Marek Ochowiak
Szymon Woziwodzki
Piotr Tomasz Mitkowski
Michał Doligalski *Editors*

Practical Aspects of Chemical Engineering

Selected Contributions from PAIC 2019

Springer

Practical Aspects of Chemical Engineering

Marek Ochowiak · Szymon Woziwodzki ·
Piotr Tomasz Mitkowski ·
Michał Doligalski
Editors

Practical Aspects of Chemical Engineering

Selected Contributions from PAIC 2019

Springer

Editors
Marek Ochowiak
Faculty of Chemical Technology
Poznan University of Technology
Poznan, Poland

Szymon Woziwodzki
Faculty of Chemical Technology
Poznan University of Technology
Poznan, Poland

Piotr Tomasz Mitkowski
Faculty of Chemical Technology
Poznan University of Technology
Poznan, Poland

Michał Doligalski
Faculty of Computer, Electrical
and Control Engineering
University of Zielona Góra
Zielona Góra, Poland

ISBN 978-3-030-39866-8 ISBN 978-3-030-39867-5 (eBook)
https://doi.org/10.1007/978-3-030-39867-5

© Springer Nature Switzerland AG 2020
This work is subject to copyright. All rights are reserved by the Publisher, whether the whole or part of the material is concerned, specifically the rights of translation, reprinting, reuse of illustrations, recitation, broadcasting, reproduction on microfilms or in any other physical way, and transmission or information storage and retrieval, electronic adaptation, computer software, or by similar or dissimilar methodology now known or hereafter developed.
The use of general descriptive names, registered names, trademarks, service marks, etc. in this publication does not imply, even in the absence of a specific statement, that such names are exempt from the relevant protective laws and regulations and therefore free for general use.
The publisher, the authors and the editors are safe to assume that the advice and information in this book are believed to be true and accurate at the date of publication. Neither the publisher nor the authors or the editors give a warranty, expressed or implied, with respect to the material contained herein or for any errors or omissions that may have been made. The publisher remains neutral with regard to jurisdictional claims in published maps and institutional affiliations.

This Springer imprint is published by the registered company Springer Nature Switzerland AG
The registered company address is: Gewerbestrasse 11, 6330 Cham, Switzerland

Preface

In Memoriam of Professor Jerzy Bałdyga (1950–2019)

> "The aim of chemical engineering is to manufacture products of the chemical industry or the wider range of products of the whole processing industries. Its most important task is to describe these processes which is the basis for design, proper exploitation, optimization and control of production installations, and to solve technical problems of process execution. Therefore, it is extremely important to transfer the results of scientific experiments to industrial practice and production of finished goods".
>
> Jerzy Bałdyga

The book is dedicated, in memoriam, to Professor Jerzy Bałdyga, a pioneer in chemical engineering in Poland, in Europe, in the world. He opened new paths in the theory and practice of chemical engineering. Professor Jerzy Bałdyga was the inspiration of the first Seminary on Practical Aspects of Chemical Engineering PAIC 2017.

Chemical engineering is the field of applied science that employs physical, chemical, and biochemical rate processes for the betterment of humanity. This sentence has been the underlying paradigm of chemical engineering and related sciences, e.g. process engineering, chemical technology, and environmental protection engineering for at least a century, through the development of modern chemical and petrochemical, biochemical, and materials processing, and into the twenty-first century as chemical engineers have applied their skills to fundamental problems in pharmaceuticals, medical devices and drug delivery systems, semiconductor manufacturing, nanoscale technology, renewable energy, environmental control, and so on.

This book aims at presenting the reader a combination of scientific research with process practice and product development, as well as the practical aspects of chemical engineering and related sciences. It contains selected issues with a detailed description of the use of research results, i.e.

- Rheological properties of fluids
- Mixing
- Single- and multi-phase flows
- Reactors
- Momentum transfer processes
- Heat and mass transfer
- Design and modelling of chemical processes and devices
- Measurement and process control
- Environmental protection engineering
- Other issues of chemical engineering.

The editors of this book hope that it will be a valuable piece of reading for both researches and students of chemical engineering and engineers working in the area of design of chemical processes and equipment. The reader is presumed to have a basic knowledge of chemical equipment design and the theory of chemical engineering.

November 2019 Marek Ochowiak

Organization

General Chair

Marek Ochowiak — Faculty of Chemical Technology, Poznan University of Technology
marek.ochowiak@put.poznan.pl

Organizing Committee

Jacek Różański
Szymon Woziwodzki
Michał Doligalski
Marcin Janczarek
Magdalena Matuszak
Piotr T. Mitkowski
Sylwia Różańska
Waldemar Szaferski
Sylwia Włodarczak
Sebastian Frankiewicz
Aleksandra Golczak
Andżelika Krupińska
Adrianna Kuczora
Agata Marecka-Migacz
Małgorzata Markowska
Patrycja Wagner

Scientific Committee

Krzysztof Alejski, Poland
Jerzy Bałdyga, Poland
Tali Bar-Kohany, Israel
Magda H. Barecka, Switzerland
Grażyna Bartelmus, Poland
Andrzej Biń, Poland
Włodzimierz Ciesielczyk, Poland
Alfonso Mauricio Sales-Cruz, Mexico
Magdalena Cudak, Poland
Krystian Czernek, Poland
Roman Dyga, Poland
Marek Dziubiński, Poland
Joanna Feder-Kubis, Poland
Zulkifli Abdul Ghaffar, Malaysia
Andrzej Gierczycki, Poland
Andrzej Górak, Germany
Farid Hammad, Egypt
Marek Henczka, Poland
Ameur Houari, Algeria
Vitalii Ivanow, Ukraine
Marcin Janczarek, Poland
Daniel Janecki, Poland

Andrzej Jarzębski, Poland
Zdzisław Jaworski, Poland
Teofil Jesionowski, Poland
Jerzy Kamieński, Poland
Władysław Kamiński, Poland
Joanna Karcz, Poland
Bożenna Kawalec-Pietrenko, Poland
Marian Kordas, Poland
Izabela Kruszelnicka, Poland
Alexander Liaposhchenko, Ukraine
Magdalena Matuszak, Poland
Piotr T. Mitkowski, Poland
Eugeniusz Molga, Poland
Arkadiusz Moskal, Poland
Grzegorz Musielak, Poland
Marek Ochowiak, Poland
Magdalena Orczykowska, Poland
Ivan Pavlenko, Ukraine
Paulina Pianko-Oprych, Poland
Rafał Rakoczy, Poland
Sylwia Różańska, Poland
Jacek Różański, Poland
Dunja Sokolović, Serbia
Tomasz R. Sosnowski, Poland
Andrzej Stankiewicz, Netherlands
Waldemar Szaferski, Poland
Jolanta Szoplik, Poland
Stanisław Witczak, Poland
Anna Witek-Krowiak, Poland
Sylwia Włodarczak, Poland
Szymon Woziwodzki, Poland
Małgorzata Wzorek, Poland
Ireneusz Zbiciński, Poland

Contents

Analysis of Thermal Distillation Process for Digestate in the Aspect of Gas, Liquid and Solid Products of Thermal Conversion 1
Mariusz Adamski and Piotr Tomasz Mitkowski

Drying of Biomaterials of Animal Origin with Superheated Steam 10
Robert Adamski, Kamil Wróbel, Zdzisław Pakowski, and Waldemar Szaferski

Copper(II) Chelating Agents 17
Przemysław Aksamitowski and Karolina Wieszczycka

Verification of Methods for Calculating Resistance in Two-Phase Gas-Liquid Mixture Flow 27
Krystian Czernek, Patryk Okoń, Waldemar Szaferski, and Stanisław Witczak

Application of Plant Design System on the Example of the ABE Mixture Separation 37
Paweł Dobrołowicz, Igor Ośkiewicz, and Szymon Woziwodzki

Cascade Impactor Study of Aerosolization Process During Passive Dry Powder Inhaler Performance Under Unsteady Versus Steady Flow Conditions 47
Agata Dorosz, Paula Martínez Cánovas, and Arkadiusz Moskal

Selected Issues of Gas-Liquid Flow Through Open-Cell Foams 58
Roman Dyga

Modified Aluminum-Magnesium Oxide Catalysts in the Process of Ethoxylation of Higher Fatty Acid Methyl Esters 69
Magdalena Emmons-Burzyńska, Marek Lukosek, and Krzysztof Alejski

Gas-Liquid Mixing in an Unbaffled Vessel with a Forward-Reverse Rotating Scaba Impeller 79
Sebastian Szymon Frankiewicz and Szymon Woziwodzki

Analysis of Mechanical Mixing in a Tank Mixer with Disturbing Elements 89
Aleksandra Golczak, Waldemar Szaferski, and Piotr Tomasz Mitkowski

Gas-Phase Synthesis of Anatase Titania Nanocrystals with Controlled Structural Properties 99
Marcin Janczarek and Ewa Kowalska

Application of Enzymatic-Based Bioreactors 110
Katarzyna Jankowska, Karolina Bachosz, Jakub Zdarta, and Teofil Jesionowski

Nanoparticles Size Determination by Dynamic Light Scattering in Real (Non-standard) Conditions Regulators - Design, Tests and Applications 122
Maciej Jarzębski, Przemysław Siejak, Arkadiusz Sawerski, Maksymilian Stasiak, Kamil Ratajczak, Łukasz Masewicz, Krzysztof Polewski, Farahnaz Fathordoobady, Yigong Guo, and Anubhav Pratap Singh

Study on the Effect of Rotating Magnetic Field on Cellular Response of Mammalian Cells 132
Magdalena Jędrzejczak-Silicka, Ewa Mijowska, Karolina Szymańska, and Rafał Rakoczy

Biodegradation of Pharmaceuticals Belonging to the Group of Non-steroidal Anti-inflammatory and Analgesic Drugs Using Activated Sludge 144
Zofia Kiersnowska, Dobrochna Ginter-Kramarczyk, Izabela Kruszelnicka, Anna Zając-Woźnialis, Joanna Zembrzuska, and Michał Michalkiewicz

Analysis of the Effect of the Atomizer Swirl Chamber on the Liquid Atomization Process 153
Franciszek Klimczak, Tomasz Burda, Marek Ochowiak, Sylwia Włodarczak, and Andżelika Krupińska

Engineering of Immobilized Enzymes: pH, Thermal Stability and Kinetic Aspects 161
Agnieszka Kołodziejczak-Radzimska and Teofil Jesionowski

Methods of Bacteriophages Production with Application of Alternate Magnetic Field 171
Maciej Konopacki, Bartłomiej Grygorcewicz, Marian Kordas, Barbara Dołęgowska, and Rafał Rakoczy

Multiphase Pressure Swirl Atomizers for Agricultural Applications . . . 183
Andżelika Krupińska, Marek Ochowiak, Sylwia Włodarczak, Małgorzata Markowska, Magdalena Matuszak, and Tomasz Szulc

Modified Moving Bed Method for Treatment of Wastewater Originating from the Pharmaceutical Industry 191
Izabela Kruszelnicka, Dobrochna Ginter-Kramarczyk, Michał Michalkiewicz, Stanisław Zajchowski, Jolanta Tomaszewska, and Przemysław Muszyński

Homogenization of O/W Emulsions Using Dynamic Membranes 199
Adrianna Kuczora and Jacek Różański

Analysis of Coal Dust Ignition Deposited in a Layer at Constant and Variable Temperature of Heating Panel 209
Bożena Kukfisz, Dorota Siuta, and Waldemar Szaferski

Synergic Nanoparticles-Cationic Surfactant Interactions for Controlling Foam Systems 216
Krzysztof Jan Legawiec and Izabela Polowczyk

Verification of the Impedance Spectroscopy Method Used in Extra Virgin Olive Oil Water Content Assessment 223
Łukasz Macioszek, Sylwia Włodarczak, and Ryszard Rybski

Standards for Rainwater Discharge in Terms of Solid Pollution Separation Process in Modified Swirl Settling Tanks 231
Małgorzata Markowska, Marek Ochowiak, Sylwia Włodarczak, and Magdalena Matuszak

Efficiency of Co-substrates Application and Thermal Processing in the Field of Methane Fermentation of the Distillers Grains 241
Natalia Mioduszewska, Mariusz Adamski, and Waldemar Szaferski

Application of HE-3 and HE-3X Agitators in Suspension Production 252
Piotr Tomasz Mitkowski, Waldemar Szaferski, Mariusz Adamski, and Robert Adamski

Flow Regulators - Design, Tests and Applications 261
Marek Ochowiak, Sylwia Włodarczak, Magdalena Matuszak, Andżelika Krupińska, and Małgorzata Markowska

Physicochemical Aspects of Aerosol Generation in Electronic Cigarettes 271
Marcin Odziomek

Application of Rotating Magnetic Field to Intensify the Processes in Airlift Reactor 282
Joanna Padiasek, Marian Kordas, Maciej Konopacki, and Rafał Rakoczy

Examination of Rheological Properties of Selected Wastewater Sludge Proposed to Biogas Production 294
Monika Pawlita-Posmyk and Małgorzata Wzorek

The Effect of Airborne Particles on Human Body Fluids 305
Agata Penconek, Urszula Michalczuk, and Arkadiusz Moskal

Analysis of the Steady-State Properties of a Bifunctional Catalyst for the Synthesis of Renewable Fuels 314
Dominik Pędzich, Natalia Reczek, Krzysztof Skrzypek-Markiewicz, and Katarzyna Bizon

Algae as a Raw Material for Third Generation Biofuels Production . . . 324
Małgorzata Płaczek

The Use of Micro Additives in Building Gypsum Materials 336
Karol Prałat, Mirosław Grabowski, and Justyna Ciemnicka

The Influence of External Recirculation Loop Design on the Hydrodynamic Properties of a Hybrid Fluidized Bed Apparatus 346
Mateusz Prończuk and Katarzyna Bizon

Impact of Electrodes Design on Their Activity in the Oxidation of Organic Pollutants 355
Tomasz Rozmanowski, Piotr Krawczyk, and Jakub Wolańczyk

Extensional Flow of Wormlike Micellar Solutions 365
Sylwia Różańska, Jacek Różański, and Patrycja Wagner

Heat Transfer Enhancement During the Flow of Drag-Reducing Surfactant Solutions 374
Jacek Różański and Sylwia Różańska

Separation of Erythritol from Fermentation Broth Using Preparative Chromatography 383
Beata Rukowicz, Kinga Polaszek, and Krzysztof Alejski

Spent Automotive Converters as a Secondary Resource of Metals 392
Martyna Rzelewska-Piekut, Mariola Saternus, Agnieszka Fornalczyk, and Magdalena Regel-Rosocka

Risk Assessment in Process Industries Using Fuzzy Logic Approach . . . 401
Dorota Siuta, Agata Kotynia, Bożena Kukfisz, and Waldemar Szaferski

Adsorption of Phosphates on Modified Eggshells - Batch and Fixed-Bed Column Process 412
Dawid Skrzypczak, Katarzyna Mikula, Daria Kocek, Grzegorz Izydorczyk, Rafał Taf, and Anna Witek-Krowiak

Experimental Analysis of the Deposition of Aerosol Droplets in the Upper Airways of Human 423
Tomasz Robert Sosnowski

Spherical Particle Technology and Engineering: Fabrication and Practical Utility 430
Małgorzata Stanisz, Łukasz Klapiszewski, and Teofil Jesionowski

Analysis and Modeling of the Process of Metal Separation from the Aqueous Phase in a Pseudo-emulsion Based Hollow Fiber Strip Dispersion 441
Katarzyna Staszak, Karolina Wieszczycka, Maciej Staszak, M. Teresa A. Reis, and M. Rosinda C. Ismael

Comparison of Emulsification in a Sieve Emulsification Mixer, Homogenizer and Mechanical Mixer 452
Waldemar Szaferski, Dorota Siuta, Bożena Kukfisz, and Krystian Czernek

Application of Flow Simulation Results in the Calculation of Gas Networks 461
Jolanta Szoplik

Metal Leaching from E-Waste with Ionic Liquids 473
Stefaan Verwimp, Magdalena Emmons-Burzyńska, Abhishek Dutta, and Magdalena Regel-Rosocka

Influence of Annealing on Structure and Corrosion Resistance of Duplex and Super Duplex Stainless Steel 483
Sylwia Włodarczak, Andżelika Krupińska, Tomasz Kachlicki, Magdalena Matuszak, Małgorzata Markowska, Piotr Krawczyk, Tomasz Rozmanowski, Marcin Janczarek, and Marek Ochowiak

Application of Morison Equation in Unsteady Mixing Characteristics . . . 491
Szymon Woziwodzki

Author Index 501

Analysis of Thermal Distillation Process for Digestate in the Aspect of Gas, Liquid and Solid Products of Thermal Conversion

Mariusz Adamski[1(✉)] and Piotr Tomasz Mitkowski[2]

[1] Institute of Biosystems Engineering, Faculty of Agriculture and Bioengineering, Poznan University of Life Sciences, Poznań, Poland
mariusz.adamski@up.poznan.pl
[2] Institute of Chemical Technology and Engineering, Faculty of Chemical Technology, Poznan University of Technology, Poznań, Poland

Abstract. The paper presents a case study for the process of thermal decomposition of digestate in order to obtain energy fractions. The aim of this work is to produce digestate and to indicate the potential of obtaining solid biofuel through thermal decomposition for the production of solid, gaseous and liquid products. In order to achieve the objective of the work, it was planned to produce digestate in mesophilic conditions, using a mixture of food and agricultural waste. The methanation process was carried out in accordance with the standard DIN 38 414 p.8. Thermal decomposition was carried out in the range of low-temperature pyrolysis at atmospheric pressure. The air-dried mass has been thermally decomposed. In the field of solid products, the acquisition of the form of carbonized biomass was assumed. The concentration of process gases was measured with the use of chemical and spectral sensors. In the scope of gas products, the observation of the emission of basic process gases (CO, CO_2, CH_4, H_2, NO_X, H_2S, O_2) was assumed. In the range of liquid products, the observation of moisture and tarry substances secretion was assumed. A case studie for digestate under dry thermal distillation conditions indicated insufficient emission of flammable gases (CO, CH_4) and the possibility of obtaining a flammable product in a low temperature range (from 200 °C to 300 °C).

1 Theoretical Fundamentals of the Thermal Decomposition

Popular methods of biomass thermal conversion include: drying, combustion, pyrolysis, gasification and torrefaction (Kratofil et al. 2014; Bis et al. 2018; Jamrozik et al. 2015; Bergman et al. 2005). The torrefraction process takes place at a temperature of range from 200 °C to 300 °C, without access to oxygen, and is known for improving the quality of biomass as a fuel (Kratofil et al. 2014; Bis et al. 2018; Agar 2017).

During the torrefraction process, solid, gas and liquid products are obtained. There is also a loss of chemical energy and a loss in the weight of the source material. The initial mass is reduced by up to 30% and the chemical energy is reduced by 10% (Kratofil et al. 2014; Bis et al. 2018; Jamrozik et al. 2015; Bergman et al. 2005; Pawlak-Kruczek and Czerep 2016; Agar 2017).

© Springer Nature Switzerland AG 2020
M. Ochowiak et al. (Eds.): PAIC 2019, *Practical Aspects of Chemical Engineering*, pp. 1–9, 2020.
https://doi.org/10.1007/978-3-030-39867-5_1

The torification method has been known for more than 70 years and is derived technologically from the drying and roasting of coffee beans (Kratofil et al. 2014; Bis et al. 2018; Jamrozik et al. 2015; Bergman et al. 2005; Pawlak-Kruczek and Czerep 2016).

In the process of thermal biomass decomposition, conversion is usually carried out at atmospheric pressure (Pawlak-Kruczek and Czerep 2016). In the process of torrefraction, the following stages can be distinguished: drying, proper thermal decomposition and cooling of the biomass (Fig. 1) (Kratofil et al. 2014; Bis et al. 2018; Pawlak-Kruczek and Czerep 2016; Tremel et al. 2012; Mełgieś and Malinska 2016; Agar 2017). Biomass drying can be carried out during the heating process or before the substrate is introduced into the thermal chamber (Pawlak-Kruczek and Czerep 2016; Jakubiak and Kordylewski 2010).

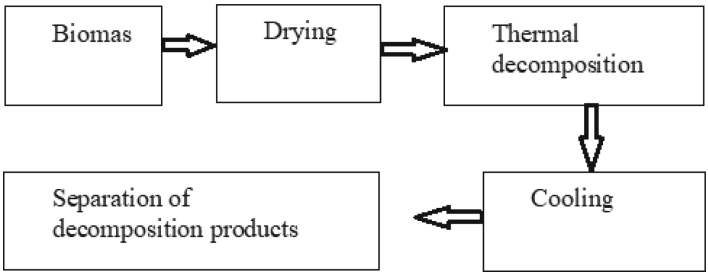

Fig. 1. Possible steps in the torrefraction process (own source)

Maintaining the process of thermal decomposition in the nominal temperature range and under atmospheric pressure allows the decomposition of fiber structures, including cellulose, hemicellulose and lignin (Kratofil et al. 2014; Bis et al. 2018; Jamrozik et al. 2015; Bergman et al. 2005; Pawlak-Kruczek and Czerep 2016; Jakubiak and Kordylewski 2010; Neugebauer et al. 2010). Therefore, the chemical composition of biomass is an important factor in determining the amount of solids and volatile components.

The most reactive ingredient is hemicellulose, which is characterized by the highest degree of decomposition at temperatures ranging from 225 °C to 325 °C.

Then, as a result of the torification process, cellulose is degraded at temperatures from 300 °C to 325 °C and lignin is decomposed, which temperature range is from 250 °C to 500 °C (Pawlak-Kruczek and Czerep 2016; Durczak et al. 2018; Mitkowski et al. 2016; Yan et al. 2009).

For these reasons, during the toryfication process, which takes place at temperatures between 200 °C and 300 °C, the highest weight loss is observed in the degradation of hemicellulose and lignin (Pawlak-Kruczek and Czerep 2016; Kaushik et al. 2018; Adamski et al. 2018; Durczak et al. 2018; Mitkowski et al. 2016; Tremel et al. 2012; Mełgieś and Malinska 2016; Agar 2017; Jakubiak and Kordylewski 2010; Neugebauer et al. 2010).

Compared to unprocessed biomass, torrefraction is characterized by higher energy density and milling susceptibility and is structurally homogeneous material. The solid thermal decomposition product resembles, by its properties, more low-calorific carbon than biomass.

During the thermal degradation process, the initial substrate mass is reduced by up to 30% by removing moisture and volatile substances (Pawlak-Kruczek and Czerep 2016; Jakubiak and Kordylewski 2010; Neugebauer et al. 2010).

The separated volatile components are the cause of energy loss, which usually does not exceed 10% of the total energy of the raw material.

The mass and energy yield for a typical thermal conversion reaction may vary depending on the type of biomass, process temperature, moisture content of the biomass and the time spent in the thermal chamber.

The volatile parts called "tor-gas" contain a lot of flammable organic components, but just as many of them are non-flammable, making it problematic to get a gas that can be burned and provide the heat required during the process.

The gas from the torrefracion process is a moist gas, because even if the raw material is dry, it can be expected that about 50% of the resulting gas mass will be water and another 10% CO_2 (Pawlak-Kruczek and Czerep 2016; Jakubiak and Kordylewski 2010; Yan et al. 2009; He et al. 2013).

For this reason, it is difficult to obtain a flammable gas that, after combustion, would supply the required heat stream to the process.

Wood pellets and wood chips are a popular material for the torrefraction process due to their density and humidity. The digestate can be an alternative to typical substrates in the thermal conversion process (Kratofil et al. 2014; Bis et el. 2018; Jamrozik et al. 2015; Bergman et al. 2005; Pawlak-Kruczek and Czerep 2016; Jakubiak and Kordylewski 2010; Neugebauer et al. 2010; Yan et al. 2009; He et al. 2013; He et al. 2018).

2 Aim of the Study

The aim of this work is to produce digestate and to indicate the potential of obtaining solid biofuel through thermal decomposition for the production of solid, gaseous and liquid products.

Thermal decomposition was carried out in the range of low-temperature pyrolysis at atmospheric pressure. The air-dried mass has been thermally decomposed. In the field of solid products, the acquisition of "bio-coal" was assumed. In the scope of gas products, the observation of the emission of basic process gases (CO, CO_2, CH_4, H_2, SO_2, NO_X, O_2) was assumed. In the range of liquid products, the observation of moisture and tarry substances secretion was assumed.

In order to achieve the objective of the work, it was planned to produce fermentation under mesophilic conditions using a mixture of food and agricultural waste. Thermal decomposition of the acquired digestate was planned within the temperature range from 200 °C to 300 °C.

3 Materials and Methods

The fermentation process and the production of digestate were carried out in accordance with DIN 38 414 p.8 (DIN 38414 S.8 2012).

Fig. 2. Research stand for the study of biogas productivity of substrates according to DIN 38414 S.8 (left), inoculum station for quasi continuous fermentation work (right) (own source)

The characteristics of liquid flow through the regulator reminded the outflow characteristics through a small opening: if there is a small opening in any shape but with rounded edges in the tank wall (Fig. 1).

The digestate was prepared on a multi-chamber stand in a periodical fermentation system. (Fig. 2). The capacity of a single fermentation chamber is 1000 ml. The produced biogas is stored in eudiometer tanks. The capacity of each biogas tank is 1200 ml (Fuldauer et al. 2018; KTBL-Heft 84 2009; Kaushik et al. 2018; Adamski et al. 2018; Durczak et al. 2018).

The substrate mixture for the fermentation process was prepared on the basis of cattle slurry, food and municipal waste (Table 1). The fermenting mixture was stirred using a hydraulic mixer in which the sedimentation and flotation layers were disturbed using gas and liquid fraction (Mitkowski et al. 2016, 2018).

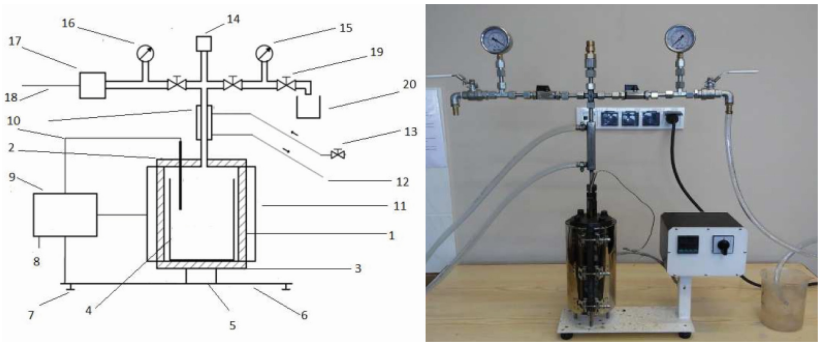

Fig. 3. Components of the thermal chamber for torrefied biomass (own source): 1 - thermal chamber, 2 - top cover, 3 - bottom cover, 4 - container for substrate, 5 - base, 6 - mounting plate, 7 - levelling regulation, 8 - 230 V power supply, 9 - process controller, 10 - temperature sensor, 11 - ceramic resistance heater, 12 - coolant supply, 13 - coolant outlet, 14 - safety valve, 15 - pressure gauge, 16 - akuometer, 17 - vacuum pump, 18 - 230 V supply, 19 - process product removal valve, 20 - liquid product container

Table 1. The composition of the fermentation mixture

Mixture	Dry matter	Proportion	Amount of dry matter	Fresh matter	Organic dry matter	Organic dry matter
Ingredient	[% m/m]	[%]	[g]	[g]	[%]	[g]
Cattle slurry	2.822	1	0.2854	10.113	40.82	0.116
Manure	16.521	7	8.259	49.995	84.02	6.939
Potatoes	1.886	4	5.150	27.269	93.91	4.836
Cauliflower	9.167	2	1.152	12.570	93.64	1.079
Fried meat	27.963	1	1.816	6.496	93.73	1.703
Salad	4.315	2	0.719	16.672	0.851	0.612
Bread	63.367	2	8.416	13.281	0.970	8.163
Sweeds	83.271	2	9.354	11.233	0.998	9.335
Grass	20.170	5	7.061	35.005	0.896	6.327
Inoculation	6.957	73	34.785	500.000	0.676	23.513
Total moisture [% m/m]	**88.72**	**Totals**	**76.999**	**682.600**		**62.624**
Total dry mass [% m/m]	**11.28**					

After a period of 64 days, the fermentation process has spontaneously stopped (DIN 38414 S.8 2012; Adamski et al. 2018; Durczak et al. 2018).

The fermentation process was carried out simultaneously in 10 fermenters to accumulate a sufficient amount of digestate. Moist post-fermentation pulp with a dry matter content of 6.35% was dried at a temperature not exceeding 67 °C.

During the extensive drying process the following material was obtained: moisture content 10.54% m/m, average dry organic matter 51.52% m/m. The dried digestate was crushed mechanically and divided into laboratory samples of weight 40 g.

The prepared material was used to study the process of thermal decomposition of biomass. A scheme of the research station is shown in Fig. 3.

The fermentation process and the production of digestate were carried out in accordance with DIN 38 414 p.8 (DIN 38414 S.8 2012).

Eudiometric tanks from the research station of the fermentation process were used to store gas products (Fig. 2). The concentration of process gases was measured with the use of chemical and spectral sensors. The measurement of process gas concentrations was performed with a multi-gas "Optima 7" meter from MRU.

4 Results and Discussion

Studies of thermal decomposition of digestate were tested in intervals of 10 °C starting from 200 °C to 300 °C. Thermal and efficiency characteristics of the gasification process indicate that the process times were maintained until the emission of the gas fraction was stopped (Fig. 4, Fig. 5).

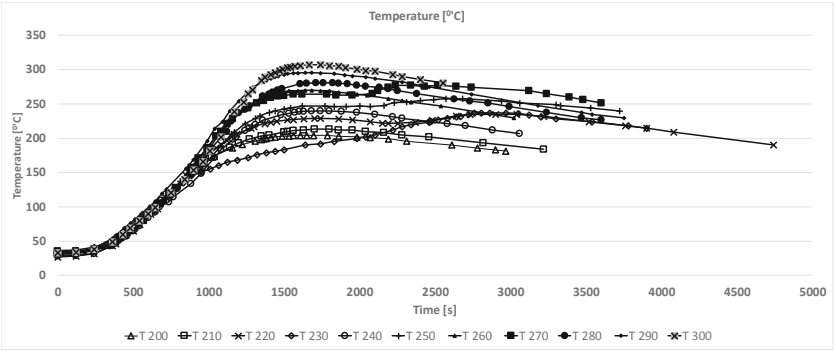

Fig. 4. Characteristics of temperature changes in the reaction chamber and time of thermal decomposition for particular ranges

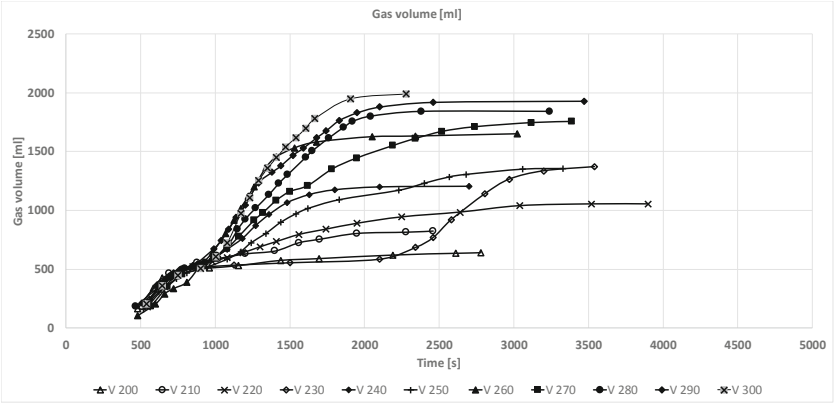

Fig. 5. Characteristics of the generated gas mixture for particular temperature ranges

Investigations of thermal decomposition of digestate allowed to obtain information on the influence of temperature on the process time and the level of emission of selected process gases (Table 2).

In the case of material with reduced raw fibre content and components of cellulose, hemicellulose and lignin, an increase in methane concentration was observed (Fuldauer et al. 2018; Adamski et al. 2018; Durczak et al. 2018).This tendency is opposite to high-temperature processes of wood biomass decomposition (Pawlak-Kruczek and Czerep 2016; Tremel et al. 2012; Mełgieś and Malinska 2016; Jakubiak and Kordylewski 2010; Yan et al. 2009).

It should be noted that the total content of combustible gases (CO, CH_4) is lower than in the case of wood biomass and cannot contribute to the balance of energy expenditure in the thermal process (Jamrozik et al. 2015; Pawlak-Kruczek and Czerep 2016; Tremel et al. 2012; Mełgieś and Malinska 2016; Jakubiak and Kordylewski 2010).

In the process of thermal decomposition no SO_2 emission was observed for each of the temperature ranges. Also no NO_2 and hydrogen emissions were observed for individual thermal ranges (Jakubiak and Kordylewski 2010).

Samples of dried digestate with an average organic matter content of 51.52% allowed for the separation of carbonizate and visible liquid fraction (Table 3).

As a result of the temperature effect, the carbonizate mass loss was observed in the range from 8% m/m to over 35% m/m.

The level of carbonizate combustible matter was observed in the range from 48% m/m to over 59% m/m.

Comparison of the obtained parameters for solid products of the process of thermal decomposition of dry digestate shows that wet or hydro-thermal gasification processes allow to better intensify the decomposition of raw fibre components for energy purposes (Yan et al. 2009; He et al. 2013; He et al. 2018).

Table 2. Emissions of gaseous products from digestate gasification

Process temperature	CO	CO_2	NO_X	CH_4	Gas volume	O_2
[°C]	[ppm]	[%]	[ppm]	[ppm]	[ml]	[%]
200	53673	7.10	419	1290	640	1.64
210	6659	2.10	53	670	825	1.16
220	39337	26.43	134	2530	1055	1.71
230	41210	64.11	940	6400	1370	1.34
240	46948	38.37	571	2230	1205	1.58
250	59205	54.88	783	5390	1355	1.40
260	56710	68.60	860	10000	1650	1.21
270	44994	76.28	1451	25850	1755	1.40
280	40096	68.83	1770	29660	1840	1.22
290	38057	64.84	1539	26130	1930	1.33
300	36207	65.62	1640	34010	1990	1.28

Table 3. Emissions of solid and liquid products from digestate gasification

Process temperature	Sample weight	Carbonizate weight	Dry organic matter	Weight loss	Combustible matter	Liquid fraction
[°C]	[g]	[g]	[% m/m]	[% m/m]	[% m/m]	[% m/m]
200	40.147	35.826	59.14	10.76	40.86	4.16
210	30.014	27.614	54.80	8.00	45.20	3.10
220	30.016	25.683	48.68	14.44	59.32	4.47
230	40.168	31.774	56.44	20.90	43.56	10.70
240	40.287	32.716	55.76	18.79	44.24	9.49
250	30.013	23.299	49.42	22.37	59.58	12.67
260	35.001	31.326	46.16	10.50	55.90	4.50
270	40.010	30.047	49.15	24.90	58.00	11.35
280	40.055	28.199	49.45	29.60	53.00	14.50
290	40.011	27.376	48.35	31.58	51.65	16.31
300	40.069	25.838	49.35	35.52	50.65	17.97

5 Conclusions

A case study for digestate under dry thermal distillation conditions indicated insufficient emission of flammable gases (CO, CH_4) and the possibility of obtaining a flammable product in a low temperature range (from 200 °C to 300 °C). The solution to the problem of high moisture content in the fermentation can be to use the digestate only after filtration of the liquid fraction and to carry out the modified wet torrefraction at 260 °C (He et al. 2018).

Acknowledgments. This research was supported by Institute of Biosystems Engineering, Poznań University of Life Sciences, Poland

References

Adamski, M., Szaferski, P.T., Gulewicz, P., Majkowski, W.: Silage of switchgrass (Panicum virgatum) as a bioenergy feedstock in Poland. In: Ochowiak, M., Woziwodzki, S., Doligalski, M., Mitkowski, P.T. (eds.) Practical Aspects of Chemical Engineering. Selected Contributions from PAIC 2017, 1–15 (2018). ISBN 978-3-319-73978-6

Agar, D.: A comparative economic analysis of torrefied pellet production based on state-of-the-art pellets. Biomass Bioenerg. **97**, 155–161 (2017)

Bergman, P., Boersma, A., Kiel, J., Prins, M., Ptasinski, K., Janssen, F.: Torrefaction for entrained-flow gasification of biomass. Technical report, Energy research Centre of the Netherlands (ECN) (2005)

Bis, Z., Kobyłecki, R., Cisłowska, M., Zarzycki, R.: Biochar – potential tool to combat climate change and drought. Ecohydrol. Hydrobiol. **18**, 441–453 (2018)

DIN 38414 S 8.: German Standardized Test Method for Water, Sewage and Sludge. Sediments and sediments (group S). Determination of fermentation characteristics (S. 8). DIN DeutchesInstitut fur Normung e. V., Berlin (2012)

Durczak, K., Adamski, M., Mitkowski, P.T., Szaferski, W., Gulewicz, P., Majkowski, W.: Chemical processing of switchgrass (panicum virgatum) and grass mixtures in terms of biogas yield in Poland. In: Ochowiak, M., Woziwodzki, S., Doligalski, M., Mitkowski, P.T. (eds.) Practical Aspects of Chemical Engineering. Selected Contributions from PAIC 2017, pp. 85-99 (2018). ISBN 978-3-319-73978-6

Fuldauer, L.I., Parker, B.M., Yaman, R., Borrion, A.: Managing anaerobic digestate from food waste in the urban environment: evaluating the feasibility from an interdisciplinary perspective. J. Clean. Prod. **185**, 929–940 (2018)

He, C., Giannis, A., Wang, J.-Y.: Conversion of sewage sludge to clean solid fuel using hydrothermal carbonization: hydrochar fuel characteristics and combustion behavior. Appl. Energy **111**, 257–66 (2013)

He, C., Tang, C., Lia, C., Yuan, J., Tran, K., Bach, Q., Qiu, R., Yang, Y.: Wet torrefaction of biomass for high quality solid fuel production: a review. Renew. Sustain. Energy Rev. **91**, 259–271 (2018)

Jakubiak, M., Kordylewski, W.: Biomass torrefaction. Archiwum Spalania **10**(1–2), 11–25 (2010)

Jamrozik, A., Pyrc, M., Świącik, M., Schab, M.: Oczyszczanie i przetwarzanie gazu generowanego ze zgazowania odpadów. J. Civil Eng. Enviro. Arch. **62**(2/15), 145–156 (2015). kwiecień-czerwiec

Kaushik, A., Basu, S., Raturi, S., Batra, V.S., Balakrishnan, M.: Recovery of antioxidants from sugarcane molasses distillery wastewater and its eject on biomethanation. J. Water Process Eng. **25**, 205–211 (2018)

Kratofil, M., Zarzycki, R., Kobyłyckie, R., Bis, Z.: Badania procesu toryfikacji biomasy. Energy Policy J. Tom 17(Zeszyt 4), 137–146 (2014)

KTBL-Heft 84: Schwachstellen an Biogasanlagen verstehen und vermeiden. Kuratorium fürTechnik und Bauwesen in der Landwirtschafte.V. (KTBL), KTBL-Heft 84, Darmstadt, Druckerei Lokay, Reinheim (2009)

Mełgieś, K., Malinska, K.: Aktualne wymagania jakościowe i prawne dla biowęgla jako nawozu i polepszacza gleby. Sci. Works Inst. Ceram. Build. Mater. **26**, 82–95 (2016)

Mitkowski, P.T., Szaferski, W., Adamski, M.: Hydraulic mixing. In: Ochowiak, M., Woziwodzki, S., Doligalski, M., Mitkowski, P.T. (eds.) Practical Aspects of Chemical Engineering. Selected Contributions from PAIC 2017, 291-306 (2018). ISBN 978-3-319-73978-6

Mitkowski, P.T., Adamski, M., Szaferski, W.: Experimental set-up of motionless hydraulic mixer and analysis of hydraulic mixing. Chem. Eng. J. **288**, 618–637 (2016)

Neugebauer, M., Piechocki, J., Sołowiej, P.: Gazyfikacja biomasy odpadowej z produkcji rolniczej. Inżynieria Rolnicza **14, 5**(123), 219-224(2010). e-ISSN 2449-5999

Pawlak-Kruczek, H., Czerep, M.: Technologia termicznej waloryzacji paliw - toryfikacja w auto termicznym reaktorze. Nowa Energia **1**, 12–18 (2016)

Tremel, A., Stemann, J., Herrmann, M., Spliethoff, E.H.: Entrained flow gasification of biocoal from hydrothermal carbonization. Fuel **102**, 396–403 (2012)

Yan, W., Acharjee, T.C., Coronella, C.J., Vsquez, V.R.: Thermal pretreatment of for HTC, future gasification experiments should also be conducted lignocellulosic biomass. Environ. Prog. Sustain Energy **28**(3), 435–40 (2009)

Drying of Biomaterials of Animal Origin with Superheated Steam

Robert Adamski[1(✉)], Kamil Wróbel[1], Zdzisław Pakowski[1], and Waldemar Szaferski[2]

[1] Safety Engineering Department, Faculty of Process and Environmental Engineering, Lodz University of Technology, Lodz, Poland
robert.adamski@p.lodz.pl
[2] Institute of Chemical Technology and Engineering, Faculty of Chemical Technology, Poznan University of Technology, Poznań, Poland

Abstract. Drying with superheated steam is an innovative method for the preparation of food products. Compared to hot air drying, this method allows obtaining higher quality products. In addition to better quality features, superheated steam has a number of other advantages, such as low energy consumption and high drying speed. The main purpose of the following work was to determine the drying curve for pork subjected to superheated steam drying. The parameter that was additionally determined was the temperature distribution in the dried material. The tests were carried out at four temperatures (120, 140, 160 and 180 °C). The drying curves determined were similar to the drying curves obtained by other scientists. The obtained results confirmed that steam drying with superheated heat at a higher temperature reduces drying time.

1 Introduction

Pork meat is the most consumed meat in Europe. According to data from 2018, in the European Union countries nearly 20 thousand tonnes of pork meat was consumed during the year, which accounted for 18% of global consumption of pork (OECD 2019). The main ingredient of meat is water, which has a direct impact on the durability and quality of food, which is caused by the fact that this ingredient causes biological and physicochemical changes occurring in food products (Castell-Palou et al. 2011). Meat also contains large amounts of protein, which is an essential component of the human diet. In addition, the meat contains vitamins among them group B vitamins (riboflavin and thiamine) and minerals such as potassium, sulfur, phosphorus, sodium and iron (Kirschmann 2007). The oldest and most commonly used method of food preservation is drying. The purpose of drying is to reduce the moisture content of the dried material, which results in reduced water activity (Singh et al. 2006). Currently, the most popular method of obtaining dried meat and meat products is drying with hot air (Castell-Palou et al. 2011). This method is used to extend the shelf life, however, it causes a deterioration in the quality characteristics of meat. Drying with superheated steam allows for higher quality products (Uengkimbuan et al. 2006). The effectiveness of SSD in obtaining higher quality products has been confirmed by many publications. (Uengkimbuan et al. 2006) conducted research aimed at explaining the effect of salt on

© Springer Nature Switzerland AG 2020
M. Ochowiak et al. (Eds.): PAIC 2019, *Practical Aspects of Chemical Engineering*, pp. 10–16, 2020.
https://doi.org/10.1007/978-3-030-39867-5_2

SSD kinetics and quality characteristics of dried pork slices. The qualitative features during these tests were meat color and the ability to rehydrate (Uengkimbuan et al. 2006). Similar studies were conducted by (Swasdisevi et al. 2006). However, in this case, apart from the meat color and rehydration ability, the effect of salt on meat contraction during SSD was also examined (Uengkimbuan et al. 2006). As a result of the conducted tests (Uengkimbuan et al. 2006), they found that along with the increase in temperature, the time of dried pieces of pork decreases. The increase in temperature also caused that the degree of meat redness increased and the brightness of dried meat decreased, which was caused by Maillard's reactions. Pork slices dried at a higher temperature had less rehydration ability compared to slices dried at a lower temperature. They drew similar conclusions after the conducted experiments (Swasdisevi et al. 2006). In addition, they observed that the addition of salt increases the drying time and increases the redness of meat. Pieces of salted meat had greater drying shrinkage but had less rehydration capacity. (Pengpongsa 2006) during his research compared two methods for drying seasoned beef slices. The first method was steam drying and the second method was combined superheated steam drying with a heat pump. As a result of the tests, it was found that the increase in drying temperature caused a shortening of the duration of the process, pork dried using a combined technique had a higher redness value, but had a lower brightness value than pork dried with superheated steam. In addition, it was found that the use of a combined technique for drying seasoned pork resulted in a decrease in the shrinkage of dried meat. Samples dried by combined technique had a greater rehydration capacity than samples dried using superheated steam. (Sa-adchom et al. 2011a) conducted research on the impact of slice thickness, seasoning and cutting direction in relation to meat fibers on drying kinetics and quality characteristics of dried pieces of pork subjected to superheated steam drying. The obtained results showed that a thinner pork slice has a shorter drying time, a lower redness value and its drying shrinkage is smaller compared to a thicker one. The addition of seasoning extends the drying time, increases the value of yellowness and reduces the strength and hardness of pieces of pork. Dried pork sliced parallel to the fiber direction had a lower percentage of shrinkage, hardness and strength than that sliced perpendicular to the fiber direction. The SSD, apart from positively influencing the quality characteristics of dried products, has other advantages. The processing of food products using superheated steam allows for pasteurization, deodorization and inactivation of microorganisms and enzymes. In addition to positively influencing the quality characteristics SSD allows for the use of pasteurization, deodorization and deactivation of microorganisms and enzymes (Sehrawat et al. 2016). Additionally, drying by superheated steam is characterized by low power consumption, small risk of fires and explosions and a high rate of drying (Mujumdar 2007). In addition, studies confirmed the effectiveness of superheated steam in decontaminating poultry skin (Kondjoyan et al. 2008).

2 Materials and Methods

2.1 Experimental Set-up

A schematic of the apparatus used during the experiments is shown in Fig. 1.

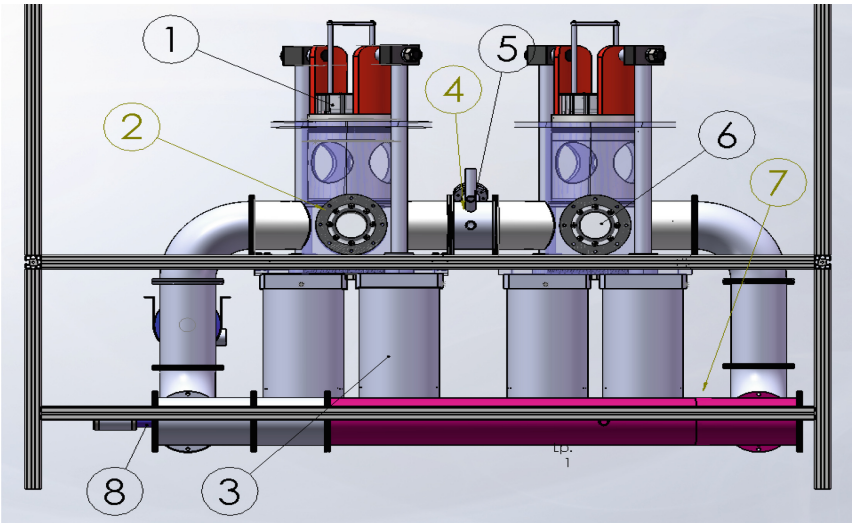

Fig. 1. Schematic of the apparatus for determining the kinetics of superheated drying: 1-sample insertion device, 2-measuring chamber, 3-sample insertion pressure cylinders, 4-pressure sensor, 5-temperature sensor, 6-window, 7-heater, 8-fan

The apparatus by means of which the SSD kinetics have been determined operates in a closed circuit and can work under a maximum pressure of 6 atmospheres. At the time of start-up, steam is supplied to the heated apparatus from the steam generator until the air contained in it is removed. Circulating steam in the apparatus it is overheated to the preset temperature by means of electric heaters (7). The steam flow is forced by a built-in fan (8). In the measuring chamber (2), the samples are placed on a strain gauge and then the chamber is sealed (1). With the help of two servomotors (3), the measuring chamber with the samples inside is lowered into the apparatus, where the tested material immediately contacts the superheated steam. The apparatus consists of two identical measuring chambers.

2.2 Materials

The material used during the experiments was pork loin, purchased from a local supermarket. The meat samples used in the tests were cylindrical with dimensions r = 9 mm and H = 70 mm and had an initial mass of about 14.6 g.

2.3 Methods

The process of drying pork with superheated steam was carried out at four temperatures (120, 140, 160 and 180 °C) at atmospheric pressure. An additional parameter measured during drying was the temperature distribution in the sample. This measurement was carried out using two thermocouples placed in the sample. The first thermocouple was located in the central part of the sample (r = 0) and the second in the middle of the distance between the center and the edge of the sample (r = 4,5 mm) The results obtained in this way allowed us to plot the drying curves, which are similar to the drying curves found in the literature (Jamradloedluk et al. 2004).

3 Results

The results are shown graphically in Figs. 2, 3, 4 and 5.

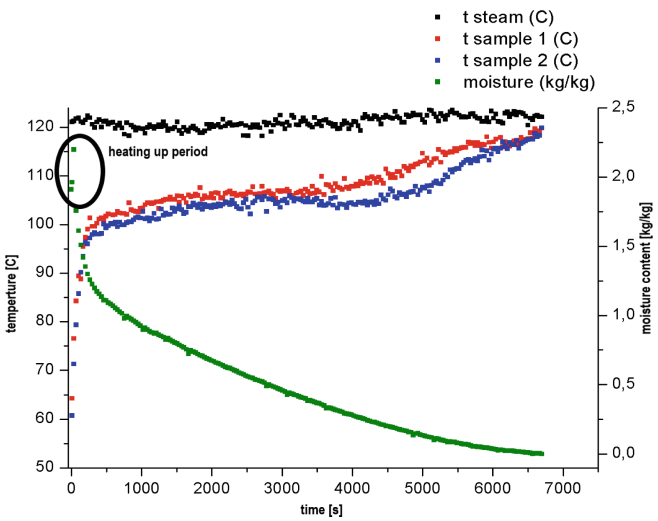

Fig. 2. Drying curve and temperature distribution at 120 °C

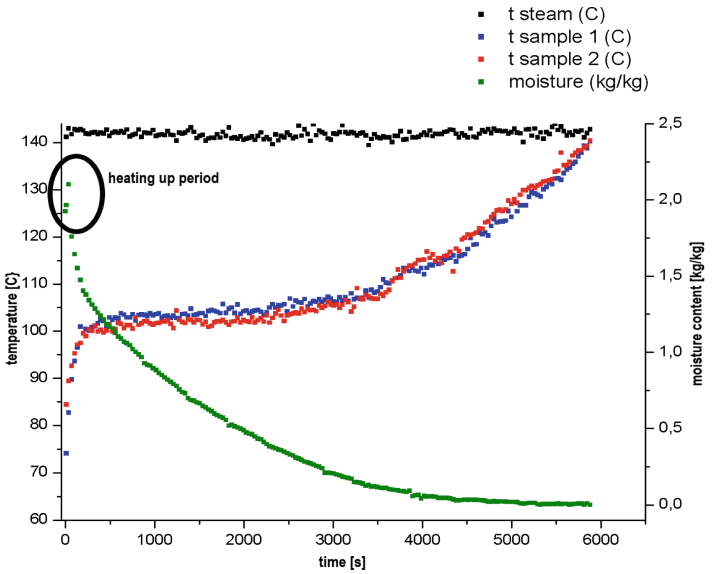

Fig. 3. Drying curve and temperature distribution at 140 °C

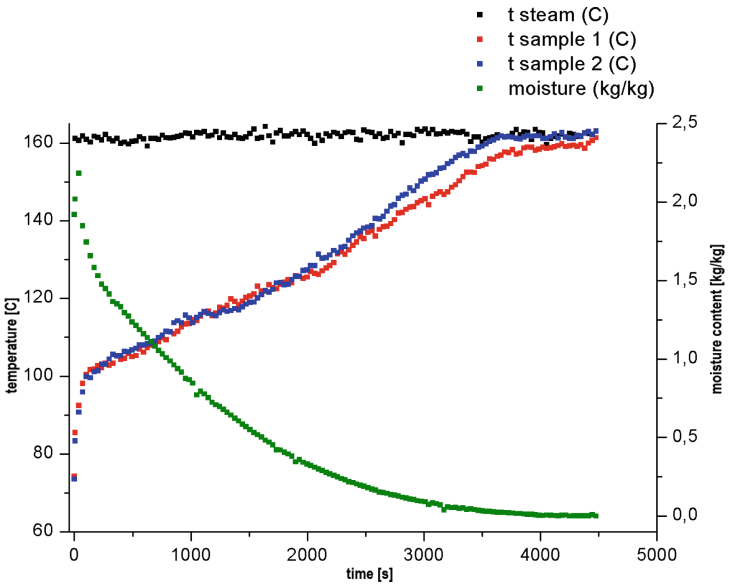

Fig. 4. Drying curve and temperature distribution at 160 °C

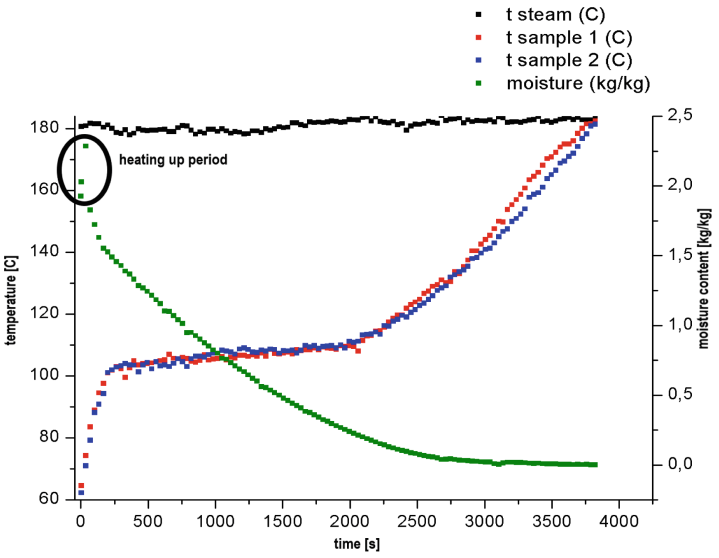

Fig. 5. Drying curve and temperature distribution at 180 °C

From the drying curves presented in the drawings, it can be seen that the rate of moisture removal from the material is related to temperature. An increase in the process temperature causes an increase in the rate of moisture removal from the dried material. Three characteristic stages of drying materials with superheated steam can also be observed in the drawings. The first stage is related to the condensation of water vapor on the dried material because the temperature of the dried material is initially lower than the temperature of the drying medium (Jamradloedluk et al. 2004). Similar observation regarding this drying step has been described by (Soponronnarit et al. 2006, Taechapairoj et al. 2006). The second is the CDR stage. This stage begins when the film of water on the dried material disappears. The rate of moisture evaporation on the surface of the material results from the rate of convective heat transfer (Mujumdar 2000). During this stage, the wet material temperature remains constant at saturation temperature (Taechapairoj et al. 2006). The third stage is the FRP stage, which begins when the moisture content of the material is lower than the critical moisture content (Taechapairoj et al. 2006). The material temperature rises to superheated steam temperature and the moisture content slowly decreases to the equilibrium moisture content (Sa-adchom et al. 2011b).

4 Conclusions

Experiments on SSD kinetics of pork performed in this work indicate that drying time to reach equilibrium MC strongly depends on steam temperature. The times were approximately equal to 6500, 4500, 3500 and 2500 s for steam temperatures 120, 140, 160 and 180 °C respectively. Condensation stage lasted approx. 250 s in each case.

In each case the obtained product has acceptable sensorial quality but further study on this aspect is required.

References

Castell-Palou, A., Simal, S.: Heat pump drying kinetics of a pressed type cheese. LWT - Food Sci. Technol. **44**(2), 489–494 (2011)

Kirschmann, J.D.: Nutrition Search Inc., Nutrition Almanac, 6th ed, 101. McGraw Hill (2007)

Singh, S., Raina, C.S., Bawa, A.S., Saxena, D.C.: Effect of pretreatments on drying and rehydration kinetics and color of sweet potato slices. Dry Technol. **24**(11), 1487–1494 (2006)

Uengkimbuan, N., Prachayawarakorn, S., Soponronnarit, S., Nathkaranakule, A.: A comparative study of pork drying using superheated steam and hot air. Dry Technol. **24**, 1665–1672 (2006)

Swasdisevi, T., Wongsri, P., Prachayawarakorn, S., Soponronnarit, S.: Effect salt on pork drying using superheated steam. J. Roy. Inst. Thai. **31**(2), 493–507 (2006)

Pengpongsa, W., et al.: Flavored pork drying using superheated steam with heat pump, In: Proceedings of the Seventh Thai Society of Agricultural Engineering Conference, Thailand, pp. 1–4 (2006)

Sa-adchom, P., Swasdisevi, T., Nathakaranakule, A., Soponronnarit, S.: Drying kinetics using superheated steam and quality attributes of dried pork slices for different thickness, seasoning and fibers distribution. J. Food Eng. (104) (2011a)

Sehrawat, R., Nema, P.K., Kaur, P.B.: Effect of superheated steam drying on properties of foodstuffs and kinetic modeling. Innov. Food Sci. Emerg. **34**, 285–301 (2016)

Mujumdar, A.S.: Handbook of industrial drying, 3rd edn, pp. 448–449. CRC Press, Florida (2007)

Kondjoyan, A., et al.: Effect of superheated steam on the inactivation of Listeria innocua surface-inoculated onto chicken skin. J. Food Eng. (87) (2008)

Jamradloedluk, J., Nathakaranakule, A., Soponronnarit, S., Prachayawarakorn, S.: Modelling of dehydration and rehydration kinetics of durian. In: The 2nd International Conference on Innovations in Food Processing Technology and Engineering, Asian Institute of Technology, Thailand, pp. 267–277 (2004)

Soponronnarit, S., Nathakaranakule, N., Jirajindalert, A., Taechapairoj, C.: Parboiling brown rice using superheated steam fluidization technique. J. Food Eng. **75**, 423–432 (2006)

Taechapairoj, C., Prachayawarakorn, S., Soponronnarit, S.: Modelling of parboiled rice in superheated steam fluidized bed. J. Food Eng. **76**, 411–419 (2006)

Mujumdar, A.S.: Superheated steam drying-technology of the future. In: Devahastin, S. (ed.) Mujumdar's Practical Guide to Industrial Drying, Canada, pp. 115–138 (2000)

Sa-adchom, P., Swasdisevi, T., Nathakaranakule, A., Soponronnarit, S.: Mathematical model of pork slice drying using superheated steam. J. Food Eng. (104), 499–507 (2011b)

OECD2019. https://data.oecd.org/agroutput/meatconsumption.htm#indicator-chart. Accessed 10 Sept 2019

Copper(II) Chelating Agents

Przemysław Aksamitowski and Karolina Wieszczycka(✉)

Institute of Chemical Technology and Engineering,
Poznan University of Technology, Poznań, Poland
karolina.wieszczycka@put.poznan.pl

Abstract. The work focuses on current state, trends and further development directions in solvent extraction of copper. The extractants used for this purpose were reviewed and new pyridine-based proposals were described. Compounds having copper chelating properties are described in detail, with particular emphasis on oxime pyridine derivatives.

1 Copper and Its Production

Copper is a malleable, ductile metal that has excellent heat conductive and electricity properties. It is also a metal resistant to corrosion (Rzadkosz et al. 2014; ICGS 2018) and exhibiting antimicrobial properties (Ochoa-Herrera et al. 2011). Copper can be found in the earth's crust as pure native copper or in combination with other elements (ICGS 2018; Pietrzyk and Tora 2018). With other elements, it occurs mainly in sulfide deposits such as chalcopyrite, bornite, chalcocite, and kovelite. In smaller quantities, carbonate deposits such as azurite or malachite and silicate deposits (chrycolla and dioptase) copper is also found. Copper and its alloys are used in a variety of applications that are necessary for a good standard of living. Its continuous production and use is necessary for the development of society. Figure 1 shows the changes in copper consumption per person compared to their population in years of 2000–2017. It can be seen that the data presented correlate with each other, indicating how necessary copper is today (ICGS 2018). The growing demand for copper can be met through the discovery of new deposits, the development of new processing technologies as well as the proper management of its waste.

There are currently two main methods for obtaining metallic copper. The first is pyrometallurgical processing of metal-rich deposits and their concentrates obtained by flotation. Hydrometallurgical (also known as LX-SX-EW) treatment is an alternative method, which can be used for poorer deposits. It consists of three stages (Fig. 2), in which the main is to obtain a solution containing metal ions by leaching of ores with an appropriate agent (Table 1) causing its dissolution (Chmielewski 1996). The leachate solutions obtained (called pregnant leach solution, PLS) are further purified by reactive liquid-liquid extraction (Wieszczycka 2018), during which metal ions are complexed by a complexing reagent. Extractant plays a key role in hydrometallurgical process. Its task is to transfer a desired component from the aqueous to the organic phase through complexation reaction, leaving undesirable components of the mixture in the aqueous

© Springer Nature Switzerland AG 2020
M. Ochowiak et al. (Eds.): PAIC 2019, *Practical Aspects of Chemical Engineering*, pp. 17–26, 2020.
https://doi.org/10.1007/978-3-030-39867-5_3

phase, and then in the reverse process (stripping), is to create the appropriate electrolyte necessary for the metal electrowinning process (Schlesinger et al. 2011).

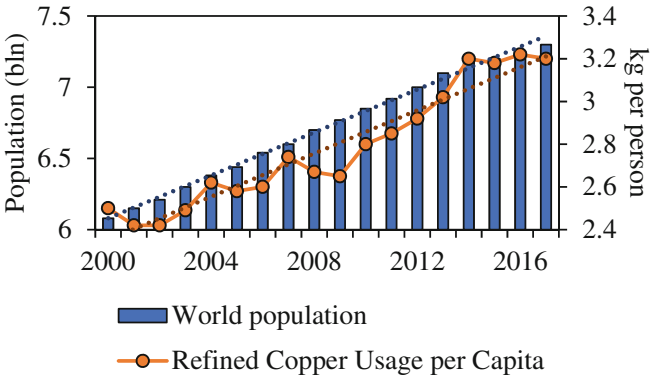

Fig. 1. Global consumption of refined copper per person compared to their population in years 2000–2017 (ICGS 2018)

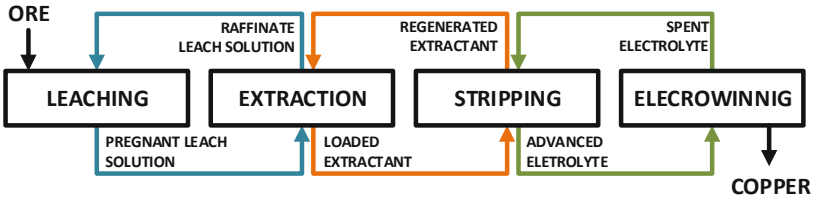

Fig. 2. Flow-sheet diagram recovery of copper from its ore in LX/SX/EW process (Rotuska and Chmielewski 2008; Schlesinger et al. 2011)

The processing of deposits within the hydrometallurgical route began to develop in the 1960s due to the discovery of extractants. Based on data published by ICSG (ICSG 2018), in 2017 refined copper production by hydrometallurgy accounted 16% of its total production (3.7 million ton of refined copper) (Fig. 3). Along with the rate of decreasing of ores containing high copper content and at the same time with the increase in copper demand, it has been estimated that SX-EW processes have become more and more popular (Norgate and Jahanshahi 2010; Rotuska and Chmielewski 2008).

Table 1. Sulphate and chloride based leaching processes of copper ore

Leaching agent	Process	Conditions
Diluted H_2SO_4	Heap leaching (Domic 2007) ROM dump leaching (Domic 2007)	Ambient temperature and atmospheric pressure
Diluted H_2SO_4 with bacteria	BacTech/Mintek (Gericke et al. 2009) BioCOP™ (Batty and Rorke 2006)	35–50 °C 65–80 °C
$FeSO_4$	Sepona (Baxter et al. 2003) Galvanox™ (Dixon et al. 2008) Albion (Hourn et al. 1999) Cobre Las Cruces Project (Fleury et al. 2010)	80 °C 80 °C 85 °C 90°
Diluted H_2SO_4 with NaCl Diluted H_2SO_4 with $CaCl_2$	BHAS (Peacey et al. 2004) CESL (Bruce and Seaman 2014) CuproChlor® (Chilean Patent 2001)	Ambient temperature Elevated temperature and pressure Ambient temperature
$FeCl_3$, $CuCl_2$, NaCl $FeCl_3$, NaCl $FeCl_3$, NaCl NaCl-NaBr	Cymet (Peacey et al. 2004) Cuprex (Peacey et al. 2004) Outukumpu (Peacey et al. 2004) Intec (Peacey et al. 2004)	75–85 °C 95 °C n.d. 80–85°
$(NH_4)_2SO_4$	BIOSHALE (Chmielewski et al. 2009; Radmehr et al. 2012)	120–180 °C 5–12 atm

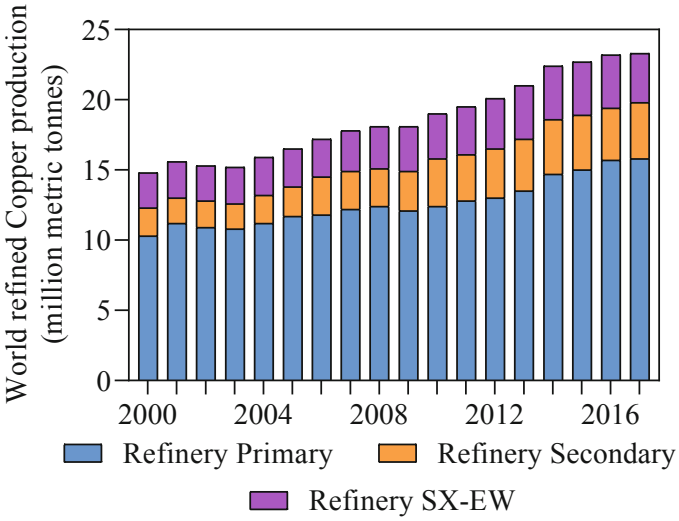

Fig. 3. World refined Copper production in the period from 2000 to 2017 (ICGS 2018)

2 Chelating Extractants

Depending on the metal leaching agent used, of various leaches may be formed i.e. sulphate, chloride, nitrate, ammoniacal or mixtures thereof, e.g. chloride-sulphate (Table 1). Therefore, a complexing agent used in the extraction step must be adequate to work in desired conditions, e.g. by using an appropriate active compound or modifier. For this, many different groups of compounds have been proposed, such as carboxylic acids, hydroxamic acids, high molecular weight amines and organic compounds based on phosphoric acid (Cheng et al. 2015; Preston 1985; Tait et al. 1995).

The α-hydroxyoxime (LIX®63) has been implemented in the industry as an extractant of copper(II) from acid solutions together with ketoxime based on 2-hydroxy-5-nonyl or -dodecylbenzophenone (LIX®64, LIX®64N, LIX®65N) Later developed compounds were based on 2-hydroxy-5-nonylacetophenone (Table 2-I) (Schlesinger et al. 2011), which, compared to previous ones, provided better extraction efficiency from dilute acid solutions with a low content of copper(II). Ketoximes provide sufficient extraction force useful in the pH range 1.6–1.8, sufficient selectivity for iron(III) ions and adequate physicochemical stability (Yáñez et al. 2017). In addition, they are characterized by excellent phase separation, low losses due to penetration into the aqueous phase and do not cause crud formation (Schlesinger et al. 2011).

Hydroxyaldoximes are the next generation of extractants (Table 2-II). Their advantages are above all even better extraction ability, especially from strongly acid solutions and better selectivity towards iron(III) ions. An important aspect is also that owing to the mutual miscibility of these compounds, we can influence on the extraction properties by adjusting them to the needs of a given process by selecting their respective ratios (Table 2-III) (Schlesinger et al. 2011).

The aforementioned compounds as well as their mixtures have also been used in the extraction processes of copper(II) from ammonia leach solutions (LIX®860N, LIX®84-I, LIX®973N) as well as β-diketone (LIX®54-100, Table 2-IV) (Alguacil and Navarro 2002; Algaucil and Regel-Rosocka 2018). All extractants based on aldoximes and ketoximes have been proposed to extract copper(II) in industrial process, but finally used with a few exceptions (LIX®54, LIX®70, LIX®71, LIX®73, XI 51, SME 530, OMG, ABF), and are still used. Currently there are three main companies on the market that produce extractants for industry. BASF (LIX extractants), Solvay (ACORGA and CYANEX) and KopperChem (Mextral extractants). Table 2 presents a summary of the currently used commercial extractants in the copper(II) removal (BASF 2019; KopperChem 2019; Solvay 2019).

3 Novel Extracting Reagents

Novel compounds that have complexing properties for copper ions have also been designed and tested over last twenty years. Much research has been devoted to compounds based on pyridine.

Table 2. Commercial copper chelating agents and their applications

No	Structure and name of active compound	Application (e.g)	Literature
I	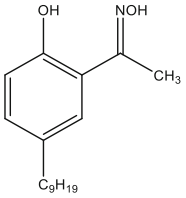	Xstrata Copper Lomas Bayas 2006, Chile pH 2.12 4.07 g/L Cu(II) 0.42 g/L Fe(III) 21%(v/v) LIX84-IC Shellsol 2046AR	(Robinson et al. 2008)
	2-hydroxy-5-nonylacetophenone oxime ACORGA®K2000, LIX®84-I, Mextral® 84-IC		
II	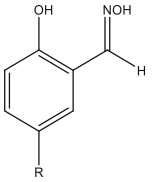	Escondida oxide 2006, Chile pH 1.6-1.8 7 g/L Cu(II) 0.5 g/L Fe(III) 17% (v/v) ACORGA®M5640 HS Shellsol 2046 AR	(Robinson et al. 2008)
	R=C_9H_{19} 5-nonylsalicylaldoxime	ACORGA®M5640, LIX®LIX®684N-LV, Mextral®5640H	
	R=$C_{12}H_{25}$ 5-dodecylsalicylaldoxime	LIX®860-IC	
III	Mixtures of aldoximes I and ketoximes II ACORGA®PT5050, LIX®973NS-LV, Mextral®5050H	Sociedad Minera Cerro Verde 2006, Peru pH 1.9-2 2.8 g/L Cu(II) 0.6 g/L Fe(III) 15% (v/v) LIX®984 NC	(Robinson et al. 2008)
	1:1 ratio LIX®984, LIX®984N 1:3 ratio LIX®9790N		
IV	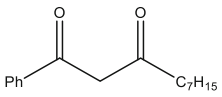	0.1 M Cu(II) pH 0-9 25% (v/v) Exxsol D80	(Gotfryd and Pietek 2012)
	1-phenyldecane-1,3-dione	LIX®54-100, Mextral®54-100	

Hydrophobic derivatives of pyridine-carboxylic acids capable of metal complexation include also the compounds with amide group, as indicated by results of the studies performed for the derivatives with amide group at positions 2, 3 or 4 of the pyridine ring and for diamides of pyridine-3,5- and -2,4-dicarboxylic acid. Similarly as for esters, the complexing and extracting properties of the amide derivatives depend on the basicity of the pyridine nitrogen, determined by the number and positions of electron-acceptor groups. Most often, an increase in the number of amide groups and their positions near the pyridine nitrogen result in a reduced extraction ability of the compound. The exception from the above rule takes place when the extraction is carried out at a low concentration of chloride ions. In such conditions the hydrophobic

derivatives with the amide group near the pyridine nitrogen are more potent extractants than the analogous amide derivatives of pyridine-3- and 4-carboxylic acids. Most probably the reason for this exceptional behavior is formation of more stable complexes in which copper atom is bonded to pyridine-2-carboxyamide and pyridine-2,6-dicarboxyamide via the pyridine nitrogen and the oxygen from amide group. Unfortunately, most of the pyridineamide easily undergo protonation, which means that the acid is moved to the organic phase (Borowiak-Resterna 1999; Borowiak-Resterna and Lenarcik 2004; Bogacki et al. 1997; Klonowska-Wieszczycka et al. 2009; Wojciechowska et al. 2017a, 2017b).

The hydrophobic pyridine ketoximes (Table 3-V) are the another type of extractant which are a combination of a chelating extractant (oxime group) and a solvating extractant (pyridine ring). This structure was expected to permit their use in different extraction systems. The presence of an oxime group along with the pyridine ring in the extractant increased the number of sites capable of metal coordination. Of particular importance is the basic nitrogen atom that has a free electron pair, capable of making a coordinate bond. Oximes comprise a weakly acidic hydrogen at hydroxyl group that can undergo deprotonation and lead to formation of a stable chelate complex. Oxime of 1-(2-pyridyl)ethane-1-one belongs to the group of polydentate ligands that are capable of forming complexes more stable than pyridine or oxime group alone. The complexes are formed mainly via coordinate bonds in which the electron pair donors are the nitrogen atoms from pyridine ring and oxime groups and the oxygen atoms, that can make coordinate or ionic bonds with metals. Also the formation of the so-called hydrogen bonds is possible, they additionally stabilize the complex and link e.g. two ligands coordinating the metal ion between them.

The search for a new extractant was undertaken in response to the hydrometallurgical industry demand for an effective, selective and stable complexing compound. In particular demand was an extractant of copper ions from chloride and sulphate solutions, and also, if copper is extracted from wastewater, from solutions of ammonium chloride. Not all of the pyridine ketoximes proposed meet all these conditions. As expected, the position of oxime group in pyridine ring determined the mechanism of metal ions complexation. When copper(II) ions are extracted from weakly acidic chloride solution, with toluene and 10% (v/v) addition of decan-1-ol as an organic solvent, the compounds with an oxime group in direct vicinity of the pyridine nitrogen complexed copper in 100% in the whole range of chloride ions studied making stable chelate-type complexes. A shift of the oxime substituent to position 3 or 4 of the pyridine ring leads to formation of complexes of different structure, and the process of metal transition significantly depends on the concentration of chloride ions in water solution (Klonowska-Wieszczycka et al. 2009; Wieszczycka et al. 2012a, 2012b; Parus et al. 2015). Unfortunately, when copper(II) ions were extracted with hydrophobic alkyl-2-pyridyl oximes, the sulphate ions prevented the metal transfer to the organic phase, as they induced precipitation of the complex formed and formation of a stable emulsion (Wieszczycka et al. 2012a, 2012b).

Table 3. Structures, names and extraction conditions

Structure and name of active compound of chelating agent	Aqueous feed/Organic feed	Extraction parameters
V 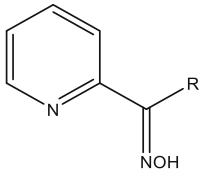	Cu(II) 0.01-0.12 M pH 1-5 Concentration of extractant 0.01-0.1 M Diluent: Heptane or toluene with 10% (v/v) decanol	Eq. time = 15min 0 M Cl^- = emulsion $Cl^- \geq 0.1$ M %E = 100 Capacity: 1 M Cu(II)/1 M HL
R=octyl, decyl, dodecyl, tetradecyl 1-(2-pyridyl)alkan-1-one oxime		
VI 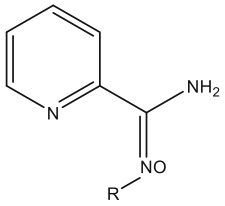	Cu(II) 0.01-0.12 M pH 1-5 Concentration of extractant 0.01-0.1 M Diluent: Heptane or toluene with 10% (v/v) decanol	Eq. time = 15min A/O = 1 O-2IA %E pH 3.5 = 97 0-4 M Cl^- %E = 99-95 Eh-2IA %E pH 3.5 = 99 0-2.5 M Cl^- %E = 40 3-4 M Cl^- %E = 60-99
R=2-ethylhexyl, octyl *N'*-alkyloxypyridine-2-carboximidamide		
VII 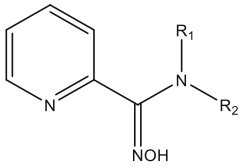	Cu(II) 0.01-0.16 M pH 1-5 Concentration of extractant 0.02-0.25 M Diluent: Heptane, Toluene, Solvesso 100, Exxsol D80	A/O = 1-10 Eq. time = 2 min pH_{50} Exxsol 1.3 pH_{50} Solvesso 2.5 pH_{50} Heptane 1.3 pH_{50} Toluene 2.8
R_1=H R_2=2-ethylhexyl, octyl, dodecyl *N*-alkyl-*N'*-hydroxyprydine-2-carboximidamide R_1=R_2=butyl, 2-ethylhexyl, hexyl, octyl *N,N*-dialkyl-*N'*-hydroxyprydine-2-carboximidamide		

The ether derivatives of pyridineamidoximes have also been studied (Wojciechowska et al. 2017a, 2017b; Wieszczycka et al. 2019) (Table 3-VI). Regardless of the type of alkyl chain (straight and branched), these compounds reached equilibrium after 15 min of shaking. However, significant differences between the compounds can be seen by observing changes in chloride ion concentration. In the case of compounds with a straight alkyl chain, the best properties are obtained in whole range of chloride ions concentration. Compounds having a 2-ethylhexyl chain exhibited completely different behavior. Effective extraction occurred at a concentration of chloride ions above 3.5 M. In addition, the compounds with branched chain had higher selectivity for iron(III) ions from the acid chloride solution. The extractants were regenerated easily using diluted (1%) sulfuric acid.

Recent literature have reported pyridine derivatives containing an imidoamide moiety (Table 3-VII), in which the amino nitrogen is attached with two alkyl chains. These compounds are characterized by very fast equilibrium achieving (120 s) and by

the extraction properties depending on the substitution in the pyridine ring. Only compounds with substitution at 2 position of the pyridine ring show adequate efficiency, which also depends on the type of used diluent. When heptane is used as a diluent, the 50% extraction is observed at pH of 1.7, while in the case of toluene, at pH 2.8. Regeneration of the extractant requires the use of a sulfuric acid solution or a spent electrolyte, which after the process can be used at an electrowinning step. Moreover, the pyridineimidamides are selective copper extractants especially in the presence of iron(II) and (III) (Aksamitowski et al. 2018; Aksamitowski et al. 2019). Other studies conducted using the hydrophobic pyridineimidamides have indicated that this compounds are promising extractant of copper(II) from a sulphate mixture containing also a high concentration of zinc(II). The length and type of alkyl chains attached to the imidamide nitrogen, as well as the diluent type have been demonstrated as the main factors influencing on the selectivity of the extraction. The results obtained have also shown that compounds having less than 6 carbon atoms in a single chain attached to the imidamide nitrogen form complexes that are too hydrophilic. The use of commercial diluent counterparts additionally improved the extraction efficiency and improved selectivity towards zinc(II). As in previous studies presented, regeneration of the extractant was carried out using the sulfuric acid solutions (Aksamitowski et al. 2018; Aksamitowski et al. 2019).

4 Summary

In the last 50 years, the hydrometallurgy ore treatment has become increasingly popular. Currently used commercial extractants have several disadvantages. The main ones include such as susceptibility to nitration or hydrolysis. Currently, also classic sulfuric acid leaching methods are gradually being abandoned in favour of solutions containing chloride ions. This is because fresh water is replaced by sea water. It is therefore necessary to consider the use of existing and new compounds under different then classic conditions. It seems important to design and research novel compounds that would have similar or better properties than commercial reagents, eliminating the disadvantages of them.

Acknowledgments. This work was supported by the Ministry of Science and Higher Education (Grant No. 03/32/SBAD/0900).

References

Aksamitowski, P., Wiesczycka, K., Wojciechowska, I.: Selective copper extraction from sulfate media with N,N-dihexyl-N′-hydroxypyridine-carboximidamides as extractants. Sep. Purif. Technol. **201**, 186–192 (2018)

Aksamitowski, P., Filipowiak, K., Wieszczycka, K.: Selective extraction of copper from Cu-Zn sulfate media by new generation extractants. Sep. Purif. Technol. **222**, 22–29 (2019)

Alguacil, F.J., Navarro, P.: Non-dispersive solvent extraction of Cu(II) by LIX 973N from ammoniacal/ammonium carbonate aqueous solutions. Hydrometallurgy **65**, 77–82 (2002)

Alguacil, F.J., Regel-Rosocka, M.: Hydrometallurgical treatment of hazardous copper Cottrell dusts to recover copper. Physicochem. Probl. Miner. Process. **54**(3), 771–780 (2018)

BASF (2019). www.mining-solutions.basf.com. Accessed 12 Sept 2019
Batty, J.D., Rorke, G.V.: Development and commercial demonstration of the BioCOP™ thermophile process. Hydrometallurgy **83**, 83–89 (2006)
Baxter, K., Dreisinger, D.B., Pratt, G.: The Sepon copper project: development of a flowsheet. In: Young, C.A., Alfantazi, A.M., Anderson, C.G., Dreisinger, D.B., Harris, B., James, A. (eds.) Hydrometallurgy, pp. 1487–1502. TMS, Warrendale (2003)
Bogacki, M.B., Borowiak-Resterna, A., Szymanowski, J.: Modification of extraction abilities of N,N,N′,N′-tetraalkyl-3,5-pyridinedicarboxamide by its association with alcohol. Solvent Extr. Ion Exc. **15**(4), 591–604 (1997)
Borowiak-Resterna, A.: Extraction of copper(II) from acid chloride solutions by N-dodecyl- and N,N-dihexylpyridinecarboxamides. Solvent Extr. Ion Exc. **17**(1), 133–148 (1999)
Borowiak-Resterna, A., Lenarcik, B.: Effect of the alkyl chain length in N,N-dialkylpyridine-3-carboxamides upon their extraction of copper(II) from aqueous chloride solutions. Solvent Extr. Ion Exc. **22**(6), 913–931 (2004)
Bruce, R., Seaman, T.: Reducing Fresh Water Use in the Production of Metals. Teck Resources Limited, Canada (2014). https://www.teck.com. Accessed 12 Sept 2019
Cheng, C.Y., Urbani, M.D., Davies, M.G., Pranolo, Y., Zhu, Z.: Recovery of nickel and cobalt from leach solutions of nickel laterites using a synergistic system consisting of Versatic 10 and Acorga CLX 50. Miner. Eng. **77**, 17–24 (2015)
Chmielewski, T.: Ługowanie metali z rud, koncentratów, półproduktów i odpadów. Physicochem. Probl. Mi. **30**, 217–231 (1996)
Chmielewski, T., Wódka, J., Iwachów, Ł.: Ammonia pressure leaching for Lubin shale middlings. Physicochem. Probl. Mi. **43**, 5–20 (2009)
CuproChlor: Chilean Patent #40891, Chile (2001)
Dixon, D.G., Mayne, D.D., Baxter, K.G.: Galvanox™ — a novel galvanically-assisted atmospheric leaching technology for copper concentrates. Can. Metall. Q. **47**, 327–336 (2008)
Domic, E.M.: A review of the development and current status of copper bioleaching operations in Chile: 25 years of successful commercial implementation. In: Rawlings, D.E., Johnson, D.B. (eds.) Biomining, pp. 81–95. Springer, Berlin (2007)
Fleury, F., Delgado, E., Collao, N.: A new technology for processing hydrometallurgical copper ore, Cobre Las Cruces Project. In: Proceedings of Copper 2010 (Hamburg, Germany). Hydrometallurgy, vol. 5, pp. 1871–1897. GDMB, Clausthal-Zellerfeld (2010)
Gericke, M., Neale, J.W., van Staden, P.J.: A Mintek perspective of the past 25 years in minerals bioleaching. J. South Afr. Inst. Min. Metall. **109**, 567–585 (2009)
Gotfryd, L., Pietek, G.: Contaminants of post-leaching copper solutions and their behavior during extraction with industrial extractants. Physicochem. Probl. Miner. Process. **49**(1), 133–143 (2012)
Hourn, M.M., Turner, D.W., Holzberger, I.R.: Atmospheric mineral leaching process. U.S. Patent 5,993,635 (1999)
ICGS (International Copper Study Group): The world copper factbook 2018 (2018). www.icsg.org. Accessed 12 Sept 2019
KopperChem (2019). http://www.mextral.com/aspx/en/index.aspx. Accessed 12 Sept 2019
Klonowska-Wieszczycka, K., Olszanowski, A., Parus, A., Zydorczak, B.: Removal of copper(II) from chloride solutions using hydrophobic pyridyl ketone oximes. Solvent Extr. Ion Exc. **27**(1), 50–62 (2009)
Norgate, T., Jahanshahi, S.: Low grade ores – smelt, leach or concentrate? Miner. Eng. **23**, 65–73 (2010)
Ochoa-Herrera, V., León, G., Banihani, Q., Field, J.A., Sierra-Alvarez, R.: Toxicity of copper(II) ions to microorganisms in biological wastewater treatment systems. Sci. Total Environ. **412–413**, 380–385 (2011)

Ochromowicz, K., Jeziorek, M., Wejman, K.: Copper(II) extraction from ammonia leach solution. Physicochem. Probl. Miner. Process. **50**(1), 327–335 (2014)

Parus, A., Jankowska, A., Wieszczycka, K.: Pyridylketoximes with branched alkyl chain as extractants of copper(II) ions from chloride solutions. Sep. Sci. Technol. **50**(2), 214–222 (2015)

Peacey, J., Guo, X., Robles, E.: Copper hydrometallurgy — current status, preliminary economics, future direction and positioning versus smelting. Trans. Nonferrous Met. Soc. China **14**, 560–568 (2004)

Pietrzyk, S., Tora, B.: Trends in global copper mining – a review. Mater. Sci. Eng. **427**, 1–10 (2018)

Preston, J.S.: Solvent extraction of metals by carboxylic acids. Hydrometallurgy **14**, 171–188 (1985)

Radmehr, V., Koleini, S.M.J., Khalesi, M.R., Tavakoli Mohammadi, M.R.: Ammonia leaching in the copper industry: a review. In: XXVI International Mineral Processing Congress (IMPC) 2012 Proceedings, New Delhi, India, 24–28 September 2012, Paper No. 487 (2012)

Robinson, T., Moats, M., Davenport, W., Karcas, G., Demetrio, S., Domic, E.: Copper solvent extraction – 2007 world operating data. In: Proceedings of ISEC 2008 International Solvent Extraction Conference, pp. 1669–1691 (2008)

Rotuska, K., Chmielewski, T.: Growing role of solvent extraction in copper ores processing. Physicochem. Probl. Miner. Process. **42**, 29–36 (2008)

Rzadkosz, S., Kranc, M., Garbacz-Klempka, A., Piękoś, M., Kozana, J., Cieślak, W.: Research on technology of alloyed copper casting. Arch. Foundry Eng. **14**(2), 79–84 (2014)

Sarangi, K., Parhi, P.K., Padhan, E., Palai, A.K., Nathsarma, K.C., Park, K.H.: Separation of iron (III), copper(II) and zinc(II) from a mixed sulphate/chloride solution using TBP, LIX 84I and Cyanex 923. Sep. Purif. Technol. **55**, 44–49 (2007)

Solvay (2019). https://www.solvay.com/en. Accessed 12 Sept 2019

Schlesinger, M.E., King, M.J., Sole, K.C., Davenport, W.G.: Extractive Metallurgy of Copper. Elsevier, Oxford (2011)

Staszak, K., Regel-Rosocka, M., Wieszczycka, K., Burmistrzak, P.: Copper(II) sulphate solutions treatment by solvent extraction with Na-Cyanex 272. Sep. Purif. Technol. **85**, 183–192 (2012)

Tait, B.K., Mdlalose, K.E., Taljaard, I.: The extraction of some metal ions by LIX 1104 dissolved in toluene. Hydrometallurgy **38**, 1–6 (1995)

Wieszczycka, K., Kaczerewska, M., Krupa, M., Parus, A., Olszanowski, A.: Solvent extraction of copper(II) from ammonium chloride and hydrochloric acid solutions with hydrophobic pyridineketoximes. Sep. Purif. Technol. **95**, 157–164 (2012a)

Wieszczycka, K., Krupa, M., Olszanowski, A.: Extraction of copper(II) ions from chloride and sulphate solutions using hydrophobic pyridyl ketoximes. Sep. Purif. Technol. **47**(9), 1278–1284 (2012b)

Wieszczycka, K.: Reactive extraction at liquid–liquid systems. Phys. Sci. Rev. **3**, 1–24 (2018)

Wieszczycka, K., Wojciechowska, I., Aksamitowski, P.: Amphiphilic amidoxime ether as Cu(I) and Cu(II) extractant from waste etch solution. Sep. Purif. Technol. **215**, 540–547 (2019)

Wojciechowska, A., Wieszczycka, K., Wojciechowska, I.: Efficient recovery of copper from aqueous solutions with pyridine extractants (oxime, ketone) and their quaternary pyridinium salts. Sep. Purif. Technol. **185**, 103–111 (2017a)

Wojciechowska, I., Wieszczycka, K., Aksamitowski, P., Wojciechowska, A.: Copper recovery from chloride solutions using liquid extraction with pyridinecarboximidamides as extractants. Sep. Purif. Technol. **187**, 319–326 (2017b)

Yáñez, H., Ardiles, L., Río, C.: High chloride in PLS and their impact on copper solvent extraction. In: Hydroprocess ICMSE, Proceedings, pp. 234–241 (2017)

Verification of Methods for Calculating Resistance in Two-Phase Gas-Liquid Mixture Flow

Krystian Czernek(✉), Patryk Okoń, Waldemar Szaferski, and Stanisław Witczak

Faculty of Mechanical Engineering, Department of Process Engineering, Opole University of Technology, Opole, Poland
k.czernek@po.edu.pl

Abstract. The chapter presents the results of research on the vertical falling flow and their analysis. Methods for calculating resistance in two-phase gas-liquid mixture flow, which are characterized by high accuracy, and are often proposed in the literature. Their accuracy was presented, as well as the method with the highest computational usefulness when designing devices in which two-phase gas-liquid flow is used.

1 Introduction

Determination of resistances in two-phase mixture flow is one of the three basic parameters, next to flow structures and volumetric phase share, to be determined when testing and analysing two-phase gas-liquid flow. Exact determination of pressure losses during flow is very significant due to operating conditions, which force correct design of devices using two-phase mixtures and well as operating costs of these devices during their use in industrial installations. Precise determination of flow resistances has an effect on the selection of feeding devices for pumps, for instance, as well.

Determination of flow resistances is very complicated due to the complex nature of two-phase mixture flow. The summary value of flow resistances in such a mixture $(\Delta P/\Delta L)_{2F}$ is determined by summing up friction resistance components $(\Delta P/\Delta L)_{2F,T}$, caused by the force of gravity $(\Delta P/\Delta L)_{2F,H,}$ and change in momentum $(\Delta P/\Delta L)_{2F,A}$:

$$\left(\frac{\Delta P}{\Delta L}\right)_{2F} = \left(\frac{\Delta P}{\Delta L}\right)_{2F,T} \pm \left(\frac{\Delta P}{\Delta L}\right)_{2F,H} + \left(\frac{\Delta P}{\Delta L}\right)_{2F,A}. \quad (1)$$

In the case of adiabatic flows, the component concerning the change in momentum is very often left out and the component concerning the resistances caused by the force of gravity is strongly dependent on the length of the channel, the diameter and the direction in which two-phase mixture is flowing. The most significant element of the equation describing pressure losses is related to the friction of the flowing mixture. The determination of the component connected with friction is based on the homogeneous-flow model or the separated-flow model. Assuming that the flow if based on the homogeneous-flow model, a two-phase mixture is to be treated as a single-phase liquid

© Springer Nature Switzerland AG 2020
M. Ochowiak et al. (Eds.): PAIC 2019, *Practical Aspects of Chemical Engineering*, pp. 27–36, 2020.
https://doi.org/10.1007/978-3-030-39867-5_4

with substitutive properties. In those methods, the friction-induced pressure loss is determined on the basis of the Darcy-Weisbach Equation:

$$\left(\frac{\Delta P}{\Delta L}\right)_{2F,T} = \lambda_{2F}\frac{g_T^2}{2D\rho_{2F}}, \tag{2}$$

where physicochemical properties of the mixture are determined from equations including proper volumetric shares of streams of individual phases or their mass shares. The homogeneous model allows achieving some accuracy mostly for bubble flow and dispersive flow.

The other group of proposed methods are those based on the separated-flow model, where mixture flow resistances are determined by the calculation of resistances of one of the phases. The most well-known method based on the separated-flow method is the method of Lockhart-Martinnelli, where the two-phase mixture flow resistances is determined with the pressure loss of a given phase which is flowing independently through the full cross-section of the channel, with use of multiplier φ^2:

$$\left(\frac{\Delta P}{\Delta L}\right)_{2F,T} = \left(\frac{\Delta P}{\Delta L}\right)_i \varphi_i^2. \tag{3}$$

In the original version of the method of Lockhart-Martinnelli, the value of multipliers φ^2 was presented in graphical form (Fig. 1) and depends on one of four types of two-phase flow characterised as laminar or turbulent flow of a given phase flowing through the full cross-section of the channel independently and on the X parameter determined from the following relation:

$$X = \left[\left(\frac{\Delta P}{\Delta L}\right)_c \Big/ \left(\frac{\Delta P}{\Delta L}\right)_g\right]^{0,5}. \tag{4}$$

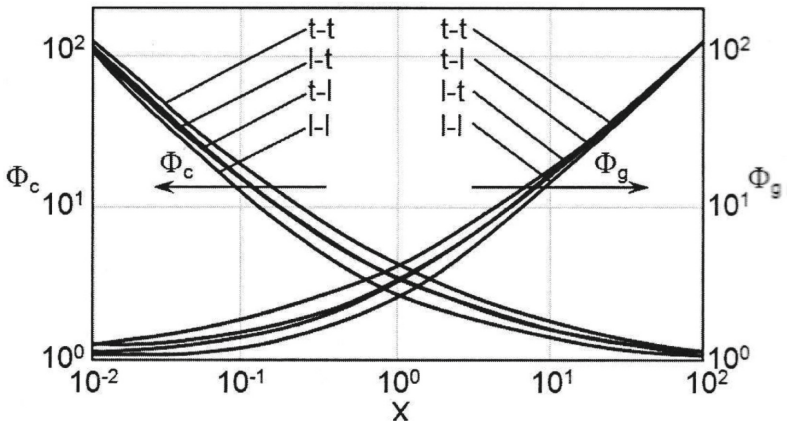

Fig. 1. Graphical interpretation of the method of Lockhart-Martinnelli (Dziubiński 2005).

The graphical interpretation proposed by Lockhart-Martinnelli is very popular, but due to the fact that it may generate a considerable error in reading the exact value of the multiplier, the method was mathematically described multiple times. One of the most often quoted descriptions is the method of Chisholm (Dziubiński 2005), where the author introduced the value of the *C* constant (Table 1).

Table 1. Constant *C* value.

Type of flow	C value
laminar-laminar (l-l)	5
laminar-turbulent (l-t)	10
turbulent-laminar (t-l)	12
turbulent-turbulent (t-t)	20

2 Test Stand

Two-phase gas-liquid mixture flow resistances were tested on the stand presented in Fig. 2, where the most important element was the vertical transparent tube with two cut-off valves (17) allowing measurement of the volumetric share of gas with the trap method.

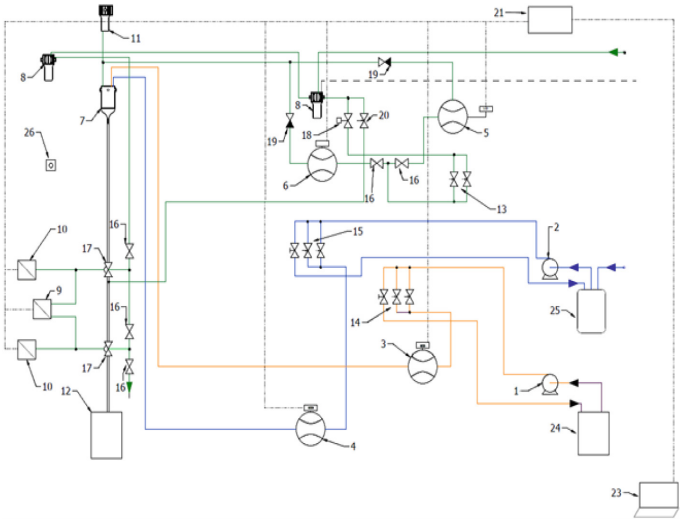

Fig. 2. Diagram of the two-phase gas-liquid flow testing installation: 1, 2 – pump 3, 4, 5, 6 – mass stream concentration gauges; 7 – mixing chamber; 8, 11 – flowmeters; 9, 10 – pressure loss measurement; 12 – terminal liquid tank; 13, 14, 15, 20 – poppet valve; 16 – ball valve; 17 – cut-off valve; 18 – controlled valve; 19 – check valve; 21 – measurement converter; 23 – computer; 24 – oil tank; 25 – water tank; 26 – power switch.

Two sensors measuring pressure losses (10) were attached to the measurement channel, at its inlet and outlet, as well as a sensor measuring pressure differences (11) in the measurement section. The tube was mounted to the mixing chamber (7), where individual phases were mixed. The gas agent was fed from the network and poppet valves (18, 20) were used to regulate the amount of gas fed to the mixing chamber. Water was also fed from the network, with a pump (2). Poppet valves (15) were used to regulate the amount of liquid fed to the measurement tube. The installation was also equipped with an additional line for feeding a liquid agent that is not water so as not to contaminate the duct through which water was forced and to allow quick change of the liquid agent used on the measurement stand. The amount of flowing agents was measured with mass concentration gauges (3, 4, 5, 6). All data obtained during measurements, pressure losses, flow concentrations and physicochemical parameters were sent to a measurement converter (21) and a computer (23).

3 Measurement Results and Calculation Analysis

Using the results obtained from the review of literature (Mishima and Hibiki 1996; Lee and Lee 2001; Kaminaga et al. 2003; Dziubiński 2005; Sun and Mishima 2013; Witczak 2013) concerning methods for calculating two-phase mixture flow resistances, it was found that a lot of methods has a very specific scope of application and that calculation models differ from each other in terms of equation forms. Therefore, it is impossible to directly compare and assess the applicability of individual methods.

Willing to analyse the applicability of individual methods for calculating two-phase mixture flow resistances, typical systems used in laboratory tests and in the industry were selected. To that end, the experiment data set of the Department of Process Engineering of the Opole University of Technology (Department of Process Engineering 2004) and the results of own tests were used. Proper data were extracted that allowed analysing the accuracy of individual calculation methods. Table 2 illustrates the surnames of researchers, diameters of measurement channels and ranges of gas and flow speed ranges with co-current downward flow.

A preliminary assessment of methods (Table 3) presented in the literature allowed to select six that allow describing two-phase mixture flow resistances. Some of them are based on a mathematical model describing the graphical interpretation of the Lockhart-Martinnelli correlation, which allows determining the value of multiplier φ^2, or present their own mathematical models determining the value of the C constant.

The assessment of the accuracy of individual methods and their usability in determining flow resistances for the purposes of design and construction work consisted in the determination of characteristic statistical parameters including the determination of the mean value of relative error δR_g and the mean value of absolute error $|\delta R|$. Detailed results of the calculations are presented in Table 4.

Table 2. List of data used for analysis.

Type of mixture	Author of test	Channel diameter, [m]	Range of speed	
			liquid, [m/s]	gas, [m/s]
air-water	Oshinowo	0.025	0.22	10–23
	Andreussi	0.024	0.03–0.3	40–85
	Okoń	0.012	0.15–0.5	0.28
	Okoń	0.012	0.3–0.45	0.56
air-steam	Janssen	0.024	0.05–3.5	3.5–40

Table 3. Methods for calculating two-phase mixture flow resistances.

Method	Method characteristics
Chisholm	$\varphi_c^2 = 1 + \frac{C}{X} + \frac{1}{X^2}$, $\varphi_g^2 = 1 + CX + X^2$
Kaminaga et al.	$\varphi_c^2 = 1 + \frac{C}{X} + \frac{E}{X^2}$, where $E = 0{,}39\left(\frac{\rho_c}{\rho_g}\right)^{0{,}15}$
Mishima and Hibiki	for circular cross-section channels: $C = 21[1 - \exp(-0{,}333 D_h]$ for rectangular cross-section channels: $C = 21[1 - \exp(-0{,}319 D_h]$
Kim and Mudawar	laminar-laminar (l-l) $C = 0{,}39 Re_{Lo}^{0{,}03} Su_{Go}^{0{,}1} \left(\frac{\rho_L}{\rho_G}\right)^{0{,}35}$ laminar-turbulent (l-t) $C = 0{,}39 Re_{Lo}^{0{,}03} Su_{Go}^{0{,}1} \left(\frac{\rho_L}{\rho_G}\right)^{0{,}35}$ turbulent-laminar (t-l) $C = 3{,}5 \cdot 10^{-5} Re_{L0}^{0{,}44} Su_{G0}^{0{,}5} (\rho_L/\rho_G)^{0{,}48}$ turbulent-turbulent (t-t) $C = 8{,}7 \cdot 10^{-4} Re_{L0}^{0{,}17} Su_{G0}^{0{,}5} (\rho_L/\rho_G)^{0{,}14}$
Lee and Lee	laminar-laminar (l-l) $C = 15 \cdot 10^{-4} Re_{L0}^{0{,}59} Su_{G0}^{0{,}19} (\rho_L/\rho_G)^{0{,}36}$ laminar-turbulent (l-t) $C = 6{,}833 \cdot 10^{-8} \lambda^{-1{,}317} \psi^{0{,}719} Re_L^{0{,}557}$ where: $\psi = \eta_L w_{L0} \sigma^{-1}, \lambda = \eta_L^2 (\rho_L \sigma D_h)^{-1}$ turbulent-laminar (t-l) $C = 6{,}185 \cdot 10^{-2} Re_L^{0{,}726}$ turbulent-turbulent (t-t) $C = 0{,}048 Re_L^{0{,}451}$
Sun and Mishima	for $Re_L < 2000$ and $Re_G < 2000$: $C = 26\left[1 + \left(\frac{Re_L}{1000}\right)\right][1 - \exp(-0{,}153(0{,}27Co + 0{,}8)^{-1})]$ for $Re_L \geq 2000$ and $Re_G \geq 2000$: $C = 1{,}79(Re_G/Re_L)^{0{,}4}[(1 - x/x)]^{0{,}5}$, wherein $\varphi_c^2 = 1 + \frac{C}{X^{1{,}19}} + \frac{1}{X^2}$

Table 4. Statistical analysis of determination of flow resistances.

Data	Method	Statistical values		
		δR_g [%]	δR	[%]
Oschinowo water-air	Chisholm	44.97	53.15	
	Kaminaga et al.	45.90	53.64	
	Mishima and Hibiki	51.38	57.46	
	Kim and Mudawar	−28.21	35.67	
	Lee and Lee	−68.70	68.70	
	Sun and Mishima	−48.30	69.49	
Andreussi water-air	Chisholm	42.21	42.21	
	Kaminaga et al.	44.44	44.44	
	Mishima and Hibiki	49.77	49.77	
	Kim and Mudawar	−8.03	24.47	
	Lee and Lee	−31.97	47.10	
	Sun and Mishima	21.24	21.24	
Okoń water-air	Chisholm	22.62	42.60	
	Kaminaga et al.	22.62	42.60	
	Mishima and Hibiki	55.57	66.01	
	Kim and Mudawar	−19.10	27.21	
	Lee and Lee	248.22	248.22	
	Sun and Mishima	4.10	29.25	
Okoń water-air	Chisholm	111.42	111.42	
	Kaminaga et al.	111.42	111.42	
	Mishima and Hibiki	183.57	183.57	
	Kim and Mudawar	11.54	27.53	
	Lee and Lee	134.63	134.63	
	Sun and Mishima	95.72	95.72	
Janssen water-steam	Chisholm	235.35	240.75	
	Kaminaga et al.	219.82	227.41	
	Mishima and Hibiki	249.39	254.41	
	Kim and Mudawar	−4.29	46.85	
	Lee and Lee	36.58	63.75	
	Sun and Mishima	−47.17	89.30	

The graphical interpretation of performed analyses is provided in Fig. 3, where the results of assessment of calculation accuracy of the compared methods are illustrated. As you can see, Kim and Mudawar's method (Fig. 4) is characterised by the highest accuracy. Calculations of pressure losses in two-phase gas-liquid flow made with the above method show that over 60% of points are located in the range of ±30% of absolute error. The method is characterised by high accuracy as the mathematical model describing it takes into account physicochemical properties of the flowing mixture as well as the nature of the flow of individual phases.

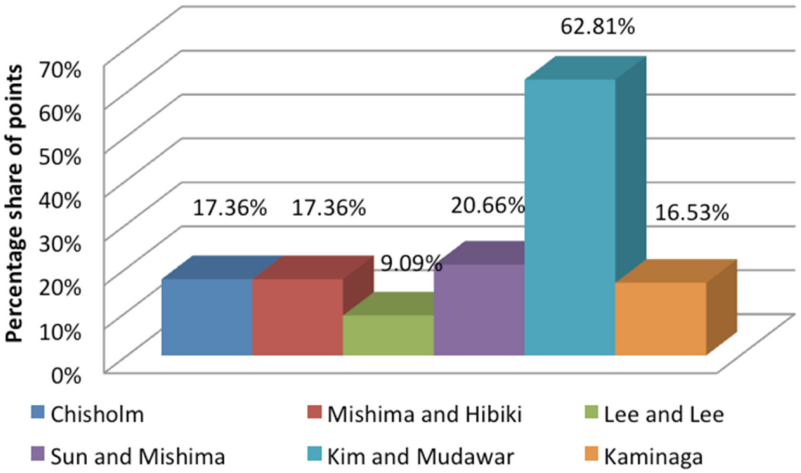

Fig. 3. Comparison of the accuracy of calculation methods for two-phase gas-liquid mixture flow resistances

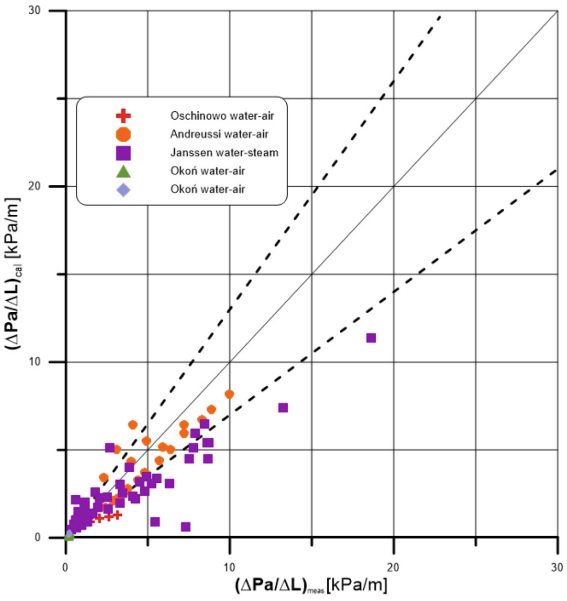

Fig. 4. Comparison of values of flow resistances measured and calculated with Kim and Mudawar's method

The study assessed the influence of selected parameters on the shaping of calculation results (distribution of points) in system $(\Delta Pa/\Delta L)_{cal} - (\Delta Pa/\Delta L)_{meas}$. Graphical interpretations of selected calculation methods for determining flow resistances for various types of two-phase mixtures are presented in Figs. 4, 5, 6 and 7.

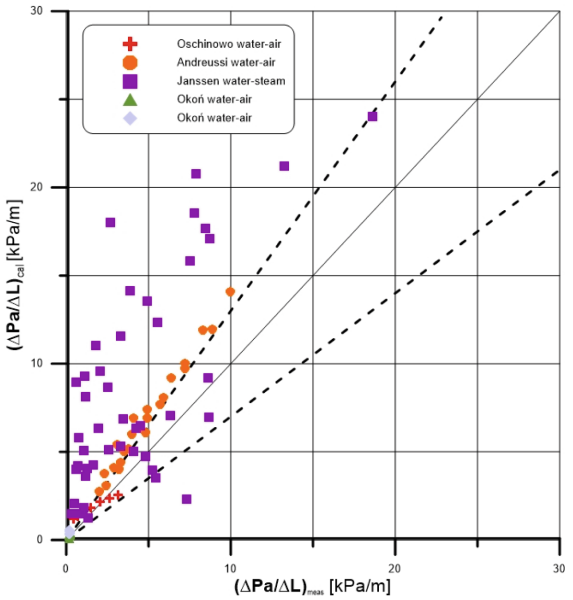

Fig. 5. Comparison of values of flow resistances measured and calculated with Chisholm's method

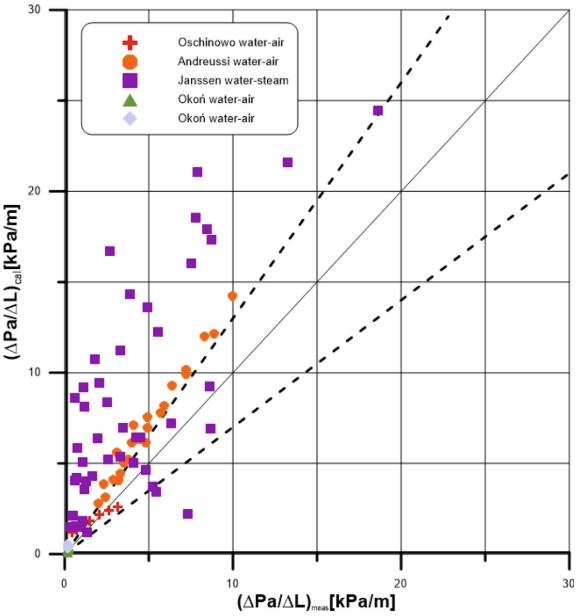

Fig. 6. Comparison of values of flow resistances measured and calculated with Kaminaga's method

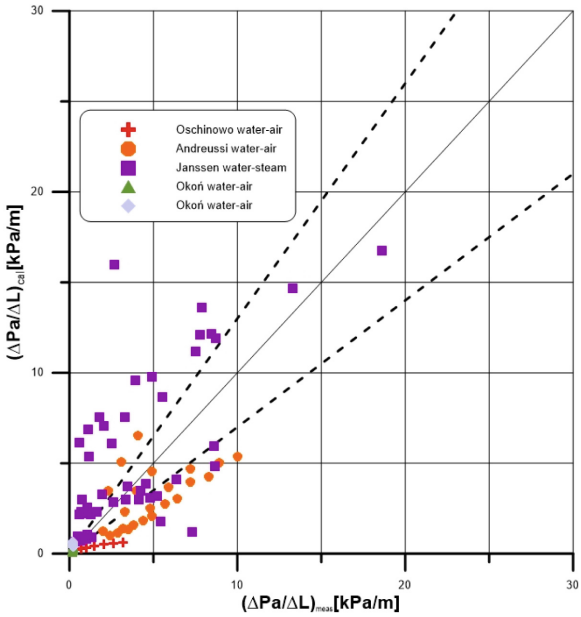

Fig. 7. Comparison of values of flow resistances measured and calculated with Lee and Lee's method

4 Conclusions

Determination of mixture flow resistances is one of the three most important parameters specifying two-phase flows. Exact determination of pressure losses is necessary for proper designing of the equipment where two-phase flows are used and for proper use of that equipment. Due to the essence of determination of flow resistances, a lot of researchers deals with determining pressure losses during flow. The literature reports a range of calculation methods proposed by them, which were developed on the basis of past tests and which are reasonable within the scope of such past tests. A lot of authors of pressure drop determination methods makes them dependent on hydrodynamic parameters and physicochemical properties of agents forming multi-phase mixtures.

As a result of the performed analysis of flow resistance calculation methods proposed by various authors, it should be noted that the calculated values do not overlap the results obtained in experiments within the obtained scope of pressure drop. In a wide range of changes in flow parameters and physicochemical properties of two-phase mixture ingredients, the highest accuracy of results was exhibited by Kim and Mudawar's method, so it can be recommended for calculating two-phase mixture flow resistances as the universal method.

References

Department of Process Engineering: Two-phase gas-liquid flows. No experiment data. Opole University of Technology (2004)

Dziubiński, M.: Hydrodynamika przepływu mieszanin dwufazowych ciecz-gaz [Hydrodynamics of two-phase gas-liquid mixture flow]. Lodz University of Technology (2005)

Kaminaga, F., Sumith, B., Matsumura, K.: Pressure drop in capillary tube in boiling two-phase flow. In: First International Conference on Microchannels and Minichannels, New York (2003)

Kim, S.M., Mudawar, I.: Review of databases and predictive methods for pressure drop in adiabatic, condensing and boiling mini/micro-channel flows. Int. J. Heat Mass Transfer **77**, 74–97 (2014)

Lee, H.J., Lee, S.Y.: Pressure drop correlation for two-phase flow within horizontal rectangular channels with small heights. Int. J. Multiphase Flow **27**, 783–796 (2001)

Mishima, K.M., Hibiki, T.: Some characteristics of air-water two-phase flow in small diameter vertical tubes. Int. J. Multiphase Flow **22**, 703–712 (1996)

Sun, L., Mishima, K.: Evaluation analysis of prediction methods for two-phase flow pressure drop in mini-channels. Int. J. Multiphase Flow **35**, 47–54 (2013)

Witczak, S.: Wrzenie naturalnych czynników chłodniczych podczas przepływu w kanałach i minikanałach [Boiling of natural coolants during flow in channels and minichannels]. Publishing house, Opole University of Technology (2013)

Application of Plant Design System on the Example of the ABE Mixture Separation

Paweł Dobrołowicz, Igor Ośkiewicz, and Szymon Woziwodzki(✉)

Institute of Chemical Technology and Engineering,
Poznan University of Technology, Poznań, Poland
szymon.woziwodzki@put.poznan.pl

Abstract. Process engineering design faces many challenges (BIM methodology or Industry 4.0). Paper presents the realization of the process installation project on the example of the separation of the acetone-benzene-ethanol mixture (ABE). The ABE mixture was separated in a processing system consisting of four distillation columns and a separator. The process simulation was performed in ChemCAD while the P&ID diagram, 3D installation model and 2D documentation were performed using the PDS software – Aveva Plant. It has been showing the data flow between process simulation software (process data) and the creation of final project documentation.

1 Introduction

Designing process installations nowadays has become a big challenge. On the one hand, designers are required to execute the project in the shortest possible time and, on the other hand, reduce project costs. This puts high demands for chemical engineers especially the 21st century is the time of mobile working using tablets, smartphones, and computers which requires chemical engineers to adapt to the new technologies. The development of technology leads to the introduction of the so-called Industry 4.0 which is usually called the fourth industrial revolution.

It involves the use of different digital technologies to connect consumers and manufacturers of products consisting of the Internet of Things (IoT), centralisation, unification, and harmonisation of various data in digital form (i.e. process and assets data), application of Best Practice (Elsevier 2017). This requires the chemical engineer to use appropriate design tools that allow the integration of process and non-process data, their exchange between different project groups (i.e. cloud sharing), the use of digital documentation from the process simulation stage to the 2D and 3D documentation release. Cooperation between designers is therefore essential, which will reduce the time and costs of projects (Bakker 2015).

This trend is undoubtedly part of the BIM (Building Information Modelling) methodology, which allows unification design documentation as well as managing and sharing information. It is introduced in many European countries and the UK is the leader.

© Springer Nature Switzerland AG 2020
M. Ochowiak et al. (Eds.): PAIC 2019, *Practical Aspects of Chemical Engineering*, pp. 37–46, 2020.
https://doi.org/10.1007/978-3-030-39867-5_5

Table 1. Exemplary PDS software

Producer	Software name	Description
Bentley	OpenPlant	P&ID, 2D and 3D models, Isometrics, Data Server Management, Supports
	AutoPLANT Modeller	Advanced 3D models of equipment, pipelines and raceways
	PlantWise	3D conceptual front-end engineering process plant designs
	AXSYS	2D conceptual plant designs
CADSchroer	MPDS	2D, 3D modelling, data management, global collaboration, P&ID, Piping, and steel design
Hexagon	Smart 3D	3D modelling
	SmartPlant P&ID	P&ID
	SmartPlant Electrical	Design of electrical installations
	SmartPlant Instrumentation	Specification, design and maintenance of all plant instrumentation and control systems
	SmartPlant Foundations	Data management, datasheets
	Smart Constructions	Constructions design
	Smart Materials	Materials management
	HxGN SDx	Assets management
	Isogen	Isometrics drawing
Autodesk	AutoCAD Plant 3D	P&ID, 3D modelling, pipelines, equipment, steel constructions, basic data management
Aveva	SimCentral, PRO/II, DYNSIM	Process simulation
	Aveva Diagrams	P&ID
	Aveva Engineering	Advance data management, datasheets and documentation
	Aveva Everything3D	3D modelling, integration of P&ID and 3D, marine and nuclear industry, mining
	Aveva Draw	2D drawings based on the 3D model
	AVEVA Electrical	Design of electrical installations
	Aveva Instrumentation	Specification, design and maintenance of all plant instrumentation and control systems
	Aveva Assets	Assets management
Alignex	Smap3D	2D/3D plant and piping design and isometrics
IT and Factory	CADISON	Project Planning, Cost Estimation & Engineering Information Management, PID, 3D modelling, electrical designing, pipe supports modeller, steel structures
Cadmatic	Cadmatic Diagram	P&ID
	Cadmatic 3D Plant Design	3D modelling
	Structural Modelling	Creating the structural parts of a project,
	Piping Design	Advance piping design
	Construction Data	Documents management

There are many software companies on the market however, the above requirements are compliant with Plant Design System (PDS). There are many PDS vendors in the software market. Some of these are shown in Table 1. The biggest ones like Aveva, Bentley, and Hexagon are trying to deliver the complete software i.e. in the field of process calculations, perform 2D and 3D documentation and managing of the installation or facility up to decommissioning.

This is a good direction, because designing and managing is performed in a one software platform and allows to limit the time lost to customise and convert various data formats in the project.

2 Project Workflows

The implementation of the project requires specific treatment. Figure 1 shows a typical simplified design schedule on the example of plant design for the separation of the ABE mixture. The first step is to discern the project (preliminary project study) in which the boundary conditions of the project are assessed, the requirements of the customer, geodetic conditions, etc.

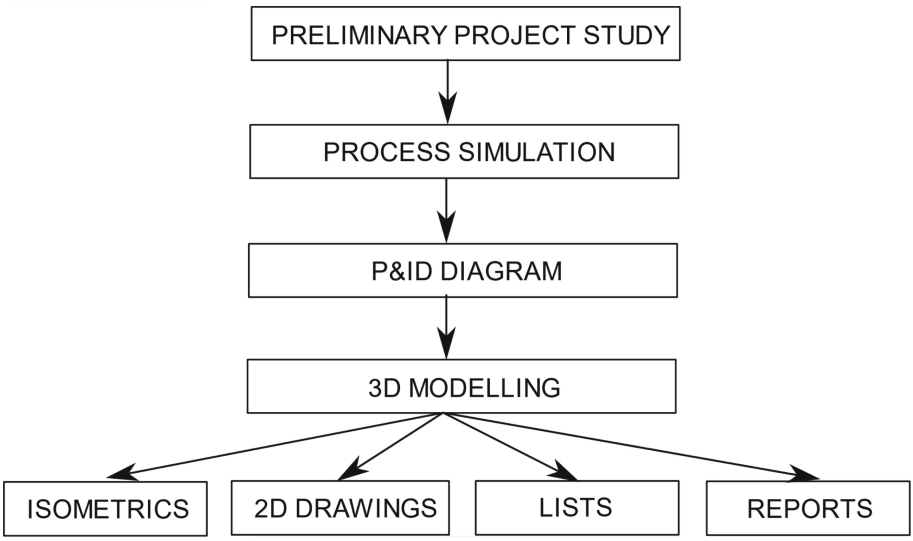

Fig. 1. Simplified project workflow

The second stage is the process simulation which results in a P&ID diagram and then a 3D model. The data contained in the 3D model allow generating documentation i.e. isometric drawing of pipelines, CAD drawings (2D), equipment list, nozzles, and other items.

2.1 Preliminary Project Study

The ABE is a mixture of acetone, butanol, and ethanol (Table 2) obtained by fermentation Sugars carried by the bacteria from the Clostridium culture (i.e. *Clostridium acetobutylicum* or *Clostridium beijerinckii*) (Kraemer et al. 2011). Currently, the ABE is obtained mainly by fermentation of raw materials as marine algae, corn waste, rice waste, etc. Due to its physical properties, the ABE can form an azeotrope between their individual components e.g. ethanol-water, butanol-water (Table 3) (Kujawska et al. 2015).

Table 2. Physiochemical properties

	Self-ignition temperature [°C]	Boiling temperature [°C]	Density [kg/m^3]	Dynamic viscosity [mPa·s]
Acetone	465	56	790	0.306
n-Butanol	345	117	810	2.54
Ethanol	425	78.4	810	1.074

Table 3. Azeotropes of ABE-water mixture [12]

Azeotrope	Temperature of azeotrope [°C]	Water mass fraction in the azeotrope	Type
Water-ethanol	78.1	0.044	Homogenous
Water-n-butanol	91.7–92.4	0.38	Heterogenous

The ABE mixture can be separated by several techniques. The most important ones are distillation, adsorption, crystallisation, extraction, pervaporation (Kujawska et al. 2015).

The designed installation is used to separate N-butanol from a water mixture acetone–ethanol–N-butanol (ABE) using distillation. It is assumed that the purpose of the installation is to receive n-Butanol of a purity of at least 0.99 (mole frac.).

Table 4 shows the presumed compositions of feed, its flux and the expected composition of the distillate (Patrascu et al. 2017).

Table 4. Project assumptions

Azeotrope	Feed mole fraction	Distillate mole fraction	Feed stream kmol/h
Water	0.97	0.99	1000
n-butanol	0.018	<0.01	
Acetone	0.01	<0.01	
Ethanol	0.002	<0.01	

The installation consisted of four distillation columns and a separator.

2.2 Process Simulation

The ChemCAD process simulation software was used in this stage. In the first stage, the PFD diagram of the installation was created. In this step, the basic conditions of simulation have been set (i.e. streams compositions). After that, the pipelines, pumps, valves were added to create a P&ID diagram (Fig. 2).

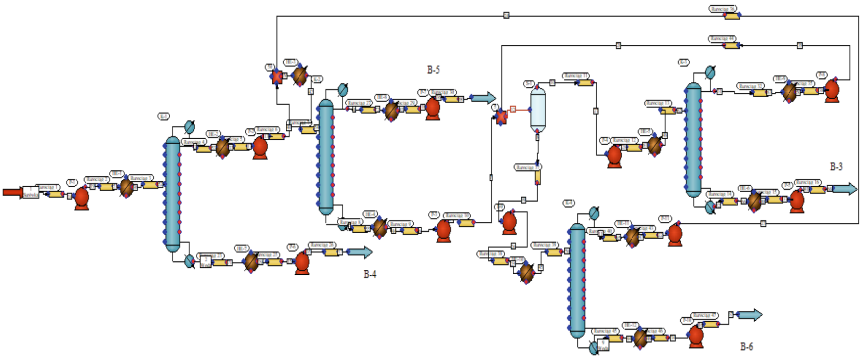

Fig. 2. Simulation diagram – ChemCAD (Dobrołowicz and Ośkiewicz 2018)

In the designed simulation, the feed is pumped by the P-1 pump to the heat exchanger HE-1, which is heated to a temperature of T = 102.06 °C and introduce to the distillation column K-1. The column shall separate the water from the other components which are discharged from the top of the column. The removed water is received from the bottom of the distillation column K-1 and after cooling in the heat exchanger HE-7 transported by the P-6 pump to the storage tank B-4 (Dobrołowicz and Ośkiewicz 2018).

The distillate leaving the distillation column K-1 is cooled in the heat exchanger HE-2 and then transported by the pump P-2 to the column K-2. In this column, acetone is removed from the mixture. The feed introduced into the K-2 column is heated in the HE-3 heat exchanger to boiling temperature (T = 100.54 °C). The lighter fraction formed after distillation in the K-2 column is propanone, which after cooling in the heat exchanger HE-8 is transported by the P-7 pump to the storage tank B-5 (Dobrołowicz and Ośkiewicz 2018). The heavier fraction remaining after distillation in the K-2 column, which is a mixture of water, n-butanol, ethanol and small quantities of propanone is cooled in the HE-4 heat exchanger and then transported by the P-3 pump to the S-1 separator. Between the P-3 pump and the S-1 separator, the upper fraction from the distillation K-3 is returned. The organic phase after separation from the water on the S-1 separator is transported by the pump P-4 to the K-3 distillation column (Dobrołowicz and Ośkiewicz 2018).

The task of the K-3 distillation column is to separate N-butanol from the ABE mixture, which due to the highest boiling point (T = 117 °C) will accumulate at the bottom of the K-3 column as a liquid. Before inputting to column K-3, the feed is heated to boiling point (T = 99.47 °C) in the heat exchanger HE-5. The lighter fraction

from the K-3 column is returned between the P-3 pump and the S-1 separator. A mixture contained in a stream of exhaust fluid consisting of N-butanol contaminated with admixtures of other components of the mixture after leaving the distillation column the K-3 is chilled to a temperature of T = 40 ° C in the heat exchanger HE-6 and then pumped by the P-5 pump to the B-3 tank, where the final product of the process is collected. The aqueous phase consisting of water, n-butanol, ethanol, and acetone is separated in the S-1 separator is pumped by the P-9 pump and then heated to boiling temperature (T = 100.09 °C) in the HE-10 heat exchanger. Next, the stream goes to the distillation column K-4, whose task is to separate water from residues of N-butanol. N-Butanol leaving the top of K-4 column is returned and entered between the distillation column K-1 and K-2. A stream of exhausted fluid which is water with small admixtures of N-butanol, after distillation in the K-4 column, is cooled in the heat exchanger HE-12 to a temperature T = 40 °C and then transported by the P-10 pump to the storage vessel B-5 (Dobrołowicz and Ośkiewicz 2018).

2.3 P&ID Diagram – AVEVA Diagrams

The next stage of work was to prepare the P&ID diagrams. For this purpose, the AVEVA Diagrams software was used. This software is based on a central database (Dabacon) in which whole project data are collected i.e. from process data as well as from the electrical and construction branches (Fig. 3). This solution facilitates data flow between different groups of designers and branches.

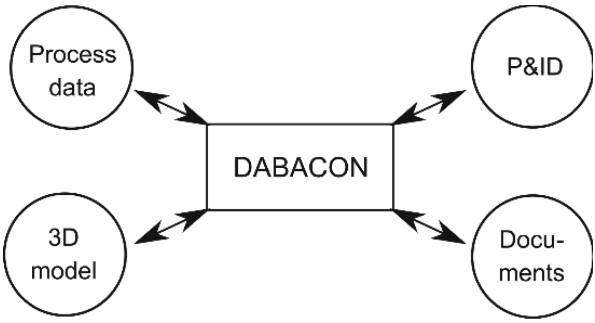

Fig. 3. Relations between software modules

Hundreds of process data are generated during the simulation. In order to introduce to the central database are imported into the AVEVA Engineering software. It deals with the management of project data as well as the work of designers, which allows assessing the stage of project completion. Such a solution facilitates data control e.g. in a situation where the project changes required by the customer.

From the AVEVA Engineering, data can be shared with other programs and branches (within a single software platform) using the Compare & Update mechanism.

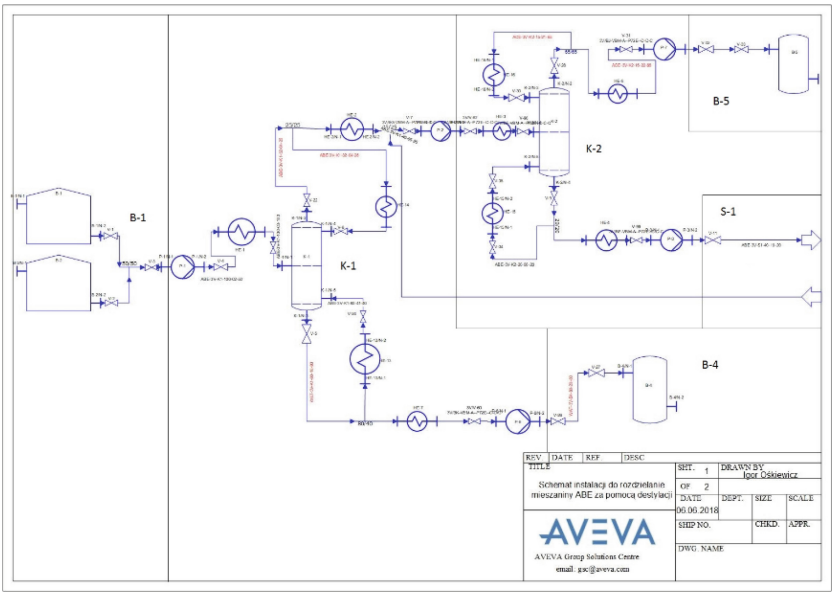

Fig. 4. P&ID diagram 1 (Dobrołowicz and Ośkiewicz 2018)

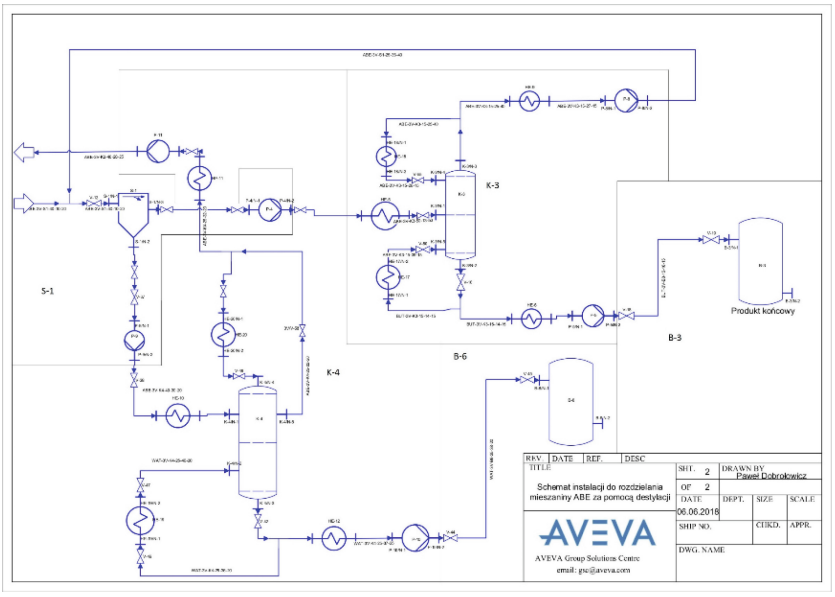

Fig. 5. P&ID diagram 2 (Dobrołowicz and Ośkiewicz 2018)

The process data introduced to AVEVA Engineering is then imported by process engineers into AVEVA Diagrams where they perform the P&ID diagrams. In the sample project, the P&ID diagrams consist of two parts which facilitate and simultaneously accelerates the work of designers.

The P&ID diagram has been divided into the following areas: B-1, K-1, B-5, S-1, B-4 (Fig. 4) and S-1, K3, K-4, B-6 and B-3 (Fig. 5). The completed P&ID diagrams had an intelligent passage which is set by OFF Page connectors and allow to view the entire diagram installation in continuous mode. Also, the statuses are used to control workflow and advancement of the project as well as the control of documentation (P&ID schemes) i.e. their subsequent version. Process data can also be presented in datasheets. The process engineer has access to them both from the AVEVA Diagrams and AVEVA Engineering.

Work on the P&ID diagram does not end until the project is released to the customer. For this reason, in order to save time, the software allows sharing parts of the P&ID diagram with other branches, i.e. a single branch or pipeline between two types of equipment.

This allows mechanism Set Release Status instruction. The shared part of the P&ID allows starting a working pipeline or equipment designers.

2.3.1 3D Model – AVEVA Everything 3D

Preparation of the P&ID diagram allows performing a 3D model of the projected installation. This model was made using AVEVA Everything 3D software (Fig. 6)

It should be noted that this model has the purpose to show the reservation of 3D space under equipment's, pipelines, structures, buildings, etc. Therefore, 3D models are not perfect. If you need to make accurate models, you should use other software such as SolidEdge or Autodesk Inventor.

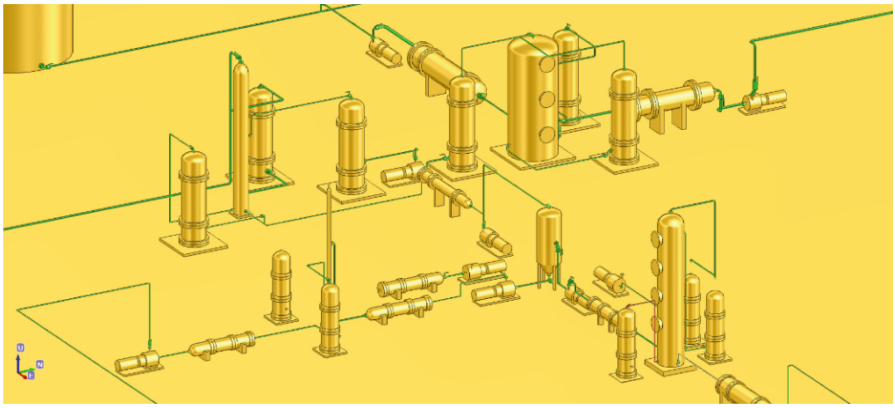

Fig. 6. 3D model (Dobrołowicz and Ośkiewicz 2018)

The 3D model is based on the information contained in the P&ID diagrams. It is imported from AVEVA Diagrams by the AVEVA 3D Integrator and the role of the designer is to give the appropriate 3D geometry, the arrangement of types of equipment and design of pipelines between them. However, this mechanism does not allow to control changes in a project. To do this, the Compare & Update mechanism should be used.

For an optimal space utilisation, it was decided to place the distillation columns on the vertices of a trapezoid and the S-1 separator in the centre of the longer base (Fig. 7). During the arrangement of the installation equipment's, the flammability of the propanone and water mixtures and the overall explosiveness of acetone was considered.

The storage tank B-5 with acetone is located at a safe distance from the other installation parts (approximately 50 m). Other storage tanks with the main and side products are located at 10 m (Moran 2015).

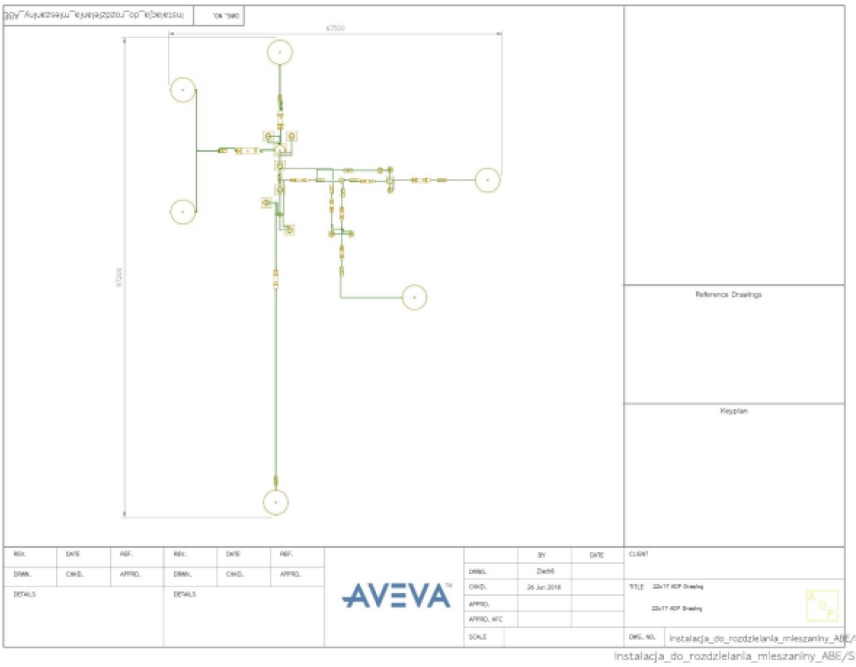

Fig. 7. Equipment location (Dobrołowicz and Ośkiewicz 2018)

Built-in pipe routing mechanisms were used in the construction of the piping model. No calculation of the pipe supports was performed, and no model was created. However, it should be noted that AVEVA E3D has bases of supports as well as steel structural components.

The final stage of the project was the implementation of project documentation. It consisted of equipment lists, piping lists, valve lists, nozzle lists, isometric drawings of pipelines, CAD drawings of installations, CAD drawings of equipment (AVEVA Draw). These drawings were made based on the previously prepared 3D model installation.

3 Conclusions

Paper present application of the PDS software (Plant Design System) on the example of separation of the ABE mixture. It has been presented the workflow in the project. In the first step, process simulation was performed. The next step was to export process data to the PDS software. Authors used the AVEVA Plant software system. Process data were collected in AVEVA Engineering and shared via the Dabacon main database to AVEVA Diagrams (P&ID diagram), AVEVA Eveything3D (3D modelling) and AVEVA Draw (2D drawings).

PDS software is a useful tool in process designing. Especially use of one system software can reduce wasting time in data exchange between various software. However, data import from process simulators still is time-consuming because the PDS software cannot perform process simulation. The use of external software is favourable.

Acknowledgements. This work was supported by the Polish Ministry of Science and Higher Education. (Grant no. 03/32/SBAD/0902).

Many thanks to Stefan Dzielendziak and Grzegorz Jabłoński from AVEVA Gmbh Poland for making the software available.

References

Industry 4.0: How Chemical Manufacturers Can Rise to the Challenges. Elsevier, Elsevier R&D Solutions for Chemicals, White papers (2017). https://chemical-materials.elsevier.com/chemical-manufacturing-excellence/chemical-companies-adapt-industry-4-0/. Accessed 16 Oct 2018

Bakker, S.: Optimising the design-to-cost cycle. Chem. Eng. **12**, 34–37 (2015)

Kraemer, K., Harwardt, A., Bronneberg, R., Marquardt, W.: Separation of butanol from acetone–butanol–ethanol fermentation by a hybrid extraction–distillation process. Comput. Chem. Eng. **35**, 949–963 (2011)

Kujawska, A., Kujawski, J., Bryjak, M., Kujawski, W.: ABE fermentation products recovery methods—a review. Renew. Sustain. Energy Rev. **48**, 648–661 (2015)

Patraşcu, I., Bîldea, C.S., Kiss, A.A.: Eco-efficient butanol separation in the ABE fermentation process. Sep. Purif. Technol. **177**, 49–61 (2017)

Moran, S.: Applied Guide to Process Design. Butterworth-Heinemann, Oxford (2015)

Dobrołowicz, P., Ośkiewicz, I.: Projekt instalacji do rozdzielania mieszaniny ABE (in polish). Poznan University of Technology, Poznan (2018)

Cascade Impactor Study of Aerosolization Process During Passive Dry Powder Inhaler Performance Under Unsteady Versus Steady Flow Conditions

Agata Dorosz[1(✉)], Paula Martínez Cánovas[2], and Arkadiusz Moskal[1]

[1] Department of Chemical and Process Engineering, Warsaw University of Technology, Warsaw, Poland
agata.dorosz.dokt@pw.edu.pl
[2] Faculty of Chemistry, University of Murcia, Murcia, Spain

Abstract. The passive Dry Powder Inhalers (DPIs) rely on the human's inspiratory airflow and negative pressure drop to create turbulent energy environment inside the inhaler. It induces the forces provided by the flow field to fluidize and disperse the drug aggregates into respirable aerosol, exposed to fluid motions. Hence, aerosolization, transport and deposition phenomena with respect to unsteady flow conditions constitute a subject of biomedical research applying methodology of chemical and process engineering. In vitro pharmacopoeia methods – inertial impaction sizing techniques – have been adopted to assess the aerodynamic performance of powder drug-device platforms. The necessity of investigating time-dependent breathing profiles during operation of DPIs renders conventional testing insufficient. Recently, a method using cascade impactor, mixing inlet and breathing simulator has been developed. The hypothesis of the study was proven to be true: the dynamics of the flow conditions influence the aerodynamic particle size distribution of a drug-passive DPI platform. Research efforts focused on mimicking DPI drug delivery with time-varying flow profile may help to develop better *in vitro – in vivo* correlation (IVIVC) when linking the information gained from compendial testing to clinical efficacy. Further insight of quality parameters in time series is desired to better understand the dynamics of aerosolization process.

1 Introduction

Nowadays all possible efforts at a worldwide level have been taken to reduce the burden of morbidity, disability and premature mortality related to chronic respiratory diseases, especially chronic obstructive pulmonary disease (COPD) and asthma. In both cases the therapy significantly improves patients' inferior quality of life. While COPD is progressive and cannot be cured, its symptoms may be relieved by an appropriate treatment that decreases the risk of death. Medication can help to attain satisfactory and long-lasting asthma control.

A basis for the treatment of chronic respiratory diseases is the delivery of inhalable pharmaceuticals via the pulmonary route, where dry powder inhalers (DPIs) provide a

© Springer Nature Switzerland AG 2020
M. Ochowiak et al. (Eds.): PAIC 2019, *Practical Aspects of Chemical Engineering*, pp. 47–57, 2020.
https://doi.org/10.1007/978-3-030-39867-5_6

notable opportunity to aerosolize the powder for further transport and deposition of aerosol particles in the lower respiratory tract. The principle of operation of the most marketed DPIs is to breath-activate the dose, since they rely both on the human's inspiratory airflow (Q) and negative pressure drop (ΔP) achieved at the mouthpiece to create adequate turbulent energy environment inside the inhaler (Azouz and Chrystyn 2012). It induces the forces provided by the flow field to fluidize and disperse the drug aggregates into respirable aerosol. The dose emission is then flow dependent, while dynamics of aerosol transport and deposition are then governed by general physical law and are determined by the non-steady local aerodynamic conditions in the whole respiratory tract. The airways together with lungs act as a separation system for particles (aerosol classifier). The smaller particles are able to penetrate deeper into alveolar region comparing to large one which deposit mainly in throat and bronchial tree. Hence, aerosolization, transport and deposition phenomena with respect to unsteady flow conditions constitute a specific subject of biomedical research related to the optimization of aerosol therapy.

2 Process Variables for Drug Powder Delivery by Inhalation

In accordance with the methodology of chemical and process engineering, all process variables responsible for efficient drug administration need to be identified. The two key factors are technical. First one is drug formulation, associated with interparticle interactions, which can be adjusted by selection, control of powder manufacturing and post-process conditioning methods. Second one is inhaler design (the interaction between device resistance and inhalation flow is related to the degree of powder dispersion, as discussed above). Other factors are patient-related, for example: the inhaled air volume, human's throat geometry and, last but not least, the factor of the highest variability and uncertainty – the inhalation technique with its varying inspiratory flow (Sosnowski 2018). The airflow through the device must match the inhaling force of the patients. The real issue is to deal with the interplay between the aforementioned process variables, leading to the high complexity of the process evaluation.

3 Indicators of the Efficacy of Dry Powder Drug Delivery

Not only the emitted drug dose itself, but also the spatial deposition distribution of drug particles within desired bronchial tree regions is a crucial piece of information. It can enlighten the interpretation of clinical outcome parameters when assessing the efficacy of the treatment. From the beginning of development of inhaler-drug platforms, it was clear to aerosol-minded researchers that, for particles to collected within different lung zones, these had to be small (in size). However, only the aerodynamic particle size distribution (APSD) allows to foresee the behavior of particles in the aerosol flow field, since the aerodynamic diameter constitutes the diameter of a standard density

(1000 kg/m^3) sphere that has the same gravitational settling velocity as the particle in question. The influence of its shape and density is also taken into account. The knowledge of the size distribution provides the ability to predict of the amount of drug that will impact in the oropharynx (particles larger than 5 μ in diameter) and helps to define where the smaller particle fractions will deposit following inhalation (particles in the range of 1 to 5 μ).

Based on the aerodynamic PSD it is possible to find the crucial indicators of the quality of drug aerosol, prerequisite for the optimization of drug delivery:

- the indicator for lung deposition, the dose of particles smaller than 5 μ – fine particle dose (FPD),
- the percentage of particles smaller than 5 μ – fine particle fraction (FPF),
- mass median aerodynamic diameter (MMAD),
- the indicator of systemic delivery – total emitted dose (TED).

Therefore, it has been a highly desirable goal to develop and properly adapt a comprehensive *in vivo* predictive *in vitro* method for process analysis in terms of aerosol particle separation on the basic of aerodynamic size ((Marple et al. 2003); (Mitchell and Nagel 2004); (Olsson et al. 2013)).

4 Conventional *in Vitro* Testing of Medicinal Aerosols

For the sake of conventional *in vitro* testing of medicinal aerosols, the particle size distribution methodology was adopted from health protection fields. A group of apparatuses has been developed, where classification is based on the differing inertia of the incoming particles of various sizes. For a given inertial classifier, construction and value of flow rate through the test setup determine the cut off points between measured size ranges deposited at the consecutive separation stages. These so-called multi-stage (cascade) impaction separators have become a natural instrument of choice to size-analyze inhaler-derived aerosols within the critical range from 0.5 to 5 μ, for three predominant reasons (Mitchell and Nagel 2004).

First, cascade impactors measure aerodynamic particle size. Second, by using a specific drug assay, cascade impactors allow to size-fractionate the incoming aerosol weighted in terms of the active pharmaceutical ingredient (API) mass (the actual drug). Thus, the APSD is not confounded with any non-drug material that may be in the sample (drug carrier from the powder blend etc.). Third, cascade impactors measure the entire dose, while the APSD measured on a sub-sample may not be representative. These advantages of inertial impaction sizing makes other methods insufficient, for example in comparison with techniques based on light scattering or time-of-flight principle. The latest impactor, the Next Generation Impactor (NGI) may be recognized as a gold standard for evaluation of DPI inhalers of different resistance values, since it enables comparison at the same pressure drop, hence at different flow rates (from the range of 30 to 100 dm^3/min and down to 15 dm^3/min).

5 *In Vitro – in Vivo* Correlation (IVIVC) and Development of Modified *in Vitro* Testing of Medicinal Aerosols Under Realistic Unsteady Flow Conditions

Research efforts to date have been focused on developing better *in vitro – in vivo* correlation (IVIVC) and bioequivalence when linking the information gained from compendial DPI testing to clinical efficacy (e.g. (Clark and Borgstrom 2002), (Delvadia et al. 2016), (Mitchell et al. 2007), (Sosnowski 2018), (Wei et al. 2017, 2018)). Numerous reports abundantly confirmed the significance of the flow rate profile. Dynamics of inhalation was proven to affect not only the deposition and the total emitted dose ((Chrystyn et al. 2015); (Colthorpe et al. 2013)). It also influences the time course and the time duration of the aerosol emission along with aerosol characteristics (measured in time series with optical methods) after being dispersed from the passive dry powder inhaler ((Dorosz et al. 2016); (Ung and Chan 2016); (Ziffels et al. 2015)).

The necessity of investigating time-dependent breathing profiles during *ex vivo* operation of different DPIs renders traditional inertial impaction method inadequate. Henceforth a new method using cascade impactor, mixing inlet and breathing simulator has been developed to consider delivery efficiency and aerodynamic performance of drug-device platforms under realistic, unsteady flow conditions possible for a given inhaler design (the method was described in e.g. (Chrystyn et al. 2015), (Colthorpe et al. 2013), (Miller et al. 2000), (Nadarassan et al. 2010)). A constant flow rate can be maintained through the cascade impactor, whilst a zero flow is drawn through the inhaler *in situ*. It is allowed by providing supplementary compressed air into the cascade impactor of the same flow value as the vacuum that passes through the sizing apparatus. A profile of a time-varying flow can be generated on demand through the DPI by a computer-controlled breathing simulator. The smooth merging of the two flow regimes (central aerosol-laden stream and surrounding sheath stream of constant flow) is achieved utilizing the above-mentioned mixing inlet.

6 Objective of the Current Study

The current paper presents a comparative *in vitro* study on the delivery efficiency and aerodynamic performance of drug-DPI device platforms, conducted using inertial classification method under unsteady versus steady flow conditions. The aim of the investigation was to verify the hypothesis: the dynamics of the flow conditions affect collectively the delivered dose uniformity and aerodynamic particle size distribution (APSD) of a model drug-passive DPI platform.

7 Materials and Methods

7.1 Development of Model Drug Powder Blend

The fabrication of lactose-based model drug powder blend was accomplished in two steps. First, the model API powder was produced utilizing model B-290 laboratory-scale spray-dryer (Buchi Labortechnik AG, Flawil, Switzerland). The feed solution (2% w/w) contained sodium fluoride (NaF) dissolved in ultrapure water. Spray-drying parameters were adjusted to obtain satisfactory product. The final process variables' values are presented in Table 1.

Table 1. Spraying conditions

Feed flow rate [ml/min]	3
Inlet temperature [°C]	120
Nozzle gas flow rate [m^3/h]	0.819
Aspirator capacity [m^3/h]	13

Secondly, milled lactose carrier (dedicated for inhalation pharmaceuticals) was selected to acquire the model powder blend for further utilization in the research – Lactohale® 200, DFE Pharma (Germany). The mixture (13 g, 20% w/w) of spray-dried NaF and carrier was prepared by turbulent tumbling mixing for 30 min at 75 rpm (Turbula T2F (Bachofen AG, Switzerland)). The model powder drug blend met the USP homogeneity criterion regarding the uniformity of the inhalation blend when exhibiting %CV value equal to 4.89% (less than 6%).

7.2 Powder Aerosolization with New Generation Cyclohaler (NGC Inhaler)

Approx. 20 mg of blend was weighed into capsules (Capsugel, USA) and dispersed from the New Generation Cyclohaler (NGC). This readily available, passive inhaler is a representative of the low-mid resistance DPIs (0.055 $hPa^{0.5}min/dm^3$, based on the own research of the authors). The airflow streams entered the dispersion chamber through two opposite tangential inlets, leading to the spinning movement of the punctured capsule around its minor axis. The loading was centrifugated out of the capsule through the holes, allowing to be further aerosolized.

7.3 Selection of Flow Profiles

Four different flow profiles were chosen to experimentally investigate aerodynamic performance of drug-DPI device platform both under unsteady and steady flow conditions (Fig. 1).

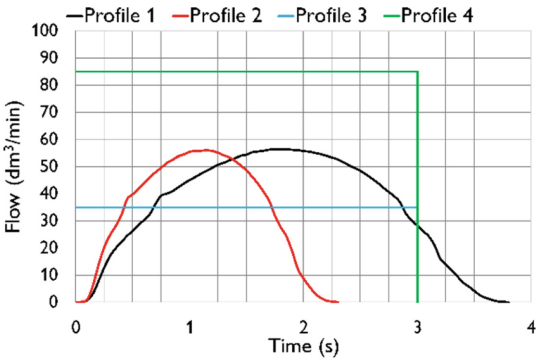

Fig. 1. Flow profiles tested throughout the study

Prior to the effects of realistic patient inhalation profiles on the aforementioned performance being assessed, two unsteady profiles 1 and 2 were utilized. These profiles mimic different ex vivo operation of DPI inhalers. Profile 2 is less deep, but a good deal more forceful and quicker than profile 1. Both of unsteady profiles are characterized by the same value of peak flow rate. The predefined time courses of profiles 1 and 2 were supplied in the experimental setup by the high capacity breathing simulator ASL 5000 XL (IngMar Medical, United States). Afterwards, two steady profiles were selected to be induced in the setup by the vacuum pump for further steady-state study. Profile 3 represents an averaged, constant flow rate calculated for the previous unsteady profiles. Profile 4 constitutes a steady flow rate providing a constant pressure drop value (in the DPI inhaler) equal to 4 kPa, as it is recommended by pharmacopeia to test inhalers of various resistances.

Defined airflow conditions for investigated profiles are shown in Table 2.

Table 2. Summary of the airflow conditions investigated throughout the study

	Profile 1	Profile 2	Profile 3	Profile 4
Total volume of inhaled aerosol [dm^3]	2.193	1.283	1.75	4.25
Whole time duration of the inhalation [s]	3.8	2.3	3.0	3.0
Peak flow rate [dm^3/min]	55	55	35	85

7.4 Experimental Setups for Conventional and Modified in Vitro Aerosol Sizing by Inertial Impaction

Figure 2 and 3 provide schematic designs of the two methods utilized in the study – the conventional and the modified inertial impaction techniques, respectively. In both cases the flow rate of air drawn through the NGC inhaler was measured in real-time during the experiments (using mass flow meter).

The first steady-state part of the study encompassed simulating two fixed flow profiles 3 and 4. These profiles were employed in *in vitro* testing using the standard NGI setup presented in Fig. 2 (Apparatus 5 (The United States Pharmacopoeial Convention 2007)). For both mentioned cases, the NGI impactor operated routinely at

constant flow rates of the tested profiles. In the second part of the study taken under unsteady flow conditions, time-varying profiles 1 and 2 were tested using the modified experimental setup depicted in Fig. 3, with supplementary flow rate of 85 dm^3/min. For all analyzed cases the model powder blend was aerosolized using NGC inhaler and discharged upon studied flow profiles 1 to 4 to the respective setup. Prior to each experimental run, ten capsules with model drug powder blend were used.

In order to assay the cumulative mass against cut-off diameter of the respective stages, the analysis of particles was done by recovering of collected samples using ultrapure water (25 ml per NGI stage, USP port and preseparator). This procedure was followed by the conductometric measurement (using conductivity meter HI 2030-02 edge (Hanna Instruments, USA)). The adequate contributions of particles were determined as the percentage of gravimetrically quantified total powder mass exiting the capsule and the inhaler device.

The APSD results were then expressed by collecting data of relevance to lung delivery: metered dose (MD), emitted dose (ED), fine particle dose (FPD), fine particle fraction (FPD), mass median aerodynamic diameter (MMAD), span (the measure of aerosol polydispersity) and geometric standard deviation (GSD).

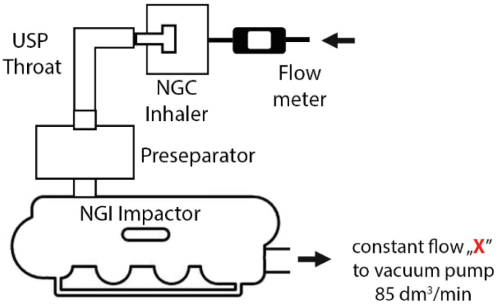

Fig. 2. Experimental setup for the conventional NGI investigation under steady flow conditions

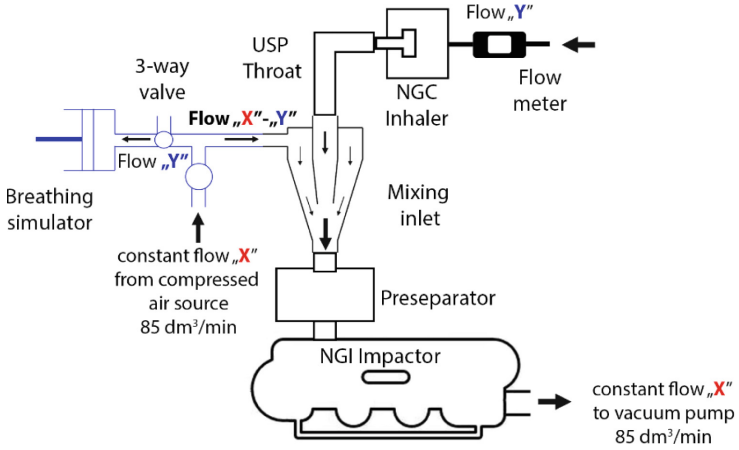

Fig. 3. Experimental setup for the modified NGI investigation under unsteady flow conditions

8 Results and Discussion

8.1 Aerodynamic Performance of Model Drug Powder Blend-DPI Inhaler Under Unsteady Versus Steady Flow Conditions

In the following section, the dose uniformity and aerodynamic particle size distribution of a drug-passive DPI platform for all studied flow profiles were discussed. The cumulative contributions of particles in APSD as the datasets were plotted against the particle size values, as presented in Fig. 4. The main observation was as follows: for unsteady profiles (1 and 2) and steady profile 4 (of 85 dm^3/min) the shapes of obtained distributions were almost identical. However, these flow conditions resulted in different DPI performances when compared to the steady profile 3 (of averaged 35 dm^3/min). Furthermore, the aerosol produced upon profile 3 appears to be of somewhat poorer quality (bigger particles) than in case of other profiles. Interestingly, it was noted that relatively high standard deviation values were achieved for profile 3. This could be attributed to the aerosolization of low stability, since the low value of 35 dm^3/min may not be efficient to trigger a reproducible, thus satisfactory aerosol dispersion.

The APSD results are supported by the findings presented in Table 3, summarizing the values of indicators of the efficacy of aerosol delivery under different flow conditions – profiles 1 to 4. At first, results concerning time-varying profiles 1 and 2 were compared. The results indicate that the DPI user is capable of receiving aerosol of similar characteristics, despite the differences in the time course, time duration of inhalation maneuver and the inhaled volume for both profiles. Table 3 also reveals that in case of profile 4 (of 85 dm^3/min), the analyzed parameters exhibited similar values (MMAD, span, GSD) or barely higher values (FPF, FPD) when compared with profiles 1 and 2. This observation decidedly confirms the formerly stated allegation (Dorosz et al. 2016), that the initial part of the inhalation maneuver is crucial for the overall process of DPI drug delivery due to the strong aerodynamic effects of unsteadiness acquired from relatively small values of flow rates. Based on the findings attained for profile 4 it was found that the distinctly higher ED along with the resulting higher FPD were attributed to the value of the drawn air volume being a good deal higher than for the other studied profiles (1, 2 and 3).

Profile 3 resulted in the highest value of MMAD and the lowest values of ED, FPD and FPF. In reality, patients do not inhale with a sudden, steady flow rate, so for compendial impaction testing a compromise is reached whereby studies are undertaken at a chosen constant flow rate. The observed discrepancies between the results for unsteady and the averaged, steady flow conditions raise a question whether the mid-inhalation flow rate may be representative of the highly time-varying inhalation flow profile.

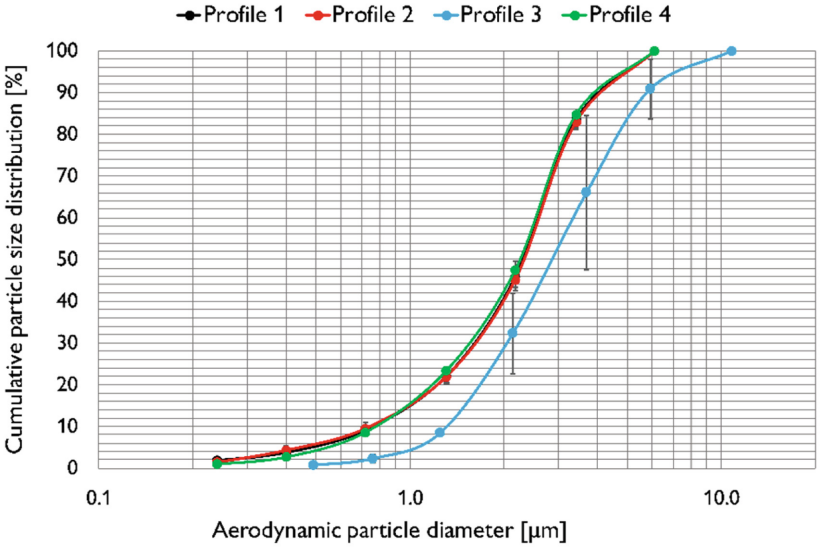

Fig. 4. Cumulative particle size distribution for all studied profiles

Table 3. Indicators of the efficacy of dry powder drug delivery for all studied profiles

Quality parameter (mean value)	Profile 1	Profile 2	Profile 3	Profile 4
MD [mg]	4.992	5.003	4.983	4.993
ED [mg]	3.494	3.505	3.381	4.259
FPD [mg]	2.820	2.664	2.090	3.095
FPF [mg]	56.490	53.257	41.959	61.984
MMAD [µm]	2.297	2.314	2.990	2.249
Span [−]	1.395	1.416	1.505	1.372
GSD [−]	1.823	1.831	1.757	1.823

9 Conclusions

It was proven to be true that the dynamics of the flow conditions influence the delivered dose uniformity and aerodynamic particle size distribution of a drug-passive DPI platform. Obtained results show that steady profile recommended by pharmacopeia (Profile 4), of flow rate providing a constant pressure drop value (in the DPI inhaler) equal to 4 kPa, can lead to overestimating emitted dose MD and fine particles fraction FPF parameters. However, the results obtained for Profile 1 and Profile 2 are very similar and it is very difficult to conclude about influence of shape of the breathing curve on the drug release process. Research efforts focused on mimicking DPI drug delivery with time-varying flow profile may help to develop better *in vitro – in vivo* correlation (IVIVC) when linking the information gained from compendial DPI testing to clinical efficacy in reality. Further insight of quality parameters in time series should

be gained to better understand the dynamics of aerosolization process. In the future, more realistic protocols of DPI testing, including cascade impactor sizing under unsteady flow rate may be desired as the next attempt to improve the clinical significance of the obtained results.

Acknowledgments. This study was supported by the National Science Centre, Poland (project no. 2017/25/N/ST8/00809).

References

Azouz, W., Chrystyn, H.: Clarifying the dilemmas about inhalation techniques for dry powder inhalers: integrating science with clinical practice. Prim. Care Respir. J. **21**(2), 208–213 (2012)

Chrystyn, H., Safioti, G., Keegstra, J.R., et al.: Effect of inhalation profile and throat geometry on predicted lung deposition of budesonide and formoterol (BF) in COPD: an in-vitro comparison of Spiromax with Turbuhaler. Int. J. Pharm. **491**(1–2), 268–276 (2015)

Clark, A.R., Borgström, L.: In vitro testing of pharmaceutical aerosols and predicting lung deposition from in vitro measurements. In: Bisgaard, K., O'Callaghan, C., Smaldone, G.C. (eds.) Drug Delivery to the Lung, pp. 105–142. Marcel Dekker, New York (2002)

Colthorpe, P., Voshaar, T., Kieckbusch, T., et al.: Delivery characteristics of a low-resistance dry-powder inhaler used to deliver the long-acting muscarinic antagonist glycopyrronium. J. Drug Assess. **2**(1), 11–16 (2013)

Delvadia, R.R., Wei, X., Longest, P.W., et al.: In Vitro tests for aerosol deposition. IV: simulating variations in human breath profiles for realistic DPI testing. J. Aerosol Med. Pulm. Drug Deliv. **29**(2), 196–206 (2016)

Dorosz, A., Penconek, A., Moskal, A.: In vitro study on the aerosol emitted from the DPI inhaler under two unsteady inhalation profiles. J. Aerosol Sci. **101**, 104–117 (2016)

Marple, V.A., Hochrainer, D., Roberts, D.L., et al.: Next generation pharmaceutical impactor (a new impactor for pharmaceutical inhaler testing). Part I: design. J. Aerosol Med. **16**(3), 283–299 (2003)

Miller, N.C., Maniaci, M.J., Dwivedi, S.K., et al.: Aerodynamic sizing with simulated inhalation profiles: total dose capture and measurement. In: Dalby, R.N., Byron, P.R., Farr, S.J., et al. (eds.) Proceedings of Respiratory Drug Delivery VII, United States of America, May 2000, vol. 1, pp. 191–196. Virginia Commonwealth University (2000)

Mitchell, J.P., Nagel, M.W.: Particle size analysis of aerosols from medicinal inhalers. KONA Powder Part. J. **22**, 32–65 (2004)

Mitchell, J., Newman, S., Chan, H.K.: In vitro and in vivo aspects of cascade impactor tests and inhaler performance: a review. AAPS PharmSciTech **8**(4), 237–248 (2007)

Nadarassan, D.K., Assi, K.H., Chrystyn, H.: Aerodynamic characteristics of a dry powder inhaler at low inhalation flows using a mixing inlet with an Andersen Cascade Impactor. Eur. J. Pharm. Sci. **39**, 348–354 (2010)

Olsson, B., Borgström, L., Lundbäck, H., Svensson, M.: Validation of a general in vitro approach for prediction of total lung deposition in healthy adults for pharmaceutical inhalation products. J. Aerosol Med. Pulm. Drug Deliv. **26**(6), 355–369 (2013)

Sosnowski, T.R.: Powder particles and technologies for medicine delivery to the respiratory system: challenges and opportunities. KONA Powder Part. J. **35**, 122–138 (2018)

The United States Pharmacopoeial Convention: United States Pharmacopoeia Thirtieth Revision - <601>Aerosols, nasal sprays, metered-dose inhalers, and dry powder inhalers, Rockville, USA (2007)

Ung, K.T., Chan, H.K.: Effects of ramp-up of inspired airflow on in vitro aerosol dose delivery performance for certain dry powder inhalers. Eur. J. Pharm. Sci. **84**, 46–54 (2016)

Wei, X., Hindle, M., Delvadia, R.R.: In vitro tests for aerosol deposition. V: using realistic testing to estimate variations in aerosol properties at the trachea. J. Aerosol Med. Pulm. Drug Deliv. **30**(5), 339–348 (2017)

Wei, X., Hindle, M., Kaviratna, A., et al.: In vitro tests for aerosol deposition. VI: realistic testing with different mouth-throat models and in vitro - in vivo correlations for a dry powder inhaler, metered dose inhaler, and soft mist inhaler. J. Aerosol Med. Pulm. Drug Deliv. **31**(6), 358–371 (2018)

Ziffels, S., Bemelmans, N.L., Durham, P.G., et al.: In vitro dry powder inhaler formulation performance considerations. J. Controlled Release **199**, 45–52 (2015)

Selected Issues of Gas-Liquid Flow Through Open-Cell Foams

Roman Dyga(✉)

Department of Chemical and Process Engineering, Faculty of Mechanical Engineering, Opole University of Technology, Opole, Poland
r.dyga@po.opole.pl

Abstract. The paper presents selected aspects of gas-liquid flow through open-cell solid foams. The construction of foams and their characteristic features have been described. The examples of use of foams in the construction of industrial equipment and achieved technological benefits are given. The state of the art in the field of hydrodynamics and heat transport during two-phase flow through a space filled with solid foam were presented.

1 Introduction

Striving to increase their efficiency and – first and foremost – effectiveness, many of technological processes expand the heat or mass transfer area or mass contact area with packings of various sorts. The packings should be characterised by high specific surface area and high porosity so that the increase in the active surface area of the equipment could be achieved with as little increase in pressure drop as possible. Those requirements are met by open-cell foams. Those are materials with fully open structure and very high porosity (up to 98%), which allows a relatively free flow of liquid through the foam-filled area.

Two types of open-cell foams are known – ceramic foams and metal foams. The latter are characterised by a relatively high effective thermal conductivity. The continuity of the skeleton limits thermal transport resistance, typical for poured and structural packings. It is possible to produce foam from a wide range of metal alloys and various ceramic materials. Consequently, foams are available the properties of which allow them to be used even under extremely adverse working conditions, e.g. at high temperatures or in chemically aggressive environments. The technology of placing catalysts on the foam surface area has been mastered to a sufficient degree. Moreover, metal foams are characterised by good workability, high plasticity and capacity to dampen vibrations, which is significant when they are used as structural elements of the equipment.

The listed features of the foams result in the fact that those materials, despite their poor availability, are more and more often seen as an alternative for other, more common packings. The literature reports use of open-cell metal foams in the construction of compact heat exchanger, rechargeable batteries and heat regenerators as well as chemical reactors, including catalytic converters. In addition, the foams are used in evaporators of cooling devices and solar energy collectors as well as in column apparatuses and bioreactors. Open-cell foams are also used as flow stabilisers, pulsation dampeners, flame arresters or filtration partitions.

© Springer Nature Switzerland AG 2020
M. Ochowiak et al. (Eds.): PAIC 2019, *Practical Aspects of Chemical Engineering*, pp. 58–68, 2020.
https://doi.org/10.1007/978-3-030-39867-5_7

Examples of various application of the foams in the construction of the process equipment are provided for instance by authors of works, Banhart (2001), Han et al. (2012), Zhao (2012). In many cases, it is equipment with multiphase systems.

2 Structure of Open-Cell Foams

Open-cell foams have the form of spatial skeleton forming large empty cells. The size of those cells is a grade higher than the transverse size of skeleton ligaments. Adjacent cells are connected with numerous openings commonly known as pores. Such a structure provides the foams with the specific surface area from several hundred to several thousand m^2/m^3 and very high porosity, usually exceeding 90%, and it allows a relatively free flow of liquids through those materials.

The geometric structure of ceramic and metal foams may be very similar, as illustrated in Fig. 1, but in the case of the metal foams there is considerable geometric diversity. For instance, Fig. 2 demonstrates 3 foams of similar porosity and cell size but of different skeleton structure.

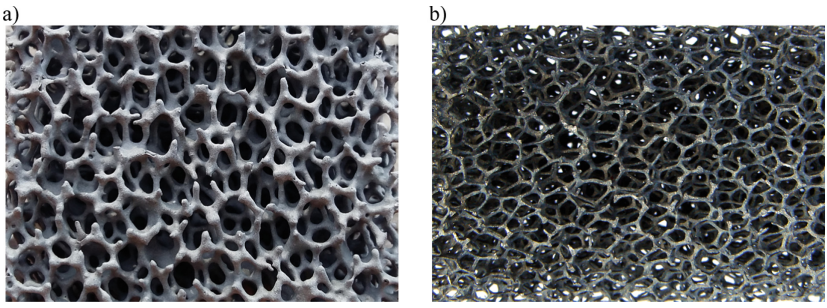

Fig. 1. Open-cell foams, **a** ceramic, **b** metal.

The cellular skeleton of the foam illustrated in Fig. 2a is characterised by relative high shape regularity. The skeleton is built of ligaments in the form of rods with nearly constant cross-section and similar length. The foam illustrated in Fig. 2b exhibits a less regular structure. In this case, the skeleton ligaments have various lengths and varying cross-section. Moreover, in some cells, at the junction of ligaments. Despite a seemingly more "closed" structure, the porosity of that foam is merely by 1.4% lower than the porosity of the foam from Fig. 2a. The skeleton of the foam illustrated in Fig. 2c is composed of bonded platelets oriented diversely. The platelets have relatively high surface areas, but their low thickness allows to obtain foams of porosity exceeding 90%.

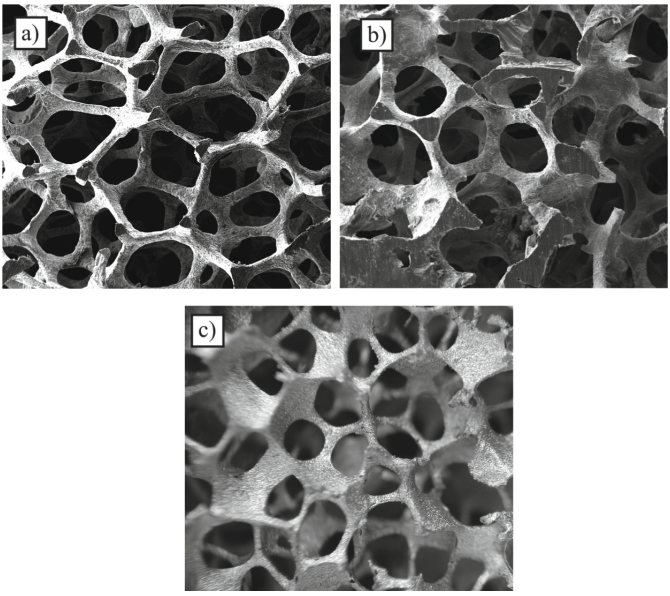

Fig. 2. Comparison of the structure of metal foams, **a** foam: 30 PPI, ε = 94.3%, **b** foam: 40 PPI, ε = 92.9%, **c** foam: 40 PPI, ε = 91.6%

The shape of the ligaments forming the cellular skeleton, their combination into a spatial network and, in turn, the shape of the cells depends on the method of foam production. The size and number of pores binding neighbouring cells may vary, but in most cases all cells may be treated as open. In foams, there are virtually no blind pores, that is pores opened on one side only, so characteristic for porous materials.

Foams are assumed to be materials of isotropic structure and their geometry is characterised on the basis of average values. The most important structural parameters of foams are the following:

- pore density, *PPI*
- porosity, ε
- specific surface area, a_{mf}
- cell diameter, d_c
- pore diameter, d_p
- skeleton ligament diameter, d_l

Pore density *PPI* means the number of pores per inch. This value is commonly used to classify foams. However, one needs to be aware that the pore density is not a size, but merely a nominal value allowing to classify given foam as a member of a given group. By standard, the pore density of solid foams ranges from 5 to 120 PPI.

The porosity of the metal foams used in practice most commonly ranges from 88 to 95%. The value of 98% is possible in some cases. When the porosity goes below 65%, foams lose their ability to let liquids through. The specific surface area of solid foams

ranges from 300 to 6000 m^2/m^3 and depends on the porosity and cell size. In general, foams with lower porosity and smaller cells have specific surface area higher than foams with larger cells.

In relation to the size of cells, pores and cross-section of skeleton ligaments, the term of 'diameter' is commonly used even though the cross-section of cells, pores and ligaments is usually not circular. In terms of numbers, the substitute cell diameter d_c equals the diameter of a circle with the area or circumference equivalent to the surface area/circumference of the cross-section of the cell. Likewise, the substitute pore diameter d_p and the substitute ligament diameter d_l are determined. The cell diameter in solid foams ranges from 0.3 to 7 mm. According to Duocel, the foam producer, the pore diameter equals 0.5–0.7 of the cell diameter. The other geometric parameters of cells are also interdependent, but to state those interdependencies precisely is quite difficult. Therefore, unambiguous description of foam requires providing more than just one structural parameter.

3 Gas-Liquid Flow Through Solid Foams

The most common case of the gas-liquid flow through open-cell foams is flow boiling. Work in this respect is carried out in a lot of centres. Their authors emphasise that the presence of foam on the boiling surface results in lower overheating point of the heating surface, necessary for the nucleation of vapour bubbles, and in the shift of the boiling crisis towards much higher heat fluxes. Hu et al. (2014) state that during the flow of boiling coolant through a flat channel packed with metal foam, the heat transfer coefficient is 1.5 to 2.6 times higher compared to the boiling on a smooth surface (channel without packing). An even higher difference – 2 to 4 times in favour of foam – occurs when the boiling happens round tubular channels. Jamal-Abad et al. (2017) assess that the thermal effectiveness of solar energy collectors after packing their evaporators with copper foam increases by up to 45% despite markedly higher pressure drops. In turn Shi et al. (2018) found that a vapour condenser in the form of a tube with an annular insert from copper foam is 30% more effective compared to a tube with micro-ribs.

Diani et al. (2015) and Zhu et al. (2015) emphasise that the use of foam on the boiling surface brings the best benefits when the process is carried out with a flow with low liquid stream density and high participation of vapour. According to Wang et al. (2013) increase in the intensity of heat exchange results from the flow disruptions in the layer at the wall caused by the foam skeleton, more intense mixing of vapour and liquid and elevated effective thermal conductivity. The merit of the last factor is underlined by Kouidri and Madani (2017) and Pangarkar et al. (2010).

The effectiveness of foam-packed equipment also depends on the energy required for forcing fluids through. Due to the specific structure of foams, that energy is low – it did not exceed 1 W/m^3 in studies performed by Lali (2017). Zhang et al. (2011) show that two-phase pressure drop in metal foams is significant but evidently lower than the pressure drops in other porous media and structural packings. According to them, the gas-liquid pressure drop equals 20% of pressure drops in mesh packings. The authors of work Stemmet et al. (2005) also registered relatively low pressure drops. Zalucky

et al. (2017) claim that the pressure drop in a foam-packed column is several times lower than in a column with a deposit of poured granules with comparative specific surface area. Moreover, the authors of the studies performed in columns filled with metal foams also found that the flow is much more stable compared to the flow through columns with other packings. Due to high porosity, the column can be charged with higher amounts of gas and liquid. In a wider range, the following flows occur: stream, stratified, bubble and dispersive. Pulsation flow in counterflow columns occurs with very strong gas stream. The void fraction of liquid can be higher than in columns filled with other materials. According to Stemmet et al. (2005), in extreme cases the void fraction reaches the value of foam porosity, especially in the case of foams of low pore density.

Use of solid foams in packed columns allows to increase the intensity of mass transfer. According to Zhang et al. (2011) the intensity of mass transfer is by ca. 40% higher compared to columns with mesh packing and the mass transfer coefficient goes up along with pore density (Stemmet et al. 2007). According to Tourvieille et al. (2015) the intensity of mass transfer may increase even by 50% as the energy used to force fluids through remains low.

When gas and liquid combined flow through foam-packed channels, specific flow structures form, understood as a manner of liquid distribution in the channel. The type of structures and the conditions under which they occur are not clear, which is very much noticeable due to a significant impact of the structures on the course and results of technological processes performed with multiphase systems.

Observation of gas-liquid flow was a subject of studies by Bamorovat et al. (2016); those authors, however, performed studies only in terms of intermittent annular flow. The results of the experiments described in work Dyga and Płaczek (2017), indicate that more diverse flow structures may occur. What is significant is that during the flow of the gas-liquid mixture through foam-packed channels, structures typical for the flow in empty channels are observed. In work Dyga and Płaczek (2017), four basic types of flow were differentiated – stratified flow, plug flow, slug flow and churn flow – illustrated in Fig. 3. The type of structure is determined by flow conditions (speed, participation and properties of fluids). No effect of the structure of foams on the type of flow structure has been demonstrated so far.

Areas of occurrence of respective flow structures can be presented in a flow regime map in a $g_L/g_G \cdot \lambda\psi$ – g_G/λ reference system, proposed by Baker for the flow through unpacked channels. In the system in question, g_L and g_G mark the mass velocity of liquid and gas and λ and ψ are dimensionless parameters reflecting relations between physical properties of gas and liquid and the properties of air and water. As in Fig. 4, in the case of the flow through metal foam-packed channels, the points corresponding to the structures observed by Dyga and Płaczek (2017), form compact areas in the Baker's system, which – however – do not fully overlap with the range of occurrence of the same structures in empty channels. When forcing the gas-liquid mixture through foams, change in the stratified flow into other forms of flow occurs at a lower ratio between the streams of liquid and gas compared to the flow through empty channels (particularly in the case of change of stratified flow into plug flow). That relation results from higher interphase slide in foam-packed channels, which is demonstrated in work Płaczek et al. (2012).

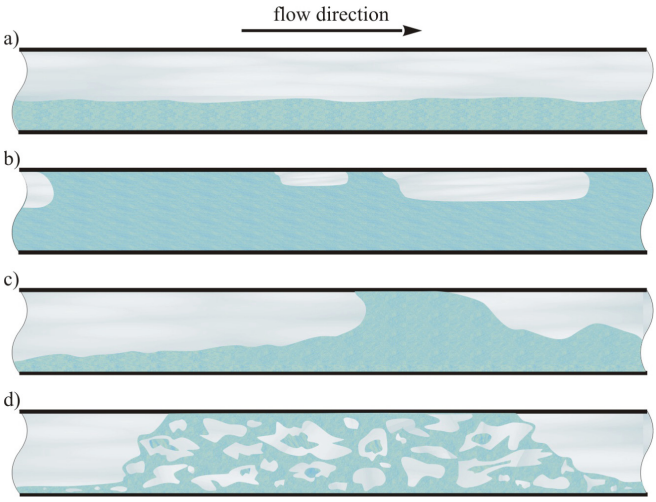

Fig. 3. Structures of gas-liquid flow in metal foam-packed channels, **a** stratified, **b** plug, **c** slug, **d** churn

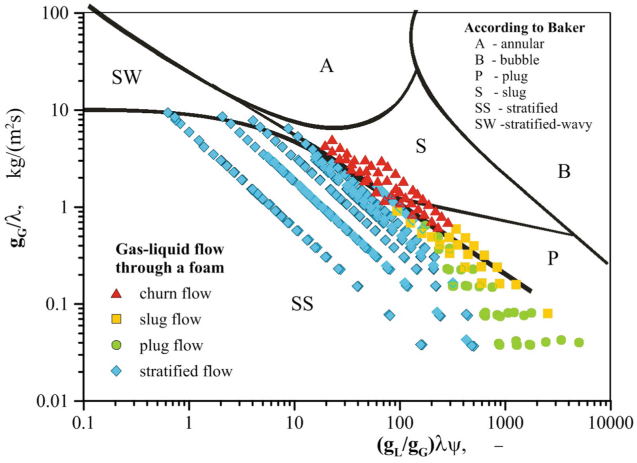

Fig. 4. The scope of occurrence of gas-liquid flow structures in the case of flow through metal foams against the Baker's map

Gas, due to its low viscosity, flows through the geometrically complex cellular space relatively freely, but liquid is stopped by the skeleton of the foam, which makes the participation of gas in the mixture much lower than the inlet participation of that phase (resulting from the ration between the streams of the flows introduced in the channel). The situation is illustrated in Fig. 5.

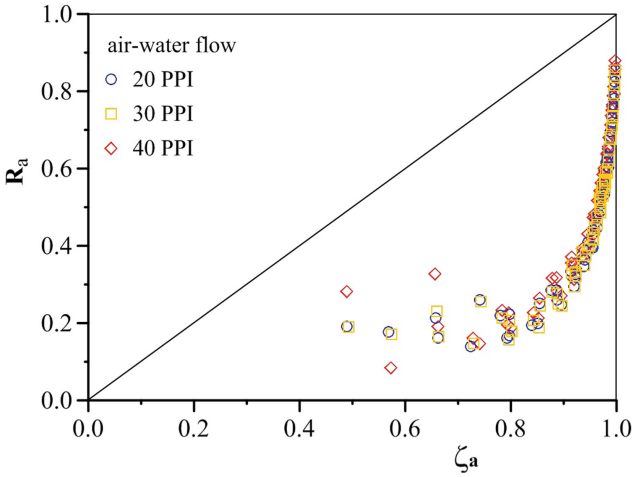

Fig. 5. Comparison of actual void fraction of air R_a with inlet participation ζ_a

The comparison of the void fraction of air R_a at the flow with water through three foams of similar structure but different in terms of porosity and cell size, illustrated in Fig. 6, indicates that the value of void fraction does not depend on the structural parameters of foams.

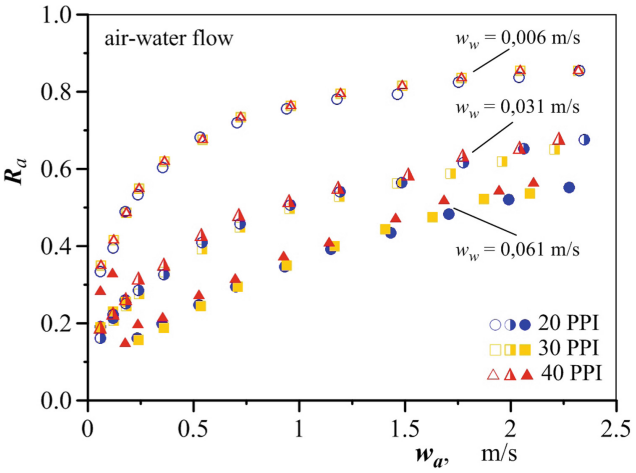

Fig. 6. Void fraction of air in the mixture with water at flow through aluminium foams with pore density 20, 30 and 40 PPI

However, the structure of foams affects the movement of air to some extent and has a very marked effect on two-phase pressure drop. Work Dyga and Troniewski (2015) found that in metal foam-packed channels, heat is exchanged first and foremost by way of heat transferring between the liquid and the wall of the channel. Foam participates in heat transport mostly by conduction. This is why the value of heat transfer coefficient depends on the hydrodynamic conditions of the flow in the first place. If comparable conditions, heat exchange intensity is higher when the foam skeleton is characterised by higher thermal conductivity k_s, which is reflected by the experiment data presented in Fig. 7, taken from work Dyga and Kos (2017).

Pressure drops of fluid in solid foams, apart from the obvious effect of hydrodynamic conditions, depend on the structure of foams and the effect of geometric parameters of the skeleton of foams on the values of pressure drops is very much evident, which is illustrated in Fig. 8 on the example of air-water flow through two types of aluminium foams. Pressure drop is much higher in the case of flow through foams with higher pore density, or with smaller cells. Similar observations as to the effect of pore density on the values of gas-liquid pressure drops were made by Hu et al. (2013) and Ji and Xu (2012) when examining the flow boiling of coolants. In turn, study Dyga (2015) demonstrated that the value of pressure drops depends not only on the cell size, but also on the shape of the cellular skeleton. In the case of flow of fluid through foams with geometrically regular skeleton, the pressure drops are markedly lower compared to flow through foams with large knots at the junction of skeleton ligaments or local skeleton deformations.

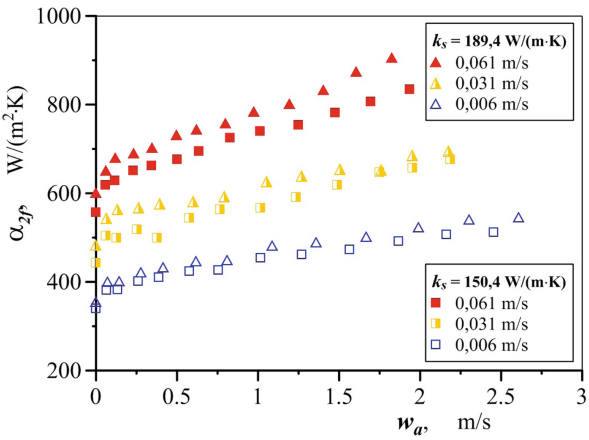

Fig. 7. Comparison of heat transfer coefficient α_{2f} at air-oil flow through foams of various thermal conductivity k_s and similar geometric parameters

In the gas-liquid flow through foam-packed channels, what is observed are changes in the pressure drops and void fraction of phases, seemingly inconsistent to the flow conditions. An example may be abrupt reduction in pressure drops despite increase in

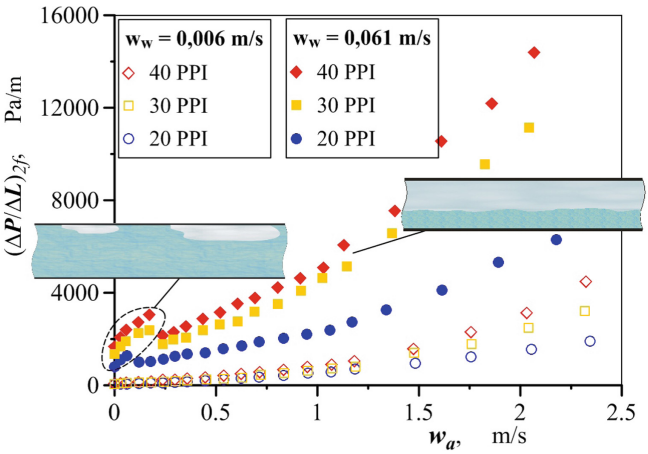

Fig. 8. Air-water pressure drop in aluminium foams of 20 and 40 PPI

phase streams (Fig. 8). Such singularities are related to changes in the structures of flow, particularly change of plug or slug flow into stratified flow.

Phenomena accompanying gas-liquid flows through solid foams are described mathematically to a limited extent, e.g. there are no analytical methods to determine the heat transfer coefficient, and there are only few studies – Gerbaux et al. (2009), Hu et al. (2013), Ji and Xu (2012) – concerning the modelling of hydrodynamics of flow.

Gerbaux et al. (2009) propose to determine gas-liquid pressure drops using the Darcy–Brinkman–Forchheimer equation, valid for single-phase flow, to which coefficients correcting the value of permeability and the inertia coefficient in two-phase flow were introduced. According to the authors of studies Hu et al. (2013), and Ji and Xu (2012), the classic Lockhart–Martinelli method can be used to calculate the pressure drops of boiling coolants in solid foams. Hu et al. (2013) indicate that the pressure drop of fluid should then be determined by the procedure proper for flow through porous deposits, which allows to take into account the parameters characterising foam (specific surface area, porosity and pore diameter) in the calculations. A similar solution was developed by Ji and Xu (2012) but in that case the pressure drop of liquid is determined on the basis of the pressure drop number defined in the manner typical for single-phase flows through solid foams. In addition, Hu et al. (2013) provide manners for calculating the void fractions in the gas-liquid flow through solid foams. They suggest determining the void fraction of liquid by evaporation of the agent on the basis of a dependence developed for flow through empty channels by Rauhani and Axelsson (1970).

The insufficient mathematical description of the gas-liquid flow through solid flows, particularly in the case of flows other than boiling of coolants, encourages to use calculation models valid for other types of packings or unpacked channels. However, the analysis presented in studies Płaczek and Dyga (2012) and Płaczek et al. (2012) indicate that the application of those models to the flow through solid foams results in too high deviations of the calculated values of void fractions from the actual values.

4 Summary

Open-cell foams can be used in the construction of various types of process equipment. There are high expectations as to the application of metal foams in the performance of the processes in participation of multiphase systems, including two-phase gas-liquid systems. The knowledge concerning the phenomena occurring in the space packed with open-cell foam requires supplementation. The information provided in this study come from few studies devoted to two-phase flows through solid foams. The analysis of those studies shows evident similarities of flows through foam-packed channels and flows through empty channels. Despite that analogy and a growing number of studies devoted to the flow through open-cell foams, it is still difficult to pinpoint the effect of foams on the examined thermal and hydrodynamic phenomena. The largest gaps can be found in the mathematical description of two-phase flow, which in general pertains to one specific case of gas-liquid flow, i.e. flow boiling. Such a state of affairs makes designing, optimisation and construction of metal foam-packed equipment very difficult.

References

Bamorovat, A.G., Moon, C., Kim, K.C.H.: Flow boiling visualization and heat transfer in metal-foam-filled mini tubes – Part I: Flow pattern map and experimental data. Int. J. Heat Mass Transf. **98**, 857–867 (2016)

Banhart, J.: Manufacture, characterisation and application of cellular metals and metal foam. Prog. Mater Sci. **46**, 559–632 (2001)

Diani, A., Mancin, S., Doretti, L., Rossetto, L.: Low-GWP refrigerants flow boiling heat transfer in a 5 PPI copper foam. Int. J. Multiphase Flow **76**, 111–121 (2015)

Dyga, R.: Opór hydrauliczny przy przepływie gaz-ciecz w kanałach wypełnionych pianami aluminiowymi. Inż. Ap. Chem. **6**, 319–320 (2015)

Dyga, R., Kos, M.: Analiza zjawisk cieplnych i hydrodynamicznych w przepływie mieszaniny gaz-ciecz przez kanał wypełniony pianami metalowymi. Wydawnictwo Instytutu Techniki Cieplnej; Gliwice, Współczesne problemy termodynamiki (2017)

Dyga, R., Płaczek, M.: Selected problems of gas-liquid flow through the channels filled with metal foams. In: E3S Web of Conferences, vol. 19 (2017)

Dyga, R., Troniewski, L.: Convective heat transfer for fluids passing through aluminum foams. Arch. Thermodyn. **36**(1), 139–156 (2015)

Gerbaux, O., Vercueil, T., Memponteil, A., Bador, B.: Experimental characterization of single and two-phase flow through nickel foams. Chem. Eng. Sci. **64**, 4186–4195 (2009)

Han, X.-H., Wang, Q., Park, Y.-G., T'Joen, C., Sommers, A., Jacobi, A.: A review of metal foam and metal matrix composites for heat exchangers and heat sink. Heat Transf. Eng. **33**(12), 1–20 (2012)

Hu, H., Zhu, Y., Ding, G., Sun, S.: Effect of oil on two-phase pressure drop of refrigerant flow boiling inside circular tubes filled with metal foam. Int. J. Refrig. **36**, 516–526 (2013)

Hu, H., Zhu, Y., Peng, H., Ding, G., Sun, S.: Effect of tube diameter on pressure drop characteristics of refrigerant-oil mixture flow boiling inside metal-foam filled tubes. Appl. Therm. Eng. **62**, 433–443 (2014)

Jamal-Abad, M.T., Saedodin, S., Aminy, M.: Experimental investigation on a solar parabolic trough collector for absorber tube filled with porous media. Renew. Energy **107**, 156–163 (2017)

Ji, X., Xu, J.: Experimental study on the two-phase pressure drop in copper foams. Heat Mass Transf. **48**, 153–164 (2012)

Kouidri, A., Madani, B.: Thermal and hydrodynamic performance of flow boiling through a heat exchanger filled with various metallic foam samples. Chem. Eng. Proc. **121**, 162–169 (2017)

Lali, F.: A hydrodynamic study of cylindrical metal foam packings: residence time distribution and two phase pressure drop. Chem. Eng. Process. **115**, 1–10 (2017)

Pangarkar, K., Schildhauer, T.J., Van Ommen, J.R., Nijenhuis, J., Moulijn, J.A., Kapteijn, F.: Heat transport in structured packings with co-current downflow of gas and liquid. Chem. Eng. Sci. **65**, 420–426 (2010)

Płaczek, M., Dyga, R.: Analiza metod obliczania udziału objętościowego gazu w przepływie gaz-ciecz w kanałach wypełnionych pianami metalowymi. Inż. Ap. Chem. **6**, 368–369 (2012)

Płaczek, M., Dyga, R., Witczak, S.: Experimental investigation of void fraction in gas-liquid flow through FeCrALY foam. Procedia Eng. **42**, 690–703 (2012)

Rauhani, S.Z., Axelsson, E.: Calculation of volume void fraction in subcooled and quality region. Int. J. Heat Mass Transfer **13**, 383–393 (1970)

Shi, J., Zheng, G., Chen, Z.: Experimental investigation on flow condensation in horizontal tubes filled with annular metal foam. Int. J. Heat Mass Transf. **116**, 920–930 (2018)

Stemmet, C.P., Jongmans, J.N., Van Der Schaaf, J., Kuster, B.F.M., Schouten, J.C.: Hydrodynamics of gas–liquid counter-current flow in solid foam packings. Chem. Eng. Sci. **60**, 6422–6429 (2005)

Stemmet, C.P., Meeuwse, M., Van der Schaaf, J., Kuster, B.F.M., Schouten, J.C.: Gas-liquid mass transfer and axial dispersion in solid foam packings. Chem. Eng. Sci. **62**, 5444–5450 (2007)

Tourvieille, J.-N., Philippe, R., De Bellefon, C.: Milli-channel with metal foams under an applied gas–liquid periodic flow: external mass transfer performance and pressure drop. Chem. Eng. J. **267**, 332–346 (2015)

Wang, P., Liu, D.Y., Xu, C.: Numerical study of heat transfer enhancement in the receiver tube of direct steam generation with parabolic trough by inserting metal foams. Appl. Energy **102**, 449–460 (2013)

Zalucky, J., Wagner, M., Schubert, M., Lange, R., Hampel, U.: Hydrodynamics of descending gas-liquid flows in solid foams: liquid holdup, multiphase pressure drop and radial dispersion. Chem. Eng. Sci. **168**, 480–494 (2017)

Zhang, W., Zhang, B., Shi, Z.: Study on hydrodynamic performance and mass transfer efficiency of nickel foam packing. Procedia Eng. **18**, 271–276 (2011)

Zhao, C.Y.: Review on thermal transport in high porosity cellular metal foams with open cells. Int. J. Heat Mass Transf. **55**, 3618–3632 (2012)

Zhu, Y., Hu, H., Sun, S., Ding, G.: Flow boiling of refrigerant in horizontal metal-foam filled tubes: Part 2 – A flow-pattern based prediction method for heat transfer. Int. J. Heat Mass Transf. **91**, 502–511 (2015)

Modified Aluminum-Magnesium Oxide Catalysts in the Process of Ethoxylation of Higher Fatty Acid Methyl Esters

Magdalena Emmons-Burzyńska[1(✉)], Marek Lukosek[2], and Krzysztof Alejski[1]

[1] Institute of Chemical Technology and Engineering, Faculty of Chemical Technology, Poznan University of Technology, Poznań, Poland
magdalena.emmons-burzynska@put.poznan.pl
[2] Institute of Heavy Organic Synthesis "Blachownia", Kędzierzyn-Koźle, Poland

1 Introduction

Oxyethylation leads to obtaining nonionic surfactants that are widely used in many branches of industry. The potential hydrophobic raw materials used in this process include, apart from widely used fatty alcohols, also fatty acid methyl esters. Direct oxyethylation of fatty acid methyl esters needs application of a catalyst to activate a hydrophobic substrate or ethylene oxide (Schick 1967). As the oxyethylated product is a mixture of homologs with polyoxyethylene chains of different length, in order to identify the dominant fraction it is necessary to use the conception of average degree of oxyethylation. Depending on the catalyst used, the range of homologs distribution in the product may vary. However, currently used catalysts allow the synthesis of products in which the main component constitutes max. 30 wt%. mixture of oxyethylates (Alejski et al. 2003a). The obtained product may contain the ethoxylated derivatives, by-products and unreacted starting material (Alejski et al. 2003b). For ethoxylated fatty acids methyl esters the by-product may be methyl monoesters of polyoxyethylated glycol and their diesters (Hama et al. 1997a; Szymanowski 2001).

2 Ethoxylation Catalysts

A typical homogenous catalyst for the oxyethylation substrates containing mobile hydrogen is hydroxide of a I group metal. The most commonly used is sodium hydroxide (Szymanowski 2005). The use of such catalysts leads to the formation of products of a wider distribution of homologs and a significant amount of unreacted alcohol (Alejski et al. 2003b). The simplest alternative to NaOH are simple or complex alkoxides of alkali metal IIA group (Szymanowski 2005). The homogeneous catalysts capable of catalyzing the oxyethylation of higher fatty acid methyl esters are those based on calcium (Hreczuch and Szymanowski 1997, 2007; Białowąs and Szymanowski 2004). With increasing degree of oxyethylation, the distribution of

© Springer Nature Switzerland AG 2020
M. Ochowiak et al. (Eds.): PAIC 2019, *Practical Aspects of Chemical Engineering*, pp. 69–78, 2020.
https://doi.org/10.1007/978-3-030-39867-5_8

oxyethylated derivatives in the product is significantly narrowed (Hreczuch 2002). Unfortunately, homogeneous calcium catalysts show relatively low activity. Additionally, there is a problem with their separation from the post-reaction mixture and a long time is needed for the reaction induction (Alejski et al. 2006).

An alternative to calcium homogeneous catalysts of the oxyethylation process can be heterogeneous ones. Literature reports point to composite aluminum-magnesium oxides that are used both in the fatty alcohol and in the fatty acid methyl esters ethoxylation process. Various methods for the preparation of aluminum-magnesium oxides are known. In general, this process is realized in two main stages. The first one is to obtain the appropriate hydroxides, while the second is their calcination at a certain temperature. Aluminum-magnesium hydroxides, being a catalyst precursors, can be produced by coprecipitation from salt solutions (Okamoto et al. 2003), dry (Nakamura et al. 1991) or wet (Nakamura et al. 1994) impregnation. Precursors of aluminum-magnesium oxide can also be natural or synthetic hydrotalcites of the general formula $M_xAl_y(OH)_z(CO_3)m{\cdot}H_2O$ (Hama et al. 1998a), commercial aluminum-magnesium hydroxides $nMgO{\cdot}Al_2O_3m\ H_2O$ (Hama et al. 1998b) or mixtures of aluminum and magnesium salts (Imanaka et al. 2003).

Literature data indicate a very strong influence of the conditions of obtaining aluminum-magnesium oxides on their physicochemical properties, which are crucial from the point of view of their activity and selectivity. Both, the step of obtaining the hydroxide precursor and its thermal treatment are important. A widely used method for producing mixed metal hydroxides is coprecipitation, however, it requires taking into account many factors affecting the physicochemical properties of the obtained product. An extremely important issue during the co-precipitation process is full control and stability of such parameters as: pH, temperature, mixing hydrodynamics, concentrations of precipitating agents and maintenance of their pH, concentration of metal ion solution. In the case of coprecipitation of two or more cations, it is particularly important to find a pH range that would allow precipitation under conditions ensuring the lowest possible losses due to the solubility of the sludge, leading to a composition consistent with the assumed target one (Sokolovskii et al. 2003).

The coprecipitation process of aluminum-magnesium oxides can be carried out in many ways. The processes are carried out at a constant pH or with pH increasing to the assumed value, differing in the ways and time of contacting streams (Shuzhi et al. 1999, Cantrell et al. 2005). The most commonly used precipitants and pH stabilizers are potassium (Di Cosimo et al. 1998; Fraile et al. 2009), sodium (Climent et al. 2004; Fishel and Davis 1994b) or ammonium carbonates and hydroxides (Shen et al. 1994; Cantrell et al. 2005). The temperature of the coprecipitation process is usually maintained at 60–65 °C (Di Cosimo et al. 1998; Climent et al. 2004; Fraile et al. 2009), lower values of around 40 °C (Shen et al. 1994; Okamoto et al. 2003) or much higher, e.g. 90 °C (Imanaka et al. 2003) are less frequently used. Conducting the coprecipitation process at high temperatures, needs a large amount of energy. It is possible to carry out precipitation at room temperature without the need for ageing process (Alejski et al. 2010a). Due to the direct effect of pH on the composition of the catalysts obtained, coprecipitation is most often carried out by feeding streams containing a mixture of aluminum and magnesium cations and a precipitating agent with the

simultaneous dosing of the pH maintaining agent. The pH used is taken from the range 7.5 (Cantrell et al. 2005)–11 (Sokolovskii et al. 2003).

The mixing of the reaction mixture is very important. The point introduction of the reagents implies inhomogeneity which may result in the lack of reproducibility of the catalysts properties. As follows from the study on mixing hydrodynamics during the coprecipitation process, the best selectivity is demonstrated by the catalysts obtained with the Reynolds number around 100,000. At low values of Reynolds numbers (range Re 30000–190000 analyzed) the range of particle diameters in the obtained oxides significantly extends towards larger diameters (Alejski et al. 2010b).

Properties of the obtained aluminum-magnesium oxides are also influenced by the total concentration of aluminum and magnesium cations. It has been observed that the increase in the used total concentration of Al^{3+}, Mg^{2+} is followed by a decrease in the specific surface area, which is associated with an increase in the content of agglomerates with diameters above 40 μm (Emmons-Burzyńska et al. 2018). Appropriately selected pH, stable during the coprecipitation process, results in the production of aluminum-magnesium oxides with a composition similar to that assumed, which indicates a complete precipitation of Al^{3+}, Mg^{2+} ions during the synthesis (Di Cosimo et al. 1998; Fraile et al. 2009).

Aluminum-magnesium oxides with an Al/(Al + Mg) molar ratio lower than 0.5 or equal to 0.5 contain in their crystalline structure only MgO [ASTM 4-0829] in the periclase type, crystallizing in a regular system. The crystallinity of the phase derived from MgO decreases with increasing aluminum content in the catalyst, which is manifested by a simultaneous increase in contribution of the peaks assigned to the spinel $MgAl_2O_4$ in the XRD spectrum. The oxides enriched in aluminum (Al/(Al + Mg) > 0,5) crystallize in a pseudo-crystalline form of Al_2O_3 [ASTM 10–425] (Fraile et al. 2009; Shen et al. 1994; Di Cosimo et al. 2000; Diez et al. 2003). The analysis of the surface composition indicates that in most cases the surface is enriched in aluminum when compared to the composition following from the elemental analysis. (Fraile et al. 2009; Fishel and Davis 1994a; Emmons-Burzyńska et al. 2018). The tested density of basic centers decreases with increasing aluminum content in the catalyst (Fraile et al. 2009; Fishel and Davis 1994b; Diez et al. 2003; Parida and Das 2000). The increase in aluminum content in the analyzed aluminum-magnesium oxides results in the increase in the specific surface area (Fraile et al. 2009; Parida and Das 2000).

The influence of pH on the physicochemical properties of the obtained aluminum-magnesium oxides was investigated. The pH values considered were 8, 9, 10, 11. According to the results, higher pH causes a higher contribution of magnesium in the hydroxide structure. However, no effect of the analyzed factor on the crystallographic structure as well as the surface area was observed (Emmons-Burzyńska et al. 2018). The use of alkali metal carbonates and hydroxides in the coprecipitation process requires rinsing to remove them. The procedure is carried out until no metal ions are found in the filtrate, which results in less than 0.1% wt. of metal ions in the catalyst (Di Cosimo et al. 1998; Fraile et al. 2009). However, it turns out that the presence of alkali metal in the aluminum-magnesium catalyst, significantly affects its physicochemical properties. The type of alkali metal used is also important. Aluminum-magnesium oxides, whose precursors are not washed, are characterized by a smaller specific surface area and porosity. X-ray analysis indicates the appearance of a small degree of ordering

coming from sodium aluminate ($NaAlO_2$), as evidenced by the relevant weak reflections (Emmons-Burzyńska et al. 2018; Fraile et al. 2009).

The problem of the influence of calcination temperature on physicochemical properties of the aluminum-magnesium catalyst has been discussed in many literature reports. It is the factor that has a significant impact on both the morphology and the catalytic properties of oxides. The aluminum-magnesium oxides studied were prepared in the temperature range of 400–950 °C. Their hydroxides were obtained by various methods differing significantly in the coprecipitation process parameters (Hama et al. 1997b; Liu et al. 2007). It has been found that irrespective of the preparation conditions, as the calcination temperature increases, the specific surface area decreases. The use of aluminum-magnesium oxides in fatty alcohols oxyethylation results in narrowing of the distribution of homologs (up to 30% wt. of the main component), reducing the unreacted substrate (<6%) and by-products, mainly polyglycols (<0.1%), (Okamoto et al. 2003; Imanaka et al. 2003). The aluminum-magnesium oxide catalysts for the process of ethoxylation of methyl esters of higher fatty acids, presented in literature, allow the synthesis of a product with a broad distribution of homologs and containing unreacted substrate (Fig. 1), (Hama et al. 1998a).

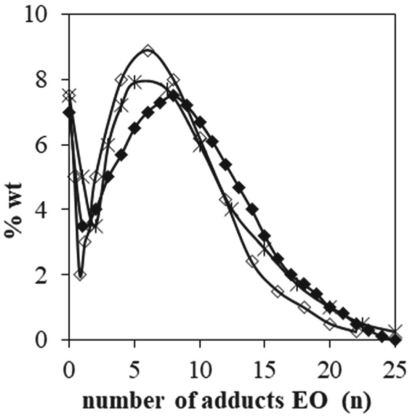

Fig. 1. Distribution of homologs in ethoxylated methyl dodecanoate using aluminum-magnesium catalysts obtained by calcination: hydroxides produced by application method (■), commercial hydroxides $2{,}5MgO{\cdot}Al_2O_3{\cdot}mH_2O$ (□), natural hydrotalcites $Mg_6Al_2(OH)_{16}$-$CO_3{\cdot}4H_2O$ (✕)

The procedure for the preparation of catalysts is very strongly reflected in the distribution of produced particles, degree of surface area development of the catalysts, internal structure and pore size distribution and characteristics of the active surface. The mentioned parameters are crucial from the point of view of catalyst activity and selectivity (Hama et al. 1997a; Szymanowski 2001; Emmons-Burzyńska et al. 2018). Analysis of the influence of a number of preparation parameters allows obtaining

aluminum-magnesium oxides with the desired morphology and catalytic properties. On the basis of our studies, we identified the conditions of modified oxide aluminum-magnesium catalysts preparation allowing the synthesis of a product with a narrow distribution of homologs and a low content of unreacted substrate. The following parameters of the coprecipitation process were analyzed: Al/Mg molar ratio, total aluminum and magnesium ions concentration, concentration of precipitating factors, maintenance of pH and pH range. It was found that the presence of an alkali metal in the aluminum-magnesium catalyst, introduced at the stage of precipitation of hydroxides, had a positive effect on the increase in the conversion of the hydrophobic substrate and the narrowing of the homolog distribution in the ethoxylated product (Fig. 2). Moreover, the type of alkali metal used was shown to affect the catalytic properties and selectivity of the tested oxides (Fig. 3).

The alkali metal content on the catalyst surface was found decisive for catalysts activity and selectivity. The catalysts containing no sodium on the surface showed very high activity because most likely there were no constraints on the activation and attachment of ethylene oxide. Too much surface sodium content (above 6%) disables the activation of ethylene oxide causing no oxide activity.

The aim of the undertaken research was to determine the methodology for obtaining modified aluminum-magnesium oxides as catalysts of ethoxylation of fatty acid methyl esters, leading to products with a narrow distribution of homologs. Because the content of alkaline cations strongly depends on the preparation conditions, which limits the possibility of controlling their content, an attempt was made to change the methodology for obtaining modified aluminum-magnesium oxides.

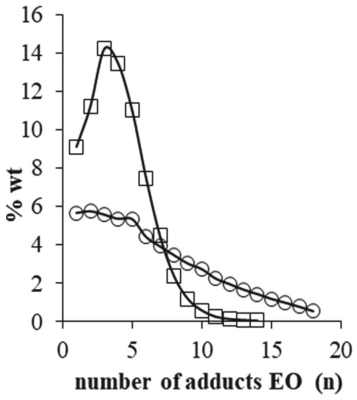

Fig. 2. Homologs distribution of oxyethylated products (n = 3) as a function of sodium content of aluminum-magnesium oxides (□ – 3% wt., ○ – 0,8% wt.)

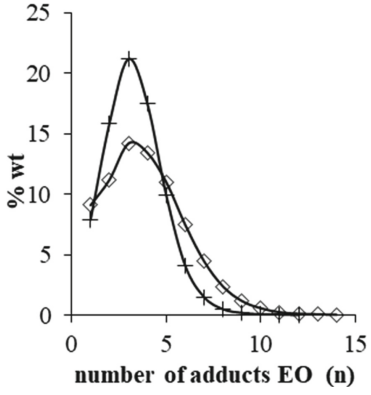

Fig. 3. Homologs distribution of oxyethylated products (n = 3) as a function of the type of alkali metal used in coprecipitation process (□ – Na +, + – K +)

3 Methodology

The tested oxide catalysts were obtained by dry impregnation of commercial $\gamma - Al_2O_3$ (Alumina Spheres 1.8/210 from SASOL with high purity). Before impregnation, the alumina was calcined for 5 h at 800 °C under nitrogen or dried overnight at 105 °C. Aluminum and magnesium cations were applied from aqueous solutions of nitrates (V) and alkali metals (Na^+, K^+) from aqueous solutions of carbonates. Aluminum and magnesium cations were applied in a molar ratio of 1:5. In the case of surface modification with alkali metal cations, the mass concentration of the corresponding alkali oxides in the catalyst was assumed to be 3 or 6%. Alkali metal cations were applied to both, the aluminum support and the oxides formed after prior application of aluminum and magnesium cations. After impregnation, the prepared catalyst precursors were dried for 24 h at 105 °C and then calcined under nitrogen for 5 h at 800 °C (Table 1).

Table 1. Conditions for the preparation of oxide catalysts

Nr	Catalysts symbol	Assumed catalysts composition [% wt.]		
		Na_2O	K_2O	MgO
I	$Al_2O_3/MgO/Na_2O$	3	–	4
II	$Al_2O_3/MgO/K_2O$	–	3	4
III	Al_2O_3/K_2O	–	3	–
IV	Al_2O_3/K_2O	–	6	–
V	Al_2O_3/Na_2O	6	–	–
VI	Al_2O_3/Na_2O	3	–	–
VII*	Al_2O_3/MgO	–	–	4
VIII	Al_2O_3/MgO	–	–	4

* Prior to impregnations the support was dried overnight at 105 °C, in other cases calcined for 5 h at 800 °C in nitrogen atmosphere.

The catalysts obtained were subjected to comprehensive characterization. Their chemical composition was determined by the ASA method using ContrAA 300, Analytik Jena. Their BET texture and specific surface area were evaluated using the ASAP 2010 porous structure analyzer from the American company Micromeritics Instrument Corporation. The activity of the obtained oxides was tested in a semi-periodic pressure reactor made of stainless steel (Autoclave Engineers, Erie, PA, USA) of 2 dm^3 capacity, equipped with a mechanical stirrer, electric heating jacket and cooling coil, pressure gauge and safety valve. The synthesis was started by loading the reactor with a defined mass of hydrophobic substrate (300 g) and catalyst (0.5% wt. of the product). The hydrophobic substrates used were lauryl methyl esters and lauryl alcohol. After loading the reactor and checking its tightness, the feedstock was purged with nitrogen at 130 °C for 30 min to remove trace amounts of water. After raising the reactor temperature to a set

value of 185 °C, automatic dosing of ethylene oxide was started. Having completed dosing of ethylene oxide, the reaction mixture was kept for 60 min at the reaction temperature to ensure the maximum conversion of substrates. After cooling to 60–80 °C, the reactor was purged with nitrogen and the resulting product was discharged, weighed and analyzed. The fractional composition of ethoxylated methyl esters was determined by gas chromatography (GC). Composition of the obtained ethoxylated product was established using a chromatograph Agilent Technologies 6890N (II/005/BA-AA) with a flame ionization detector equipped with a non-polar, high-temperature ZB-5HT column measuring 15 × 0.25 mm × 0.10 μm. Chromatograph working conditions: 380 °C/det. 400 °C/furnace: 60 °C (2 min), 15 °C/min 380 °C (5 min)/carrier gas (helium): 2.0 ml/min/split: 100:1/injection: 0,4 μl (manual).

4 Results

The results were analyzed to determine the impact of the conditions for obtaining catalysts on their physicochemical properties and activity in the ethoxylation process. The actual composition of Al_2O_3/Na_2O oxides is very similar to the assumed one. The potassium content in Al_2O_3/K_2O oxides differed significantly from the assumed one and constituted about 40% (catalyst 3) and 70% (catalyst 4) of the initial value. The lowest deposition efficiency was noted for the oxides obtained by modification of the aluminum support surface with the cations of both aluminum, magnesium and alkali metals (Table 1, Table 2).

Table 2. Physicochemical parameters of oxide catalysts

Nr	Specific surface area [m^2/g]	Real composition of catalyst [% wt.]		
		Na_2O	K_2O	MgO
I	130	0,88	–	0,38
II	140	–	0,45	0,38
III	151	–	1,24	–
IV	135	–	4,25	–
V	125	5,40	–	–
VI	137	2,58	–	–

Analysis of the pore distribution in the oxides obtained, indicates that there are mainly pores with diameters of about 10 nm. The pore distributions in the catalysts are very similar, only in Al_2O_3/Na_2O (6%) oxide there is a shift in the maximum pore contribution towards slightly higher values, which results in the largest decrease in the specific surface area to 125 m^2/g in relation to the aluminum support (157 m^2/g) (Table 1, Fig. 4). Under the assumed conditions of the ethoxylation process, when using either lauryl alcohol or lauryl methyl esters the active catalysts were only the oxides modified with aluminum and magnesium cations and the aluminum support.

Analysis of the ethoxylated product indicates that it contains about 40% of unreacted substrate and about 6% of by-products, including only about 1% of PEG. The maximum distribution of homologs is shifted towards lower values in relation to the assumed n = 3. The oxyethylated derivative containing one molecule of attached ethylene oxide is formed in the largest amount. The analysis of product composition shows that the nature of the modified catalytic surface allows attachment of up to 6 ethylene oxide molecules (Fig. 5).

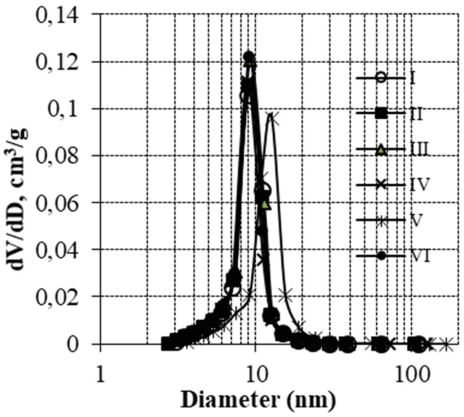

Fig. 4. Pore diameter distribution of obtained oxide catalysts

In the presence of lauryl alcohol the oxides showed greater activity expressed in the rate of ethylene oxide attachment reaction and it was almost 3 times higher than the catalytic activity of the unmodified support. When using lauryl methyl esters, the catalytic activity was very similar, which may suggest that the surface modification did not generate centers active in the process of ethoxylation of higher fatty acid methyl esters (Table 3).

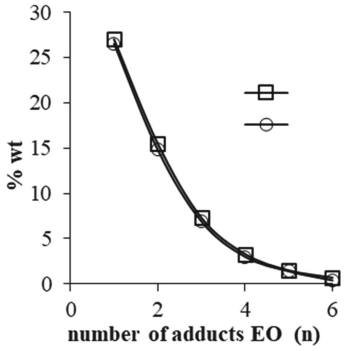

Fig. 5. Homolog distribution of oxyethylated products (n = 3) using aluminum-magnesium catalysts

Table 3. Catalytic activity of aluminum-magnesium catalysts.

Nr	Raw material	Average rate of ethoxylation [molEO/g-cat*h]
γ- Al_2O_3	lauryl alcohol	0,13
VII		0,35
VIII		0,38
γ- Al_2O_3	lauryl acid methyl esters	0,12
VII		0,13
VIII		0,13

5 Conclusions

The actual composition of oxide catalysts is different from the assumed one. Magnesium and alkali metal oxides were incorporated to a lower degree than expected. The specific surface area of each catalyst is lower than that of support and decreases with increasing degree of coverage. The porosities of the modified oxides are very similar, regardless of the conditions of their preparation. Contrary to expectations, the oxides modified with alkali metal cations did not show catalytic activity, irrespective of the preparation conditions and the type of hydrophobic substrate used. The resulting product was a mixture of ethoxylates containing 3–6 attached EO adducts. The catalyst activity was in the range 0.13–0.38 molEO/g-cat*h and was higher when lauryl alcohol was used.

Acknowledgements. The work was supported by the Polish Ministry of Science and Higher Education (Grant No. 03/32/SBAD/0907).

References

Alejski, K., Białowąs, E., Hreczuch, W., Szymanowski, J.: Modeling of fatty acid methyl ester oxyethylation. La Rivista Italiana Delle Sostanze Grasse **80**, 317–322 (2003a)

Alejski, K., Białowąs, E., Hreczuch, W., Trathnigg, B., Szymanowski, J.: Oxyethylation of fatty acid methyl esters. Molar ratio and temperature effects. Pressure drop modeling. Ind. Eng. Chem. Res. **42**, 2924–2933 (2003b)

Alejski, K., Emmons, M., Lukosek, M., Miesiąc, I., Wesołowski, P.: Sposób otrzymywania katalizatorów oksyalkilenowania. Pat. pol. P-216 810 (2010a)

Alejski, K., Emmons, M., Lukosek, M., Wesołowski, P.: Wpływ hydrodynamiki na proces otrzymywania i charakterystykę heterogenicznych glinowo-magnezowych katalizatorów oksyetylenowania. Inż. Ap. Chem **3**, 19–20 (2010b)

Alejski, K., Emmons, M., Sobczyńska, A., Lukosek, M.: Kinetics of oxyethylation of fatty acid methyl ester in a batch reactor. Chem. Process Eng. **27**, 1399–1410 (2006)

Białowąs, E., Szymanowski, J.: Catalysts for Oxyethylation of Alcohols and Fatty Acid Methyl Esters. Ind. Eng. Chem. Res. **43**, 6267–6280 (2004)

Cantrell, D.G., Gillie, L.J., Lee, A.F., Wilson, K.: Structure-reactivity correlations in Al-Mg hydrotalcite catalysts for biodiesel synthesis. Appl. Catal. A: Gen. **287**, 183–190 (2005)

Climent, M.J., Corma, A., Iborra, S., Epping, K., Velty, A.: Increasing the basicity and catalytic activity of hydrotalcites by different synthesis procedures. J. Catal. **225**, 316–326 (2004)

Di Cosimo, J.I., Apesteguia, C.R., Gines, M.J.L., Iglesia, E.: Structural requirement and reaction pathways in condensation reactions of alcohols on Mg_yAlO_x catalysts. J. Catal. **190**, 261–275 (2000)

Di Cosimo, J.I., Diez, V.K., Xu, M., Iglesia, E., Apesteguia, C.R.: Structure and surface properties of Al-Mg basic oxides; J. Catal. **178**:499–510 (22) (1998)

Diez, V.K., Apesteguia, C.R., Di Cosimo, J.I.: Effect of the chemical composition on the catalytic performance of Mg_yAlO_x catalysts for alcohol elimination reactions. J. Catal. **215**, 220–233 (2003)

Emmons-Burzyńska, M., Lukosek, M., Paukszta, D., Alejski, K.: Preparatyka katalizatorów glinowo-magnezowych do procesu oksyetylenowania metylowych estrów wyższych kwasów tłuszczowych. Przem. Chem. **97**(12), 2004–2008 (2018)

Fishel, Ch.T., Davis, R.J.: Use of catalytic reactions to probe Mg-Al mixed oxide surface. Catal. Lett. **25**, 87–95 (1994a)

Fishel, ChT, Davis, R.J.: Characterization of Al-Mg mixed oxides by temperature-programmed reaction of 2-propanol. Langmuir **10**, 159–165 (1994b)

Fraile, J.M., Garcia, N., Mayoral, J.A., Pires, E., Roldan, L.: The influence of alkaline metals on the strong basicity of Mg-Al mixed oxides: the case of transesterification reactions. Appl. Catal. A: Gen. **364**, 87–94 (2009)

Hama, I., et al.: Method of manufacturing a fatty acid ester of poloxyalkylene alkyl ether. Pat. am. 6184400 2001, Pat. am 5817844 (1998a)

Hama, I., et al.: Method of producing an alkylene oxide adduct of compound having one or more active hydrogen. Pat am. 5750796 (1998b)

Hama, I., Okamoto, T., Hidai, E., Yamada, K.: Direct ethoxylation of fatty methyl ester over Al-Mg composite oxide catalyst. J. Am. Oil Chem. **74**, 19–24 (1997a)

Hama, J., Sasamoto, H., Okamoto, T.: Influence of catalyst structure on direct ethoxylation of fatty methyl esters over Al-Mg composite oxide catalyst. J. Am. Oil Chem. **74**, 817–822 (1997b)

Hreczuch, W.: Temperature-related reaction kinetics and product composition of ethoxylated fatty acid methyl esters. J. Chem. Technol. Biotechnol. **77**, 511–516 (2002)

Hreczuch, W., Szymanowski, J.: Katalizator procesu oksyalkilenowania. Pat. pl. 171663 (1997)

Hreczuch, W., Szymanowski, J.: Sposób oksyetylenowania estrów. Pat. pl. 194888 (2007)

Imanaka, H., et al.: Alkoxylation catalyst, process for the preparation of the catalyst and process for preparing alkoxylate with the use of the catalyst. Pat. am. 5686379 1997, Pat eur. 684872 (2003)

Liu, Y., Lotero, E., Goodwin Jr., J.G., Mo, X.: Transesterification of poultry fat with methanol using Mg-Al hydrotalcite derived catalysts. Appl. Catal. A: Gen. **331**, 138–148 (2007)

Nakamura, H., et al.: Alkoxylation catalyst. Pat. am. 5012012 (1991)

Nakamura, H., et al.: Method and manufacturing of fatty acid esters of polyoxyalkylene alkyl ethers. Pat. am. 5374750 (1994)

Okamoto, T., et al.: Alkoxylation catalyst and method for producing the same and method for producing alkylene oxide adduct using the catalyst. Pat. am. 6504061, EP 0 965 382 B1

Parida, K., Das, J.: Mg/Al hydrotalcites: preparation, characterisation and ketonisation of acetic acid. J. Mol. Catal. A: Chem. **151**, 185–192 (2000)

Schick, M.J.: Nonionic Surfactant. Marcel Dekker, New York (1967)

Shen, J., Kobe, J.M., Chen, Y., Dumesic, J.A.: Synthesis and surface acid/base properties of magnesium-aluminum mixed oxides obtained from hydrotalcites. Langmuir **10**, 3902–3908 (1994)

Shuzhi, L., Bangwei, Z., Xiaolin, S., Yifang, O., Haowen, X., Zhongyu, X.: The structure and infrared spectra of nanostructured MgO-Al2O3 solid solution powders prepared by the chemical method. J. Mater. Process. Tech. **89–90**, 405–409 (1999)

Sokolovskii, A.E., Bobkova, N.M., Radion, E.V.: Conditions for the chemical precipitation of the starting substances from solutions for the synthesis of aluminosponels. Russ. J. Appl. Chem. + **79**, 349–350 (18) (2003)

Szymanowski, J.: Ethoxylation of fatty acid methyl esters. La Rivista Italiana Delle Sostanze Grasse **78**, 279–284 (2001)

Szymanowski, J.: Nowoczesne katalizatory oksyetylenowania. Przem. Chem. **84**, 567–569 (2005)

Gas-Liquid Mixing in an Unbaffled Vessel with a Forward-Reverse Rotating Scaba Impeller

Sebastian Szymon Frankiewicz and Szymon Woziwodzki(✉)

Institute of Chemical Technology and Engineering,
Poznan University of Technology, Poznań, Poland
szymon.woziwodzki@put.poznan.pl

Abstract. Mixing is one of the most important unit operations carried out in the chemical, food and related industries. It is still in the research of many scientists because of its high energy consumption. Unsteady mixing with an emphasis on its use in gas-liquid systems is presented. In such a mixing there is no need to use baffles e.g. in the food and pharmaceutical industries. In brewing, even with steady mixing, baffles are not used because it makes the washing process too difficult and affects its frequency. An experiment was conducted for the Scaba 6SRGT to compare the unsteady and steady mixing power in both a single-phase and a two-phase gas-liquid system. One would like to achieve an improvement in mixing power through the use of forward-reverse mixing. Different oscillation frequencies are used for unsteady mixing using a triangular time-course of impeller speed. Using forward-reverse mixing in a single-phase system has caused an increase in mixing power by about 80%. For forward-reverse mixing in the gas-liquid system, lower RPD values are observed compared to steady mixing, which shows greater power decreases caused by gas introduction.

1 Introduction

One of the most commonly used unit operations in the industry is mechanical mixing. Because of its high energy and time consumption, there is a need for continuous development. Conventional mechanical mixing uses impeller, which rotates in one direction and constant rotational speed (steady mixing). In an unbaffled vessel, this kind of rotation leads to the formation of the central vortex and fluid swirling (Nagata 1975; Ciofalo et al. 1996; Myers et al. 2002). These phenomena are disadvantageous because it causes a fall in mixing power. The solution to this is the use of baffles. Baffled mixing eliminates vortexing and circumferential flow however it is not an ideal solution because it causes problems itself e.g. (1) the occurrence of insufficient mixing zones, (2) the need to clean baffles periodically (Yoshida et al. 1996, 2001b). Baffles can also cause agglomeration of the catalyst in heterogeneous catalysis (Woziwodzki 2011) and hinder the growth of crystals in processes where crystallization occurs (Yoshida 2011).

Sometimes, the use of baffles is not recommended e.g. in the food and pharmaceutical industries, where keeping cleanliness is very important. To improve the mixing

© Springer Nature Switzerland AG 2020
M. Ochowiak et al. (Eds.): PAIC 2019, *Practical Aspects of Chemical Engineering*, pp. 79–88, 2020.
https://doi.org/10.1007/978-3-030-39867-5_9

efficiency in tanks without baffles, two methods are used: eccentrically located impeller (Joosten et al. 1977; Nishikawa et al. 1977; Karcz et al. 2005) or mixing in which the direction of rotation or impeller speed changes (unsteady mixing) (Kobayashi 1964). Also, unsteady mixing can also reduce some problems such as (1) formation of cavities behind the impeller blades, (2) flooding of the impeller by gas bubbles which limits the range of gas sparging rate, (3) low probability of turbulence in the vicinity of the gas-liquid interface (Yoshida et al. 2001b). These reasons make it necessary to research and to develop an unsteady mixing technique. In particular, gas-liquid mixing is a study as there is little information in the literature about this.

2 Unsteady Mixing

Various authors report the use of oscillation to intensify mixing and mass exchange. It is used in standard stirred vessels for various systems such as gas-liquid, liquid-liquids (Yoshida et al. 2002; Woziwodzki 2011) and vessels with multiple impellers (Yoshida et al. 2001a; Woziwodzki 2013). Also, Cabaret et al. (2008) used a dual shaft stirred vessel with two off-centred shafts operating in counter-rotating and co-rotating modes, whereas Komoda et al. (2000, 2019), Hirata et al. (2007) and Senda et al. (2015) applied a disk impeller reciprocating up and down. Oscillations can be successfully used in OBC (Oscillatory Baffled Column) or OBR (Oscillatory Baffled Reactor) devices (Ni and Gao 1996).

Unsteady mixing in the literature is carried out using various types of time course. Woziwodzki (2017) used various triangular impeller speed-course, both in one and two directions of rotation. For two directions they were symmetrical, symmetrical with a break between changes of direction and asymmetrical, all for different oscillation frequencies. Yoshida et al. (1996) used sinusoidal waves, while Roy and Acharya (2011) a sinusoidal variation of the impeller speed and a step function. A significant effect of this time-course on the results got was observed. Using a trapezoidal wave appeared in newer publications (Gu et al. 2017). Also, attempts are being made to change impellers for unsteady mixing (Frankiewicz 2017; Frankiewicz and Woziwodzki 2018a, b).

The literature analysis shows that studies of unsteady mixing in the gas-liquid system were usually conducted for two types of impeller time-course: sinusoidal and triangular time course of impeller speed. The research was carried out for various types of the impeller, both in single and multiple systems for various types of liquids as the dispersing phase. Triangular wave research was carried out for impellers: RT, PBT, SC3, A310, A315, HE-3, HE-3W (Woziwodzki and Broniarz-Press 2014a, b; Woziwodzki et al. 2015; Woziwodzki 2017). For the sinusoidal course, the research was conducted by Yoshida et al. (2002) for delta and RT impellers. Table 1 summarises the values of the turbulent power numbers for various types of impellers for steady and unsteady water mixing. It has been shown that the use of unsteady motion increases the mixing power. This increase is explained by the formation of disturbance areas behind the agitator blades, which increases the mixing turbulence and thus increases the power number (Yoshida et al. 2002, Woziwodzki 2017).

Table 1. Power number comparison for steady and unsteady turbulent mixing

Impeller	Steady	Unsteady
CD delta type (Yoshida et al. 2002)	0.254	0.43
RT (Yoshida et al. 2002)	0.483	1.09
RT (Woziwodzki 2011)	4.9	7.14
ST (Woziwodzki 2011)	3.2	4.74
PBT (Woziwodzki 2011)	1.1	1.64
A310 (Woziwodzki et al. 2015)	1.06	0.72
HE-3 (Woziwodzki 2017)	–	1.49
A315 (Woziwodzki 2017)	–	2.98
SC-3 (Woziwodzki 2017)	–	0.88
BT-6 (Frankiewicz 2017)	3.78	4.37

The mixing power in a gas-liquid system is usually represented by the relative power demand (RPD), which is the ratio of power in a gas system and the power in an ungassed one. With steady mixing, introducing gas into the system causes a decrease in mixing power, which results from density decrease and gas accumulation behind the blades (gas caverns) (Kamieński 2004). Studies carried out by various researchers show that for unsteady mixing higher relative power values are obtained than for steady mixing (Frankiewicz and Woziwodzki 2018b). This is probably the result of the destabilisation of gas caverns. In unsteady mixing, it destroys caverns formed behind the impeller blades during acceleration of impeller because of deceleration and change of rotation direction. In this way, their effect on mixing power is smaller, which is helpful.

During unsteady mixing, two main forces occur inertia and drag. Which of the forces prevails depends on the Keulegan-Carpenter number KC defined as follows:

$$KC = \frac{n_{max}}{f} \tag{1}$$

where $n_{\max}$ is the maximum impeller speed and f is the oscillation frequency (Woziwodzki 2017). There are three various ranges of force domination. For the value $KC < 4$, the inertia force dominates, for $4 < KC < 15$, both the drag force and the inertia force have a significant impact on unsteady mixing, and for $KC > 15$ the dominance of the drag force is observing (Woziwodzki 2017). It was noticed that for mixing in the range of resistance forces ($KC > 15$) and turbulent flow, mixing power in a single-phase system is a constant and independent of Keulegan-Carpenter number.

One of the most important features in the mixing of gas-liquid systems is the gas hold-up. Usually, the purpose is to increase the amount of gas in the liquid and thus increases mass transport. Experimental studies show that during unsteady mixing the gas hold-up is greater compared to steady mixing (Yoshida et al. 1996; Woziwodzki et al. 2015; Frankiewicz 2017; Woziwodzki 2017). This may be because of increased turbulence, which leads to an intensified bubble break-ups by eddies (Kresta 2015). In this way, more gas is dispersed in the liquid. In addition, the influence of various parameters on the gas hold-up, i.e. the oscillation frequency, the viscosity of the

continuous phase, the time-course and the gas supply method was studied (Yoshida et al. 1996, 2003; Woziwodzki 2017).

Another important parameter used to determine the efficiency of gas-liquid mixing is the volumetric mass transfer coefficient k_La, which describes the mass exchange between gas and liquid. Usually, k_La is represented by the equation:

$$k_L a = a \cdot \left(\frac{P_g}{V}\right)^b \cdot w_g^c \tag{2}$$

where a, b and c are coefficients, P_g/V is an average energy dissipation per volume and w_g is superficial gas velocity. The volumetric mass transfer coefficient k_La also depends on the physicochemical parameters of the continuous and the dispersed phase. The research by Yoshida (2011) and Woziwodzki et al. (2015) have shown that for different impellers, the use of oscillation causes a significant increase in the volumetric mass exchange coefficient. The increase in gas hold-up caused by unsteady mixing, cause an increase in the volumetric mass exchange. Only at high average energy dissipation rates, k_La values for steady mixing are similar or slightly lower values compared to steady mixing. The average energy dissipation rates from which the steady mixing takes higher k_La values are depending on the impeller, e.g. for PBT $P_g/V > 200$ W/m^3 (Woziwodzki and Broniarz-Press 2016) while for RT $P_g/V > 1000$ W/m^3 (Woziwodzki and Broniarz-Press 2014a).

3 Experimental

The experimental setup has shown in Fig. 1. Mixing was carried out in a flat-bottomed vessel. The diameter of the vessel D and the height of the liquid H was 0.29 m. Air was introduced into the system using an air compressor and then a ring sparger of diameter 0.085 m. To measure the volumetric mass transfer coefficient, an oxygen electrode with an oxygen meter and a temperature sensor were used. Compressed nitrogen introduced into the system using a porous stone was used to remove oxygen from a liquid.

The impeller was mounted on the shaft (D_s = 0.012 m) connected to an electric motor (Electrim SF400L4A) via a transmission belt. The pDrive MX Eco inverter with a curve generator delivered by Schneider Electric Company and the MatriX-3.2 computer program controlled the engine.

Thanks to this, changes in the impeller speed and direction of rotation were possible as a function of time. The applied impeller speed-course can be described by a triangular wave with different oscillation frequencies f, represented by the equation (Woziwodzki 2011):

$$n = \frac{8}{\pi^2} \cdot n_{max} \cdot \left(\sin(2\pi ft) - \frac{1}{9}\sin(6\pi ft) + \frac{1}{25}\sin(10\pi ft)\right) \tag{3}$$

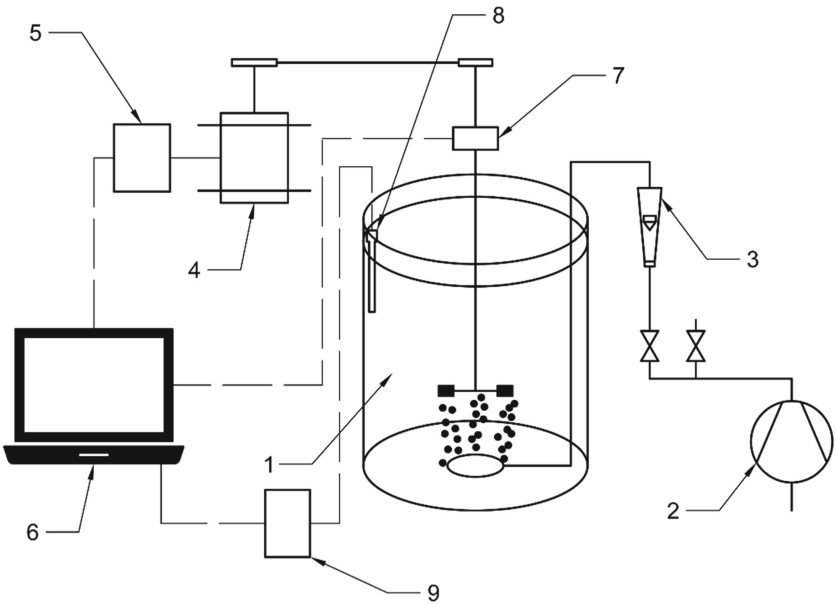

Fig. 1. Experimental setup 1 – tank, 2 – air compressor, 3 – rotameter, 4 – engine, 5 – inverter, 6 – computer, 7 – torque meter, 8 – oxygen electrode, 9 – oxygen meter

The time-course of impeller speed obtained when applying the triangular wave is shown in Fig. 2. The torque was measured using a torque meter Mt2 from Sensor AT. The Scaba 6SRGT turbine was the impeller (Fig. 3). For steady mixing, the impeller speed n ranged from 3 to 12 1/s and gas flow rates from 0.5 to 2.5 m^3/s. For the unsteady mixing, tests were carried out for three oscillation frequencies f = 0.23 Hz, f = 0.46 Hz and f = 0.92 Hz. Average rotation frequencies ranged from n = 2.6 1/s to n = 7.4 1/s. All studies were conducted in a turbulent flow in the range of KC number from 5 to 60.

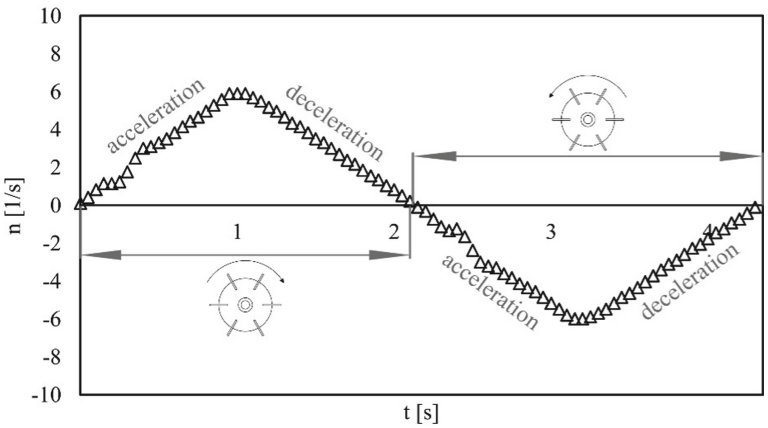

Fig. 2. Time-course of impeller speed for unsteady mixing (triangular wave)

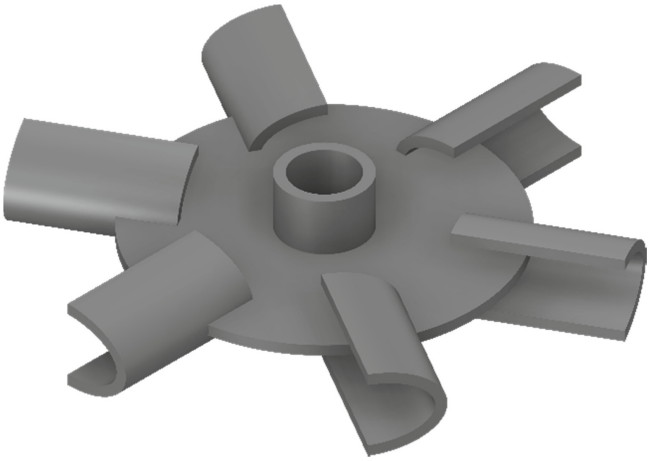

Fig. 3. Scaba 6SRGT

Figure 4 shows the relationship between power number Ne and Reynolds number Re obtained during steady and unsteady mixing, respectively. With steady mixing, the power number is 2.07 ± 0.05 and does not change with the Reynolds number than expected. Saito et al. (1992) report that the value of the turbulent power number for Scaba 6SRGT impeller (H/D = 1, d = 1/3 D) is about 1.7. The values are similar. The power number is influenced by many parameters such as tank geometry, which may cause a difference in values. Using oscillation leads to an increase in power demand (Ne = 3.68 ± 0.09). For unsteady mixing in a single-phase system, no influence of oscillation frequency is observed (KC∈(5-62)). This is confirmed by the experiments of other researchers.

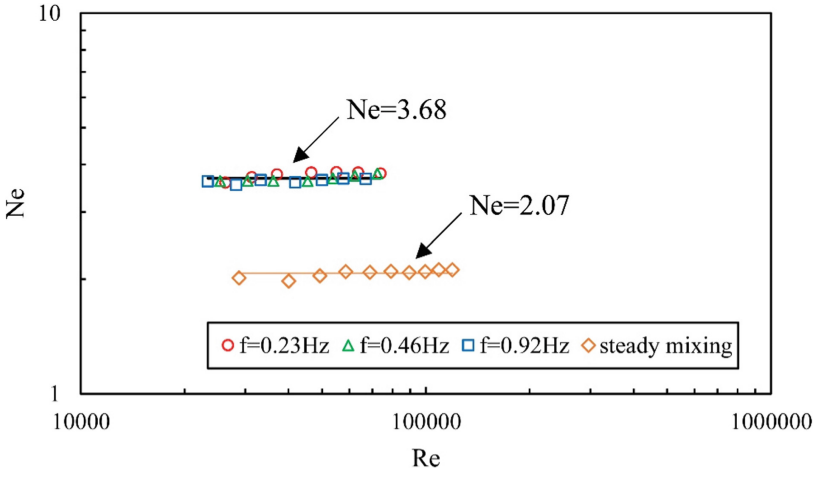

Fig. 4. Relation between power number and Reynolds number for Scaba 6SRGT

Figure 5 shows the relative power demand in a gas-liquid system as a function of gas flow number Fl_g for steady mixing. The analysis shows that as the impeller speed increases, the relative power decreases until a constant level of about 1 is achieved. The RPD value is constant in the Fl_g range from 0.01 to 0.06.

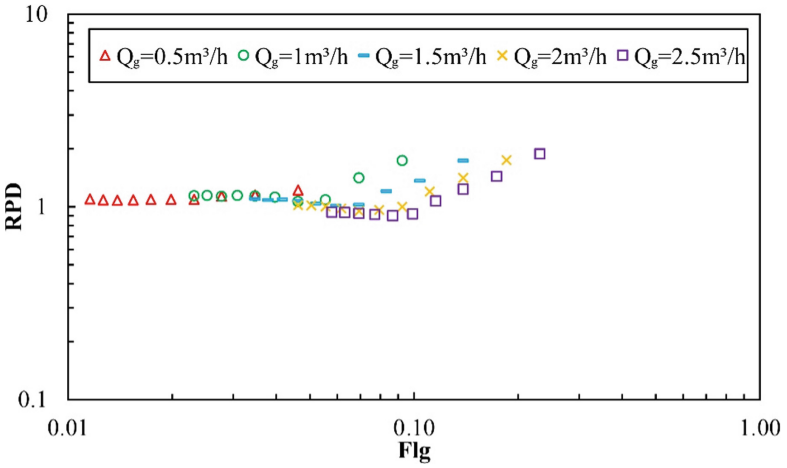

Fig. 5. Relation between relative power demand RPD and gas flow number Fl_g for Scaba (steady mixing)

Figure 6 shows the relative power demand in a gas-liquid system as a function of gas flow number Fl_g for unsteady mixing. The analysis shows that a decrease in RPD is observed ($Fl_g < 0.15$) with an increase in Fl_g for all oscillation frequencies.

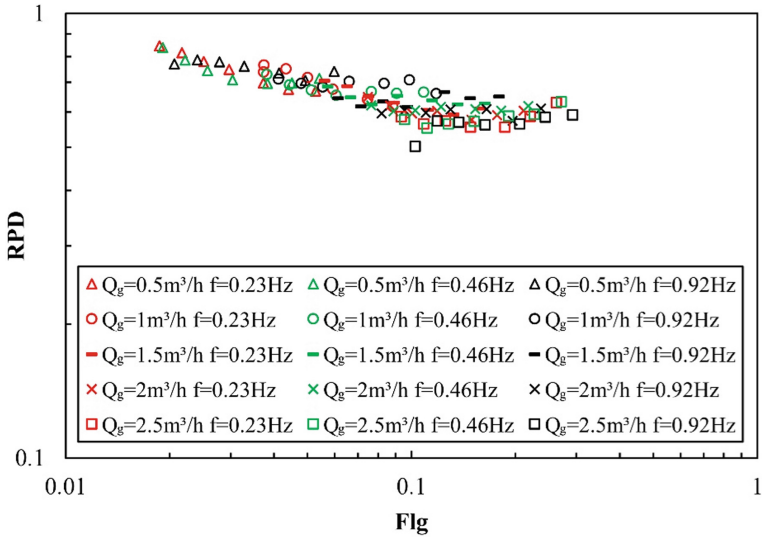

Fig. 6. Relation between relative power demand RPD and gas flow number Fl_g for Scaba (unsteady mixing)

After reaching the value of $Fl_g = 0.15$, the RPD slightly increases with gas flow number. The values obtained for all oscillation frequencies are similar.

It has been observed a slight effect of oscillation frequencies on RPD. The highest RPD is observed for oscillation frequency f = 0.92 Hz and gas flow 0.5 m^3/h and 1.0 m^3/h. The effect of oscillation frequency decreases with volumetric gas flow i.e. for Q_g = 2.5 m^3/h it is practical negligible.

4 Summary

The Scaba 6SRGT has a very high relative power demand, close to 1, which proves its good mixing properties of gas-liquid systems in terms of unidirectional mixing power.

Using forward-reverse mixing in a single-phase system has caused an increase in mixing power by about 80%. It suggests that unsteady mixing of gas-liquid systems in a vessel equipped with Scaba impeller enhance mixing, namely an increase in the mixing power and in the volumetric mass transfer coefficient. To confirm this, it would be necessary to investigate the mass exchange in forward-reverse gas-liquid mixing and the gas hold-up, which is to be a further step in the research.

Acknowledgements. This work was supported by the Polish Ministry of Science and Higher Education (Grant no. 03/32/SBAD/0902).

References

Cabaret, F., Fradette, L., Tanguy, P.A.: Gas-liquid mass transfer in unbaffled dual-impeller mixers. Chem. Eng. Sci. **63**, 1636–1647 (2008). https://doi.org/10.1016/j.ces.2007.11.028

Ciofalo, M., Brucato, A., Grisafi, F., Torraca, N.: Turbulent flow in closed and free surface unbaffled tanks stirred by radial impellers. Chem. Eng. Sci. **51**, 3557–3573 (1996). https://doi.org/10.1016/0009-2509(96)00004-8

Frankiewicz, S.: Projekt i badania podstawowe zmodyfikowanego mieszadła BT-6. Poznan University of Technology (2017)

Frankiewicz, S., Woziwodzki, S.: Mieszanie gaz-ciecz w mieszalniku z asymetrycznym mieszadłem BT-6. Inż. Apar. Chem. **57**, 59–60 (2018a)

Frankiewicz, S., Woziwodzki, S.: Effect of blade shape on unsteady mixing of gas-liquid systems. In: Ochowiak, M., Woziwodzki, S., Doligalski, M., Mitkowski, P.T. (eds.) Practical Aspects of Chemical Engineering, pp. 127–136. Springer, Cham (2018b)

Gu, D., Liu, Z., Li, J., et al.: Intensification of chaotic mixing in a stirred tank with a punched rigid-flexible impeller and a chaotic motor. Chem. Eng. Process. Process. Intensif. **122**, 1–9 (2017). https://doi.org/10.1016/j.cep.2017.08.017

Hirata, Y., Dote, T., Yoshioka, T., et al.: Performance of chaotic mixing caused by reciprocating a disk in a cylindrical vessel. Chem. Eng. Res. Des. **85**, 576–582 (2007)

Joosten, G.E.H., Schilder, J.G.M., Broere, A.M.: The suspension of floating solids in stirred vessels. Chem. Eng. Res. Des. **55**, 220–222 (1977)

Kamieński, J.: Mieszanie układów wielofazowych. Wydawnictwa Naukowo-Techniczne (2004)

Karcz, J., Cudak, M., Szoplik, J.: Stirring of a liquid in a stirred tank with an eccentrically located impeller. Chem. Eng. Sci. – Chem. Eng. Sci. **60**, 2369–2380 (2005). https://doi.org/10.1016/j.ces.2004.11.018

Kobayashi, R.: Dissolution of polyvinyl alcohol by forward-reverse rotating agitator. Shimazaki Eng. News 5–7 (1964)

Komoda, Y., Inoue, Y., Hirata, Y.: Mixing performance by reciprocating disk in cylindrical vessel. J. Chem. Eng. Jpn **33**, 879–885 (2000). https://doi.org/10.1252/jcej.33.879

Komoda, Y., Tomimasu, F., Hidema, R., Suzuki, H.: Frequency analysis of torque variation of a rotationally reciprocating impeller using Newtonian and viscoelastic fluids. Chem. Eng. Res. Des. **142**, 327–335 (2019). https://doi.org/10.1016/j.cherd.2018.12.022

Kresta, S.M.: Turbulent mixing fundamentals. In: Pharmaceutical Blending and Mixing, pp. 27–41. Wiley (2015)

Myers, K.J., Reeder, M.F., Fasano, J.: Optimise mixing by using the proper baffles. Chem. Eng. Prog. **98**, 42–47 (2002)

Nagata, S.: Mixing: Principles and Applications. Kodansha (1975)

Ni, X., Gao, S.: Scale-up correlation for mass transfer coefficients in pulsed baffled reactors. Chem. Eng. J. Biochem. Eng. J. **63**, 157–166 (1996). https://doi.org/10.1016/S0923-0467(96)03120-X

Nishikawa, M., Ashiwake, K., Hashimoto, N., Nagata, S.: Agitation power and mixing time at off-centered mixing. Kagaku Kogaku Ronbun **3**, 467–472 (1977). https://doi.org/10.1252/kakoronbunshu.3.467

Roy, S., Acharya, S.: Perturbed turbulent stirred tank flows with amplitude and mode-shape variations. Chem. Eng. Sci. **66**, 5703–5722 (2011). https://doi.org/10.1016/j.ces.2011.08.005

Saito, F., Nienow, A.W., Chatwin, S., Moore, I.P.T.: Power, gas dispersion and homogenisation characteristics of Scaba SRGT and Rushton turbine impellers. Chem. Eng. Jpn. **25**, 281–287 (1992). https://doi.org/10.1252/jcej.25.281

Senda, S., Yamagami, N., Komoda, Y., et al.: Power characteristics of a rotationally reciprocating impeller. J. Chem. Eng. Jpn. **48**, 885–890 (2015). https://doi.org/10.1252/jcej.14we392

Woziwodzki, S.: Unsteady mixing characteristics in a vessel with forward-reverse rotating impeller. Chem. Eng. Technol. **34**, 767–774 (2011). https://doi.org/10.1002/ceat.201000455

Woziwodzki, S.: Turbulent forward–reverse mixing characteristics in a vessel with multiple-turbine impellers. J. Chem. Technol. Biotechnol. **88**, 483–490 (2013). https://doi.org/10.1002/jctb.3871

Woziwodzki, S.: Mieszanie nieustalone - analiza i wybrane zastosowania. Wydawnictwo Politechniki Poznańskiej, Poznań (2017)

Woziwodzki, S., Broniarz-Press, L.: Mass transfer intensification in a vessel with unsteadily rotating impeller. In: Proceedings of 21st International Congress of Chemical and Process Engineering. Prague (2014a)

Woziwodzki, S., Broniarz-Press, L.: Power characteristics of unsteadily rotating Rushton turbine in aerated vessel. Czas Tech Chem Zesz 2-Ch 24 2014 (2014b)

Woziwodzki, S., Broniarz-Press, L.: Wpływ mieszania nieustalonego na wymianę masy w mieszalniku z mieszadłem promieniowym i osiowym. In: Proceedings of 22nd Polish Conference of Chemical and Process Engineering. Spała (2016)

Woziwodzki, S., Broniarz-Press, L., Radecki, R.: Mieszanie układów ciecz-gaz w mieszalniku z mieszadłem A310 wykonującym ruch nieustalony. Inż. Apar. Chem. **54**, 364–365 (2015)

Yoshida, M.: Gas-liquid mass transfer in an unbaffled vessel agitated by unsteadily forward-reverse rotating multiple impellers. In: Mass Transfer in Multiphase Systems and its Applications, Chap. 6. IntechOpen, Rijeka (2011)

Yoshida, M., Ito, A., Yamagiwa, K., et al.: Power characteristics of unsteadily forward–reverse rotating impellers in an unbaffled aerated agitated vessel. J. Chem. Technol. Biotechnol. **76**, 383–392 (2001a). https://doi.org/10.1002/jctb.394

Yoshida, M., Kitamura, A., Yamagiwa, K., Ohkawa, A.: Gas hold-up and volumetric oxygen transfer coefficient in an aerated agitated vessel without baffles having forward-reverse rotating impellers. Can. J. Chem. Eng. **74**, 31–39 (1996). https://doi.org/10.1002/cjce.5450740105

Yoshida, M., Taguchi, Y., Yamagiwa, K., et al.: Design and operation of unbaffled aerated agitated vessels with unsteadily forward–reverse rotating impellers handling viscous Newtonian liquids. J. Chem. Technol. Biotechnol. **78**, 474–483 (2003). https://doi.org/10.1002/jctb.813

Yoshida, M., Watanabe, M., Yamagiwa, K., et al.: Behaviour of gas-liquid mixtures in an unbaffled reactor with unsteadily forward–reverse rotating impellers. J. Chem. Technol. Biotechnol. **77**, 678–684 (2002). https://doi.org/10.1002/jctb.620

Yoshida, M., Yamagiwa, K., Ito, A., et al.: Flow and mass transfer in aerated viscous Newtonian liquids in an unbaffled agitated vessel having alternating forward–reverse rotating impellers. J. Chem. Technol. Biotechnol. **76**, 1185–1193 (2001b). https://doi.org/10.1002/jctb.498

Analysis of Mechanical Mixing in a Tank Mixer with Disturbing Elements

Aleksandra Golczak, Waldemar Szaferski(✉), and Piotr Tomasz Mitkowski

Institute of Chemical Technology and Engineering, Faculty of Chemical Technology, Poznan University of Technology, Poznań, Poland
waldemar.szaferski@put.poznan.pl

Abstract. Mechanical mixing of liquids in tanks can be performed with various agitators which can be accompanied by baffles or other disturbing elements. Such elements are not fixed to any part of the mixer but move freely within the mixed volume. In this contribution, the experimental results of chaotic mixing with spherical disturbing elements are presented along with the proposed methodology for determining the mixing time based on the change of colour. The proposed methodology utilizes the captured movie, which was split into frames, and their analysis using the vTask Studio and Adobe Photoshop 7.0 software, followed by calculations in Microsoft Excel.

1 Introduction

The efficiency of the mechanical mixing process is determined by the mixing power and time. The mixing time is determined by analysis of concentration of a selected component or the change of colour intensity at a specific point or points in the mixing space. The analysis of concentration is usually carried out based on the analysis of changes in pH (Woziwodzki et al. 2013). Nevertheless, a dye can be used to evaluate the mixing process (Mitkowski et al. 2016). Evaluation of the colour change is easy in qualitative terms, however quantitative analysis is challenging.

Takanashi and Motoda (2009) reported studies regarding the improvement of mixing efficiency in a mechanical mixer using spherical polypropylene capsules with different diameters as disturbance objects. The objects were shaped like disks, cylinders and oval balls. The mixing process was carried out in a transparent acrylic resin tank equipped with four baffles and a Rushton turbine. The experiment was conducted using an aqueous corn syrup solution and the Reynolds numbers were in laminar regime. The disturbing element was filled with barium sulphate. In order to investigate the mixing process and mixing time, the decolourization reaction of iodine with sodium thiosulfate was applied. It was observed that the capsule moves under and above the agitator, and forms circulation loops in accordance with the radial circulation of the Rushton turbine. The researchers confirmed that the inserted element is moving and destroying the isolated mixing areas below and above the mixer. The mixing times were significantly

© Springer Nature Switzerland AG 2020
M. Ochowiak et al. (Eds.): PAIC 2019, *Practical Aspects of Chemical Engineering*, pp. 89–98, 2020.
https://doi.org/10.1007/978-3-030-39867-5_10

reduced, especially in case of larger disturbing elements. The best performance was achieved for lower Reynolds number values.

Hirata (2007) investigated chaotic mixing by means of reciprocating motion of the disk in the tank. The power demand and mixing time were measured when the disk moved up and down at relatively low amplitudes. The disk generated four different flow regimes. The mixing was carried out in a liquid-liquid system and started when the two liquids were at equilibrium. When the disk moved upwards, the fluid entered the vortex created behind the disk. In the further part of the experiment, simple shear between fluids occurred.

The process was completed in a few seconds with few disk rotations due to the created high turbulence. Chaotic mixing in combination with a strong turbulence ensures fast mixing, which is not possible with conventional rotary mixing. In addition, the change from rotary to reciprocating motion increased the mixing area of both fluids (Hirata et al. 2007; Wójtowicz 2017).

The high viscosity of the liquids has a negative effect on the mixing efficiency because it causes the formation of isolated mixing regions (IMR) in the mixer. The viscous fluids can be mixed in mixers with two agitators on a common shaft. The process is carried out in the laminar and, partially, in the transition range. The occurrence of low mixing areas is problematic in the food industry, biotechnology and processing of plastics, in case of which it is important to ensure the quality of the final product and eliminate concentration or temperature gradients. Woziwodzki (2013) presented a comparison of mixing efficiency of two turbine mixers placed acentrically and in forward-reverse mixing mode, which can be also included into the group of chaotic mixing. It was determined that IMR areas occur mainly in the surroundings of agitators and are formed by applying agitators located in a non-centric position. For forward-reverse mixing, a fibber structure is formed, in case of which the fluid flows in the form of thin streams. After research and comparison of mixing times, it was concluded that forward-reverse mixing can result in increased mixing efficiency in different industries, in which fluids with significant viscosity (i.e. approximately 1 Pa·s) are used.

Although there is a vast diversity of various ways of mixing, the authors of this study report the experimental result of the mixing process in tanks with additional disturbing elements, i.e. table tennis balls. The balls possessed holes of various diameters, through which aqueous solutions characterized by different physicochemical parameters were eluted. The experiments were carried out in a mixer without baffles in a two-phase liquid-liquid system. The dye solution in the initial state of the system was only inside the ball. The important part of the research was to find a suitable methodology for recorded movies which would allow for a quantitative analysis of the obtained results.

2 Experimental Set-up and Materials

The experimental set-up consisted of a cylindrical mechanical mixer located vertically with Rushton turbine (Fig. 1). One of the main elements was a standard tank (height of liquid in the tank (H) to diameter (D) of the tank equal to 1, distance from tank bottom to impeller center line (h) to diameter (D) equal to 1/3) with the following flat bottom dimensions: inner diameter D_{in} = 290 mm and outer diameter D_{out} = 300 mm. The working volume was V = 0.0192 m^3. The used agitator with a diameter d = 100 mm was mounted at a height h = 100 mm. Table tennis balls with the outer diameter $d_{b,\ out}$ = 40 mm were used as the disturbing element. The internal volume of a single ball was $V_b = 3.351 \cdot 10^{-5}$ m^3. Each ball possessed two holes, along the ball diameter, with diameters of 1, 2 or 3 mm. Due to the additional disturbing element, no baffles were installed in the mixer.

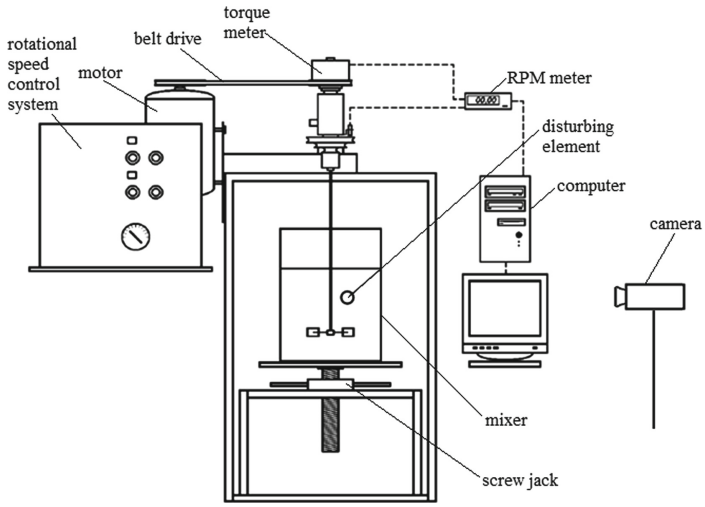

Fig. 1. Scheme of the measuring station (based on Szaferski and Mitkowski 2016)

The DC motor powered the agitator and the control system kept the agitator speed constant. A torque gauge was used to measure the torque, which was an average value taken from 10 measurements. Torque measurement were recorded and saved with an accuracy of ±0.01 rpm. The process was recorded with a digital camera (Canon EOS 60D). The experiments were carried out in the same system configuration, under the same temperature and lighting conditions (measured with Sekonic Illuminemeter i-346).

Distilled water with a temperature of 21 ± 1 °C and density of 998.02 g/cm^3 was the main medium used in the experiment. A solution of malachite green (alkaline dye) and Rokrysol WF1 polyacrylamide were used to fill the inserted balls.

Rokrysol WF1 (PCC EXOL S.A.) is a solution of partially hydrolysed polyacrylamide. It is a synthetic flocculant with non-ionic character in the form of a colourless to light yellow gel, recommended especially for concentration and filtration of inorganic suspensions characterized by a very high content of dry matter. The dynamic viscosity of Rokrysol WF1 at 25 °C is equal to 6 mPa·s and its density is equal to 1.01 g/cm^3.

3 Experimental Framework

The experiments focused on the final distribution of the dye solution in the mixer in the most efficient way and in the shortest possible time. The rate of solution release from the sphere was investigated as the result of the concentration change of mixed solution and as the dependence of the hole diameters in spheres. The contents of spheres were under ambient pressure.

The used framework for colour analysis is presented in Fig. 2. Based on the obtained movies divided into frames, the colour was examined in 10 selected points within the mixer, which were described separately using the RBG mathematical system. The obtained RGB components are a basis for calculating the hue (so called average colour). It is possible to determine the dye concentration as a function of time, knowing the value of the hue at the beginning and at the end of the process as well as at specific intervals. All experiments of chaotic mixing with disturbing elements were carried out using the measurement set-up presented in Fig. 1. The balls were filled with a solution of malachite green and Rokrysol WF1 polyacrylamide dissolved in distilled water with concentration of 1000, 2000 or 3000 ppm. The solution eluted during experiment through various holes (1, 2 or 3 mm in diameter).

The rotational speed n and torque M were measured during mixing. The results were recorded automatically with use of the computer. The experiment was recorded under constant conditions, i.e. with a constant artificial light source and without changing the position of the camera in relation to the tested system. The movie was divided into frames at intervals of 10 s using Free Video to JPG Converter (Digital Wave Ltd.). An individual frame showed a mixer containing a liquid with different colours depending on the time of mixing with a ball containing the dye. The values of RGB colour components were taken from each frame at 10 points on the surface of the mixer (Fig. 3).

The points are placed in the form of a grid. In order to improve the work, a script for image processing using vTask Studio application has been developed (Vista Software). vTask Studio is an application which stores keyboard and mouse actions based on the coordinates on the screen. It is also possible to create loops of any action.

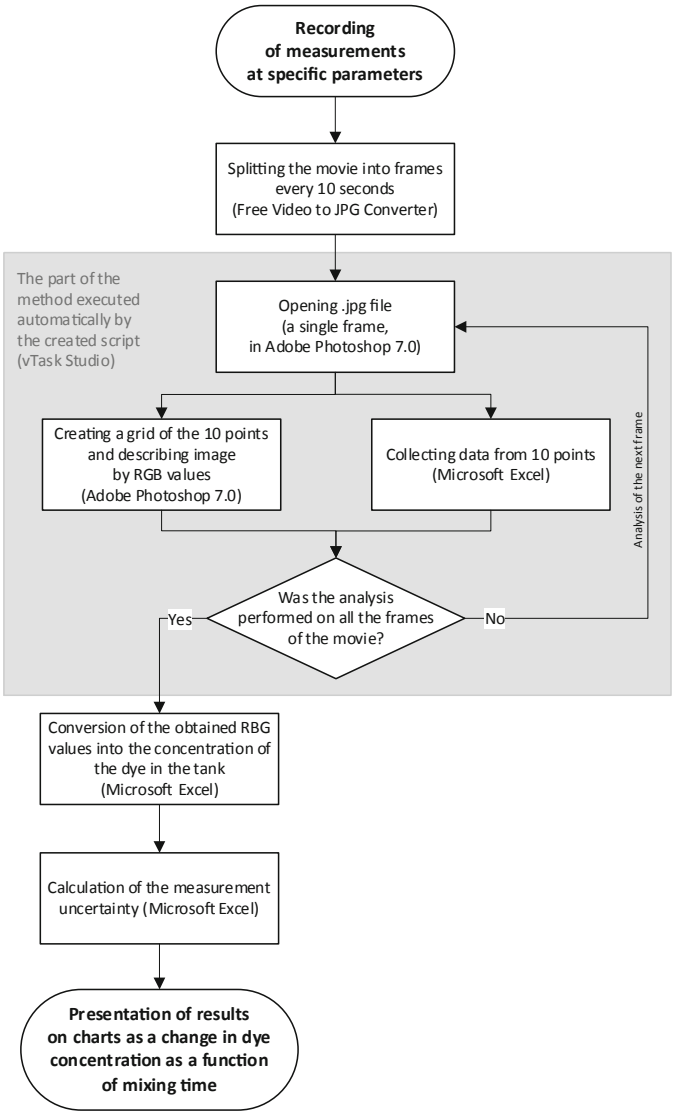

Fig. 2. Experimental framework for analysis of chaotic mixing

The images were described by RGB values in Adobe Photoshop 7.0. The data from all the points were collected in a Microsoft Excel spreadsheet. The obtained RGB values were averaged. Visualization of the mean colour was performed using the added function in Visual Basic for Applications. A macro which changes the fill colour of a cell in the table has been created. The mixing time was determined based on the assumption that the colour will not change further after releasing all the dye from the

disturbing element. On the basis of the experimental studies, the dependence between the dye concentration in the mixer tank and the time was determined by means of a camera and computer software (Dąbrowa and Krajewska 2000; Tarasiuk 2008).

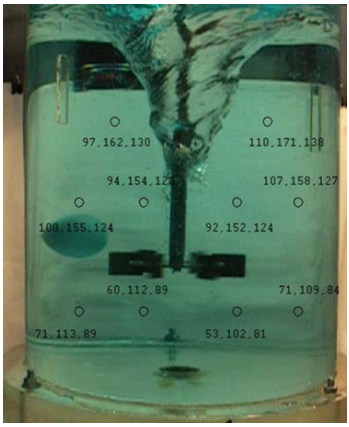

Fig. 3. Example of a photo showing the position of a grid of points

There are several important details which should be taken into consideration while using a script written in vTask Studio. First, it is designed for a computer with a specific operating system and screen resolution. It can be used in its original version or easily adapted to other requirements by changing the screen coordinates for repeatable activities.

Any number of photos which need to be processed (Fig. 4) must be opened in Adobe Photoshop and the full-screen mode should be activated (zoom 100%). The next step is to choose a regular brush (3px) and black as the basic colour. The recommended font is Arial of size 24.

Microsoft Excel spreadsheet requires previous preparation. Furthermore, the first cell in the first empty row should be selected before the script in vTask in Excel is activated. While the program is running, it is not allowed to move the cursor or to press any keys on the keyboard. Processing one photo takes approx. 4 min, but the duration of the loop depends on the capabilities of the computer.

Random errors must be removed from the data sheet. They may be manifested by series of data for which the colour sampler was located on the ball and the colour differs significantly from other results. The remaining data can be used to calculate the arithmetic average. The average values can be represented as a cell with the colour obtained after using the appropriate formula coded in the Visual Basic for Applications in Microsoft Excel. The obtained results are further processed in order to achieve plots of averaged dye concentration in function of process time with adequate colours as a background for better representation of mixing.

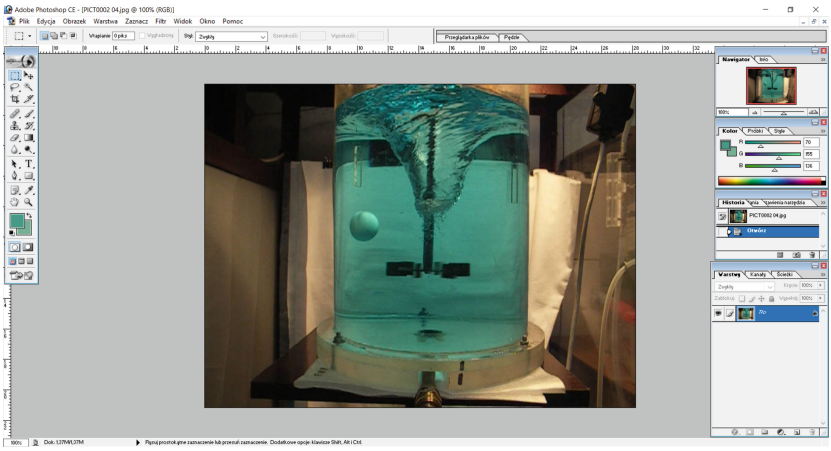

Fig. 4. Example frame of a movie before processing in Adobe Photoshop 7.0

After the calculations were finished and the results of concentrations for individual times were obtained, the errors of the results were considered. Random errors were rejected in the framework of an earlier stage. The uncertainty of type A was calculated, which occurs during repeated measurements and is caused by a random scattering of the measured quantity. The concentration was the tested parameter, which was calculated separately for each of 10 measurements in series.

The uncertainty of the final result (the arithmetic average) is defined as the standard deviation, which is the square root of the variance. The standard deviation is defined as a measure of the distribution of a random variable of x_i (i.e. concentration of dye) obtained in n measurements (i.e. 10 measurements placed on the grid):

$$\sigma_{\bar{x}} = \sqrt{\frac{\sum_{i=1}^{n} (x_i - \bar{x})^2}{n(n-1)}} \tag{1}$$

The number of measurements did not meet the condition n > 60 and it was necessary to extend the confidence interval by multiplying the standard deviation by Student's t-factor. The factor value is 2.262 for a confidence level of 0.95 and 10 measurements (Oleśkowicz-Popiel and Wojtkowiak 2007).

$$\Delta x_{A,\,0.95} = t_{n,\,0.95} \cdot \sigma_{\bar{x}} \tag{2}$$

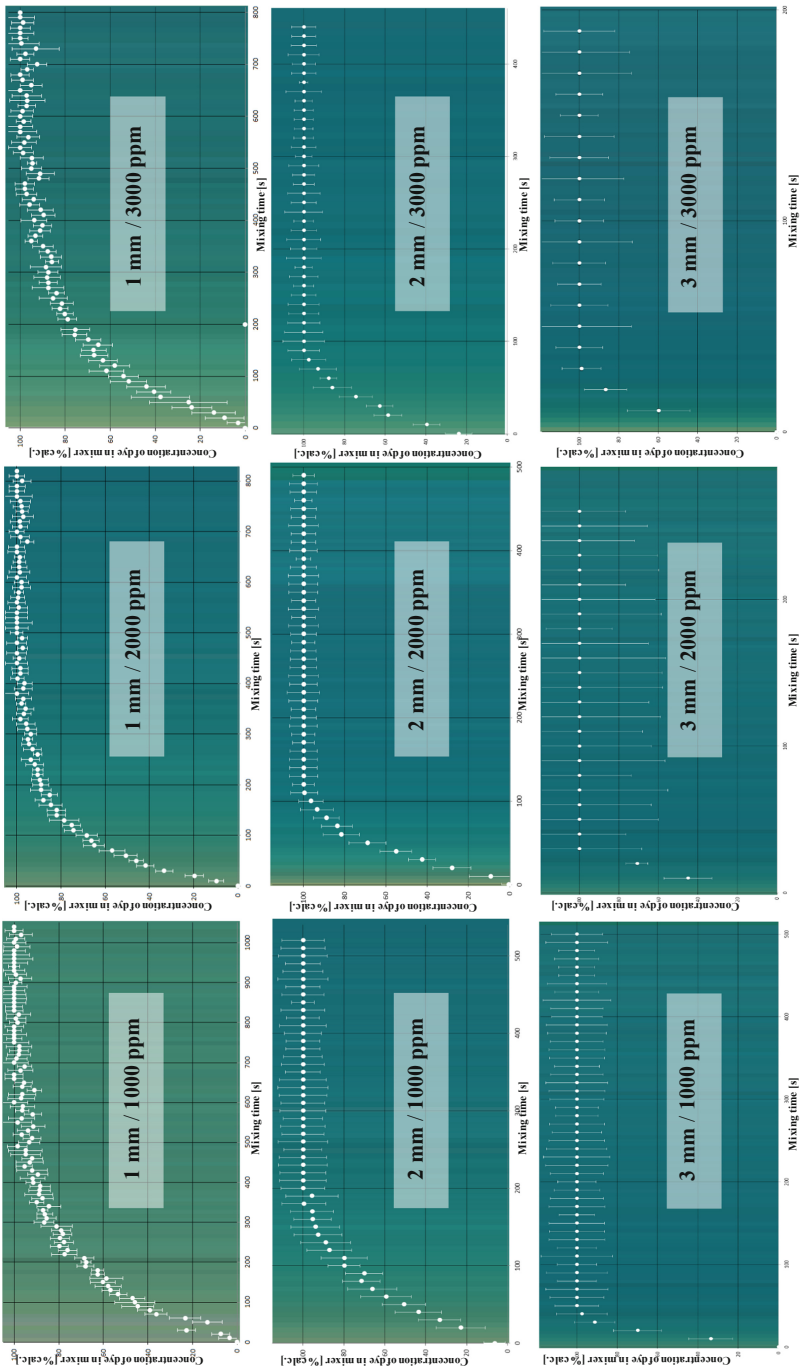

Fig. 5. Diagrams of color and concentration dependence on time for balls with holes with diameters of 1, 2 or 3 mm and for concentration of solution of dye with Rokrysol WF1 1000, 2000 or 3000 ppm.

4 Results

The obtained results are presented in Fig. 5. The concentration was calculated on the basis of hue using the RGB mathematical system. The final time of the individual processes was obtained after reaching 100% concentration. The background under the graph shows the change of colour in the mixer over time.

The mixing process has been accurately analysed during the release of dye *via* the holes in the ball according to the framework presented above. The colour and concentration in the mixer became stable after specific times which are reported in Table 1. The final time is the time after which the solution of malachite green and polyacrylamide Rokrysol WF1 has been completely released from the disturbing element.

Table 1. Final mixing time in dependence of hole's diameter and concentration of Rokrysol WF1

Concentration of aqueous solution of Rokrysol WF1 in a ball [ppm]	Diameter of holes [mm]		
	1	2	3
1000	810 [s]	290 [s]	80 [s]
2000	560 [s]	150 [s]	50 [s]
3000	630 [s]	150 [s]	50 [s]

5 Conclusions

The analysis of changes of dye concentration during chaotic mixing over the processing time for different diameters of holes within balls and for variable concentration of Rokrysol WF1 has been presented. It can be concluded that the fastest mixing occurred for the ball with 3 mm holes for solutions of 2000 ppm and 3000 ppm. The longest time was obtained for the ball with 1 mm holes. Almost the same mixing times have been obtained for solutions of 2000 ppm and 3000 ppm. In general, the mixing time decreases with the increase of hole diameter.

The important output of that research is the framework which presents all individual steps of analysis of the recording. One of the important outputs of the framework are coloured graphs which visualize the chaotic mixing. There are some measuring points on the graphs which do not comply with the assumption that the concentration of the dye in the mixer increases with time. Incorrect average values may be caused by the low quality of the camera used to record movies or by deviations in the used the RGB colour imaging system.

Acknowledgments. This research was supported by the Ministry of Science and Higher Education in Poland subsidy for Poznan University of Technology, Faculty of Chemical Technology (Grand No.: 03/32/SBAD/0902).

References

Dąbrowa, T., Krajewska, E.: Różnica barw w reprodukcji poligraficznej i sposoby jej określania (2000). http://archiwum.swiatdruku.eu/archiwum/2000_10/02.htm. Accessed 25 July 2018

Digital Wave Ltd.: Free Video to JPG Converter. https://www.dvdvideosoft.com/products/dvd/Free-Video-to-JPG-Converter.htm. Accessed 29 Apr 2019

Hirata, Y., Dote, T., Yoshioka, T., et al.: Performance of chaotic mixing caused by reciprocating a disk in a cylindrical vessel. Chem. Eng. Res. Des. **87**, 576–582 (2007)

Mitkowski, P.T., Adamski, M., Szaferski, W.: Experimental set-up of motionless hydraulic mixer and analysis of hydraulic mixing. Chem. Eng. J. **288**, 618–637 (2016). https://doi.org/10.1016/j.cej.2015.12.012

Oleśkowicz-Popiel, C., Wojtkowiak, J.: Eksperymenty w wymianie ciepła. Wydawnictwo PP, Poznań (2007)

Szaferski, W., Mitkowski, P.T.: Aeration of liquid-liquid systems with use of various agitators in mixer equipped with membrane diffuser. Chem. Eng. Technol. **39**, 2370–2379 (2016). https://doi.org/10.1002/ceat.201500248

Takanashi, K., Motoda, M.: Chaotic mixing created by object inserted in a vessel agitated by an impeller. IChemE **87**, 386–390 (2009)

Tarasiuk, J.: Wprowadzenie do grafiki komputerowej v.2008. Podstawy teorii koloru (2008). http://home.agh.edu.pl/~tarasiuk/dydaktyka/doc/GFK/S/03.pdf. Accessed 29 Apr 2019

Vista Software I vTask Studio. http://www.vtaskstudio.com/help/intro.htm. Accessed 14 Aug 2017

Wójtowicz, R.: Flow pattern and power consumption in a vibromixer. Chem. Eng. Sci. **172**, 622–635 (2017). https://doi.org/10.1016/j.ces.2017.07.010

Woziwodzki, S., Broniarz-Press, L., Jędrzejczak, Ł., Zaworska, K.: Porównanie sposobów zwiększenia efektywności mieszania płynów lepkich w mieszalniku z dwoma mieszadłami. Inż. Ap. Chem. **52**, 378–379 (2013)

Gas-Phase Synthesis of Anatase Titania Nanocrystals with Controlled Structural Properties

Marcin Janczarek[1(✉)] and Ewa Kowalska[2]

[1] Institute of Chemical Technology and Engineering, Poznan University of Technology, Poznan, Poland
marcin.janczarek@put.poznan.pl
[2] Institute for Catalysis, Hokkaido University, Sapporo, Japan

Abstract. The chapter focuses on the application of gas-phase preparation methods for the synthesis of anatase titania nanocrystals with an emphasis on their morphology. The general principles of powders' synthesis have been presented with the distinction for two groups of gas-phase preparation methods. The key role of the flow character of reaction mixture in the gas-phase crystallization process of titania has been shown. The chapter concludes that better understanding of the particles' formation principles, kinetic theory of gases and molecular dynamics is crucial to propose the proper engineering solutions.

1 Introduction

Titanium (IV) oxide (TiO_2; titanium dioxide) is widely used, among others as a pigment, food and pharmaceutical additive, as well as biocomposites, catalysts and photocatalysts. Due to the growing demand for titanium dioxide with strictly specified structural characteristics (e.g. phase composition, particle size and particle morphology), correlated with the resultant properties (absorption/reflection, activity, stability, etc.), industrial-scale synthesis methods have been sought intensively. A special role is attributed to TiO_2 occurring in the form of nanoparticles/nanocrystals, which significantly expands the perspective of potential application due to the incorporation of new properties that are not present in the case of particles with micrometer sizes (Chen and Mao 2007; Cargnello et al. 2014; Rahimi et al. 2016; Zhang et al. 2009).

For the production of TiO_2 on an industrial scale, traditional technological solutions such as the sulfate and chloride methods are most often used (Braun et al. 1992). Although these methods have been successfully used for many years to obtain large quantity of titania products world-wide (mainly for pigment applications), two shortcomings, i.e., the inability (i) to produce materials with nanoparticle characteristics, and (ii) to control structural properties precisely, hinder their application in modern nanotechnology. Therefore, other methods have been proposed to produce TiO_2 in nanometric sizes, which are mainly concentrated in two areas: hydrolysis from dissolved titanium salts and pyrolysis hydrolysis in the gas phase. Both approaches, however, are associated with advanced technological solutions, limitations in production efficiency, additional liquid-solid separation processes, and thus with high production costs of these materials.

© Springer Nature Switzerland AG 2020
M. Ochowiak et al. (Eds.): PAIC 2019, *Practical Aspects of Chemical Engineering*, pp. 99–109, 2020.
https://doi.org/10.1007/978-3-030-39867-5_11

It should be pointed out that besides the nanometric size, the shape of nanomaterials is crucial for resultant activity, and thus specific applications. The crystal shape strongly influences the functionality and quality of the final products, and the ability to design processes through the modification of the crystallization process conditions to obtain target crystal shapes has been defined as the crystal shape engineering (Lovette et al. 2008). Obtaining materials based on titanium(IV) oxide with a specific morphological structure is a particular challenge. Over the last decade, the development of laboratory-scale methods, based on reactions carried out under hydrothermal conditions, has been observed, which allows the production of semiconductor materials with different morphological structure (Liu et al. 2011). However, the main disadvantage of these methods is the strong adsorption of the reagents responsible for the morphology control on titania surface, which can influence the resultant performance, e.g., decrease the catalytic activity. In addition, many of these compounds (primarily fluorine-containing compounds) are transformed at higher temperatures to products that are highly toxic and corrosive, which limits the potential applicability of these methods. The issue of enlarging the scale of these processes is also debatable, resulting from the difficulties to precisely control the properties of the final product, especially as part of a continuous technological process.

The strategy for obtaining TiO_2 nanoparticles that allows extensive control of product properties, with particular emphasis on the morphology of nanoparticles, is to use the preparation methods based on gas phase reactions. The advantages of this strategy are also the elimination of costly stages from the technological process, such as liquid-solid separation, washing and drying, as well as much wider possibilities of increasing the scale of the process (Wegner and Pratsinis 2005).

2 General Principles of Powder Synthesis in the Gas Phase

Powder synthesis in the gas-phase has many advantages, such as preparation of particles in continuous mode, high purity and easy control of process parameter. Moreover, production of solid particles in the gas phase does not involve the liquid byproducts characteristic for wet chemistry processes. Finally, obtained particles are separated from the gas stream without any additional operations. These processes can be divided in two groups relying on: (i) evaporation and/or reaction of suspended solid particles or precursor liquid droplets (particle-to-particle conversion), and (ii) reaction of precursor gases at high temperature (gas-to-particle conversion) (Pratsinis and Vemury 1996).

Important difference between these two groups of processes is the fact that with the particle-to-particle conversion the target particle size is achieved by size reduction of larger particles, especially sprayed droplets, but in the case of gas-to-particle conversion particles are built from molecules all the way up to target size.

Analyzing gas-to-particle conversion, the molecules form quickly the particles either by uninhibited molecular collisions (coagulation-driven process) or by nucleation of subcrtitical molecular clusters (nucleation-driven process). The growth of the particles occurs by condensation and/or coagulation (Fig. 1). The strong point of this conversion route is the narrow particle size distribution. However, the weak point of

this process is the possible agglomeration of primary particles resulting from the competition between coagulation and sintering. In the case of particle-to-particle conversion the precursor liquid droplets (or solid particles) are suspended in gas streams where the product powder is formed as the consequence of the reaction with another gas or by pyrolysis. The size distribution of resultant particles depends on the primary particle size distribution, and the produced particles are rarely agglomerated (Pratsinis and Vemury 1996; Ulrich and Subramanian 1977).

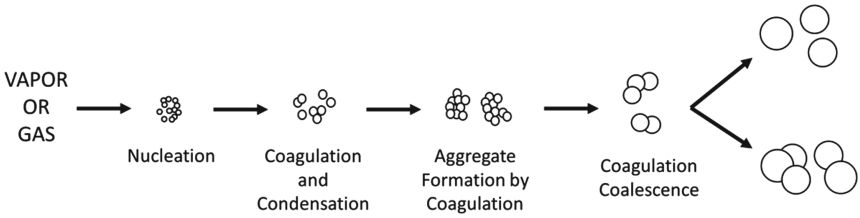

Fig. 1. Gas-to-particle conversion – scheme of particle formation and growth (adapted from (Pratsinis 2000))

3 Production of Anatase Nanocrystals by Gas Phase Methods

Anatase is the crystal form of TiO_2 (ditetragonal dipyramidal) that is particularly desirable as an active semiconductor material in such new field of application as photocatalysis. Morphology of single-crystalline anatase particles can be decisive parameter for their photocatalytic activity. Surface atomic arrangement and coordination change with crystal facets located in different orientations (Selloni 2008; Selcuk and Selloni 2016). According to the Wulff construction and the calculated surface energy, the shape of anatase under equilibrium conditions is a truncated tetragonal bipyramid (decahedral morphology) enclosed in eight isosceles trapezoidal surfaces of {101} and two top squares of {001} of small area, as shown in Fig. 2 (Oliver et al. 1997; Lazzeri et al. 2001). Preparation of such nanocrystals with well-defined facets (faceted morphology) having different {001}/{101} ratio and controlled size with narrow distribution is still an important challenge in the context of large-scale production.

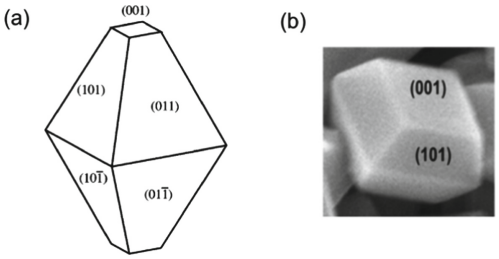

Fig. 2. The equilibrium shape of a TiO_2 in the anatase phase (a) (Lazzeri et al. 2001); SEM image of anatase crystal with decahedral morphology (b)

To obtain anatase particles with faceted morphology by gas phase synthesis, the sufficiently high reactor temperature is necessary, i.e., above 900 °C (Ahonen et al. 2002). With an increase in the reaction temperature, the shape of particles changes from spherical to irregular, and finally to a faceted one. The proper production technology should also consider the temperature for anatase to rutile (the most thermodynamically stable form of titania) irreversible transformation, which can be found in the temperature range of 400–1200 °C depending on several factors, such as the presence of defects in anatase crystals (Shannon and Pask 1965; Kumar et al. 1993), crystallite size (Gribb and Banfield 1997), the content of reaction atmosphere and the presence of impurities and additives (Shannon and Pask 1965; Akthar and Pratsinis 1992). Therefore, the selection of gas-phase method and establishing of the necessary process conditions are the key points to obtain anatase single crystals with controlled morphology at good efficiency.

3.1 Synthesis Strategy Based on Particle-to-Particle Conversion

Ahonen et al. proposed the gas-phase preparation method of faceted anatase particles by a "droplet" particle-to-particle conversion starting from titanium tetraisopropoxide (TTIP) as a titania precursor (Ahonen et al. 2001; Ahonen et al. 2002). In this method, TTIP was atomized to droplets and carried by nitrogen as a carrier gas. The produced aerosol was supplied with a flow of pressurized air. A fraction of the aerosol was directly transferred to an aerosol tubular reactor with a high temperature zone (up to 1200 °C). In the reactor, the hydrated TiO_2 particles were firstly formed. At elevated temperatures these primary particles were thermally decomposed and resultant titania particles were synthesized. The character of reaction mixture flow was identified as a laminar for all considered temperatures. Pertaining to the reactor configuration the different residence times in the reaction zone were observed.

In the case of horizontally-oriented tubular reactor the nanocrystalline anatase particles started to transform to rutile at 800 °C and average residence times in the heated zone were: 17.3 and 7.6 s for temperatures of 500 °C and 1500 °C, respectively (Ahonen et al. 2001). Their results confirm previous findings showing that rutile phase starts to appear at 700–850 °C, when titania alkoxide is used as a precursor (Schleich et al. 1997). Schleich et al. observed the presence of rutile at these temperatures, but in oxygen atmosphere and for much longer residence time (>1 min).

In the next Ahonen's study (Ahonen et al. 2002), the reactor configuration was changed to vertical orientation. Furthermore, a sample was taken from the reactor axis by using a smaller sampling tube. This solution provided a better control of residence time of particles in comparison to sampling from entire reactor volume. The Reynolds number in the case of process conducted at 1100 °C was 25 and a residence time was ca. 1 s – there were significantly lower than for previous reactor configuration. The faceted anatase particles has been obtained at 1000–1200 °C. Therefore, the reactor configuration and experimental conditions allowed to keep the high degree of stability of the anatase phase, resulting from the fact that the obtained particles were defect-free,

and thus free of crystal-crystal attachment points for calcination in gas phase. Furthermore, it was proposed that the faceted crystal shape caused an increase in an activation energy of anatase-to-rutile conversion (Ahonen et al. 2002).

Moreover, Ahonen et al. performed detail analysis of temperature distribution in the reactor tube at 800 °C (Ahonen et al. 2002). The simulations of temperature distribution (Fig. 3) by computer fluid dynamics (CFD) agree with the centerline thermocouple measurements, and experimentally obtained residence times taking advantage of vertical reactor orientation. They found that as the flow moved downstream in highest temperatures, it became more fully developed, and the axial velocity formed a parabolic profile characteristic for the laminar flow. Accordingly, the key-role of reactor configuration to keep an identifiable reaction conditions (distribution of temperature and residence time) was confirmed.

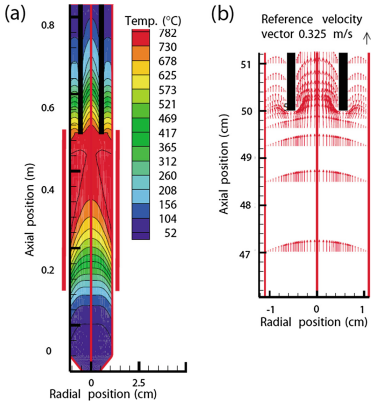

Fig. 3. Results of CFD simulation showing temperature contours in the entire aerosol reactor (a) with velocity vectors and captured flow streamlines (b) (Ahonen et al. 2002)

Pertaining to titania particle size distribution, the correlation with the properties of generated aerosol (nebulizer output) was found. The particle size was reduced as the reaction temperature was changed from room temperature to 500 °C. At the higher temperatures (up to 1200 °C), particle size remained quite constant, as shown in Fig. 4. The first temperature range (up to 500 °C) is attributed to the combustion and outgassing of organic species of alkoxy ligands (from TTIP) inducing the significant decrease of particle size (from 40 to ca. 20 nm). Chemical reactions are completed at ca. 500 °C, and the crystallization of anatase phase starts. At the temperatures above 700 °C, a slight increase of particle size was observed, resulting from a change in a particle morphology to the faceted structure (Ahonen et al. 2002).

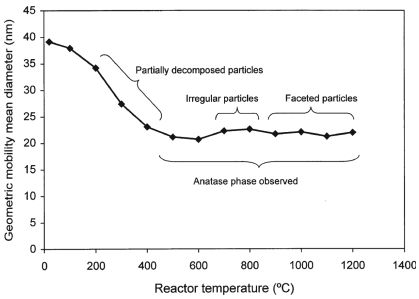

Fig. 4. Development of particle size and shape at different temperatures (Ahonen et al. 2002)

Additionally, Ahonen et al. analyzed the morphology of anatase at different calcination temperatures (500–1200 °C) (Ahonen et al. 2002). Particles which were synthesized at 500–600 °C had spherical or deformed shape. As the temperature increased, the particle shape changed from spherical to irregular, and finally faceted crystals were observed at temperatures higher than 1000 °C with similar morphology to equilibrium shape of anatase crystal (see Fig. 2).

3.2 Synthesis Strategy Based on Gas-to-Particle Conversion

3.2.1 Diffusion Flame Reactor

Preparation of anatase single crystals by the gas-phase method with gas-to-particle transformation is mainly based on using $TiCl_4$ as a titania precursor. The key-stage of chloride industrial process of TiO_2 production relays on supplying $TiCl_4$ and oxygen at almost stoichiometric conditions in gas-phase flame reactors operating under near atmospheric pressure and high temperatures in the range of 1000–1500 °C. Rutile form is the main titania phase produced by typical chloride process (Gázquez et al. 2014). Aeroxide® TiO_2 P25 is known as a widely-used reference material for photocatalytic processes. It is produced from $TiCl_4$ in the flame reactor using a mixture of air and hydrogen. Non-faceted particles with not specified morphology are obtained as a mixture of anatase (ca. 80%) and rutile (ca. 20%) (Pratsinis 1998; Koirala et al. 2016). The principle of operation of flame reactors is connected with the fact that the flame energy is used to drive chemical reactions of precursor compounds that results in the formation of product molecules, which then nucleate to form resultant particles (Pratsinis 2000).

The application of flame reactors (Fig. 5) to titania production, and the phenomenon of particles' formation in flames have been extensively studied by Pratsinis' group. They have examined the effect of additives on the phase composition of titania produced by $TiCl_4$ oxidation in a diffusion flame reactor. The addition of silica inhibits anatase-to-rutile conversion, in contrast to the addition of $AlCl_3$ accelerating the phase transition, due to the formation of oxygen vacancies on titania surface (Pratsinis and Vemury 1996). Additionally, the effect of gas mixing, precursor concentration, particle residence time and flame configuration on the particle size and the phase composition has been investigated during the titania synthesis in the flame reactor. It has been found

out that low $TiCl_4$ concentration, low residence times and low flame temperatures favor the synthesis of small anatase particles (Pratsinis et al. 1996). In the case of flame reactors, the particle morphology issue was analyzed mainly from the point of their agglomeration, and the role of flame configuration and residence times has been underlined – direct influence on the competition between particle coagulation and sintering (Pratsinis 2000).

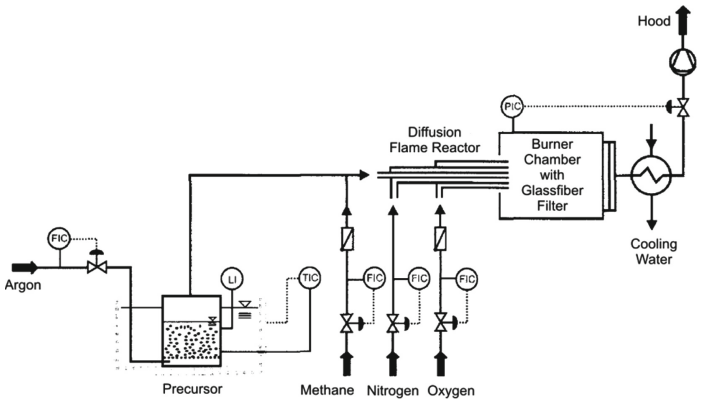

Fig. 5. Diffusion flame reactor set-up for nanoparticle synthesis (adapted from (Pratsinis 2000))

3.2.2 Tubular Gas Flow Reactor

The application of tubular gas flow reactors with external heat source (a furnace) to proceed gas-to-particle conversion strategy for preparation of titania nanocrystals with controlled morphology from $TiCl_4$ is very promising strategy. The extensive studies on this issue has been performed in Ohtani's group where single-crystalline anatase particles with decahedral morphology has been prepared (Amano et al. 2009; Janczarek et al. 2016).

The base element of the conception was to apply rapid heating (up to 1100–1200 °C) and rapid quenching of reaction mixture to enable homogeneous nucleation, and subsequent particle growth to the faceted anatase crystals. Furthermore, a narrow heating zone prevents formation of aggregates with grain boundaries (Amano et al. 2009; Janczarek et al. 2016). The first attempt was to apply an oxyhydrogen flame burner as an external heat source of a quartz glass reaction tube (Amano et al. 2009). The vapor of $TiCl_4$ was liberated by bubbling argon through a titanium tetrachloride solution at 85 °C, and then mixed with an oxygen gas. This mixture was fed to a reaction quartz glass tube. The tube was rotated to ensure homogeneous heating. The resultant anatase particles with decahedral morphology were collected at downstream by a glass-fiber filter (Amano et al. 2009).

However, the above-presented reactor set-up had some limitations. A flame burner temperature was controlled by the mixing ratio of hydrogen and oxygen, thus, the control of the temperature in the heating zone was not precise. The lack of real

continuous mode of reactor and ineffective control of process parameters were additional shortcomings of this design. Therefore, the source of heat was changed to an infrared furnace equipped with platinum foil connected with thermocouple, located in the center part of a reaction tube. In this solution only the platinum foil (and subsequently a narrow part of a reactor tube) was heated by absorption of infrared light emitted from the infrared furnace (T-3; 1100–1200 °C; Fig. 6). The intensity of infrared radiation was precisely regulated by a temperature controller. To establish accurate and continuous addition of titania precursor, the $TiCl_4$ feeding system was reorganized. A portion of liquid $TiCl_4$ was continuously fed to a vaporizer (T-1; 180 °C) with a controlled flowrate, and simultaneously argon was passed as the carrier gas for $TiCl_4$ (Fig. 6). The mixture of $TiCl_4$ vapor and argon was directed to a preheating zone tube (T-2; 200 °C). Oxygen was also preheated, but without contact with $TiCl_4$/Ar stream, and was passed directly to the reaction zone through a small tube placed coaxially inside the preheating zone. To assure stable conditions for crystallization and high yield of powder production, the process proceeded under low vacuum. Furthermore, a shower-type scrubber with Raschig rings packing was used to remove liberated chlorine from the exhaust gas. Anatase decahedral particles with small fraction of rutile (2–3%) were successfully obtained (Janczarek et al. 2016).

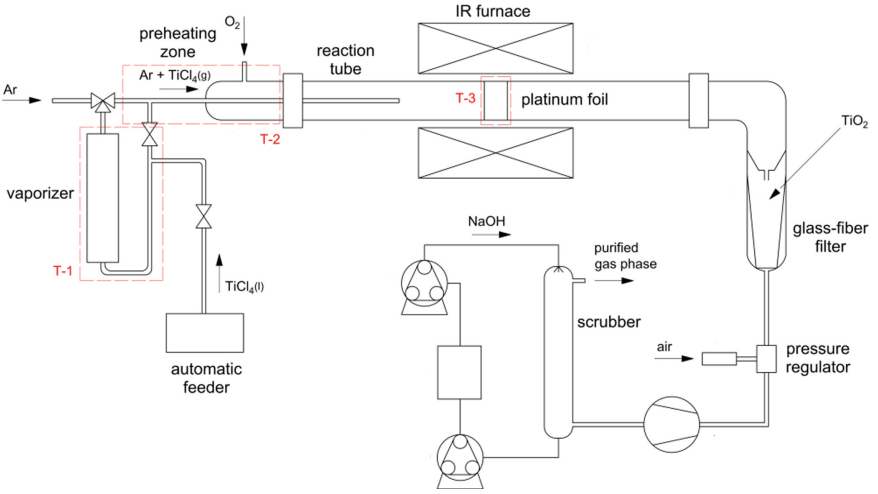

Fig. 6. Coaxial-flow gas-phase tubular reactor set-up for preparation of anatase decahedral-shaped particles: (T-1) vaporizer heating zone, (T-2) preheating zone of gases, (T-3) reaction heating zone (adapted from (Janczarek et al. 2016))

The properties of the final product were precisely controlled by the three main parameters: concentration of $TiCl_4$ vapors, temperature in the reaction zone and line speed ratio (relation between line speeds of $TiCl_4$/Ar mixture and oxygen). The flow character of gas reaction mixture was described as a laminar flow (Reynolds numbers at the range: 5.3–21.5), and the corresponding residence times were 0.5–1.8 s. The

laminar tubular flow profile in the reaction zone was showed in Fig. 7. It was proposed that despite very high reaction temperatures, short residence times (below 2 s) inhibited the anatase-to-rutile conversion. Furthermore, the excess of oxygen was responsible for low density of oxygen defects, and thus in consequence also favoring the inhibition of this transformation. It was found that the concentration of $TiCl_4$ vapors had a dominant influence on the particle size and the morphology. Moreover, it was proposed that the parallel adjustment of the line speed ratio allowed to perform smaller changes in the particles' morphology, to reduce the content of aggregated crystals and to narrow particle size distribution. The reaction temperature was decisive for the quality of the product – the number of faceted particles quickly droped at the temperatures below 1000 °C. Therefore, the reaction temperature, the amount of precursor and the flow character determine the final properties of obtained titania powders. The clear correlations between main process parameters and the properties of the product might contribute to the scaling up of this continuously proceeded synthesis of faceted anatase single crystals (Janczarek et al. 2016).

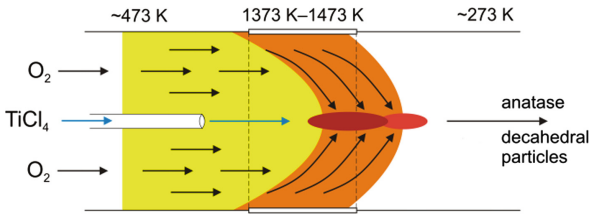

Fig. 7. Flow character profile in the coaxial-flow gas-phase tubular reactor (Janczarek et al. 2016)

4 Summary and Perspectives

The industrial synthesis of anatase crystals with high quality and strictly controlled properties is still an important challenge. In this chapter the present state of application of gas-phase preparation methods for the synthesis of anatase nanocrystals with an emphasis on their morphology has been discussed. The general principles of powders' synthesis have been presented with the distinction for two groups of gas-phase preparation methods, i.e., particle-to-particle and gas-to-particle conversions. The main examples of these methods with different types of reactor solutions such as aerosol tubular reactor, diffusion flame reactor and tubular gas flow reactor have been described with an emphasis on the relation between reactor configuration, process parameters and the properties of the final product. The fundamental role of the flow character of reaction mixture in the gas-phase crystallization process of titania has been shown. The better understanding of the particles' formation principles, kinetic theory of gases and molecular dynamics is still needed to properly describe these systems, and to propose the proper engineering solutions, particularly in the preparation of particles with controlled shape. In this regard, the wider application of CFD simulations in the gas-phase reactors' design is recommended.

Acknowledgments. This work was supported by PUT research grant No. 03/32/SBAD/902.

References

Ahonen, P.P., Joutsensaari, J., Richard, O., Tapper, U., Brown, D.P., Jokiniemi, J.K., Kauppinen, E.I.: Mobility size development and the crystallization path during aerosol decomposition synthesis of TiO_2 particles. Aerosol Sci. **32**, 615–630 (2001)

Ahonen, P.P., Moisala, A., Tapper, U., Brown, D.P., Jokiniemi, J.K., Kauppinen, E.I.: Gas-phase crystallization of titanium dioxide nanoparticles. J. Nanopart. Res. **4**, 43–52 (2002)

Amano, F., Prieto-Mahaney, O.O., Terada, Y., Yasumoto, T., Shibayama, T., Ohtani, B.: Decahedral single-crystalline particles of anatase titanium(IV) oxide with high photocatalytic activity. Chem. Mater. **21**, 2601–2603 (2009)

Akthar, M.K., Pratsinis, S.E.: Dopants in vapor-phase synthesis of titania powders. J. Am. Ceram. Soc. **75**, 3408–3416 (1992)

Braun, J.H., Baidins, A., Marganski, R.E.: TiO_2 pigment technology: a review. Prog. Org. Coat. **20**, 105–138 (1992)

Cargnello, M., Gordon, T.R., Murray, C.B.: Solution-phase synthesis of titanium dioxide nanoparticles and nanocrystals. Chem. Rev. **114**, 9319–9345 (2014)

Chen, X., Mao, S.S.: Titanium dioxide nanomaterials: synthesis, properties, modifications, and applications. Chem. Rev. **107**, 2891–2959 (2007)

Gázquez, M.J., Bolivar, J.P., Garcia-Tenorio, R., Vaca, F.: A review of the production cycle of titanium dioxide pigment. Mater. Sci. Appl. **5**, 441–458 (2014)

Gribb, A.A., Banfield, J.F.: Particle size effects on transformation kinetics and phase stability in nanocrystalline TiO_2. Am. Mineral. **82**, 717–728 (1997)

Janczarek, M., Kowalska, E., Ohtani, B.: Decahedral-shaped anatase titania photocatalyst particles: Synthesis in a newly developed coaxial-flow gas-phase reactor. Chem. Eng. J. **289**, 502–512 (2016)

Koirala, R., Pratsinis, S.E., Baiker, A.: Synthesis of catalytic materials in flames: opportunities and challenges. Chem. Soc. Rev. **45**, 3053–3068 (2016)

Kumar, K.N.P., Keizer, K., Burggraaf, A.J.: Textural evolution and phase transformation in titania membranes: part 1 – unsupported membranes. J. Mater. Chem. **3**, 1141–1149 (1993)

Lazzeri, M., Vittadini, A., Selloni, A.: Structure and energetics of stoichiometric TiO_2 anatase surfaces. Phys. Chem. Rev. B **63**, 155409 (2001)

Liu, G., Yu, J.C., Lu, G.Q., Cheng, H.M.: Crystal facet engineering of semiconductor photocatalysts: motivations, advances and unique properties. Chem. Commun. **47**, 6763–6783 (2011)

Lovette, M.A., Browning, A.R., Griffin, D.W., Sizemore, J.P., Snyder, R.C., Doherty, M.F.: Crystal shape engineering. Ind. Eng. Chem. Res. **47**, 9812–9833 (2008)

Oliver, P.M., Watson, G.W., Kelsey, E.T., Parker, S.C.: Atomistic simulation of the surface structure of the polymorphs rutile and anatase. J. Mater. Chem. **7**, 563–568 (1997)

Pratsinis, S.E., Vemury, S.: Particle formation in gases: a review. Powder Technol. **88**, 267–273 (1996)

Pratsinis, S.E., Zhu, W., Vemury, S.: The role of gas mixing in flame synthesis of titania powders. Powder Technol. **86**, 87–93 (1996)

Pratsinis, S.E.: Flame aerosol synthesis of ceramic powders. Prog. Energy Combust. Sci. **24**, 197–219 (1998)

Pratsinis, S.E., Spicer, P.T.: Competition between gas phase and surface oxidation of $TiCl_4$ during synthesis of TiO_2 particles. Chem. Eng. Sci. **53**, 1861–1868 (1998)

Pratsinis, S.E.: Aerosol flame reactors for the synthesis of nanoparticles. KONA **18**, 170–182 (2000)

Rahimi, N., Pax, R.A., Gray, E.M.: Review of functional titanium oxides. I: TiO_2 and its modifications. Prog. Solid State Chem. **44**, 86–105 (2016)

Selcuk, S., Selloni, A.: Facet-dependent trapping and dynamics of excess electrons at anatase TiO_2 surfaces and aqueous interfaces. Nat. Mater. **15**, 1107–1113 (2016)

Selloni, A.: Anatase shows its reactive side. Nat. Mater. **7**, 613–615 (2008)

Shannon, R.D., Pask, J.A.: Kinetics of the anatase-rutile transformation. J. Am. Ceramic. Soc. **48**, 391–398 (1965)

Schleich, D.M., Walter, B.: Formation of titania nanoparticles by vapor phase reactions of titanium tetraisopropoxide in oxygen/ozone containing atmospheres. NanoStr. Mater. **8**, 579–586 (1997)

Wegner, K., Pratsinis, S.E.: Gas-phase synthesis of nanoparticles: scale-up and design of flame reactors. Powder Technol. **150**, 117–122 (2005)

Ulrich, G.D., Subramanian, N.S.: Particle growth in flames III. Coalescence as a rate-controlling process. Combust. Sci. Technol. **17**, 119–126 (1977)

Zhang, H., Chen, B., Banfield, J.F.: The size dependence of the surface free energy of titania nanocrystals. Phys. Chem. Chem. Phys. **11**, 2553–2558 (2009)

Application of Enzymatic-Based Bioreactors

Katarzyna Jankowska, Karolina Bachosz, Jakub Zdarta, and Teofil Jesionowski(✉)

Institute of Chemical Technology and Engineering, Poznan University of Technology, Poznań, Poland
teofil.jesionowski@put.poznan.pl

Abstract. In the modern era, the use of environmentally friendly and sustainable solutions for effective performance of biocatalytic conversion is of key importance due to high efficiencies of the above-mentioned reactions and mild process conditions. In this context, the use of enzymatic bioreactors (EBR) with the option for highly efficient and continuous biocatalytic conversion of substrates of the reaction for conversion of biomass components as well as for removal of hazardous pollutants from wastewaters offers numerous benefits and seems to be particularly interesting. Enzymatic membrane reactors (EMR) should also be mentioned as an attractive improvement of the classic enzymatic reactors. By using the presented solution, simultaneous conversion of substrates and separation of reaction products can be achieved, which additionally reduces the operational costs and is time effective. Although the general criteria for a bioreactor design include low shear stress, high mass transfer and efficient mixing for proper substrate-enzyme interactions, it should be clearly stated that prior selection of the most suitable reactor configuration and enzyme form as well as the type of the process is required every time in order to achieve high removal efficiency. Thus, in the framework of this chapter, we present an overview of the impact of the type of bioreactor and its configuration as well as the form of enzymatic beads on the efficiencies of the biocatalytic reactions carried out using bioreactors. Finally, future perspectives regarding the use of biocatalytic processes involving free and immobilized enzymes and their application in biocatalytic reactors for removal of environmental pollutants and biomass conversion were discussed.

1 Introduction

Due to the continuously increasing interest in the practical application of biocatalytic reactions in various processes, such as biomass conversion or removal of hazardous environmental pollutants, there is a need to evaluate and develop cost-effective, eco-friendly and, most importantly, efficient solutions for their performance. One of the most promising solutions is based on the use of bioreactors with free or immobilized enzymes (Gosawami 2018). Enzymatic bioreactors (EBR) are usually characterized by good flow regime and significant reduction of the mass transfer limitations which are commonly observed in heterogeneous catalysis (Luckarift 2008). As consequence, the processes carried out in EBR offer high selectivity and efficiency. Nevertheless, it should be clearly stated that the efficiency of the EBRs is usually enhanced using

© Springer Nature Switzerland AG 2020
M. Ochowiak et al. (Eds.): PAIC 2019, *Practical Aspects of Chemical Engineering*, pp. 110–121, 2020.
https://doi.org/10.1007/978-3-030-39867-5_12

immobilized biocatalysts due to the improved stability of the enzymes against reaction conditions and increase of their reusability (Husain 2017).

In the practical application many various types and configurations of the biocatalytic reactors have been developed over recent years, which in general, can be divided into: (i) classic enzymatic bioreactors (EBRs) and (ii) enzymatic membrane reactors (EMRs) (Nanba et al. 2007). Both types of the reactors differ notably. Classic enzymatic bioreactors can be used in different operational modes, however, in order to improve the biocatalytic process efficiency, the batch and continuous modes are applied most frequently. Although the EBRs offer good reaction control, an additional step is required after the process to separate free or immobilized enzymes from the reaction mixture and to obtain pure stream of the products. In contrast, in case of enzymatic membrane reactors the catalytic action occurs simultaneously with membrane separation (Sanchez-Marcano and Tsotsis 2002).

Nevertheless, both types of bioreactors can work in three operational modes: (i) batch, (ii) semi-continuous and (iii) continuous mode (see Fig. 1), depending on how the substrate is fed. Batch and semi-continuous mode bioreactors are the most commonly used at an industrial scale, especially in the production of biofuels or biomass saccharification. However, continuous-mode processes are characterized by the highest efficiency (Pino et al. 2018). In addition, other types of bioreactors are also available, such as stirred-tank and plug-flow reactors. Among others, the stirred-tank reactors play an important role, because they ensure immediate and direct contact of the substrate and the enzymes. In case of their application in biomass conversion, it is important to select the orientation of the reactor and the method of reagents mixing. Some scientists claim that horizontal orientation is more effective due to the possibility of using gravitational or free-fall mixing. In contrast, others suggest that the use of vertical tanks with typical impellers, such as the Rushton turbine or anchor impeller, is more efficient (Modenbach and Nokes 2013).

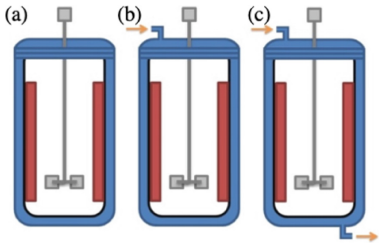

Fig. 1. Types of bioreactors in different modes: (a) batch mode, (b) fed-batch mode, (c) continuous mode

As already mentioned, most of the enzymatic processes in the industry are carried out in periodic reactors, which is associated with some limitations regarding the need of enzyme recovery and the differences between separation of consecutive portions of the product. The selection of the most suitable type of reactor depends on several important factors, such as:

- form of the enzyme (free or immobilized),
- physical properties of substrates,
- scale of reaction,
- requirement for pH and temperature control,
- stability of the enzymes,
- total costs.

Thus, there is no single standard rule for selection of an enzymatic bioreactor. All factors should be taken into account and the decision must be made on their basis (Bagheri and Mirbagheri 2018).

As it has been previously mentioned, both EBR and EMR may be used for biocatalytic biomass conversion and removal of toxic substances from wastewaters. However, particular attention should be paid to enzymatic membrane reactors, mainly due to reduced number of operational steps and higher products purity compared to the EBR. The membrane reactors are classified according to the mechanism by which the enzyme can be contacted with the substrate. According to this classification, the following enzymatic membrane reactors can be distinguished:

- direct contact membrane reactors,
- diffusion membrane reactors,
- multiphase membrane reactors.

Direct contact membrane reactors allow the contact between the substrate and enzyme immediately after being introduced into the reactor. In diffusion membrane reactors, the contact is preceded by the diffusion of the substrate by a microporous film separating the enzyme compartment. In turn, multiphase membrane reactors enable the contact between the enzyme and the substrate in a membrane matrix and interfacial transport is the main mechanism (Prazeres and Cabral 1994). The advantages and disadvantages of enzymatic membrane reactors for biomass conversion were presented in Table 1 (Rios et al. 2004; Al-Zuhair et al. 2013).

Table 1. Advantages and disadvantages of enzymatic membrane reactors (EMR).

Enzymatic membrane reactors (EMR)	
Advantages	Disadvantages
Continuous mode	Decrease of enzyme activity
Reuse of the enzyme	Heterogeneity of reaction conditions
Reduction in substrate inhibition	Membrane fouling
High selectivity and specificity	Polarization layer
Enhanced control possibilities	Leakage of enzyme

The above-mentioned features of enzymatic membrane reactors relate to the case in which the native (free) enzyme is present in the reaction mixture. However, it is possible to effectively reduce some of these disadvantages by the use of immobilized enzymes. The key advantage of immobilized biocatalysts is the increase of their

stability and resistance to inhibitors and/or process conditions as well as facilitated reusability. The methods of enzyme immobilization for use in membrane bioreactors were presented in Fig. 2.

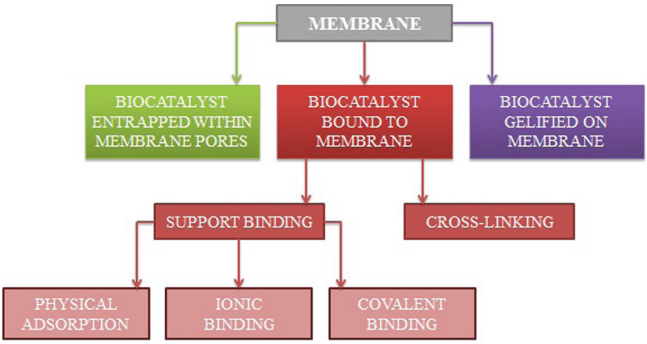

Fig. 2. Examples of enzyme immobilization methods for use in enzymatic membrane reactors

2 Application of Enzymatic Bioreactors

2.1 Biomass Conversion

Due to the constantly growing social awareness, more stringent regulations regarding environmental protection and use of natural resources, there is an increasing interest in the application of biomass. Therefore, it became popular to convert biomass components, such as cellulose and hemicelluloses, to chemical compounds at lower molecular weight, which could be used in many branches of industry. Biomass conversion can be carried out using enzymatic methods which allow to develop technologies which are completely environmentally friendly. In addition, these processes offer many advantages, i.e. low energy consumption, use of non-toxic solvents, limited number of by-products and mild environmental conditions (Alvira et al. 2010). Nevertheless, it should be noted that the processing of a large amount of substrates in bioreactors involves a number of disadvantages, which include low reaction yield, variable product quality and loss of biocatalysts activity due to the presence of inhibitors (Rios et al. 2004).

During the conversion of biomass, a wide variety of chemical compounds is synthesized. Their presence in the reaction mixture may lead to the inhibition of biocatalysts as well as to the promotion of thermodynamically unfavorable reactions (Bhatt and Bal 2019). The application of enzymatic membrane reactors (EMR) seems to be promising solution of the problem (Chakraborty et al. 2016). It is an ideal solution for reactions such as hydrolysis of cellulose, xylan, maltodextrin or starch (Prazeres and Cabral 1994). For instance, Ghazali et al. used an ultrafiltration membrane during the enzymatic cellulose hydrolysis process, which allowed the separation of glucose from the reaction mixture. As a result, a significant increase in the reaction efficiency, which was 4 times higher than in case of a batch reactor, was achieved. Additionally, it has

been confirmed that there are no meaningful changes in the activity of the enzymes depending on the operational mode used (Ghazali et al. 2017).

In the industry, the main problem is associated with the efficient separation of small-molecule products after biomass conversion. These problems are directly related to the fact that monosaccharides possess similar structures and size. A possible solution has been presented by Morthensen with co-workers, who designed an enzymatic membrane bioreactor for separation of xylose and glucose. The reactor was equipped with a nanofiltration membrane, which was used as a carrier for glucose oxidase, enzyme responsible for the conversion of glucose to gluconic acid. This solution allows for effective simultaneous enzymatic conversion and separation of xylose and gluconic acid due to the difference of charge in both compounds. At pH 5.5, gluconic acid is repelled by the membrane surface and remains in the reaction mixture, whereas xylose penetrates the pores of the membrane and passes into the permeate (Morthensen et al. 2017).

To further improve the efficiency of the enzymatic membrane bioreactor for cellulose conversion and simultaneously reduce the fouling effect by *in-situ* foulant degradation, Gebreyohannes with co-workers have used a superparamagnetic biocatalytic membrane reactor. The idea is to reversibly immobilize cellulolytic enzymes on a superparamagnetic polymeric membrane using an external magnetic field. The presented solution possesses numerous advantages, such as limited enzyme product inhibition due to simultaneous separation of the product and reduced fouling of the membrane due to dynamic layer of bionanocomposites (magnetic nanoparticles and enzymes) on the membrane surface. In consequence, a 50% increase in enzyme efficiency was noticed, as compared to the batch reactor. Furthermore, endo-glucanase and β-glucosidase immobilized onto magnetic nanoparticles were applied for *in-situ* membrane cleaning as glucose and other reaction products were recovered (Gebreyohannes et al. 2018).

Nevertheless, enzymatic membrane reactors are not the only option to improve the efficiency of biomass conversion. The use of fluidized bed reactors also seems to be promising. For example, Ricca with co-workers carried out the enzymatic hydrolysis of inulin, a polysaccharide found in many plants, to produce a fructose. From the point of view of general costs, this process is definitely more beneficial than the classic isomerization of glucose. Using the methacrylic membrane support, the inulinase from *Aspergillus* sp. was covalently immobilized. Initially, the biocatalyst was tested under industrial conditions in a batch reactor, however due to insufficient hydrolysis rate, a fluidized bed reactor was used. Although, the tests have shown that the efficiency obtained in both bioreactors is comparable, the fluidized bed reactor seems to be more time-effective, as hydrolysis occurred in a shorter time. Thus, the fluidized bed reactors are an interesting alternative especially in the processes of conversion of natural raw materials in the form of unclarified solutions (Ricca et al. 2010).

It could be briefly summarized that the data presented above and other aspects regarding the types of bioreactors and the enzyme immobilization for biomass conversion confirm the hypothesis that each system should be treated individually, particularly in the case of biocatalytic reactions. Furthermore, the fact that biomass is used as a substrate is the source of a great variety of compounds which may inhibit enzymes and decrease the process efficiency. However, the enzymatic-based bioreactors used for

biomass conversion are gaining popularity due to their overall potential and correspondence with the principles of green chemistry. Moreover, they allow to reduce the process costs and facilitate the obtaining of wide range of valuable products under mild conditions.

2.2 Environmental Protection

Currently, one of the challenges that humanity must face is to protect the natural environment from pollution, which mainly results from various branches of the industry, such as pharmaceutical, textile or automotive industry. Pollution of wastewater is particularly dangerous for the living organisms, as such substances may be easily introduced to the surface water, and then to drinking water. This may cause several negative consequences for the natural environment and human health, such as the extinction of ecosystems, or numerous human diseases, such as allergies, cardiology and neurology disorders or even cancers (Bayramoglu et al. 2019). The possible sources of environmental pollution and their negative effects were briefly summarized in Fig. 3.

Fig. 3. The possible sources of environmental pollution and their adverse effects

Biomolecules from the oxidoreductases group are enzymes which deserve special attention in the field of environmental protection. Biocatalysts such as laccase, tyrosinase or various peroxidases are used in the bioremoval of phenolic compounds and their derivatives. The structure of oxidoreductases, their co-factors and reaction mechanisms differ significantly for each of the enzymes, which means that different reaction conditions should be applied depending on the type of enzyme used, degraded compound and conditions of the reaction, and different efficiencies may be obtained (Zdarta et al. 2018a). The use of the above-mentioned enzymes in bioreactors allows to biodegrade hazardous compounds from wastewaters under controlled, mild reaction

conditions with the possibility of changing selected parameters, such as the volume of the initial solution and/or amount of the biocatalysts (Guzik et al. 2014).

Aside from the selection of the enzymes that will participate in the biocatalytic reaction, the selection of a suitable reactor configuration is an important parameter. It has a notable impact on the biocatalytic systems, their effectiveness and activity of the used enzymes (Lema et al. 2010). The reactors with the batch systems and continuous reactors are mainly used in environmental protection processes. The main difference between batch and continuous reactors is the presence of inlet and outlet flow during biodegradation process using a continuous system. The first ones find application when the mechanism of the biocatalytic reaction plays an important role and is closely related to the reaction kinetics. Continuous flow reactors are used when there is a need to purify relatively high volumes of aqueous solutions. On the other hand, batch reactors are usually applied for biodegradation of hazardous compounds from lower volumes of wastewater. The types of bioreactors used for the removal of environmental pollution were summarized in Fig. 4.

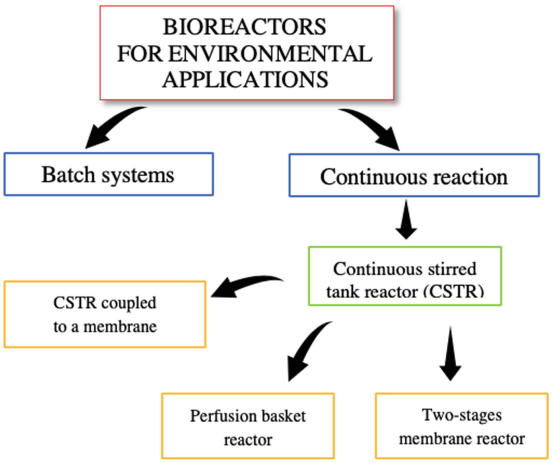

Fig. 4. The types of bioreactors used in removal of environmental pollutants

2.2.1 Free Enzymes-Based Bioreactors

Hitherto many scientists have designed the enzymatic bioreactors which could remove or convert compounds found in industrial wastewater by means of biocatalytic reactions. Dyes are among the compounds which pose a danger to the environment as their presence in sewage can be toxic for organisms living in water due to the limitation of photosynthesis process in water reservoirs (Antecka et al. 2018). In case of decolorization of azo dye Orange II from an aqueous solution, López et al. used the native manganese peroxidase in a batch reactor and CSTR coupled with an ultrafiltration membrane. The main aim of the investigation was the verification of operational strategies, such as batch and continuous systems and determination of enzyme activity during catalytic cycle. The highest removal rates of the dye (over 85%) were obtained

using a continuous reactor after 18 days of reaction. Moreover, enzymatic inactivation has been strongly limited (López et al. 2004). In another study, Kalaiarasan and Palvannan used a native enzyme, namely horseradish peroxidase, in a batch reactor for removal of phenol and Malachite Green dye from wastewaters. The scientists focused on the investigation of the effect of stabilizers of native HRP and optimization of the degradation process. It is worth noticing that guar gum and galactose showed the best performance in terms of high enzyme activity. Moreover, the optimized process allowed to remove over 95% of the pollutant from a model solution (Kalaiarasan and Palvannan 2015).

The next group of compounds that might be hazardous for environment and human health are natural or synthetic estrogens which originate from pharmaceutical industry and municipal sewage. The similarity of these compounds to hormones may cause serious diseases after their penetration into the human body. Bioreactors with free enzymes could also be used for their removal. For example, Mao with co-workers removed estrogens such as estrone (E1), 17β-estradiol (E2), 17α-ethinylestradiol (E22) and estriol (E3) using native lignin peroxidase in a batch reactor. The enzyme converted selected estrogens to dimers and trimers, which could be further separated from an aqueous solution using membrane techniques (Mao et al. 2010). The same compounds were also removed using a batch reactor by Lloret and co-workers. They used native laccase from *M. thermophila* at various reaction conditions, such as pH and the presence of mediators. The degradation products in the form of dimers and trimers are less toxic than the parent compounds as was confirmed in their work (Lloret et al. 2010). Thus, the bioreactors with native enzymes may be used for the removal of various compounds which contaminate the environment, not only dyes and pharmaceuticals. Unfortunately, the drawback of using native enzymes in bioreactors is often associated with relatively high costs of the process, due to the inability to reuse the biocatalyst.

2.2.2 Immobilized Enzymes-Based Bioreactors

Immobilized enzyme-based bioreactors are more popular bioreactors, compared to bioreactors with native enzymes. This is caused by numerous advantages of the immobilized enzymes. The biomolecules immobilized using solid supports can be used in numerous reaction cycles and retain high biocatalytic activity. Currently, tubular reactors, such as fluidized bed reactors or two-stage tubular reactors, are the most popular for removing impurities with immobilized enzymes. In these bioreactors, enzymes may be immobilized by numerous available methods, such as covalent binding, adsorption or inside membrane pores (Zdarta et al. 2018b, Jesionowski et al. 2014).

In the work of Bayramoglu and co-workers, immobilized horseradish peroxidase was used to degrade phenol and *p*-chlorophenol. The application of a magnetically stabilized fluidized bed reactor allowed to maintain high activity of HRP during the process and successfully conduct the biodegradation process in a large-scale continuous reactor (Bayramoglu et al. 2008). On the other hand, Nicolucci et al. removed bisphenol A (BPA), bisphenol F (BPF), bisphenol B (BPB) and tetrachlorobisphenol A (TCBPA) using tyrosinase immobilized onto polyacrylonitrile beads in a fluidized bed reactor. These compounds are used in the production of plastic items for everyday use.

However, they can be released into wastewater in the form of free compounds. During the investigation, BPF was removed from the aqueous solution with the highest efficiency. Furthermore, the catalytic stability of the obtained system after 30 days was over 80%. It is worth noticing that the use of fluidized bed bioreactor enables the exchange of the carrier with the enzyme and controlled flow of the solution with hazardous compounds (Nicolucci et al. 2011). In another study, Lloret et al. carried out biocatalytic degradation of Acid Green 27 dye and estrogens, such as estrone (E1), 17β-estradiol and 17α-ethinylestradiol using a packed bed reactor with laccase immobilized on Eupergit C and Eupergit C 250L. The total removal efficiency of endocrine disrupting chemicals was over 65%. However, enzymatic degradation reached an efficiency of approx. 50% as the remaining 15% of the compounds were removed by the adsorption (Lloret et al. 2012).

Examples of enzyme co-immobilization for environmental protection can also be found. For example, Krastanov removed phenols using co-immobilized laccase and tyrosinase in a fixed-bed tubular bioreactor. This method enabled the removal of 40 to approx. 90% of various phenolic compounds by a single passage through the bioreactor. The operational stability of the co-immobilized enzymes was between 10 to 90 h, depending on the phenolic substrate (Krastanov 2000).

Free enzymes and immobilized-based bioreactors find applications in environmental protection. The types of used bioreactors and enzymes strictly depend on the biocatalytic reaction, types of removed compounds and conditions of processes. Moreover, the choice between batch system and continuous reactor depends on the volumes of wastewaters and their density. Despite the satisfactory results of removing dangerous compounds from wastewaters, it is still necessary to find new enzymes-based bioreactors and to improve the entire biocatalytic processes carried out in bioreactors. This fact is caused by the constantly emerging new environmental pollutants with complex structures.

3 Summary and Future Perspectives

Toxic environmental pollutants, such as phenolic compounds, as well as natural and synthetic dyes are present as wastes in effluents from many branches of the industry and, consequently, they occur in waters and soils. Thus, there is a need to evaluate the effective ways of their removal. Moreover, direct conversion, upgrade and separation of the biomass components, such as transformation of monosaccharides into more valuable compounds, are overlooked areas. The above-mentioned queries might be solved by the use of free or immobilized enzymes from the groups of oxidoreductases (dehydrogenases, peroxidases) as well as hydrolases (cellulases, amylases) in the form of catalytic beads. However, to achieve high conversion efficiencies in a more cost-effective way, the use of various enzymatic bioreactors is required. Application of the various modes of the EBR with free or immobilized enzymes for catalytic conversion of environmental pollutants or biomass components appears to be a promising option for large-scale processes under mild conditions in the future. It means that these processes can be carried out at mild conditions and in accordance with the principles of green chemistry.

In the presented chapter, we have shown a brief overview regarding the application of the free or immobilized enzymes-based bioreactors for bioremediation processes and biomass conversion. We have emphasized the advantages of this approach and established that with their use:

(i) bioconversion of valuable biomass components as well as removal of pollutants is carried out under mild conditions, without organic solvents, in accordance with the principles of green chemistry;
(ii) total conversion of the above-mentioned compounds can be achieved in more efficient and cost-effective ways;
(iii) one-step conversion/removal and separation of the conversion products is possible to obtain an effluent stream of high purity.

We have also summarized the most frequently used operational modes of bioreactors, which facilitate high reaction yields and enhance the reusability of the enzymes.

However, further studies are required to identify the most suitable and most long-term operational modes and conditions of the enzymatic bioreactors. Moreover, the development of the novel, more efficient configurations of the bioreactors will be investigated. It should also be added that future development of the tailored made support/carrier materials characterized by improved operational stability and biocompatibility should be carried out to achieve high reactions rates. Finally, future studies should focus on the implementation of the developed solutions at large-scale applications for the bioremediation of wastewaters and biomass conversion. We hope that the presented chapter may provide important and valuable information, suggestions and ideas for the design, development and implementation of innovative, highly efficient solutions for conversion of biomass components and removal of hazardous compounds from wastewater with the use of enzymatic bioreactors.

Acknowledgements. This study was funded by Ministry of Science and Higher Education (Poland) as financial subsidy to PUT under the grant no. 03/32/SBAD/0906.

References

Alvira, P., Tomas-Pejo, E., Ballesteros, M., Negro, M.J.: Preatreatment technologies for an efficient bioethanol production process based on enzymatic hydrolysis: a review. Bioresour. Technol. **101**, 4851–4861 (2010)

Al-Zuhair, S., Al-Hosany, M., Zooba, Y., Al-Hammadi, A., Al-Kaabi, S.: Development of a membrane bioreactor for enzymatic hydrolysis of cellulose. Renew. Energy **56**, 85–89 (2013)

Antecka, K., Zdarta, J., Siwińska-Stefańska, K., Sztuk, G., Jankowska, E., Oleskowicz-Popiel, P., Jesionowski, T.: Synergistic degradation of dye wastewaters using binary or ternary oxide systems with immobilized laccase. Catalysts **402**(8), 1–18 (2018)

Bagheri, M., Mirbagheri, S.: Critical review of fouling mitigation strategies in membrane bioreactors treating water and wastewater. Bioresour. Technol. **258**, 318–334 (2018)

Bayramoglu, G., Arica, M.Y.: Enzymatic removal of phenol and p-chlorophenol in enzyme reactor: horseradish peroxidase immobilized on magnetic beads. J. Hazard. Mater. **156**, 148–155 (2008)

Bayramoglu, G., Salih, B., Akbulut, A., Arica, M.Y.: Biodegradation of Cibacron Blue 3GA by insolubulized laccase and identification of enzymatic byproduct using MALDI-ToF-MS: Toxicity assessment studies by Daphnia magna and Chlorella vulgaris. Ecotoxical. Environ. Safe **170**, 453–460 (2019)

Bhatt, S.M., Bal, J.S.: Bioprocessing perspective in biorefineries. In: Sustainable Approaches for Biofuels Production, vol. 7, pp. 1–23. Springer, Cham (2019)

Chakraborty, S., Rusli, H., Nath, A., Sikder, J., Bhattacharjee, C., Curcio, S., Drioli, E.: Immobilized biocatalytic process development and potential application in membrane separation: a review. Crit. Rev. Biotechnol. **36**, 43–58 (2016)

Gebreyohannes, A.Y., Dharmjeet, M., Swusten, T., Mertens, M., Verspreet, J., Verbiest, T., Courtind, C.M., Vankelecom, I.F.V.: Simultaneous glucose production from cellulose and fouling reduction using a magnetic responsive membrane reactor with superparamagnetic nanoparticles carrying cellulolytic enzymes. Bioresour. Technol. **263**, 532–540 (2018)

Ghazali, N.F., Pahlawi, Q.A., Hanim, K.M., Makhtar, N.A.: Enzymatic hydrolysis of oil palm empty fruit bunch using membrane reactor. Chem. Eng. Trans. **56**, 1543–1548 (2017)

Goswami, L., Kumar, R.V., Borah, S.N., Manikandan, N.A., Paksirajan, K., Pugazhenthi, G.: Membrane bioreactors and integrated membrane bioreactor systems for micropollutants removal from wastewater: a review. J. Water Process Eng. **26**, 314–328 (2018)

Guzik, U., Hupert-Kocurek, K., Wojcieszynska, D.: Immobilization as a strategy for improving enzyme properties – application to oxidoreductases. Molecules **19**(7), 8995–9018 (2014)

Husain, Q.: Nanomaterials as novel supports for the immobilization of amylolytic enzymes and their applications: a review. Biocatalysis **3**, 37–53 (2017)

Jesionowski, T., Zdarta, J., Krajewska, B.: Enzyme immobilization by adsorption: a review. Adsorption **20**, 801–821 (2014)

Kalaiarasan, E., Palvannan, T.: Efficiency of carbohydrate additives on the stability of horseradish peroxidase (HRP): HRP-catalyzed removal of phenol and malachite green decolorization from wastewater. CLEAN – Soil, Air, Water **43**, 846–856 (2015)

Krastanov, A.: Removal of phenols from mixtures by co-immobilized laccase/tyrosinase and Polyclar adsorption. J. Ind. Microbiol. Biotechnol. **24**, 383–388 (2000)

Lema, J.M., López, C., Eibes, G., Taboada-Puig, R., Moreira, M.T., Feijoo, G.: Reactor engineering. In: Torres, E., Ayala, M. (eds.) Biocatalysis Based on Heme Peroxidases as Potential Industrial Biocatalysts. Springer, Heidelberg (2010)

Lloret, L., Eibes, G., Lu-Chau, T.A., Moreira, M.T., Feijoo, G., Lema, J.M.: Laccase-catalyzed degradation of anti-inflammatories and estrogens. Biochem. Eng. J. **51**, 124–131 (2010)

Lloret, L., Hollmann, F., Eibes, G., Feijoo, G., Moreira, M.T., Lema, J.M.: Immobilisation of laccase on Eupergit supports and its application for the removal of endocrine disrupting chemicals in a packed-bed reactor. Biodegradation **23**, 373–386 (2012)

Lopez, C., Moreira, M.T., Feijoo, G., Lema, J.M.: Dye decolorization by manganese peroxidase in an enzymatic membrane bioreactor. Biotechnol. Prog. **20**, 74–81 (2004)

Luckarift, H.R.: Silica-immobilized enzyme reactors. J. Liq. Chromatogr. Relat. Technol. **31**, 1568–1592 (2008)

Mao, L., Lu, J., Habteselassie, M., Luo, Q., Gao, S., Cabrera, M., Huang, Q.: Ligninase-mediated removal of natural and synthetic estrogens from water: II. Reactions of 17beta-estradiol. Environ. Sci. Technol. **44**, 2599–2604 (2010)

Modenbach, A.A., Nokes, S.E.: Enzymatic hydrolysis of biomass at high-solids loadings – a review. Biomass Bioenergy **56**, 526–544 (2013)

Morthensen, S.T., Meyer, A.S., Jorgensen, H., Pinelo, M.: Significance of membrane bioreactor design on the biocatalytic performance of glucose oxidase and catalase: free vs immobilized enzyme systems. Biochem. Eng. J. **117**, 41–47 (2017)

Nanba, H., Yasohara, Y., Hasegawa, J., Takahashi, S.: Bioreactor systems for the production of optically active amino acids and alcohols. Org. Process Res. Dev. **11**, 503–508 (2007)

Nicolucci, C., Rossi, S., Menale, C., Godjevargova, T., Ivanov, Y., Bianco, M., Mita, L., Bencivenga, U., Mita, D., Diano, N.: Biodegradation of bisphenols with immobilized laccase or tyrosinase on polyacrylonitrile beads. Biodegradation **22**, 673–683 (2011)

Pino, M.S., Rodriguez-Jasso, R.M., Michelin, M., Flores-Gallegos, A.C., Morales-Rodriguez, R., Teixiera, J.A., Ruiz, H.A.: Bioreactor design for enzymatic hydrolysis of biomass under the biorefinery concept. Chem. Eng. J. **347**, 119–136 (2018)

Prazeres, D.M.F., Cabral, J.M.S.: Enzymatic membrane bioreactors and their applications. Enzyme Microb. Technol. **16**, 738–750 (1994)

Ricca, E., Calabro, V., Curcio, S., Basso, A., Gardossi, L., Iorio, G.: Fructose production by inulinase covalently immobilized on sepabeads in batch and fluidized bed bioreactor. Int. J. Mol. Sci. **11**, 1180–1189 (2010)

Rios, G.M., Belleville, M.P., Paolucci, D., Sanchez, J.: Progress in enzymatic membrane reactor – a review. J. Membr. Sci **242**, 189–196 (2004)

Sanchez-Marcano, J., Tsotsis, T.T.: Catalytic Membranes and Membrane Reactors. Wiley VCH, Weinheim (2002)

Zdarta, J., Antecka, K., Frankowski, R., Zgoła-Grześkowiak, A., Ehrlich, H., Jesionowski, T.: The effect of operational parameters on the biodegradation of bisphenols by Trametes versicolor laccase immobilized on Hippospongia communis spongin scaffolds. Sci. Total Environ. **615**, 784–795 (2018a)

Zdarta, J., Meyer, A.S., Jesionowski, T., Pinelo, M.: Developments in support materials for immobilization of oxidoreductases: a comprehensive review. Adv. Colloids Interface Sci. **258**, 1–20 (2018b)

Nanoparticles Size Determination by Dynamic Light Scattering in Real (Non-standard) Conditions Regulators - Design, Tests and Applications

Maciej Jarzębski[1(✉)], Przemysław Siejak[1], Arkadiusz Sawerski[1], Maksymilian Stasiak[1], Kamil Ratajczak[1], Łukasz Masewicz[1], Krzysztof Polewski[1], Farahnaz Fathordoobady[2], Yigong Guo[2], and Anubhav Pratap Singh[2]

[1] Department of Physics and Biophysics, Poznan University of Life Sciences, Poznań, Poland
maciej.jarzebski@up.poznan.pl
[2] Faculty of Land and Food Systems (LFS), University of British Columbia, Vancouver, Canada

Abstract. Dynamic light scattering (DLS) is one of the most commonly used for rapid particle size determination. The advantages of DLS for fast and simple colloid systems (i.e. food, emulsions) and nanoparticles dispersion characterization is limited due to particle shape and possible interactions between the sample and the measuring solution. In this paper, we present the results of monodispersed polystyrene standardized nanobeads, silver and polydispersed submicron-sized fluorinated particles (HFBMA) and silica synthesized by a modified Stöber method. We compared the obtained results in "standard conditions" with non-standard situations, such as using tap water or employing Ringer solution as a dispersant. Furthermore, the studies were performed at both room temperature (20 °C) and elevated temperature (37 °C) to simulate various possible applications of nanosystem investigations in the biomedical field. The results show that sample behaviours might not only vary with temperature and dispersant changes, but may also fluctuate during the time of measurement (i.e. aggregation process could be observed). Presented results will open discussion about factors other than dilution and concentrations for observing behavior of the nanoparticles and submicron particles in "real conditions". Our studies confirmed the hypothesis that more than one particle size determination technique is recommended. Moreover, particle size verification is recommended during long-term storage and when environmental conditions change.

1 Introduction

Nanotechnology is an approach to develop processes for the manipulation of materials in nanoscales and can result in new products. Particle size under 100 nm is commonly considered as particles with unique properties and novel applications. Nanotechnology covers science and technologies including chemistry, physics, engineering, and biotechnology and has the potential to open opportunities in R&D and add novelty in many areas, including cosmetics, medicine, agriculture and food industry (Chaudhry

© Springer Nature Switzerland AG 2020
M. Ochowiak et al. (Eds.): PAIC 2019, *Practical Aspects of Chemical Engineering*, pp. 122–131, 2020.
https://doi.org/10.1007/978-3-030-39867-5_13

et al. 2008). Most materials, including foods and other biomaterials, show dissimilar properties when they are converted into nano-size structures (Aguilera 2005). These materials, when converted to nanoscale, may aid in improving safety properties, nutritional value, and bioavailability of nutrients and health supplements, as well as the potential functional properties which can affect the molecular synthesis of new ingredients (Bai et al. 2006). The convergence of nanotechnology with other technologies can result in development in food processing and safety, color and flavor, delivery methods, detection of pathogens, functional properties of foods, and storage benefits. The product development, method designs, and instrumentation may also get advantage from nanotechnology (Rashidi and Khosravi-Darani 2011). Hence, many companies in the food segment are exploring the potential of using nanotechnology in their processing and product development (Chaudhry et al. 2008).

Dynamic light scattering (DLS) is one of the most commonly employed technique in the food and bioproducts industries for particle size determinations wherein a laser beam is employed to illuminate a suspension of particles undergoing Brownian motion (Dahneke 1983). An autocorrelator then analyzes the signal, G, of the time-dependent fluctuations in the intensity of the scattered light to measure the speed of Brownian motion. This signal decays exponentially at a rate dependent on the diffusion coefficient (D) of the particle (Dahneke 1983), as shown in Eq. (1), which is then correlated to the hydrodynamic diameter (d_H) of the particle using the Stokes-Einstein equation (Eq. 2).

$$G = \int_0^\infty I(t) \cdot I(t+\tau)dt = B + A \cdot e^{-\frac{32 \cdot \pi^2 \cdot \mu^2 \cdot D \cdot \tau}{\lambda_o^2} sin^2 \frac{\theta}{2}} \tag{1}$$

$$d_H = \frac{k \cdot T}{3 \cdot \pi \cdot \eta \cdot D} \tag{2}$$

where A is the amplitude, B is the baseline, D is the translational diffusion coefficient, θ is the scattering angle, λ_o is the vacuum wavelength of the laser, k is the Boltzmann constant, μ is the solvent refractive index, η is the dispersant viscosity and T is the temperature (Kaszuba et al. 2008). The minimum size limit for the DLS technique depends on difference in the light scattering characteristics of the matter being studied & the dispersant in question. This in turn depends on multiple factors such as the nature of the laser source, detector sensitivity, instrument configurations, concentration of the sample and the refractive indices of the sample and dispersant. Usually to minimize deviations due to the dispersant for enabling a low minimum detection limit, investigations are performed in highly defined and "sterile" dispersant, such us deionized and Millipore water and with additional purification processes, such as filtration.

In this paper, we focused on understanding what happens on using non-ideal systems as dispersants for particle size determination using DLS. We choose tap water (which conditions might be determined by local water supplier) and Ringer solution as a measurements environment. Presented results will open discussion for factors other than dilution and concentration to observe the behavior of the nanoparticles and submicron particles in "real conditions".

2 Materials and Methods

2.1 Materials

2.1.1 Latex Standardized Nanobeads

Size standard polystyrene (PS) beads dispersed in water with 216 nm ± 4 nm (cat. 3220 A) were purchased from Thermo Scientific™. Size Standards The latex standards were used as delivered without further purification. Typically 50 μL of stock solution was dissolved in 1 mL of selected solvent. Then the suspension was vortexed for 60 s before the test.

2.1.2 Silver Nanoparticles

The silver nanoparticles (Ag60, 0.02 mg/ml) dispersion were purchased as silver nanoparticles (60 nm, TEM confirmed by manufacturer) dispersion in aqueous buffer, containing sodium citrate as stabilizer from Sigma Aldrich (Poland) and used without further purification. For the analysis, 100 μl of stock dispersion was added to 1 ml of the test solutions.

2.1.3 Silica

Fluorescent silica submicron particles (SiO) were synthesized as described in more details in our previous works (Jarzębski et al. 2017a; Gapiński et al. 2016) according to modified Stöber method (Verhaegh and van Blaaderen 1994). As a fluorescent dye, Rhodamine B isothiocyanate (RBITC) in anhydrous 99.8% methanol from Sigma Aldrich and 3-aminopropyltriethoxysiliane (APS) from Fluka (Germany) were used. Before the DLS examinations, fluorescent silica samples were centrifuged several times and re-suspended in fresh ethanol and water in order to remove the non-coupled fluorescent dye. Then, highly dispersed aqueous dispersion was used for the measurements (typically 10 μL silica dispersion in 1 mL of the solution).

2.1.4 HFMBA Polymeric Particles

Fluorescent polymeric submicron-sized HFBMA (H1) based on 1H, 1H-Heptafluoro-n-butyl methacrylate 97% (SynQuest Labs, USA) with ethylene glycoldi-methacrylate (Acros Organics, Germany) as crosslinker (Koenderink et al. 2001; Sacanna et al. 2004; Jarzębski et al. 2016) was used without further purification. Due to insoluble residue the reaction mixture was investigated as is after synthesis.

2.2 Methods

The hydrodynamic diameters (d_H) of the nanoparticles dispersion were determined by dynamic light scattering (DLS) technique, using Zetasizer Nano ZS90 (Malvern). For DLS measurements scattered light was recorded at the angle of 90°. The autocorellation curves were registered at temperatures of 20 °C and 37 °C. The measurements were performed using automatic settings adjusted for the latex spheres. The average values of the particle size distribution were obtained from 10 measurements.

The measurements were performed in deionized water, tap water (from local water supplier Aquanet) and Ringer solution Fresenius (Fresenius Kabi, Poland) as infusion

solution (natrii chloridum + Kalii chloridum + Calcii chloridum dihydricum). For the results presentation and unification, average particle diameter was summarized up to full nanometer (i.e. 203.2 nm, 203.9 nm → 204 nm).

3 Results and Discussion

Berne and Pecora in (1976) presented the principles of the dynamic light scattering technique for particle size characterization. In general, Brownian motion of the particles indicates fluctuation of scattered light intensity. As a light source for colloidal dispersions illumination different lasers beams was used. The laser length should be strictly defined for the calculation of hydrodynamic diameter of the investigated particles.

What is more, the scattering light detection angle plays one of the crucial roles of the particle size characterization (see Eq. 1). Kaszuba et al. (2008) pointed that frequently used detection angle of 90° may not be enough sensitive and accurate enough for the small particles characterizations. Furthermore, they suggested that at 173° backscatter, the scattering light from smaller particles increased dramatically (up to 8 times than 90°).

Nowadays, a lot of DLS devices manufacturers have offered two or three detection angles for small (backscatter angles at 173 or 175°) and big particles (forward angles 13 or 15°). Bhattacharjee (2016) defined that the samples which PDI index is ≤ 0.1 shows highly monodisperse values. In the range of 0.1–0.4 exhibit moderate polydispersity. Beyound PDI value >0.4 are considered as highly polydisperse samples. In this paper we presented the results of selected nanoparticles and submicron particles with low and high polydispersity (PDI) index. The results presented in Table 1, were recorded at 90° detection angle.

Typically, the recommended conditions for the DLS measurement solution were: used deionized water (i.e. millipored water, 0.055μS/cm), additional purification processes such as filtration might be needed, then dispersed particles in the previously prepared solution and stabilized as prepared samples for few minutes at the desired temperature. Nevertheless, suggested measuring conditions were suitable for standardization of the DLS technique. Using additional purification processes, the samples were preserved from the aggregations, agglomeration, and impact on other conditions, such as interaction between the particles and the ions in the solution. Unfortunately, "live samples" including human fluidics, food or cosmetic systems do not behave as a model system. So, we performed our measurements in tap water and Ringer solution.

Table 1. Average diameters of PS, Ag60, SiO and H1 samples: z-ave, peak maximum and PDI index, obtained in deionized water, tap water and Ringer solution.

Sample	Temperature (°C)	Deionized water			Tap water			Ringer solution		
		d_H (z-avg) (nm)	d_H – peak maximum (nm)	PDI	d_H (z-avg) (nm)	d_H – peak maximum (nm)	PDI	d_H (z-avg) (nm)	d_H – peak maximum (nm)	PDI
PS	20	200 ± 2	225	0.099 ± 0.022	190 ± 3	217	0.126 ± 0.026	191 ± 3	237	0.184 ± 0.021
	37	201 ± 2	220	0.080 ± 0.014	160 ± 13	189	0.150 ± 0.026	193 ± 2	219	0.113 ± 0.021
Ag60	20	62 ± 1	75	0.191 ± 0.021	125 ± 41	148	0.200 ± 0.039	221 ± 31	266	0.251 ± 0.035
	37	64 ± 2	70	0.215 ± 0.013	745 ± 197	766	0.568 ± 0.110	466 ± 65	537	0.530 ± 0.045
SiO	20	778 ± 34	819	0.093 ± 0.056	711 ± 77	742	0.109 ± 0.080	803 ± 37	860	0.056 ± 0.038
	37	710 ± 35	746	0.054 ± 0.028	762 ± 154	804	0.191 ± 0.181	601 ± 90	555	0.658 ± 0.385
H1	20	215 ± 3	224	0.042 ± 0.026	214 ± 3	225	0.030 ± 0.022	218 ± 4	228	0.029 ± 0.027
	37	219 ± 2	226	0.016 ± 0.009	210 ± 5	216	0.044 ± 0.021	221 ± 2	229	0.027 ± 0.018

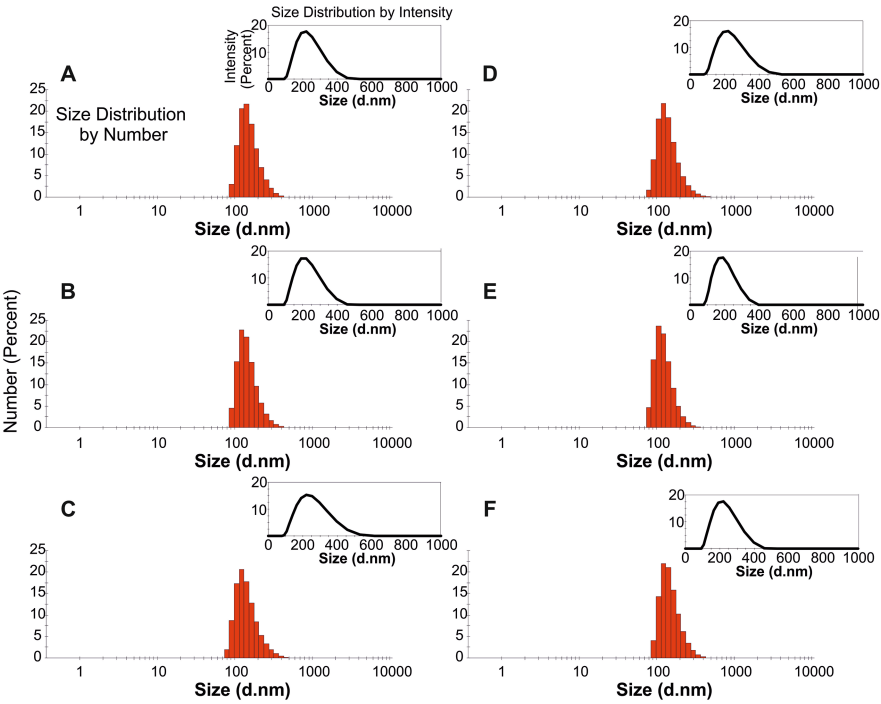

Fig. 1. Results of DLS measurements of latex standard nanobeads (PS) (number by size – red bars, size distribution by intensity – black curves), obtained in: A. 20 °C deionized water, B. 20 °C tap water, C. 20 °C Ringer solution, D. 37 °C deionized water, E. 37 °C tap water, F. 37 °C Ringer solution.

In Figs. 1, 2, 3 and 4 the particles size distribution by number and particles size distribution by light scattering intensity were presented. In the DLS studies, two main parameters are usually given to characterize the hydrodynamic diameter of the investigated samples: z-average (z-ave) and peak maximum. Z-ave parameter corresponds to cumulant method, which is less vulnerable to noise than other algorithms and not recommended for the high polydispersed samples (Maulucciet al. 2005; Bhattacharjee 2016). The second algorithm, which is most used in measuring devices is CONTIN. This one has been recommended for more detailed studies of inhomogeneous samples (Bhattacharjee 2016; Varga et al. 2014). The proves of this recommendation can be easy observed in Table 1 where the z-ave were in good agreement with peak maximum for the PS and Ag60 measured in standard conditions (deionized water). Standardized latex beads presented stable values of d_H and relation between z-ave and peak maximum (see Fig. 1), even when the environmental condition changed (tap water or Ringer solution used). The differences between z-ave and peak maximum were observed for Ag60 sample. In deionized water, the d_H of Ag60 was in good agreement with the declaration of the supplier. When tap water and Ringer solution and higher temperature were used, the values of z-ave and average peak maximum increased.

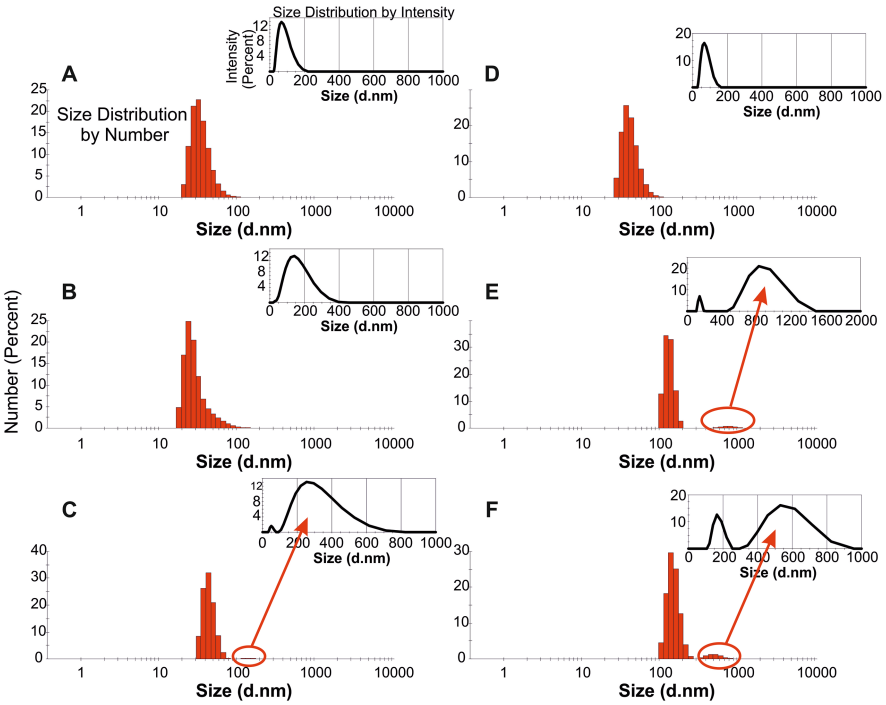

Fig. 2. Results of DLS measurements of silver nanoparticles (Ag60) (number by size – red bars, size distribution by intensity – black curves), obtained in: A. 20 °C deionized water, B. 20 °C tap water, C. 20 °C Ringer solution, D. 37 °C deionized water, E. 37 °C tap water, F. 37 °C Ringer solution.

Nevertheless, detailed studies presented in Fig. 2, shows that there is was plenty of the particles which their size corresponded to base d_H of Ag60. The histograms which presented particles size distribution by number showed two main fractions (samples dispersed in tap water and Ringer solution). First, bigger fraction of smaller particles gave weaker signal for presented size distribution by intensity. It means that occurring aggregates, which possibly were made by interaction between particles and the ions in dispersion phase, strongly had impact on the registered signal from scattered light. It can be easy observed in Fig. 2C, E, F that minor fraction presented on the histogram size by number, gave strong signal where the size distribution was correlated with the light scattering intensity. For that reason, we recommend more detailed studies, both graph (or data) of particle size distribution by number and intensity. This solution might be interesting, where the changes in the behavior of the sample occur during the time, temperature or environmental changes should be considered.

Figure 3 presented the graphs of the particle size distribution of the samples with high PDI index. Obtained from Stöber method silica submicron particles were detailed characterized in (Kaszuba et al. 2008).

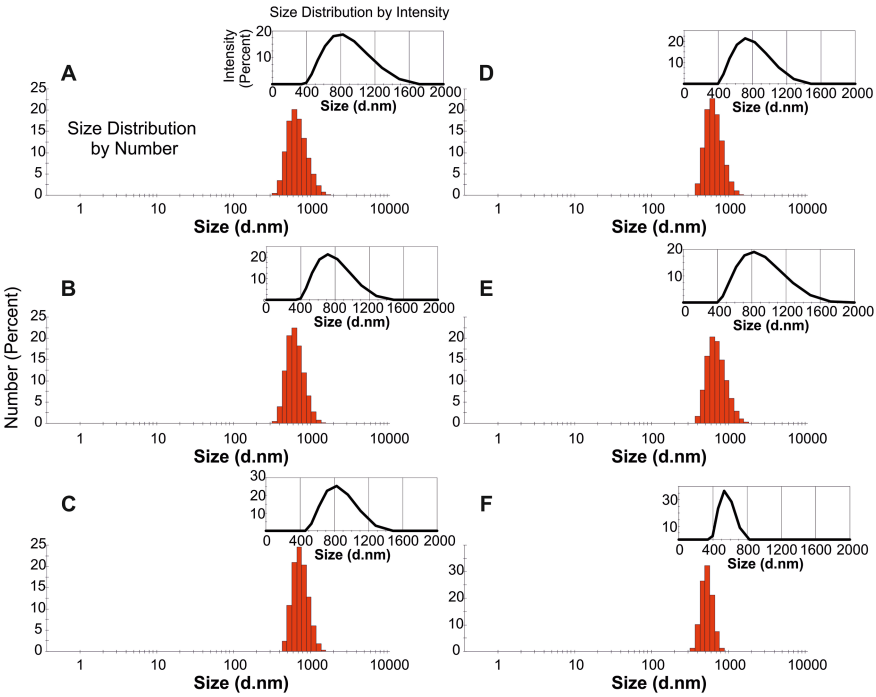

Fig. 3. Results of DLS measurements of polydispersed silica submicron particles SiO (number by size – red bars, size distribution by intensity – black curves), obtained in: A. 20 °C deionized water, B. 20 °C tap water, C. 20 °C Ringer solution, D. 37 °C deionized water, E. 37 °C tap water, F. 37 °C Ringer solution.

Presented DLS measurements correspond to the results obtained from scanning electron microscopy (SEM) and nanoparticle tracking analysis (NTA). Further studies of SEM gave more detailed information about the purposes of the high PDI index. It was pointed that twin or triple particles occurred during the synthesis (Jarzębski et al. 2017b). Moreover, NTA and FCS (fluorescence correlation spectroscopy) allowed to confirm the efficiency of the incorporation of fluorescent agent into the nanoparticles.

One of the biggest benefits of DLS is the rapid evaluation of the particle size (Varga et al. 2014; Bell et al. 2012). DLS technique had been frequently used for the synthesis, such as polymerization, progress evaluation. Moreover, DLS is a useful tool for evaluation of post-process behavior of the samples validation. Figure 4 presents the results of HFMBA particles investigations which were made eight years after synthesis. The results confirmed the high stability of submicron-sized HFMBA samples, even when measuring condition changed. No significant differences in d_H values were observed when tap water and Ringer solution with 20 and 37 °C were used.

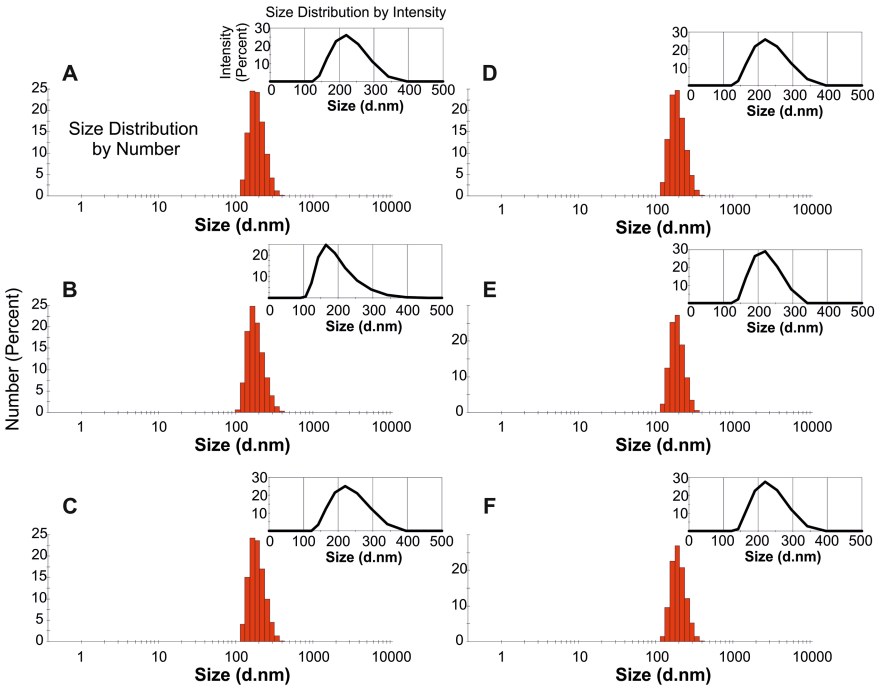

Fig. 4. Results of DLS measurements of fluorinated particles H1 (number by size – red bars, size distribution by intensity – black curves), obtained in: A. 20 °C deionized water, B. 20 °C tap water, C. 20 °C Ringer solution, D. 37 °C deionized water, E. 37 °C tap water, F. 37 °C Ringer solution.

4 Conclusions and Final Remarks

Dynamic light scattering technique was recommended for the sphere-like nano- and submicron particles. Some mathematical models allowed to study the non-spherical samples, but the results need recalculation and shape factor should be taken into account (Arenas-Guerrero et al. 2018). DLS allowed to perform rapid particle size determination during the synthesis. What is more, DLS is a useful tool for "on-line" changes registration, which might be caused by temperature, environmental changes (in this case of using liquid with ions) or other "non-standard" conditions. Our studies on silver nanoparticles showed that aggregation progress might be controlled by DLS. Presented study also showed that the results should be considered not only for the intensity of the scattered light versus particles size distribution but hydrodynamic diameter versus particles number. On the other hand, more than one technique is recommended for particle size evaluation. One of the most popular combinations was using DLS with electron microscopy.

Acknowledgments. Authors' also acknowledge the financial support provided by the Dr. and Mrs. A. S. Dekaban Foundation for supporting the stay of Maciej Jarzebski at the UBC Food Process Engineering Laboratory, Vancouver, Canada.

References

Aguilera, J.M.: Why food microstructure? J. Food Eng. **67**(1–2), 3–11 (2005)

Arenas-Guerrero, P., et al.: Determination of the size distribution of non-spherical nanoparticles by electric birefringence-based methods. Sci. Rep. **8**, 950 (2018)

Bai, Y.X., Li, Y.F., Yang, Y., Yi, L.X.: Covalent immobilization of triacylglycerol lipase onto functionalized nanoscale SiO_2 spheres. Process Biochem. **41**, 770–777 (2006)

Bell, N.C., Minelli, C., Tompkins, J., Stevens, M.M., Shard, A.G.: Emerging techniques for submicrometer particle sizing applied to Stöber silica. Langmuir **28**, 10860–10872 (2012)

Berne, B.J., Pecora, R.: Dynamic Light Scattering: With Applications to Chemistry, Biology, and Physics. Dover Publications, Mineola (1976)

Bhattacharjee, S.: DLS and zeta potential – what they are and what they are not? J. Controlled Release **235**, 337–351 (2016)

Chaudhry, Q., Scotter, M., Blackburn, J., Ross, B., Boxall, A., Castle, L.: Applications and implications of nanotechnologies for the food sector. Food Addit. Contam. Part A **25**(3), 241–258 (2008)

Dahneke, B.E.: Measurement of Suspended Particles by Quasi-elastic Light Scattering. Wiley, New York (1983)

Gapinski, J., Jarzębski, M., Buitenhuis, J., Deptula, T., Mazuryk, J., Patkowski, A.: Structure and dimensions of core-shell nanoparticles comparable to the confocal volume studied by means of fluorescence correlation spectroscopy. Langmuir **32**(10), 2482–2491 (2016)

Jarzebski, M., et al.: Core–shell fluorinated methacrylate nanoparticles with Rhodamine-B for confocal microscopy and fluorescence correlation spectroscopy applications. J. Fluor. Chem. **183**, 92–99 (2016)

Jarzębski, M., et al.: Submicron sized fluorescent silica particles characterization. Nucl. Instrum. Methods Phys. Res., Sect. B **411**, 78–84 (2017a)

Jarzębski, M., et al.: Particle tracking analysis in food and hydrocolloids investigations Food Hydrocolloids **68,** 90–101 (2017b)

Kaszuba, M., McKnight, D., Connah, M.T., McNeil-Watson, F.K., Nobbmann, U.: Measuring subnanometre sizes using dynamic light scattering. J. Nanopart. Res. **10**, 823–829 (2008)

Koenderink, G.H., Sacanna, S., Pathmamanoharan, C., Rasa, M., Philipse, A.P.: Preparation and properties of optically transparent aqueous dispersions of monodisperse fluorinated colloids. Langmuir **17**, 6086–6093 (2001)

Maulucci, G., et al.: Particle size distribution in DMPC vesicles solutions undergoing different sonication times. Biophys. J. **88**, 3545–3550 (2005)

Rashidi, L., Khosravi-Darani, K.: The applications of nanotechnology in food industry. Crit. Rev. Food Sci. Nutr. **51**(8), 723–730 (2011)

Sacanna, S., Koenderink, G.H., Philipse, A.P.: Microemulsion synthesis of fluorinated latex spheres. Langmuir **20**, 8398–8400 (2004)

Varga, Z., et al.: Towards traceable size determination of extracellular vesicles. J. Extracellular Vesicles **3**(1) (2014)

Verhaegh, N.A.M., van Blaaderen, A.: Dispersions of rhodamine-labeled silica spheres: synthesis, characterization, and fluorescence confocal scanning laser microscopy. Langumir **10**, 1427–1438 (1994)

Study on the Effect of Rotating Magnetic Field on Cellular Response of Mammalian Cells

Magdalena Jędrzejczak-Silicka[1], Ewa Mijowska[2], Karolina Szymańska[2], and Rafał Rakoczy[2(✉)]

[1] Faculty of Biotechnology and Animal Husbandry, West Pomeranian University of Technology in Szczecin, Szczecin, Poland
[2] Faculty of Chemical Technology and Engineering, West Pomeranian University of Technology in Szczecin, Szczecin, Poland
rrakoczy@zut.edu.pl

Abstract. The effect of magnetic fields (MFs) on mammalian cells *in vitro* has been studied to clarify in greater details potential influence on biological systems. In spite of the numerous and valuable experiments, the MF molecular mechanisms that affect cells still remain unclear. Thus, the aim of the study was to evaluate the cellular response of L929 fibroblast cell line to a rotating magnetic field (RMF) for 8-h exposure incubation period. We conclude that the exposure of L929 fibroblasts to the rotating magnetic field (RMF) in tested magnetic flux density range alerted the cellular dehydrogenases metabolism in a dose-dependent manner, with the highest values in dehydrogenases activity for cells incubated at 10.06 mT and lowest incubated at 1.23 mT of RMF.

1 Introduction

The biological effectiveness of magnetic fields (MFs) on mammalian cells has been studied for a couple of decades. Some of the MF molecular mechanisms that affect mammalian cells have still not been clearly defined (Feng et al. 2013). The increasing number of publications which demonstrate the effects of MFs on *in vivo* and *in vitro* models do not clarify intracellular mechanisms and do not allow the researchers to formulate the clear conclusions (Rosen 2003; Pozzi et al. 2007; Marędziak et al. 2014).

Different biological systems have been investigated (from bacteria to animal and human cells) in an effort to detect the biological effects of static magnetic field (SMF). Current state of the art in this field indicates that SMF effect depends on many aspects e.g. type of magnetic field, exposure protocols, magnetic induction level and duration time of the experiments, type of cellular *in vitro* models, different assays used for cellular response in the experiments (Teodori et al. 2002). The type of cells chosen for the experiments has crucial impact on the obtained results from *in vitro* models. For example, strong SMF (greater than 0.2 T) have been applied in biological systems to study e.g. genotoxic effect and mutation studies (Ikehata et al. 2002); chromosomal damage (Nakahara et al. 2002); DNA damage (Mahdi et al. 1994); proliferation (Iwasaka et al. 2004); gene expression (Potenza et al. 2004); metabolic activity (Huang et al. 2006); aggregation and cell adhesion (Testorf et al. 2002).

© Springer Nature Switzerland AG 2020
M. Ochowiak et al. (Eds.): PAIC 2019, *Practical Aspects of Chemical Engineering*, pp. 132–143, 2020.
https://doi.org/10.1007/978-3-030-39867-5_14

Magnetotherapy has been used to accelerate the regeneration of injured tissues e.g. bones, cartilage, tendons and is one of the forms of physiotherapy (Rosen 2003; Marędziak et al. 2014). It has been reported that the low frequency electromagnetic field (50–60 Hz) stimulates e.g. nerve regeneration, modifies gene transcription and may play a synergistic role in the cellular proliferation (Rusovan and Kanje 1992; Phillips et al. 1992; Manni et al. 2002). It was found that electrical stimulation at 20 Hz can influence the orientation and growth of neurite or motoneuron regeneration (Brushart et al. 2002). The application of low frequency magnetic fields (60 Hz and 100 Gauss) accelerates the healing process of the skin in Balb-C mouse (Cordova-Fraga et al. 2014). Fathi et al. (2017) analysed rat adipose-derived MSC (mesenchymal stem cells) exposed to extremely low frequency electromagnetic field (ELF-EMF) of 50 Hz and 20 mT and evaluated effect of ELF-EMF in the presence of zinc sulphate ($ZnSO_4$) on telomerase reverse transcriptase (TERT) gene expression and aging process in MSCs. The effect of ELF-EMFs on cells is related with changes in the expressions of genes involved not only in the metabolic pathways, response to stress, cell proliferation, but also aging and death. A number of studies showed correlation between Zn^{2+} and apoptosis, and suggested that Zn^{2+} play role as an antioxidant with the ability to minimize oxidative damage in cells. The cells exposed to ELF-EMF in the presence of zinc sulphate could significantly increase of TERT and decrease the aging of MSCs (Fathi et al. 2017). From the therapeutic point of view the subset of ELF electromagnetic fields such as pulsed electromagnetic field (PEMF) can be non-invasively used in treatment for non-union bone fractures, failed joint fusions, congenital pseudarthroses, musculoskeletal disorders, rheumatological disorders, spinal fusions, soft-tissue regeneration, pelvic pain, neurological disorders (Shupak 2003, Iannitti et al. 2013). The long-term exposure to extremely low frequency of (ELF) magnetic field (MF) induces also testicular germ cell apoptosis and impair spermatogenesis process (Lee et al. 2004; Kim et al. 2009; Kim et al. 2014).

From the data available in literature it is clear that the attention has not been focused on the experimental studies of the influence of RMF on the cellular response of mammalian cells. Thus, the aim of this study was the evaluation of a RMF intensity (at different magnetic induction values from 1.23 to 10.06 mT) on the cellular response of L929 - mouse fibroblasts.

2 Experimental Details

L929 mouse fibroblast cell line (the L929 cell line was purchased from the American Type Culture Collection; ATCC no. CCL-1) was seeded into 96-well plates at the density of 4×10^3/well, and cultured in 200 μL cell culture medium per well. Complete DMEM culture medium (Gibco, Langley, OK, USA) was supplemented with 10% heat-inactivated foetal bovine serum (Gibco, Langley, OK, USA), 2 mM L-glutamine (Sigma-Aldrich, St. Louis, MO, USA), 0.4% streptomycin/penicillin (Sigma-Aldrich, St. Louis, MO, USA) and 10 mM HEPES (Sigma-Aldrich, St. Louis, MO, USA). Cells were maintained in standard cell culture conditions at 37 °C, 5% CO_2, 95% humidity, and were visualized with a Nikon TS-100 microscope (NIS Elements F Package, camera Nikon DS-Fi1, Nikon, Melville, NY, USA). Sham-exposure samples were incubated for

8 h in the water bath at temperature 37 °C ± 0.5 °C. The untreated cells were used as the negative control. The positive control was obtained by treated L929 cells with 10% solution of DMSO (Sigma-Aldrich, St. Louis, MO, USA).

Experiments on the influence of rotating magnetic field (RMF) on L929 cell cultures were performed using self-designed equipment and adopted for the biological studies experimental set-up previously described by Masiuk et al. (Masiuk et al. 2008). This set-up is schematically presented in Fig. 1.

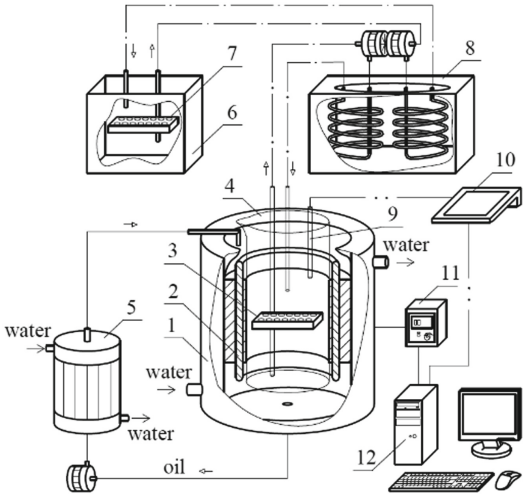

Fig. 1. The sketch of experimental set-up: 1 – cooling jacket, 2 – RMF generator, 3 – test plate, 4 – cylindrical glass vessel, 5 – heat exchanger for cooling system, 6 – water batch for control probes, 7 – control plate, 8 – thermostat, 9 – microprocessor temperature sensor, 10 – multifunctional meter, 11 – transistorized inverter, 12 – personal computer.

The experimental set-up contained a generator of the RMF, made of a three-phase stator of an induction squirrel cage motor, and a glass container filled with the demineralized water that was a water bath incubator for the tested material placed inside it during the exposition. The glass container was axially aligned with the RMF generator and positioned symmetrically with the respect to its lower and upper ends. The microplates with L929 cells were placed in the glass container in the center of the coil.

In the case of this experimental work the RMF was generated by means of the modified three-phase stator of an induction squirrel cage motor. The frequencies of the RMF were changed by the transistorized inverter (Commander SK, APATOR, Poland). The investigations were realized for the frequency equaled to 50 Hz. The incubation temperature during the exposition to the RMF was controlled by the thermostat (UTU-3, ZEAMiL, Poland), the cooling jacket and the circulating pump (WZ-250/BY, Poland). This system was used to keep the water flow rate constant in time and to set the constant temperature of the water bath (37 °C ± 0.5 °C). The temperature fluctuation inside the glass container during the experiment was measured using the microprocessor temperature sensors (LM-61B, National Semiconductor Corporation, USA).

The values of magnetic induction, B, inside the each well of the 96-well cell culture plate were detected by using the Hall probe (Smart Magnetic Sensor-102, Asonik, Poland) and a personal computer. The measurement of magnetic induction at the tested RMF frequency (f = 50 Hz) was repeated several times and mean values of magnetic induction was calculated. It is seen that the RMF distribution is strongly dependent on the spatial coordinates (see Fig. 2).

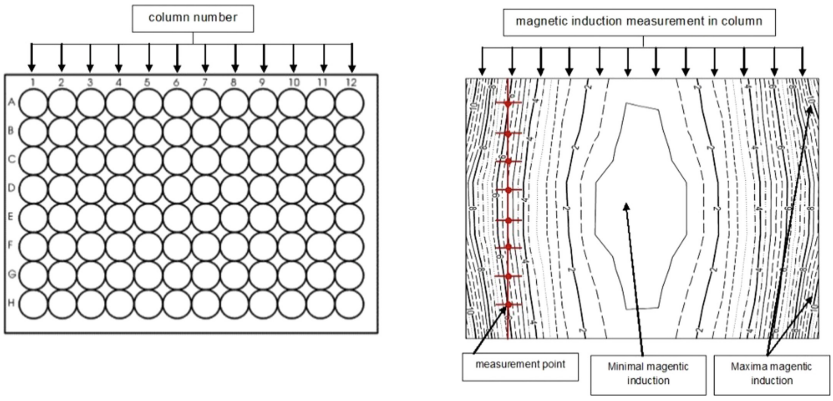

Fig. 2. The spatial distribution of the magnetic induction inside the 96-well cell culture plate for the tested operational condition (f_{RMF} = 50 Hz).

As follows from the analysis of the obtained data, the mean values of the magnetic induction are varied in the range between 1.23 and 10.06 mT. L929 cell line exposed to RMF at different magnetic induction 1.23, 1.57, 2.36, 3.95, 6.58 and 10.06 mT and control/sham culture samples were observed by phase contrast inverted Nikon TS-100 microscope (NIS Elements F Package, camera Nikon DS-Fi1, Nikon, Melville, NY, USA) at 400x magnification.

Cell viability and the effect of RMF on cell cultures were determined using the WST-1 Cell Proliferation Reagent (Roche Applied Science, Mannheim, Germany). The WST-1 cell proliferation assay is based on the reduction of water soluble tetrazolium salts to red formazan by cellular dehydrogenases from metabolically active cells. The amount of formazan dye formed correlates to the number of metabolically active cells. After 72-h cell cultures were exposed to RMF for 8 h. To study RMF effect to each well of microplates 20 μL of WST-1 solution was added and incubated for additional 60 min at 37 °C. After incubation the absorbance at 450 nm (with a reference wavelength at 630 nm), according to manufacturer's instructions, was recorded on a Sunrise Absorbance Reader (Sunrise, Tecan, Männedorf, Switzerland).

The RMF effect rate on cellular metabolic activity can be calculated using the following formula (1):

$$RMF_{effect\ rate} = \frac{\{OD\ value\}_{RMF} - \{OD\ value\}_{control}}{\{OD\ value\}_{control}} 100\% \quad (1)$$

where OD is optical density.

The cytotoxicity effects of RMF were determined using the LDH CytoTox 96® Non-Radioactive Cytotoxicity Assay (Promega, Madison, WI, USA). The LDH CytoTox 96® Non-Radioactive Cytotoxicity Assay measures lactate dehydrogenase (LDH) enzyme released upon cell lysis. After the experimental treatment for the maximum LDH release 10x lysis solution (Promega, Madison, WI, USA) was added and incubated at 37 °C, 5% CO_2 for 45 min. After the incubation period the plates were centrifuged at 240 × g for 4 min and the supernatant was transferred into new 96-well plates. The supernatant was mixed with Substrate Mix (Promega, Madison, WI, USA) and incubated for 30 min at room temperature (wrapped in aluminum foil to protect samples from light). Finally, 50 μL of Stop Solution (Promega, Madison, WI, USA) was added and the absorbance at 490 nm was measured using a microplate spectrophotometer reader (Sunrise, Tecan, Männedorf, Switzerland).

The percentage of LDH released (cytotoxicity) after 8-h exposure was calculated using the formula:

$$\%LDH\ released = \frac{A490\ nm\ of\ treated\ and\ untreated\ cells - A490\ nm\ of\ control}{A490\ nm\ of\ maximum\ of\ untreated\ cells - A490\ nm\ of\ control} 100\% \quad (2)$$

where A is absorbance.

Total LDH level present in cell cultures exposed to RMF were determined using the LDH CytoTox 96® Non-Radioactive Cytotoxicity Assay. To the all walls of microplate the 10x lysis solution (Promega, Madison, WI, USA) was added and incubated at 37 °C for 45 min. After incubation the supernatant of lysed cells was transferred to the enzymatic assay plate. The Substrate Mix (Promega, Madison, WI, USA) was added into the enzymatic assay plate and incubated for 30 min at room temperature. After incubation Stop Solution (Promega, Madison, WI, USA) was added and absorbance was measured at 490 nm. Equation (1) allows the calculation of RMF effect rate for data obtained from total LDH level.

The neutral red uptake assay was performed briefly, after 8-h exposition of L929 to the RMF. The medium was collected and the cells were washed with phosphate buffered saline (1xDPBS) (Gibco, Langley, OK, USA). Fresh complete DMEM containing 10% neutral red (In Vitro Toxicology Assay Kit, Neutral Red based, Sigma-Aldrich, St. Louis, MO, USA) was added to the culture. L929 cells were incubated at 37 °C, 5% CO_2 and 95% relative humidity for 3 h. Next, cells were washed with DPBS and Neutral Red Assay Solubilization Solution (Sigma-Aldrich, St. Louis, MO, USA) was added to release the incorporated dye from the cells. The cultures were allowed to rest for 10 min at room temperature, then were gentle stirred for 10 min and the absorbance at 540 nm was measured (the background absorbance of multiwell plates at 690 nm) in Tecan Sunrise microplate reader (Tecan, Männedorf, Switzerland). The RMF effect rate for neutral red uptake assay was calculated using Eq. (1).

3 Results and Discussion

Figure 3 presents microscopic observation of untreated L929 cells and cells exposed to RMF. The population of cells exposed to RMF revealed the typical fibroblast morphology and did not show morphological changes even after the exposure of cells to the highest magnetic induction (10.06 mT, 50 Hz). The analysis of cells did not show the tendency of multi-layer aggregates formation (Fig. 3).

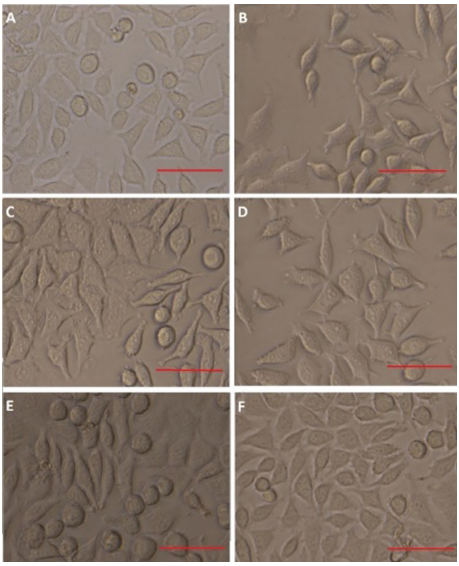

Fig. 3. Morphology of L929 cells in (a) control culture; after 8-hour incubation in rotating magnetic field (magnetic induction 1.57 mT) (b); magnetic induction 2.36 mT (c); magnetic induction 3.95 mT (d); magnetic induction 6.58 mT (e); magnetic induction 10.06 mT (f). Scale bar: 50 μm.

The dehydrogenases activity of cells exposed to non-homogenous RMF (the applied field is characterized by the different values of the magnetic induction inside the 96-well plate) was determined using WST-1 assay.

Interestingly, the cell cultures treated with the highest magnetic induction (10.06 mT, 50 Hz) showed higher dehydrogenases activity than the cells exposed to the lower magnetic flux density (1.23 mT–6.58 mT). The groups of cells incubated for 8 h within the range of 1.23 to 6.58 mT of RMF showed also lower OD values in WST-1 assay than the sham-exposure samples (Fig. 4; $p \leq 0.05$). The analysis of relative cellular dehydrogenases metabolism showed that the magnetic field might have stimulating effect on the cellular activity of L929 cell line in higher values of magnetic flux density. This finding present that in the experimental condition the magnetic flux density (above 6.58 mT) exhibit the stimulatory effect.

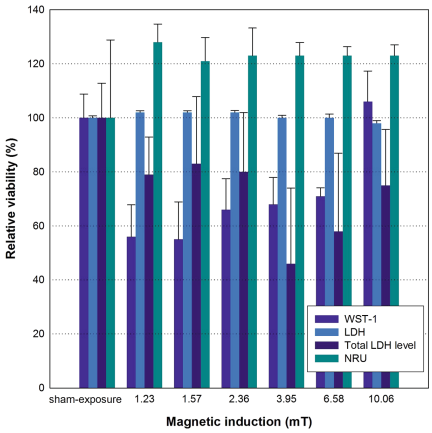

Fig. 4. Relative viability of L929 cells after exposure to different magnetic induction of RMF (all samples were compared to sham-exposure).

The lactate dehydrogenase leakage assay shows that RMF slightly affected the cell membrane integrity in comparison to sham exposure samples. It has been noticed that 10.06 of RMF evoked the highest cytotoxic effect (2.0%; $p \leq 0.05$). The lowest LDH leakage was recorded for magnetic intensity in the rage of 1.23 to 3.95 mT of RMF ($p \leq 0.05$). The level of LDH release for 1.23 ($p \leq 0.05$), 1.57 ($p \leq 0.05$) and 2.36 mT ($p \leq 0.05$) was marginally lower than for sham exposure samples (Fig. 4). The cellular response upon the exposure to RMF affected cells in a dose-dependent manner similarly as it was noticed for WST-1 assay. Results obtained from LDH assay suggests that the cytotoxic effect might be obtained in higher magnetic flux density values – above 6.58 mT.

Using the CytoTox 96® Assay the total LDH level was also evaluated. The addition of lysis solution to each well allows the total LDH level quantitation (live and dead). Figure 4 shows that the RMF influence total LDH level, but not in dose-dependent manner. The highest total LDH level was determined for 1.23, 1.57 and 2.36 mT. In the contrary, the lowest total LDH level was recorded for cells exposed to 3.95 mT of RMF. This tendency was similar to result obtained from WST-1 assay. The obtained results of this assay is presented in graph (see Fig. 4).

Both assays, WST-1 and LDH are based on enzymatic activity, thus to verify the effect of RMF on enzymatic cell activity another test was performed. For that purpose we used the neutral red uptake assay to determine lysosomal uptake of toluylene red. As was presented in Fig. 4, the tiny difference was noticed for the cells incubated in different RMF magnetic induction. For the cell population exposed to 1.23 mT of RMF the lysosomal uptake of toluylene red was minimal higher than for the cell population incubated in 10.06 mT of RMF. The statistical analysis shows significant differences between NR results for 1.23 mT and other records obtained for the cells tested in the range of 1.57–10.06 mT of magnetic induction. This result might suggest that in presented experimental condition RMF in higher values of magnetic flux density affect enzymatic activity of L929 cell line.

The effect of magnetic fields on living systems is a sum of the physical and biological mechanisms. From the physical point of view the main mechanisms by which MF affect living systems is in accordance with the Faraday's Law. It is known that the biological tissues are diamagnetic (some few exceptions are also known). According to Faraday's Law mechanical actions (relative motions) of a conducting medium and static magnetic determine changes of surface charges on the cell membranes. Those processes are related with changes in membrane potential, re-orientation of the diamagentic membrane phospholipids, sodium and calcium content or affects potassium-efflux (Hildebrandt et al. 2002; Hristov and Perez 2011). Other effects of MF on living matter is based on the magnetic field properties that cause not only cellular membrane penetration but deep MF penetration into cell body. In this context, Liu et al. (2012) demonstrated the mechanism of temporary membrane permeabilization (similarly as it happened during the cell electroporation). The membrane permeabilization was repairable when the cell were exposed to weak RMF, due to magnetopores undergo resealing (Liu et al. 2012). As noticed by Tenuzzo et al. (2008) the reorientation of diamagnetic anisotropic molecules in the cell membrane is capable of distorting ion channels to the point of altering their function. Ca^{2+} could also affect morphology, phagocytosis rate, by interfering with the polymerisation of microtubules and the assembly of actin filaments (Tenuzzo et al. 2006). Another finding suggest that MF affect cytoskeletal organization (e.g. cellular shape, mitotic apparatus, endoplasmic reticulum) due to reorganization of the electrostatically negative charged actin filaments (Hildebrandt et al. 2002). It is be stressed that Larmor precession also defines MF effect on biological systems at the level of subcellular structures, mainly those in motion (Hristov and Perez 2011).

Calcium gradient between the extracellular and intracellular fluid is crucial in signal transduction processes. Calcium is regarded to be intracellular transduction second messenger (Bouschet and Henley 2005) and its gradient is maintained in several ways that could potentially be affected by electromagnetic and magnetic fields. The cellular response to MF may be due to the changes in enzymatic activities (e.g., enzymes involved in mitochondrial metabolism), the ion concentration changes, changes in the Ca^{2+} distribution or the transmembrane voltage (Fig. 5).

Walleczek (1992) concluded that membrane-mediated Ca^{2+} signalling processes are involved in the mediation of field effects on the cells of the immune system (e.g., human lymphocytes, murine cytotoxic T cells (CTLL-1), and also human lymphoma cells). Ca^{2+} mobilization is an effect of binding of a ligand (e.g., antigens, mitogens, receptor antibodies) to a appropriate receptor structure exposed on the outer cell surface. The ligand-induced Ca^{2+} mobilization is reflected by an initial rise in Ca^{2+}caused by inositol 1, 4, 5-triphosphate-induced release of Ca^{2+} from the extracellular medium. Any changes and perturbation of mentioned above events with chemical agents (e.g., Ca^{2+} channel blockers, Ca^{2+}-specific ionophores, or by lowering the extracellular Ca^{2+} concentration using chelators can lead to changes in Ca^{2+}-membrane fluxes and modification in cellular activity such as cell proliferation, DNA synthesis, RNA transcription, secretion, motility and cytotoxicity (Walleczek 1992).

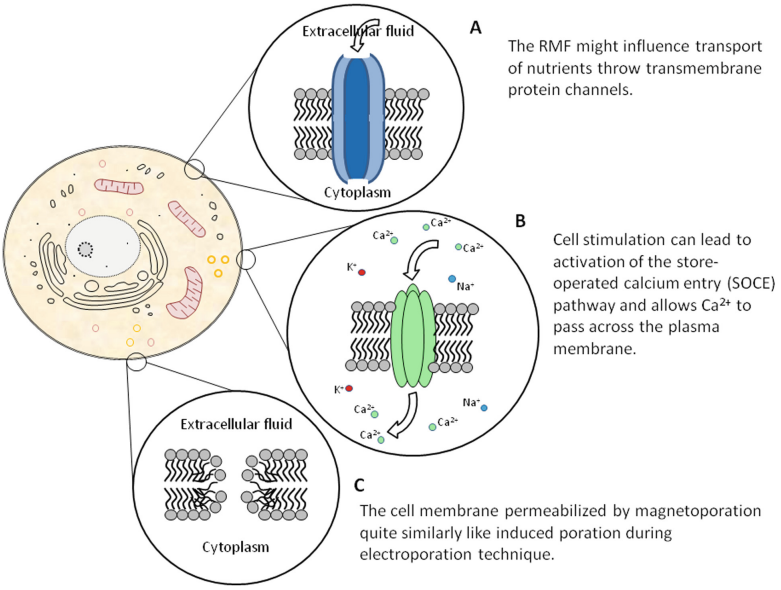

Fig. 5. Potential mechanisms of cellular response to rotating magnetic field.

The magnetic field effect on *in vitro* models is also related to the energy absorbed by cells (e.g., microorganisms) during the time of exposure. For example, the SMF do not evoke energy transmission to cells, but may affect the energy level of the some selected molecules (Hildebrandt et al. 2002; Hristov and Perez 2011). Moreover, the culture medium may be conductive due to presence of additional ions and the eddy currents in medium may be induced (in the case of the RMF exposition). The RMF creates the mixing process at the micro-level. The additional mixing effect may strongly influence the transfer processes between the living cells and the culture medium (Scharenberg et al. 2007; Jedrzejczak-Silicka et al. 2017). The other mechanisms such as activation of the store-operated calcium entry (SOCE) pathway and Ca^{2+} distribution to pass across the plasma membrane may be also evoke by the RMF exposition (Scharenberg et al. 2007).

In the context of some biological aspects, the mixing process at micro-level and the heat dissipation are two processes affecting the cell metabolism and evoke heat-shock response that refer to the micro-level dynamo concept (MLD) (Liu et al. 2012). Results obtained from WST-1 assay show that cellular dehydrogenases activity increases when the magnetic flux density is higher than 6.58 mT. An increase in total LDH level (total LDH level assay) confirms results from WST-1 assay suggesting that the enzymatic cell activity might be effectively affected by RMF exposition. The small rate of LDH leakage and NR uptake ability show that, in the range between 1.23 and 10.06 mT and 50 Hz, RMF did not affect the cellular membrane integrity and the findings presented by Liu et al. (2012) were not confirmed in the presented study. Despite presented study has the preliminary nature, obtained results show that the rotating magnetic field could be applied as a form of novel therapeutic strategy (in anticancer therapies or/and in

wound healing processes), but due to increasing interest in the application of magnetic fields on cellular models in vitro, the knowledge about mechanism of MFs still requires more attentive analysis.

4 Conclusions

We conclude that the exposition of L929 fibroblast cell line to the rotating magnetic field in tested magnetic flux density range (B values from 1.23 to 10.06 mT) has slight effect on cellular enzymatic activity and membrane integrity. The results present higher metabolic activity and positive effects on examined *in vitro* model when cells were exposed to higher magnetic induction values (higher than 6.58 mT for WST-1, LDH and total LDH level assays). Additionally, the morphology of the cells in the performed experimental conditions remained unchanged. The tendency of multi-layer aggregates formation was not detected. The data obtained from LDH leakage and NR uptake assays shows that the magnetic flux density in the range 1.23 to 10.06 mT did not affect the membrane integrity. Due to interesting results obtained from presented analysis the higher magnetic flux density should be applied to evaluate the response of cellular models in vitro to obtain the knowledge about mechanism of RMF.

Acknowledgments. This study was supported by the National Science Centre within OPUS program (UMO-2011/03/B/ST5/03239).

References

Bouschet, T., Henley, J.M.: Calcium as an extracellular signalling molecule: perspectives on the calcium sensing receptor in the brain. C. R. Biol. **328**, 691–700 (2005)

Brushart, M.T., Hoffman, P.N., Royall, R.M., Murinson, B.B., Witzell, C., Gordon, T.: Electrical stimulation promotes motoneuron regeneration without increasing its speed or conditioning the neuron. J. Neursci. **22**, 6631–6638 (2002)

Cordova-Fraga, T., Espinoza-Garcia, A.A., Barbosa-Sabanero, G., Pérez-Olivas, H.A., Rosas-Padilla, E.F., Matrinez-Espinoza, J.C., Bernal Alvardo, J.J.: Increasing survival study of kidney HEK-293T cells in magnetic field vortices and nano-fluid. IJEIT **4**, 222–225 (2014)

Fathi, E., Farahzadi, R., Rahbarghazi, R., Kafil, H.S., Yolmeh, R.: Rat adipose-derived mesenchymal stem cells aging reduction by zinc sulphate under extremely low frequency electromagnetic field exposure in associated with increased telomerase reverse transcriptase gene expression. Vet. Res. Forum **8**, 89–96 (2017)

Feng, J., Sheng, H., Zhu, C., Jiang, H., Ma, S.: Effect of adjuvant magnetic fields in radiotherapy on non-small lung cancer cells in vitro. Bio. Med. Res. Int. **10**, 657259–657265 (2013)

Hildebrandt, B., Wust, P., Ahlers, O., Dieing, A., Sreenivasa, G., Kerner, T., Felix, R., Riess, H.: The cellular and molecular basis of hyperthermia. Crit. Rev. Oncol. Hematol. **4**, 33–56 (2002)

Hristov, J., Perez, H.V.: Critical analysis of data concerning Saccharomyces cerevisiae free-cell proliferations and fermentations assisted by magnetic and electromagnetic fields. Int. Rev. Chem. Eng. **3**, 3–20 (2011)

Huang, H.M., Lee, S.Y., Yao, W.C., Lin, C.T., Yeh, C.Y.: Static magnetic fields up-regulate osteoblast maturity by affecting local differentiation factors. Clin. Orthop. Relat. Res. **447**, 201–208 (2006)

Iannitti, T., Fistetto, G., Rottigni, V., Palmieri, B.: Pulsed electromagnetic field therapy for management of osteoarthritis-related pain, stiffness and physical function: clinical experience in the elderly. Clin. Interv. Aging **8**, 1289–1293 (2013)

Ikehata, M., Iwasaka, M., Miyakoshi, J., Ueno, S., Koana, T.: Effects of intense magnetic field on sedimentation pattern and gene expression profile in budding yeast. J. Appl. Phys. **93**, 6724–6726 (2002)

Iwasaka, M., Ikehata, M., Miyakoshi, J., Ueno, S.: Strong static magnetic field effects on yeast proliferation and distribution. Bioelectrochemistry **65**, 59–68 (2004)

Jedrzejczak-Silicka, M., Urbas, K., Mijowska, E., Rakoczy, R.: The covalent and non-covalent of graphene oxide with hydroxycampotothecin in hyperthermia for its anticancer activity. J. Alloys Compd. **709**, 112–124 (2017)

Kim, H.S., Park, B.J., Jang, H.J., Ipper, N.S., Kim, S.H., Kim, Y.J., Jeon, S.H., Lee, K.S., Lee, S. K., Kim, N., Ju, Y.J., Gimm, Y.M., Kim, Y.W.: Continuous exposure to 60 Hz magnetic fields induces duration- and dose-dependent apoptosis of testicular germ cells. Bioelectromagnetics **35**, 100–107 (2014)

Kim, Y.W., Kim, H.S., Lee, J.S., Kim, Y.J., Lee, S.K., Seo, J.N., Jung, K.C., Kim, N., Gimm, Y. M.: Effects of 60 Hz 14 mT magnetic field on the apoptosis of testicular germ cell in mice. Bioelectromagnetics **30**, 66–72 (2009)

Lee, J.S., Ahn, S.S., Jung, K.C., Kim, Y.W., Lee, S.K.: Effects of 60 Hz electromagnetic field exposure on testicular germ cell apoptosis in mice. Asian J. Androl. **6**, 29–34 (2004)

Liu, D., Wang, L., Wang, Z., Cuschieri, A.: Magnetoporation and magnetolysis of cancer cells via carbon nanotubes induced by rotating magnetic fields. NanoLett. **12**, 5117–5121 (2012)

Mahdi, A., Gowland, P.A., Mansfield, P., Coupland, R.E., Lloyd, R.G.: The effects of static 3.0 T and 0.5 T magnetic fields and the echo-planar imaging experiment at 0.5 T on E. coli. Br. J. Radiol. **67**, 983–987 (1994)

Manni, V., Lisi, A., Pozzi, D., Rieti, S., Serafino, A., Giuliani, L., Grimaldi, S.: Effects of extremely low frequency (50 Hz) magnetic field on morphological and biochemical properties of human keranocytes. Bioelectromagnetics **23**, 298–305 (2002)

Marędziak, M., Marycz, K., Śmieszek, A., Lewandowski, D., Toker, N.Y.: The influence of static magnetic fields on canine and equine mesenchymal stem cells derived from adipose tissue. Vitro Cell. Dev. Biol. Animal. **50**, 562–571 (2014)

Masiuk, M., Rakoczy, R., Masiuk, S., Kordas, M.: The expression and intracellular distribution of nucleolin in HL-60 and K-562 cells after repeated, short-term exposition to rotating magnetic fields. Int. J. Rad. Biol. **84**, 752–760 (2008)

Nakahara, T., Yaguchi, H., Yoshida, M., Miyakoshi, J.: Effects of exposure of CHO-K1 Cells to a 10-T static magnetic field. Radiology **224**, 817–822 (2002)

Phillips, J.L., Haggren, W., Thomas, W.J., Ishida-Jones, T., Adey, W.: Magnetic field-induced changes in specific gene transcription. Biochim. Biophys. Acta **1132**, 140–144 (1992)

Potenza, L., Ubaldi, L., De Sanctis, R., De Bellis, R., Cucchiarini, L., Dacha, M.: Effects of a static magnetic field on cell growth and gene expression in Escherichia coli. Mutat. Res. Fund. Mol. M. **561**, 53–62 (2004)

Pozzi, D., Grimaldi, S., Ledda, M., De Carlo, F., Modesti, A., Scarpa, S., Foletti, A., Lisi, A.: Effect of 50 Hz magnetic field exposure on neuroblastoma morphology. Int. J. Integr. Biol. **1**, 12–17 (2007)

Rosen, A.D.: Mechanism of action of moderate-intensity static magnetic fields on biological systems. Cell Biochem. Biophys. **39**, 163–173 (2003)

Rusovan, A., Kanje, M.: Magnetic field stimulate peripheral nerve regeneration in hypophysectiomized rats. Neruoreport **3**, 1039–1041 (1992)

Scharenberg, A.M., Humphries, L.A., Rawlings, D.J.: Calcium signalling and cell-fate choice in B cells. Nat. Rev. Immunol. **7**, 778–789 (2007)

Shupak, N.M.: Therapeutic uses of pulsed magnetic-filed exposure: a review. Radio Sci. Bul. **307**, 9–32 (2003)

Tenuzzo, B., Chionna, A., Panzarini, E., Lanubile, R., Tarantino, P., Di Jeso, B., Dwikat, M., Dini, L.: Biological effects of 6 mT static magnetic fields on induction of apoptosis: a comparative study in different cell types. Bioelectromagnetics **27**, 560–577 (2006)

Tenuzzo, B., Dwikat, M., Dini, L.: Static magnetic field selects undifferentiated myelomonocytes from low-glutamine concentration stimulated U937 cells. Tissue Cell **40**, 177–184 (2008)

Teodori, L., Grabarek, J., Smolewski, P., Ghibelli, L., Bergamaschi, A., De Nicola, M., Darzynkiewicz, Z.: Exposure of cells to static magnetic field accelerates loss of integrity of plasma membrane during apoptosis. Cytometry **49**, 113–118 (2002)

Testorf, M.F., Oberg, P.A., Iwasaka, M., Ueno, S.: Melanophore aggregation in strong magnetic fields. Bioelectromagnetics **23**, 444–449 (2002)

Walleczek, J.: Electromagnetic field effects on cells of the immune system: the role of calcium signalling. FASEB J. **6**, 3177–3185 (1992)

Biodegradation of Pharmaceuticals Belonging to the Group of Non-steroidal Anti-inflammatory and Analgesic Drugs Using Activated Sludge

Zofia Kiersnowska[1], Dobrochna Ginter-Kramarczyk[2(✉)], Izabela Kruszelnicka[2], Anna Zając-Woźnialis[2], Joanna Zembrzuska[3], and Michał Michalkiewicz[2]

[1] Medical University of Lodz, Warsaw, Poland
zofiakiersnowska.p@gmail.com
[2] Institute of Environmental Engineering and Building Installations, Poznan University of Technology, Poznań, Poland
{dobrochna.ginter-kramarczyk, izabela.kruszelnicka, michal.michalkiewicz}@put.poznan.pl, anna_zajac87@wp.pl
[3] Institute of Chemistry and Technical Electrochemistry, Poznan University of Technology, Poznań, Poland
joanna.zembrzuska@put.poznan.pl

Abstract. The chapter presents the results of field studies confirming the presence of selected compounds from the group of non-steroidal anti-inflammatory drugs (NSAIDs) in the aquatic environment and in selected points of the technological process of the Central Wastewater Treatment Plant in Kozieglowy. The first stage examined the occurrence and distribution of concentrations of selected drugs (fenoprofen, ibuprofen, ketoprofen, naproxen, paracetamol and tolmetin) in the Warta river, in the area of the city Poznan. The second stage of the study allowed to estimate the types and concentrations of the above mentioned drugs on four sections of WWTP in Kozieglowy. The collection points included: the sewage pumping stations, denitrification chamber, nitrification chamber and drainage section of the sewage purified to the Warta river. Analysis of drug occurrence in the Warta river and their ability to decompose in WWTP in Kozieglowy, carried out under real conditions. Analysis of drug occurrence in the Warta river and their ability to decompose in WWTP in Kozieglowy, carried out under real conditions.

1 Introduction

Compounds which exhibit toxic properties despite their very low concentration are a serious threat to aquatic ecosystems. Such pollutants are of concern regarding environmental changes. Among this group of pollutants, the group of pharmaceutical substances in significant in terms of environmental changes caused by their toxic effects (Luo et al. 2014). The highest load of this type of pollution originates from hospitals, households, veterinary centres and breeding farms. Pharmaceuticals are

© Springer Nature Switzerland AG 2020
M. Ochowiak et al. (Eds.): PAIC 2019, *Practical Aspects of Chemical Engineering*, pp. 144–152, 2020.
https://doi.org/10.1007/978-3-030-39867-5_15

mainly excreted as metabolites. Unchanged active substances are only a small percentage of compounds which enter the environment. Both the starting form of the drug and its metabolites are compounds with various physicochemical properties, often with a complex structure, which significantly hinders their detection and removal from the environment (Luo et al. 2014). Companies and factories which produce pharmaceutical products are also a significant source of therapeutically active pollutants. Post-production sewage is often discharged directly into the receiver or discharged into the municipal sewage network, without checking the residues of the pharmaceuticals it contains. Studies carried out by scientific centres from various parts of the world indicate that conventional methods of active sludge treatment, intended mainly for the treatment of domestic and domestic wastewater, do not completely remove pharmaceutical substances. Therefore, the treated wastewater transported to the receivers contains the residues of pharmaceutical products and their metabolites. Due to the fact that intensified research regarding the presence of pharmaceuticals and their impact on the environment has been conducted for approx. 10 years, there are currently no known and predictable long-term consequences associated with the accumulation of pharmaceuticals in the aquatic (sewage disposal) and soil (natural use) environment (Fent et al. 2006; Martín et al. 2012; Ashfaq et al. 2017). The scale of pharmaceutical production, including non-steroidal anti-inflammatory drugs, is becoming an increasingly significant environmental issue. This study was devoted to removal of selected drugs from the group of non-steroidal anti-inflammatory drugs (NSAIDs) transported to the municipal wastewater treatment plant (CSTP Poznań, Poland), originating from pharmaceutical plants and their impact on the quality of treated wastewater discharged to the water receiver. The mentioned sewage treatment plant operates using biological methods of treatment with activated sludge. The conducted biodegradation studies (NSAIDs) using activated sludge and determination of their biodegradation efficiency allowed us to conclude whether the sewage discharged into the municipal sewage system, which originated from plants containing a high load of pollutants, and the long-term presence of drugs interferes with the ability of activated sludge microorganisms to decompose the compounds present in the wastewater. Inefficient removal of pharmaceuticals in wastewater treatment processes leads to surface water pollution, which is the basic source of drinking water. Currently, there are no legal regulations which indicate the highest admissible concentrations of pharmaceutical compounds in wastewater for plants which generate pharmaceutical substances and discharge them into municipal sewage networks as well as for recipients of such wastes (sewage treatment plants). It is therefore necessary to urgently introduce regulations at international and national levels which would set the permitted and safe maximum concentrations for pharmaceutical substances in the environment and drinking water (Ginter-Kramarczyk et al. 2013).

2 Pharmaceutical Compounds

Pharmaceutical compounds are medicinal products with a very wide range of applications. Their main purpose is therapeutic action, which leads to elimination of both minor nuisances as well as very complicated types of diseases and the accompanying

symptoms. Currently, the development of the pharmaceutical market has specialized in the design and production of antidote drugs for the vast majority of diseases or ailments that medicine is currently struggling with. The process of creating new pharmaceutical products is continuous and very dynamic. This is primarily due to the enormous competition in this field as well as the demand for new generation drugs.

Analgesic and anti-inflammatory drugs are among the most popular groups of drugs available mostly without prescription. The list of most bought products includes ibuprofen, paracetamol, naproxen, diclofenac carbamazepine and salicylic acid (Felis et al. 2005; Khetan and Collins 2007). Ibuprofen is in the top ten most popular drugs in the world ranking (Murdoch and Hay 2015). These pharmaceuticals, together with their metabolites, have been detected in surface waters, drinking waters and sewage (Felis et al. 2005; Kosjek et al. 2007; Adamek et al. 2011). The drug life cycle begins with the planning and development of the drug formula followed by many years of research and observation. After a patent for the analysed substance is obtained, the manufacturing process begins. The drugs are transported from production plants to distributors: pharmacies, non-pharmacy outlets, such as shops or supermarkets, or other suppliers. Individuals can be the recipients of drugs (predominantly analgesic and anti-inflammatory drugs). Hence, domestic and household sewage contains pharmaceutical residues either in their original form or as their metabolites due to biotransformation of the initial substances. Hospitals, drug factories and wastewater from illegal drug production also contribute to an increased load of pharmaceutical contaminants in wastewater.

Despite the fact that the concentrations of pharmaceutical compounds present in domestic sewage are at trace levels, conventional sewage treatment plants do not allow for their complete removal. Some pharmaceutical substances are decomposed during biological treatment methods into simple inorganic compounds, in the form of carbon dioxide and water. Sometimes, the removal of such substances is also possible by means of adsorption in bottom sediments. However, the effectiveness of this method depends on the electrostatic interactions of drugs with solid particles and its physicochemical properties. Drugs with a lyophilic character (e.g. estrogens) are much better adsorbed on bottom sediments compared to hydrophilic drugs. Another parameter which determines the adsorption is pH. Acidic drugs, which include most NSAIDs, e.g. acetylsalicylic acid, diclofenac, ketoprofen or naproxen, are poorly adsorbed and circulate in the water phase, but pharmaceuticals from the group of antibiotics, e.g. tetracyclines, macrolytes and sulfonamides, are well adsorbed on bottom sediments. The drug removal processes by means of adsorption on bottom sediments carry the risk of surface and groundwater pollution. The use of sludge for fertilization of the soil may result in the introduction of adsorbed pharmaceuticals into the soil and thus, in the penetration into groundwater due to the infiltration process (Szymonik and Lach 2012).

3 Activated Sludge

Wastewater which flows into the treatment plant and contains admixtures of pharmaceutical substances is subjected to treatment using conventional technological solutions. The activated sludge method is one of the basic methods used in wastewater treatment processes. Active sludge is a complex biological system, which includes both

physical and biochemical processes, as a result of which sewage treatment is possible. Microorganisms are a flocculent suspension. Adsorption of organic substances occurs on the surface of the flocs. This allows for the distribution of larger fragments, which are then absorbed directly into the core of the floc, in which further changes occur. The microorganisms which constitute the activated sludge produce catalytic enzymes, which enable the decomposition of multiparticulates (e.g. proteins, fats, carbohydrates) into simple inorganic products (e.g. CO_2, H_2O, NO_3^-, PO_4^{3-}, SO_4^{2-}) (Dymaczewski 2011). The process of activated sludge formation occurs during aeration of wastewater, while the microorganisms present in the wastewater form larger agglomerates. The proper course of flock formation affects numerous factors. The most important include:

- bacterial production of mucilaginous coatings which allow cells to merge into larger clusters,
- positively charged ions allow attachment of negatively charged cells,
- the production of very thin polysaccharide threads by some types of bacteria facilitates the agglomeration of cells (Kocwa-Haluch and Woźniakiewicz 2011).

The effectiveness of drug removal in treatment plants varies and depends on the type of pharmaceutical compound, its concentration at the entrance and the technological parameters of the system. According to literature data, none of the pharmaceutical compounds analysed in the research have been completely removed, as reported by (Quintana et al. 2005; Nakada et al. 2006; Samaras et al. 2013; Pereira et al. 2017). As a consequence, water receivers, which are a source of drinking water, are not free from drug residues upon introduction of purified sewage (Zając et al. 2013).

Pharmaceuticals transported to municipal wastewater treatment plants can be biodegraded during aerobic and anaerobic wastewater treatment. Both diclofenac and ibuprofen are susceptible to purification using activated sludge methods and the removal efficiency depends on the changing environmental conditions. It can be observed that with longer wastewater retention, some compounds, such as diclofenac, are removed up to 70% (Table 1). Ibuprofen, on the other hand, is degraded to hydroxyl- and carboxyl- derivatives. Studies indicate that, in terms of oxygen concentration, ibuprofen is characterized by the highest reduction efficiency under aerobic conditions (>95%, after two days of biodegradation the concentration of ibuprofen reaches a value below the detection limit of the device) (Kujawa-Roeleveld et al. 2008).

Table 1. Effectiveness of diclofenac removal using selected biological methods based on activated sludge, according to literature data (Zając 2017).

Diclofenac reduction efficiency [%]	Treatment method	Reference
75%	Activated sludge, mesophilic conditions, SRT: 10d	Zhou et al. (2013)
72%	Activated sludge, thermophilic conditions, STR: 6d	Zhou et al. (2013)
17%	Outflow from a municipal sewage treatment plant	Heberer (2002)
23–30%	Outflow from a municipal sewage treatment plant	Quintana et al. (2005)
71%	Outflow from a municipal sewage treatment plant	Roberts and Thomas (2006)

(*continued*)

Table 1. (*continued*)

Diclofenac reduction efficiency [%]	Treatment method	Reference
75%	Conventional activated sludge, HRT: 3h	Kimura et al. (2005)
65%	Conventional wastewater treatment	Gomez et al. (2007)
25%	Activated sludge processes	Martin et al. (2012)
<50%	MBR, SRT: 10-55d, HRT: 0,5 - 4,0d	Clara et al. (2005)
75%	Conventional biological wastewater treatment, SRT: 8d, HRT: 9h	Samaras et al. (2013)
39%	Conventional biological wastewater treatment, SRT: 18d, HRT: 23h	Samaras et al. (2013)
0–87,4%	Membrane bioreactors	Tadkaew et al. (2011)
22%	Conventional biological wastewater treatment with chemical removal of phosphorus	Benz et al. (2005)
9–21%	Initial wastewater treatment	Larsson et al. (2014)
92–98%	Conventional biological wastewater treatment	Larsson et al. (2014)
45,6%	Activated sludge	Pereira et al. (2015)
About 70%	Conventional wastewater treatment, SRT: 10d, HRT: 6h	Anumol et al. (2016)
About 70%	Conventional wastewater treatment, SRT: 6d, HRT: 6h	Anumol et al. (2016)
>50%	MBBR	Tang et al. (2017)

In contrast, under anaerobic conditions the effectiveness of ibuprofen removal reached a maximum of 40%, regardless of temperature (Suarez et al. 2010). Metabolites may exhibit higher or lower resistance to degradation compared to the original drug forms. In most cases (Table 2), the effectiveness of ibuprofen removal using traditional wastewater treatment methods remained at a level of >90%.

The efficiency of pollutant removal using biological treatment methods depends on many variables, including ambient temperature, pH, sludge age, or sewage retention time (SRT, solid retention time). Higher temperature accelerates the decomposition process of both diclofenac and ibuprofen (at the temperature of 10 °C the decomposition was much slower than at 20 °C). SRT (sludge retention time) and HRT (hydraulic retention time) are important parameters which influence the improvement and quantity of removed pollutants.

Table 2. Efficiency of ibuprofen removal using selected biological methods based on activated sludge (Zając 2017).

Ibuprofen reduction efficiency [%]	Treatment method	Reference
25–53%	Initial wastewater treatment	Larsson et al. (2014)
99%	Conventional biological wastewater treatment	Larsson et al. (2014)
99%	Outflow from a municipal sewage treatment plant	Thomas and Foster (2004)
53–79%	Outflow from a municipal sewage treatment plant	Tauxe-Wuersch et al. (2005)
97%	Outflow from a municipal sewage treatment plant	Quintana et al. (2005)
98%	Outflow from a municipal sewage treatment plant	Roberts et al. (2006)
37%	Purified wastewater; Hajdów, Lublin	Czerwiński et al. (2015)
59%	Purified wastewater; Gdańsk, Wschód	Czerwiński et al. (2015)
42%	Purified wastewater; Szczecin, Pomorzany	Czerwiński et al. (2015)
>90%	Membrane bioreactors	Tadkaew et al. (2011)

Increase of the age of the sludge may contribute to an increased removal of pollutants. These conditions are particularly favourable in case of nitrifying bacteria because they multiply slowly. Studies indicate that nitrifying bacteria effectively remove some types of drugs, such as ibuprofen, naproxen, trimethoprim, erythromycin as well as bisphenol A and nonylphenol (Luo et al. 2014). Research conducted by Clara and co-workers (Clara et al. 2005) showed that nitrogen removal at SRT >10 days can improve the removal efficiency of biodegradable pharmaceutical compounds, such as ibuprofen, bezafibrate, bisphenol A or natural estrogens. The value of the hydraulic retention time, assumed for the effective treatment of drugs from municipal wastewater, ranges from 0.5 to 3.0 d (Jenicek et al. 1996). For the removal of acidic pharmaceuticals, which also include ibuprofen and diclofenac, the pH is the key parameter for decreasing the concentration of the drug in wastewater. Kimura K. and co-workers presented the conclusions that lowering the pH from 7.0 to 6.0 allows to almost double the reduction of the concentration of these compounds (Kimura et al. 2010).

4 Studies

Studies carried out at the Institute of Environmental Engineering of the Poznan University of Technology included, among others, the determination of the degradation efficiency of selected analgesic drugs at the Central Sewage Treatment Plant (CSTP) of the city of Poznań in Koziegłowy. This treatment plant uses activated sludge in the treatment process. The obtained results showed that all analysed types of NSAIDs drugs flow together with municipal wastewater into the CSTP in Koziegłowy. In

addition to determining the concentration of selected types of NSAIDs present in the wastewater flowing into the treatment plant, their reduction efficiency achieved at the selected sections of the technological process in CSTP in Koziegłowy was also assessed (Figs. 1 and 2). The main mechanisms responsible for the removal of pharmaceutical compounds in wastewater include biodegradation and sorption on flocs. Paracetamol (99.97%) exhibited the highest reduction efficiency in the section from the raw sewage pumping station to the section of the treated sewage discharge.

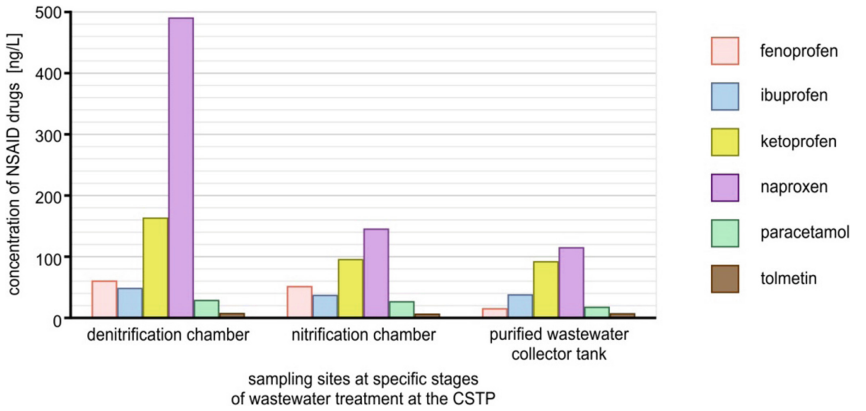

Fig. 1. Concentration of selected NSAIDs at the selected points of technological sequence at the CSTP.

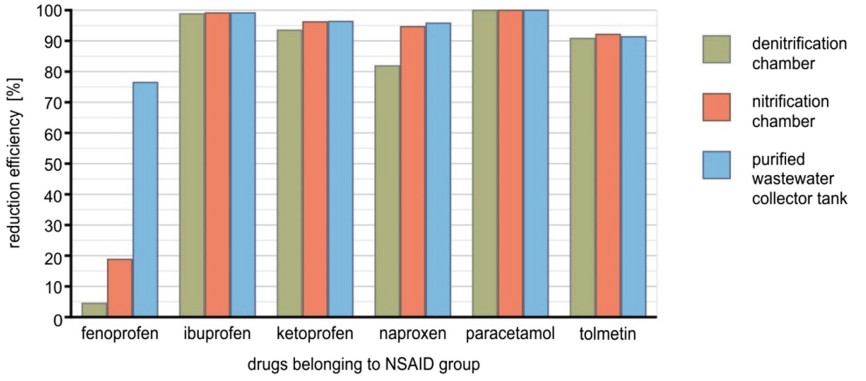

Fig. 2. Reduction efficiency of selected NSAIDs at the selected points of technological sequence at the CSTP in relation to raw sewage.

The highest reduction of the analysed drugs (ibuporofen, ketoprofen, naproxen, paracetamol and tolmetin) was observed between the sewage pumping station and the denitrification chamber. On the other hand, fenoprofen exhibited the highest reduction efficiency in the section after the secondary settler. This leads to the conclusion that

drugs are susceptible to degradation not only under aerobic conditions but also under anaerobic conditions (Suarez et al. 2010). A high degree of reduction of ibuprofen, ketoprofen, paracetamol, tolmetin, above 90%, was observed at the section from the inflow of raw sewage into the CSTP in Koziegłowy to the denitrification chamber.

The percentage of drug removal which occurs as a result of biodegradation was not clearly defined. An increase of the concentration of ibuprofen and tolmentin at the outflow from the treatment plant may suggest that these drugs are partially adsorbed on flocs, which, as a result of the long-time of wastewater retention or the long age of sludge, are released again into the supernatant liquid.

5 Summary

Activated sludge microorganisms possess the ability to remove compounds from the group of non-steroidal anti-inflammatory drugs. The removal efficiency depends on the physicochemical parameters such as temperature, pH, sludge load with impurities and oxygen concentration. Diclofenac and ibuprofen may be an additional source of organic carbon for activated sludge bacteria which enables them to carry out life processes.

Acknowledgments. The studies were carried out as part of the Ministry of Science and Higher Education project no. 01/13DS-PB 0891/2018.

References

Ashfaq, M., Khan, K.N., Ur Rehman, M.S., Mustafa, G., Nazar, M.F., Sun, Q., Iqbal, J., Mulla, S.I., Yu, C.-P.: Ecological risk assessment of pharmaceuticals in the receiving environment of pharmaceutical wastewater in Pakistan. Ecotoxicol. Environ. Saf. **136**, 31–39 (2017)

Adamek, E., Jakubczyk, E., Baran, W., Makowski, A., Lipska, I., Ziemiańska, J., Sobczak, A.: Fotodegradacja wybranych leków przeciwzapalnych w środowisku wodnym. Proc. ECOpole **5**(1), 147–153 (2011)

Clara, M., Kreuzinger, N., Strenn, B., Gans, O., Kroiss, H.: The solids retention time – a suitable design parameter to evaluate the capacity of wastewater treatment plants to remove micropollutants. Water Res. **39**, 97–106 (2005)

Dymaczewski, Z.: Poradnik Eksploatatora Oczyszczalni Ścieków, praca zbiorowa, wyd. Polskie Zrzeszenie Inżynierów i Techników Sanitarnych Oddział Wielkopolski, Poznań (2011)

Felis, E., Miksch, K., Sikora, J.: Występowanie i możliwości usuwania farmaceutyków w Polsce, Materiały konferencyjne, VII Ogólnopolska Sesja Popularnonaukowa„Środowisko a zdrowie - 2005", Częstochowa (2005)

Fent, K., Weston, A.A., Caminada, D.: Ecotoxicology of human pharmaceuticals. Aquat. Toxicol. **76**, 122–159 (2006)

Ginter-Kramarczyk, D., Zając, A., Kruszelnicka, I., Zembrzuska, J., Budnik, I.: Teraźniejszość i przyszłość produktów leczniczych w społeczeństwie i środowisku. Przemysł Chemiczny **92** (5), 596–600 (2013)

Jenicek, P., Zabranska, J., Dohanyos, M.: The influence of anaerobic pretreatment on the nitrogen removal from biosynthetic pharmaceutical wastewaters. Anton. Leeuw. **69**, 41–46 (1996)

Khetan, S.K., Collins, T.J.: Human pharmaceuticals in the aquatic environment: a challenge to green chemistry. Chem. Rev. **107**, 2319–2364 (2007)

Kimura, K., Hara, H., Watanabe, Y.: Elimination of selected pharmaceuticals by biosolids from municipal wastewater treatment plants: importance of modest pH change and degree of mineralization. Water Sci. Technol. **62**, 5 (2010). IWA Publishing

Kocwa-Haluch, R., Woźniakiewicz, T.: Analiza mikroskopowa osadu czynnego i jej rola w kontroli procesu technologicznego oczyszczania ścieków, Środowisko. Czasopismo Techniczne wydawnictwo Politechniki Krakowskiej **6**, 141–162 (2011)

Kosjek, T., Heath, E., Kompare, B.: Removal of pharmaceutical residues in a pilot wastewater treatment plant. Anal. Bioanal. Chem. **387**(4), 1379–1387 (2007). Springer-Verlag

Kujawa-Roeleveld., K., Schuman, K., Grotenhuis, K., Kragić, K., Mels, A., Zeeman, G.: Biodegradability of human pharmaceutically active compounds (PhAC) in biological systems treating source separated wastewater streams. In: Switch Scientific Meeting, Wageningen, The Netherlands (2008)

Luo, Y., Guo, W., Ngo, H.-H., Nghiem, L.-D., Hai, F.-I., Zhang, J., Liang, S., Wang, X.C.: A review on the occurrence of micropollutants in the aquatic environment and their fate and removal during wastewater treatment. Sci. Total Environ. **619**, 473–474 (2014)

Martín, J., Camacho-Munoz, D., Santos, J.L., Aparicio, I., Alonso, E.: Occurrence of pharmaceutical compounds in wastewater and sludge from wastewater treatment plants: Removal and ecotoxicological impact of wastewater discharges and sludge disposal. J. Hazard. Mater. **239–240**, 40–47 (2012)

Murdoch, R.W., Hay, A.G.: The biodegradation of ibuprofen to trihydroxyibuprofen in activated sludge and by Variovorax Ibu-1. Biodegradation **26**, 105–113 (2015)

Nakada, N., Tanishima, T., Shinoohara, H., Kiri, K., Takada, H.: Pharmaceutical chemicals and endocrine disrupters in municipal wastewater in Tokyo and their removal during activated sludge treatment. Water Res. **40**, 3297–3303 (2006)

Pereira, A.M., Silva, L.J., Meisel, L.M., Lino, C.M., Pena, A.: Environmental impact of pharmaceuticals from Portuguese wastewaters: geographical and seasonal occurrence, removal and risk assessment. Environ. Res. **136**, 108–119 (2015)

Pereira, A.M., Silva, L.J., Meisel, L.M., Lino, C.M., Pena, A.: A critical evaluation of different parameters for estimating pharmaceutical exposure seeking an improved environmental risk assessment. Sci. Total Environ. **603–604**, 226–236 (2017)

Samaras, V.G., Stasinakis, A.S., Mamais, D., Thomaidis, N.S., Lekkas, T.D.: Fate of selected pharmaceuticals and synthetic endocrine disrupting compounds during wastewater treatment and sludge anaerobic digestion. J. Hazard. Mater. **244–245**, 259–267 (2013)

Suarez, S., Lema, J.M., Omil, F.: Removal of Pharmaceutical and Personal Care Products (PPCPs) under nitrifying and denitrifying conditions. Water Res. **44**, 3214–3224 (2010)

Szymonik, A., Lach, J.: Zagrożenia środowiska wodnego obecnością środków farmaceutycznych. Inżynieria i Ochrona Środowiska **15**(3), 249–263 (2012)

Quintana, J.B., Weiss, S., Reemttsma, T.: Pathways and metabolites of microbial degradation of selected acidic pharmaceutical and their occurrence in municipal wastewater treated by a membrane bioreactor. Water Res. **39**(12), 2654–2664 (2005)

Zając, A., Budnik, I., Zembrzuska, J., Kruszelnicka, I., Ginter-Kramarczyk, D.: Droga farmaceutyków w środowisku przyrodniczym na terenie województwa wielkopolskiego - źródła występowania, obecność, zagrożenia, Materiały konferencyjne z II studenckiej konferencji naukowej „Produkcja, ekonomia, zarządzanie, marketing i ochrona środowiska – jak to się robi w Wielkopolsce", Gniezno (2013)

Zając, A.: Effectiveness of removal of selected nonsteroidal anti-inflammatory drugs from wastewater by the activated sludge method, PhD thesis (2017)

Analysis of the Effect of the Atomizer Swirl Chamber on the Liquid Atomization Process

Franciszek Klimczak, Tomasz Burda, Marek Ochowiak(✉), Sylwia Włodarczak, and Andżelika Krupińska

Institute of Chemical Technology and Engineering, Poznan University of Technology, Poznań, Poland
marek.ochowiak@put.poznan.pl

Abstract. The chapter presents an analysis of the effect of the swirl chamber of atomizer on the liquid atomization process. Atomization is a process, which involves the conversion of liquid to form an aerosol. Atomization occurs in atomizers. Atomizers have not only different sizes but also the presence of a core-hole. The paper presents experimental results obtained for the modified pressure-swirl atomizers. Examined factors are pressure drop, discharge coefficient and spray angle.

1 Introduction

1.1 Theoretical Fundamental of Atomization

Atomization is a process, which involves the conversion of liquid to form aerosol. It is used in many industries, because atomization of liquids allows to obtain larger area of liquid, when it has aerosol form in comparison to stream of liquid. Atomization is also used in processes, which require that the area should be evenly covered in liquid. Currently there are many types of atomizers, including a pneumatic, rotary, jet and pressure-swirl type (Bending 2002).

The subject of this research are pressure-swirl atomizers, which are among the most popular atomizers. Although, their constructions are relatively simple, knowledge about them is still not sufficient. Pressure-swirl atomizers are characterized by reliable operation and they do not require large input of energy. Their construction and energy efficiency means that they are relatively cheap and very often used in comparison to another devices. Pressure-swirl atomizers consist of three basic elements: inlet port, swirl chamber, and outlet port. Liquid delivered to device creating swirl movement inside the chamber. Liquid leaves device by hole of low diameter, then liquid undergoes a different types of hydrodynamic effects, and that is how droplets are formed (Broniarzz-Press et al. 2013; Broniarz-Press et al. 2015).

Low energy demand also has connection with liquid velocity in chamber, and more precisely this velocity is low in circumference of chamber, which results in low resistance at walls. The liquid velocity increases due to the increase of swirl as the chamber axis approach. Finally it reaches high value at outflow. Originally flow coming out from atomizer takes the conical form, which causes faster breakup of film to droplets, than in case of using another types of atomizers, at the same flow rate.

© Springer Nature Switzerland AG 2020
M. Ochowiak et al. (Eds.): PAIC 2019, *Practical Aspects of Chemical Engineering*, pp. 153–160, 2020.
https://doi.org/10.1007/978-3-030-39867-5_16

Atomization process in pressure-swirl atomizers is well-known and unchanging, however experimental research results indicate that this process can be affected by a lot of factors, which cause discrepancies in designated dependencies. These factors are operating conditions, measuring equipment using in research and especially construction of atomizers themselves (Orzechowski and Prywer 2008; Chinn 2009; Guangchao 2008; Liu 2017, Maly et al. 2019; Nonnenmacher and Piesche 2000; Orzechowski et al. 1997; Rashad et al. 2016; Rashid et al. 2012; Widger and Yule 1996).

Obtained pressure drop values were used to calculate discharge coefficient by using correlation (Orzechowski et al. 1997):

$$C_D = \frac{w_L \rho_L}{(2\rho_L \Delta P)^{0.5}} \tag{1}$$

Discharge coefficient is often presented as a function of Reynolds number. The Reynolds number is defined as follows:

$$\mathrm{Re} = \frac{w_L d_L \rho_L}{\eta_L} \tag{2}$$

When liquid is atomized at different flow rates, four different atomization phases were observed (Fig. 1): distorted pencil, onion, tulip, fully developed spray (Lefebvre and McDonell 2017):

- Distorted pencil phase – liquid stream leaves atomizer as a distorted lane.
- Onion phase – a phase where liquid stream creates cone twice. First stream forms a bubble, which undergoes atomization and second cone is created.
- Tulip phase – liquid stream undergoes atomization after outlet port and creates cone which has large drops at the edges.
- Fully developed spray – the most important phase, in which liquid stream right after leaving atomizer is atomized to small droplets.

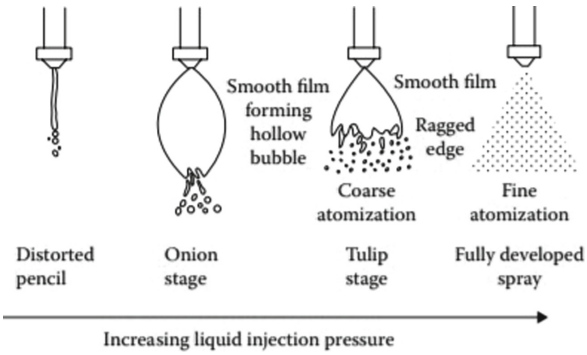

Fig. 1. Atomization phases (Lefebvre and McDonell 2017).

2 Design and Tests of Atomizers

Presenting research concerns pressure-swirl atomizers with one, cylindrical inlet nozzle and with cylindrical outlet. Two groups of pressure-swirl atomizers were tested. One of them was characterized by constant diameter of swirl chamber (D = 30 mm) and with variable chamber height (H = 20, 30, 40, 60, 90, 120 mm). Second group was described by constant height of swirl chamber (H = 30 mm) and variable chambers diameter (D = 20, 30, 40, 50 mm). Furthermore, some of the atomizers have "core-hole" of diameter d = 4 mm. Cylindrical outlet has diameter of 3 mm. Figure 2 presents the construction of pressure-swirl used in experimental studies.

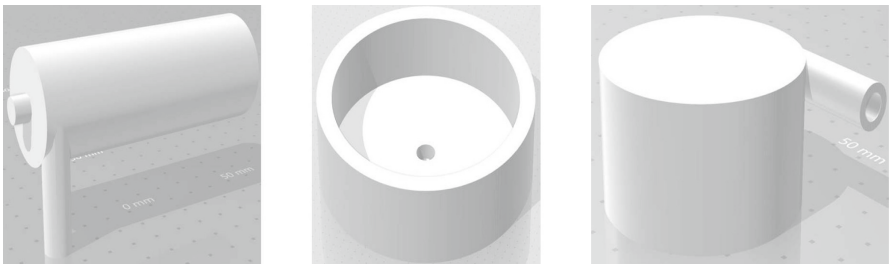

Fig. 2. Construction of pressure-swirl atomizers used in experimental studies.

Water was used as the liquid. The studies were carried out in the range of volumetric flow rate 0–250 l/h at temperature T = 20 °C. In the atomization process, the most important issue is turbulent flow, therefore to further analysis we took into consideration only the results with the calculated Reynolds number from 8820 to 29400. In this range, appropriate liquid atomization occurs. For each operating conditions pressure drop was measured and visualization of process of the liquid atomization by photographic method was performed. Afterwards, in the program called ImageJ an analysis of photos was carried out and spray angle was determined. The difference in the construction of tested devices and the influence of atomizer geometry (especially height and diameter) on pressure drop, spray angle (and discharge coefficient) were discussed.

It was found after photo analysis that onion phase is created when velocity is 1.57 m/s (40 l/h), but only in case of atomizers without core-hole. In case of atomizers with core-hole the formation of onion phase is skipped and the third phase was immediately observed. This phase is tulip. Fully developed spray phase is formed at two different ranges of flow rate. It depends on the presence of the core-hole.

In case of atomizers without core-hole, transition from 3rd to 4th phase takes place in the velocity range 5.9–6.88 m/s (150–175 l/h), however in case of atomizers with core-hole, it occurs only with the higher values of velocity 6.88–7.86 m/s (175–200 l/h). This phenomenon allows us to conclude that occurrence of core-hole enforces using higher value of flow ratio to reach fully developed spray than in the case when atomizer is without core-hole. The characteristic atomization phases obtained during experimental studies were shown in Fig. 3.

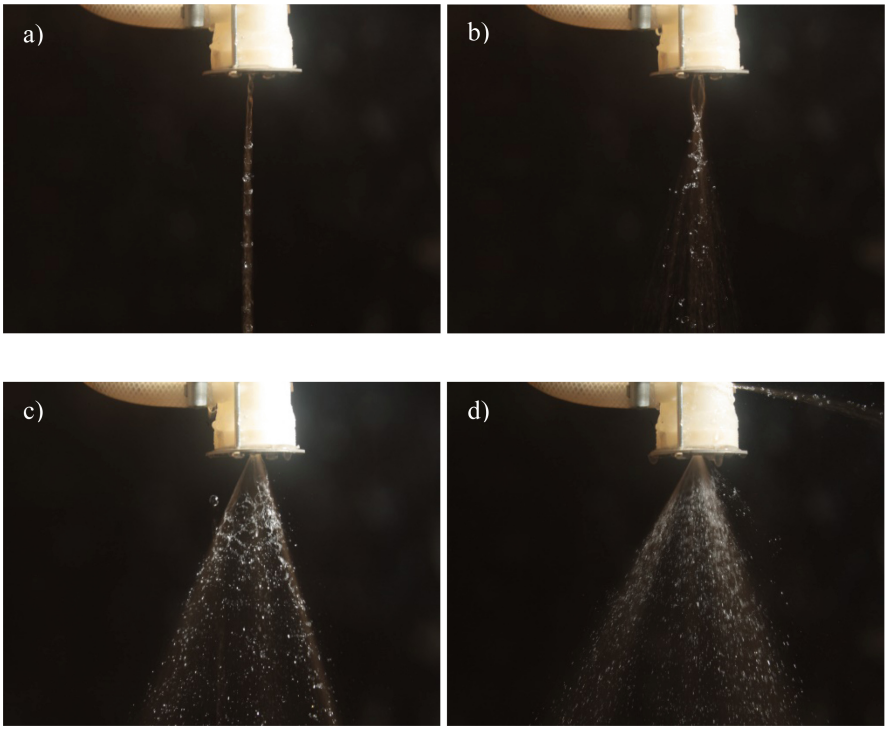

Fig. 3. Atomization phases for experimental studies: **a** Distorted pencil phase, **b** Onion phase, **c** Tulip phase, **d** Fully developed spray phase.

However, occurrence of core-hole results in reduced pressure drop in the atomizer. Almost in every case, when we compare pressure drop at a given volumetric flow rate, pressure drop in the atomizer with core-hole is much more less in comparison to atomizers without core-hole, in some cases its value reaches even ca. 100 000 Pa (Figs. 4 and 5).

When analyzing the spray angle, it is observed that in almost every case (the exception is a device with D = 30 mm, H = 120 mm) a larger spray angle is obtained for atomizers with core-hole than in the case of a device without this modernization.

For every device, only at determined flow rate of 75 l/h the atomization of liquid begins (Re = 8820). Above mentioned differences in results were showed in our analysis. In the case of atomizers with core-hole, the highest obtained spray angle was 85°. In the case of atomizers without core-hole, the highest obtained spray angle was 77°.

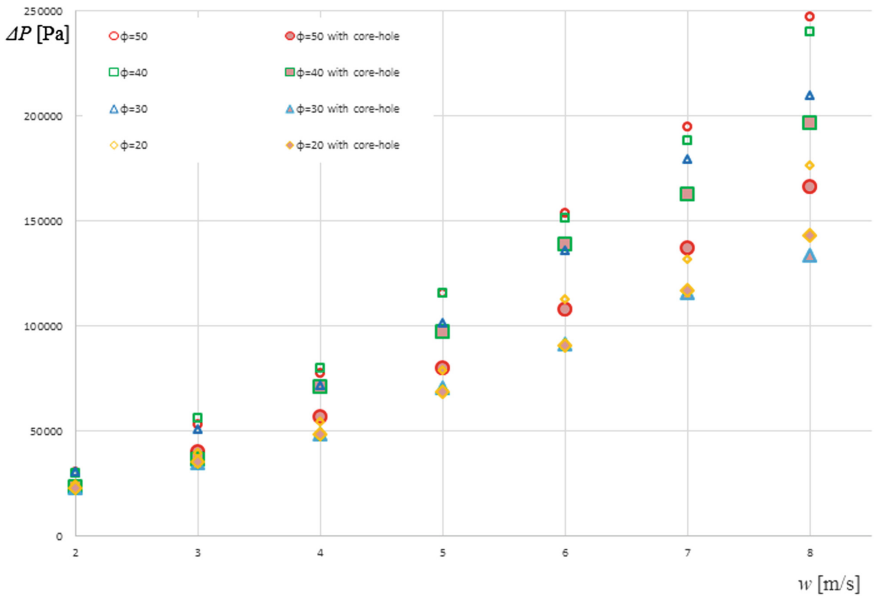

Fig. 4. Relationship of pressure drop in function of liquid velocity for constant height of atomizer.

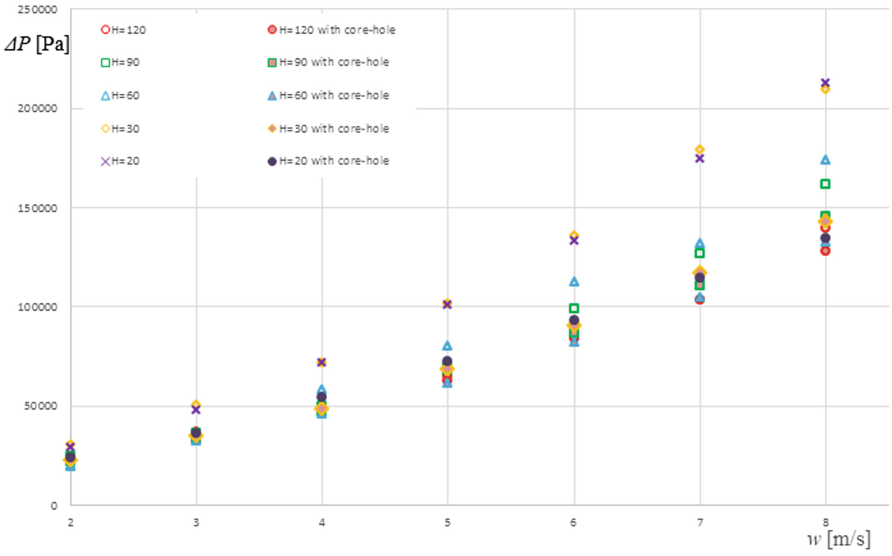

Fig. 5. Relationship of pressure drop in function of liquid velocity for constant diameter of atomizer.

For atomizers with core-hole with constant diameter (30 mm), spray angle increases with decreasing height of atomizers chamber, while for devices without core-hole spray angle decreases with decreasing height of atomizers chamber (Table 1).

Table 1. Values of spray angle for atomizers with different diameter.

Atomizers with core-hole					
Height [mm]	120	90	60	30	20
Spray angle [°]	66	69	75	85	85
Atomizers without core-hole					
Height [mm]	120	90	60	30	20
Spray angle [°]	77	62	41	46	54

The application of core-hole also influences on values of discharge coefficient. In the case of atomizers, which were constructed without any extras, lower discharge coefficient was obtained than for devices with core-hole (Figs. 6 and 7).

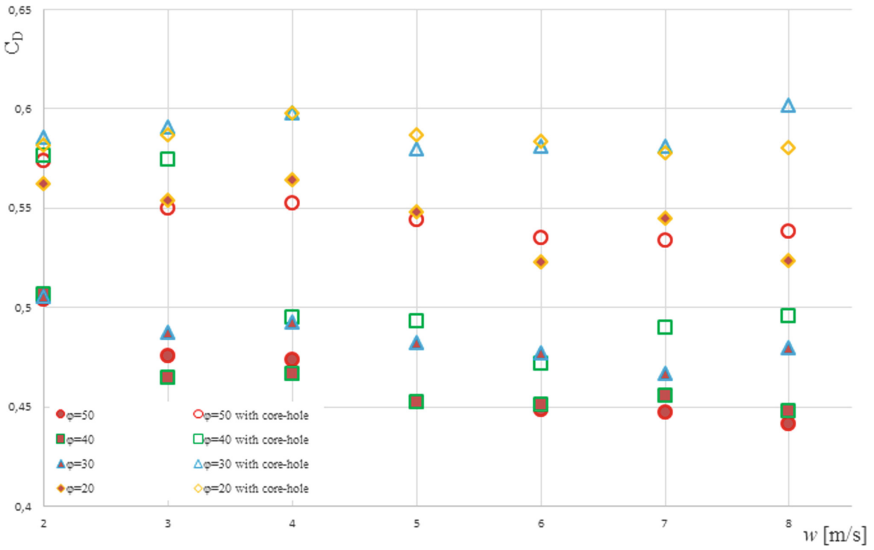

Fig. 6. Relationship of discharge coefficient vs. liquid velocity for atomizers with constant height (H = 30 mm).

Adjustment of atomizers' dimensions also brings few dependencies resulting from the introduced changes. A decrease of atomizer diameter at constant height results in a decrease in the pressure drop value. However this phenomenon was observed also in the case of atomizers without core-hole. In case of height changing at constant diameter for atomizers without core-hole the trend is reversed. When chamber height decreases,

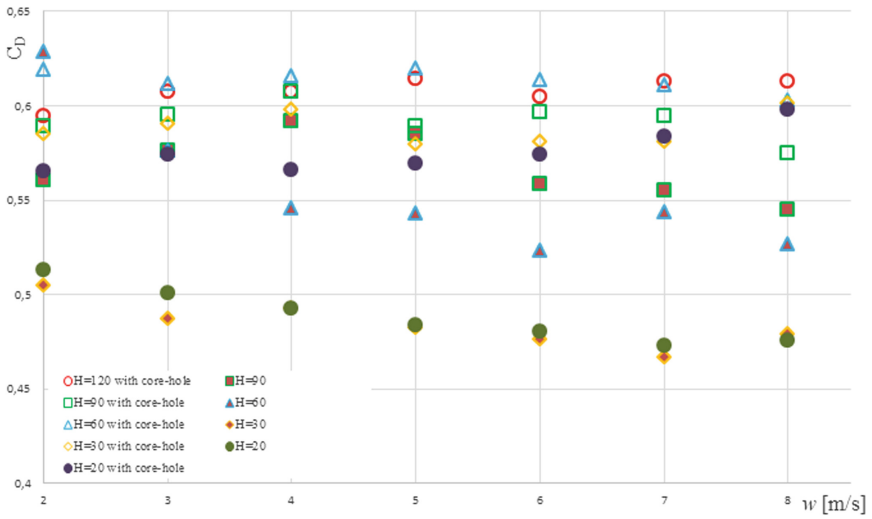

Fig. 7. Relationship of discharge coefficient vs. liquid velocity for atomizers with constant diameter (D = 30 mm).

pressure drops increase and discharge coefficient decreases. But these dependencies were observed also in the case of atomizers without core-hole. The highest values of discharge coefficient were obtained for atomizer with core-hole of following dimensions: diameter D = 30 mm and height H = 60 mm.

3 Summary

From the above results we can pull out following conclusions:

- In the case atomizers without core-hole every four phases of atomization were occurred and these atomizers need lower flow rate to reach appropriate atomization phase.
- Atomizers with core-hole need higher flow rate to reach appropriate atomization phase, but in this case onion phase was not occurred.
- Application of core-hole causes, that lower pressure drops, larger spray angles and also higher discharge coefficients were obtained. Furthermore changing geometry of atomizer also show that when diameter decreases (at constant height), pressure drops simultaneously decrease and discharge coefficient increases, but if height decreases (at constant diameter), the reverse situation occurs. Pressure drops increase, but discharge coefficient decreases.
- Discharge coefficient is the highest for device with core hole for diameter 30 mm and height 60 mm, and its value is 0.62. The application of a core-hole has a positive effect on the atomization process. It increases the spray angle and flow rate. For the atomizers with a core-hole, an increase in the spray angle and the discharge coefficient was achieved.

- Spray angle is the highest for device with core-hole for diameter 30 mm and height 20 mm and its value is 85°.
- Application of core-hole has an essential influence on the change of spray angle, because afterwards, the spray angle is larger than in case of atomizer with the same sizes but without core-hole. Simultaneous decrease of chamber height also causes the increase of spray angle.

Acknowledgments. This research was supported by Ministry of Science and Higher Education through grant PUT 03/32/SBAD/0902.

References

Bending, L., et al.: Industrial Sprays and Atomization. Springer-Verlag, London (2002)
Broniarz-Press, L., et al.: Analiza współczynnika wypływu cieczy dla rozpylaczy wirowych o różnych kształtach otworu wylotowego. Inż. Ap. Chem. **52**(5), 403–404 (2013). (in Polish)
Broniarz-Press, L., Włodarczak, S., Ochowiak, M.: Analiza kąta rozpylania dla rozpylaczy o stożkowej komorze wirowej. Inż. Ap. Chem. **54**(5), 230–232 (2015). (in Polish)
Chinn, J.J.: An appraisal of swirl atomizer inviscid flow analysis, part 2: inviscid spray cone angle analysis and comparison of inviscid methods with experimental results for discharge coefficient, air core radius and spray cone angle. Atomization Sprays **19**(3), 283–308 (2009)
Guangchao, L., Huiming, F., Huiren, Z.: Discharge coefficient of 3-in-1 hole with various inclination angle and hole pitch. Chin. J. Aeronaut. **21**, 385–392 (2008)
Lefebvre, A., McDonell, V.: Atomization and Sprays, 2nd edn. Taylor & Francis, CRC Press, Boca Raton (2017)
Liu, Z., Huang, Y., Sun, L.: Studies on air core size in a simplex pressure-swirl atomizer. Int. J. Hydrogen Energy **42**, 18649–18657 (2017)
Maly, M., et al.: Effect of spill orifice geometry on spray and control characteristics of spill-return pressure-swirl atomizers. Exp. Thermal Fluid Sci. **106**, 159–170 (2019)
Nonnenmacher, S., Piesche, M.: Design of hollow cone pressure swirl nozzles to atomize Newtonian fluids. Chem. Eng. Sci. **55**, 4339–4348 (2000)
Orzechowski, Z., et al.: Mechanika płynów w inżynierii środowiska. Wydawnictwa Naukowo-Techniczne, Warszawa (1997). (in Polish)
Orzechowski, Z., Prywer, J.: Wytwarzanie i zastosowanie rozpylonej cieczy. Wydawnictwo Naukowo-Techniczne, Warszawa (2008). (in Polish)
Rashad, M., Yong, H., Zekun, Z.: Effect of geometric parameters on spray characteristics of pressure swirl atomizers. Int. J. Hydrogen Energy **41**, 15790–15799 (2016)
Rashid, M., Hamid, A., Sheng, O., Ghaffar, Z.: Effect of inlet slot number on the spray cone angle and discharge coefficient of swirl atomizer. Procedia Eng. **41**, 1781–1786 (2012)
Widger, I., Yule, A.: Swirl atomizers operating at high water pressure. Int. J. Mech. Sci. **38**, 981–999 (1996)

Engineering of Immobilized Enzymes: pH, Thermal Stability and Kinetic Aspects

Agnieszka Kołodziejczak-Radzimska(✉) and Teofil Jesionowski

Institute of Chemical Technology and Engineering,
Poznan University of Technology, Poznań, Poland
Agnieszka.Kolodziejczak-Radzimska@put.poznan.pl

Abstract. Enzymes are important catalysts which have gained much attention in various branches of science. The catalytic proteins are immobilized on various materials to increase their resistance to the unfavorable effects of pH, temperature or other denaturants present in the reaction mixture. The heterogeneous form of biocatalytic systems is the most important advantage of the immobilization process, and leads to the prolonging of catalytic activity. This chapter reviews the use of immobilization as a useful technique for improving the thermal and chemical stability of enzymes. Kinetic aspects of the immobilization process are also discussed.

1 Enzymes: General Information

Enzymes are macromolecular, three-dimensional protein structures which catalyze certain biochemical reactions. This occurs due to reduction of the activation energy of one of the possible reaction paths and stabilization of the high-energy transition state of the substrate-enzyme system, as a result of which the state of chemical equilibrium is achieved more rapidly (Murray et al. 1995; Stryer 2003).

X-ray studies have shown that in the structure of an enzyme there is a slit containing side chains of amino acids, which are responsible for binding the corresponding substrate, as well as other structures known as cofactors, which are essential for the process of catalysis. This slit is called an active site, and constitutes the catalytic center of the enzyme (McDonald et al. 2014). The active site accounts for only a small part of the enzyme's total volume, and has a three-dimensional structure. The formation and breaking of bonds between the enzyme and substrate requires that the shape, geometry and arrangement of functional groups in the substrate be precisely matched to the active site. Only a few molecules of the substrate are able to fit perfectly into the active site of a specific enzyme; hence enzymes are said to have high specificity and selectivity, and the resulting product exhibits precisely defined properties (Pleiss 2014).

Enzymology has developed to an enormous extent in recent decades. In the 1950s information was available on 659 enzymes; by 1992 the number was larger by a factor of five, while by the end of 2014 almost 5600 enzymes had been discovered, and their number continues to rise (Cornich-Bowden et al. 2014).

The wide range of discovered biocatalysts led to difficulties in nomenclature. For this reason, in the second half of the last century the International Union of Biochemistry and Molecular Biology (IUBMB) appointed an Enzyme Commission (EC), whose tasks

© Springer Nature Switzerland AG 2020
M. Ochowiak et al. (Eds.): PAIC 2019, *Practical Aspects of Chemical Engineering*, pp. 161–170, 2020.
https://doi.org/10.1007/978-3-030-39867-5_17

included the creation of a unified classification for enzymes. The Commission's 1961 report contains a list of enzymes classified according to the type of reaction that they catalyze. This division remains in use today, and newly discovered enzymes are assigned to the appropriate groups (Tipton et al. 2000). The top-level classification of enzymes consists of the following:

- EC 1 – oxidoreductases: catalyze oxidation/reduction reactions;
- EC 2 – transferases: transfer a functional group (e.g. a methyl or phosphate group);
- EC 3 – hydrolases: catalyze the hydrolysis of various bonds;
- EC 4 – lyases: cleave various bonds by means other than hydrolysis and oxidation;
- EC 5 – isomerases: catalyze isomerization changes within a single molecule;
- EC 6 – ligases: join two molecules with covalent bonds.

Enzymes, as important catalysts, significantly accelerate many processes taking place both within living organisms and on an industrial scale. However, in view of the low stability of biocatalysts and the rapid loss of their catalytic properties, the process conditions and the reaction environment in which they function have a decisive impact on the yield of the catalyzed reactions and on the catalysts' lifetime. It is important to maintain the properties of enzymes at an adequate level by carefully selecting the reaction conditions and continuously monitoring them.

2 Immobilized Enzymes

Biocatalysts perform best in their natural environment (for instance, in living organisms). The use of enzymes on an industrial scale is associated with a number of difficulties resulting from the poor adaptability of those compounds in a foreign environment (Faber 2017). The most important problems relating to enzymes include:

- instability in the conditions of industrial reactions, leading to reduced catalytic activity, autoxidation or denaturation;
- difficulties in separating the enzyme from substrates or products;
- limited resistance to high concentrations of the substrate and to temperatures different from those in which the enzymes occur naturally.

To reduce the risk of occurrence of the aforementioned problems, the technique of immobilization is used. Enzymes may be immobilized on various types of support. Such immobilized systems may be used in a wide range of pH and temperature, and most importantly they have a heterogeneous form, which enables them to be used multiple times in catalytic processes (Zdarta et al. 2018a). The immobilization of enzymes on various types of support may be carried out using a wide range of chemical and physical methods (Fig. 1). The most popular method of immobilizing biocatalysts is adsorption, which makes use of physical interactions between the enzyme and the support (Hanefeld et al. 2008; Jesionowski et al. 2014). The adsorptive method is simpler than other immobilization techniques and enables higher mobility of the enzyme, which in many cases results in significant enzyme activity. However, the adsorbed enzyme may be subject to desorption, by which it becomes detached from the surface of the support—particularly in industrial conditions where high concentrations

of reagents and products are present. This is a result of the weak physical interactions between the enzyme and support (van der Waals forces, electrostatic interaction). A more durable method of attachment is covalent immobilization. Here it is important that amino acid radicals should not form covalent bonds with the support, as this may reduce the high catalytic activity of the enzyme. This condition is quite difficult to achieve; hence this form of immobilization is used in industry mainly in cases where penetration of the enzyme into the reaction environment may disrupt the entire technological process (Brena et al. 2006; Zhang et al. 2016).

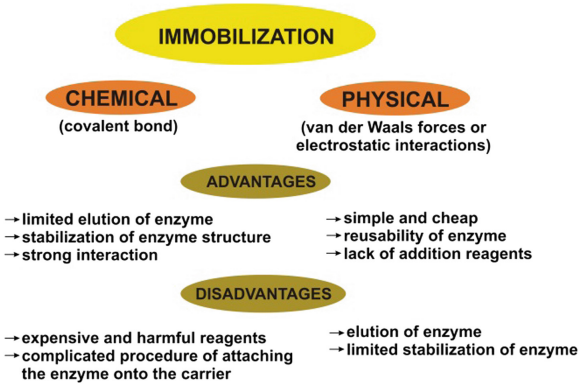

Fig. 1. Enzyme immobilization methods and their advantages and disadvantages

3 Morphology, Structure and Chemistry of Supports

An important role in the immobilization process is played by the supports used. The selection of the support material is a key challenge, due to the major impact that this material may have on the resulting properties. There is an extremely wide and varied range of materials that may be used as supports in immobilization processes. Supports include both organic and inorganic materials, and differ in terms of morphology, structure and chemical properties. The most important properties that supports should offer are presented in Fig. 2.

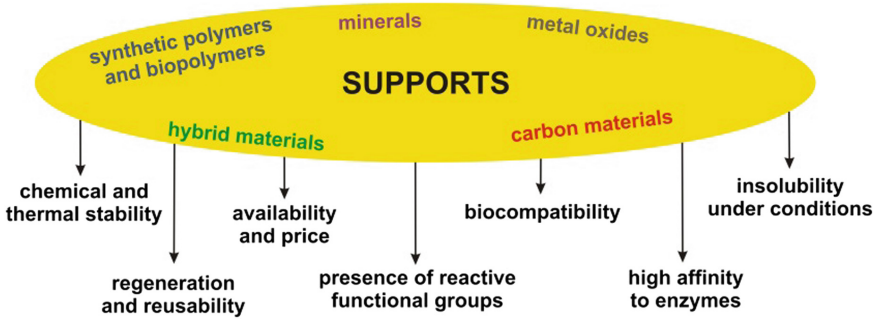

Fig. 2. Main properties of materials used as supports in the immobilization of enzymes

The type of enzyme and process in which the immobilized enzyme will be used is very important when it comes to choosing appropriate supports. Materials which have high stability, availability, relatively low price, and high affinity to the bound enzymes, are most commonly used in immobilization process. (Cao 2005; Zdarta et al. 2018b). One of the important parameters determining the use of a given support in an immobilization process is its chemical structure. The material should have a high content of reactive functional groups, such as hydroxyl, epoxide and amino groups. These have high affinity to the chemical groups contained in the protein structure, and thus ensure effective attachment of the enzyme (Zhang et al. 2016; Song et al. 2018). If direct binding of the enzyme is not possible, the chemistry of the support should be such that it can be easily modified to introduce the chemical groups required for bonding. Important parameters determining the potential use of a material as a support include its morphological and porous structure—the size and shape of particles, the size and volume of the pores of the material, and its specific surface area. The materials that attract the greatest interest have specific surface areas above 100 m^2/g, in addition to high porosity (pore diameter above 3 nm) (Magner 2013). The choice of support is one of the most important questions in the development of an immobilization process, and has direct impact on the properties of the resulting biocatalytic system. When choosing an appropriate support it must be remembered that, in spite of the availability of numerous substances on which an enzyme may be immobilized, the final selection is a highly individual matter. It depends greatly on both the properties of the biocatalyst and the technological conditions of the catalyzed process. Table 1 lists examples of materials used as supports for enzyme immobilization (Marschelke et al. 2019).

Table 1. Examples of materials used as supports for enzyme immobilization, and their parameters.

Material	Parameter	Examples	References
Synthetic polymers	Presence of reactive functional groups, solubility, porosity, stability and mechanical properties, low cost	Polyamide/laccase Polyvinyl/alcohol/amylase	Song et al. 2018 Porto et al. 2019
Biopolymers	Biodegradability to harmless products, biocompatibility and nontoxicity, affinity to proteins	Chitosan/lipase Cellulose/lipase	Chen et al. 2014 Karra-Chaabouni et al. 2008
Minerals	Occur in nature, easily available, high biocompatibility, can be used as obtained without further advanced treatment and purification	Montmorillonite/glucoamylase Halloysite/acylase	Sanjay et al. 2008 Kolodziejczak-Radzimska et al. 2019
Metal oxide	Thermal and chemical resistance and good mechanical properties, good sorption capacity	Silica/lipase Zirconia/lipase	Amirkhani et al. 2016 Zivkovic et al. 2015
Carbon-based	Well-developed porous structure; high surface area-up to 1000 m^2/g; high adsorption capacity	Graphene/laccase *MWCNT/lipase	Chen et al. 2017 Marzuki et al. 2015
Hybrid materials	Thermal and chemical stability, good sorption capacity, well-developed porous structure	Polyamide/chitosan laccase Chitosan/Fe_2O_3/lipase	Maryskova et al. 2016 Osuna et al. 2015

**MWCNT – multi-walled carbon nanotubes*

4 Useful Features of Immobilized Enzymes

As noted above, free enzymes exhibit high catalytic activity within a limited range of pH and temperature. This is because they function mainly within the natural environment found in living organisms. Many factors can affect the stability of an enzyme, including pH, temperature, the solvent, and the presence of metals and surfactants. While free enzymes exhibit high activity in a narrow pH range, their immobilized forms retain high activity in a pH range from 4 to 10. At higher temperatures, most enzymes tend to become inactivated or unfolded, and in consequence are no longer capable of catalyzing the target reaction (Amin et al. 2017; Bilal et al. 2019). The increased stability of enzymes that results from their immobilization is often attributed to the inherent characteristics of specific immobilization procedures, and can be determined by stabilization factors (Mateo et al. 2007).

Zare et al. (2019) showed that, while the activity of the free enzyme was greatly reduced, lipase immobilized on modified polyether sulfonate with MOF (metal-organic framework nanoparticles) retained more than 60% of its initial activity at 60 °C. This improvement in thermal stability may be the result of a hydrophobic interaction between the enzyme molecules and the MOF-based membrane. Additionally, the pH stability was determined. While at acidic pH there was no substantial difference between the free and immobilized lipase, a significant improvement in pH stability was observed for immobilized lipase at an extreme alkaline pH (retaining approximately 60% of its initial activity).

Another study (Zdarta et al. 2017) showed that the new prepared biocatalytic system lipase/spongin-based scaffolds has a high enzymatic activity at temperature range 30–60 °C and in the pH range 6–9. This research demonstrate that obtained biocatalysts have a better catalytic activity then free lipase. The lipase/spongin-based scaffolds retain about 80–90% of its initial activity in conditions present above.

Lin et al. (2017) proposed a biocatalytic system type of cellulase/magnetic Fe_3O_4-chitosan. The results of carried out studies showed that immobilized cellulase indicated better pH adaptability and heat tolerance to compare with the native protein. That situation could be associated with the good bonding of enzyme to the support. Immobilized cellulase is more durable to structural changes caused by the high value of pH and temperature.

5 Kinetic Parameters of Immobilized Enzymes

In 1913, Michaelis and Menten published their now classic paper, *Die Kinetik der Invertinwerkung* (Michaelis and Menten 1913). They proposed a mechanism to explain the dependence of the initial rate of enzyme-catalyzed reaction concentration. They considered the following model, in which *ES* is the enzyme-substrate complex (Johnson et al. 2011):

$$E + S \overset{k_1}{\leftrightarrow} ES \overset{k_2}{\rightarrow} P + E \tag{1}$$

$$V = \frac{dP}{dt} = k_2 \times ES \tag{2}$$

$$E_0 = E + ES \tag{3}$$

$$V = k_{2t} E_0 \frac{S}{S + k_1} = \frac{V_{max} S}{S + k_1} \tag{4}$$

Following a number of further investigations, the Michaelis–Menten equation used to determine the kinetic parameters of an immobilization process was presented in the following form (5):

$$V = \frac{V_{max}[S]}{K_M + [S]} \tag{5}$$

Equation (5) states that the initial rate (V) is equal to the product of the maximum initial rate (V_{max}) and the initial substrate concentration (S), divided by the *Michaelis constant*, K_M (k_1), plus the initial substrate concentration (S) (Potratz 2018).

The definition of Michaelis constant (K_M) describe that it is "the substrate concentration at which half of the enzyme active sites are filled by substrate molecules" (Luo et al. 2018). In many cases the value of the K_M is equal with the constant of the enzyme-substrate complex (ES). This is an important parameter, because the value of K_M indicates the durability of binding created due to immobilization. The bonds are weaker if the Michaelis constant is larger (Segal 1975; Marangoni 2002). The changes on temperature, the nature of the substrate, pH, ionic strength, and other reaction conditions have an influence on the value of K_M (Nigh 1976).

$$V_{max} = k_2 E_0 \tag{6}$$

In the equation (6) the k_2 is called the "*turnover number"* (or *catalytic constant,* k_{cat}). The catalytic constant (k_2) describes the maximum amount of substrate which was converted to product in the presence of enzyme and in one second. The ratio k_{cat}/K_M is a constant which evaluates the catalytic efficiency of an enzyme (Northrop 1998; Miller et al. 2002).

The basic kinetic data of an enzymatic reaction are calculated using spectrophotometric methods. The substrate properties and reaction conditions (temperature and pH) have a lot of influence on the measurement by this method. Alternatively, the calorimetric methods can be used. The reaction rate are measured based on the enthalpy changes, which is omnipresent in most enzymatic reactions (Luo et al. 2018).

Sample K_M and V_{max} values obtained for various free and immobilized enzymes are given in Table 2. As the table shows, the value of V_{max} decreased upon immobilization in all cases. That results show that the kinetic parameters are changed after the immobilization process. The changes mostly depend on the electrostatic and hydrophobic interactions created during the adsorption of enzyme onto the support, which could cause changes in the protein structure (Amirkhani et al. 2016; Zivkovic et al. 2015). The values of K_M and V_{max}, because of the lower flexibility of enzyme

which is smaller after immobilization, respectively increase and decrease. That suggests a lower affinity of immobilized enzyme to the substrate. This is probably associated with the steric barrier occurred during the immobilization process (Wang et al. 2006; Zdarta et al. 2016). On the other hand, a decrease in K_M leads to an increase in the enzyme's affinity to the substrate. This probably occurs when the electric charges on the support and substrate are of different sign (Ling et al. 2016; Yuan et al. 2016).

The factors, which are caused the changes in the kinetic parameters, it:

- changes in the protein structure appearing due to interactions between the support and the enzyme;
- the immobilization methods, which—in the case of covalent attachment—can involve different amino acid radicals;
- steric hindrances and diffusional effects introduced by the grafted monomers or by the spacer (De Maio et al. 2003).

Table 2. Kinetic parameters of various free and immobilized enzymes.

Material	K_M, mM	V_{max}, μmol/min	References
Free urease	18.1	11.5	Di Martino et al. 2003
Urease/nylon membrane	25.8	8.7	
Free catalase	26.7	19.5	Barreca et al. 2018
Catalase/graphene	376.3	1.74	
Free lipase	3.9	71.5	Amirkhani et al. 2016
Lipase/SiO_2	8,9	20.4	
Free acylase	47.2	0.44	Jiang et al. 2018
Acylase/SiO_2	144.3	0.38	
Free amylase	6.8	1.30	Mardani et al. 2018
amylase/chitosan/montmorillonite	9.1	0.62	
Free cellulose	4.82	0.06	Yuan et al. 2016
Cellulose/polymer	3.64	0.04	
Free laccase	0.05	0.04	Antecka et al. 2018
Laccase/TiO_2•ZrO_2	0.10	0.03	
Free trypsin	1.03	1.48	Zdarta et al. 2018c
Trypsin/Fe_2O_3/lignin	1.86	0.89	

6 Summary

Catalysis based on immobilized enzymes has become one of the most important disciplines in bioorganic synthesis, and has played a noteworthy role in the development of many chemical industries. Immobilization enhances the catalytic stability and activity of enzymes and reduces the overall cost burden of the enzyme. The kinetic parameters (K_M and V_{max}) are of great significance for the immobilization process. Changes in the values of these parameters reflect the effectiveness of the process. Such changes are naturally influenced by the immobilization method, the support used, and

the nature of the enzyme itself. The technique of immobilization is coming to be used widely for the successful development of sustainable and environmentally responsive catalytic processes.

Acknowledgments. This work was supported by the Polish Ministry of Science and Higher Education (Grant No. 0912/SDAB/2006).

References

Amin, F., Bhatti, H.N., Bilal, M., Asgher, M.: Improvement of activity, thermo-stability and fruit juice clarification characteristics of fungal exo-polygalactofructonase. Int. J. Biol. Marcomol. **95**, 974–984 (2017)

Amirkhani, L., Moghaddas, J., Jafarizadeh-Malmiri, H.: *Candida rugosa* lipase immobilization on magnetic silica aerogel nanodispersion. RSC Adv. **6**, 12676–12687 (2016)

Antecka, K., Zdarta, J., Siwińska-Stefańska, K., Sztuk, G., Jankowska, E., Oleskowicz-Popiel, P., Jesionowski, T.: Synergistic degradation of dye wastewaters using binary or ternary oxide systems with immobilized laccase. Catalysts **8**, 402–420 (2018)

Barreca, D., Neri, G., Scala, A., Fazio, E., Gentile, D., Rescifina, A., Piperno, A.: Covalently immobilized catalase on functionalized graphene: effect on the activity, immobilization efficiency, and tetramer stability. Biomater. Sci. **6**, 3231–3240 (2018)

Bilal, M., Zhao, Y., Noreen, S., Shah, S.Z.H., Bharagava, R.N., Iqbal, H.M.N.: Modifying bio-catalytic properties of enzymes for efficient biocatalysis: a review from immobilization strategies vewpoint. Biocatal. Biotransformation **37**, 159–182 (2019)

Brena, B.M., Batista-Viera, F.: Immobilization of enzymes. In: Guisan, J.M. (ed.) Methods in Biotechnology: Immobilization of Enzymes and Cells. Humana Press Inc., New York (2006)

Cao, L.: Carrier-Bound Immobilized Enzymes. Wiley-VCH, Weinheim (2005)

Cornish-Bowden, A.: Current IUBMB recommendations on enzyme nomenclature and kinetics. Perspect. Sci. **1**, 74–87 (2014)

Chen, J., Leng, J., Yang, X., Liao, L., Liu, L., Xiao, A.: Enhanced performance of magnetic graphene oxide-immobilized laccase and its application for the decolorization of dyes. Molecules **22**, 221–232 (2017)

Chen, Y., Liu, J., Xia, C., Zhao, C., Ren, Z., Zhang, W.: Immobilization of lipase on porous monodisperse chitosan microspheres. Biotechnol. Appl. Biochem. **62**, 101–106 (2014)

De Maio, A., El-Masry, M.M., Portaccio, M., Diano, N., Di Martino, S., Mattei, A., Bencivenga, U., Mita, D.G.: Influence of the spacer length on the activity of enzymes immobilized on nylon/polyGMA membranes: Part 1. Isothermal conditions. J. Mol. Catal. B Enzymatic **21**, 239–252 (2003)

Di Martino, S., El-Sheriff, H., Diano, N., De Maio, A., Grano, V., Rossi, S., Bencivenga, U., Mattei, A., Mita, G.: Urea removal from agricultural waste waters by means of urease immobilized on nylon membranes grafted with cyclohexyl-methacrylate. Appl. Catal. B **46**, 613–629 (2003)

Faber, K.: Biotransformation in Organic Chemistry. Springer, Heidelberg (2017)

Hanefeld, U., Gardossib, L., Magner, E.: Understanding enzyme immobilisation. Chem. Soc. Rev. **38**, 453–468 (2008)

Jiang, Y., Zhai, J., Zhou, L., He, Y., Ma, L., Gao, J.: Enzyme@silica hybrid nanoflowers shielding in polydopamine layer for the improvement of enzyme stability. Biochem. Eng. J. **132**, 196–205 (2018)

Jesionowski, T., Zdarta, J., Krajewska, B.: Enzyme immobilization by adsorption. Adsorption **20**, 801–821 (2014)

Johnson, K.A., Goody, R.S.: The original Michaelis constant: translation of the 1913 Michaelis-Menten paper. Biochemistry **50**, 8264–8269 (2011)

Kolodziejczak-Radzimska, A., Jesionowski, T.: Characterization of amino-, epoxy- and carbonyl-functionalized halloysite and its application in the immobilization of aminoacylase from *Aspergillus melleus*. Physicochem. Probl. Miner. Process. **55**, 128–139 (2019)

Karra-Chaabouni, M., Bouaziz, I., Boufi, S., Botelho do Rego, A.M., Gargouri, Y.: Physical immobilization of *Rhizopus oryzae* lipase onto cellulose substrate: Activity and stability studies. Colloids Surf. B **66**, 168–177 (2008)

Lin, Y., Liu, X., Xing, Z., Geng, Y., Wilson, J., Wu, D., Kong, H.: Preparation and characterization of magnetic Fe3O4–chitosan nanoparticles for cellulase immobilization. Cellulose **24**, 5541–5550 (2017)

Ling, X.M., Wang, X.Y., Ma, P., Yang, Y., Qin, J.M., Zhang, X.J., Zhang, Y.W.: Covalent immobilization of Penicillin G Acylase onto Fe3O4@chitosan magnetic nanoparticles. J. Microbiol. Biotechnol. **26**, 829–836 (2016)

Luo, Q., Chen, D., Boom, R.M., Janssen, A.E.M.: Revisiting the enzymatic kinetics of pepsin using isothermal titration calorimetry. Food Chem. **268**, 94–100 (2018)

Magner, E.: Immobilization of enzymes on mesoporous silicate materials. Chem. Soc. Rev. **42**, 6213–6222 (2013)

Marangoni, A.G.: Enzyme Kinetics: A Modern Approach. Wiley, Chichester (2002)

Mardani, T., Khiabani, M.S., Mokarram, R.R., Hamishehkar, H.: Immobilization of α-amylase on chitosan-montmorillonite nanocomposite beads. Int. J. Biol. Macromol. **120**, 354–360 (2018)

Marschelke, C., Müller, M., Köpke, D., Matura, A., Sallat, M., Synytska, A.: Hairy particles with immobilized enzymes: impact of particle topology on the catalytic activity. ACS Appl. Mater. Interfaces. **11**, 1645–1654 (2019)

Marzuki, C.N.H., Mahat, N.A., Huyop, F., Buang, N.A., Wahab, R.A.: *Candida rugosa* lipase immobilized onto acid-functionalized multi-walled carbon nanotubes for sustainable production of methyl oleate. Appl. Biochem. Biotech. **177**, 967–984 (2015)

Mateo, C., Palomo, J.M., Fernandez-Lorente, G., Guisan, J.M., Lafuente, R.F.: Improvement of enzyme activity, stability and selectivity via immobilization techniques. Enzyme Microb. Technol. **40**, 1451–1463 (2007)

Maryskova, M., Ardao, I., Garcia-Gonzalez, C.A., Martinova, L., Rotkova, J., Sevcu, A.: Polyamide 6/chitosan nanofibers as support for the immobilization of *Trametes versicolor* laccase for the elimination of endocrine disrupting chemicals. Enzyme Microb. Technol. **89**, 31–38 (2016)

Michaelis, L., Menten, M.L.: Die Kinetik der Invertinwirkung. Biochem Z **49**, 333–369 (1913)

Miller, B.G., Wolfenden, R.: Catalytic proficiency: the unusual case of OMP decarboxylase. Annu. Rev. Biochem. **71**, 847–885 (2002)

McDonald, A.G., Tipton, K.F.: Fifty-five years of enzyme classification: advances and difficulties. FEBS J. **281**, 583–592 (2014)

Murray, R.K., Granner, D.K., Mayes, P.A., Podwell, W.V.: Biochemia Harpera. Wydawnictwo Lekarskie PZWL, Warszawa (1995)

Nigh, W.G.: A kinetic investigation of an enzyme-catalyzed reaction. J. Chem. Educ. **53**, 668–669 (1976)

Northrop, D.B.: On the meaning of K_m and V = K in enzyme kinetics. J. Chem. Educ. **75**, 1153–1157 (1998)

Osuna, Y., Sandoval, J., Saade, H., López, R.G., Martinez, J.L., Colunga, E.M., de la Cruz, G., Segura, E.P., Arévalo, F.J., Zon, M.A., Fernández, H., Ilyina, A.: Immobilization of *Aspergillus niger* lipase on chitosan-coated magnetic nanoparticles using two covalent-binding methods. Bioprocess Biosyst. Eng. **38**, 1437–1445 (2015)

Pleiss, J.: Systematic analysis of large enzyme families: Identification of specificity- and selectivity-determining hotspots. ChemCatChem **6**, 944–950 (2014)

Potratz, J.P.: Making enzyme kinetics dynamic via simulation software. J. Chem. Educ. **95**, 482–486 (2018)

Porto, M.D.A., dos Santos, J.P., Hackbart, H., Bruni, G.P., Fonseca, L.M., Zavareze, E.R., Dias, A.R.G.: Immobilization of α-amylase in ultrafine polyvinyl alcohol (PVA) fibers via electrospinning and their stability on different substrates. Int. J. Biol. Macromol. **126**, 834–841 (2019)

Sanjay, G., Sugunan, S.: Acid activated montmorillonite: an efficient immobilization support for improving reusability, storage stability and operational stability of enzymes. J. Porous Mater. **15**, 359–367 (2008)

Segal, I.H.: Enzyme Kinetics. Wiley, New York (1975)

Song, J.E., Kim, H.R., Lee, S.H.: Effect of enzymatic hydrolysis on developing support of pol amide woven fabric for enzyme immobilization. Text. Res. J. **89**, 1345–1360 (2018)

Stryer, L.: Biochemia. Wydawnictwo Naukowe PWN, Warszawa (2003)

Tipton, K., Boyce, S.: History of the enzyme nomenclature system. Bioinformatic **16**, 34–40 (2000)

Wang, Z.G., Wang, J.Q., Xu, Z.K.: Immobilization of lipase from *Candida rugosa* on electrospun polysulfone nanofibrous membranes by adsorption. J. Mol. Catal. B **42**, 45–51 (2006)

Yuan, Y., Luan, X., Rana, X.K., Hassana, M.E., Dou, D.: Covalent immobilization of cellulase in application of biotransformation of ginsenoside Rb_1. J. Mol. Catal. B: Enzymatic **133**, S525–S532 (2016)

Zare, A., Bordbar, A.K., Razmjou, A., Jafarian, F.: The immobilization of *Candida rugosa* lipase on the modified polyethersulfone with MOF nanoparticles as an excellent performance bioreactor membrane. J. Biotechnol. **10**, 55–63 (2019)

Zdarta, J., Antecka, K., Jędrzak, A., Synoradzki, K., Łuczak, M., Jesionowski, T.: Biopolymers conjugated with magnetite as support materials for trypsin immobilization and protein digestion. Colloids Surf. B Biointerfaces **169**, 118–125 (2018a)

Zdarta, J., Norman, M., Smułek, W., Moszynski, D., Kaczorek, E., Stelling, A.L., Ehrlich, H., Jesionowski, T.: Spongin-based scaffolds from *Hippospongia communis* demosponge as an effective support for lipase immobilization. Catalysts **7**, 147–167 (2017)

Zdarta, J., Meyer, A.S., Jesionowski, T., Pinelo, M.: Developments in support materials for immobilization of oxidoreductases: a comprehensive review. Adv. Colloid Interface Sci. **258**, 1–20 (2018b)

Zdarta, J., Meyer, A.S., Jesionowski, T., Pinelo, M.: A general overview of support materials for enzyme immobilization: characteristics, properties, practical utility. Catalysts **8**, 92–109 (2018c)

Zhang, D., Hegab, H.E., Lvov, Y., Snow, L.D., Palmer, J.: Immobilization of cellulase on a silica gel substrate modified using a 3-APTES self-assembled monolayer. Springerplus **5**, 48–68 (2016)

Zivkovic, L.T.I., Zivkovic, L.S., Babicb, B.M., Kokunesoski, M.J., Jokic, B.M., Karadzic, I.M.: Immobilization of *Candida rugosa* lipase by adsorption onto biosafe meso/macroporous silica and zirconia. Biochem. Eng. J. **93**, 73–83 (2015)

Methods of Bacteriophages Production with Application of Alternate Magnetic Field

Maciej Konopacki[1(✉)], Bartłomiej Grygorcewicz[2], Marian Kordas[1], Barbara Dołęgowska[2], and Rafał Rakoczy[1]

[1] Faculty of Chemical Technology and Engineering, West Pomeranian University of Technology, Szczecin, Poland
mkonopacki@zut.edu.pl
[2] Department of Microbiology, Immunology and Laboratory Medicine, Pomeranian Medical University, Szczecin, Poland

Abstract. The chapter presents the methods of bacteriophage production with the application of the alternate magnetic field. Bacteriophages are viruses that can infect and destroy bacteria cells. Up to date, numerous types of phages have been discovered. Nevertheless, the basic mechanisms and properties are common. Nowadays, the growing interest of the application of bacteriophages in a different field (e.g. medical, pharmaceutical, food preservation, biosensors, nanomaterials) causes the improved methods of phage's production are necessary to design. The magnetically assisted bacteriophages production method was then proposed. The preliminary results suggest, that electromagnetic stimulation may lead to process improvement by the increased number of produced virions and their lytic activity.

1 Theoretical Fundamental of Bacteriophages

Bacteriophages (or commonly phages) are specialized viruses, which attack selected bacteria strains or groups. Bacteriophages can be divided into two basic types: lytic and lysogenic (Kropinski 2018). The lytic (also called virulent) phages multiplying inside the bacterial cell and finally destroying them. These properties result in high application potential in medicine, especially in the treatment of antibiotic resistant bacterial infection. (Herada et al. 2018). In short, the lytic phages use one of two proteins to destroy the host cell: holins or lysins. The holins can perforate the bacterial cytoplasmic membrane. This situation creates an opportunity for endolysins to destruct the bacterial cell wall. The lysins can rapidly destroy the bacteria cell wall, by cleaving peptidoglycan, which is the major cell wall component. (Cisek et al. 2014). The second kind of bacteriophage, representing the lysogenic life cycle is known as temperate phages. They could integrate the viral genome into host DNA. Such DNA replicates as part of the bacterial chromosome and is noninfectious (called a prophage). The prophage in specific circumstances can force host bacteria to create phage particles in the lytic cycle. Nevertheless, temperate phages can live together with bacteria in cooperation, which can give advantages to both sides. The overview of the main differences between the lytic and the lysogenic bacteriophages' life cycle is presented in Fig. 1.

© Springer Nature Switzerland AG 2020
M. Ochowiak et al. (Eds.): PAIC 2019, *Practical Aspects of Chemical Engineering*, pp. 171–182, 2020.
https://doi.org/10.1007/978-3-030-39867-5_18

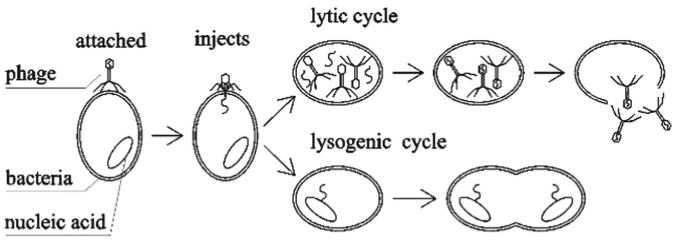

Fig. 1. Bacteriophage life cycles

The beginning of the bacteriophage studies was in 1915, when Frederick Twort, a British physician described the probable occurrence of an "ultramicroscopic virus" that could destroy bacteria. He discovered during work on vaccinia preparations "glassy and transparent" spots within colonies of bacteria suggesting dead bacteria zones. One of the possible explanations given by Twort was the presence of viruses but he could not confirm this hypothesis (Twort et al. 2011). In 1917 Felix d'Herelle observed a very similar phenomenon. He was convinced that bacteria were destroyed by an invisible microbe which he named bacteriophage (Kakasis and Panitsa 2019). This discovery led to a new idea of phage therapy and it was implemented in many studies, but after the discovery of antibiotics and their application during the Second World War, the bacteriophage area research was generally subsided. A small number of experiments of phage therapy still carried on was mainly failure. The reasons for phage therapy failure were inappropriate phage preparation, selection, and storage (Gill and Hyman 2010). Additionally, bacteriophages pose high application potentials in other fields, such as components of materials in batteries, fuel cells, sensors, optics, food preservations and other disciples so far (Herada et al. 2018; Kakasis and Panitsa 2019; Warner et al. 2014; Kilcher and Loessner 2019). This potential increases the interest in bacteriophage research.

1.1 Structures and Functions of Bacteriophages

Bacteriophages are viruses that requiring host bacteria to the replication of their genetic material and new virions production (Hyman and Abedon 2009; Skurnik and Strauch 2006). The average size of phage virion is generally about 50–200 nm, but the largest known bacteriophages are bigger than 400 nm in length (Cuervo and Carrascosa 2012). The most of the discovered (over 5100 types) phages are classified in Caudovirales order, the Myoviridae, Podoviridae, Ackermannviridae, Herelleviridae and Siphoviridae families. (Adriaenssens et al. 2018). Basing on the type of genetic material, bacteriophages can be divided into four groups: double-stranded DNA phages, single-stranded DNA phages, double-stranded RNA phages, single-stranded RNA phages (Herada et al. 2018). Caudovirales phages share a similar structure, like an icosahedral capsid, that stores genetic information in the form of double-stranded DNA, with attached spike tail with fibers (Ackermann 2007). Virion has a permanent dipole moment because of charges position - the head structure possesses a negative charge when the tail fibers have a positive charge. The tail fibers structure, attached to

bacteriophage baseplate, depends on the phage family and determining the bacterial host specificity (Leiman and Shneider 2012). There are also different phage families like Inoviridae (e.g. M13 phage, characterized by the filamentous structure of virion) or Leviviridae (e.g. MS2 phage, almost spherical). The main difference of these phages, behind the structure, is the genetic information that is stored in single-stranded RNA or DNA (Baran and Bloomfield 1978). The typical structure of Caudovirales phage is presented in Fig. 2.

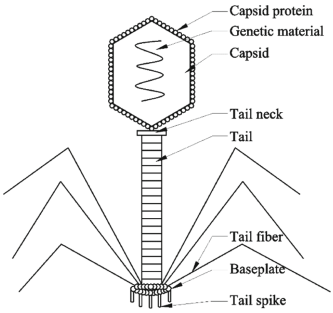

Fig. 2. Typical structure of Caudovirales bacteriophage

The multiplication of virions required recognition of the proper bacteria host cell which results in the precise and often multistep identification process. The electrostatic interactions play a key role in the initial recognition. The surface of bacteria, which is negatively charged is attracting phage tail fibers (positively charged). Following specific receptor-binding proteins are utilized to recognize the proper bacterial-host (Richter et al. 2018). Next, the phage tail fibers bound to the host surface towards it. Reorientation of the tail fibers does not occur in free bacteriophage, but only on the host cell surface and without any chemical energy (Herada et al. 2018). One of the proposed mechanisms explaining this phenomenon based on theory, that during phage encounters bacteria host an only a small amount of tail fibers (one or two) binds to surface receptors. Attached phage is then subjected to the action of molecular motions (convective current and thermally induced movements, Brownian motions) and movement created by swimming bacteria (Herada et al. 2018). The second proposed mechanism relates to the phage calcium requirement for bacterial infection. Molecules, such as proteins, and polysaccharides, on the host surface, bind divalent cations, which results in their higher concentration near the surface. This situation can promote changes in the conformation of the phage baseplate with an extension of the tail fibers (Herada et al. 2018). Finally, the phages use the bacteria intercellular transport mechanism to transfer its genome inside the cell, where their progeny virions are produced. in a consequence of a lytic cycle through host cell lysis virions are released. (Richter et al. 2018; Martinez et al. 2018).

1.2 Application of Bacteriophages

Bacteriophages have wide application in modern technology, not only for diagnostic and treatment purposes but also is such branches as food safety, pharmaceutic, energetic, sensors, electronic and other (Herada et al. 2018; Kakasis and Panitsa 2019; Warner et al. 2014; Kilcher et al. Martinez et al. 2018; Monteiro et al. 2018). Nowadays, bacteriophages are a very desired alternative for antibiotic therapy due to the increment of antibiotic resistance, mostly of highly morbific bacteria. This situation is generally caused by to over-utilization of antibiotics (unreasonable treatment, excessive application in animal breeding) or improper application (self-treatment, preventive use) (Herada et al. 2018). Bacteriophages naturally kill bacteria by making them burst or lyse. Moreover, they are highly specific, which results in action only on target bacteria without harmful effects on the natural bacterial flora of the patient. Phages do not need application of many doses – one use is often enough because after application their concentration raising due to multiplication in host bacteria until host bacteria depleting. (Kropinski 2018; Nobrega et al. 2015). Thanks to those abilities, phages have numerous advantages in comparison with the antibiotic treatment (Monteiro et al. 2018). Nevertheless, bacteriophages similarly sometimes do not kill all bacteria, because of the presence of bacteriophage resistant mutants. For this reason, the mixed treatments are proposed, where combined phages and antibiotics are applied (Kakasis and Panitsa 2019; Chang et al. 2018). Moreover, in case of rapid destroy of bacteria, treated organisms can be poisoned by bacteria decomposition products (Kakasis and Panitsa 2019; Nobrega et al. 2015). Bacteriophage action may induce immunological reaction or can affect body tissues and non-target bacteria by transducing DNA between bacteria or expressing virulence genes (Abedon et al. 2011). However, modern methods of genome sequencing allow avoiding unwanted situations (Abedon 2017).

Bacteriophages for medical applications may be applied by the inhalation, ingestion, injection or transdermal methods (e.g. ointments, creams, lotions) (Kakasis and Panitsa 2019). In respiratory tract infection, therapeutic phages can be applied by inhalation through nose, mouth or inside inhalation chambers. Those methods were tested on animals (e.g. mice) (Abedon 2018) and humans (Chang et al. 2018). This kind of therapy was reported in Easter Europe (Georgia, Poland, and Russia) and was continuously improved (Chang et al. 2018). Phages in the form of an ointment impregnated dressing directly on the skin are utilized in wound infection treatment and diabetic foot ulcers, mainly against Pseudomonas aeruginosa and Staphylococcus aureus bacteria (Abedon 2018). Moreover, bacteriophages can be used in new generation vaccines (Herada et al. 2018). Two different approaches can be highlighted – first, based on the production of immunogenic phage particles, which surface is coated by foreign antigens due to fusion with selected structural proteins of virion; second approach use incorporation of foreign antigens into phage's genome under control of strong eukaryotic promotors. In this case, bacteriophage acts as a passive carrier of foreign DNA into mammalian cells, where the gene expressions taking place. These two approaches are often combined (Herada et al. 2018). Bacteriophages can be also applied to decrease the impact of the food industry on the environment. They are a promising alternative for traditional food preservation techniques and at the same time allow a reduction of antibiotics usage in animal breeding (Martinez et al. 2018). Phages

are used in bio conservation of food, e.g. to protect before E. coli and Salmonella bacteria (Richter et al. 2018) and to detect pathogens in food of animal origin (Martinez et al. 2018; Fister et al. 2019). This mechanism bases on destroying pathogens harmful for food and crops, which results in an increment of food production safety and harvest size. The effectiveness of phage in crop protection is comparable to conventional plant protection products. (Herada et al. 2018) Additionally application of bacteriophages can reduce the number of pathogens transferred in food and help in the control of slaughterhouses and process plants (Fister et al. 2019). The disadvantages of these techniques are often the necessary application of phage cocktails, horizontal transfer of genes, phage resistant bacteria mutants and virulence transmission (Martinez et al. 2018). Bacteriophages also may be used in the following applications:

1. As nano-carriers to precise gene delivery in specific regions. The phage coat protects DNA from degradation after injection. Moreover, targeting of specific cells in enables due to the ability of foreign molecules display on the phage coat (Herada et al. 2018; Kilcher and Loessner 2019).
2. Bacterial biosensors, thanks to the possibility of detection of bacteria by bacteriophage particles. Addition of bacteriophage to sample results in changes in impedance when the target bacteria is present due to conductivity changes of the medium caused by microorganisms. This happens, when microorganisms transforming uncharged metabolites into charged molecules (e.g. acids). Moreover, phages identify the specific structure of the bacteria surface, which can help in auxiliary bacteria detection. (Herada et al. 2018; Martinez et al. 2018).
3. Surface disinfection through bacteria growth control, especially in health care and food processing facilities. Most difficult to remove are bacteria forming biofilms, but bacteriophages can hydrolysis of the peptidoglycan layer of cell wall causing an osmotic imbalance which results in loss of the structural integrity and lysis (Herada et al. 2018; Martinez et al. 2018).
4. In nanomaterials production as vectors or matrix for the creation of new nanodevices. Some of the phages (filamentous, MS2, λ, T) can be used in the form of nano-carriers for target drug delivery in therapeutic and diagnostic applications. There is three major potential application in drug delivery: target imaging, drug targeting, and gene therapy. Phages can deliver specific genes efficiently to a cell or tissue thanks to engineering peptide sequences on capsid surface, specifying directly its target (Farr et al. 2014; Merzlyak et al. 2006), but also, they are protecting genes from degradation (Herada et al. 2018).
5. In material corrosion control – bacteria can cause corrosion on metal surfaces by chemical changes that occur during bacteria growth. Bacteria biofilms are an important issue in the oilfield system (Baldwin et al. 2012). Nowadays, biofilm control in gas and oil industries is carried on by physical and chemical treatment. Those methods can be efficient, but incomplete removal of biofilm can cause bacteria regrowth after treatment. Bacteriophage lytic cycle is a very good alternative to inhibit corrosion-causing bacteria growth, generally by phage's self-replication ability, which is the main advantage of this technique (Zarasvand and Rai 2014).

1.3 Bacteriophage Production Methods

Isolation of bacteriophages can be performed from any environmental source, that containing the target microorganism. The biggest source of phages is sewage and wastewaters, especially from the hospital, where phages of clinically relevant bacteria can be found (Latz et al. 2016). The simplest method to isolate bacteriophages is to remove from sample unwanted microorganisms by sterilization. Next, the sample is plated to bacteria host to evaluate the formation of the plaques (Gill and Hyman 2010). Thereafter, isolated bacteriophages should be genetically sequenced and characterized in the purpose of therapeutic applications. The keys parameters to select proper phages are their efficacy, specificity, possible side effects (Weber-Dąbrowska et al. 2016). Bacteriophage production methods can be divided into the batch, semi-continuous and continuous, single or two-stage processes. The cultivation methods vary generally on way of bacteria multiplication and phage isolation. Typically, bacteriophages are produced in shaker flask (about a few liters volume) or bioreactor with mechanical stirrer (Grieco et al. 2009). The batch method is the simplest and most popular method. Host bacteria solution is prepared with a certain concentration and then inoculate with bacteriophages. After some time, the cycle process is ended, thus phages are centrifuged and isolated (Chen and Lim 1996; Oh et al. 2005). The biggest advantages of this method are its simplicity, lack of problems with process control and residence time. Although, a lot of manpower is required as usually in the batch process and its capital costs are very high. Moreover, the throughput is limited by the high proportion between downtime and production time, which results in small cost or time efficiency (Sauvageau and Cooper 2010). The continuous and semi-continuous methods are generally characterized by more complicated equipment and procedures. Single-stage methods use one tank, where the proper temperature is set to cultivate demanded bacteria concentration and then the temperature is modified (Park and Park 2000). Two-stage methods utilize two separate tanks. In the first one bacteria growth and multiplication are conducted and then the suspension is transferred to the second tank, where after the addition of phages cell lysis process and product formation taking place (Oh et al. 2005). This method allows us to obtain high volumetric throughputs, nevertheless many disadvantages are known. The main issue is very hard to obtain a stable and consistent production system and they are dependent on the population density for infection control (Chen and Lim 1996). Continuous phage production is very time-sensitive and creating difficulties in the system maintain which often results in small final phage titers (Oh et al. 2005). Many problems are also connected with the estimation of residence time distribution (Chen and Lim 1996; Oh et al. 2005). Nevertheless, it is possible to combine these two methods to obtain high phage titers, high volumetric throughput by utilizing a proper designed semi-continuous process (Sauvageau and Cooper 2010). In Table 1 short compartment of different production methods is presented, considering the type of bacteriophages, bacteria host and general process conditions.

Tab. 1. Review of bacteriophages production methods

Ref.	Type	Bacteriophage	Host cultivation	Phage production
(Sargeant et al. 1968)	Batch	T7	E. coli B, 37 °C	Tanks: 3 L and 10 L, 37 °C
(de Czekala et al. 1972)	Batch	Phage lambda mutant (XCI857)	E. coli 3102 (XCI857) E. coli C-600 (indicator) 32 °C (i) a modified Vogel-Bonner medium, (ii) 1% tryptone broth	10 L of broth in 20 L tank 40 °C
(Warner et al. 2014)	Batch	M13	XL1-Blue MRF' E. coli, 37 °C, 225 rpm LB or TB medium supplemented with 20 mg/mL tetracycline, 1% (v/v) glycerol or D-glucose	250 mL and 4 L shaker flasks, (1.2 L and 75 mL of medium), 50 mL tube spin reactors, (15 mL medium), Cultures were incubated in 32 °C for 20 h
(Chen and Lim 1996)	Batch/semi-batch continuous	Q-mutant of bacteriophage λ	E. coli, the medium of tryptone and yeast extract	n/a
(Park and Park 2000)	Continuous	Bacteriophage λ	E. coli CY15050	1 l bioreactors 30 °C to 38 °C–40 °C
(Oh et al. 2005)	Batch, continuous	Bacteriophage λHL1	E. coli P90c	1 l bioreactors (500 ml working volume), 33 °C to 40 °C (45/12 h)
(Sauvageau and Cooper 2010)	Batch, continuous	T4 ATCC 11303	E. coli ATCC 11303, 37 °C 250 rpm	1 l working volume, 37°C, 200 rpm, 0.5 vvm aeration

2 Magnetically Assisted Bacteriophage Production

Stimulation of living cells for intensification of biotechnological processes and effective production of demanded compounds is possible thanks to the utilization of different factors (Domingues et al. 2000). Nowadays, the application of various force fields (e.g. magnetic or electric field, ultrasounds) to increase biomass production is very interesting and excessively studied. The electromagnetic field is also used in enzymes production, biochemical and enzymatic process intensification and utilization of this kind of field is the aim of many theoretical and experimental studies (Wang et al. 2017; Rakoczy et al. 2017). The new idea is to apply the alternating magnetic field, AMF (e.g. rotating magnetic field, RMF) to bioprocess assist. AMF is a magnetic field created by electric charges which move vary in time and/or in space (e.g. in a result of direct current flow), which spread in space in form of electromagnetic wave. Our previous studies showed, that in specific conditions under AMF exposition the stimulation of biomass production, cell proliferation, and metabolic activity increment is possible (Konopacki and Rakoczy 2019). Both gram-positive and gram-negative bacteria were tested but various results were obtained: stimulation of gram-positive and inhibition of gram-negative bacteria. Received data suggested, that AMF can affect intercellular transport and alter the permeability of cell walls (Konopacki and Rakoczy 2019). The production of bioethanol utilizing yeast (Konopacka et al. 2019) and

bacteria-formed cellulose (Fijałkowski et al. 2015) was also studied. In both cases, an intensification of processes increased yield, and proliferation of microorganisms and their metabolic activity were obtained. Such a result suggests, that AMF can be successfully applied to improve bioprocesses. Moreover, the influence of the external electromagnetic field on lambdoidal bacteriophages was tested (Struk et al. 2017). Received data indicated, that AMF exposition (B = 34 mT, f = 50 Hz) increased the production of induced lambdoidal phages. It was assumed, that a similar phenomenon can be observed for lytic bacteriophages and phages characterized by chronic infection. In the next step, the preliminary studies of AMF application in lytic bacteriophage production were tested. Bacteriophages were cultivated using the batch method in a single tank, without a mechanical agitator but assisted with the RMF generator. The RMF can create a micromixing effect, that can improve mass and heat transfer inside the tank, but with smaller shear stresses in comparison to the standard agitator. The experimental set-up is presented in Fig. 3

The main element of the experimental set-up is the RMF generator in the form of three-phase coils situated inside the tank, which is powered by the alternated current of controlled parameters (using phase inverter). Inside the generator culture tank is axially situated, where the studied biologic material can be placed. The temperature of the system is controlled by proper system and heat created by coils is recuperated in a plate heat exchanger and then taken to heat-up the cultures, which result in no additional heat source is required.

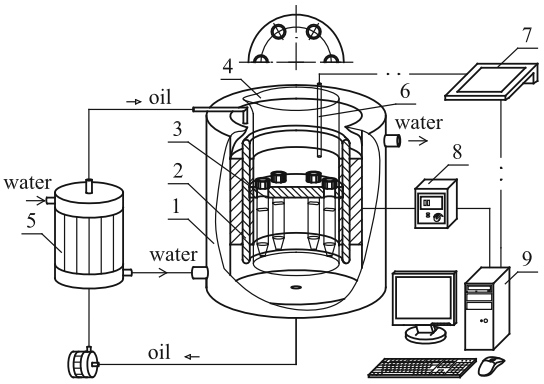

Fig. 3. Experimental set-up: 1 – tank, 2 – the RMF generator, 3 – sample, 4 – cultivation tank, 5 – heat exchanger, 6 – temperature sensor, 7 – multifunctional reader, 8 – phase inverter, 9 – PC

In present studies, the multiplication of bacteriophages and phage-host interaction under the action of AMF were tested. The T4 lytic cycle bacteriophage and E. coli bacteria as hosts were chosen for these preliminary studies. In the beginning, the bacteria suspension was transferred to the generator for 20 min and exposed to the AMF. After this time, the culture tank was inoculated by phages suspension and left for 1 h of exposition. The samples were collected every five minutes and then the

bacteriophage cycle, its amount and its lytic activity were evaluated. The same experiment, but without the exposition of AMF was performed as the control process. The exemplary results are presented in Figs. 4 and 5.

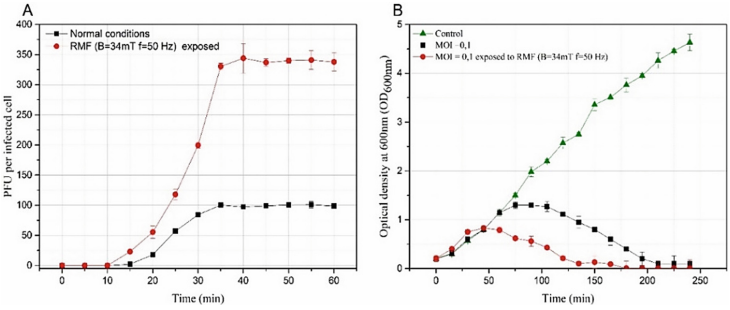

Fig. 4. Bacteria growth (A) and phage's lytic activity (B) under RMF exposure

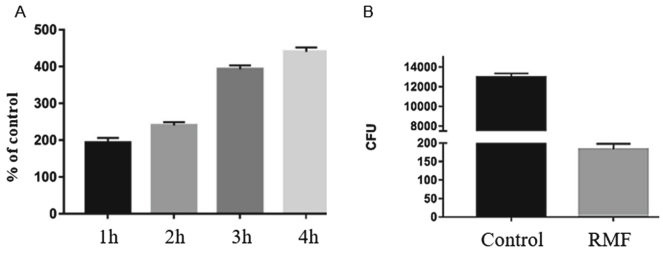

Fig. 5. Number of produced phages (A) and phage-resistant mutants (B)

The result of preliminary studies showed, that AMF exposition modified the bacteriophage life cycle and its lytic activity. It was observed, that the latent period of T4 lytic cycle was shortened from 20 to 15 min (without adsorption time). Additionally, the bacteriophage burst size was significantly increased from 103 to 330 PFU per infected cell. Moreover, the presented results showed the higher lytic activity of this phage on liquid cultures of E. coli after 1 h of exposition. This preliminary result showing great potential for AMF application in bacteriophage studies and production. Additionally, conducted experiments indicated a highly increased (up to 400%) number of produced bacteriophages and decrement of phage-resistant mutants in the process with AMF exposition, which can be utilized in the production process. Those results allowed to formulate an idea of magnetically assisted bacteriophage production. In the near future, the batch method, which has its limitation is planned to upgrade into the semi-continuous two-stage process. The goal is to design new technology to phage production characterized in a high amount of bacteriophage in a short time, that can be utilized in the treatment of antibiotic-resistant bacterial infections. Presented results confirmed the possibility of stimulation of bioprocess by application of proper AMF setup.

3 Summary

The literature analysis showed that bacteriophages pose high application potential in modern technology, not only in therapeutic processes but also in food processing and other industries, increasing researchers' interest of this topic (Warner et al. 2014). Due to the rising number of studies, very important is to design a proper, so efficient and low-cost bacteriophage production, also for the industrial scale. Many of the works concern the isolation of phages and optimization of cultivation parameters, such as temperature and environmental conditions (Kim and Park 2000). The proper production method needs to be taken into account and currently, the semi-continuous type seems to be optimal, but not so easy to design and operate as batch methods (Oh et al. 2005). An alternative for improving the process can be the stimulation of phages by force field applications, especially AMF (Konopacki and Rakoczy 2019; Konopacka et al. 2019). Multiplication of phages can be stimulated by proper AMF. This kind of field also facilitates phage adsorption to host bacteria, which can be very interesting in terms of antibiotic-resistant bacteria infections treatment.

Acknowledgments. This study was supported by the National Science Centre, Poland [OPUS 16, Project No.UMO-2018/31/B/ST8/03170, granted to Rafal Rakoczy].

References

Abedon, S.T.: Bacteriophage clinical use as antibacterial "drugs": utility and precedent. Microbiol. Spectr. **5**(4) (2017)

Abedon, S.T.: Use of phage therapy to treat long-standing, persistent, or chronic bacterial infections. Adv. Drug Deliv. Rev. **145**, 18–39 (2018)

Abedon, S.T., Kuhl, S.J., Blasdel, B.G., Kutter, E.M.: Phage treatment of human infections. Bacteriophage **1**(2), 66–85 (2011)

Ackermann, H.W.: 5500 Phages examined in the electron microscope. Arch. Virol. **152**(2), 227–243 (2007)

Adriaenssens, E.M., Wittmann, J., Kuhn, J.H., Turner, D., Sullivan, M.B., Dutilh, B.E., Jang, H. B., van Zyl, L.J., Klumpp, J., Lobocka, M., Switt, A.I.M., Rumnieks, J., Edwards, R.A., Uchiyama, J., Alfenas-Zerbini, P., Petty, N.K., Kropinski, A.M., Barylski, J., Gillis, A., Clokie, M.R.C., Prangishvili, D., Lavigne, R., Aziz, R.K., Duffy, S., Krupovic, M., Poranen, M.M., Knezevic, P., Enault, F., Tong, Y., Oksanen, H.M., Brister, J.R.: Taxonomy of prokaryotic viruses: 2017 update from the ICTV bacterial and archaeal viruses subcommittee. Arch. Virol. **163**(4), 1125–1129 (2018)

Baldwin, D., Summer, N.S.: Prevention and remediation of petroleum reservoir souring and corrosion by treatment with virulent bacteriophage. Patent number: US8168419 B2 (2012)

Baran, G.J., Bloomfield, V.A.: Tail-fiber attachment in bacteriophage T4D studied by quasielastic light scattering-band electrophoresis. Biopolymers **17**, 2015–2028 (1978)

Chang, R.Y.K., Wallin, M., Lin, Y., Leung, S.S.Y., Wang, H., Morales, S., Chan, H.K.: Phage therapy for respiratory infections. Adv. Drug Deliver Rev. **133**, 76–86 (2018)

Chen, B.Y., Lim, H.C.: Bioreactor studies on temperature induction of the Q-mutant of bacteriophage λ in Escherichia coli. J. Biotechnol. **51**, 1–20 (1996)

Cisek, A.A., Dabrowska, I., Gregorczyk, K.P., Wyzewski, Z.: Phage therapy in bacterial infections treatment: one hundred years after the discovery of bacteriophages. Curr. Microbiol. **74**(2), 277–283 (2014)

Cuervo, A., Carrascosa, J.L. (eds.): Bacteriophages: Structure. Wiley, Hoboken (2012)

de Czekala, A., Luk, D., Bartl, P.: Large-scale production of lambda Bacteriophage and purified lambda deoxyribonucleic acid. Appl. Microbiol. **23**(4), 791–796 (1972)

Domingues, L., Vicente, A.A., Lima, N., Teixeira, J.A.: Applications of yeast flocculation in biotechnological processes. Biotechnol. Bioprocess Eng. **5**, 288–305 (2000)

Farr, R., Choi, D.S., Lee, S.W.: Phage-based nanomaterials for biomedical applications. Acta Biomater. **10**(4), 1741–1750 (2014)

Fijałkowski, K., Żywicka, A., Drozd, R., Niemczyk, A., Junka, A.F., Peitler, D., Kordas, M., Konopacki, M., Szymczyk, P., El Fray, M., Rakoczy, R.: Modification of bacterial cellulose through exposure to the rotating magnetic field. Carbohyd. Polym. **133**, 52–60 (2015)

Fister, S., Mester, P., Witte, A.K., Sommer, J., Schoder, D., Rossmanith, P.: Part of the problem or the solution? Indiscriminate use of bacteriophages in the food industry can reduce their potential and impair growth-based detection methods. Trends Food Sci. Tech. **90**, 170–174 (2019)

Gill, J.J., Hyman, P.: Phage choice, isolation, and preparation for phage therapy. Curr. Pharm. Biotechnol. **11**(1), 2–14 (2010)

Grieco, S.H.H., Lee, S., Dunbar, S.W., MacGillivray, R.T.A., Curtis, S.B.: Maximizing filamentous phage yield during computer controlled fermentation. Bioprocess Biosyst. Eng. **32**, 773–779 (2009)

Herada, L.K., Silva, E.C., Campos, W.F., del Fiol, F.S., Vila, M., Dąbrowska, K., Krylov, V.N., Balcão, V.M.: Biotechnological applications of bacteriophages: state of the art. Microbiol. Res. **212–213**, 38–58 (2018)

Hyman, P., Abedon, S.T.: Practical methods for determining phage growth parameters. Methods Mol. Biol. **501**, 175–202 (2009)

Kakasis, A., Panitsa, G.: Bacteriophage therapy as an alternative treatment for human in-fections. A comprehensive review. Int. J. Antimicrob. Ag. **53**, 16–21 (2019)

Kilcher, S., Loessner, M.J.: Engineering Bacteriophages as versatile biologics. Trends Microbiol. **27**(4), 355–367 (2019)

Kim, T.S., Park, T.H.: Optimization of bacteriophage λ Q-contatin recombinant Escherichia coli fermentation process. Bioprocess. Eng. **23**, 187–190 (2000)

Konopacka, A., Rakoczy, R., Konopacki, M.: The effect of rotating magnetic field on bio-ethanol production by yeast strain modified by ferrimagnetic nanoparticles. J. Magn. Magn. Mater. **473**, 176–183 (2019)

Konopacki, M., Rakoczy, R.: The analysis of rotating magnetic field as a trigger of Gram-positive and Gram-negative bacteria growth. Biochem. Eng. J. **141**, 259–267 (2019)

Kropinski, A.M.: Bacteriophage research - what we have learnt and what still needs to be addressed. Res. Microbiol. **169**, 481–487 (2018)

Latz, S., Wahida, A., Arif, A., Häfner, H., Hoß, M., Ritter, K., Horz, H.P.: Preliminary survey of local bacteriophages with lytic activity against multi-drug resistant bacteria. J. Basic Microbiol. **56**(10), 1117–1123 (2016). https://doi.org/10.1002/jobm.201600108

Leiman, P.G., Shneider, M.M.: Contractile tail machines of bacteriophages. In: Michael Rossmann, G., Venigalla Rao, B. (eds.) Viral Molecular Machines, Advances in Experimental Medicine and Biology, vol. 726, pp. 1–978 Ch. 5. Springer (2012). ISBN 978-1-4614-0979-3

Martinez, B., Garcia, P., Rodriguez, A.: Swapping the roles of bacteriocins and bacteriophages in food biotechnology. Curr. Opin. Biotechnol. **56**, 1–6 (2018)

Merzlyak, A., Lee, S.W.: Phage as templates for hybrid materials and mediators for nanomaterial synthesis. Curr. Opin. Chem. Biol. **10**(3), 246–252 (2006)

Monteiro, R., Pires, D.P., Costa, A.R., Azeredo, J.: Phage therapy: going temperate? Trends Microbiol. (2018)

Nobrega, F.L., Costa, A.R., Kluskens, L.D., Azeredo, J.: Revisiting phage therapy: new applications for old resources. Trends Microbiol. **23**(4), 185–191 (2015)

Oh, J.S., Cho, D., Park, T.H.: Two-stage continuous operation of recombinant Escherichia coli using the bacteriophage λ Q vector. Bioprocess Biosys. Eng. **28**, 1–7 (2005)

Park, S.H., Park, T.H.: Analysis of two-stage continuous operation of Escherichia coli containing bacteriophage λ vector. Bioprocess. Eng. **23**, 557–563 (2000)

Rakoczy, R., Przybył, A., Kordas, M., Konopacki, M., Drozd, R., Fijałkowski, K.: The study of influence of a rotating magnetic field on mixing efficiency. Chem Eng. Process. Process Intensification **112**, 1–8 (2017)

Richter, Ł., Janczuk-Richter, M., Niedziółka-Jönsson, J., Paczesny, J., Hołyst, R.: Recent advances in bacteriophage-based methods for bacteria detection. Drug Discov. Today Technol. **23**(2), 448–455 (2018)

Sargeant, K., Yeo, R.G., Lethbridge, J.H., Shooter, K.V.: Production of Bacteriophage T7. Appl. Microbiol. **16**(10), 1483–1488 (1968)

Sauvageau, D., Cooper, D.G.: Two-stage, self-cycling process for the production of bacteriophages. Microb. Cell Fact. **9**, 81 (2010)

Skurnik, M., Strauch, E.: Phage therapy: facts and fiction. Int. J. Med. Microb. **296**, 5–14 (2006)

Struk, M., Grygorcewicz, B., Nawrotek, P., Augustyniak, A., Konopacki, M., Kordas, M., Rakoczy, R.: Enhancing effect of 50 Hz rotating magnetic field on induction of Shiga toxin-converting lambdoid prophages. Microb. Pathog. **109**, 4–7 (2017)

Twort, F.W., L.R.C.P. Lond., M.R.C.S.: An investigation on the nature of ultra-microscopic viruses. Bacteriophage **1**(3), 127–129 (2011)

Wang, Z., Liu, X., Ni, S.Q., Zhang, J., Zhang, X., Ahmad, H.A., Gao, B.: Weak magnetic field: a powerful strategy to enhance partial nitrification. Water Res. **120**, 190–198 (2017)

Warner, C.M., Barker, N., Lee, S.W., Perkins, E.J.: M13 bacteriophage production for large-scale applications. Bioprocess Biosyst. Eng. **37**, 2067–2072 (2014)

Weber-Dabrowska, B., Jonczyk-Matysiak, E., Zaczek, M., Łobocka, M., Łusiak-Szelachowska, M., Górski, A.: Bacteriophage procurement for therapeutic purposes. Front. Microb. **7**, 1177 (2016)

Zarasvand, K.A., Rai, V.R.: Microorganisms: induction and inhibition of corrosion in met-als. Int. Biodeterior. Biodegr. **87**, 66–74 (2014)

Multiphase Pressure Swirl Atomizers for Agricultural Applications

Andżelika Krupińska[1(✉)], Marek Ochowiak[1], Sylwia Włodarczak[1], Małgorzata Markowska[1], Magdalena Matuszak[1], and Tomasz Szulc[2]

[1] Institute of Chemical Technology and Engineering, Poznan University of Technology, Poznan, Poland
andzelika.krupinska@doctorate.put.poznan.pl
[2] Łukasiewicz Research Network - Industrial Institute of Agricultural Engineering, Poznan, Poland

Abstract. In order to obtain abundant crops of satisfactory quality, it is necessary to apply liquid chemicals during agrotechnical procedures. It is important to target the treatment for a specific purpose and reduce the losses of applied chemicals. The aim of a precise protection technique is to provide the active substance in the proper place, in sufficient quantity and in the appropriate form. One of the approaches to modify the physicochemical properties of plant protection products is the addition of small amounts of polymers. The efficiency and safety of spraying process is determined by properly selected atomizers. In the agriculture section on spatial cultivation and vegetables, vortex atomizers are usually used in the spraying process. Two new constructions of two-phase atomizers with a swirl flow and the experimental results on the spraying of aqueous solutions of sodium carboxymethylcellulose with various concentrations were shown in this chapter. The obtained results were compared with the data obtained when spraying water. The addition of polymer allows to obtain a much larger number of droplets with large diameters and reduces the share of the smallest sized droplets. As the concentration of polymer increased, larger diameter droplets were obtained and the spray angle was reduced. The obtained results confirm the application possibility of the developed constructions in the agriculture area.

1 Introduction

Chemical substances and mixtures are widely present and used in agriculture. Their application is aimed at combating unwanted organisms, stimulating plant resistance to pathogens, and broadly understood protection against the influence of destructive factors. During all agrotechnical treatments, the most abundant crops of highest quality are strived (Grausz 2015; Li et al. 2019). An important aspect that must necessarily be considered is the issue of minimizing risks to people and environment associated with the use of plant protection products. In connection with the regulations (Rozporządzenie Ministra Rolnictwa i Rozwoju Wsi z dnia 18 kwietnia 2013 r. w sprawie wymagań integrowanej ochrony roślin (Dz.U. z 2013 r. poz. 505)) the concept of integrated plant protection was introduced. The priority of this approach is undertaking

© Springer Nature Switzerland AG 2020
M. Ochowiak et al. (Eds.): PAIC 2019, *Practical Aspects of Chemical Engineering*, pp. 183–190, 2020.
https://doi.org/10.1007/978-3-030-39867-5_19

actions in accordance with the concept of sustainable development. The correct implementation of the procedure will allow achieving the intended efficiency, while maintaining ecological and economic considerations. By the modification of the composition of solution to be sprayed, the effectiveness of spraying can be improved. The addition of small amounts of polymers may contribute to improving the properties of solution (Mun et al. 1998; Harrison et al. 1999). The main aim is to minimize the formation of droplets of smallest diameters during the spraying process. Small droplets are susceptible to drift by wind, which results in adverse effects on the surrounding environment (Hermansky and Krause 1997). The other research purpose is to increase the stabilization of herbicides in the solution and to reduce the surface tension (Harrison et al. 1999). Harrison and Mun explain the effect of polymer addition primarily as extensional viscosity modifier, which results in the reduction of droplet decay and hindering of satellite droplet formation.

In the agriculture section on spatial cultivation and vegetables, vortex atomizers are usually used in the spraying process. It is necessary to obtain an aerosol of appropriate quality. In order to protect the cultivated plant efficiently, aerosol droplets of certain size and coverage uniformity should be formed. Modification of classic constructions, widely known and described vortex atomizers, by changing the swirl chamber geometry and introduction of second gas phase, allows for smaller droplets' sizes with a more monodisperse size distribution (Ochowiak et al. 2018).

2 Sodium Carboxymethylcellulose

Sodium carboxymethylcellulose (Na-CMC) is water soluble, etherified cellulose salt. It is formed as a result of the reaction of alkali cellulose with sodium chloroacetate (Kukrety et al. 2018).

Sodium carboxymethylcellulose has a hydrophilic nature, satisfactory film-forming properties and high viscosity. It is a white or grayish granular powder, tasteless, odorless. It is widely used in many industry branches, including as thickening agent, but also as a filler, dietary fiber, anti-caking agent, component of varnishes, dyes and emulsifier. It is also used as a modifier in solutions of substances applied for plant protection (Kukrety et al. 2018).

3 Two-Phase Atomizers with a Swirled Flow

Among all types of atomizers, there is still growing interest in swirl atomizers and their variations. They show a number of features that promote them among other constructions. They stand out, among others:

- durability and reliability,
- simple construction,
- stability,
- energy efficiency,

- high quality of the obtained spray,
- decent price (Lefebvre 2000; Wimmer and Brenn 2013).

They are used during drying, painting, humidifying, burning, cooling or plant protection (Moon et al. 2009; Liu et al. 2019). During agrotechnical operations, mainly swirl atomizers with a full cone are applied (Halder et al. 2004).

The swirl atomizers consist of three main elements: tangential inlet ports, swirl chamber and outlet port. For spraying, they use the energy of liquid itself, which is spent to form a swirl inside the atomizer. The generated swirl supports the air core inside the chamber. Stability of the gas core (constant shape and height) is one of the most important distinguishing features of swirl atomizers. The liquid rotates inside the swirl chamber as a result of centrifugal force. The peripheral velocity of liquid flow increases as soon as it passes the outlet port. The centrifugal force also increases. The thin layer of liquid film closes the outlet port and breaks into droplets (Rashad et al. 2016). A core of air is formed along the atomizer axis. The outlet port is then filled with liquid only on the circumference and its center is filled with air. The proper use of the swirl motion of liquid stream is one of the ways to improve the spraying process and its optimization (Włodarczak 2016).

Due to many advantages, there is a growing interest in the two-phase spraying technique that uses the phenomenon of swirl motion. Two-phase atomizers have low sensitivity to the rheological properties of sprayed liquid, with a wide range of liquid flow rates, which ensures good spraying (Sovani et al. 2001). They allow to obtain small droplets while maintaining high operational reliability and efficiency (Ramamurthi et al. 2009; Wimmer and Brenn 2013). Substantial saving of liquid can be observed, and the process itself is more controlled, which results from the use of additional gas stream.

An important issue in the two-phase spraying process is the atomizer construction, the modification of which can significantly affect the parameters of sprayed stream (Lefebvre 1989; Rashad et al. 2016; Ochowiak et al. 2017). The most important geometric invariants are:

- $H_S/D_{S,}$
- h_0/d_0,
- D_S/d_0,

where: H_S – height of swirl chamber, D_S – diameter of swirl chamber, h_0 – height of outlet port, d_0 – diameter of outlet port (Rashad et al. 2016). In their works, Eltkob (1978) and Rashad (2016) show that there is a value of H_S/D_S ratio at which the most favorable parameters of sprayed stream are obtained. In the publication (Rashad et al. 2016) it was shown that this value is 3.75. For the H_S/D_S range from 1.25 to 3.75, the spray angle was independent of this geometric invariant, while a decreasing trend was observed in the range from 3.75 to 5. This can be explained by the correlation of further increase of swirl chamber height with simultaneous increase in energy losses. Similar observations concerned the value of average droplet diameter. For H_S/D_S the *SMD* value was practically constant up to 3.75, however, after exceeding this point, this value increased rapidly. The explanation of this phenomenon also includes the aspect of energy losses occurring with increasing the height of swirl chamber above the

optimal value. Energy losses arise due to the large interaction between the liquid elements and the swirl chamber wall, which permanently reduces the liquid angular momentum. As a result, the diameter of the air core decreases and the thickness of liquid layer inside the swirl chamber increases, so that the *SMD* increases. Eltkob (1978) determined the value of H_S/D_S ratio of 2.75 as a critical one. Ochowiak et al. (2018) showed that with H_S/D_S higher than 3 a rapid increase in *SMD* was observed. The spraying process is also influenced by the properties and parameters of the sprayed liquid. The most important liquid properties are: density, surface tension and viscosity.

The work of two-phase atomizer with a swirled stream is best described by such parameters of the sprayed stream as: discharge coefficient, spray angle, volume-surface average droplet diameter (Sauter diameter) and liquid distribution in sprayed stream. These data are useful when designing this type of atomizers. There are many correlation equations in the literature describing the basic quantities characterizing the spraying process, combining the construction of atomizer, spraying liquid properties and operational parameters (Włodarczak 2016; Rashad et al. 2016; Ochowiak et al. 2018). However, they take into account a limited number of input variables and pertain to a specific constructional solution. Due to this fact, it seems reasonable to conduct research aimed at proposing a new model and correlation equations allowing design and more precise selection of such construction type. It will also allow to extend the knowledge about the phenomenon of two-phase spraying, the principles of operation of two-phase atomizers with a swirl flow and the mechanism of aerosol formation.

To determine the spray quality, the spray angle and to examine the nature of resulting stream, the experimental set-up consisting of the following elements was used:

- liquid tank with a rotameter and valves enabling controlled regulation of the flow rate of tested liquid,
- compressor and rotameter for determining gas flow,
- tested atomizer placed on the crane traveling along the designated track,
- measuring system - Spraytec optical unit (i.e. particle size analyzer) and a computer with the appropriate Spraytec software.

The experiments were carried out at a constant temperature $T = 20 \pm 1$ °C, in the range of air flow rates not exceeding $6.94 \cdot 10^{-4}$ m^3/s and in the range of solution flow rates not exceeding $6.94 \cdot 10^{-5}$ m^3/s. The influence of atomizer constructions with a swirl motion, operational parameters, liquid properties on the spray angle, volumetric values as well as radial distributions of droplet diameter and mean Sauter diameter were determined. The considered atomizers differed in the dimensions of mixing chamber. A simplified atomizer scheme was shown in Fig. 1. Detailed dimensions of tested atomizers were presented in the publication (Ochowiak et al. 2018). The model liquids were water and aqueous solutions of sodium carboxymethyl cellulose of various concentrations. The rheological properties of considered Na-CMC solutions were described using the Ostwald-de Waele power model:

$$\tau = k \cdot \dot{\gamma}^n \tag{1}$$

The values of characteristic flow index n, consistency factor k, density and surface tension for individual concentrations of aqueous solutions of Na-CMC were presented in Table 1.

Table 1. Rheological parameters of the Ostwald-de Waele power model.

Solution	k [Pa·s]	n [-]	σ [N/m]	ρ [kg/m^3]
0.05% Na-CMC (aq)	0.0053	0.91	71.9	999.8
0.1% Na-CMC (aq)	0.0134	0.85	71.5	999.8
0.2% Na-CMC (aq)	0.0486	0.77	70.9	999.6

The concept of spray angle and its significance were described, among others, in the work of Rashad et al. (2016). The tangens of half spray angle can be determined by the tangential and axial velocity ratio. Knowledge of the spray angle is essential, e.g. when designing gas turbine combustors. Ochowiak (2014) defines the spray angle as the tip angle of droplets stream, which together with coverage characterizes its external shape. Figure 1 presents the obtained values of spray angle as a function of different applied constructions and the sprayed liquid properties.

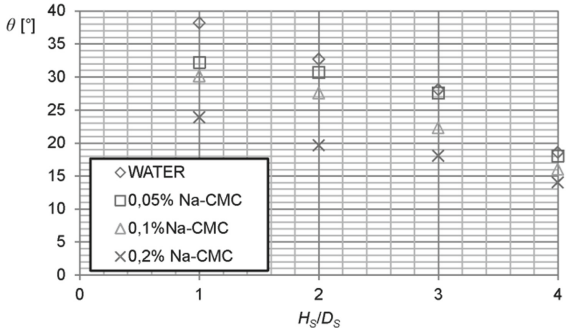

Fig. 1. The dependence of the spray angle on the construction geometry for solution with different concentration

It can be noticed that as the concentration of Na-CMC and the H_S/D_S ratio are increased, spray angles are getting smaller. Furthermore, the spray angle increases as the flow of liquid and gas increases. This observation is consistent with literature reports (Harrison et al. 1999; Rashad et al. 2016). Rizk and Lefebvre also showed an inverse relationship between the spray angle and the viscosity of liquid (Rizk and Lefebvre 1987). Dafsari et al. (2019) explained the decrease of the spray angle as the liquid viscosity increases through the increase in energy losses and the reduction of the liquid angular momentum.

Figure 2 shows the volumetric distribution of diameters of droplets obtained for an exemplary atomizer with the same operating parameters for different liquids. By juxtaposing the obtained results, it can be noticed that the addition of polymer results in the reduction in the number of small droplets formed and the formation of higher number of droplets with large diameters. This is a desirable effect in the case of application of these atomizers in agriculture.

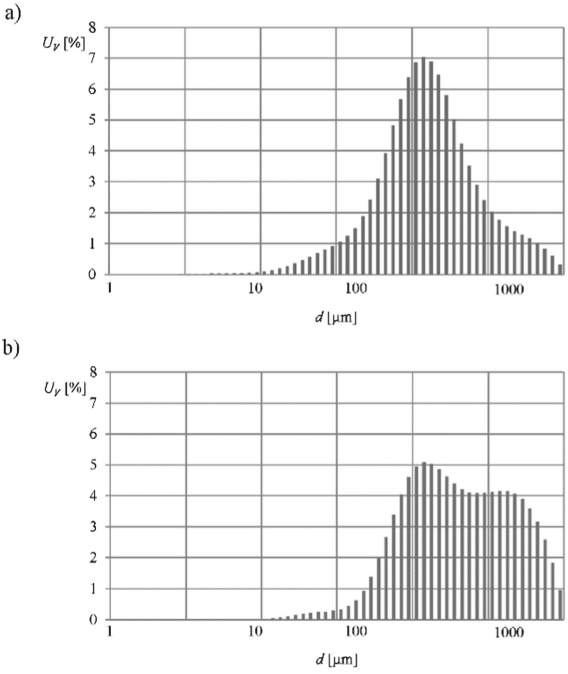

Fig. 2. Exemplary droplet size distribution for CSA1 atomizer at volumetric flow rate of gas $\dot{V}_G = 1.94 \cdot 10^{-4} \frac{m^3}{s}$ and liquid $\dot{V}_L = 8.33 \cdot 10^{-6} \frac{m^3}{s}$: (a) water (b) 0.2% Na-CMC solution

The addition of polymer also changes the value of average diameters of obtained droplets and the nature of stream. The higher Na-CMC concentration in the solution, the larger droplets formed during the spraying process. Lefebvre (1998) and Rashad et al. (2016) correlated the value of obtained average droplet diameter with the properties of sprayed liquid and the operational process parameters. The higher the viscosity, the liquid surface tension and the liquid mass flow rate, the larger the average droplet diameter (Lefebvre 1998; Rashad et al. 2016). For the highest Na-CMC concentration used during the experiments, the nature of stream was changed as well, a larger polydispersity was observed. Aerosols obtained with analyzed atomizers for water and lower concentrations of sodium carboxymethyl cellulose have a monodisperse nature. The above trends were showed in Fig. 3.

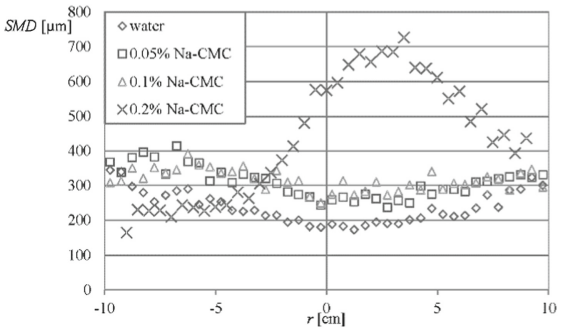

Fig. 3. Average droplet size distribution in the liquid stream at volumetric flow rate of gas $\dot{V}_G = 1.94 \cdot 10^{-4} \frac{m^3}{s}$ and liquid $\dot{V}_L = 8.33 \cdot 10^{-6} \frac{m^3}{s}$ for CSA2 atomizer

4 Summary

Agriculture is the area of economy characterized by the receptivity of modern technologies. The development of plant protection through the use of efficient spraying results in an increase in the amount of crops obtained, a reduction in costs, while respecting environmental protection requirements. Improvement of the spraying process allows for more precise dosing of liquid fertilizers, which results in their lower consumption. This fact subsequently influences a reduction in fertilization costs and contributes to a reduction in the amount of fertilizer entering the environment.

This chapter presents the construction solutions for two-phase atomizers with a swirl flow that can be used in agriculture to improve the spraying process for spatial crops. On the basis of the determined values of individual parameters and their trends, it is possible to create correlation equations, which will enable optimal design and selection of atomizers for specific application.

Acknowledgments. This research was supported by Ministry of Science and Higher Education through grant PUT 03/32/SBAD/0921.

References

Dafsari, R.A., Lee, H.J., Han, J., Park, D.C., Lee, J.: Viscosity effect on the pressure swirl atomization of an alternative aviation. Fuel **240**, 179–191 (2019)

Eltkob, M.M., Rafat, N.M., Hanna, M.A.: The influence of swirl atomizer geometry on the atomization performance. In: Proceedings of the 1st International Conference on Liquid Atomization and Spray Systems, pp. 109–115 (1978)

Grausz, T.W.: Chemia dla rolników poradnik BHP. Państwowa Inspekcja Pracy Główny Inspektorat Pracy, Warszawa (2015). in Polish

Halder, M.R., Dash, S.H., Som, S.K.: A numerical and experimental investigation on the coefficients of discharge and the spray cone angle of a solid cone swirl nozzle. Int. J. Therm. Sci. **28**, 297–305 (2004)

Harrison, G.M., Mun, R., Cooper, G., Boger, D.V.: A note on the effect of polymer rigidity and concentration on spray atomisation. J. Non-Newtonian Fluid Mech. **85**, 93–104 (1999)
Hermansky, C.G., Krause, G.F.: Relevant physical property measurement for adjuvants. In: Proceedings 4th International Conference, pp. 20–22 (1997)
Kukrety, A., Singh, R.J., Singh, P., Ray, S.S.: Comprehension on the synthesis of Carboxymethyl-cellulose (CMC) utilizing various cellulose rich waste biomass resources. Waste Biomass Valori. **9**, 1587–1595 (2018)
Lefebvre, A.H.: Atomization and Sprays. Hemisphere, New York (1989)
Lefebvre, A.H.: Gas Turbine Combustion. CRC Press, Taylor and Francis, Philadelphia (1998)
Lefebvre, A.H.: Fifty years of gas turbine fuel injection. Atom. Sprays **102**, 251–276 (2000)
Li, J., Huang, Q., Liu, B.: A pest control model with birth pulse and residual and delay effects of pesticides. Adv. Differ. Equ. 117 (2019, in print)
Liu, C., Liu, F., Yang, J., Mu, Y., Hu, C.: Experimental investigations of spray generated by a pressure swirl atomizer. J. Energy Inst. **92**, 210–221 (2019)
Moon, S., Abo-Serie, E., Bae, Ch.: Air flow and pressure inside a pressure-swirl spray and their effects on spray development. Exp. Thermal Fluid Sci. **33**, 222–231 (2009)
Mun, R.: The effects of polymer concentration and molecular weight on the breakup of laminar capillary jets. J. Non Newtonian Fluid Mech. **74**, 285–297 (1998)
Ochowiak, M.: Analiza procesu rozpylania cieczy w rozpylaczach pęcherzykowych i pęcherzykowo- wirowych. Wydawnictwo Politechniki Poznańskiej, Poznań (2014). in Polish
Ochowiak, M., Krupińska, A., Włodarczak, S., Matuszak, M., Szulc, T.: The studies of the two-phase flow for conical pressure-swirl atomizers. Chem. Eng. Equip. **56**(6), 215–216 (2017)
Ochowiak, M., Lytvynenko, O., Włodarczak, S., Matuszak, M., Krupińska, A.: Design and study of conical pressure-swirl atomizers. design, simulation, manufacturing: the innovation exchange In: DSMIE 2018: Advances in Design, Simulation and Manufacturing, pp. 472–480 (2018)
Ramamurthi, K., Sarkar, L.K., Raghunandan, B.N.: Performance characteristics of effervescent atomizer in different flow regimes. Atom. Sprays **19**, 41–56 (2009)
Rashad, M., Yong, H., Zekun, Z.: Effect of geometric parameters on spray characteristics of pressure swirl atomizers. Int. J. Hydrog. Energy **41**, 15790–15799 (2016)
Rizk, N.K., Lefebvre, A.H.: Prediction of velocity coefficient and spray cone angle for simplex swirl atomizers. Int. J. Turbo Jet Engines **4**, 65–74 (1987)
Rozporządzenie Ministra Rolnictwa i Rozwoju Wsi z dnia 18 kwietnia 2013 r. w sprawie wymagań integrowanej ochrony roślin (Dz.U. z 2013 r. poz. 505). in Polish
Sovani, S.D., Sojka, P.E., Lefebvre, A.H.: Effervescent atomization. Prog. Energy Comb. Sci. **27**, 483–521 (2001)
Wimmer, E., Brenn, G.: Viscous flow through the swirl chamber of a pressure-swirl atomizer. Int. J. Multiphase Flow **53**, 100–113 (2013)
Włodarczak, S.: Analiza hydrodynamiki w rozpylaczach wirowych. Rozprawa doktorska, Poznań (2016). in Polish

Modified Moving Bed Method for Treatment of Wastewater Originating from the Pharmaceutical Industry

Izabela Kruszelnicka[1(✉)], Dobrochna Ginter-Kramarczyk[1], Michał Michalkiewicz[1], Stanisław Zajchowski[2], Jolanta Tomaszewska[2], and Przemysław Muszyński[1]

[1] Institute of Environmental Engineering and Building Installations, Poznan University of Technology, Poznan, Poland
{izabela.kruszelnicka, dobrochna.ginter-kramarczyk, michal.michalkiewicz, przemyslaw.muszynski}@put.poznan.pl
[2] Faculty of Chemical Technology and Engineering, BydgoszczUniversity of Technology and Life Sciences, Bydgoszcz, Poland
{stanislaw.zajchowski, jolanta.tomaszowska}@utp.edu.pl

Abstract. The chapter presents the information about composite materials, which due to their properties, can be used as fill/carrier in the technology of wastewater treatment using a bed biofilm reactor MBBR (Moving Bed Biofilm Reactor). In this work the susceptibility of surface of carriers made from the wood-polymer composites (WPC) to the formation of biofilm in the wastewater treatment process was investigated. Based on the carried out analyses, it was found that the use of fittings consisting of wood polymer composite as a carrier allow for the concentration of microorganisms in the bioreactor.

1 Introduction

The scale of production of pharmaceutical compounds, including non-steroidal anti-inflammatory drugs, is becoming an increasingly notable environmental issue. Inefficient removal of pharmaceutical compounds during wastewater treatment processes results in the pollution of surface water, which is the primary source of drinking water. The increase in the production of drugs is influenced by factors such as aging of the population, increase of the population's income, increase of the incidence of civilization and chronic diseases as well as a change in public awareness of health issues (Koszowska et al. 2015; Tang et al. 2015; Wydro et al. 2016).

In English-language literature, the term *Pharmaceuticals and Personal Care Products* (PPCPs) encompasses a number of biologically active compounds. PPCPs are a group of bioactive chemical compounds used in medicine, veterinary medicine and breeding farms. This group includes drugs used in case of both humans and animals, active substances used in medicine and pharmaceuticals, food supplements and nutrients as well as all types of cosmetics. These are compounds with various

© Springer Nature Switzerland AG 2020
M. Ochowiak et al. (Eds.): PAIC 2019, *Practical Aspects of Chemical Engineering*, pp. 191–198, 2020.
https://doi.org/10.1007/978-3-030-39867-5_20

physicochemical properties, often characterized by a complex structure, which significantly hinders their identification and removal from the environment (Donlan 2002; Kruszelnicka and Ginter-Kramarczyk 2017).

Modified MBBR technology can be an alternative to traditional methods of pharmaceutical wastewater treatment. The MBBR (Moving Bed Biofilm Reactor) technology was first developed by Professor Hallvard Ødegaard of the Norwegian University of Science and Technology. A biological membrane composed of microorganisms develops on the surface of the moving bed. Wastewater is delivered at a fixed, controlled flow rate to the bed and contact between the organic compounds contained in the wastewater, microorganisms and other organisms immediately occurs. Living organisms absorb and consume the dissolved organic compounds for their life processes, and their mass increases as a result (Koszowska et al. 2015), Flemming et al. (2016) and Torresi et al. (2017) (Fig. 1).

Chemical compounds are retained on the surface of the biological membrane layer. As a result, the biofilm acts as a semi-selectively permeable biological membrane. Atmospheric oxygen plays an important role because it penetrates the biofilm layer and intensifies the processes of biological decomposition carried out by settled microorganisms in the outer part, called the aerobic layer. An anaerobic layer forms in the inner part, where substances are decomposed in the framework of anaerobic processes. Colonization of various surfaces by microorganisms is possible due to their adhesive properties, and the structure of the produced biofilm is stabilized by extracellular secreted polymeric substances, called EPS (Fig. 1). The biofilm is formed by complex multicellular structures in which numerous microbial cells surround the mucus layer. Cells of microorganisms which build the biofilm specialize in performing various functions in enzymatic processes and exhibit different characteristics than those living separately in the form of free cells. The design of such clusters protects microorganisms against the adverse effects of external factors, and microorganisms in the biofilm are much more resistant to changes of pH and temperature, which is why the biofilm can function under conditions which would be difficult and in many cases even impossible to survive by individual cells (Donlan 2002; Flemming and Wingender 2010; Kołwzan 2011; Łaskawiec 2015).

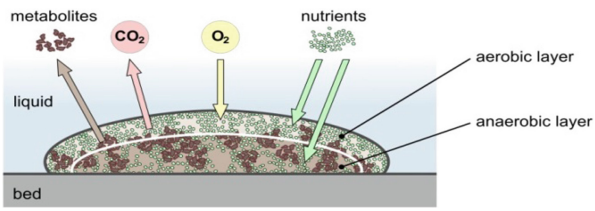

Fig. 1. Structure of the biofilm (Tang et al. 2015).

The type of filling used has a significant impact on the treatment efficiency. Most often it consists of a selected natural or artificial material. Synthetic fillings includes various loose fittings or blocks from polystyrene, polyvinyl chloride, polyamide, polypropylene, polyethylene, etc. Synthetic deposits possess a specific surface in the range of up to 2000 m^2/m^3. This type of filling ensures better flow and even distribution of wastewater when using lower loads and prevents the clogging of pores in case higher loads. Currently, carriers of various shapes and sizes are used. In each case, they should be designed to provide a large protected surface in order to create optimal conditions for growth and maintain proper biological membrane activity. The use of polymer composites with natural fillers (mainly WPC-Wood Polymer Composites) as carriers in MBBR technology is an interesting option with can be successfully used for removal of pharmaceuticals, primarily due to the large active surface available for development biological membrane. Due to economic factors, i.e. increasing prices of raw materials for the production of polymers (oil and gas) as well as a very high demand for these materials, the composite materials based on the polymer matrix find applications in an increasing number of industries. The dynamic development of the production of polymer-wood composites results, among others, from the good combination of properties of polymer components and natural additives. Ecological considerations play an additional role since defective and post-use wood can be used to produce WPC (Kruszelnicka et al. 2014a, b; Kruszelnicka et al. 2018a, b).

2 Research Methodology

Studies focused on the assessment of the removal efficiency of a non-steroidal anti-inflammatory drug (NSAID), diclofenac, were carried out in a reactor filled with carriers (Fig. 2) which consisted of a polymer-wood composite. The matrix was polyethylene. A scheme of a 12-L research reactor was presented in Fig. 3.

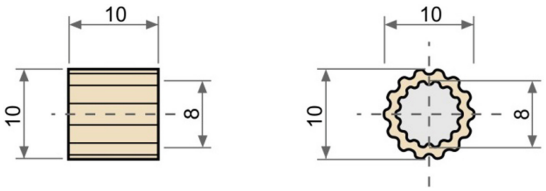

Fig. 2. Scheme of the biological membrane carrier.

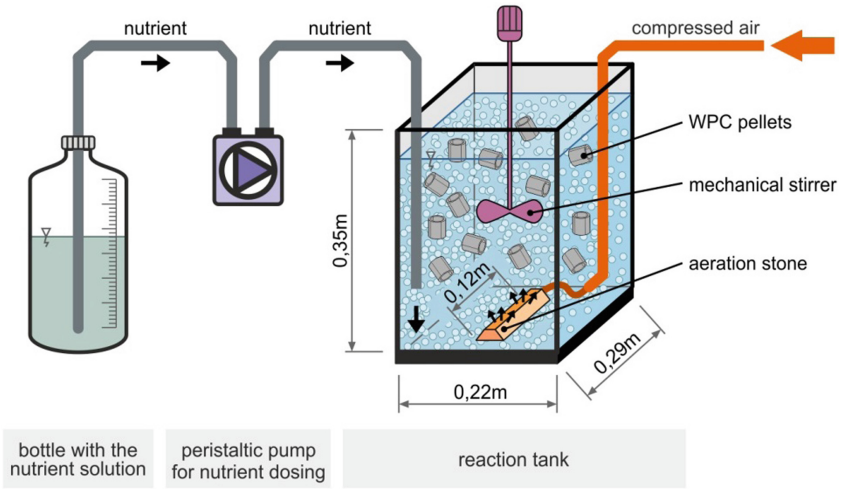

Fig. 3. Scheme of the research reactor.

Coniferous flour under the trade name Lignocel type C120 with particle sizes in the range of 70–150 μm was used as the filler. The laboratory experiment was divided into 2 stages; bed working time and pharmaceutical dosage period. A nutrient solution was dosed during the preparation of the bed as described in Table 1.

Table 1. Composition of the dosed nutrient solution.

Compound name	Dose [g/2L] bed preparation time	Dose [g/2L] diclofenac dosing period
Casein peptone	22,0	16,0
Meat extract	22,0	16,0
Urea	6,0	5,4
NaCl	2,2	2,2
K_2HPO_4	5,6	5,2
Glucose	37,0	18,0

The nutrient solution was prepared in a concentrated form and then diluted. A the end of the working period, an appropriate concentration of diclofenac was added to the system. The dilution was of the pharmaceutical compounds was equal to 1 mg/L, 5 mg/L, 10 mg/L, respectively. The value of pH was an additional parameter that was artificially set in the reactor. The experiments were carried out at pH equal to: 7.0, 6.5 and 6.0. (Table 2). Microscopic analysis was performed using a Carl Zeiss Jena optical microscope with 12.5× eyepiece, 5× and 10× lens and 1.5× tube at 93.75× and/or 187.5× magnification.

Table 2. Diclofenac dosing schedule.

Series	Diclofenac concentration [mg/L]	Level of imposed pH
I	1	–
I	5	–
I	10	–
II	1	7,5
II	5	7,5
II	10	7,5
III	1	6,5
III	5	6,5
III	10	6,5
IV	1	6,0
IV	5	6,0
IV	10	6,0
V	1	–
V	5	–
V	10	–

3 Results

Microbiological analysis showed that there was a change in the quality and quantity of microorganisms present in the system as a result of dosing the pharmaceutical compound. A high variety of microorganisms was achieved in the WPC reactor. In the activated sludge originating from the MBBR reactor, it was observed that the testate amoebae *Arcella sp.* classified as amoebic shell was the most common bacterium. Her presence confirmed the proper course of the nitrification process. *Rotaria rotatora* rotifer was another group of organisms. The presence of rotifers and nematodes indicates a long age of the sludge. In the sediment there were also microorganisms such as: *Vorticella convallaria*, *Carchesium polypinum* and *Colpidium colpoda*. The presence

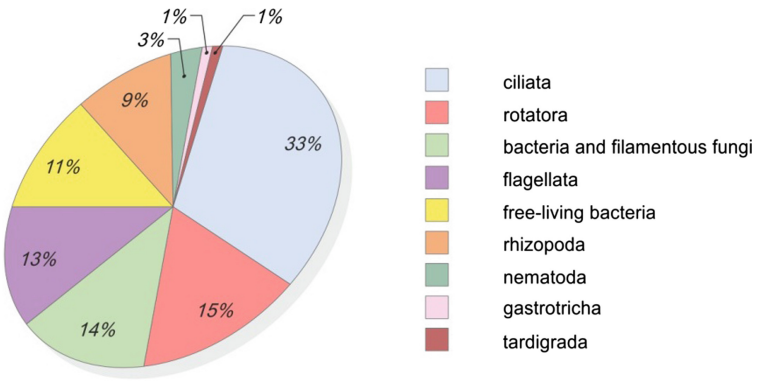

Fig. 4. Percentage distribution of bacteria occurring during the diclofenac dosing period.

of the first of these bacteria may indicate the correct concentration of dissolved oxygen in the reactor. An interesting observation is that at the time of diclofenac dosing (for the first fourteen days), flagellates were very numerous, among them the *Bodo sp.* microorganism (Fig. 4).

The studies have confirmed that the extent of diclofenac removal strongly depends on the concentration of hydrogen ions. Analysis of the graph (Fig. 5) allows to observe that the decrease of pH in the system contributes to an increase of the treatment efficiency of the test substance. The most significant changes were observed on days 50 to 62.

The chemical oxygen demand value was determined using the dichromate method throughout the diclofenac dosing period (Fig. 6). The COD level was very low throughout the entire cycle. The COD of medium with diclofenac at 10 mg/L was equal to 775 mg/L on the average. The lowest COD value was recorded on day 70 of the experiment, which was equal to 0.70 mg/L.

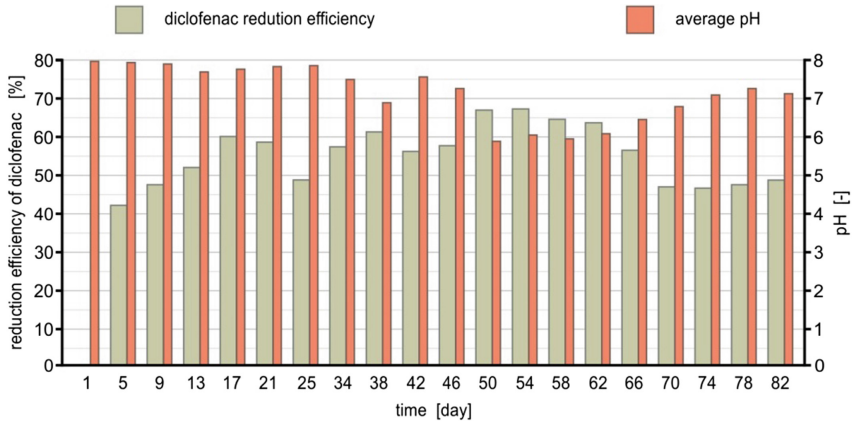

Fig. 5. The pH level in the reactor during the diclofenac dosing period.

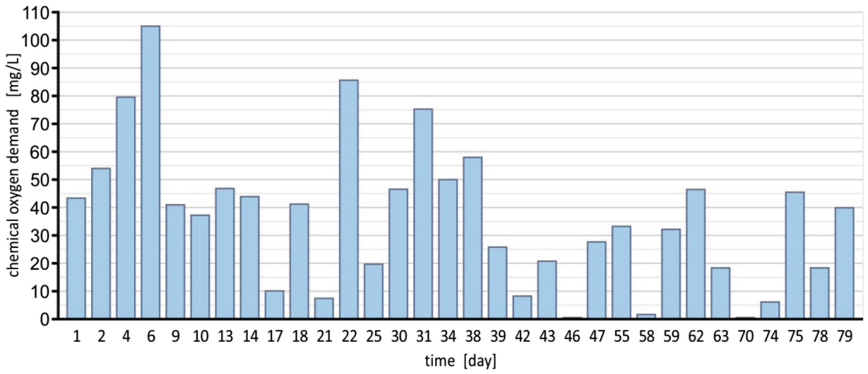

Fig. 6. Chemical oxygen demand value.

Low values of chemical oxygen demand indicate a very good distribution of organic compounds present in the medium, primarily the test substance – diclofenac.

4 Summary

The aim of the studies was to check and determine whether polymer-wood composites can find application as materials for the production of components used in a moving bed for the treatment of sewage containing diclofenac. Based on the carried out analyses, it was found that the use of fittings consisting of wood polymer composite as a carrier allow for the concentration of microorganisms in the bioreactor. In addition, due to the well-developed active surface of the carrier, the susceptibility of living organisms to adverse environmental conditions is reduced.

Acknowledgments. The studies were carried out as part of the Ministry of Science and Higher Education project no. 01/13DS-PB 0891/2018.

References

Donlan, R.M.: Biofilms: microbial life on surfaces. Emerg. Infect. Dis. **8**, 881–890 (2002)

Flemming, H.C., Wingender, J.: The biofilm matrix. Nat. Rev. Microbiol. **8**, 623–633 (2010)

Flemming, H.C., Wingender, J., Szewzyk, U., Steinberg, P., Rice, S.A., Kjelleberg, S.: Biofilms: an emergent form of bacterial life. Nat. Rev. Microbiol. **14**, 563–575 (2016)

Kołwzan, B.: Analiza zjawiska biofilmu – warunki jego powstania i funkcjonowania. Ochrona Środowiska **4**, 3–14 (2011)

Koszowska, A., Ebisz, M., Krzyśko–Łupicka, T.: Obecność farmaceutyków i środków kosmetycznych w środowisku wodnym jako nowy problem zdrowia środowiskowego. Env. Med. **18**(1), 62–69 (2015)

Kruszelnicka, I., Ginter–Kramarczyk, D.: Nowe nośniki w technologii złoża ruchomego. III Konferencja Przedsiębiorstw Wodociągowo – Komunalnych Miast i Wsi (2017)

Kruszelnicka, I., Ginter-Kramarczyk, D., Michałkiewicz, M., Kloziński, A., Zajchowski, S., Jakubowska, P., Tomaszewska, J.: Kompozyty polimerowo-drzewne w technologii zawieszonego złoża ruchomego. Polimery **10**, 739–746 (2014a)

Kruszelnicka, I., Ginter-Kramarczyk, D., Michałkiewicz, M., Zajchowski, S., Kloziński, A., Tomaszewska, J.: The use of wood-polymer composites in a moving bed biofilm reactor technology. Polimery **5**, 423–426 (2014b)

Kruszelnicka, I., Ginter-Kramarczyk, D., Poszwa, P., Stręk, T.: Influence of MBBR carriers' geometry on its flow characteristics. Chem. Eng. Process. Process Intensif. **130**, 134–139 (2018a)

Kruszelnicka, I., Ginter-Kramarczyk, D., Rudawska, A., Michałkiewicz, M., Zajchowski, S., Tomaszewska, J.: Wpływ zwilżalności powierzchni kompozytów polimerowo-drzewnych na tworzenie biofilmu w procesach oczyszczania ścieków. Polimery **9**, 619–625 (2018b)

Łaskawiec, E.: Biofilm - an instrument for wastewater treatment technology. Edukacja biologiczna i Środowiskowa **1**, 20–26 (2015)

Tang, K., Ooi, G., Litty, K., Sundmark, K., Kaarsholm, K., Sund, C., Kragelund, C., Christensson, M., Bester, K., Andersen, H.: Removal of pharmaceuticals in conventionally treated wastewater by a polishing moving bed biofilm reactor (MBBR) with intermittent feeding. Bioresour. Technol. **236**, 77–86 (2015)

Torresi, E., Plósz, B., Christensson, M., Smets, B.: Removal of micropollutants in moving bed biofilm reactors (MBBRs). Technical University of Denmark (2017)

Wydro, U., Wołejka, E., Struk–Sokołowska, J., Puchlik, M.: Pozostałości farmaceutyków w środowisku wodnym oraz możliwości ich usuwania. Interdyscyplinarne zagadnienia w inżynierii i Ochronie Środowiska, pp. 286–299 (2016)

Homogenization of O/W Emulsions Using Dynamic Membranes

Adrianna Kuczora and Jacek Różański(✉)

Institute of Chemical Technology and Engineering,
Poznan University of Technology, Poznań, Poland
jacek.rozanski@put.poznan.pl

Abstract. The paper discusses different methods of formulating emulsions, and presents a structural solution employed in the design and construction of an experimental stand for the formulation of emulsions based on the method of premix membrane emulsification. The main element of the designed stand was a pressure tank suitable for the formulation of a premix which was then forced through a membrane. The designed experimental stand can be used for the formulation of emulsions using both conventional and dynamic membranes (packed bed of spherical microparticles). Tests of the stand showed that it was suitable for formulating emulsions with droplet diameters approximately 70% smaller than the original emulsion.

1 Methods of Emulsion Formulation

An emulsion is a system consisting of two immiscible liquids. One liquid (the dispersed phase) is dispersed in the other (the continuous phase). The third necessary component of an emulsion is an emulsifier which, in addition to reducing interfacial tension and facilitating the formation of the developed interfacial surface, stabilizes the emulsion by preventing droplets from coalescing (Alvarado and Marsden 1979). Simple emulsions can be divided into two types: oil-in-water (O/W) and water-in-oil (W/O). Phase "W" is usually water or an aqueous solution, while phase "O", regardless of its chemical nature and composition, is typically referred to as oil (Zieliński 2017).

Emulsions can be formulated in several different ways. The most commonly used methods are based on various types of homogenizers (rotor-stator, pressure, ultrasonic types), colloid mills, and mixers (Fig. 1). The choice of formulation method depends primarily on emulsion viscosity and changes in the viscosity of emulsions that may occur during their homogenization.

Other factors that should be considered when choosing a method for formulating emulsions include their thermal sensitivity and the potential need to pump the final product (Fellows 2017). Using high-speed mixers, it is possible to obtain emulsions with droplet diameters ranging from 2 to 10 μm. Colloid mills operate with very high shear stresses between the rotary and stationary elements, which allows a reduction in drop diameter to 1–5 μm. The devices are suitable for formulating highly viscous

© Springer Nature Switzerland AG 2020
M. Ochowiak et al. (Eds.): PAIC 2019, *Practical Aspects of Chemical Engineering*, pp. 199–208, 2020.
https://doi.org/10.1007/978-3-030-39867-5_21

emulsions. High-pressure homogenizers make it possible to obtain emulsions with droplet sizes ranging from 0.1 μm to 2 μm. In these devices, the break-up of droplets occurs under the effect of shear stresses, cavitation and turbulence.

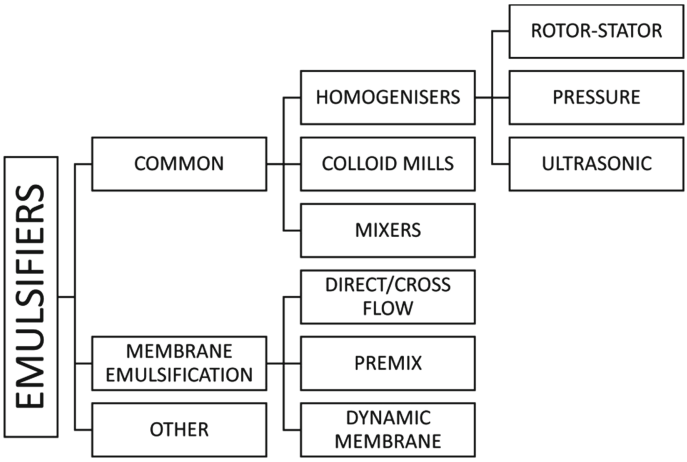

Fig. 1. Methods of emulsion formulation

2 Formulation of Emulsions Using Membranes

Over the past few decades, a number of new emulsion formulation methods offering superior control of droplet diameter and droplet size distribution have been proposed. One of them is based on the use of membranes (membrane emulsification, ME). The original variant of membrane emulsification, direct/cross flow ME, was proposed by Nakashima and Shimzu in a Japanese paper published in 1993 (Nakashima and Shimizu 1993). This method involves forcing the dispersed phase directly into the continuous phase through a membrane (Fig. 2a). Compared to the methods of emulsion formulation used at that time, direct ME made it possible to easily control droplet sizes, and obtain monodisperse emulsions. Only two main preconditions must be met. The membrane must have narrow pore size distribution, and must not be wetted by the dispersed phase. Unfortunately, the stability of the process of emulsion formulation can be assured within a limited range of flow rates of the continuous phase (typically 0.01–0.1 $m^3/(m^2\ h)$), resulting in low productivity (Abrahamse et al. 2002; Kobayashi et al. 2003; Vladisavljević and Williams 2005).

In 1996, Suzuki, Shuto and Hagura (Suzuki et al. 1996) proposed a modification of the membrane method of formulating emulsions, called premix ME. The process of emulsion formulation was divided into 2 stages: formulation of a premix with relatively large droplets (premix/coarse emulsion) by mixing the phases (i), and forcing the premix through a membrane (ii) (Fig. 2b). If the membrane is well wettable by the dispersion phase, and appropriate emulsifiers are used, phase inversion may occur (after being forced through the membrane the continuous phase of the premix becomes

the dispersed phase of the final (fine emulsion) (Fig. 2c) (Suzuki et al. 1999). Compared to the direct method, the new variant has several advantages (Vladisavljević and Williams 2005):

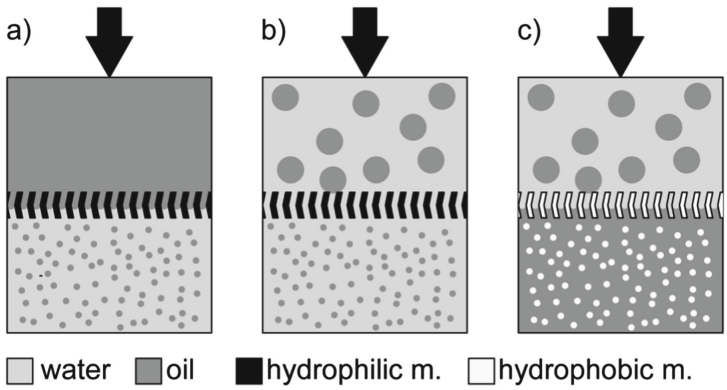

Fig. 2 Membrane emulsification (a) direct, (b) premix, (c) premix with phase inversion (based on Vladisavljević et al. 2004)

- possibility to apply higher flow rates (above 1 $m^3/(m^2 \cdot h)$),
- possibility to achieve smaller droplet diameters using the same membrane and composition,
- simplified design of the experimental stand (no moving parts),
- easier control of the emulsification process.

The disadvantages of premix ME include the formation of emulsions with wider droplet distribution than when using direct ME, and problems with pore blocking (depth fouling). For these reasons, a solution was sought that would combine the advantages of both types of membrane emulsification. Zwan, Schroën and Bloom (van der Zwan et al. 2008) proposed replacing conventional membranes with a packed bed of spherical particles (so-called dynamic membrane). A benefit of this solution is simplified pore cleaning due to the possibility of separating the packed bed into constituent parts. Moreover, pumping the emulsion through the packed bed several times results in the narrowing of droplet size distribution (Vladisavljević et al. 2004).

3 Emulsion Flow Through Porous Packed Bed

Emulsion flow through a porous packed bed can be classified based on its stability and the size of pores and droplets of the dispersed phase (Soo and Radke 1984). In the case of diluted, relatively unstable emulsions with a very low mean droplet size to pore size ratio (Spielman and Goren 1970; Spielman and Su 1977), two flow regimes are distinguished. One of them is distinctive for the presence of oil droplets dispersed in water,

while the other is characterized by the flow of the continuous oil phase resulting from droplet coalescence (Scheidegger 1974). The flow of emulsions of this type does not induce changes in permeability.

Studies examining the flow of quite stable emulsions through a porous packed bed were initiated by McAuliffe (McAuliffe 1973), Alvarado and Madsen (Alvarado and Marsden 1979) in the 1970s. Experiments conducted by these authors show that key factors determining packed bed permeability include the droplet size to pore size ratio, and the injection rate. Droplets with size comparable to the size of pore constrictions (Fig. 3b) are retained in the packed bed by capillary forces, which leads to a significant reduction in permeability. It is only the balancing of capillary forces with viscous forces (e.g. by increasing the injection rate) that promotes droplet deformation and flow through the constriction (Romero et al. 2007). If the size of droplets is smaller than the size of constrictions (Fig. 3a), the droplets are not deformed during their flow through the constrictions. If the size of emulsion droplets exceeds the size of the pores (Fig. 3c), the droplets are too large to pass through the constriction (Zhou et al. 2018).

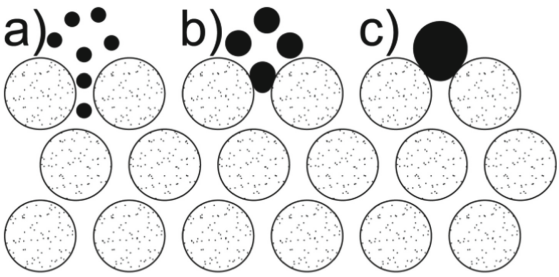

Fig. 3. Flow of emulsions with varying droplet size to pore size ratio through porous bed (based on Zhou et al. 2018)

An emulsion is able to form by flowing through a membrane when the transmembrane pressure is higher than the critical pressure p_c. The emulsion droplet diameter resulting from this operation (d_2) is affected by the ratio of the initial droplet diameter (d_1) to the pore diameter (d_1/d_m), and shear stresses at the pore wall, which can be determined by the equation:

$$\sigma_{w,p} = \frac{8\eta_e J \xi}{\varepsilon d_m} \tag{1}$$

where η_e - mean viscosity of emulsion inside the pores, J – transmembrane flux, ξ – mean tortuosity factor of the pore, ε – mean membrane porosity, d_m – mean pore size (Vladisavljević et al. 2004). At low shear stress values, the resulting droplets have diameters larger than pore diameters ($d_2 > d_m$, Fig. 4b).

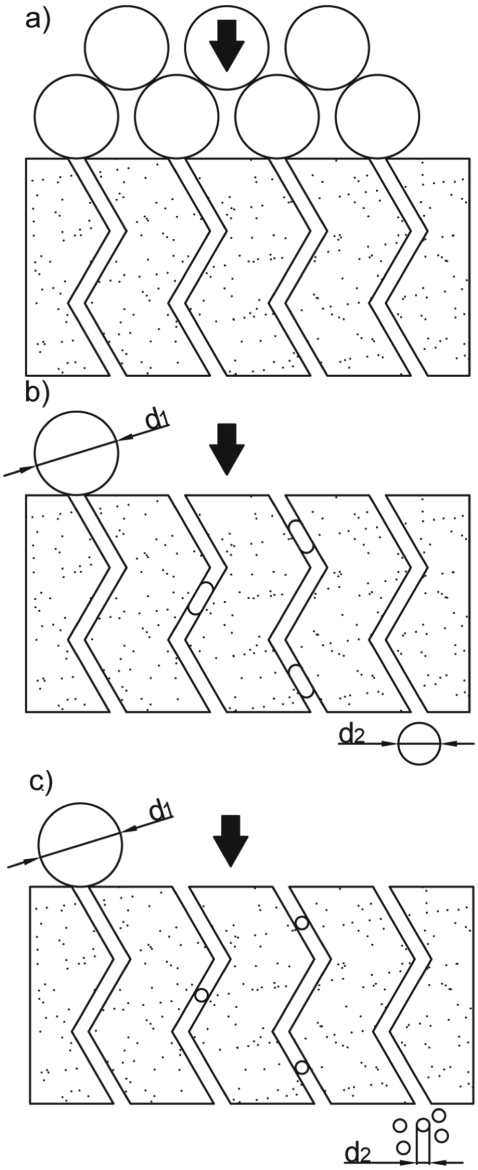

Fig. 4. Break-up of droplets in the porous medium – (a) droplet retention below the critical pressure, (b) moderate shear stresses ($d_m < d_2 < d_1$), (c) high shear stress values ($d_2 < d_m < d_1$) (based on Vladisavljević et al. 2004)

In this case, the droplets become deformed at the pore inlets, which is due to friction against their walls. At the pore outlets, the droplets regain their spherical shape. If high shear stresses occur, droplets collide with one other and with the pore walls, producing droplets with diameters smaller than the pore diameter ($d_2 < d_m$, Fig. 4c)

(Vladisavljević et al. 2004). If the initial droplet diameter to the pore diameter ratio $a = d_1/d_m$ is close to one, the critical pressure can be determined from the equation:

$$p_c = \frac{\gamma_{OW}\left[2 + \frac{2a^6}{\sqrt{2a^6-1}} \cdot \arccos\left(\frac{1}{a^3}\right) - 4a^2\right]}{a + \sqrt{a^2 - 1}} \tag{2}$$

where γ_{OW} is the interfacial tension at oil/water interface. However, if the ratio of the diameters is $a = d_1/d_m \gg 1$, the critical pressure is equal to the capillary pressure:

$$p_c = \frac{4\gamma_{OW}\cos\theta}{d_m} \tag{3}$$

where θ - contact angle between disperse phase droplets and membrane surface in continuous phase (Vladisavljević et al. 2004).

4 Emulsion Formulation in Packed Bed of Glass Microbeads

This paper addresses the structural solution for a device designed for premix membrane emulsification, and characterizes emulsions formulated with the device.

The schematic representation of the device is given in Fig. 5, and detailed design is shown in Fig. 6. Both emulsion phases and an emulsifier are transferred into the pressure tank (4). An Aquael FAN Plus motor (2) creates a rotating magnetic field that causes the magnet (1) on the agitator shaft to rotate.

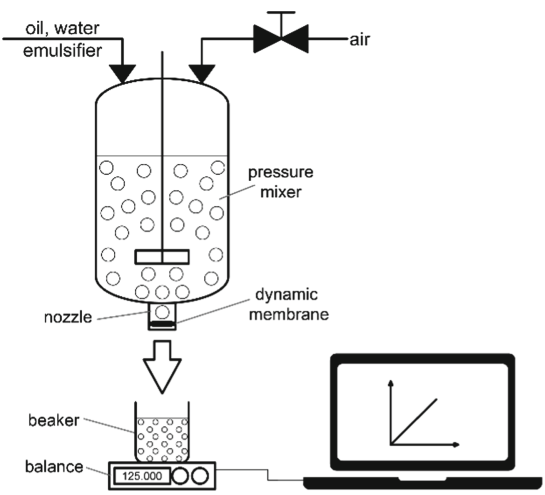

Fig. 5. Schematic representation of the experimental stand

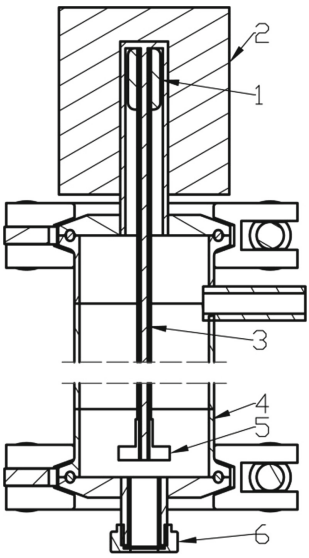

Fig. 6. Cross-section through the pressure tank of the experimental stand

In the course of mixing (5), a premix is formed, which is then forced through a dynamic membrane located in the nozzle (6). The emulsion flowing out of the nozzle goes to a beaker placed on a Radwag WTC 200 balance (reading accuracy: 0.001 g). Integration of the balance with the R-Lab computer programme enables registration of weight gain in time. Pressure in the tank is measured by means of EMS-20L digital pressure gauge (Meraserw5) with a measuring range of $0 \div 690$ kPa (resolution: 0.01 kPa up to 100 kPa, resolution: 0.1 kPa above 100 kPa).

In order to assess the usefulness of dynamic membranes for the formulation of emulsions, it was necessary to determine the parameters of the premix obtained using the impeller, and the time of mixing after which the droplet size of the premix stabilizes at a constant level. To this end, a series of tests was carried out. Formulated emulsions were subjected to mixing for 15 s to 300 s, following which their droplet diameter was determined. The result of the tests in the form of a correlation between the Sauter diameter d_{32} and the mass diameter d_{43}, and the mixing time, is shown in Fig. 7. On their basis, it was found that the greatest changes in emulsion droplet diameters occurred within the initial 90 s, while after approximately 200 s mixing did not lead to any change in diameter.

In the constructed device, the packed bed of glass beads is placed on a sieve made of 12/64 Dutch woven mesh (warp diameter 0.06 mm, weft diameter 0.04 mm). In order to evaluate the effect of the mesh used in the device on droplet size, an experiment was conducted in which the premix was forced through a sieve at various pressure levels. As shown in the data in Fig. 8, during the flow of the premix through the mesh, the diameters d_{32} and d_{43} decrease by more than half.

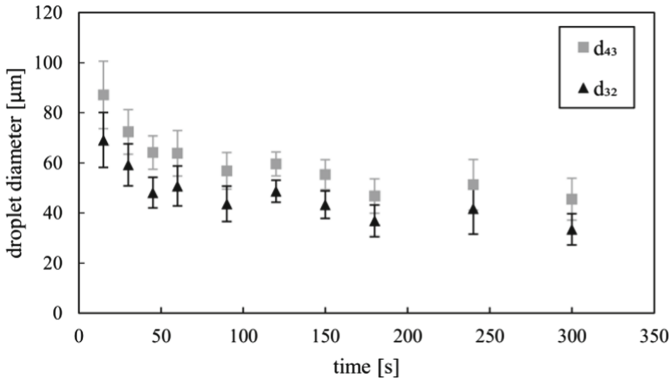

Fig. 7. Effect of mixing on premix droplet size

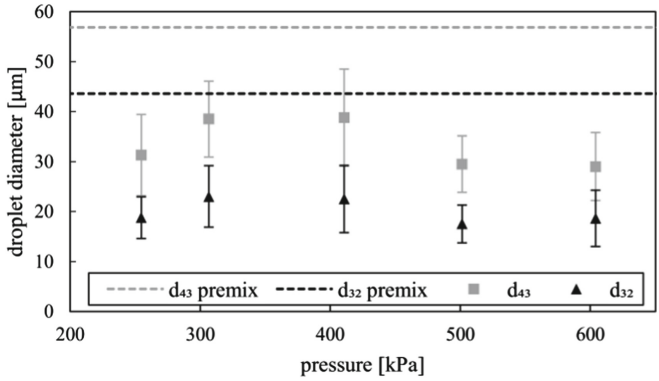

Fig. 8. Effect of pressure on droplet diameter of emulsions forced through mesh

After determining the parameters of premix formulation and evaluating the effect of mesh on droplet diameter, the proper experiment was carried out using a dynamic membrane. To this end, a layer of packed bed of glass microspheres with a grain size of 71–100 µm was employed (d_{32} = 84.98 µm, d_{43} = 85.68 µm, polydispersity index 1.03, span 0.21). The resulting premix was forced through a dynamic membrane at various pressure levels (from 250 kPa to 620 kPa). As shown by the data presented in Fig. 9, the use of a dynamic membrane results in a reduced diameter of premix droplets. The extent of the reduction is greater than when mesh alone is used, ranging from approximately 30% to 25% of the initial value. The impact of pressure on the mean diameter of droplets is also noticeable. The higher the applied pressure, the smaller the droplet diameter.

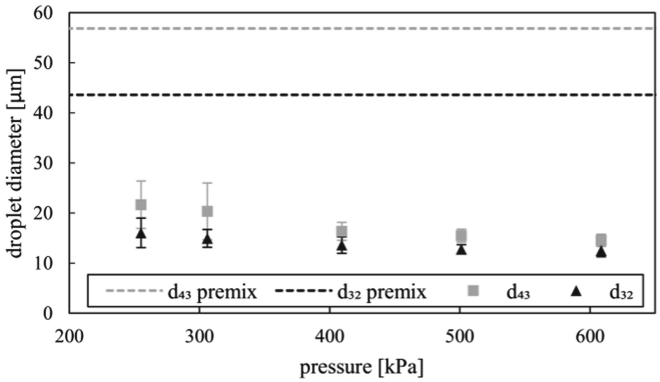

Fig. 9. Effect of pressure on the droplet diameter of emulsions forced through a packed bed of microbeads

5 Summary

The paper discusses different methods of formulating emulsions, and presents an original structural solution employed in the design and construction of an experimental stand for the formulation of emulsions based on the method of premix membrane emulsification. The main element of the designed stand is a pressure tank suitable for the formulation of a premix which is then forced through a membrane (in the form of mesh or packed bed of glass beads) in order to obtain a fine emulsion. Dutch woven mesh reduces the diameters of emulsion droplets by more than half, while the dynamic membrane of glass beads (with diameters from 71 μm to 100 μm, height 5 mm) allows obtaining emulsions with droplet diameters approximately 70% smaller than the initial value.

Acknowledgments. The work was financed by the Ministry of Science and Higher Education (03/32/SBAD/0902).

References

Abrahamse, A.J., van Lierop, R., van der Sman, R.G.M., et al.: Analysis of droplet formation and interactions during cross-flow membrane emulsification. J. Membr. Sci. **204**, 125–137 (2002). https://doi.org/10.1016/s0376-7388(02)00028-5

Alvarado, D.A., Marsden Jr., S.S.: Flow of oil-in-water emulsions through tubes and porous media. **19**, 369–377 (1979). SPE-5859-PA. https://doi.org/10.2118/5859-pa

Fellows, P.J.: Size reduction. In: Fellows, P.J. (ed.) Food Processing Technology, 4th edn., pp. 291–328. Woodhead Publishing, Sawston (2017)

Kobayashi, I., Nakajima, M., Mukataka, S.: Preparation characteristics of oil-in-water emulsions using differently charged surfactants in straight-through microchannel emulsification. Colloids Surf. Physicochem. Eng. Asp. **229**, 33–41 (2003). https://doi.org/10.1016/j.colsurfa.2003.08.005

McAuliffe, C.D.: Oil-in-water emulsions and their flow properties in porous media. **25**, 727–733 (1973). SPE-4369-PA. https://doi.org/10.2118/4369-pa

Nakashima, T., Shimizu, M.: Preparation of monodispersed O/W emulsion by porous glass membrane. Kagaku Kogaku Ronbunshu **19**, 984–990 (1993). https://doi.org/10.1252/kakoronbunshu.19.984

Romero, C., Bazin, B., Zaitoun, A., Leal-Calderon, F.: Behavior of a scale inhibitor water-in-oil emulsion in porous media. **22**, 191–201 (2007). SPE-98275-PA. https://doi.org/10.2118/98275-pa

Scheidegger, A.E.: The Physics of Flow Through Porous Media, 3rd edn. University of Toronto Press, Toronto (1974)

Soo, H., Radke, C.J.: Flow mechanism of dilute, stable emulsions in porous media. Ind. Eng. Chem. Fundam. **23**, 342–347 (1984). https://doi.org/10.1021/i100015a014

Spielman, L.A., Goren, S.L.: Progress in induced coalescence and a new theoretical framework for coalescence by porous media. Ind. Eng. Chem. **62**, 10–24 (1970). https://doi.org/10.1021/ie50730a003

Spielman, L.A., Su, Y.-P.: Coalescence of oil-in-water suspensions by flow through porous media. Ind. Eng. Chem. Fundam. **16**, 272–282 (1977). https://doi.org/10.1021/i160062a018

Suzuki, K., Hayakawa, K., Hagura, Y.: Preparation of high concentration O/W and W/O emulsions by the membrane phase inversion emulsification using PTFE membranes. Food Sci. Technol. Res. **5**, 234–238 (1999). https://doi.org/10.3136/fstr.5.234

Suzuki, K., Shuto, I., Hagura, Y.: Characteristics of the membrane emulsification method combined with preliminary emulsification for preparing corn oil-in-water emulsions. Food Sci. Technol. Int. Tokyo **2**, 43–47 (1996). https://doi.org/10.3136/fsti9596t9798.2.43

van der Zwan, E.A., Schroën, C.G.P.H., Boom, R.M.: Premix membrane emulsification by using a packed layer of glass beads. AIChE J. **54**, 2190–2197 (2008). https://doi.org/10.1002/aic.11508

Vladisavljević, G.T., Shimizu, M., Nakashima, T.: Preparation of monodisperse multiple emulsions at high production rates by multi-stage premix membrane emulsification. J. Membr. Sci. **244**, 97–106 (2004). https://doi.org/10.1016/j.memsci.2004.07.008

Vladisavljević, G.T., Williams, R.A.: Recent developments in manufacturing emulsions and particulate products using membranes. Adv. Colloid Interface Sci. **113**, 1–20 (2005). https://doi.org/10.1016/j.cis.2004.10.002

Zhou, Y., Yin, D., Wang, D., Gao, X.: Emulsion particle size in porous media and its effect on the displacement efficiency. J. Dispersion Sci. Technol. **39**, 1532–1536 (2018). https://doi.org/10.1080/01932691.2017.1421082

Zieliński, R.: Surfaktanty. Budowa, właściwości, zastosowania. Wydawnictwo Uniwersytetu Ekonomicznego w Poznaniu (2017)

Analysis of Coal Dust Ignition Deposited in a Layer at Constant and Variable Temperature of Heating Panel

Bożena Kukfisz[1(✉)], Dorota Siuta[2], and Waldemar Szaferski[3]

[1] Faculty of Security Engineering and Civil Protection, The Main School of Fire Service, Warsaw, Poland
bkukfisz@sgsp.edu.pl
[2] Faculty of Process and Environmental Engineering, Lodz University of Technology, Lodz, Poland
[3] Institute of Chemical Technology and Engineering, Faculty of Chemical Technology, Poznan University of Technology, Poznan, Poland

Abstract. The present work analyses the tendency of ignition of the "Barbara" coal dust from a heated surface. Minimum coal dust layer ignition temperature was measured at a fixed temperature of heating plate (standard method) and at temperature of the heating plate increasing at constant rate. Dust layers of thickness ranging from 5 to 50 mm were tested. Permissible temperature of surfaces of electrical equipment were determined on the basis of PN-EN 60079-14 standard requirements concerning the method of lowering the permissible equipment surface temperature along with the increasing thickness of the layer from 5 mm to 50 mm in order to maintain an adequately high safety margin. Based on the results, significant differences were found for both methods of determination. For a 5 mm dust layer, the permissible temperature of equipment differed by ca. 140 °C and they decreased as the layer thickness rose, down to ca. 40 °C for a 50 mm dust layer.

1 Introduction

One of the main dangers that occur nowadays in various branches of industry, resulting from widespread use of dusts in technological processes, is the risk of fire or explosion of powdered materials. Such risks appear in all the places where milling, fragment or grinding of products is performed during mechanical processing, storage, packaging and transport. According to Eckhoff (2003), the greatest number of events connected with explosion of dust occurs in wood industry – 34% and grain processing – 24%. Slightly fewer events – 14% - are generated by plastic dusts and 10% of events occurs in the presence of coal and metal dusts. Coal dust generated in various technological processes can present a fire risk, if it takes a form of layer deposited on hot surface of equipment or machines. Taking into account the passive explosion protection, the parameter of minimum dust layer ignition temperature is significant. Minimum dust layer ignition temperature is determined as the lowest temperature of hot surface at which a dust layer of given thickness deposited on that surface ignites. Fire protection related to occurrence of organic dust in the layer is connected mostly with smouldering,

© Springer Nature Switzerland AG 2020
M. Ochowiak et al. (Eds.): PAIC 2019, *Practical Aspects of Chemical Engineering*, pp. 209–215, 2020.
https://doi.org/10.1007/978-3-030-39867-5_22

incandescence, self-ignition and ignition. Smoldering is slow burning of materials without emission of visible light, characterized by release of smoke and increase in temperature. Incandescence is burning of materials in solid phase, without flame, but with emission of light from the combustion zone. Self-ignition of dust occurs when the rate of generating heat as a result of a series of reactions (biological, chemical) exceeds the rate of releasing heat to the environment.

2 Minimum Dust Layer Ignition Temperature – Analysis of References

Palmer and Butlin (1972) analysed the phenomenon of incandescence and smouldering of beech wood dust in horizontal layers. In his analyses he took into account the distribution of dust grains, movement of air above the layer and type of material on which the dust is deposited. The results of his work confirmed the influence of all the above-mentioned factors upon the minimum dust ignition temperature.

Lebecki et al. (2003) described the results of experiments performed to determine the minimum dust layer ignition temperature on the basis of experimental studies of coal dust for 5 mm and 50 mm layers. The measurements were performed with use of two methods; the first one was a standard method of constant temperature of the heated plate (CTHP), described in PN-EN 50281-2-1, which assumes determining the minimum ignition temperature of dust layer deposited on a heated plate of constant temperature. The second method was constant rate of heat generation (CRHG). The results indicated that the lowest values of minimum dust layer ignition temperature were noted in the CRHG method, the differences reached as much as several degrees for both thicknesses of layers, yet the differences decreased as the layer thickness grew. The results show that application of the procedure recommended in the standard can be connected with a serious statistical error in a great deal of practical cases. More work is required to develop a more universal method of testing that will reflect the actual conditions better, while at the same time fulfilling the safety requirement.

Kim and Hwang (1996), on the basis of experimental studies, developed a mathematical model which reflects the heating and ignition of dust in a layer, and, in addition to that, takes into account the shrinking of the combustible material. Having analysed the impact of shrinking of the dust layer on the temperature distribution in the layer, and, consequently, the impact on the minimum dust layer ignition temperature, Kim and Hwang concluded that the dust layer thickness is the most important parameter affecting the minimum dust layer ignition temperature. Dyduch and Majcher (2006) used a one-dimensional model of dust layer ignition placed on a heated plate to calculate the temperature field. The calculation results were compared with the results of the experimental studies from the CRHG method, and the comparison turned out to be satisfactory with reference to dust layers of thickness below 10 mm. In the case of layers of thickness exceeding 10 mm, a reliable description should contain more than one dimension, because in the event of dust layer thickness comparable with the radius diameter, one cannot neglect the two-dimensionality of heat transfer in dust, and one should then take into account the heat transfer through the ring. Nevertheless, such a

situation fails to reflect the actual industrial conditions, as the deposited dust layers do not form high cylinders confined by metal rings.

Querol et al. (2006) published results of testing a minimum dust layer ignition temperature of thickness 75 mm with use of modified procedure from the standard PN-EN 50281-2-1. Besides the description of the method and the criteria of ignition, the standard contains a chapter regarding the scope of applicability of results and the method of linear interpolation and extrapolation of the minimum ignition temperature to results other than the measured dust layer thickness. To that end a logarithm of layer thickness in an inverse function of the minimum ignition temperature expressed in degrees Kelvin is used. The values measured by Querol et al. show high conformity with the method of forecasting suggested by the standard.

Janes et al. (2008) analysed correlations between the values of minimum dust layer and dust cloud ignition temperatures, which are the values obtained with use of method A and B. Using the relations they developed it is possible to calculate the minimum layer ignition temperature on the basis of minimum dust cloud ignition temperature, knowing the Biot number. The Biot number is a dimensionless number that defines the ratio between the heat conduction resistance by a body and the resistance of heat transfer from its surface.

3 Experimental Set-up and Materials

Currently, minimum dust layer and dust cloud ignition temperatures are determined based on the requirements of PN-EN ISO 60079-14. Until 15 November 2019, the standard PN-EN 50281-2-1 was a binding document in that regard in European and Polish law, whereas in American law it was ASTM E2021. The current standard PN-EN ISO 60079-14 distinguishes between two test methods: A and B, the method of testing dust layer on the heated plate of and the method of testing dust cloud in furnace of constant temperature, respectively. They enable to determine the minimum dust layer ignition temperature and the minimum dust cloud ignition temperature.

The standard distinguishes between the visual and temperature-related criteria of dust layer ignition. Smouldering or flame burning indicates ignition of the layer. Furthermore, if the measured temperature of the layer is higher than 450 °C or if the difference between the temperature of the heated plate and the measured temperature of the dust layer is higher than 250 °C, then, according to the standard, the measurements should be also terminated with the results showing the occurrence of ignition. The current standard indicates that it should be assumed that ignition of the sample did not occur only in the event that none of the conditions confirming the occurrence of ignition is fulfilled within 60 min from starting the test. The test cycle should be interrupted, if the dust layer ignition does not occur within a cycle of three measurements at a temperature of the heated plate equal to 400 °C, and in that event, it should be assumed that the minimum dust ignition temperature is higher than 400 °C at the given dust layer thickness. The measurements and the method of bisection should be applied until the minimum ignition temperature is determined with an accuracy of 10 °C. Test stand used for determination of dust layer minimum ignition temperature is shown in Fig. 1.

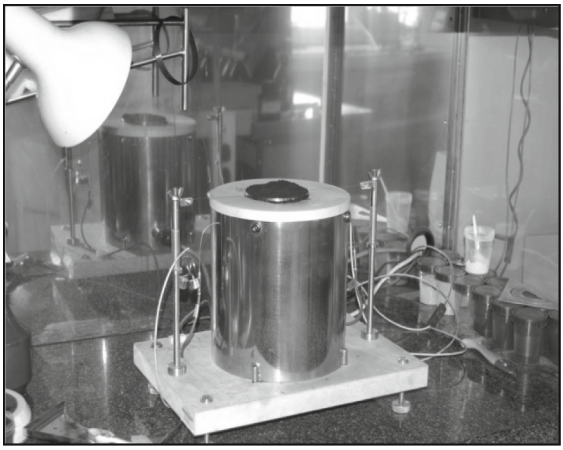

Fig. 1. Test stand for determination of dust layer minimum ignition temperature

For the purpose of this article a series of experimental studies were performed in relation to the "Barbara" coal dust which has the properties shown in Table 1 and Table 2, aimed at determining the impact of the layer thickness on the minimum ignition temperature defined at the constant temperature of heated plate and at constant increment of heated place of 3 °C/min.

Table 1. Percentage of mass fraction passing the sieve of dust tested

Percentage of mass fraction passing the sieve of	"Barbara" coal dust
0.200 mm	100.0
0.100 mm	81.5
0.075 mm	76.0
0.063 mm	72.5

Table 2. Properties of dust tested

Properties of dust tested	"Barbara" coal dust
Average ash content [%]	13.9
Average volatile content [%]	39.2
Average moisture content [%]	5.7
Bulk density [kg/m^3]	542.0
Specific heat [J/kg K]	1323.0
Heat of combustion [kJ/kg]	24396.0

The tested dust was the "Barbara" dust. It was selected because of its uniform distribution of grains between fractions and due to increasing health and safety problems in the mining industry. All the measurements were performed at an air temperature of 21 ± 2 °C and atmospheric pressure of 1000 ± 5 hPa. Minimum ignition temperature of the dust layer for a thickness of 5 mm, 10 mm, 12.5 mm, 15 mm, 25 mm and 50 mm was determined.

4 Results

A difference between the results obtained with use of two different methods of determining dust layer ignition temperature (CRHG and CTHP) is visible. A significant difference of ca. 140 °C is highest for dust thickness of 5 mm and decreases to ca. 50 °C for a layer of 50 mm. The obtained results are presented in Table 3.

Table 3. Results of determination of minimum ignition temperature of the "Barbara" coal dust

Coal dust layer thickness [mm]	Minimum dust layer ignition temperature at a constant temperature of heated plate [°C]	Permissible temperature of the electrical equipment surface [°C]	Minimum dust layer ignition temperature with constant rate of increase in the temperature of the heated plate [°C]	Permissible temperature of the electrical equipment surface [°C]	Difference in the permissible temperature of the electrical equipment surface [°C]
5	320	245	180	105	140
10	250	210	150	150	60
12.5	230	190	140	140	50
15	210	180	130	130	50
20	180	165	120	110	55
25	160	150	110	90	60
50	150	100	100	60	40

Temperature 75 °C lower than the minimum ignition temperature is the maximum permissible temperature of the equipment surface on which a max. 5 mm layer of tested dust can be deposited, with concurrent sufficiently high safety margin. The PN-EN 60079-14 standard contains a suggestion on how to lower the permissible equipment surface temperature along with the increasing thickness of the layer from 5 mm to 50 mm in order to maintain an adequately high safety margin (Fig. 2).

For thin layers, the difference reaches 140 °C for coal dust. For thick layers there are some indications showing that the difference stabilizes at the level of 40–60 °C. The difference can be directly attributable to an increase in the temperature of the heated plate in the CRHG experiments, when the heat transfer reaching the dust layer is constant throughout the entire experiment, which consequently prevents from the loss of heat as a result of the boundary touching the heated plate. During the CTHP tests, the heated plate starts acting as a radiator and lowers the ignition temperature, and the thicker the dust layer, the weaker the effect of heated plate as a radiator.

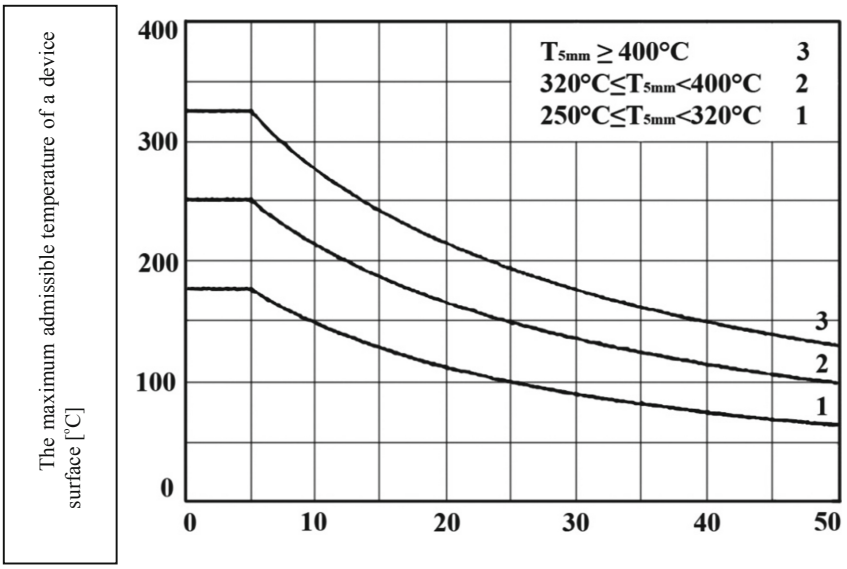

Fig. 2. Decrease of maximum permissible equipment surface temperature along with the increasing thickness of dust layer.

A method of estimating maximum permissible temperature of the device enclosure surface for dust layers up to 50 mm depends on the minimum ignition temperature estimated for a 5 mm dust layer of thickness and the thickness of the actual layer (based on the selection of the curve – Fig. 2).

5 Conclusions

In the actual conditions the temperature of electric equipment enclosure on which a layer of dust is deposited can increase significantly due to insulating properties of the dust layer. That relation is confirmed by the measurement of the minimum ignition temperature of the "Barbara" coal dust layer at a constant temperature of heated plate (standard method) and at constant speed of increase in the temperature of heated plate. The relation was confirmed for the analysed layers of coal dust of thickness ranging between 5 and 50 mm. For the dust, the estimated minimum ignition temperature of the dust layer at a constant temperature of the heated plate was higher than the estimated minimum ignition temperature at a constant increment of the temperature of the heated plate for each tested layer thickness. The noted difference was highest for thin layers (140 °C) and decreased as the layer thickness got thicker, to reach a difference of 40 °C. The results suggest that in the simulated actual conditions ignition of the dust layer can occur at temperatures lower than suggested by requirements of the standard.

Acknowledgments. The study was funded by the National Centre for Research and Development under project no. DOB-BIO9/18/01/2018.

References

ASTM E2021: Standard Test Method for Hot-Surface Ignition Temperature of Dust Layers (2013)

Dyduch, Z., Majcher, B.: Ignition of a dust layer by a constant heat flux-heat transport in the layer. J. Loss Prevent. Proc. **19**, 233–237 (2006). https://doi.org/10.1016/j.jlp.2005.06.027

Eckhoff, R.K.: Dust Explosions in the Process Industries. Elsevier, New York (2003)

Janes, A., Carson, D., Accorsi, A., Chaineaux, J., Tribouilloy, B., Morainvillers, D.: Correlation between self-ignition of a dust layer on a hot surface and in baskets in an oven. J. Hazard. Mater. **159**, 528–535 (2008). https://doi.org/10.1016/j.jhazmat.2008.02.057

Kim, H.M., Hwang, C.C.: Heating and ignition of combustible dust layers on a hot surface Influence of layer shrinkage. Combust. Flame **105**, 471–485 (1996). https://doi.org/10.1016/0010-2180(95)00110-7

Lebecki, K., Dyduch, Z., Fibich, A., Śliż, J.: Ignition of a dust layer by a constant heat flux. J Loss Prevent. Proc. **16**, 243–248 (2003). https://doi.org/10.1016/s0950-4230(03)00041-x

Palmer, K.N., Butlin, R.N.: Dust explosibility tests and their application. Powder Technol. **6**, 149–157 (1972). https://doi.org/10.1016/0032-5910(72)80071-8

PN-EN 50281-2-1: Urządzenia elektryczne do stoso-wania w obecności pyłów palnych – Część 2-1: Metody badania – Metody oznaczania minimalnej temperatury zapłonu pyłu (2002)

PN-EN 60079-14: Atmosfery wybuchowe – Część 14: Projektowanie, dobór i montaż instalacji elektrycz-nych (2013)

Querol, E., Torrent, J.G., Bennett, D., Gummer, J., Fritze, J.P.: Ignition tests for electrical and mechanical equipment subjected to hot surface. J Loss Prevent. Proc. **19**, 639–644 (2006). https://doi.org/10.1016/j.jlp.2006.03.007

Synergic Nanoparticles-Cationic Surfactant Interactions for Controlling Foam Systems

Krzysztof Jan Legawiec(✉) and Izabela Polowczyk

Faculty of Chemistry, Wroclaw University of Science and Technology, Wrocław, Poland
krzysztof.legawiec@pwr.edu.pl

Abstract. In this chapter we discussed the results of application of silica dioxide nanoparticles as foam modifiers prepared with cationic surfactant – CTAB and their potential to control foamability. Foams are interesting systems and their stabilization mechanism is still not fully known, cause it depends on many factors included physicochemistry parameters of gas-liquid interface. After nanoparticles being introduced into the foam system most of its parameters change, especially the stability which is important due to flotation process. The results indicate a potential for reducing the use of synthetic surfactants, which gives a chance for the development of this method as more environmentally friendly.

1 Introduction

Foams are gases dispersed in liquids, which not only surround humans in everyday life, but are also an integral part of many technological processes including flotation - the most widely used separation technique, whose main purpose is to separate minerals from their ores (Fuerstenau et al. 2007). The stability of the foam plays a key role in the final stage of flotation, which is the transport the solid particles to the foam formed on the surface of flotation tank. This stage determines the effectiveness of further operations leading to flotation concentrate (Scheludko et al. 1976).

Due to the large specific surface area and lack of thermodynamic stability, the description of such systems becomes much more difficult. In a typical flotation operation, synthetic surfactants are used to reduce the surface tension and thus to produce foam stable enough to maintain the air-solution boundary with floated mineral particles. These compounds – frothers and other flotation reagents – are difficult to biodegrade and represent a significant environmental problem (Karakashev and Grozdanova 2012). The variable quality composition of the ore additionally causes a decrease in the energy of surfactants adhesion at the phase boundary, which in consequence contributes to desorption of these substances, causing faster liquid outflow and foam degradation. The effect of this phenomena is the loss of possibility for foam to carry solid particles (Crawford and Ralston 1988).

Increasing popularity of nanoparticles in industrial processes has also contributed to the attempts to use them as nanostructures controlling the stability of dispersion systems, including foam systems. It was found that nanoparticles with appropriate surface

© Springer Nature Switzerland AG 2020
M. Ochowiak et al. (Eds.): PAIC 2019, *Practical Aspects of Chemical Engineering*, pp. 216–222, 2020.
https://doi.org/10.1007/978-3-030-39867-5_23

properties can act synergistically with surfactants in terms of regulation of foam lifetime (Kim et al. 2016). An additional advantage in favour of attempts to implement such solutions in industrials processes seems to be relatively low cost of dispersion generation and measurable environmental effects in the form of reducing the amount of consumed surfactants (Arriaga et al. 2012).

The key to understanding the mechanisms ruling the stabilisation of dispersion systems discussed in this paper seems to be controlling the hydrophobicity of nanoparticles' surfaces (Yang and Pelton 2011). As it turns out, it is the adsorption of nanoparticles with surfaces modified with cationic surfactant that prevents the drainage of liquid film, which is an important element of the morphology of the foam system (Horozov 2008). Moreover, the emerging steric barrier counteracts the process of ageing this type of system, i.e. coalescence of gas bubbles.

2 Methodology

For this experiments a commercial available hydrophilic fumed silica dioxide nanoparticles (SNPs) AEROSIL 200 was used. Table 1 shows the physiochemical characteristics of SNPs used in this research. Below data has been provided by the manufacturer, Evonik Resource Efficiency GmbH (Essen, Germany).

Table 1. Physicochemical characteristics of AEROSIL 200

S_{BET}	pH value in 4% weight dispersion	SiO_2 content	Tamped density
$m^2 \cdot g^{-1}$	–	%	$g \cdot l^{-1}$
175–225	3.7–4.5	>99.8	~50

Cationic hexadecyltrimethylammonium bromide of an analytical grade (Alpha Aesar, Haverhill, USA) was used as an ionic surfactant. All solutions have been prepared using Millipore ultrapure water with conductivity about 0,055 $\mu S \cdot cm^{-1}$ from Milli-Q water purification system (Merck, Darmstadt, Germany).

The surface tension of the surfactant SNPs solutions were determined by the Du Noüy ring method, using a T-100 tensiometer (Krüss, Germany).

Foam stability tests were carried out using a glass column with a flattened wall and had a height of 400 mm and had a diameter of 50 mm. A speed camera MiriM120 (Phantom, USA) and LED light source was attached to the column to allow observation of foam dynamics transformations. The liquid was dispersed by air pumped via peristaltic pump with a volumetric flow rate of 250 $cm^3 \cdot min^{-1}$. The gas was distributed through a blotting-paper filter at the bottom of the column. Size of the aggregates was measured with the Photocor Complex (Photocor, Estonia) particle analyser. Foam drainage kinetics was investigated using turbidimetric Turbiscan La*b*-expert (Formulaction, France) analyser.

3 Foam System Analysis

3.1 Properties of SNPs in CTAB Dispersion

By definition, surfactants are a group of compounds that have the ability to reduce surface tension. The mechanism of this phenomenon is based on the adsorption of this very specific molecules at the interface (Fuerstenau et al. 2007). In Fig. 1.A one can see a change in surface tension progressing with a change in concentration. Apparently, there is a tendency for the surface tension to decrease (from 59,5 to 36,0 mN · m^{-1}) with increasing surfactant concentration (from 10 to 1000 mg · dm^{-3}). For CTAB solution we note adsorption region in the aqueous phase where surfactants can create micellar aggregates, called critical micellisation concentration (CMC).

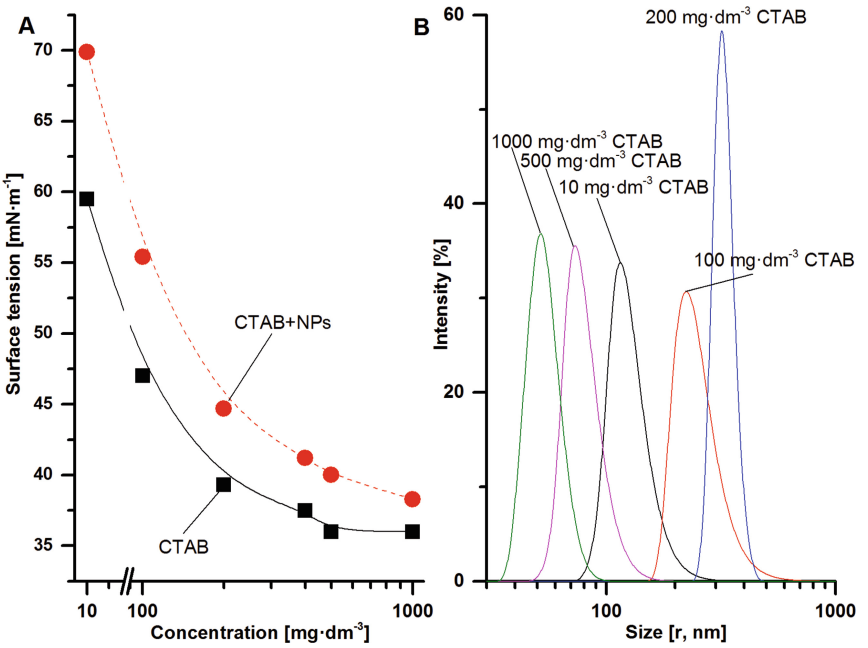

Fig. 1. **(A)** Change of surface tension in the presence (dash line) and in absence (black line) SNPs, **(B)** diagram of scattering intensity for SNPs dispersions.

For CTAB molecule according to literature CMC is approximately 335 mg · dm^{-3} (Liu et al. 2013). Black line symbolises lowering the surface tension for CTAB solution. The dash line in Fig. 1.A indicates the values of surface tension measured for surfactant concentration in a range 10–1000 mg · dm^{-3} but with the addition of 0.1% v/w of SNPs. It is evident that the surface tension is higher in the presence of SNPs and the CMC is not reached in this case comparing to surfactant solution. This is the result of cationic surfactant adsorption on the negatively charged surface of the SNPs. Some of the molecules adsorbed by electrostatic interactions reduce the concentration of free

surfactants monomers, so that the critical concentration for micellisation act is not reached at the interface where surface tension is measured.

Interactions between nanoparticles in aqueous solutions depend on the electrical condition of the surface, so-called zeta potential. In this system zeta potential is regulated by the surfactants molecules attached to SNPs surface. Figure 1.B shows the results of nanoparticles aggregates size distribution in dispersion using the dynamics light scattering technique. The change of aggregates size has a non-linear progression with respect to concentration. At lover than CMC values, quite large aggregates of SNPs (250–375 nm) are observed, which is caused by their aggregation and probably by interactions between monomeric and premicellar structures with the surface of the solid matter (Takeshita et al. 2014). The structures interact by hydrophobic moyetes of surfactant molecules (Nana et al. 2018). This orientation towards solution contributes directly to the process so-called hydrophobic coagulation. The SNPs aggregation tendency increases until the CMC value is reached. When CMC is reached then, the size of aggregates is becoming progressively smaller. This is due to the repulsion of two layers of surfactants created on the SNPs surface. Positively charged surfactants head interact electrostatically with each other and thus prevent coagulation (Liu et al. 2013).

3.2 Foamability and Foam Stability

Figure 2 shows two causes of results. The solid-line series indicate foamability of solution without and with 0,1% v/w SNPs, respectively with increasing surfactant concentration. The dash-line series represent the half-life of foam. As expected, in a system without nanoparticles, initial foam height increases with increasing cationic

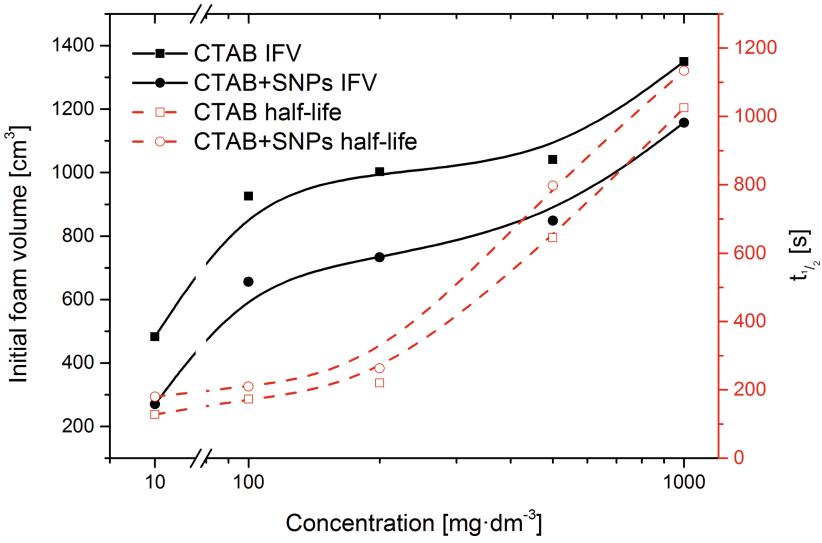

Fig. 2. Foam statics and half-time life.

surfactant concentration. In the presence of nanoparticles, one can point out that SNPs lower initial foam volume in the column test. Decreased foam volume formation in the presence of SNPs might be associated with surfactant adsorption on the solid surface, which causes a decrease in the concentration of monomers and other groups of CTAB molecules that could be sorbed on the surface of a thin liquid film. A constant increment of change in initial volume can be observed for the same concentrations of surfactant in the presence or absence of SNPs. Initial foam volumes ranges from 200 to 250 cm^3 for surfactant concentration in the range of 10–1000 mg · dm^{-3}. Moreover, according to the literature, we can conclude that the lower foamability is also reflects the changes in viscosity. Liu and his co-workers (AlYousef et al. 2018) found that in the presence of nanoparticles the viscosity of surfactants solutions increases. This makes it harder to disperse gas in the liquid, and thus the formation of gas bubbles is more difficult.

The opposite effect can be noticed when analysing foam stability in the presence of SNPs. An increase in the half-life time of decay is observed by roughly 150 s. This effect is the result of the growing hydrophobicity of the particles. When surfactant concentration increase, more hydrophobic tails are directed towards the air trapped in the foam. This effect is enhanced when the CMC is reached, as monolayers are formed in a kind of a scaffolding which prevent the coalescence effect. As the CMC is increasingly exceeded, aliphatic chains interact with each other in a way of tail-to-tail interactions, causing the drainage of liquid film to slow down. Furthermore, not only does the electric charge decrease on the surface, but also the adhesion energy in the interphase region increases.

Another interesting aspect of foam stability is the kinetic rate which the liquid drains out. Foams in practice are systems in which there are dynamics changes in their structural elements – foam cells. This causes some difficulties in quantitative and qualitative analysis of the processes taking place at the interphase boundary. The turbulence phenomena occurring in foam nodes contribute the basic ageing process – liquid drainage – influencing the stability of this systems. The effect of this fact causing the pressure fluctuations and thus disturbances of thermodynamics balance (Subrahamanyam and Forssberg 1988). The response of the system in an extreme situation, when liquid drained out, may result in a rupture of thin liquid film, which in effect leads to collapse of the dispersion structure.

In case under consideration, several techniques for measuring this phenomenon have already been developed, but the most accurate seems to be the turbidimetric method. This technique is based on the measurement of kinetics for destabilisation of dispersion placed in the measuring cell. Definition of kinetic effects is based on comparison in time of both: transmittance and back-scattering values for light of defined length (880 nm) passing through the sample. Measuring cell is made of glass and is 55 mm high with a diameter of 20 mm. Among numerous software options one can also find a module calculating the increment of the continuous phase. Device precisely detects changes in position of the boundary between continuous phase and foam system. This boundary changes during the time – as the film drainages, the height peaks increase.

Figure 3 shows height variability during the time. On the basis of the curves one can easily determine which of foam dispersions has slower film draining. In general,

with the increasing concentration of surfactants, the tendency to increase height of continuous liquid phase in the sample decreased. The most interesting effect can be observed at concentrations of 200 and 500 mg · dm^{-3} with SNPs. It can be seen that to achieve more stable system there is no need to use more cationic surfactant, because after adding SNPs drainage is more effectively slowed down.

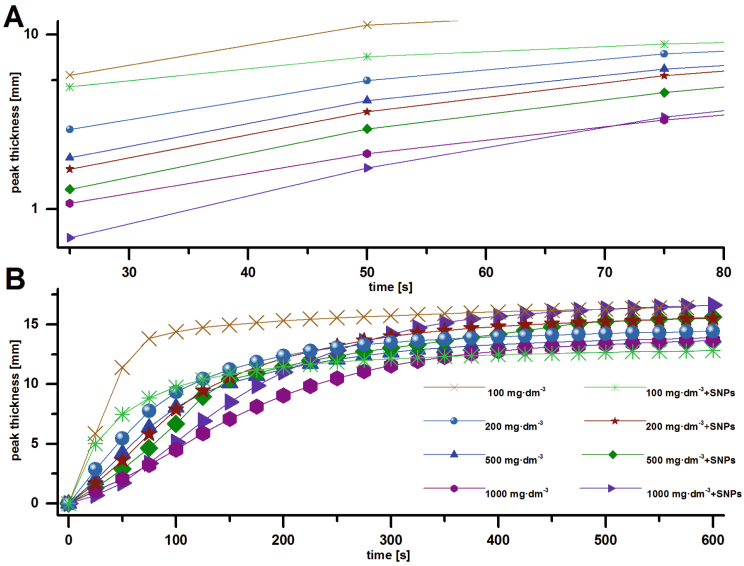

Fig. 3. Peak thickness kinetics in measure cells. **(A)** zoom in on range of 25–80 s of measurement, **(B)** general relationship between the change in height over time.

4 Conclusions

At the beginning of the 21st century, the way that we look at foams has changed. The potential for partially controlled foam lifetime has been recognised and could be used not only in the metal ore processing industry but also in various applications.

The stability of foam is controlled by SNPs interaction with electrostatically adsorbed CTAB molecules. Stability of the prepared and investigated systems increases with surfactant concentrations. Due to additional interactions between the surfactant hydrophobic tails and, as a result, creation of a barrier preventing rapid drainage of the liquid film located between trapped air bubbles in the foam cells.

That synergic effect of using SNPs – ionic surfactant mixture has a potential in reducing the consumption of surfactants, so this concept fits into the spirit of sustainable development. Also, it can be a milestone in finding the rules for designing the lifetime of the foam with greater precision.

Acknowledgements. This work was financially supported by a statutory activity subsidy from the Polish Ministry of Science and Higher Education for the Faculty of Chemistry of Wroclaw University of Science and Technology.

References

AlYousef, Z.A., Almobarky, M.A., Schechter, D.S.: The effect of nanoparticle aggregation on surfactant foam stability. J. Colloid Interface Sci. **511**, 365–373 (2018)

Arriaga, L.R., Drenckhan, W., Salonen, A., Rodrigues, J.A., Iniguez-Palomares, R., Rio, E., Langevin, D.: On the long-term stability of foams stabilised by mixtures of nanoparticles and oppositely charged short chain surfactants. Soft Matter **8**, 11085–11097 (2012)

Crawford, R., Ralston, J.: The influence of particle size and contact angle in mineral flotation. Int. J. Miner. Process. **23**, 1–24 (1988)

Fuerstenau, M., Jameson, G., Yoon, R.: Froth Flotation: A Century of Innovation. Society for Mining, Metallurgy, and Exploration, Littleton (2007)

Horozov, T.S.: Foams and foam films stabilised by solid particles. Curr. Opin. Colloid Interface Sci. **13**, 134–140 (2008)

Karakashev, S.I., Grozdanova, M.V.: Foams and antifoams. Adv. Colloid Interface **176–777**, 1–17 (2012)

Kim, I., Worthen, A.J., Johnston, K.P., DiCarlo, D.A., Huh, C.: Size-dependent properties of silica nanoparticles for pickering stabilization of emulsions and foams. J. Nanopart. Res. **18**, 82 (2016)

Liu, Y., Tourbin, M., Lachaize, S., Guiraud, P.: Silica nanoparticles separation from water: aggregation by cetyltrimethylammonium bromide (CTAB). Chemosph **92**, 681–687 (2013)

Nana, H., Yanfeib, L., Zhaolianga, W., Kea, L., Dia, H., Wei, L.: Foams stabilization by silica nanoparticle with cationic and anionic surfactants in column flotation: effects of particle size. J. Taiwan Inst. Chem. E. **88**, 62–69 (2018)

Scheludko, A., Toshev, B.V., Bojadijev, D.T.: Attachement of particles to a liquid surface (capillary theory of flotation). J. Chem. Soc. Faraday Trans. **72**, 2815–2828 (1976)

Subrahamanyam, T.V., Forssberg, E.: Froth stability, particle entertainment and drainage in flotation – a review. Int. J. Miner. Process. **23**, 33–53 (1988)

Takeshita, N., Paradis, L.A., Oner, D., McCarthy, T.J., Chen, W.: Simultaneous tailoring of surface topography and chemical structure for controlled wettability. Langmuir **20**, 8131–8136 (2004)

Yang, S., Pelton, R.: Nanoparticle flotation collectors II: the role of nanoparticle hydrophobicity. Langmuir **27**, 11409–11415 (2011)

Verification of the Impedance Spectroscopy Method Used in Extra Virgin Olive Oil Water Content Assessment

Łukasz Macioszek[1(✉)], Sylwia Włodarczak[2], and Ryszard Rybski[1]

[1] Institute of Metrology, Electronics and Computer Science, University of Zielona Góra, Zielona Góra, Poland
l.macioszek@imei.uz.zgora.pl
[2] Institute of Chemical Technology and Engineering, Poznan University of Technology, Poznań, Poland

Abstract. Authors have used impedance spectroscopy to assess water content in diesel fuel successfully. The lack of similar research to compare obtained results induced authors to verify the same methodology with a substance that would be free of some aspects that make diesel analysis very complicated but with similar electrical properties. Impedance of samples containing 500 ml of extra virgin olive oil (EVOO) with known water contents were examined in the frequency range of 0.02–500 Hz at a constant temperature. Obtained results were used to fit equivalent circuit elements values. Similarly to diesel, water added to EVOO caused major change in the equivalent resistance. The tests' findings presented in the chapter show that basing either on the measured impedance modulus or calculated resistance one can assess the water content in EVOO with the use of impedance spectroscopy, therefore it confirms that the methodology proposed by authors was also proper to be used with diesel fuel.

1 Introduction

Among other, research conducted at the University of Zielona Góra (Poland) Institute of Metrology, Electronics and Computer Science includes water content assessment in diesel fuel. The results obtained so far confirm the thesis that impedance spectroscopy (IS) method can be used to estimate the water content in fuel (Macioszek and Rybski 2015, 2016). Complex chemical composition, lack of repeatability of the samples and the manufacturer's confidentiality of substances added during production make diesel analysis very difficult. Very few research institutes are studying electrical properties of fuel, including its impedance. They have to be studied at refinery laboratories but the results are not publicly available. In such a case information can be only obtained via private talk with people working in those facilities. The publicly available publications are mainly focused on fossil diesel rather than modern commercially sold fuel, which contain up to 7% of Fatty Acid Methyl Esters (FAME). Therefore, the authors are unable to make any comparison of the obtained at the Institute results with other research.

© Springer Nature Switzerland AG 2020
M. Ochowiak et al. (Eds.): PAIC 2019, *Practical Aspects of Chemical Engineering*, pp. 223–230, 2020.
https://doi.org/10.1007/978-3-030-39867-5_24

Aforementioned difficulties induced authors to verify their methodology with different, yet similar mixture. From electrical point of view diesel can be considered as a dielectric (De Souza et al. 2013), therefore using the same methodology to test the water content of a similar dielectric, one should also expect reliable results. In terms of dielectric constant of about 2 very close to diesel fuel is transformer oil which is one of the greatest dielectrics available. However, water solubility limit (at 20 °C) in this oil is ultra-low [below 60 ppm (Du et al. 2001)] and therefore it could not be used to test the same methodology that was used before, as the EN 590 standard allows 0.2 g/kg of water in diesel oil. Olive oil has slightly higher dielectric constant of about 3.1 (Paranjpe and Deshpande 1935) but still this value is far away from that for the water itself (about 80). One of the commercial types of olive oils according to International Olive Council is extra virgin olive oil (EVOO). It has 0.3–2.0 g/kg of water at the moment of purchase (Ragni et al. 2013), thus its water solubility limit is very high. Karl Fischer titration (AOAC 1998) and drying by heating (ISO 662 1998) are the most commonly accepted methods of measuring water content in olive oil. The aforementioned Council limits water amount in commercially sold EVOO to 2 g/kg, as it affects the taste, stability and preservation of quality during storage (Ambrosone et al. 2007). Therefore, water in various amounts naturally occurring in olive makes this oil a good material for a comparative research. The closest to this research were so far studies of the olive's electrical properties that concerned the estimation of water content by measuring electrical capacity (Ragni et al. 2013) and olive free acidity estimation with the use of electrochemical impedance spectroscopy, thus the oil under test had to be mixed with a chemical reagent to create an emulsion to be electrically characterized (Grossi et al. 2014).

Olive oils composition varies with the altitude, cultivar, time of harvest and used extraction processes. It consists of fatty acids including oleic acid (from 70 up to 83%), linoleic acid (10–21%) and 12–20% palmitic acid (Velíšek 2013; Kunachowicz et al. 2017). Although its composition is different than diesel's, it is better known and does not contain additives that are a secret of producer, like for example some sort of conductive polymers that may be added to increase fuel conductivity and thus safety in transport (Macioszek 2016). Authors believe that the changes in EVOO properties caused by different water content addition could be detected with the use of impedance spectroscopy making water content possible to assess. That would be a step forward in confirmation of the IS method effectiveness when used to assess water content in different oils, including diesel fuel.

2 Materials and Methods

The main objective of the study was to check experimentally water addition influence on the impedance of extra virgin olive oil measured with the use of impedance spectroscopy. The olive was obtained from a grocery store, bottled in Portugal and filtered during production. It had a density of 904,40 kg/m^3 and water content of 454 mg/kg at the moment of purchase. For testing, the oil was divided into 500 ml samples containing different distilled water contents by adding known amounts of 100, 200, 300, 400, 500 and 600 µl. These volumes formed samples with the total water content of

454 (no added water), 674, 895, 1115, 1335, 1555 and 1775 mg/kg respectively. Prepared samples were stirred for one hour before and during the measurements with the use of magnetic stirrer. Although much more efficient ways to mix water and oil exist, authors consequently tried to use the same exact methodology that they have been using with the diesel oil experiments. Oil samples were examined at the temperature of 26 ± 0.5 °C.

Extra virgin olive oil samples' impedance was measured in the frequency range of 0.2–500 Hz with a 100 mV RMS voltage. An EG&G/Princeton Applied Research electrochemical impedance spectroscopy laboratory system was used. It consisted of 263A Potentiostat/Galvanostat, 5210 Lock-In Amplifier, PC computer with dedicated software and electrodes. Diagram of the system is shown in Fig. 1.

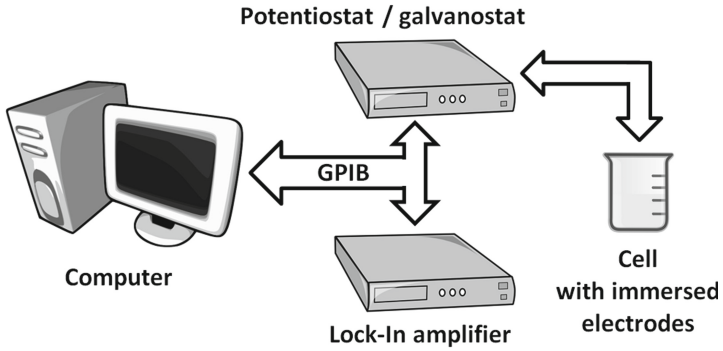

Fig. 1. Measurement system diagram

The measurements were performed with two circular parallel electrodes made of gold coated copper (shown in Fig. 2) with the surface area of 25 cm^2 each, spaced by 0.8 mm, which were immersed in olive samples (Fig. 3).

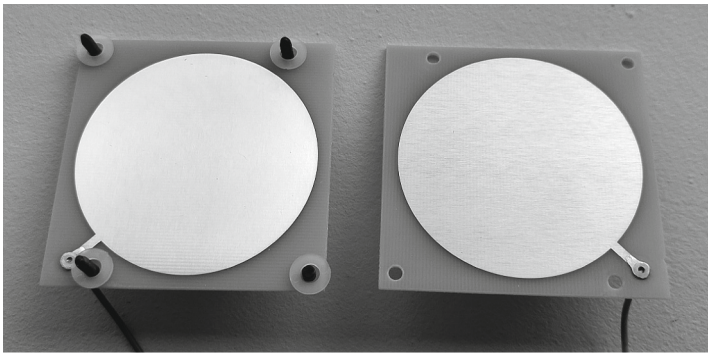

Fig. 2. Symmetrical electrodes used in experiment

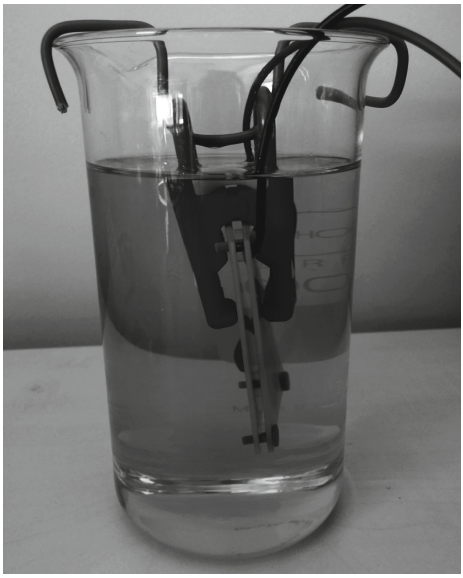

Fig. 3. Olive sample with immersed electrodes

The measured impedance in the form of:

$$Z^*(\omega) = Z'(\omega) - jZ''(\omega) \tag{1}$$

was used to fit equivalent circuit elements values. The circuit was simple (shown in Fig. 4) and contained the resistor with parallel constant phase element (CPE) and was already used elsewhere to describe diesel oil properties (De Souza et al. 2013; Macioszek and Rybski 2015).

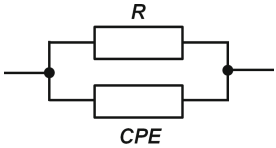

Fig. 4. Electrical equivalent circuit used in experiment

Using the constant phase element instead of ideal capacitor in the equivalent circuit has resulted in satisfactorily small fitting errors so far. Impedance of such circuit is described by:

$$Z^*(\omega) = R/[1 + QR(j\omega)^n] \tag{2}$$

where Q is the CPE admittance $1/|Z|$ at $\omega = 1$ rad/s, real n satisfies $0 \leq n \leq 1$. When $n = 1$ the CPE is identical to the capacitor.

3 Results and Discussion

Extra virgin olive oil samples consisting the aforementioned water contents from 454 up to 1775 mg/kg were examined. Figure 5 presents the Nyquist plot with measured real and imaginary impedance parts of seven olive samples. It can be seen that values form single semicircles. Small but visible differences in the shape (angle) of the right ends result from temperature fluctuations between measurements of subsequent samples. Better temperature stability would allow to obtain more similar semicircles. Nevertheless, the results obtained seemed to be sufficient for this preliminary study. Although some of the right ends of semicircles are a bit raised, a further decrease in frequency did not reveal second semicircles (not shown in Fig. 5). This raise may be associated with diffusion phenomena occurring in the dielectric when a metal electrode is being used (Ming and Toh-Ming 2012) and was not treated as a primary and dominant phenomenon. It is worth noting that the raise is more visible than with water contaminated diesel and it may correspond to significantly higher water content in olive oil.

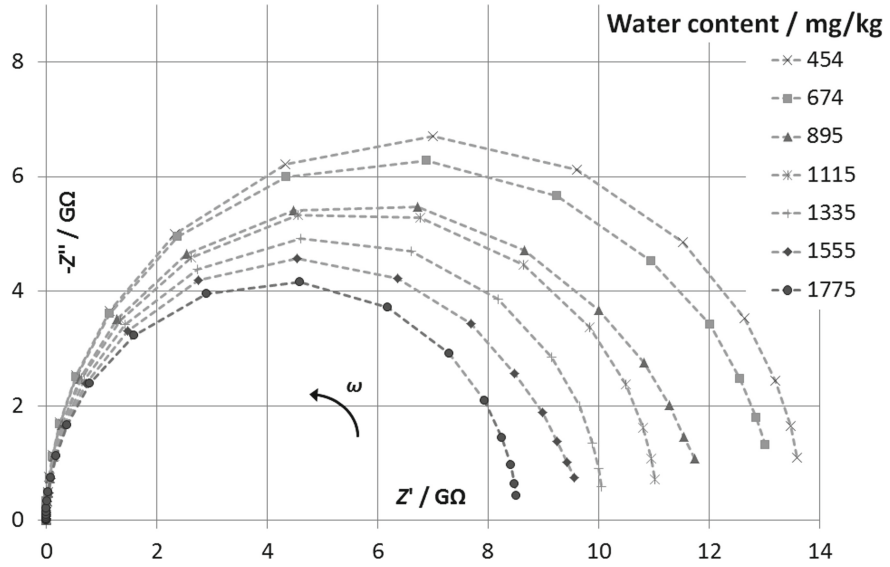

Fig. 5. Nyquist plot of examined olive oil samples

Note that with the raise of water content resistivity decreases – semicircles have smaller diameters. Such behaviour was observed in diesel fuel before. This may suggest that distilled water addition is responsible for increasing conductivity of oils significantly, thus changed impedance can be detected with the use of impedance spectroscopy. It seems that none of the additives in diesel suppressed this phenomenon confirming that measurements of diesel fuel impedance may be reasonable.

Table 1 contains fitted values of equivalent circuit elements and the corresponding χ^2 modelling errors. For calculations, the EIS Spectrum Analyser software was used (Bondarenko and Ragoisha 2005). Relative errors of fitting individual values did not exceed 1.8% in the presented samples.

Table 1. Fitted values of electrical equivalent circuit and corresponding modelling errors

Added water/% (v/v)	Total water amount/mg/kg	R/GΩ	Q/pS · s^n	n	χ^2
0	454	13.71	45.48	0.9858	0.00061
0.02	674	13.04	45.51	0.9862	0.00057
0.04	895	11.60	45.56	0.9854	0.00065
0.06	1115	11.09	45.53	0.9858	0.00060
0.08	1335	10.11	45.55	0.9859	0.00059
0.10	1555	9.47	45.45	0.9859	0.00056
0.12	1775	8.54	45.51	0.9861	0.00058

Note that the most changing value is the parallel resistivity of equivalent circuit with 13.71 GΩ calculated for the sample containing 454 mg/kg of water and only 8.54 GΩ for the 1775 mg/kg sample. Values of the constant phase element Q parameter seem not to change and oscillate around 45.5 pS · s^n. Slightly bigger, but still very small variation was observed in diesel fuel but it was hard to assess its trend and again their differences were not so significant as resistance R. Fitted value of the parameter n, the other describing the CPE, for all tested samples reaches a value of approximately 0.986. Although it is close to 1, the use of an ideal capacitor (which is the same as CPE with $n = 1$) in the equivalent circuit resulted in unacceptably large modeling errors. It is associated with a visible decrease in the semicircle centers relative to the real impedance part axis of the Nyquist plot (Fig. 5). For comparison, the measured impedance of connected in parallel resistor and capacitor on the Nyquist plot creates semicircle with center lying exactly on the real impedance part axis. Values of χ^2 modelling errors do not exceed 0.00065 for each sample tested, which confirms the good choice of the equivalent circuit.

Given the values in Table 1, it is possible to create a calibration curve based on the fitted value of resistance R. In this particular case, this curve takes the form of a straight line shown in Fig. 6. The value of R^2 correlation of 0.9904 is high and would be even higher with better temperature stability during measurements.

Some points deviations are visible, caused mainly by the temperature, which has a very significant impact on the dielectric impedance. The examined range of water content almost completely covered the most common values (0.454–1.775 g/kg as against 0.3–2 g/kg). Very complicated reactions take place in water-in-oil mixtures and their analytical description is very difficult or even impossible. Their electrochemical nature was not within the scope of this paper, therefore it was not presented.

Increasing the precision of estimating the water content of olive oil certainly requires either increasing temperature stability during measurements or taking into

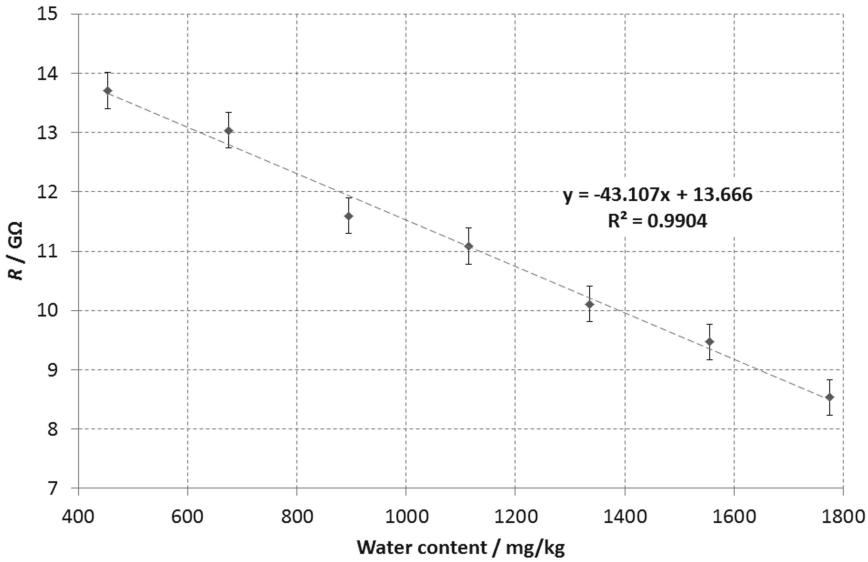

Fig. 6. Calibration curve based on the fitted value of resistance *R*

account its effect on olive impedance. Further research on the selection of the best electrode geometry and size would also be recommended. However, the results obtained seem to be sufficient for the purposes of this paper, as it was possible to detect changes in olive impedance as a function of water quantity.

4 Conclusion

In this paper, the use of impedance spectroscopy for water content in the extra virgin olive oil assessment was discussed. Experimental results were reported and analysed. The electric equivalent circuit modelling olive oil properties was proposed and eventually the calibration curve was determined based on the circuit element fitted values.

The experimental results show that impedance of extra virgin olive oil in the function of water content changes significantly, wherein the most changing value is calculated resistance which is the part of used equivalent circuit. These changes can be detected with the use of impedance spectroscopy, thus it confirms that the evaluation of water in olive oil with the use of this particular measuring methodology is possible. The proposed circuit, although it was previously used to model the properties of another oil, also in this case proved to be good for a similar range of used measurement frequencies, relatively low water concentrations, used electrodes and primarily mixture type (water-in-oil). Despite the fact that extra virgin olive oil and diesel fuel have different chemical contents, their impedance seem to react similarly to water addition. After all, from an electrical point of view both can be considered as dielectrics, therefore the tests' findings confirm that the proposed methodology may be suitable to assess water content both in olive oil and diesel fuel.

References

Ambrosone, L., Mosca, M., Ceglie, A.: Impact of edible surfactants on the oxidation of olive oil in water-in-oil emulsions. Food Hydrocoll. **21**, 1163–1171 (2007)

AOAC Official Method 984.20: Moisture in Oils and Fats. Karl Fischer Method. Official Methods of Analysis of AOAC International, 16th edn., vol. I, pp. 41–42. AOAC, Gaithersburg, MD (1998)

Bondarenko, A.S., Ragoisha, G.A.: Inverse problem in potentiodynamic electrochemical impedance spectroscopy. In: Pomerantsev, A.L. (ed.) Progress in Chemometrics Research, pp. 89–102. Nova Science Publishers, New York (2005)

De Souza, J.E., Scherer, M.D., Cáceres, J.A.S., et al.: A close dielectric spectroscopic analysis of diesel/biodiesel blends and potential dielectric approaches for biodiesel content assessment. Fuel **105**, 705–710 (2013)

Du, Y., Mamishev, A.V., Lesieutre, B.C., et al.: Moisture solubility for differently conditioned transformer oils. IEEE Trans. Dielectr. Electr. Insul. **8**, 805–811 (2001)

Grossi, M., Di Lecce, G., Gallina Toschi, T., et al.: Fast and accurate determination of olive oil acidity by electrochemical impedance spectroscopy. IEEE Sens. J. **14**, 2947–2954 (2014)

ISO 662: Animal and Vegetable Fats and Oils – Determination of Moisture and Volatile Matter Content, 2nd edn. (1998)

Kunachowicz, H., Przygoda, B., Nadolna, I., et al.: Food Composition Tables, p. 311. Wyd Lek PZWL, Warszawa (2017)

Macioszek, Ł.: Temperature influence on parameters of summer diesel fuel measured with the use of impedance spectroscopy. Przeglad Elektrotechniczny **92**, 213–216 (2016)

Macioszek, Ł., Rybski, R.: Evaluation of water content in diesel fuel using impedance spectroscopy. Paper Presented at the XXI IMEKO World Congress Measurement in Research and Industry, Czech Technical University, Prague, 30 August–4 September 2015 (2015)

Macioszek, Ł., Rybski, R.: Low-frequency dielectric spectroscopy approach to water content in winter premium diesel fuel assessment. In: Kanoun, O. (ed.) Progress Reports on Impedance Spectroscopy: Measurements, Modeling, and Application, pp. 73–80. De Gruyter, Oldenburg (2016)

Ming, H., Toh-Ming, L.: Metal-Dielectric Diffusion Processes: Fundamentals, pp. 11–20. Springer, New York (2012)

Paranjpe, G.R., Deshpande, P.Y.: Dielectric properties of some vegetable oils. Proc. Indian Acad. Sci. **1**, 880–886 (1935)

Ragni, L., Iaccheri, E., Cevoli, C., et al.: A capacitive technique to assess water content in extra virgin olive oils. J. Food Eng. **116**, 246–252 (2013)

Velíšek, J.: The Chemistry of Food. Wiley, Blackwell, Hoboken (2013)

Standards for Rainwater Discharge in Terms of Solid Pollution Separation Process in Modified Swirl Settling Tanks

Małgorzata Markowska(✉), Marek Ochowiak, Sylwia Włodarczak, and Magdalena Matuszak

Institute of Chemical Technology and Engineering, Poznan University of Technology, Poznań, Poland
malgorzata.markowska@doctorate.put.poznan.pl

Abstract. The chapter describes the standards for rainwater discharge to the environment, it is discussed the legislation and paid attention to economic issues. Also the review aims to examine requirement of aquaculture solids and petroleum management strategies. Focused on defining the maximum concentration values of the most important pollutants present in the runoff water and the conditions which must be satisfied in the selection of the separators. Reference was also innovative solutions in terms of separators design and research on improving the efficiency of pollution reduction in liquid separators, compared to commercial solutions. The study was focused on relations between purification efficiency and dispersion medium viscosity. Conclusion was the assortment of the analyzed constructions to be more productive. It is known that for light fraction separation with increasing continuous phase's viscosity, highest purification efficiency is gained from construction with relocated baffle towards the outlet from the separator.

1 Introduction

The accessibility of water resources is an essential requirement to sustain life. It is indispensable for the most aspects of human activity, that also includes industry. Both quality and quantity of useable catchment impact the health and safety of population, economic and industrial development, non-production segments (like tourism) and condition of natural environment (Bąk et al. 2010; Zanotti et al. 2019). Any kind of rainwater pollution should be under an appropriate supervision of valid decrees. They impose reduction of adverse systems and substances in rainwater flow guided to manifold types of sectors after proper processing (pre-treatment, thickening, disinfection etc.) (Abdullah 2016; Recko 2018). Presently the public awareness of unarranged sewage disposal hazardous is rising. The current rules and regulations entail duty of wastewater treatment from cities, industrial areas, transportation depots, etc. (Królikowska 2011; Fashae et al. 2019).

The aim of this paper is to bring economic and legal aspects of rainwater treatment closer to the reader. Pointing the current ecological problems and possible engineer solutions provides fresh look at present natural environment condition.

© Springer Nature Switzerland AG 2020
M. Ochowiak et al. (Eds.): PAIC 2019, *Practical Aspects of Chemical Engineering*, pp. 231–240, 2020.
https://doi.org/10.1007/978-3-030-39867-5_25

2 Legislation and Economic Issues of the Rainwater Treatment in Poland

Management processes consist of following elements: manufacturing, division, exchange and consumption. Existence of connections between firms based on cause-and-effect relationship, creates complete chain of environment aggravating process (Marciniak 2013). These relations are presented in the scheme in Fig. 1. The environmental abilities of absorption and regeneration are limited and nowadays even insufficient for constant development of anthropogenic factors. That is why it is an obligation to obey fundamental laws and ecological principles (Królikowska 2011; Marciniak 2013). Manufacturing as a production process of public goods proving apposite needs, results in increasing consumption. In both cases wastes still arise. Significant part of them can be recycled. Rest is undeveloped and has a negative impact on the environment (Marciniak 2013).

The amendments of legislation in European Union in last few years led to improvement and development of Polish legal provisions about water management and environmental protection. The demand is to unequivocally establish wastewater as an item of cities sustainability using methods that mimic flow and rain retention in natural conditions. There is also required expansion, maintenance and modernization of existing sewerage, and also construction of the new ones (Królikowska 2011).

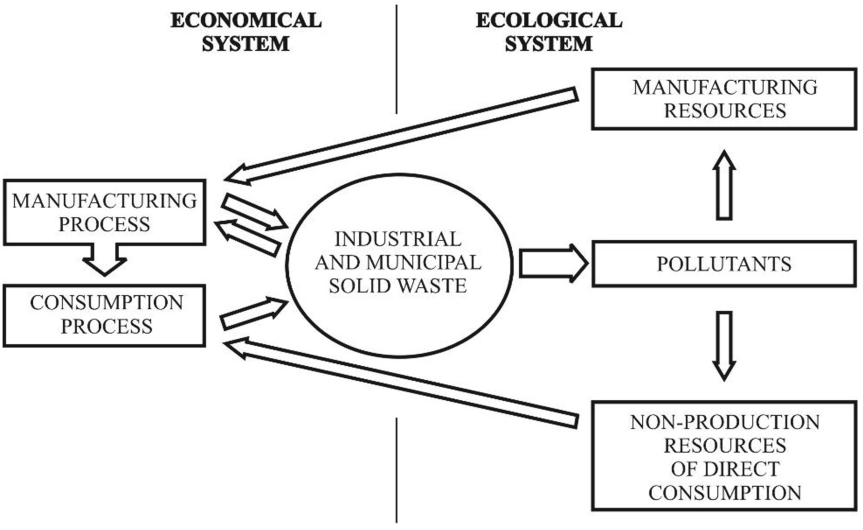

Fig. 1. The relations between economical and ecological systems based on Marciniak (2013).

The sustainable development is a keystone in EU regulations. The environmental protection law area includes over 70 directives and over 20 decrees. This attitude is going to suppress the negative influence of traditional methods applied in wastewater

management, and also rehabilitate it as much as possible (Królikowska 2011). Few of the primary rules are:

- the principle of application the best available technology,
- the principle of knowable information about environment's condition
- the principle about how to prevent contamination or dispose of it at the source
- the principle of financial responsibility of contaminant emitter.

In Poland the requirements that must be fulfilled at draining sewage to water or soil and concerning substances particularly harmful for water environment, are regulated by the Ordinance of Minister of Environment of 18th November 2014 (Dz.U. z 2014 r. nr 023, poz. 1800). Additionally, two Laws can be distinguished: Water Law Act of 18th July 2001 and Environmental Protection Law Act of 27th April 2001 (Królikowska 2011; Sawicka-Siarkiewicz 2011; Bąk et al. 2012). First one regulates methods of water management according to sustainable development, it defines the instruments applied at that matter, hydrological documentation and waters proprietorship. Second Law pertains to obligations, programs and requirements of registration, report or notification about operations within environmental protection (Dz.U. nr 62, poz. 627 z późn. zm.; Dz.U. nr 115, poz. 1229, z późn. zm.). In case of groundwater pollution by oil and petroleum substances the ordinance of Minister of Environment of 23rd July 2008 in matter of criterion and groundwater assessment method and Act 30th May 2014 (Dz. U. 2014, poz. 850) as an expletive regulation are applied. Surface waters are regulated by decree of Minister of Environment of 21st July 2016 in matters of classification methods of uniform surface waters sections condition and qualitative environmental standards for priority substances (Dz. U. 2016, poz. 1187). Moreover, there is applied the Chemical Hazard Identification and Assessment Tool (CHIAT) for chemical danger assessment, that had the desired result of selecting compounds of supreme environmental threat (Sakson et al. 2014). Preparation of priority lists of wastewater pollutants took five steps: determination of pollution root's and characterization of affected area, identification of problems and risk, threat evaluation, and finally selection of substances by group of experts. The selection is based on i.a. retention in natural surroundings (decay vulnerability, bioaccumulation, toxicity), effect on living organisms (i.a. carcinogenic and mutagenic potential, reproduction and hormonal disorder, allergy) as well as technical and esthetic issues (precipitation, smell) (Eriksson et al. 2007; Sakson et al. 2014).

2.1 Type and Contents of Pollution in Rainwater Run-off

Main contaminations identified in rainwater run-off from roads and involved facilities/areas are: suspensions, fat, oil and grease (FOG), petroleum hydrocarbons, other substances extracted by petroleum ether (SEPE), heavy metals (lead, zinc, copper, cadmium, chromium, nickel, etc.), organic and inorganic compounds that can be defined by total and organic carbon content and also by biochemical (BOD) and chemical (COD) oxygen demand, chlorides, sodium, magnesium, calcium, thick floating contaminants, biogenic substances (nitrogen, phosphorus, potassium), micro-contaminants (arenes) (Królikowska 2011; Bąk et al. 2012; Abdullah 2016; Fashae et al.2019; Dz.U. z 2014 r. nr 023, poz. 1800).

Currently substances subjected with special attention are petroleum hydrocarbons. It is a group of compounds that can be distinguished fuel, solvents, resins, vaselines, paraffins, naphthenes and arenes mixture (Dz.U. z 2014 r. nr 023, poz. 1800). They are characterized as non-polar, lipophilic and very slightly soluble in water. Furthermore, if petroleum hydrocarbons are emitted to the environment it causes formation of thin layer on water surface and impedes gas exchange or disturbs biological balance in natural reservoirs (Lazim et al. 2019; Dz. U. 2016, poz. 1187). Among them few are harmful in particular: benzene, naphthalene, fluoranthene, benzo(a)pyrene, benzo(a) fluoranthene, benzo(k)fluoranthene, benzo(ghi)perylene and indene(1,2,3-cd)pyrene (Dz. U. 2016, poz. 1187; Włodarczyk-Makuła 2016).

Distinctly it is difficult to provide an accurate value of contamination due to reliance to geographical localization, climatic zone, season or national economic. Table 1 presents few selected rainwater pollutants depending on the data source.

Table 1. Analyzed concentration of selected pollutants in rainwater flow according to research source.

Data source	Brombach et al. 2002	Bąk et al. 2012	Langeveld et al. 2012	Sakson et al. 2014
Type of pollutant	Concentration value range [mg/L]			
Suspension (TSS)	29–1535	144–272	11–874	11–1450
Lead (Pb)	0.007–2.408	0.096–1.405	0.01–0.129	0.021–2.458
Cadmium (Cd)	0.00046–0.030	0.007–0.090	0.0003–0.024	0.0002–0.008
Zink (Zn)	0.024–3.563	0.107–0.858	0.130–0.520	0.247–12.357
Petroleum hydrocarbons	no data	no data	no data	0.15–7.25

As shown in the table above, contamination concentration reaches different values and it is hard to lay down the average characteristic of rainwater run-off. There are many factors that effect on quality and properties of sewage: way of management and formation of catchment area, type of roads surface and how are they utilized and supported, class and intensity of traffic, atmosphere contamination, specific of precipitation (rain, snow, hail, break length between ones, intensity and time of falling) (Królikowska 2011).

2.2 Permissible Pollution Concentration Values in Rainwater Run-off in Order to Legal Regulations

While effectuating rainwater flow in sealed surface it is necessary to provide for legal regulations and normative prescriptions. Permissible concentration of contaminants in wastewaters that can be drained either to surface waters or soil, derived from industrial and deposit areas, transportation bases, docks, airports, cities, railways, national, regional and district roads class G, car parks over 0.1 ha, storage and fuel distribution facilities is regulated by the Ordinance of Minister of Environment of 18th November 2014 (Dz.U. z 2014 r. nr 023, poz. 1800) (Sawicka-Siarkiewicz 2011). According to

the law maximum value for total suspended solids (TSS) is 100 mg/L, and for petroleum hydrocarbons is 15 mg/L. In case of run-off from storage and fuel distribution facilities, mentioned regulations are in effect for precipitation with frequency once a year and 15 min long but not less than wastewaters drained from 1 ha of sealed surface from fall flow of 77 L per second (Sawicka-Siarkiewicz 2011; Bąk et al. 2012; Sakson et al. 2014; Rećko 2018). Earlier mentioned petroleum hydrocarbons are strictly determined in matter of maximum concentration in sewage. Table 2 shows provision of ministerial ordinance about surface waters.

Table 2. Permissible concentration of petroleum hydrocarbons in surface waters according to (Dz. U. 2016, poz. 1187)

Indicator	Uniform waters sections (stream, brook, river, canal, lake, reservoirs)	Uniform temporary and coastal waters sections
	Maximum concentration mg/L$\times$ 10^3	
Benzene	50	50
Naphthalene	2.4	1.2
Fluoranthene	1	1
Benzo(a)pyrene	0.1	0.01
Bezno(b)fluoranthene	0.03	0.03
Benzo(k)fluoranthene	0.03	0.03
Benzo(ghi)perylene	0.002	0.002
Indene(1,2,3-cd) pyrene	0.002	0.002

With reference to groundwater valid regulation is the ordinance about criterions and assessment methods of their condition (Dz. U. nr 143, poz. 896). Following compounds are mentioned: BTX (volatile aromatic hydrocarbons as benzene, toluene, xylenes) benzo(a)pyrene and PAH (polycyclic aromatic hydrocarbons) (Włodarczyk-Makuła 2016).

3 Assortment and Legally Preconditions of the Liquid Separators Characteristic in Poland

Reduction of suspensions in rainwater flow is performed with sedimentation phenomenon and takes place in retention and gravitational devices. In case of petroleum hydrocarbons the separation is caused by flotation processes and buoyant force (Wu et al. 2010; Królikowska 2011; Sawicka-Siarkiewicz 2011). Fundamental rule is to use the differences in density between oil and water phase. Oil is collecting in top layers of separator and after that it is disposed of. Application of devices configured in a way to stop arising excessive turbulences gives satisfying results and supports oil drops coalescence (Rećko 2018).

Separators practiced in rainwater treatment must comply with adequate legal regulations. Reference standard number PN-S-02204:1997 contains the information about

drainage and depurative road equipment. It is defined that drainage units must be characterized with specific technical requirements in the matter of planning, design, construction and proper usage. In addition, basic ecological requirements are discussed including roads desiccating and beside that, calculative process for control reasons. To engineer petroleum hydrocarbons separator it is recommended to comply with the PN-EN 858-1:2005 + A1:2007 and PN-EN 858-2:2005 standards and also technological approval from the Institute of Environment Protection (Sawicka-Siarkiewicz 2011; Rećko 2018). Part one of PN-EN 858:2005 defines rules about product design, usage and analysis ability, marking and quality control. Part two characterizes choice of nominal dimensions, installing, exploitation and service. Both pertain to light fluids classifier (for substances with weight density below 0,95 g/cm^3) (Rećko 2018). Heavy pollutant separator, so-called settling tanks, should carry out regulations about volume criterion defined in the PN-EN 858-2:2005 standard. Volume values cannot be equal less than 100, 200 or 300 times of separators nominal capacity (Sawicka-Siarkiewicz 2011).

3.1 Suspension Separators

Settling tanks are applied in order to separate suspended solids. They are characterized by simple construction and often massive sizes. The reason is a needful long way of solid particles falling to separate phases. Settlers area is determined as a proportion of rainwater volumetric flow and permissible maximum hydraulic load (Wu et al. 2010; Sawicka-Siarkiewicz 2011). Technological assuming is that on every 1 m^3/h of liquid flow the necessity is at least 0.24 m^2 of active area. This allows to sustain over 50% separator efficiency, which is measured as a performance of stopping suspension particles in the device. However, there are many factors effecting on the sedimentation efficiency as particles' dimensions, shape and density, suspension concentration or continuous phase's temperature (Królikowska 2011; Sawicka-Siarkiewicz 2011). Recently, new construction of settling tank which keeps remote gross covered area arrangement and is characterized by vortex movement extending particles falling pathway has been applied. They gain comparable results with 2 to 5 times greater hydraulic load (Królikowska 2011).

3.2 Petroleum Separators

Separation of petroleum hydrocarbons is connected to application of specific constructional elements to create chamber for blocking out light fraction inside the tank. This process can be affected gravitationally by flotation or it can be supported by coalescence, where microparticles of oil substance merge together into larger drops (Sawicka-Siarkiewicz 2011; Rećko 2018). Efficiency of separation increases by applying coalescence frustums such as polyurethane sponges or batches with honeycomb structure (Rećko 2018; Lazim et al. 2019). The basal work parameters are as follows: nominal capacity as flow volume in time unit, materials and equipment of the tank, content of storage of light fraction and allowable thickness of oil substance layer inside the tank (Sawicka-Siarkiewicz 2011).

3.3 Other Concepts of Pollution Separators

Nowadays liquid separators are being improved and developed in order to create purifying constructions that can unite both sedimentation and petroleum tanks' characteristic. The reasons are also energy and management area savings.

One of the currently analysis pertained to the relation of continuous phase's viscosity on precipitation process of pollutant particles with lesser density than the dispersion medium. The aim of the study was to determine the effect of separator's construction on separation process efficiency and also to characterize the liquid damming and flow resistance inside the tank. It conditions capacitive and hydraulic capabilities of separators. Ochowiak et al. (2017) presented modified settling tanks designed to separate heavy fraction from the water stream. This concept was developed on chosen constructions in order to improve existing separators.

Two settling tanks constructions were operated (Fig. 2) and they were characterized by total height $H = 0.69$ m, internal diameter $D = 0.19$ m, inlet and outlet lines internal diameter $d = 0.03$ m, escape from inlet line height $h_1 = 0.2$ m and from the outlet $h_2 = 0.4$ m, baffle hang height $h_b = 0.3$ m. These constructions differed in baffle location in reference to tank's axle: $l = 0$ m or $l = 0.055$ m (half distance from the middle and the outlet of the separator). The analysis was performed in room temperature 20°C. Hydraulic load range set for the analysis was from 20 to 57 $m^3/(m^2 \cdot h)$. Dispersion mediums were water from the pipeline and aqueous glycerol solutions with percentage weight concentration 59% (11.5 cP), 55% (9.4 cP), 50% (6.8 cP), 41% (4.2 cP) and 24% (2 cP). Research material was granulated low-density polyethylene with density 0.928 g/cm^3 and particles diameter $d_s > 0.6$ mm and 0.5–0.6 mm.

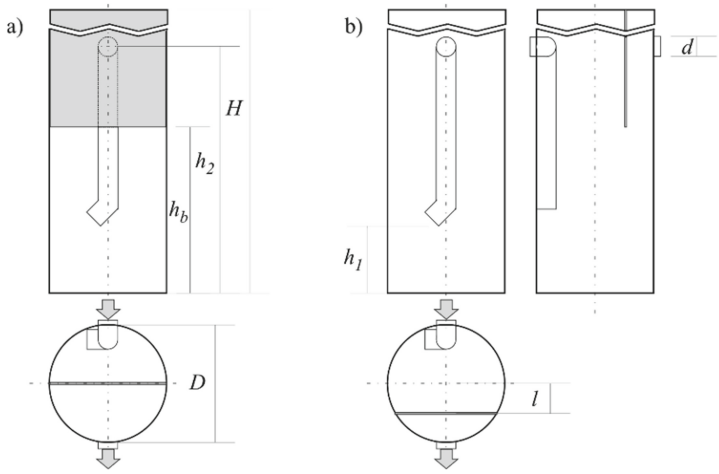

Fig. 2. Technical diagram of analyzed modified settling tanks characterized by baffle: **a** located in tank's axle, **b** relocated in the half way between tank's axle and outlet

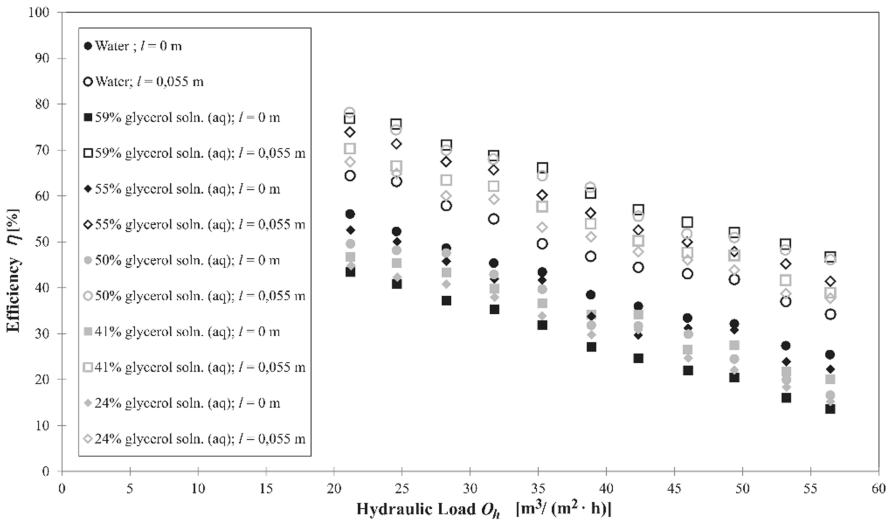

Fig. 3. Settling tanks' liquid stream purifying efficiency from light solid pollutant particles with size over 0.6 mm in dependence of hydraulic load

Selected material was supposed to represent pollutant of lower density than continuous phase, for example: dust, ash, organic remnants from vegetation, litter from cigarettes and food packages.

The study result was the choice of construction characterized by the highest efficiency of light fraction separation in relation to liquid's viscosity. It was determined that the settling tank with relocated baffle achieved the highest performance among studied with increasing continuous phase's viscosity (Fig. 3), which valued maximum 80%. This result was connected with larger volume of inlet chamber where light fraction was ejected up by the liquid and then stopped by the baffle. Second construction with baffle located in the tank's axle was distinguished by opposite relation with liquid's viscosity. Arguably, the reason was that glycerol solution were characterized by lesser hydraulic resistance so it was easier for the liquid flow to dragged out solid particle from the separator.

4 Summary

Gravity separator tanks are used to separate solids and oil from water in treatment units. Achieving the maximum removal efficiency is related to the construction that is chosen for processing. It is appertained to absolutely remember about purification the wastewater flow before the drainage to the environment. It is based on application of purification devices with diversified performance. In matter of assortment the qualified information should be presented by the designer but it is also suitably to be aware of the available possibilities and what should be complied with the professional requirements. Fundamental rules in that case are: learn about current state of knowledge related to

obligatory regulations on wastewater purification process, define quantity and quality of sewage flow drained from the catchment area, choose the appropriate type of separator based on the technical specification, abide installation and device's exploitation provisions. Continuation of studies performed on separators seems reasonable owing to the fact that it could bring more satisfying results with similar labor input.

Acknowledgments. This work was supported by the Polish Ministry of Science and Higher Education (03/32/SBAD/0902).

References

Abdullah, R., Hussein, H.A., Sald, M.A.M.: Experimental and computational investigations of baffle location effect on the performance of oil and water separator tanks. In: MATEC Web of Conferences, vol. 47, p. 05002 (2016)

Bąk, Ł., Górski, J., Górska, K., Szeląg, B.: Zawartość zawiesin i metali ciężkich w wybranych falach ścieków deszczowych w zlewni miejskiej. Ochrona Środowiska **34**(2), 49–52 (2012)

Brombach, H., Fuchs, S.: Datenpool gemessener Verschmutzungskonzentrationen von Trocken– und Regenwetterabflüssen in Misch– und Trennkanalisationene. Abschlussbericht Langfassung, ATV-DVWK (2002)

Eriksson, E., Baun, A., Scholes, L., Ledin, A., Ahlman, S., Revitt, M., Noutsopolous, C., Mikkelsen, P.S.: Selected stormwater priority pollutants – a European perspective. Sci. Total Environ. **383**, 41–51 (2007)

Fashae, O.A., Ayorinde, H.A., Olusola, A.O., Obateru, R.O.: Landuse and surface water quality in an emerging urban city. Appl. Water Sci. **9**, 25 (2019)

Królikowska, J.: Swirl chamber equipment applied in sewage networks for desoreasing suspended particle load in stormwater sewage. Inżynieria Ekologiczna **26**, 156–170 (2011)

Langeveld, J.G., Liefting, H.J., Boogaard, F.C.: Uncertainties of stormwater characteristics and removal rates of stormwater treatment facilities: Implication for stormwater handling. Water Res. **46**, 6868–6880 (2012)

Lazim, A.M., Musbah, D.L., Chin, C.C., Abdullah, I., Mustapa, M.H.A., Azfaralariff, A.: Oil removal from water Surface using reusable and absorptive foams via simple fabrication of liquid natural rubber (LNR). Polym. Test. **73**, 39–50 (2019)

Marciniak, S., Nauk, R.: Makro- i mikroekonomia: Podstawowe problem współczesności. PWN, Warszawa (2013)

Ochowiak, M., Matuszak, M., Włodarczak, S., Ancukiewicz, M.: The modified swirl sedimentation tanks for water purification. J. Environ. Manage. **189**, 22–28 (2017)

PN-EN 858-1:2005/A1:2007 Instalacje oddzielaczy cieczy lekkich (np. olej i benzyna) – Część 1: Zasady projektowania, właściwości użytkowe i badania, znakowanie i sterowanie jakością

PN-EN 858-2:2005 Instalacje oddzielaczy cieczy lekkich (np. olej i benzyna) – Część 2: Dobór wielkości nominalnych, instalowanie, użytkowanie i eksploatacja

PN-S-02204:1997 Drogi samochodowe – Odwodnienie dróg

Rećko, K.: The separator for oil-derived substances - an important element to the wastewater discharge system at a station for dismantling of exploited vehicles. Autobusy – Technika, Eksploatacja, Systemy Transportowe **19**(9), 66–70 (2018)

Rozporządzenie Ministra Środowiska z dnia 23 lipca 2008 r. w sprawie kryteriów i sposobu oceny stanu wód podziemnych (Dz. U. nr 143, poz. 896)

Rozporządzenie Ministra Środowiska z dnia 18 listopada 2014 r. w sprawie warunków, jakie należy spełnić przy wprowadzaniu ścieków do wód lub do ziemi, oraz w sprawie substancji szczególnie szkodliwych dla środowiska wodnego (Dz.U. z 2014 r. nr 023, poz. 1800)

Rozporządzenie Ministra Środowiska z dnia 21 lipca 2016 r. w sprawie sposobu klasyfikacji stanu jednolitych części wód powierzchniowych oraz środowiskowych norm jakości dla substancji priorytetowych (Dz. U. 2016, poz. 1187)

Sakson, G., Zawilski, M., Badowska, E., Brzezińska, A.: Stromwater pollution as the basis of choice the method of their management. JCEEA **61**, 253–264 (2014)

Sawicka-Siarkiewicz, H.: Storm-water treatment in oil-separators and sedimentation tanks in the context of the legal acts and regulations. Sci. Rev. Eng. Environ. Sci. **52**, 140–152 (2011)

Ustawa Prawo Ochrony Środowiska z dnia 27 kwietnia 2001 r. (Dz.U. nr 62, poz. 627 z późn. zm.)

Ustawa Prawo Wodne z dnia 18 lipca 2001 r. (Dz.U. nr 115, poz. 1229, z późn. zm.)

Ustawa z dnia 30 maja 2014 r. o zmianie ustawy - Prawo wodne oraz niektórych innych ustaw (Dz. U. 2014, poz. 850)

Włodarczyk-Makuła, M.: Zagrożenie zanieczyszczenia środowiska wodnego związkami ropopochodnymi. LAB Laboratoria, Aparatura, Badania **21**(1), 12–16 (2016)

Wu, J., He, C.: Experimental and modeling investigation of sewage solids sedimentation based on particle size distribution and fractal dimension. Int. J. Environ. Sci. Technol. **7**(1), 37–46 (2010)

Zanotti, C., Rotiroti, M., Fumagalli, L., Stefania, G.A., Canonaco, F., Stefenelli, G., Prevot, A.S. H., Leoni, B., Bonomi, T.: Groundwater and surface water quality characterization through positive matrix factorization combined with GIS approach. Water Res. **159**, 122–134 (2019)

Efficiency of Co-substrates Application and Thermal Processing in the Field of Methane Fermentation of the Distillers Grains

Natalia Mioduszewska[1], Mariusz Adamski[1(✉)], and Waldemar Szaferski[2]

[1] Institute of Biosystems Engineering, Poznan University of Life Sciences, Poznan, Poland
mariusz.adamski@up.poznan.pl
[2] Institute of Chemical Technology and Engineering, Faculty of Chemical Technology, Poznan University of Technology, Poznan, Poland

Abstract. The aim of the work is to consider the influence of thermal processing and dosing of target components in order to maintain optimal parameters of the methanation process of the distillers grains and optimal pH level. Molasses and aluminium phosphate were indicated as intentional supplements. The purpose of the additives is to increase the alkalinity buffer in terms of acidogenesis and hydrolysis. In order to achieve the aim of the study, the following methods were used: methodology according to DIN 38 414 s8 and methodological guidelines related to the determination of physical and chemical parameters of the distillery brew, target additives and inoculum. In the study the following determination was made: volume of biogas and concentrations of biogas components such as CH_4, CO_2, H_2S, O_2. The yield of biogas was compared with reference to: mixtures of distillers grains, not thermally processed and thermally processed in the presence of the indicated ingredients. The thermal method of distillers grains processing allowed to accelerate the hydrolysis process and changed the pH of the substrate only slightly. Distillers grains not thermally treated showed a biogas yield that was about 67% higher than the unprocessed distillers grains. The best results of the pH stabilization process for the distillers grains were obtained for the mixture with molasses. The biogas yield of the mixture has increased by 2.7 times in relation to the heated WDGS.

1 Introduction

Distillers grains together with soluble substances (WDGS) is a by-product of the production of ethyl alcohol in the alcoholic fermentation process (Bhoite, Vaidya 2018). Wet distillers grains with solubles (WDGS) and dried distillers grains (DDGS) are used as high-protein feeds (Laurinavichene et al. 2018).

WDGS contains only 5–8% dry matter, stored in humid rooms it quickly moulds and is useful as feed for short periods of time. Drying or ensilaging is the perfect way to

© Springer Nature Switzerland AG 2020
M. Ochowiak et al. (Eds.): PAIC 2019, *Practical Aspects of Chemical Engineering*, pp. 241–251, 2020.
https://doi.org/10.1007/978-3-030-39867-5_26

conserve distillers grains. The liquid fraction, rich in vitamins, minerals and fat, is concentrated into a syrup that resembles molasses.

The chemical composition, physical properties and nutritional value of dried distillers grains (DDGS) depend on the alcoholic fermentation feedstock and the drying and granulation temperatures. Too high drying temperature and medium pressure granulation contribute to the decomposition of sugars and protein, which results in carbonization and reduction of nutrients in relation to unprocessed substrate. Under the influence of temperature, irreversible protein denaturation may occur.

Raw and wet distillers grains contains a significant amount of energy, the average is 2.25 Mcal/kg (Bell et al. 2019).

The distiller grains can be classified according to the substrate of the fermentation process into starch and sugar brew. The fermentation process causes an imbalance in the main nutrients: nitrogen, phosphorus and potassium. The problem is that the phosphorus content is lower than the content of nitrogen and potassium.

The use of distiller grains as fertilizer means that the lack of nutrients must be supplemented by the use of mineral fertilizers. An important factor that hinders the use of raw distillery stock as a fertilizer is the low dry matter content.

Another problem is the low pH. Composting with the addition of targeted structural components is a technology that can allow to change unfavourable physical properties and balance nutrients (Bustamantea et al. 2008). Composting means the release of biological heat and the emission of heat results in the dehydration of the distiller grains (Semitela et al. 2019).

Therefore, thermal processing appears in many technologies related to the management of biomass after the alcoholic fermentation process (Basu et al. 2015; Trajer et al. 2015).

Biological stabilisation of biomass in anaerobic processes also allows modification of physical and chemical properties (Pant, Adholeya 2007). Methane fermentation requires precisely defined process parameters such as anaerobic conditions, temperature, mixing, moisture level, nutrient content and balance, absence of inhibitors (Durczak et al. 2017).

The availability of plant substrate nutrients is limited by the levels of raw fibre, lignin, cellulose and hemicellulose (Sakdaronnarong et al. 2015; Adamski et al. 2017).

Liquid or semi-liquid substrates are suitable for the methane fermentation process (Iglinski, B. et al. 2012). This results from the possibility of using different mixing techniques such as mechanical, hydraulic and pneumatic mixers (Mitkowski et al. 2018).

2 Aim of the Study

Due to the physical and chemical properties of the distillers grains, it is possible to connect the method of applying intentional additives and the thermal method with the process of anaerobic stabilisation.

The aim of the study is to analyze the influence of thermal processing and dosing of target components such as molasses and aluminum phosphate on maintaining optimal parameters of the anaerobic stabilization process.

Two research assumptions have been formulated and tested: thermal processing of the distillers grains will increase the pH and target components with a high pH (pH > 7) will increase the biogas yield. A range of detailed activities were formulated to achieve the objective of the work.

- Acquisition of the distillers grains together with the description of physical and chemical parameters.
- Application of the thermal processing technique for distillers grains.
- A change of the ph-value of the distillers grains through the use of additives in the form of molasses and aluminium phosphate.
- Testing of biogas yield of the selected distillers grains samples on a laboratory scale and using the methodology of DIN 38414 p.8.

3 Materials and Methods

Potato based distillers grains was used for the study. Characteristic parameters have been presented in Table 1.

Table 1. Physical and chemical parameters of the wet distillers grains (WDGS)

	Parameter	Unit of Measure	Value
1.	pH before thermal processing	pH	3.68
2.	Dry Matter (DM)	%	12.67
3.	Organic Dry Matter (ODM)	%	94.39
4.	Nitrogen xpressed in protein	%	2.80
5.	Crude Fat	%	<1.00
6.	Starch	%	<1.20
7.	Sugar calculated as sucrose	%	<1.00
8.	Sodium	$mg \cdot kg^{-1}$	68
9.	Potassium	%	<0.135
10.	Phosphorus	%	<0.10
11	Nitrate and nitrite content	$mg \cdot kg^{-1}$	15.8

In order to produce mixtures for the methane fermentation process, 4.5% m/m aqueous Aluminium phosphate solution and sugar-beet molasses were used. Both intentional substrates were doped to the distillers grains in order to obtain the initial pH of the mixture at the level of 7.45.

The process of thermal processing of the distillers grains (WDGS) was carried out at atmospheric pressure. The distillers (WDGS) was adjusted to a temperature close to boiling point and then the temperature was maintained with observation of substrate pH changes. The condensate was returned to the process (Fig. 1).

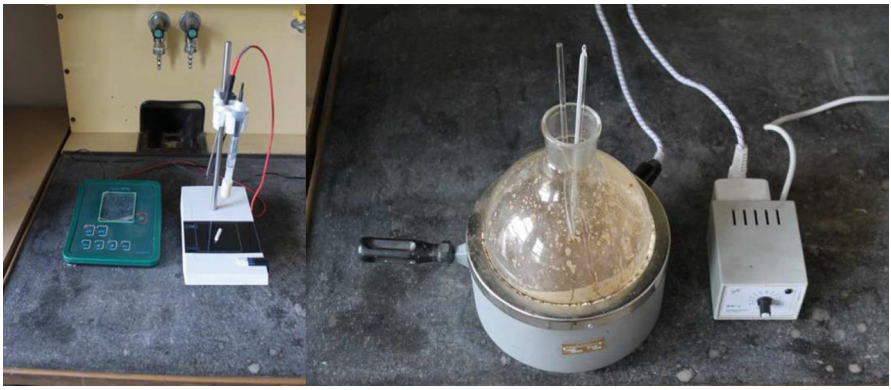

Fig. 1. Thermal processing and pH measurement stand

In order to achieve the aim of the study, the methodology of biogas yield testing (DIN 38 414 s.8, 2012) and methodological instructions related to the determination of physical and chemical parameters of the distillers grains, targeted additives and inoculum were used (KTBL Heft 84, 2009).

In the research, the biogas component gas detection system (CH_4, CO_2, H_2S, O_2) was used.

The research was carried out on a test stand consisting of a reaction chamber with a capacity of 1 dm^3 and an eudiometric tank storing process gases with a capacity of 1.2 dm^3. Biogas productivity studies were conducted in three repetitions (Fig. 2).

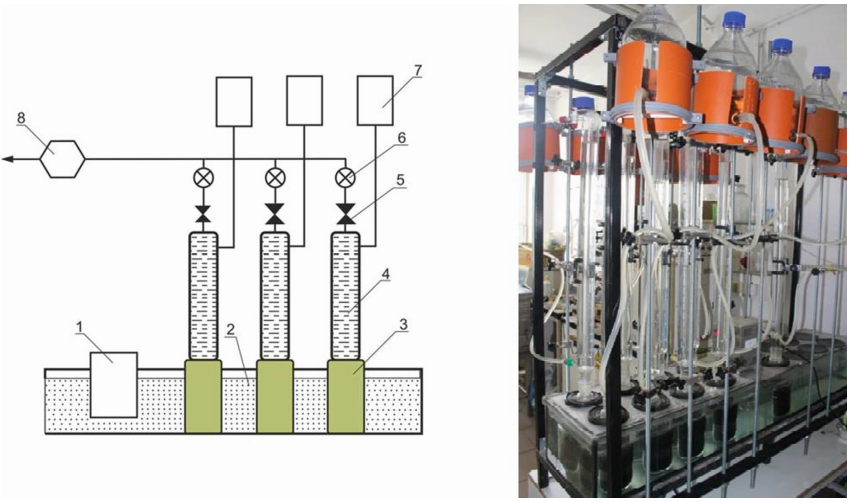

Fig. 2. Research station scheme for methane fermentation process: 1. water heater with temperature regulator, 2. glass water jacket, 3. reactors with a capacity of 1 dm^3, 4. cylindrical tanks in which gas is stored with a capacity of 1.2 dm^3, 5. shut-off valve, 6. gas flow meter, 7. equalizing tank, 8. measuring station: gas analyzer AG-BIO by Alter, pH-meter, CP-215 by Elmetron, two temperature sensors, multimeter CX 401 by Elmetron

4 Results

Thermal processing was based on heating the distillery to boiling point and keeping it boiling for specific periods of time (15 min, 30 min, 45 min and 60 min). The result of the thermal conversion process was an increase in pH by 0.1. The heating process of the wet distillers grains is shown in Fig. 3.

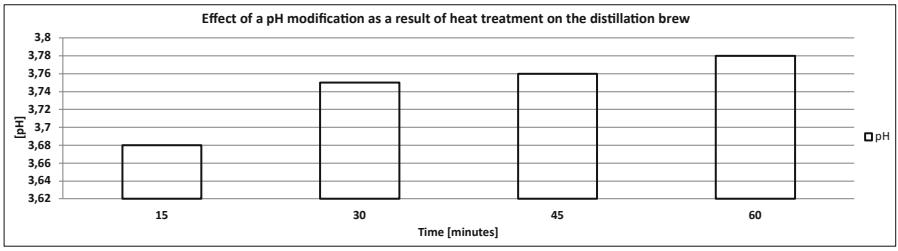

Fig. 3. Result of the pH thermal modification for WDGS sample

Using raw and thermally processed distillers grains (WDGS), new test mixtures were made. The behavior of four standard mixtures was studied: M1 - with heated WDGS without additives, M2 - with heated WDGS with aluminium phosphate, M3 - with heated WDGS with molasses, M4 - with unheated WDGS without additives. The composition of the blends has been presented in tabular form (Table 2).

Table 2. Initial composition of mixtures for biogas production process

Mixture	Dry matter	Ratio	Amount of dry matter	Fresh matter	Organic dry matter	Organic dry matter
M1	[% m/m]	[%]	[g]	[g]	[%]	[g]
WDGS heated	9.32	25	11.650	125.00	92.35	10.759
Inoculation	4.42	75	17.010	384.90	59.56	10.133
Total Moisture	94.38					
Total Dry Matter	5.62		28.660	509.90		20.893
M2	[% m/m]	[%]	[g]	[g]	[%]	[g]
WDGS heated	9.32	23	11.650	125.00	92.35	10.759
Inoculation	4.42	72	16.973	384.00	59.56	10.110
Alum. Phosphate	51.21	5	12.579	24.56	5.10	0.642
Total Moisture	92.28					
Total Dry Matter	7.72		41.202	533.56		27.158
M3	[% m/m]	[%]	[g]	[g]	[%]	[g]
WDGS heated	9.32	23	11.650	125.00	92.35	10.759
Inoculation	4.42	72	16.973	384.00	59.56	10.110

(*continued*)

Table 2. (*continued*)

Mixture	Dry matter	Ratio	Amount of dry matter	Fresh matter	Organic dry matter	Organic dry matter
Molasses	82.14	5	20.535	25.00	87.45	17.958
Total Moisture	90.79					
Total Dry Matter	9.21		49.158	534.00		38.827
M4	[% m/m]	[%]	[g]	[g]	[%]	[g]
WDGS	12.67	25	15.838	125.00	94.39	14.950
Inoculation	4.42	75	16.973	384.00	59.56	10.110
Total Moisture						
Total Dry Mass			32.810	509.00		25.059

Mixing during the fermentation process was carried out with the use of author's pneumatic-hydraulic system of a hybrid mixer (Mitkowski et al. 2016). The fermentation of the mixtures was carried out to spontaneously suppress the process. The biogas efficiency of intentional blends (Table 3) was determined together with the characteristics of daily and cumulative biogas emission.

Table 3. Biogas yield characteristics for tested mixtures

Values	Productivity of biogas per mass unit [$m^3 \cdot Mg^{-1}$]			
	M1	M2	M3	M4
Fresh Matter	11.85	29.55	29.43	19.77
Dry Matter	210.73	382.63	319.68	306.73
Organic Dry Matter	289.10	580.48	504.72	401.61
Average methane concentration (maximum*)	39 (67*)	59 (72*)	58 (72*)	45 (67*)
Average concentration of carbon dioxide (current value**)	23 (32**)	35 (27**)	18 (20**)	23 (22**)
Average hydrogen sulphide concentration (current value**)	271 (655)	390 (309)	446 (63)	481 (775)
Average oxygen concentration	0.67	0.54	0.79	0.75
* Maximum value in the hydraulic retention time (HRT) range				
** Current value for the maximum methane concentration				

The process of thermal treatment of the distillers grains caused a slight increase in pH (to pH = 3.78), but led to a decrease in the dry matter content (Table 2). Protein denaturation was shown to be irreversible and this had an impact on the fermentation process. A lower biogas yield of the distillers grains after thermal processing was obtained (Table 3).

The results of the fermentation process under the conditions of the periodical experiment were calculated from the laboratory scale to the technical scale and expressed for the charge in Mg unit of fresh matter, dry matter and dry organic matter. The characteristics of discrete data were connected with the trend line (Fig. 4).

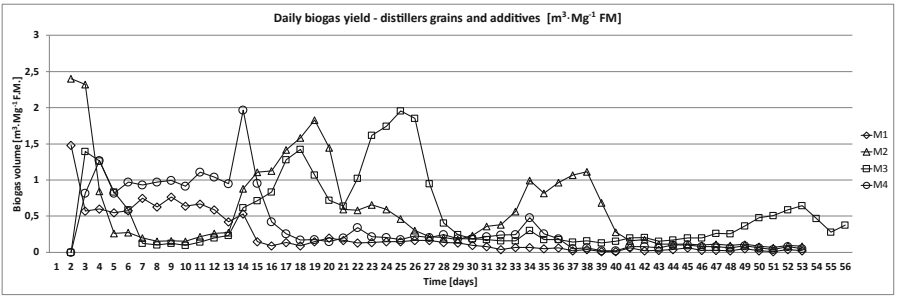

Fig. 4. Characteristics of temporary (daily) biogas yield expressed in Mg of fresh matter

Despite maintaining the initial pH value at 7.45 and mixing the feedstock under mesophilic conditions (35 °C), the daily biogas productivity trend lines of all samples showed a discrepancy from the typical asymptotic characteristics (Fig. 4).

Characteristics of the cumulative biogas efficiency of the tested mixtures showed a slowdown (M2, M3) in relation to the typical normal characteristics (Fig. 5).

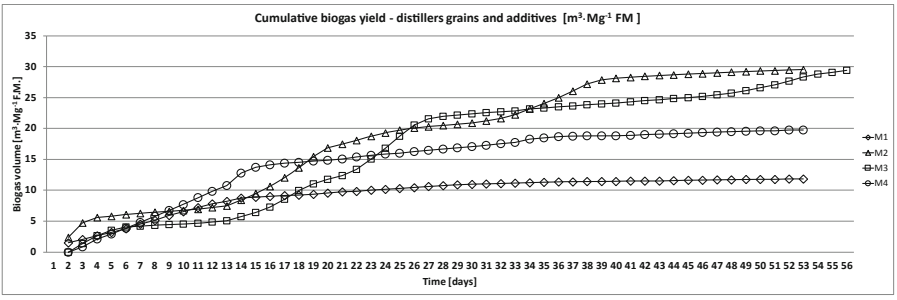

Fig. 5. Characteristics of cumulative biogas yield expressed in Mg of fresh matter

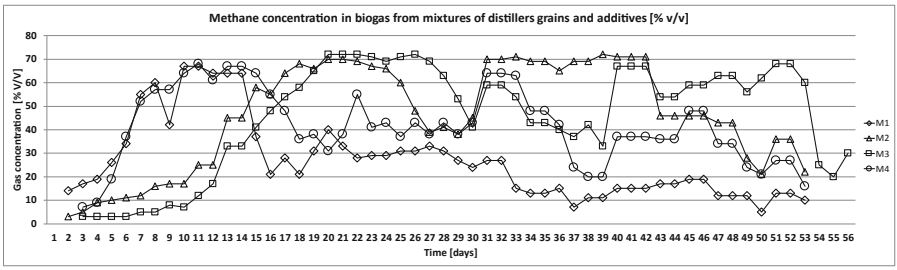

Fig. 6. Daily characteristics of methane concentrations in the process of mixtures fermentation

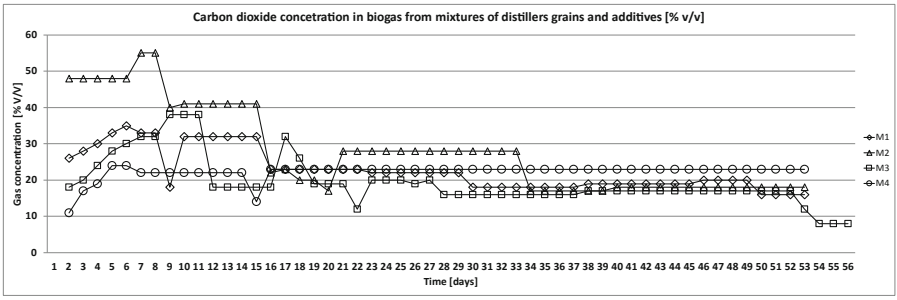

Fig. 7. Daily characteristics of carbon dioxide concentrations in the process of mixtures fermentation

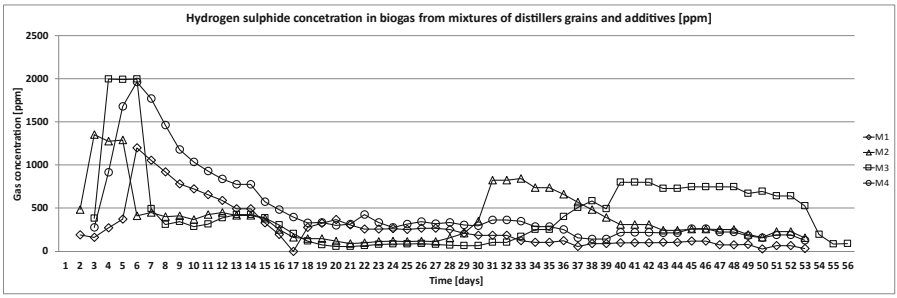

Fig. 8. Daily characteristics of hydrogen sulphide concentrations in the process of mixtures fermentation

The extinguishing of biogas production with the use of nutrients resulted in a reduction of carbon dioxide (Fig. 7) and hydrogen sulfide (Fig. 8) emissions. Methane emission in mixtures of M2 and M3 (Fig. 6) was still high even after exceeding the HRT interval (O'Shea et al. 2017).

5 Discussion and Conclusions

The obtained results of cumulated biogas productivity for thermally processed distillers grains indicate that irreversible protein denaturing has an impact on the decrease of biogas productivity in relation to unprocessed distillers grains.

Diagrams of daily biogas efficiency allowed to indicate the parameter of biomass retention time in the reaction chamber.

For the thermally processed distillery grains (M1 probe), the HRT inter val time (Hydraulic Retention Time) can be estimated to be 33 days. For the distillery grains not thermally processed, the HRT factor may be estimated to be 36 days. The mixture of distillery grains with aluminium phosphate increased the HRT index to 41 days. The mixture of distillery grains with the addition of molasses obtained an average HRT time period of 30 days.

The addition of aluminium phosphate balanced the shares of macro-nutrients (N:P:K), which leads to a more complete use of nutrients.

The best biogas productivity results were obtained for the thermally processed stock with addition of aluminum phosphate aqueous solution (580.48 $m^3 \cdot Mg^{-1}$ ODM). The mixture M3 with added molasses, despite a significant energy addition, increased content of organic matter and sugars, reached a maximum biogas yield of 504.72 $m^3 \cdot Mg^{-1}$ ODM.

For wet distillery waste fermented under thermophilic conditions, on a microscale, the daily biogas yield of the wet distillery waste is given at a level of 2900 $ml \cdot dm^{-3} \cdot day^{-1}$ and a methane concentration of up to 50% v/v, up to 6600 $ml \cdot dm^{-3} \cdot day^{-1}$ and a methane concentration of about 40% v/v. However, these results are unstable in relation to the results obtained from the tested thermal and mixed method (Jiang et al. 2013).

Waste Vinasse, comparable in parameters to distillery waste and WDGS, from the process of ethanol production from sugar cane allows to obtain 10 m^3 to 26.4 m^3 of biogas from 1 m^3 Vinasse at a concentration of 60% methane under mesophilic conditions of methane fermentation. Methanation of Vinasse with a content of 2.7% to 8.1% of dry matter was tested. In this case, the method of mixing and thermal processing tested in the article gives better results at a similar dry matter content (9.32% DM) (Parsaee et al. 2019).

Methods of methane fermentation based on COD (Chemical Oxygene Demand) reduction, e.g. methods of oxidation and wet-air processing, allow to obtain methane concentration of 15% v/v to 65% v/v of methane and methane yield of 31.6 $m^3 \cdot Mg^{-1}$ of fresh matter. The results are therefore similar to the method of mixing with target substrates (Sarat Chandra et al. 2014).

Compared to dark fermentation for cellulose and starch substrates, the thermal method used does not offer the possibility to produce hydrogen. However, the tested method significantly reduces the chemical processing necessary to stabilize the pH parameter (Łukajtis et al. 2018).

Many dark fermentation processes are also based on the addition of a inoculum (10% m/m to 25% m/m) and the pH range of 4.4 to 5.5 is extremely difficult to maintain and requires chemical processing with HCl and NaOH (Wicher et al. 2013).

In conclusion, the thermal method did not bring the expected result of increased pH and increased efficiency of the methanation process. The combination of the thermal method with the addition of target substrates gave a significant impulse for the direction of modification of the energy properties for the distillery waste and WDGS.

Acknowledgments. This research was supported by Institute of Biosystems Engineering, Pozna University of Life Sciences, Poland

References

Adamski, M., Szaferski, P.T., Gulewicz, P., Majkowski, W.: Silage of switchgrass (panicum virgatum) as a bioenergy feedstock in Poland. In: Ochowiak, M., Woziwodzki, S., Doligalski, M., Mitkowski, P.T. (eds.) Practical Aspects of Chemical Engineering: Selected Contributions from PAIC 2017, pp. 1–15. Springer, Cham (2018). ISBN 978-3-319-73978-6

Basu, S., Mukherjee, S., Kaushik, A., Batra, V., Balakrishnan, M.: Integrated treatment of molasses distillery wastewater using MicroFiltration (MF). J. Environ. Manage. **158**, 55–60 (2015)

Bell, J., Farquhar, J., McDowell, M.: Distillery by-products, livestock feed and bio-energy use in Scotland. A Review commissioned under the Scottish Government RESAS Policy Underpinning: Special Economic Studie, SRUC, July 2019

Bhoite, G., Vaidya, P.: Iron-catalyzed wet air oxidation of biomethanated distillery wastewater for enhanced biogas recovery. J. Environ. Manage. **226**, 241–248 (2018)

Bustamantea, M.A., Paredes, C., Marhuenda-Egea, F.C., Pérez-Espinosa, A., Bernal, M.P., Moral, R.: Co-composting of distillery wastes with animal manures: carbon and nitrogen transformations in the evaluation of compost stability. Chemosphere **72**(4), 551–557 (2008)

DIN 38414 S 8: German standardized test method for water, sewage and sludge. Sediments and sediments (group S). Determination of fermentation characteristics (S. 8). DIN DeutchesInstitut fur Normung e. V., Berlin (2012)

Durczak, K., Adamski, M., Mitkowski, P.T., Szaferski, W., Gulewicz, P., Majkowski, W.: Chemical processing of switchgrass (panicum virgatum) and grass mixtures in terms of biogas yield in Poland. In: Ochowiak, M., Woziwodzki, S., Doligalski, M., Mitkowski, P.T. (eds.) Practical Aspects of Chemical Engineering: Selected Contributions from PAIC 2017. Springer, Cham (2018). ISBN 978-3-319-73978-6, 85-99

Iglinski, B., Buczkowski, R., Iglinska, A., Cichosz, M., Piechota, G., Kujawski, W.: Agricultural biogas plants in Poland: investment process, economical and environmental aspects, biogas potential. Renew. Sustain. Energy Rev. **16**, 4890–4900 (2012)

Jiang, X., Hayashi, J., Yong, S.Z., Yang, L., Tang, Y., Oshibe, H., Osaka, N., Kida, K.: Improving biogas production from protein-rich distillery wastewater by decreasing ammonia inhibition. Process Biochem. **48**, 1778–1784 (2013)

KTBL-Heft 84: Schwachstellen an Biogasanlagen verstehen und vermeiden. Kuratorium fürTechnik und Bauwesen in der Landwirtschafte.V. (KTBL), KTBL-Heft 84, Darmstadt, DruckereiLokay, Reinheim (2009)

Laurinavichene, T., Tekucheva, D., Laurinavichius, K., Tsygankov, A.: Utilization of distillery wastewater for hydrogen production in one-stage and two-stage processes involving photofermentation. Enzyme Microb. Technol. **110**, 1–7 (2018)

Łukajtis, R., Hołowacz, I., Kucharska, K., Glinka, M., Rybarczyk, P., Przyjazny, A., Kamiński, M.: Hydrogen production from biomass using dark fermentation. Renew. Sustain. Energy Rev. **91**, 665–694 (2018)

Mitkowski, P.T., Szaferski, W., Adamski, M.: Hydraulic mixing. In: Ochowiak, M., Woziwodzki, S., Doligalski, M., Mitkowski, P.T. (eds.) Practical Aspects of Chemical Engineering: Selected Contributions from PAIC 2017. Springer, Cham (2018). ISBN 978-3-319-73978-6, 291-306

Mitkowski, P.T., Adamski, M., Szaferski, W.: Experimental set-up of motionless hydraulic mixer and analysis of hydraulic mixing. Chem. Eng. J. **288**, 618–637 (2016)

O'Shea, R., Wall, D.M., McDonagh, S., Murphy, J.D.: The potential of power to gas to provide green gas utilising existing CO2 sources from industries, distilleries and wastewater treatment facilities. Renew. Energy **114**, 1090–1100 (2017)

Pant, D., Adholeya, A.: Biological approaches for treatment of distillery wastewater: a review. Biores. Technol. **98**, 2321–2334 (2007)

Parsaee, M., Kiani Deh Kiani, M., Karimi, K.: A review of biogas production from sugarcane vinasse. Biomass Bioenergy **122**, 117–125 (2019)

Sakdaronnarong, Ch., Ittitanakam, A., Tanubumrungsuk, W., Chaithong, S., Thanosawan, S., Sinbuathong, N., Jeraputra, Ch.: Potential of lignin as a mediator in combined systems for biomethane and electricity production from ethanol stillage wastewater. Renew. Energy **76**, 242–248 (2015)

Sarat Chandra, T., Malik, S., Suvidha, G., Padmere, M., Shanmugam, P., Mudliar, S.: Wet air oxidation pretreatment of biomethanated distillery effluent: mapping pretreatment efficiency in terms color, toxicity reduction and biogas generation. Biores. Technol. **158**, 135–140 (2014)

Semitela, S., Pirra, A., Fernando, G., Braga, F.G.: Impact of mesophilic co-composting conditions on the quality of substrates produced from winery waste activated sludge and grape stalks: Lab-scale and pilot-scale studies. Biores. Technol. **289**, 121–622 (2019). October 2009

Trajer, J., Golisz, E., Wojdalski, J.: Analysis of energy-consumption of bioethanol production in agricultural distilleries in Poland. Agric. Agric. Sci. Proc. **7**, 265–271 (2015)

Wicher, E., Seifert, K., Zagrodnik, R., Pietrzyk, B., Laniecki, M.: Hydrogen gas production from distillery wastewater by dark fermentation. Int. J. Hydrogen Energy **38**, 7767–7773 (2013)

Application of HE-3 and HE-3X Agitators in Suspension Production

Piotr Tomasz Mitkowski[1(✉)], Waldemar Szaferski[1], Mariusz Adamski[2], and Robert Adamski[3]

[1] Institute of Chemical Technology and Engineering, Faculty of Chemical Technology, Poznan University of Technology, Poznań, Poland
piotr.mitkowski@put.poznan.pl
[2] Faculty of Agriculture and Bioengineering, Institute of Biosystems Engineering, Poznan University of Life Sciences, Poznań, Poland
[3] Laboratory of Thermal and Diffusion Processes, Department of Environmental Engineering, Faculty of Process and Environmental Engineering, Lodz University of Technology, Łódź, Poland

Abstract. Formation of a solid suspension in liquids is possible at a sufficiently high axial velocity of the liquid in the mixer. The formation of a slurry in the mixer is described by the minimum rotational frequency of the agitator, i.e. the lowest frequency at which the desired suspension is obtained within the mixer. Due to the hydrodynamic conditions within the mixer during the formation of a suspension with a solid phase, which is characterized by density greater than the liquid density, the agitator must possess high pumping properties towards the liquid surface. However, in the case of a solid with a density lower than the density of the liquid, its suction from the liquid surface towards the bottom and dissipation in the entire volume must be ensured. The use of excessive rotational frequency of the agitator is not economically justified because of the rapid increase of mixing power, which is disproportionate to the simultaneous mass exchange, and thus an increase in the operating costs occurs. In order to minimize these costs, an attempt was carried out to search for structural changes to the HE-3 agitator and compare them with modified HE-3X and Rushton turbine.

1 Formation of Conventional and Non-conventional Suspensions

In two phase solid-liquid systems, the dispersion phase is composed of solid particles which are dispersed in liquid, called as continuous phase, and such mixtures are defined as suspensions. These systems are very widely found in different sectors of the industry, e.g. pharmaceutical, food, chemical, cosmetic, petrochemical, chemical, rubber, plastic, recycling of solid waste and molding (Paul et al. 2004). Suspensions are also found in every process, in which the system changes from single to double phase and vice versa, such as catalyst reactions, fermentation processes, extraction (e.g. extraction of microorganisms (Lisiecki et al. 2014)) or formation of slurries (Paul et al. 2004). It is estimated that 60% of all mixing processes is associate with liquid-solid

© Springer Nature Switzerland AG 2020
M. Ochowiak et al. (Eds.): PAIC 2019, *Practical Aspects of Chemical Engineering*, pp. 252–260, 2020.
https://doi.org/10.1007/978-3-030-39867-5_27

multiphase systems (Ceres et al. 2010). Most of the liquid-solid systems include conventional suspensions, in which the dispersed phase density is higher than that of continuous phase. Without a forced flow in a mixer, the solid particles in such systems will settle on the bottom of the apparatus. However, there are systems in which solids exhibit lower density than the liquid, and their particles float near the liquid surface because of buoyancy force. Such cases are called non-conventional suspensions or light suspensions (Jaworski et al. 2000; Wesołowski and Szaferski 2002; Wójtowicz and Kamieński 2009; Szaferski et al. 2011; Kacperski and Karcz 2015).

In conventional suspensions, after starting the agitation of the liquid in a mixer by providing the rotary movement using a mechanical stirrer, the solid particles are raised from the bottom of the vessel and then dispersed in the liquid. With the increase of the number of stirrer revolutions (i.e. rotational frequency), the number of solid particles which are raised from the bottom is also increased until minimum frequency of stirrer rotation (n_0) is reached, at which the complete suspension is formed. Actually, every mixer set-up possesses its own characteristic n_0 parameter, which exceeds constant movement of all solid particles, resulting in the formation of the total suspension. Such frequency of the stirrers' rotation is sufficient to run most technological processes (Kiełbus-Rąpała and Karcz 2009, 2010).

In order to obtain non-conventional suspensions in a mechanical mixer, the hydrodynamic conditions and rotational frequency of the stirrer have to be used in the setup, which will result in sucking solid particles down from the surface inside the created suspension and result in an even distribution within the volume of the vessel. Formation of non-conventional suspensions depends on physical parameters of the mixed substances, geometrical parameters of solid particles (Wesołowski and Szaferski 2002) as well as the configuration and construction of the stirrer-mixer setup (Wójtowicz and Kamieński 2009).

Formation of light suspensions can be divided into several stages. In the first step, when no rotation is applied, the whole volume of the solid phase floats near the surface of the liquid because of dominating buoyancy force. After setting the agitator into motion, a part of the particles is separated from main aggregation, then a funnel is created with its centre located above a stirrer disc or, in general, above the agitator. Single particles reach the height below the agitator and some reach the bottom of the vessel. Increase of the rotational frequency sets all particles into motion. The bigger and heavier particles are sucked below the agitator, lower than in the previous step. Small aggregations of particles can be observed on the surface of the liquid, the velocity of which is definitely lower than others. Big aggregation of the stationary phase elements is also located directly underneath the stirrer and close to the shaft. Continuous increase of rotational frequency results in reaching the n_0 value, at which particles are distributed equally in the set-up and formation of total suspension can be observed. Further increase of rotational frequency beyond that value does not improve the total level of mixing and only results in increased consumption of energy.

2 Assessment Criterium of the Obtained Suspension

During the production of suspensions, the issue of defining the moment at which the mixing of solids within the mixture reaches the state of perfect mixing, resulting in creation of the total suspension, is of great importance. Literature sources distinguish several criteria of the total suspension. At first, a visual assessment of that moment is allowed. Meeting the criteria allows for experimental assignation of the minimal rotational frequency of the agitators which is necessary for realization of the process. However, during the use of visual methods, observation of the exact moment when perfect mixing occurs is very difficult. An example of visual criterium is that provided by Gates (1976). That criterium composed of a 10° scale of assessment, and the measurement consisted of rating the change of volume of the liquid which was filled with solid particles. Another criterium is the so-called Staudinger criterium (Staudinger and Moser 1976), which distinguishes three basic types of suspensions. Total suspension is achieved, when most of solid particles are suspended in the liquid and only small aggregations of the dispersed phase can be located near the bottom of the vessel. The second is "one hundred percent" suspension, when none of the solid particles are present at the bottom of the vessel. The last type is a homogenous suspension, when the concentration of the solids is equal in every part of the suspension. Another example is the Oldshue criterium (Oldshue 1969). Oldshue (1969) distinguished five steps of suspension creation. These are as follows: occupation of a given height of liquid by the suspension, fixing the remains of a sold layer with is placed on the bottom of the vessel, putting all the particles which remain on a bottom of the vessel in motion (at this step, the mixture is not yet a suspension), complete lifting of solid particles from the bottom (this step is characterized by substantial increase of energy input), perfect mixing at which homogenous suspension within the whole volume of the liquid is achieved.

The Zwietering criterium is used very often, although it arouses certain controversies (Zwietering 1958). The author of that assessment method realized that finding the exact moment when the suspension is created is very complicated. This results from the fact, that even when high speed stirrers are used, a part of the dispersed particles remains in contact with each other, or is located near the bottom of the vessel for some time. Because of that, Zwietering (1958) proposed a two-step assessment scale, which distinguishes only "complete" and "incomplete" suspensions. The condition to acknowledge that a suspension is "complete" is such movement of elements of the dispersed phase, in which none of the solid particles are in contact with bottom of the vessel for longer than 1 s (Kasat 2005). Every state of a mixture which does not fulfill this assumption makes the suspension "incomplete" or unmixed.

In conjunction with the fact, that Zwietering criterium was formulated for conventional suspensions, this criterium was modified in case of light suspensions studies. Because of that, the moment at which "one second criterium" is fulfilled, when the state of the mixture at which none of the dispersed phase elements floats near the liquids surface for longer than one second is achieved.

Another type of criterium, which can be used for assessment of the mixing level of suspension is based on the analysis of solid particles behaviour in the liquid. The analysis relies on measuring local concentrations of the dispersed phase in the mixer.

The results are applied to average concentration in the whole suspension and then standard deviation is calculated (Kamieński 2004). Standard deviation value is very high when the rotational frequency of stirrers is low, and it remains practically constant. Then its value decreases and settles at a certain level, which is influenced only by the concentration of the dispersed phase in the mixed volume. The lower the standard deviation is, the better the mixing of the suspension, and achievement of the lowest standard deviation equals corresponds to the formation of a homogenous suspension. The decrease of standard deviation is observed when the concentration of the dispersed phase in the mixer increases.

The minimum rotational frequency at which perfect mixing in the whole volume is achieved can also be defined by pressure measurement. The principle of such techniques is based on the fact, that the density of the mixture is higher than liquids after the distribution of solid particles in the liquid. Because of that, static pressure which is measured at the bottom of the tank will increase together with the amount of solids dispersed in the liquid. There is a mathematical correlation which describes the increase of static pressure created by suspension of solids and its mass in the liquid (Micale et al. 2002).

3 Application of the HE-3X Agitator

An interesting application found in literature, and also known from industrial applications, is to connect a HE-3 agitator with a Smith turbine on a common shaft (Junker et al. 2000). The original HE-3 agitator, produced by Chemineer (2019), is a high-speed agitator which pumps the liquid from the top to the bottom of the tank. It is therefore used in most cases as an overhead stirrer. This system works well in fermentation processes, resulting in a uniform dispersion of oxygen in the fermenter and providing good mixing times for the additives (Junker et al. 2000).

In order to increase the versatility of the HE-3 agitator, its modification was carried out, which consisted of adding the disk known from the Rushton turbine. This resulted in the design of the HE-3X mixer. Szaferski et al. (2013) presented the analysis of power demand during the formation of a suspension with use of either the HE-3, HE-3X or Rushton turbine. In that work, an aqueous solution of Arabic gum and polypropylene granulate with an equivalent particle diameter of 3.80 mm were used as the dispersed system. Dependence of the power number (Ne) and the Reynold's number (Re) for measurements carried out in distilled water indicated that the HE-3X agitator achieves similar results to the HE-3 agitator, while obtaining up to 10 times lower values of the Ne than the Rushton (Fig. 1). The influence of the solids mass content in the suspension ranging from 0.005 to 0.05 on the minimum rotational frequencies of the agitator was confirmed for distilled water and 2.5–10% (by weight) Arabic gum aqueous solutions. On the other hand, no significant effect of Arabic gum concentration in the tested range on the minimum rotational frequencies during the formation of suspensions was observed.

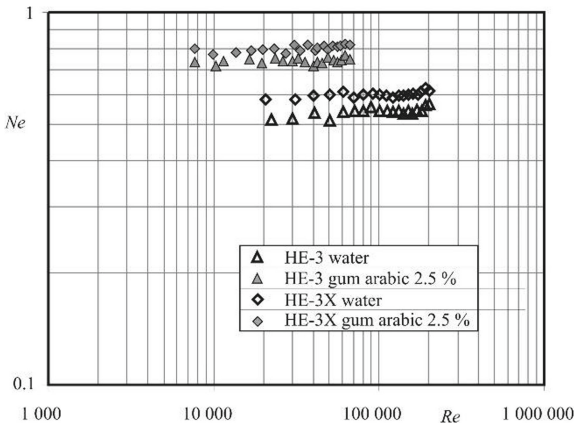

Fig. 1. Power numbers (Ne) in function of Reynolds number (Re) during mixing of distilled water and 2.5% aqueous solution of Arabic gum (Based on Szaferski et al. 2013)

The use of the modified HE-3X agitator during the formation of the gas-liquid systems was reported by Broniarz-Press et al. (2014). It has been found that the modification of the agitator increases the amount of gas retained in the mixture compared to the HE-3 agitator and is slightly below compared to the Rushton turbine. It has been shown that the modified design of the stirrer reduces the mixing power while maintaining the aeration efficiency (gas hold-up) of the system, similar to that achieved with other agitators. The slightly lower value of gas hold-up accompanied by the smaller value of energy needed to produce the two-phase system means that the agitator modification can be a good option in industrial cases. Improved efficiency of mixing gas-liquid systems with lower energy expenditure is especially desirable in wastewater treatment plants. It has been observed that the modified HE-3X agitator feeds gas into the dead zones to a greater extent than other tested mixers.

The production of a solid-liquid system (suspension) with use of HE-3 and HE-3X agitators was presented in (Szaferski et al. 2016). The polypropylene and polyethylene granules with equivalent diameters equal to 5.63 mm and 3.85, respectively, were used to obtain a light suspension in aqueous solutions of the polyacrylamide Rokrysol WF1 with concentrations ranging between 2000 and 4000 ppm. It has been shown that the suspension produced by the modified HE-3X agitator in relation to the HE-3 agitator occurs at lower values of the minimum rotational frequency and their increase is affected by the increase of the concentration of the used polymer solution. In the examined range of equivalent diameters, no influence of that parameter on the pumping characteristic of agitators was observed. The analysis of the power numbers of mixing indicated its increase with the increase of the granulates fractions in the mixtures and increase of the polymer concentrations.

During the investigation of further possibilities of using the HE-3X agitator, a number of tests were carried out for the suspension in which the density of the solid will be higher than the density of the continuous medium. It was assumed in advance that this difference should be relatively small, therefore granules from the family of styrene block copolymers with the trade name “OnFlex” were utilized. The tests were carried out

using a stand, which consisted of a transparent polymethyl methacrylate tank, with an internal diameter of 0.290 m, equipped with four standard flat baffles. A single agitator with a diameter of 0.100 m was used in the mixer, either the Chemineer HE-3 or HE-3X, and (for comparison purposes) a Rushton turbine and Smith turbine (ST). The mixer shaft was located centrally in the apparatus axis and in two non-standard positions with a 40 mm offset to the right or left in relation to the standard position. The used experimental set-up was consistent with that used elsewhere (Mitkowski and Szaferski 2016).

The solid used in this study was a thermoplastic granulate, styrene elastomer, with a density of 1220 kg/m^3 with equivalent particle diameter equal to 2.96 mm. The granules were added into the mixture with the mass fraction of solids (X_S) ranging from 0.0053 to 0.0552. Distilled water or aqueous solution of polyacrylamide Rokrysol WF1 at a concentration between 0.1 and 0.4% were used as the continuous medium. In order to determine the properties of the polymer solution, rheological tests were carried out using the Physica MCR-501 rheometer. The results of the rheological tests are presented in Table 1. All analysed systems proved to be exponent fluids and followed the Eq. (1).

$$\tau_w = K' \cdot \dot{\gamma}_w^m \tag{1}$$

where: τ_w – shear stress (Pa), $\dot{\gamma}_w$ – shear rate (1/s), K' – consistency ratio (Pa·s), m – flow ratio (-).

During the first part of the experimental research, an analysis of power characteristics for the used agitators was performed (Fig. 2). When considering the power number as an assessment criterium, the best stirrers for both distilled water and aqueous solution of polyacrylamide were HE-3X and HE-3, which completed and confirmed the earlier studies (Szaferski et al. 2013, 2016; Broniarz-Press et al. 2014). These two agitators were characterized by the lowest values of Newton number which corresponds to the fact that while working under same conditions as other agitators, they require the lowest process costs and maintain a similar mixing efficiency.

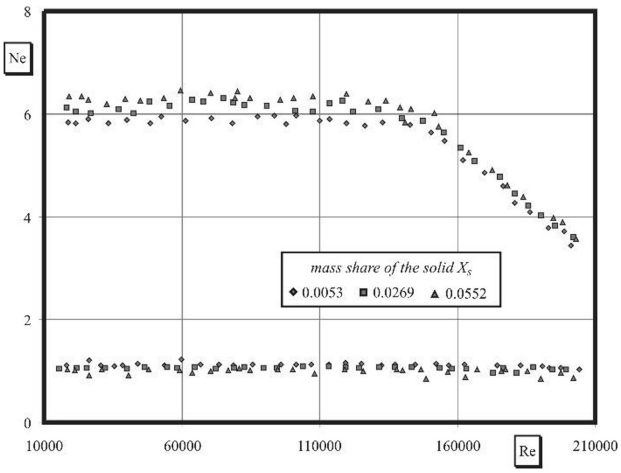

Fig. 2. Example power characteristics of the tested agitators

In the next step of experimental data analysis, the minimal rotational frequency of agitators needed to create highly-dispersed suspension was investigated (Fig. 3). The Zwietering visual criterium was used for that purpose. In all the attempts, the best results were achieved while using the Rushton turbine stirrer. The tests confirmed that both HE-3 and HE-3X stirrers failed in the formation of suspension in experiments in which the continuous phase consisted of polyacrylamide solution with concentrations between 0.3 and 0.4%. At lower concentrations of polyacrylamide, the obtained minimum rotational frequency was relatively high. Additionally, it was observed that RT and ST exhibit a tendency to aerate the mixture more than other configurations, and this can be used in processes carried out in wastewater treatment. Finally, an attempt of moving the stirrers' axle of shaft eccentrically within the mixer did not result in any desirable effects.

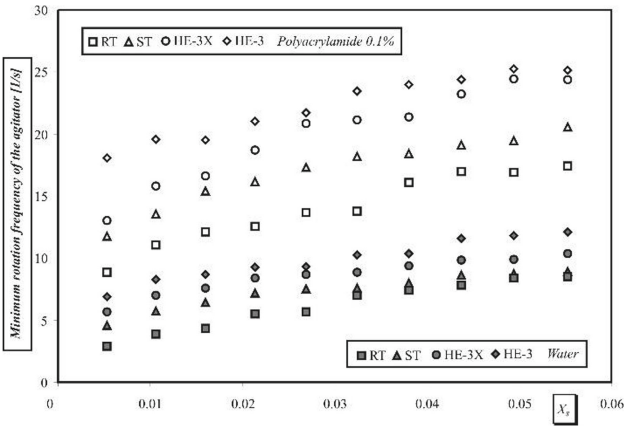

Fig. 3. Example of experimental results obtained for the formed suspensions of 0.1% polyacrylamide aqueous solution and water

Table 1. Rheological parameters of Eq. (1) for mixtures used in experimental tests

Rokrysol WF1 concentration in aqueous solution [%]	K'	m
0.1	0.055	0.670
0.2	0.134	0.627
0.3	0.230	0.576
0.4	0.310	0.517

4 Conclusions

The studies have indicated that the proposed design changes introduced to the HE-3 agitator allowed to increase the applicability of the proposed HE-3X mixer. It has found application in gas-liquid and liquid-solid systems. However, some limitations were also established during the production of suspensions of solids with higher density than the continuous medium when its viscosity is high.

Acknowledgments. This research was supported by the Ministry of Science and Higher Education in Poland subsidy for Poznan University of Technology, Faculty of Chemical Technology (Grand No.: 03/32/SBAD/0902).

References

Broniarz-Press, L., Szaferski, W., Mitkowski, P.T., Marecka, A.: Wykorzystanie układu dyfuzor membranowy-mieszadłoo HE-3X w procesach napowietrzania cieczy. Inżynieria i Apar. Chem. **53**, 225–226 (2014)

Ceres, D., Moravec, J., Jirout, T., Rieger, F.: Mixing of suspensions with pitched six blade turbines. Inżynieria i Apar. Chem. **49**, 25–26 (2010)

Gates, L.E., Morton, J.R., Fondy, P.L.: Selecting agitator systems to suspend solids in liquids. Chem. Eng. **83**, 144–150 (1976)

Jaworski, Z., Bujalski, W., Otomo, N., Nienow, A.W.: CFD study of homogenization with dual rushton turbines - comparison with experimental results, Part I: initial studies. Chem. Eng. Res. Des. **78**, 327–333 (2000)

Junker, B.H., Mann, Z., Hunt, G.: CD-6 Impeller in Fermentation Vessels Retrofit of CD-6 (Smith) Impeller in Fermentation Vessels (2000)

Kacperski, Ł., Karcz, J.: Badania numeryczne wpływu wysokości zawieszenia mieszadła PBT na jakość wytwarzanej zawiesiny lekkiej. Inżynieria i Apar. Chem. **54**, 328–329 (2015). https://doi.org/10.1205/02638760

Kamieński, J.: Mieszanie układów wielofazowych. Wydawnictwa Naukowo-Techniczne, Warszawa (2004)

Kasat, G.: Review on mixing characteristics in solid-liquid and solid-liquid-gas reactor vessels. Can. J. Chem. Eng. **83** (2005). https://doi.org/10.1002/cjce.5450830403

Kiełbus-Rąpała, A., Karcz, J.: Warunki wytwarzania układu ciecz-ciało stałe w mieszalnikach różnej skali. Inżynieria i Apar. Chem. **4**, 66–67 (2009)

Kiełbus-Rąpała, A., Karcz, J.: Solid suspension and gas dispersion in gas-solid-liquid agitated systems. Chem. Pap. **64**, 154–162 (2010). https://doi.org/10.2478/s11696-009-0104-9

Lisiecki, P., Chrzanowski, Ł., Szulc, A., et al.: Biodegradation of diesel/biodiesel blends in saturated sand microcosms. Fuel **116**, 321–327 (2014). https://doi.org/10.1016/j.fuel.2013.08.009

Micale, G., Grisafi, F., Brucato, A.: Assessment of particle suspension conditions in stirred vessels by means of pressure gauge technique. Chem. Eng. Res. Des. **80**, 893–902 (2002). https://doi.org/10.1205/026387602321143444

Mitkowski, P.T., Szaferski, W.: Aeration of liquid-liquid systems in mixer equipped with membrane diffuser and various agitators. Chem. Eng. Technol. **39**, 2370–2379 (2016). https://doi.org/10.1002/ceat.201500248

Oldshue, J.Y.: Suspending solids and dispersing gases in mixing vessel. Ind. Eng. Chem. **61**, 79–89 (1969). https://doi.org/10.1021/ie50717a010

Paul, E.L., Atiemo-Obeng, V.A., Kresta, S.M.: Handbook of Industrial Mixing. Wiley, Hoboken (2004)

Staudinger, G., Moser, F.: "100proz. Suspension" von Feststoffen im Rührgefäß – Definition und Berechnung. Chemie Ing. Tech. **48**, 1071 (1976). https://doi.org/10.1002/cite.330481128

Szaferski, W., Broniarz-Press, L., Dulska, D.: Suspending of floated solid particles in a mixer of non-standard geometry. Przem. Chem. **90**, 1686–1688 (2011)

Szaferski, W., Mitkowski, P.T., Kondras, A.: Wytwarzanie zawiesin zmodyfi kowanym mieszadłem HE-3X. Inżynieria i Apar. Chem. **52**, 566–567 (2013). https://doi.org/10.1016/0009-2509(58)85031-9

Szaferski, W., Mitkowski, P.T., Marecka, A., Słowińska, K., Szuster, M., Matelska, E.: Właściwości pompujące zmodyfikowanego mieszadła HE-3X. Inż. Ap. Chem. **55**(5), 205–207 (2016)

Wesołowski, P., Szaferski, W.: Wpływ geometrii granulatów tworzyw sztucznych na wytwarzanie modelowych "zawiesin lekkich" (English: The influence of the geometric parameters of the polymer granulate on the "light suspensions" generation). Inżynieria i Apar. Chem. **4**, 145–146 (2002)

Wójtowicz, R., Kamieński, J.: Minimalna częstość obrotów mieszadła podczas wytwarzania zawiesin lekkich w mieszalniku mechanicznym. Inżynieria i Apar. Chem. **48**, 126–127 (2009)

Zwietering, T.N.: Suspending of solid particles in liquid by agitators. Chem. Eng. Sci. **8**, 244–253 (1958). https://doi.org/10.1016/0009-2509(58)85031-9

Chemineer – Impellers (2019). https://www.chemineer.com/products/chemineer/impellers.html. Accessed 1 Aug 2019

Flow Regulators - Design, Tests and Applications

Marek Ochowiak(✉), Sylwia Włodarczak, Magdalena Matuszak, Andżelika Krupińska, and Małgorzata Markowska

Institute of Chemical Technology and Engineering, Poznan University of Technology, Poznań, Poland
marek.ochowiak@put.poznan.pl

Abstract. The chapter presents the theoretical fundamentals of liquid flow regulation. The description of the operation of vortex regulators is reduced to the Toricelli formula, in which the flow factor is determined experimentally. Flow regulators are devices that reduce fluid flow. They consist of inlet and outlet ports and a vortex chamber, which can have different shapes and geometric dimensions. Designed regulators differ in the shape of the vortex chamber and the presence of a core-hole. Their prototypes were made of reinforced ABS copolymer using the 3D printing technique, which is resistant to high temperature and mechanical damage. The paper presents experimental results of the modified vortex flow regulators, characteristics of liquid flow and discharge coefficients.

1 Theoretical Fundamental of Flow Regulation

In the era of increasingly frequent climatic anomalies, which we observe in recent years (droughts, torrential rain, floods), the awareness of necessities for the regulation of small watercourses, rain runoffs and the construction of small retention systems is increasing. The continuous development of civilization is also the reason why rainwater used to be once treated conventionally as clean nowadays is sewage that carries dangerous pollution washed out from polluted atmosphere (acids, dusts) and from urban areas (old parts of tires, road surfaces, oils as well as other persistent organic pollutants) and rural (liquid manure, washed fertilizers and agricultural chemicals). Therefore, in order to protect the aquatic environment, we have to increasingly clean rainwater sewage, not only mechanically, but also biologically, and even perform its disinfection (Ekol-Unicon 2017).

Due to the wave nature of rain runoffs and flows in surface watercourses, the construction of any sewage treatment systems encounters the basic problem of temporary hydraulic overloads occurring at the moment of culmination of the flow wave. This problem can be solved by equipping sewage and melioration structures with retention or overflow installations cooperating with flow regulators (Zwara 2004; Ekol-Unicon 2017).

© Springer Nature Switzerland AG 2020
M. Ochowiak et al. (Eds.): PAIC 2019, *Practical Aspects of Chemical Engineering*, pp. 261–270, 2020.
https://doi.org/10.1007/978-3-030-39867-5_28

Working with tanks, flow regulators ensure flow wave alignment and limit the maximum flows, thereby moderating the hydraulic impacts caused by, among others, storm and freshet flows. Their proper application also allows the connection of new drainage areas to existing municipal collectors, without the risk of overloading them. New legal regulations regarding rainwater open wide possibilities of application of flow regulators for overflow systems of rainwater pre-treatment installations, individual types of regulators are adapted to different flow ranges and assembly conditions (Zwara 2004). Traditional throttling devices, such as orifices, reducers or gate valves, allow limiting this flow by reducing the active cross-section of the regulator. As a result, however, it may cause clogging, especially in the case of contaminated liquids. Furthermore, movable mechanical parts decrease the reliability of such devices. Vortex regulators are devoid of these disadvantages (Wójtowicz and Kotowski 2008a). The original design of the device has been considered in many studies that aimed to optimize the geometric parameters of the device to obtain the best hydraulic efficiency, i.e. as high as possible value of ratio of throttling and free flow resistance. Such devices are used, among others, on bypass lines in power plants (Brombach 1972a; Elalfy 1979). They are also applied to suppress fluctuations in the water table in water closures and in front of water-air tanks, in order to dampen hydraulic impacts (Huber and Prenner 1999; Haakh 2003).

Vortex controllers are used in water construction as energy dissipation devices in bottom sinks (Brombach 1972b), in microflow technology (Anduze et al. 2001). The vortex chamber is also used as a device to swirl the liquid stream into sewage pumps, which reduces their power (Brombach 1972a; Mays 2001; Wójtowicz 2007). In water supply and sewage systems, they are mainly used to throttle the flow of liquids in water and wastewater treatment facilities (Kotowski and Wójtowicz 2008; Wójtowicz and Kotowski 2008b). The effect of throttling the flow in regulators is achieved by forcing a swirl flow in the device (Brombach 1972a; Mays 2001; Wójtowicz 2007). The swirl intensity depends on the pressure of the liquid flowing into the device. At the beginning, when the inflow is small, there is no throttling and the liquid flows freely. As the inflow increases, the free flow changes to pressure flow. The rising pressure causes at some point the closure of the air pillar in the upper part of the vortex chamber. The entrapped air becomes the source of extra resistance and turbulence, and the potential energy of liquid is converted into the vortex energy. In this way, despite the absence of orifices, a throttling effect is formed, corresponding to the use of a reducer with a several times smaller cross-section than the cross-section of regulator (Ekol-Unicon 2017).

The characteristics of liquid flow through the regulator reminded the outflow characteristics through a small opening: if there is a small opening in any shape but with rounded edges in the tank wall (Fig. 1). For a liquid stream starting on its free surface 1 and ending in opening 2, the Bernoulli equation can be used:

$$\frac{w_1^2}{2g} + \frac{p_a}{g\rho} + H = \frac{w_2^2}{2g} + \frac{p_a}{g\rho} \tag{1}$$

The w_1 speed results from the flow continuity:

$$w_1 A_1 = w_2 A_2 \tag{2}$$

After the substitution one obtains:

$$w_2 = \sqrt{\frac{2g\rho}{1 - \left(\frac{A_2}{A_1}\right)^2}} \tag{3}$$

$A_2 < A_1$ and $A_2^2 \ll A_1^2$ for small openings, so that the familiar Toricelli formula is obtained:

$$w_2 = \sqrt{2gH} \tag{4}$$

It can be seen that the outflow liquid velocity through the opening in the open tank depends only on the height (slope) H. The volume flow $\dot{V}$ of the outgoing liquid is (Orzechowski et al. 1997):

$$\dot{V} = w_2 A_2 = A_2 \sqrt{2gH} \tag{5}$$

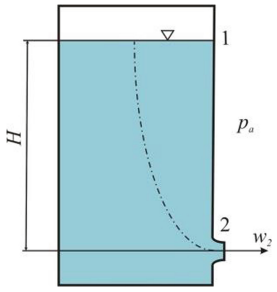

Fig. 1. Outflow through a small opening

In the above considerations, it was assumed that the opening has rounded edges, thanks to this the liquid flows out without disruptions, as in Fig. 2a. In the case of a sharp-edged opening, the outflow image is different, as shown in Fig. 2b. It can be seen that the cross-section area of stream A_2 is much smaller than the cross-section area of the opening $A = \pi\frac{d^2}{4}$. This is due to the fact that in the Sect. 1, there is a two-dimensional flow with an axial component w_{x1} and a radial component w_{r1}, which causes the narrowing of the stream. The outflow becomes one-dimensional in the Sect. 2, whose distance s is $s \geq d/2$ (Orzechowski et al. 1997).

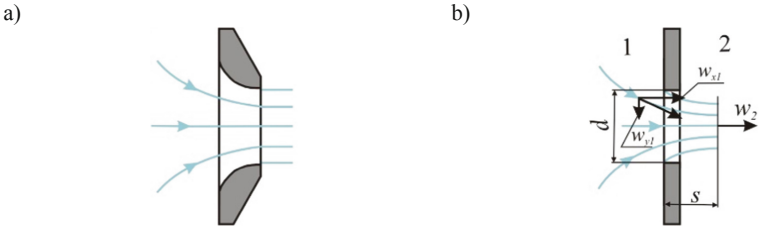

Fig. 2. Liquid outflow from the opening: (a) rounded, (b) sharp-edged.

The ratio of the cross-section area of the stream A_2 to the area of opening A is called the contraction (narrowing) coefficient of the stream:

$$\beta = \frac{A_2}{A_1} \tag{6}$$

The contraction ratio β can be determined theoretically and experimentally. Experiments show that this coefficient is not a constant value but depends on the Reynolds number described by the following formula:

$$Re = \frac{wd\rho}{\eta} \tag{7}$$

It was showed that large values of Re number, the value of β coefficient tends to the theoretically calculated value of $\beta = 0.61$ for a non-viscous liquid. This is due to the fact that during high speed flow the inertial forces predominate the viscous forces, which makes the flow similar to the flow of non-viscous liquid. Thus, it can be seen that the stream contraction is the result of the inertia of stream and not the liquid viscosity (Orzechowski et al. 1997).

However, the viscosity effect takes into account the coefficient of velocity loss φ, which is equal to the ratio of the real velocity w_2 to the theoretical velocity $w_{2,t}$:

$$\varphi = \frac{w_2}{w_{2,t}} \tag{8}$$

The coefficient φ is also a function of *Re* number. For large values of *Re* number one can take $\varphi \approx 0{,}98$ (Fig. 8) (Orzechowski et al. 1997).

The product of the contraction coefficient β and the coefficient of velocity loss φ is defined as discharge (outflow) coefficient μ:

$$\mu = \beta\varphi \tag{9}$$

As can be concluded from the above dependence, the value of μ coefficient for openings with circular cross-section is almost constant in the range of large *Re* numbers and amounts to approximately 0,60–0,66 (Orzechowski et al. 1997; Jeżowiecka-Kabsch and Szewczyk 2001).

The volume flow rate for sharp-edged openings is calculated taking into account the μ coefficient from Eq. (9), which takes the form:

$$\dot{V} = A_2 w^2 = \beta\varphi A w_{2,t} = \mu A w_{2,t} = \mu A\sqrt{2gH} \tag{10}$$

The mass stream $\dot{M}_c$ amounts respectively:

$$\dot{M} = \rho\dot{V} = \mu A\rho\sqrt{2gH} = \mu A\sqrt{2\rho\Delta P} \tag{11}$$

where $\Delta P = g\rho H$ is defined as the pressure drop during the outflow (Orzechowski et al. 1997; Jeżowiecka-Kabsch and Szewczyk 2001).

Taking into consideration normal conditions, the discharge coefficient μ is constant for a given opening. Whereas for regulators, the value of μ coefficient varies with the pressure change of inflow liquid from the initial value μ' to the value of μ'', typical for each type of device. Therefore, the flow characteristics for regulators are the combination of characteristics for two openings with different μ coefficients (Ekol-Unicon 2017).

2 Design and Tests of Flow Regulators

In the example of a cylindrical vortex regulator (Fig. 3), the liquid flows into the device through a connection tangent to the generatrix of cylinder, due to this its swirl motion is transmitted, which is maintained over the entire width of chamber up to the outlet port in the bottom of cylinder. In this motion, the peripheral velocity of the liquid increases as the cylinder's axis approaches, and due to the centrifugal force in the vortex chamber, the pressure decreases in the direction of its axis, so that the pressure reaches the ambient pressure value on the air core surface. The generated air core has a significant impact on the effectiveness of the device's throttling effect. The sprayed liquid forms a cone with the flare angle γ at the outlet (Wójtowicz and Kotowski 2008a).

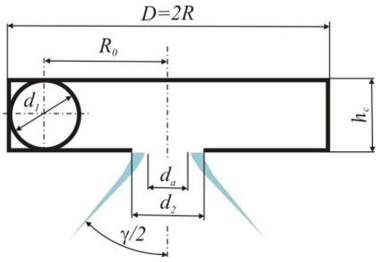

Fig. 3. Scheme of cylindrical vortex regulator

The first applied vortex regulators had a cylindrical chamber, and at the end of the '70s regulators with a conical vortex chamber were introduced (Brombach 1980). Such regulators are characterized by lower hydraulic resistance at free flow in comparison with cylindrical regulators (Fig. 4) (Wójtowicz and Kotowski 2008a). In a conical vortex regulator, the liquid flows into the device through the inlet port (1), placed in the larger base of the cone, thus it is given a swirl motion that is maintained along the entire length of the chamber (2) up to the outlet port (3) at the upper end of the truncated cone. In this motion, the peripheral velocity increases as the cone's axis approaches, and due to the centrifugal force in the vortex chamber, the pressure decreases in the direction of its axis, so that the pressure reaches the ambient pressure value on the air core surface (4). The generated air core has a significant impact on the effectiveness of the device's throttling effect. The axis of the cone is most often deviated from the horizontal level by a certain angle, so that one of the generatrix of cone is horizontal so that the device itself dewatering. Sprayed liquid on the regulator outflow forms a cone with the flare angle γ (Wójtowicz and Kotowski 2008b).

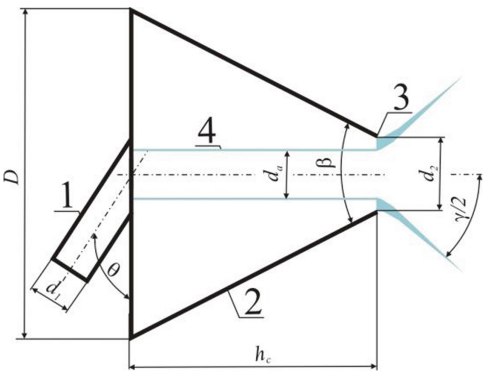

Fig. 4. Scheme of cylindrical vortex regulator

Taking into account the fact that the momentum on the swirl radius $R_0 = R - r_1$ on the regulator's input causes swirl motion, in which the predominant peripheral velocity depends on the surface area of the inlet port (r_1^2), and the centrifugal force in the outlet section is inversely proportional to the third power of the radius of the outlet port (r_2^3), a geometric constant K can be used to describe the discharge coefficient:

$$K = \frac{2R_0 \cos\theta d_1^2}{d_2^3} \tag{12}$$

which contains a trigonometric function $\cos\theta$ – the entry angle of inlet connector.

For the values of Reynolds number below 50000, the discharge coefficient is described by the following dependence:

$$\mu = 0,027\frac{d_2}{d_1} + 0,0056\frac{h_c}{d_1} - 0,0018\frac{D}{d_1} + 0,49K^{-0,19} - 0,005\left(\tan\frac{\gamma}{2}\right)^{4,9} - 0,214 \tag{13}$$

where:

$$\tan\left(\frac{\gamma}{2}\right) = 2,8K^{1,61}(\cos\theta)^{-1,36}\left(\frac{d_2}{d_1}\right)^{5,2}\left(\frac{h_c}{d_1}\right)^{-0,077}\left(\frac{D}{d_1}\right)^{-1,82} \tag{14}$$

The Reynolds number is defined as follows:

$$Re = \frac{2Q\rho}{\pi\eta r_1} \tag{15}$$

where: ρ is liquid density and η is liquid viscosity.

The analysis of Eq. (13) shows that the value of discharge coefficient is the lowest for the regulator with the inlet connector tangent to the chamber wall and perpendicular to its axis of symmetry – this construction variant was subjected to further analysis. Based on the analysis of data presented by Kim et al. (2007) and Kim et al. (2009) describing the modification of atomizer to stabilize the film thickness based on the preparation of so-called cylindrical *core-hole* in the axis of vortex chamber, flow regulators in the classic version and with the *core-hole* have been made.

Research on atomizers confirmed that this modification allows to obtain virtually constant thickness of liquid film, moreover, it is smaller than in the case of standard solution. This modification also resulted in a more regular outline of the sprayed stream (Włodarczak et al. 2018). By transferring this constructional solution to flow regulators under definite conditions, one can influence the values of liquid discharge coefficient (Ochowiak et al. 2018). The task of *core hole* is to stabilize the gas core forming in the outlet opening and in the vortex chamber.

Six vortex flow regulators were designed: cylindrical, conical, profiled and regulators with a *core hole* of the mentioned shapes. Their geometrical dimensions (developed on the basis of literature data and manufacturers' catalogs) were presented in Table 1, and the visualization was shown in Fig. 5. The completed projects were based on the system of rapid production of models of so-called 3D print in FDM technology.

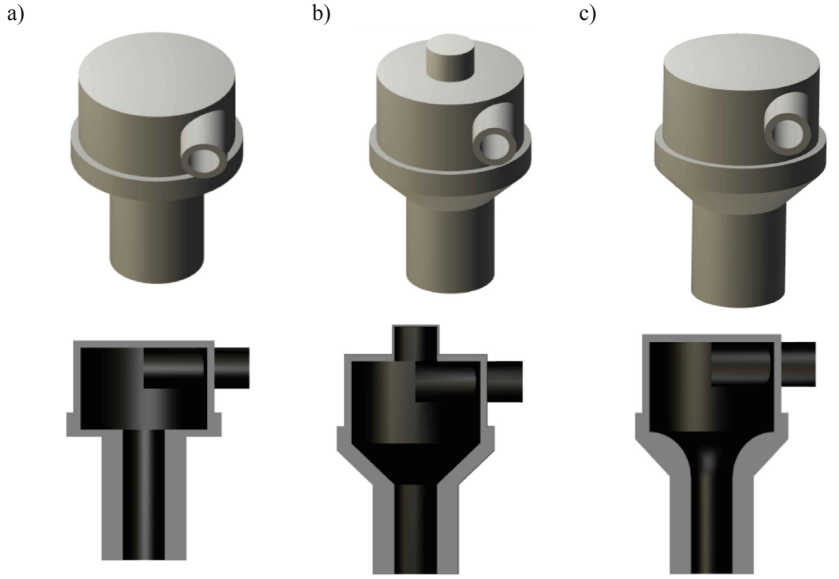

Fig. 5. Selected constructions of vortex regulators (front view and cross-section): (a) cylindrical, (b) conical, (c) profiled.

Table 1. Technical data of the regulators.

Description	Symbol	Value in meters
Inner diameter of inlet port	d_1	0.008
Inner diameter of outlet port	d_2	0.012
Inner diameter of vortex chamber	D	0.036
Height of vortex chamber	h_c	0.024
Inner diameter of *core hole*	d_3	0.014
Height of *core hole*	h_o	0.008

An exemplary graph of the dependence of the discharge coefficient on the Reynolds number calculated on the inlet port cross-section was shown in Fig. 6. The average values of discharge coefficients for the tested regulators with turbulent flow were summarized in Table 2. The accuracy of μ value was ± 0.01.

It was shown that the lowest values were characteristic for cylindrical regulators, and the highest values – profiled ones. Unfortunately, it was not possible to fully confirm the advantageous effect of the *core hole* on the value of discharge coefficient, which may result from the interaction of the geometry (dimensions) of the regulator and the *core hole* on the formation of gas core, and subsequently on the value of discharge coefficient. The application of *core hole* slightly reduced the discharge coefficient in the case of profiled regulator.

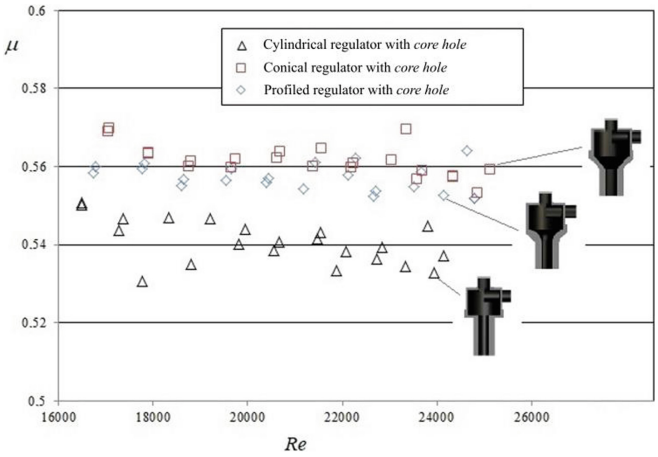

Fig. 6. Selected experimental results for vortex flow regulators with *core hole*.

Table 2. Discharge coefficient values.

Conventional flow regulator	μ	Flow regulator with *core hole*	μ
Cylindrical	0.53	Cylindrical	0.53
Conical	0.54	Conical	0.56
Profiled	0.62	Profiled	0.56

3 Summary

The obtained results are not only cognitive significance, but also practical one, because the proposed constructions of flow regulators are characterized not only by discharge coefficients comparable with other types of regulators (lower μ values compared to the opening and adapter ($\mu = 0.84$)), but also relatively simple construction not requiring movable elements. In this context, it seems advisable to conduct further research.

Acknowledgments. This research was supported by Ministry of Science and Higher Education through grant PUT 03/32/SBAD/0902.

References

Anduze, M., et al.: Analysis and testing of a fluidic vortex microdiode. J. Micromech. Microeng. **11**, 108–112 (2001)

Brombach, H.: Bistable vortex throttles for sewer flow control. In: Proceedings of IFAC Symposium of "Pneumatic & Hydraulic Components", Warszawa (1980)

Brombach, H.: Untersuchung Stromungsmechanischer Elemente (Auidik) und die Moglichkeit der Anwendung von Wirbelkammerelementen im Wasserbau. Ph.D. Thesis, Mitteilungen des Instituts fiir Wasserbau der Universitiit Stuttgart, Stuttgart (1972a)

Brombach, H.: Vortex devices in hydraulic engineering. In: Proceedings of 5th Cranfield Fluidics Conference, BHRA, Fluid Engineering, Cranfield, Bedford (1972b)

Ekol-Unicon Sp. z o.o.: Katalog regulatorów (2017)

Elalfy, Y.E.: Untersuchung der Stromungsvorglinge in Wirbelkammerdioden und Drosseln, Ph. D. Thesis, Mitteilungen des Instituts fiir Wasserbau der Universitlit Stuttgart, Stuttgart (1979)

Haakh, F.: Vortex chamber diodes as throttle devices in pipe systems. Computation of transient flow. J. Hydraul. Res. **41**(1), 53–59 (2003)

Huber, B., Prenner, R.: The influence of a vortex-flow throttle on transmission and reflection of pressure wave. In: Proceedings of 28th IAHR Congress, Graz (1999)

Jeżowiecka-Kabsch, K., Szewczyk, H.: Mechanika Płynów. Oficyna Wydawnicza Politechniki Wrocławskiej, Wrocław (2001)

Kim, S., Khil, T., Kim, D., Yoon, T.: Effect of geometric parameters on the liquid film thickness and air core formation in a swirl injector. Meas. Sci. Tech. **21**(3), 1–11 (2009)

Kim, S., Kim, D., Khil, T., Yoon, Y.: Effect of geometry on the liquid film thickness and formation of air core in a swirl injector. In: The 43rd AIAA/ASME/SAE/ASEE Joint Propulsion Conference & Exhibit 2007, Cincinnati, AIAA-2007-5460, pp. 1–8 (2007)

Kotowski, A., Wójtowicz, P.: Podstawy projektowania i zasady stosowania regulatorów wirowych przepływu cieczy w systemach wodociągowych i kanalizacyjnych. Etap III - raport końcowy. Politechnika Wrocławska, Instytut Inżynierii Ochrony Środowiska, Raport Serii SPR-1, Wrocław (2008)

Mays, L.W.: Stormwater Collection Systems Design Handbook. McGraw-Hill, New York (2001)

Ochowiak, M., Woziwodzki, S., Matuszak, M., Włodarczak, S.: Zgłoszenie patentowe P. 424372 pt.: Wirowy regulator przepływu cieczy (2018)

Orzechowski, Z., Prywer, J., Zarzycki, R.: Mechanika płynów w inżynierii środowiska. Wydawnictwa Naukowo-Techniczne, Warszawa (1997)

Włodarczak, S., Ochowiak, M., Matuszak, M., Markowska, M., Szewczyk, K.: Wpływ cylindrycznej przegrody na proces rozpylania w rozpylaczach wirowych. Inż. Ap. Chem. **57** (5), 158–159 (2018)

Wójtowicz, P., Kotowski, A.: Badania modelowe cylindrycznych regulatorów hydrodynamicznych. Ochrona Środowiska **30**, 35–41 (2008a)

Wójtowicz, P., Kotowski, A.: Badania modelowe stożkowych regulatorów hydrodynamicznych. Ochrona Środowiska **30**, 37–44 (2008b)

Wójtowicz, P.: Wpływ parametrów konstrukcyjnych i eksploatacyjnych wybranych regulatorów wirowych na ich charakterystykę hydrauliczną. Praca doktorska, Politechnika Wrocławska, Wroclaw (2007)

Zwara, W.: Oczyszczanie wód opadowych w infrastrukturze drogowej. Zeszyty Naukowo-Techniczne Stowarzyszenia Inżynierów i Techników Komunikacji Rzeczpospolitej Polskiej Oddział w Krakowie – materiały konferencyjne **62**(112), 115–135 (2004)

Physicochemical Aspects of Aerosol Generation in Electronic Cigarettes

Marcin Odziomek(✉)

Faculty of Chemical and Process Engineering,
Warsaw University of Technology, Warsaw, Poland
marcin.odziomek@pw.edu.pl

Abstract. Electronic cigarettes (e-cigarettes) have become popular consumer products being claimed both safer than tobacco cigarettes and helpful in smoking cessation. However, answering the questions concerning the safety and the possible health outcome of inhaling EC-aerosols requires reasonable predictions of preferred sites of their deposition in the respiratory system. It becomes necessary to have extensive knowledge of their physical properties, therefore, the aim of this work was to describe factors of the greatest influence on aerosols released from e-cigarettes. Generally, the generation process and the dynamics of an EC-aerosol forming from a gaseous mixture of e-liquids constituents is expressed by the detailed interplay between nucleation, evaporation, condensation and coalescence. As it was shown, the key role plays vapor saturation ratio that depends on the thermophysical properties of the individual compounds constituting e-liquid, the vaping topography that reflects individual habits of e-cigarettes users, the power applied to the heating coil and its construction.

1 Introduction

Tobacco became popular all over the world shortly after Columbus found "strange leaves" in the New World. Its rapid spread and growing popularity can be primarily explained by the psychoactive and highly addictive action of nicotine which constitutes approximately 0.6–3.0% of the dry weight of tobacco (Hoffmann and Hoffmann 1998). During centuries the mode of nicotine delivery has changed. In the 18th century, snuff taking became widespread throughout the world whereas since the 19th century tobacco was started to be burned, initially in the form of cigars and later of cigarettes. Burning tobacco allows to create an aerosol of nanosized particles that carry nicotine into the lungs, where it is absorbed and then delivered to the brain with blood. There it attaches to nicotine receptors and releases a chemical called dopamine which appear to be the primary factor in causing addiction (Mackay and Eriksen 2002).

Starting mass production of cigarettes in the 20th century contributed to greatly increased number of smokers. At the same time, the social awareness of the harmfulness of smoking grew very slowly. In the last decades, it has been scientifically proven that the combustion process of tobacco generates carcinogens, oxidizing agents, and other toxins which causes cancer (e.g., lung, oral cavity, esophagus, larynx, pancreas, bladder, kidney), chronic obstructive pulmonary disease (COPD), myocardial

© Springer Nature Switzerland AG 2020
M. Ochowiak et al. (Eds.): PAIC 2019, *Practical Aspects of Chemical Engineering*, pp. 271–281, 2020.
https://doi.org/10.1007/978-3-030-39867-5_29

infarction, and stroke (Mackay and Eriksen 2002). It can be said without exaggeration that smoking is the cause of the most deadly epidemic of modern times responsible for death of approximately 5–6 million people annually worldwide. No wonder that efforts have been made to develop less harmful cigarettes. One of the first innovations with the promise of harm reduction was the development of cigarettes with filters. The next major modification of cigarettes with safety implications was "low-yield" cigarettes, however, none of taken actions did not solve the problem.

Since the beginning of current century, high hopes for decreasing negative effects of cigarette smoking have been placed in electronic cigarettes (e-cigarettes). Like their classic counterparts, e-cigarettes create an inhalable aerosols (EC-aerosols) of ultrafine and submicrometer particles that rapidly delivers nicotine to the brain. However, reversely to them, e-cigarettes produce an aerosol without high temperature combustion of tobacco (Glantz and Bareham 2018).

Typical e-cigarette comprises a battery that powers a small heating element (heating coil) placed in the part called clearomizer (Fig. 1). The heater may be placed at either the top or bottom of the clearomizer.

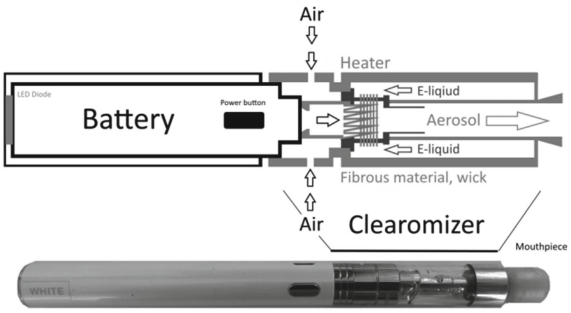

Fig. 1. Diagram showing an e-cigarette construction.

Clearomizer is filled with special solution for inhalation commonly known as e-liquid. It is a mixture of vegetable glycerin (VG) and propylene glycol (PG) that constitute together 95% of e-liquid volume, nicotine (0–30 mg/ml) and flavoring agents. When the user pushes a power button, or activates a pressure sensor by drawing air through device, the heating element heats e-liquid to the relatively low temperatures (100–250 °C) minimizing the level of carcinogens that could arise by thermal decomposition of e-liquid constituents (National Academies of Sciences, Engineering, and Medicine 2018; Glantz and Bareham et al. 2018). In consequence, e-cigarettes may pose less cancer risk to users but this doesn't mean that they are completely safe. Vapers (e-cigarettes users) are still exposed to high levels of droplets that can act as carriers for toxins. E-liquids and fibrous material that is used to absorb the e-liquid for heating and conversion to an aerosol come into contact with coil heater that contain heavy metals (tin, nickel, copper, lead, chromium). Williams et al. (2013) found nanoparticles of heavy metals in samples of e-cigarette liquids and aerosol. They can deposit with aerosol droplets into respiratory tract potentially causing local respiratory

toxicity or entering the bloodstream. The health effects depend on the area of aerosol deposition which is strictly related to the aerosol droplets size distribution. The most important factors that influence the size of droplets released from e-cigarettes are: the construction of the device, the power applied to the heating coil, composition and properties of inhaled liquids and so called vaping topography that reflects individual habits of e-cigarettes users. The main purpose of this work is to clarify the influence of mentioned factors on generation process and properties of aerosols released from e-cigarettes.

2 E-cigarette Operating Principle

In e-cigarettes aerosol is formed from a multicomponent gas mixture during rapid cooling when external air is drawn through device during inhalation. Under such conditions e-liquid vapor achieves high saturation level what is necessary for nucleation process. For each e-liquid constituent (x) saturation ratio of its vapor S_x is defined as the ratio of its current partial pressure in vapor phase P_x to its saturation vapor pressure over the flat surface of pure e-liquid constituent at the same temperature (Eq. 1):

$$S_x = \frac{P_x}{P_x^e} \tag{1}$$

When the vapor saturation ratio significantly exceeds unity ($S_x \gg 1$) the generation of new liquid phase is more energetically favorable. Under these conditions, thermal agitation of large number of gas molecules promotes density fluctuations that generate small aggregates of gas molecules (clusters). The increase of their volume by addition of new molecules causes energy gain (vapor's latent energy is released back into the surrounding as heat). However, the expansion of the cluster surface demands simultaneously energy to overcome the forces of surface tension. The competition between these two effects describes Eq. 2: (Curtius 2009; Jacobson 2005)

$$\Delta G = -\frac{4}{3}\pi R_p^3 \frac{k * T}{V_l} ln S_x + 4\pi R_p^2 \sigma_x \tag{2}$$

where: ΔG – the change in Gibbs free energy during nucleation as a function of the nucleating particle's radius R_p, k – Boltzmann constant, T – temperature, V_l – the volume occupied by molecule, σ_x – the surface tension of constituent x.

The first term of Eq. 2 is the driving force for the phase transition and in consequence the increase of the cluster's volume, the second one is the energy cost of creating new surface (Fig. 2).

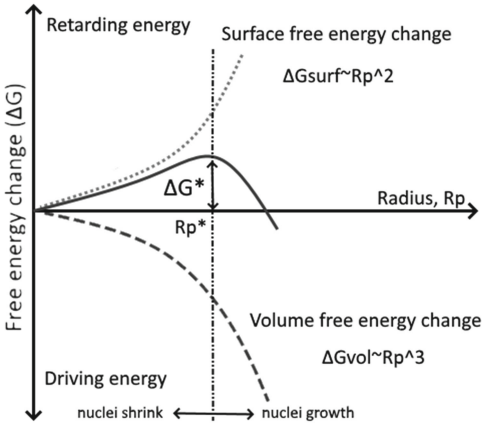

Fig. 2. Schematic diagram of the energies involved in homogeneous nucleation

The rate of increase of volume and that of surface area of clusters are not proportional. For a spherical structure volume increases as the cube of its radius, whereas the surface area shows increase in squares. This causes that initially, for very small clusters surface area expands with growing radius at a higher rate as compared to the volume and therefore the energy required to overcome surface tension forces exceeds the energy gain from creating new volume of liquid phase. This difference constitutes nucleation barrier which reaches maximum (ΔG^*) for clusters with critical radius R_p^* (Eq. 3). In simple terms, clusters of higher than R_p^* radius (critical nuclei) are mostly stable and grow by absorption of other molecules present in gas phase. Smaller clusters evaporate since as it was stated earlier this is more energetically favorable (Curtius 2009; Jacobson 2005).

$$\Delta G^* = \frac{4\pi}{3}\sigma_x R_p^{*2} = \frac{4\pi}{3}\sigma_x \left(\frac{2\sigma_x V_l}{kTlnS_x}\right)^2 \tag{3}$$

The height of the Gibbs free-energy barrier ΔG^* depends on the vapor saturation ratio. At the smallest supersaturation, closest to $S_x = 1$ the sizes of critical radius and the energy barrier are significantly larger than at higher values of S_x. High level of supersaturation decreases the maximum nucleation barrier and increases the nucleation rate – the number of clusters that grow beyond the critical size per second. The nucleation rate is connected to the height of the nucleation barrier by the Eq. 4: (Curtius 2009; Moody and Attard 2002)

$$J = \mathrm{C} * \exp\left(-\frac{\Delta G^*}{kT}\right) \tag{4}$$

The nucleation process may be facilitated by ambient particles as these inhaled during e-cigarettes vaping what is known as heterogeneous nucleation. The nucleation

barrier for heterogeneous nucleation is much lower than for homogeneous nucleation since the part of free energy equation related to surface expansion is in this case proportional not to the surface area of whole sphere but only to its part. This is due to the fact that the part of the nucleus boundary is accommodated by the surface or impurity onto which it is nucleating (Curtius 2009; Vehkamaki 2006).

3 Factors Affecting Nucleation Process and Aerosol Formation in E-cigarettes

3.1 E-liquids Composition and Physicochemical Properties of Their Constituents

The aerosol generation in e-cigarettes is strongly dependent on some thermophysical properties of the individual compounds constituting the multicomponent gas mixture. At given conditions the saturation ratio of e-liquids constituents in vapor phase may differ due to differences in their volatility which describes the tendency of a vapor to condense into a liquid. Volatility has no defined numerical value, but it can be described using vapor pressures or boiling points. High vapor pressures indicate a high volatility, while high boiling points indicate low volatility. Less volatile substances will more readily condense from a vapor than highly volatile ones (Nordlund and Kuczaj 2016; Wright et al. 2016).

The boiling points and saturated vapor pressures of the main e-liquid constituents in 20 °C are shown in Table 1.

Table 1. The boiling points and saturated vapor pressures in 20 °C of the main e-liquids components (Duell et al. 2018; Sosnowski and Odziomek 2018)

E-liquid constituent	Saturated vapor pressure in 20 °C [Pa]	Boiling point [°C]
VG	10^{-2}	290
PG	20	188,6
Nicotine	3,28	247
Water	2337	100

Comparing to water which is sometimes used as viscosity regulator in e-liquids the saturated vapor pressure of VG, PG and nicotine in 20 °C is relatively low. Simultaneously, the saturation vapor pressure for VG is approximately four orders of magnitude lower than that of PG. It has significant consequence for aerosol formation process in e-cigarettes. Assuming that Raoult's law can be used for e-liquid (ideal solution) that is heated to 100 °C and obtained vapor of partial pressure that can be calculated from Antoine equation (Duell et al. 2018) is then cooled to temperature of the interior of respiratory tract (37 °C), the saturation ratio from a e-liquid solution of PG, VG, nicotine and water with mole fractions of 0.29/0.65/0.05/0.01, respectively, would be 12.5 (PG), 32,700 (VG), 4.0 (nicotine), and 1.16 (water) (Floyd et al. 2018). It clearly shows that VG has high saturation ratio that is sufficient to initiate ultrafine particle nucleation and continue to drive condensation growth as the EC vapor cools in

the mouthpiece and oral cavity. The simulations of Nordlund and Kuczaj (2016) proved that glycerin plays key role in aerosol formation process. Absence of this compound in multicomponent gas mixture and lack of other nucleation centers may result that minor compounds of the gas mixture may not be able to reach supersaturation alone and therefore could not generate aerosol droplets.

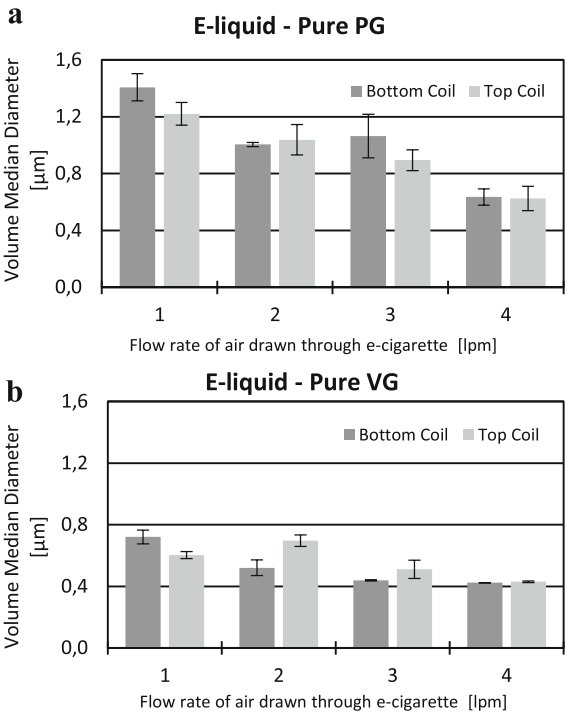

Fig. 3. Volume Median Diameter of aerosols released at different air flow rates from e-cigarettes equipped with a bottom and top coil clearomizer, e-liquid: **a** – pure propylene glycol (PG), **b** – pure vegetable glycerin (VG), mean with SD error bars, number of replicates r = 3

However, in real conditions, there is possible to generate aerosol even from e-liquid without glycerin. There are very popular liquids based in 100% on pure PG for vapers who like a stronger "throat hit", similar to that of tobacco cigarettes. Also experimental results indicate that it is possibility to generate aerosol from pure PG. As it was shown in Fig. 3 the Volume Median Diameter (VMD) of aerosol generated from pure PG is significantly higher than for pure VG aerosol.

Presented in Fig. 3 author's results were obtained with e-cigarette Navy V4 (Volish) equipped with top (Crystal CE10+) and bottom (Volitank) coil clearomizer operating at similar power level and laser diffractometer (Spraytec, Malvern, UK) which is more suitable for studies of concentrated aerosols such as those released by TCs or ECs than techniques that require dilution of the samples (Sosnowski and Odziomek 2018).

One explanation for the significant differences in VMD might be higher saturation vapor pressure of pure PG when compared to VG. On the one hand, this makes it difficult to achieve high levels of vapor saturation, but on the other hand the presence of nucleation centers in ambient air drawn through e-cigarette decreases nucleation barrier and facilitate forming droplets of pure PG. Simultaneously, there is more PG vapor available to form a greater number of particles that next can grow by condensation and coagulation. Another explanation might be related to viscosities of both compounds. At high levels of power applied to the heater the e-liquid transport through wicking material surrounding the heating coil may constitute limiting step regardless of the clearomizer construction (top or bottom coil). This is especially plausible for highly viscous liquids as those with high content of glycerin. When the wick soaked with viscous liquid approaches its maximum flow rate, the energy loss from e-liquid evaporation becomes limited. It causes that any further power applied to the heating coil will result only in higher coil temperature but not more vaporization (Floyd et al. 2018). It increases risk of thermal decomposition of glycerol. Literature data shows that the higher the percentage ratio of VG to PG, the higher the concentrations of the carbonyl compounds emitted especially the acetaldehyde, benzaldehyde, acrolein, and acetone (Ooi et al. 2019).

3.2 Flow Rate of External Air Drawn Through Device During Inhalation

As it was shown in the Fig. 3 the flow rate of air drawn through e-cigarette during inhalation significantly affects VMD of the released aerosol what is clearly seen for both e-liquids compositions. VMD decreases with growing flow rate what can be explained by intensifying dilution of e-liquid vapor. This entails decrease of vapor saturation ratio what has direct influence on the number of created critical nuclei and their further growth by vapor absorption and coagulation.

Normally, the flow rate of air drawn through e-cigarette is unsteady and strictly related to the vaping topography – the term referring to pattern of how a person uses e-cigarette including number of puffs, puff volume, duration, and velocity (Behar et al. 2015). Puff volume from ECs can be between ~30 and more than 350 mL depending on e-cigarette user. Also, the median flow rate during puffing and the puffing time is scattered (~25–100 mL/s and 0.7–6.9 s, respectively). Generally, according to work of Robinson et al. (Robinson et al. 2015) there are three, the most frequent patterns of vaping (shown in Table 2).

Table 2. Three representative puff topographies of electronic cigarettes users (Robinson et al. 2015)

Puff topography	Puff duration [s]	Flow rate [ml/s]	Flow rate [lpm]	Puff volume [ml]	Puff interval [s]	Puff period [s]
Many short	1.4	30	1.8	42	18.4	19.8
Typical	3.7	39	2.3	144	48.7	52.4
Fewer long	6.9	44	2.6	304	47.7	54.6

Use of the breathing simulator (ASL 5000XL, Ingmar Medical, USA) allowed to release aerosol from e-cigarette (iKonn 220, Eleaf) operated at 40 W in the air flow conditions reflecting vaping patterns listed in Table 2. Measurements of droplet size distribution made with laser diffractometer (shown in Fig. 4) indicate that aerosol of the highest VMD was released when the volume of inhaled air was the smallest and the time of inhalation was the shortest. This suggest that produced vapor reaches the highest saturation ratio in this vaping topography regardless the shortest time of heater supply what should limit e-liquid temperature and the amount of vaporized mass. This suggest that the key factor influencing the properties of aerosol released at given heating coil construction and applied power was the smallest air flow drawn through e-cigarette.

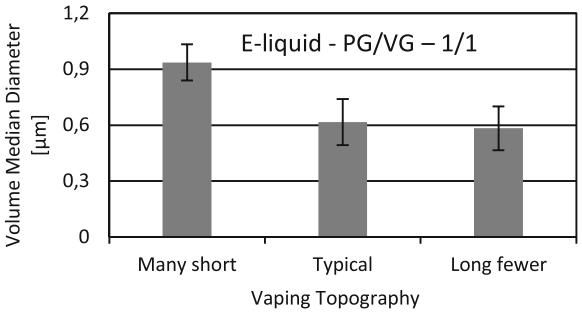

Fig. 4. Volume Median Diameter of aerosol released from e-cigarette at different vaping topographies (According to Table 2), mean with SD error bars, number of replicates r = 3

3.3 Construction and the Power Applied to the Heating Coil

According to Joule's first law the amount of heat emitted during current flow through an electric conductor is directly proportional to the product of the electric resistance of the conductor R, the square of the current I and the current flow time t (Eq. 5):

$$Q = R \cdot I^2 \cdot t \tag{5}$$

The product of R and I^2 is the electrical power consumed by an electrical appliance such as the heating coil in e-cigarette. Generally, the amount of power that is dissipated in the heater is equal the work done in pushing an electric charge round an electrical circuit in time t. Joule's law can be combined with Ohm's law to obtain alternative expressions for the amount of power applied to the heater and dissipated as heat (Eq. 6):

$$P = R \cdot I^2 = U \cdot I = \frac{U^2}{R} \tag{6}$$

where: U is the electric potential or voltage.

If e-cigarette would be equipped with source giving constant current the heater coil of higher resistance would allow to generate more power. However, heaters in e-cigarettes are supplied with a constant voltage what causes that to achieve higher power a lower resistance heater is required. Author's experimental data obtained with laser diffractometer and e-cigarette e-Grip (Joyetech) equipped with heating coils of different resistances *R*, and the power fixed at 30 Watts show that low resistance heaters (0.25 and 0.5 Ω) - intended to DTL (Direct to Lung) vaping technique produce aerosol of higher VMDs (1.36 ± 0.46 and 1.58 ± 0.07 μm respectively) than high resistance heating coil intendent to MTL (Mouth to Lung) vaping technique (0.68 ± 0.03 μm). It can be explained by higher temperature of low resistance coils due to increased current flow and more intensive e-liquid vaporization.

As fallows from the Eq. 6 the level of power dissipated by heating coil can be regulated by change of the voltage. Author's experimental results shown in Fig. 5 indicate that such changes significantly affects the VMD of released aerosol.

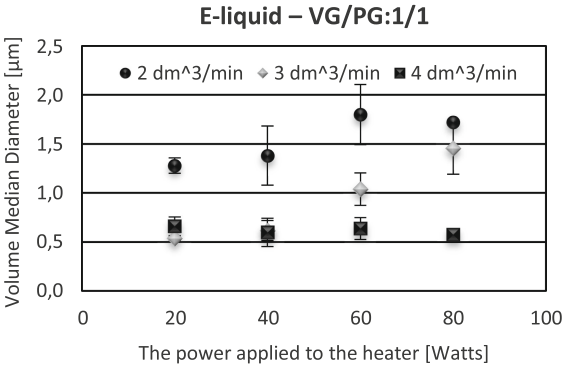

Fig. 5. The influence of the power applied to the heater on VMD of aerosols released from e-cigarettes at different flow rates of air drawn through device, mean with SD error bars, number of replicates r = 3

As the power was increased more e-liquid was vaporized, resulting in a greater saturation ratio and more vapor mass available to form primary particles. Increased number of primary particles intensify their growth due to coagulation and condensation. This effect if clearly visible especially for low air flow rates (2 lpm) when the dilution of vapor was not as high as for higher air flow rate (4 lpm).

On the other hand, the temperature reached by the liquid and the amount of vaporized mass depends also on the effectiveness of heat exchange between the coil and the e-liquid. The heating coils used in e-cigarettes can be single, double, triple or even quadruple with the same or similar resistance *R*. This is due to the fact that heating coils can be made from materials that differ in internal resistance (kanthal, stainless steel, nichrome) and from wires of different gauge and length (thicker wires have smaller resistance). In consequence, the surface of heat exchange with e-liquid may significantly vary. Results of author's measurements with e-cigarette iKonn 220 (Eleaf)

equipped with heaters of similar resistance (HW3 – 0.2 Ω and HW4 – 0.3 Ω) but different number of coils (triple and quadruple respectively) and the power fixed at 40 W (air flow rate 2 lpm) confirms that the surface of heat exchange between heating coil and e-liquid may have significant influence of aerosol properties (VMD equal 1.90 ± 0.16 for Triple Coil and 2.14 ± 0.10 μm for Quadruple Coil).

4 Conclusions

The generation process and the dynamics of an EC-aerosols forming from a gaseous mixtures of e-liquids constituents is expressed by the detailed interplay between evaporation, nucleation, condensation and coalescence. The key role plays vapor saturation ratio that depends on the thermophysical properties of the individual compounds constituting e-liquid, the vaping topography and power applied to the heating coil and its construction. Since there are many factors influencing properties of EC-aerosols the possible health outcome from their using is difficult to assess and demands further intensive examination.

Acknowledgments. The author would like to thank: Professor Tomasz R. Sosnowski for helpful suggestions and discussions regarding the contents of this paper, Ms. Magdalena Ryszkowska and Ms. Marta Biaduń for help in experimental measurements.

This work was financially supported by National Science Centre in Poland under the Project No. 2015/19/D/ST8/00822.

References

Behar, R.Z., Hua, M., Talbot, P.: Puffing topography and nicotine intake of electronic cigarette users. PLoS ONE **10**(2) (2015). https://doi.org/10.1371/journal.pone.0117222

Curtius, J.: Nucleation of atmospheric particles. Eur. Phys. J. Conf. **1**, 199–209 (2009)

Duell, A.K., Pankow, J.F., Gillette, S.M., Peyton, D.H.: Boiling points of the propylene glycol + glycerol system at 1 atmosphere pressure: 188.6–292 °C without and with added water or nicotine. Chem. Eng. Commun. **205**(12), 1691–1700 (2018)

Floyd, E.L., Queimado, L., Wang, J., Regens, J.L., Johnson, D.L.: Electronic cigarette power affects count concentration and particle size distribution of vaping aerosol. PLoS ONE **13**(12), 1–15 (2018)

Glantz, S.A., Bareham, D.W.: E-cigarettes: use, effects on smoking, risks, and policy implications. Ann. Rev. Public Health **39**, 215–235 (2018)

Hoffman, D., Hoffman, I.: Chemistry and toxicology. In: Shopland, D.R. (ed) Smoking and Tobacco Control Monograph No. 9. National Cancer Institute (NCI), U.S. Dept. of Health and Human Services, National Institutes of Health, National Cancer Institute (1998)

Jacobson, M.Z.: Fundamentals of Atmospheric Modelling. Cambridge University Press, New York (2005)

Mackay, J., Eriksen, M.: The Tobacco Atlas. World Health Organization, Geneva (2002)

Moody, P.M., Attard, P.: Homogeneous nucleation of droplets from a supersaturated vapor phase. J. Chem. Phys. **117**(14), 6705–6714 (2002)

National Academies of Sciences, Engineering, and Medicine: Toxicology of e-cigarette constituents. In: Eaton, D.L., Kwan, L.Y., Stratton, K. (ed.) Public Health Consequences of E-Cigarettes, pp. 155–216. National Academies Press (US), Washington DC (2018)

Nordlund, M., Kuczaj, A.K.: Modeling aerosol formation in an electrically heated tobacco product. Int. J. Chem. Mol. Eng. **10**(4), 373–385 (2016)

Ooi, B.O., Dutta, D., Kazipeta, K., Chong, N.S.: Influence of the e-cigarette emission profile by the ratio of glycerol to propylene glycol in e-liquid composition. ACS Omega **4**, 13338–13348 (2019)

Robinson, R.J., Hensel, E.C., Morabito, P.N., Roundtree, K.A.: Electronic cigarette topography in the natural environment. PLoS ONE **10**(6) (2015). https://doi.org/10.1371/journal.pone.0129296

Sosnowski, T.R., Odziomek, M.: Particle size dynamics: toward a better understanding of electronic cigarette aerosol interactions with the respiratory system. Front. Physiol. **9**, 853 (2018). https://doi.org/10.3389/fphys.2018.00853

Williams, M., Villarreal, A., Bozhilov, K., Lin, S., Talbot, P.: Metal and silicate particles including nanoparticles are present in electronic cigarette cartomizer fluid and aerosol. PLoS One **8**(3), 1–11 (2013)

Wright, T.P., Song, C., Sears, S., Petters, M.D.: Thermodynamic and kinetic behavior of glycerol aerosol. Aerosol. Sci. Tech. **50**(12), 1385–1396 (2016)

Vehkamaki, H.: Classical Nucleation Theory in Multicomponent Systems. Springer, Heidelberg (2006)

Application of Rotating Magnetic Field to Intensify the Processes in Airlift Reactor

Joanna Padiasek, Marian Kordas, Maciej Konopacki, and Rafał Rakoczy(✉)

Faculty of Chemical Technology and Engineering,
West Pomeranian University of Technology, Szczecin, Poland
rrakoczy@zut.edu.pl

Abstract. The chapter presents the experimental investigation of influence of the rotating magnetic field (RMF) on the hydrodynamic parameters and the oxygen mass transfer process in the novel construction external loop airlift reactor. The results show that the usage of RMF generator leads to the improvement of gas hold-up and the overall volumetric mass transfer coefficient, k_La, in the tested apparatus. Moreover, it is also proved that the mixing time under RMF exposition reaches significantly lower values in comparison to standard non-magnetically assisted airlift reactor.

1 Introduction

Good bioreactor design is a key factor in many biological processes (Chisti and Moo-Young 1987). Despite the intensive development of the bioreactors, such problems as maintaining stability and the rate of the bioprocess are still not eliminated. The possible reason for these failures might be the inadequate construction of the bioreactor leading to insufficient mixing (Mahmood et al. 2015). Considering that many of the biological processes, especially cellular respiration, are aerobic, the oxygen transfer rate is also a limiting factor affecting the process performance (Garcia-Ochoa and Gomez 2009). Traditionally, in most aerobic bioprocesses the gas-liquid or gas-slurry reactors are used (Chisti and Moo-Young 1987). The parameters characterizing the amount of the gas phase deposited in the liquid phase and the oxygen transfer rate through the interfacial surface area the basic quantities determined for processes taking place in gas-liquid reactors. The gas hold-up is one of the most important parameters characterizing hydrodynamics of airlift reactor and expresses quantitatively the amount of gas-phase dispersed in liquid phase in the form of bubbles. The oxygen transfer rate in bioreactors can be characterized by the overall volumetric gas-liquid mass transfer coefficient k_La (Fadavi and Chisti 2005).

The enhancement of the mass transfer rate in bioreactors is often realized by the augmentation of the interfacial area between gas and liquid phases. The stirred tanks are commonly used reactors for carrying out gas-liquid processes. These devices ensure efficient development of the interfacial area due to the mechanical break-up of bubbles. However, stirred reactors are characterized by high operating costs and energy

© Springer Nature Switzerland AG 2020
M. Ochowiak et al. (Eds.): PAIC 2019, *Practical Aspects of Chemical Engineering*, pp. 282–293, 2020.
https://doi.org/10.1007/978-3-030-39867-5_30

requirements (Mahmood et al. 2015). Nowadays, the pneumatically agitated bioreactors are the most important group of multiphase contactors used in biological and chemical processes (Moraveji et al. 2011). One of the groups of bubble reactors used in the gas-liquid processes is the airlift reactors. The construction of these reactors and the hydrostatic pressure differences in the main bioreactor sections enable the circulation of fluids in the apparatus. In comparison to the stirred tanks, the airlifts characterize simple, non-mechanical construction and good mass and heat transfer properties (Chisti 1989, Drandev et al. 2016).

The airlift reactors belong to the group of bubble columns and usually consist of four distinct sections: two vertical columns (riser and downcomer) and two horizontal sections (bottom connector and top gas separator). The geometry of the airlift reactor provides the liquid circulation between the riser and the downcomer sections. The energy of the gas stream is introduced into the reactor at the bottom of the riser. It generates the flow of the liquid and dispersed gas phase upwards into the disengagement section where most of the bubbles are lost (Guieysse et al. 2011). The weakly-aerated liquid phase flows into the downcomer section where fluids move downward. The hydrostatic pressure difference between the riser and the downcomer sections provides the driving force for the liquid circulation (Drandev et al. 2016).

Some recent studies have been focused on the application of magnetic fields (MFs) in the different areas of biological and chemical engineering (Rakoczy et al. 2016). Previous research has established that the three-phase rotating magnetic field (RMF) can be efficiently used to enhance the gas-liquid mass transfer process in the bubble column (Rakoczy et al. 2017; Rakoczy et al. 2018). Hristov (2002) presented a series of reviews introducing the mass transfer process in the magnetically assisted reactors. Al-Qodah (2000) in his study demonstrated that the continuous production of penicillin antibiotics in a three-phase airlift fermenter can be enhanced with the transverse magnetic field. Moreover, the increase in gas phase hold-up and gas-liquid mass transfer coefficient in airlift with magnetic particles under the influence of the external magnetic field was proved (Al-Qodah and Al-Hassan 2000). Chen and Leu (2001) also provide that the gas hold-up and the mass transfer coefficient increased with the increase in the MF intensity. Li et al. (2007) shown that electromagnetic field effects on the algal growth and nutrition composition in a magnetic airlift photo-bioreactor. It has been demonstrated that a magnetically assisted airlift reactor can be used to increase the phenol degradation rate using the microorganism (Rao et al. 1997). Hristov (2005) pointed out that the variation of MF intensity can influence the liquid circulation velocity and gas hold-up. It has been suggested that the magnetically stabilized bed may control the hydrodynamics in an external loop airlift reactor (EL-ALR) instead of the variation of gas velocity.

The main aim of this work is to present the experimentally confirmed influence of a rotating magnetic field on mixing efficiency and gas-liquid oxygen transfer in a novel construction of magnetically assisted EL-ALR (MA-EL-ALR).

2 Experimental Details

The measurements were carried out using the experimental set-up presented in Fig. 1. The reactor was made of stainless steel (body) and reinforced silicone pipe (reactor columns). Two vertical sections: the riser (1) and the downcomer (2) were connected by the bottom section (built of T-connectors (3, 4) and connector (10)) and gas disengagement section (9). The vertical pipes have an inner diameter equal to 0.1 m. The height of the riser and downcomer section was equal to 0.84 m. The length of the bottom section (between axes of the vertical zones) was equal to 0.52 m. The dimensions of the gas disengagement section were equal to 0.79 m (length), 0.28 m (width) and 0.36 m (height). However, the liquid height in this part of the apparatus was 0.05 m. The working volume of the MA-EL-ALR was equal to 29.4 dm^3. The apparatus was equipped with four-probe taps, each two of them were placed in the riser section and the downcomer, respectively. The distance between probes located in the vertical sections was equal to 0.63 m. The airlift reactor was equipped with two rotating magnetic fields generators (6, 7) located in the riser and the downcomer. The frequency of RMF was controlled using electronic control boxes and two AC transistorized inverters (14, 15). The maintaining of the constant temperature during measurement was achieved by using a cooling system. The generators were placed inside the internal coils (13). All these elements were submerged in the transformer oil. Moreover, the transformer oil was recirculated using the pump (11) through the plate heat exchanger (12) supplied with cold water.

The applied rotating magnetic field was generated using two 3-phase stators of the squirrel cage induction motors. The frequency of the supplied current was changed in the range f = 10–50 s^{-1} and the voltage supplied to the windings was varied between 10 and 100 V. The control and change of the frequency of generated RMF were realized by two PC (see Fig. 1) equipped with the software. The generated RMF was characterized by the magnetic induction, B, depending on the AC frequency. The usage of the standard transverse probe was proposed for establishing the values of B at a different point inside the riser and downcomer sections. The detailed procedure of the magnetic induction determination values inside the generators was presented in the previous paper (Lechowska et al. 2019). Based on the presented experimental results in the mentioned work, it should be noticed that the applied magnetic field is strongly non-homogenous and spatially distributed. The maximal values of the magnetic induction were recorded in the middle of the height of the RMF generator and close to the windings (values strongly decrease with the distance from the windings). The obtained values of the magnetic induction, B, determined for different points in the RMF generator, were averaged. The B_{avg} values changed in the range from 9.77 mT (for f = 10 s^{-1}) to 14.70 mT (for f = 50 s^{-1}).

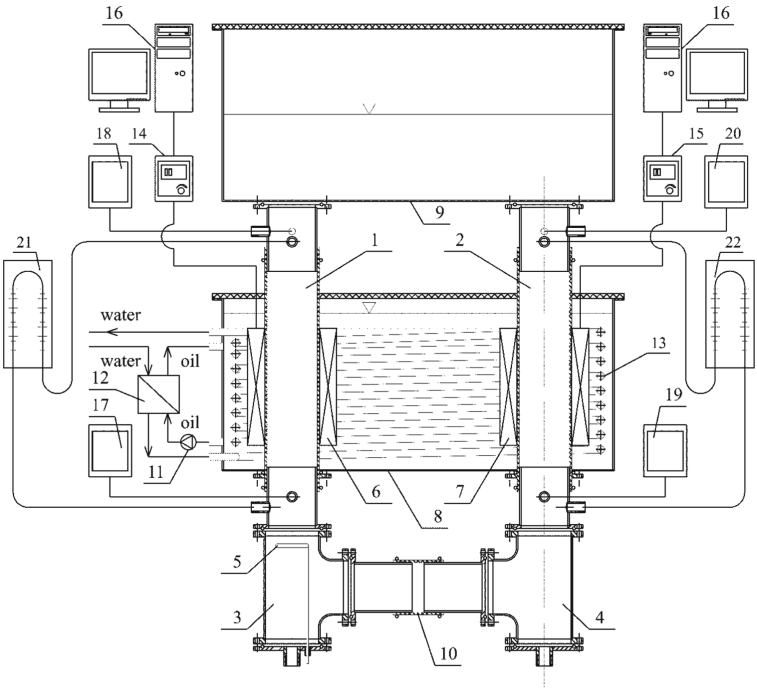

Fig. 1. Experimental set-up: 1 – riser; 2 – downcomer; 3, 4 – T-connector; 5 – sparger; 6, 7 – RMF generator; 8 – housing; 9 – disengagement section; 10 – connector; 11 – pump; 12 – heat exchanger; 13 – internal coil; 14, 15 – transistorized inverter; 16 – personal computer; 17–20 – multifunctional meter; 21–22 – U-tube manometer

In the presented experiments, tap water was used as a working liquid and compressed air as a gas phase. The gas flow rate was varied between 2 and 14 $dm^3\ min^{-1}$. The temperature of the liquid phase during the measurements was controlled to be constant and was equal to 24 ± 1 °C.

The volumetric gas hold-up of a gas-liquid dispersion was determined by measuring the differential pressure between two probe taps using the inverted U-tube manometer method (El Azher et al. 2005). The experimental set-up was equipped with two U-tube manometers located in the riser and downcomer sections, respectively (see Fig. 1). The hold-up values were determined separately for the riser and downcomer sections and calculated as follows:

$$\varepsilon = \frac{\Delta h}{\Delta z}\,\frac{\rho_L - \rho_G}{\rho_L} \tag{1}$$

where: ρ_G – gas-phase density, kg m^{-3}; ρ_L – liquid phase density, kg m^{-3}; Δh – liquid level difference in U-tube manometer, m; Δz – the distance between stub pipes, m.

The overall liquid-side volumetric mass transfer coefficient k_La was obtained using the dynamic oxygen desorption method (El Azher et al. 2005; Shah et al. 2012). Oxygen was desorbed by introducing nitrogen into the liquid phase through the sparger. The volumetric gas flow rates of nitrogen and compressed air were controlled by rotameters. First, the liquid phase was purged with nitrogen until the oxygen concentration became lower than 1% of saturation. Then the air stream was injected into the airlift reactor. The dissolved oxygen concentration was measured simultaneously using four COG probes and recorded by four multifunctional meters. The airflow into the reactor was followed until the liquid becomes nearly saturated with oxygen. The oxygen transfer rate characterized by the overall volumetric gas-liquid mass transfer coefficient k_La can be described by the following equation (Fadavi and Chisti 2005):

$$\frac{dC_L}{dt} = k_La(C^* - C_L) \tag{2}$$

where: k_La – volumetric mass transfer coefficient, s^{-1}; C^* – saturation concentration of dissolved oxygen in the liquid phase, kmol m^{-3}; C_L – the instantaneous oxygen concentration, kmol m^{-3}.

In the dynamic method, integration of the above-mentioned formula (taking into account that $C_L = C_0$ at $t = 0$ and $C_L = C_L$ at $t = t$) results as follows:

$$k_La = -\frac{1}{t}\ln\left(\frac{c^* - c}{c^* - c_0}\right) \tag{3}$$

where: c_0 – initial concentration of dissolved oxygen, kmol m^{-3}; c^* – saturation concentration of dissolved oxygen, kmol m^{-3}; c – instantaneous concentration of dissolved oxygen, kmol m^{-3}; k_La – volumetric liquid-side mass transfer coefficient, s^{-1}; t – time, s.

The mixing time values were determined using the tracer response method (Chisti 1989). In the conducted experiments, the saturated solution of NaCl was used as a tracer. The solution was introduced into the water at the top of the downcomer section. The tracer responses were measured using four conductive probes located in two vertical sections (every 2 probes in riser and downcomer sections, respectively). The conductivity values were recorded by four multifunctional meters. Signals from conductivity probes were normalized to minimalize effects of different probe gains by using the following equations (Paul et al. 2004):

$$\sigma_n = \left|\frac{\sigma(t) - \sigma_0}{\sigma_\infty - \sigma_0}\right| \tag{4}$$

where: σ_n – normalized probe output; $\sigma(t)$ – instantaneous conductivity of liquid, $\mu S \cdot cm^{-1}$; σ_0, σ_∞ – initial and final conductivity of the liquid, respectively, $\mu S \cdot cm^{-1}$.

Then, the mixing time was calculated using the RMS variance described by the following relation (Paul et al. 2004):

$$\log \sigma^2 = \log\left\{\frac{1}{4}\left[(\sigma_{n1}-1)^2+(\sigma_{n2}-1)^2+(\sigma_{n3}-1)^2+(\sigma_{n4}-1)^2\right]\right\} \quad (5)$$

where: $log\ \sigma^2$ – RMS variance; σ_{n1}, σ_{n2}, $\sigma_{n3,}$ σ_{n4} – dimensionless conductivity of liquid detected by probes 1–4, respectively.

3 Results and Discussion

The gas hold-up values were determined separately in the riser and downcomer sections. In the conducted experiments were changed three operating parameters: the gas flow rate (expressed as superficial gas velocity), location of exposition of rotating magnetic field and RMF frequency. During the experiments, three operation modes were performed: (i) exposition of RMF was turned-off on both riser and downcomer sections, (ii) the RMF exposition was turned on in the riser section and turned off in the downcomer section, respectively, and (iii) the RMF exposition was turned on in the downcomer section and turned off in the riser section, respectively.

The obtained values of gas hold-up (ε) in the riser and downcomer sections are presented in Fig. 2. Figure 2a illustrates the influence of gas flow rate and RMF exposition in riser section (f_R = 0, 10 and 50 s^{-1}) on gas hold-up in the riser (ε_R) and downcomer (ε_D) sections. The hold-up values in the presence of RMF in the downcomer section (f_D = 0, 10 and 50 s^{-1}) are shown in Fig. 2b.

As can be noticed based on the above-presented figures, the gas hold-up values in both riser and downcomer sections are strongly dependent on the volumetric gas flow rate of the compressed air stream. The riser section characterizes the significantly higher values of gas hold-up than the downcomer section. It should be noticed that the driving force of the circulation of the fluid in the airlift reactor is related to the difference of gas hold-up values in both riser and downcomer sections. Changes in the gas hold-up range are connected to increasing or decreasing of the circulation rate. The volumetric gas stream flow rate corresponds to the flow pattern in the bubble reactors. In the homogenous regime (when the superficial gas velocity is low) the size of gas bubbles is uniform. However, the heterogeneous regime characterizes the coalescence into larger bubbles which have higher velocity and shorter residence time thus determining the decrease in the gas hold-up. The application of RMF results in the augmentation of the gas hold-up in both main sections of the analyzed airlift reactor. This observation may be related to the residence time of the bubbles under the influence of the rotating magnetic field. The exposition of the external magnetic field may lead to an increase in the bubble residence time increasing gas hold-up (Al-Qodah and Al-Hassan 2000). It was also proved by Rakoczy et al. (2017) that the gas bubbles can be directed towards the magnetic field generator source where the intensity of MF is maximal.

a)

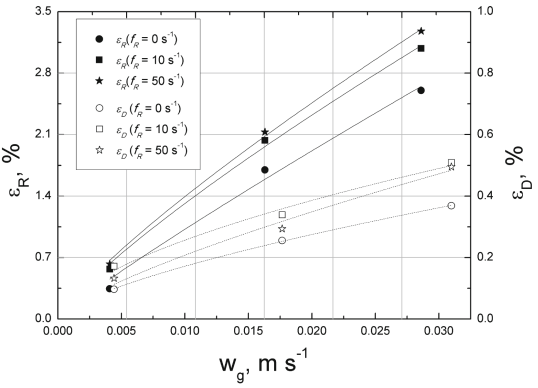

b)

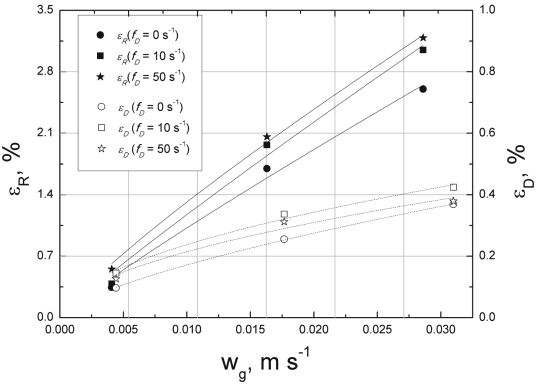

Fig. 2. Gas hold-up vales in the riser (ε_R) and downcomer (ε_D) sections as a function of superficial gas velocity w_g and frequency of RMF (0–50 s^{-1}) exposed in the riser section (a) and downcomer section (b)

The oxygen concentration in the liquid phase was measured by four oxygen probes. The probes were placed in the upper and lower stub pipes in the riser and downcomer sections, respectively (see Fig. 1). The system of the sensors allowed us to determine the value of the k_La coefficient in these four locations. Values of k_La for the riser section were determined as an average of the k_La obtained in the upper and lower location in this section. Similarly, the value of k_La was determined for the downcomer section. The characteristic of the RMF influence on the mass transfer process in the apparatus was based on the averaged value of k_La for the entire volume of airlift reactor in the presence of RMF in riser or downcomer section. The obtained results were described by the following power function:

$$k_La = p_1 w_g^{p_2} \tag{6}$$

where: p_1, p_2 – parameters; w_g – superficial gas velocity, m · s^{-1}.

The efficiency of the influence of RMF generation on the oxygen transfer rate in the novel type of MA-EL-ALR was determined by evaluating the effectiveness factor for the k_La coefficient values. The improvement factor (E) was defined for both modes: in the presence of RMF in the riser and the downcomer section, respectively:

$$E = \frac{k_La|_{WPM} - k_La|_{WPM=0}}{k_La|_{WPM=0}} \cdot 100\% \quad (7)$$

where: $k_La|_{WPM}$ - averaged k_La coefficient in the presence of RMF in the riser or downcomer section, respectively, s^{-1}; $k_La|_{WPM=0}$ - averaged k_La coefficient without exposition of RMF, s^{-1}.

The calculated values of the E-factor are graphically presented in Fig. 3. Table 1 presents the obtained mathematical correlations for the effectiveness factor.

Table 1. Obtained correlations between the effectiveness factors and superficial gas velocity for the tested operational conditions.

RMF location	RMF frequency/induction	Relation
Riser – on	f = 10 s^{-1}	$E_R = 3.0527 w_g^{-0.4115}$ (8)
Downcomer – off	B_{avg} = 9.77 mT	
Riser – on	f = 50 s^{-1}	$E_R = 0.9129 w_g^{-0.5802}$ (9)
Downcomer – off	B_{avg} = 14.70 mT	
Riser – off	f = 10 s^{-1}	$E_D = 0.1523 w_g^{-0.9989}$ (10)
Downcomer – on	B_{avg} = 9.77 mT	
Riser – off	f = 50 s^{-1}	$E_D = 0.0713 w_g^{-1.1249}$ (11)
Downcomer – on	B_{avg} = 14.70 mT	

According to the presented data the following conclusions may be observed. It has been proved that the rotating magnetic field generation increases the mass transfer rate in a magnetically assisted airlift reactor. It should be noticed that significantly higher values of efficiency factor were obtained during RMF exposition in the downcomer section than for the RMF exposition in the riser section for the lowest value of superficial gas velocity and frequency of RMF equals to 10 s^{-1}. However, the increase of w_g results in the sharp decline of the E-factor values as can be observed in Fig. 3b. The exposure of the rotating magnetic field in the riser zone results in lower but more gently decreasing values of the efficiency coefficient. The conducted hydrodynamic experiments might be useful for the explanation of the above observed phenomena. It should be noticed the hydrodynamics and mass transfer processes in the airlift reactors are strongly dependent on the gas flow rate and gas hold-up values in the entire apparatus. The driving force of the liquid circulation in the airlift columns is the consequence of the difference of gas hold-up values between the riser and downcomer sections. It is obvious that the bigger the difference between ε values, the faster the liquid circulation in the reactor. The hydrodynamic parameters in bubble and airlift columns are primarily controlled by the cycling rate and liquid turbulence that is

a)

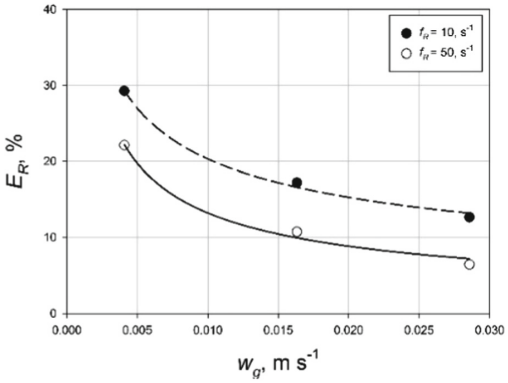

b)

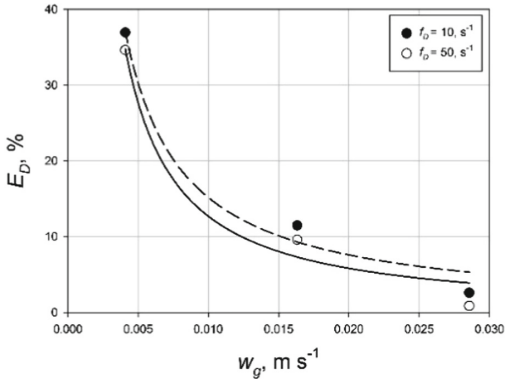

Fig. 3. Effectiveness factor values as a function of superficial gas velocity and frequency of RMF exposed in the riser section (a) and the downcomer section (b)

enhanced by the increase of the superficial gas velocity. Figure 4 presents the *E*-factor values for mixing time obtained in the presence of RMF exposition in the riser section (Fig. 4a) and in the downcomer (Fig. 4b).

The presented results of mixing time investigation in the airlift reactor indicated the effects of rotating magnetic field exposition in both riser and downcomer sections on the tested parameter. The *E*-factor values decrease with increasing RMF frequency and the most positive effect is observed for the lowest w_g values. The lowest values of mixing time were obtained for the RMF exposure in the downcomer section at the superficial gas velocity equal to 0.005–0.01 m • s^{-1} and the RMF frequency equal to 50 s^{-1}.

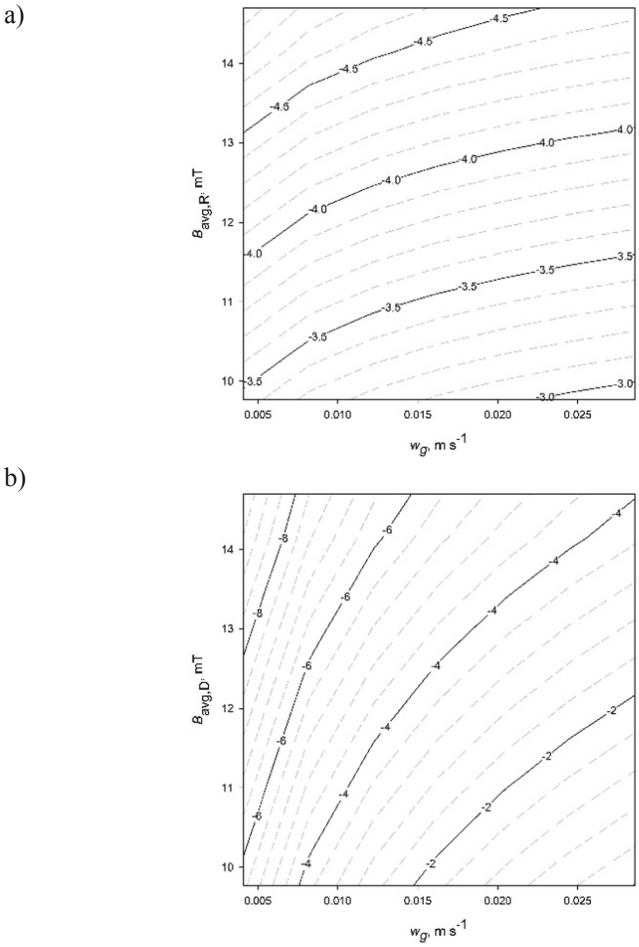

Fig. 4. The *E*-factor for the mixing time in the presence of RMF in the riser (a) and downcomer (b) column

4 Conclusions

The presented studies confirmed that the usage of rotating magnetic field generators successfully leads to the improvement of the mixing process and oxygen transfer in the novel construction of the airlift reactor. It should be noticed that hydrodynamics, mixing and mass transfer in airlift columns are strongly dependent on the flow structure. The gas-liquid mixture at the low gas velocities can be described as a homogenous bubbly flow regime and characterized by small bubble size distribution and rarely occurred bubble-bubble interactions. In the papers (Rakoczy et al. 2017, Rakoczy et al. 2018), it was investigated and proved that the rotating magnetic field strongly affects the homogenous gas-liquid flow and the bubbles are directed toward the wall of the

tested reactor due to the exposition of RMF. The observed phenomena result from the strongly paramagnetic properties of oxygen contained in the supplied air mixture. Moreover, the observed stronger effect of rotating magnetic field on k_La coefficient and mixing time during RMF generation in the downcomer section is directly affected by the flow pattern structure. Before the gas-liquid mixture introduces the downcomer section, most of the bubble disengage in the separation section and only small bubbles can be carried to the downcomer. The conducted experiments (Lechowska et al. 2019) confirmed that the smaller bubbles exposed to RMF, the stronger effect can be achieved. What is more, the airlift reactors characterize two types of mixing: axial and radial mixing. Axial mixing results from the rising gas bubble movement. In this case, the radial mixing was improved by the bubbles moved toward the RMF generators walls consequently enhancing the mixing phenomena. It was stated by Hristov (2010) at externally applied magnetic fields exposed on the substances with magnetic properties and charged particles generate eddy currents in the liquid. Then, these currents introduce their rotation and movement of liquid in the micro-scale. Finally, it can be stated that the obtained observations allow the successful application of the novel type of magnetically assisted airlift reactor in the bioprocessing.

Acknowledgments. This study was supported by the National Centre for Research and Development in Poland (Grant no. LIDER/011/221/L-5/13/NCBR/2014).

References

Al-Qodah, Z.: Continuous production of antibiotics in an airlift fermentor utilizing a transverse magnetic field. Appl. Biochem. Biotech. **87**(1), 37–55 (2000)

Al-Qodah, Z., Al-Hassan, M.: Phase holdup and gas-to-liquid mass transfer coefficient in magneto stabilized GLS airlift fermenter. Chem. Eng. J. **79**(1), 41–52 (2000)

Chen, C.M., Leu, L.P.: Hydrodynamics and mass transfer in three-phase magnetic fluidized beds. Powder Technol. **117**(3), 198–206 (2001)

Chisti, M.Y.: Airlift Bioreactors. Elsevier Applied Science, London and New York (1989)

Chisti, M.Y., Moo-Young, M.: Airlift reactors: characteristics, applications and design considerations. Chem. Eng. Commun. **60**(1–6), 195–242 (1987)

Drandev, S., Penev, K.I., Karamanev, D.: Study of the hydrodynamics and mass transfer in a rectangular air-lift bioreactor. Chem. Eng. Sci. **146**, 180–188 (2016)

El Azher, N., Gourich, B., Vial, C., Bellhaj, M.S., Bouzidi, A., Barkaoui, M., Ziyad, M.: Influence of alcohol addition on gas hold-up, liquid circulation velocity and mass transfer coefficient in a split-rectangular airlift bioreactor. Biochem. Eng. J. **23**(2), 161–167 (2005)

Fadavi, A., Chisti, Y.: Gas–liquid mass transfer in a novel forced circulation loop reactor. Chem. Eng. J. **112**(1–3), 73–80 (2005)

Garcia-Ochoa, F., Gomez, E.: Bioreactor scale-up and oxygen transfer rate in microbial processes: an overview. Biotechnol. Adv. **27**(2), 153–176 (2009)

Guieysse, B., Quijano, G., Muñoz, R.: Bioreactors – design—airlift bioreactors. In: Moo-Young, M. (ed.) Comprehensive Biotechnology, 2nd edn., vol. 2, pp. 199–212. Elsevier, Amsterdam (2011)

Hristov, J.: Magnetic field assisted fluidization–a unified approach: a series of review papers. Rev. Chem. Eng. **18**(4–5), I–IV (2002)

Hristov, J.: External loop airlift with magnetically controlled liquid circulation. Powder Technol. **149**(2–3), 180–194 (2005)

Hristov, J.: Magnetic field assisted fluidization–a unified approach. Part 8. Mass transfer: magnetically assisted bioprocesses. Rev. Chem. Eng. **26**(3–4), 55–128 (2010)

Lechowska, J., Kordas, M., Konopacki, M., Fijałkowski, K., Drozd, R., Rakoczy, R.: Hydrodynamic studies in magnetically assisted external-loop airlift reactor. Chem. Eng. J. **362**, 298–309 (2019)

Li, Z.Y., Guo, S.Y., Li, L., Cai, M.Y.: Effects of electromagnetic field on the batch cultivation and nutritional composition of Spirulina platensis in an air-lift photobioreactor. Bioresour. Technol. **98**(3), 700–705 (2007)

Mahmood, K.A., Wilkinson, S.J., Zimmerman, W.B.: Airlift bioreactor for biological applications with microbubble mediated transport processes. Chem. Eng. Sci. **137**, 243–253 (2015)

Moraveji, M.K., Sajjadi, B., Davarnejad, R.: Gas-liquid hydrodynamics and mass transfer in aqueous alcohol solutions in a split-cylinder airlift reactor. Chem. Eng. Technol. **34**(3), 465–474 (2011)

Paul, E.L., Atiemo-Obeng, V.A., Kresta, S.M.: Handbook of Industrial Mixing. Science and Practice. Wiley, Canada (2004)

Rakoczy, R., Konopacki, M., Fijałkowski, K.: The influence of a ferrofluid in the presence of an external rotating magnetic field on the growth rate and cell metabolic activity of a wine yeast strain. Biochem. Eng. J. **109**, 43–50 (2016)

Rakoczy, R., Lechowska, J., Kordas, M., Konopacki, M., Fijałkowski, K., Drozd, R.: Effects of a rotating magnetic field on gas-liquid mass transfer coefficient. Chem. Eng. J. **327**, 608–617 (2017)

Rakoczy, R., Konopacki, M., Lechowska, J., Bubnowska, M., Hürter, A., Kordas, M., Fijałkowski, K.: Gas to liquid mass transfer in mixing system with application of rotating magnetic field. Chem. Eng. Process. **130**, 11–18 (2018)

Rao, T.R., Sonolikar, R.L., Saheb, S.P.: Influence of magnetic field on the performance of bubble columns and airlift bioreactor with submersed microorganisms. Chem. Eng. Sci. **52**(21–22), 4155–4160 (1997)

Shah, M., Kiss, A.A., Zondervan, E., van der Schaaf, J., de Haan, A.B.: Gas holdup, axial dispersion, and mass transfer studies in bubble columns. Ind. Eng. Chem. Res. **51**(43), 14268–14278 (2012)

Examination of Rheological Properties of Selected Wastewater Sludge Proposed to Biogas Production

Monika Pawlita-Posmyk(✉) and Małgorzata Wzorek

Department of Process Engineering, Faculty of Mechanical Engineering, Opole University of Technology, Opole, Poland
mpawlita@wp.pl

Abstract. The determination of rheological parameters is very important in sewage sludge management in terms of designing and efficient operation of the mixing process or transport in the process of biogas production. This paper presents the results of examination of rheological properties of selected two types of sewage sludge, i.e. from the municipal (MWTP) and domestic (DSTP) sewage treatment plant. Experimental tests were performed with rotary viscometer Rheotest 2 with spinning coaxial cylinders. The tests were performed at various shear rates, i.e. from 3 s^{-1} to 800 s^{-1}, at temperatures corresponding to mesophilic fermentation, in which the process of biogas production is conducted most frequently. The tests showed that the analysed sewage sludge is non-linear (non-Binghamian) fluid. A significant difference in apparent viscosity for analysed sludge was observed.

1 Introduction

The process of biogas production is an important link in waste management, one where it is possible to use organic waste, which is difficult to manage with other methods such as sewage sludge from municipal and domestic sewage treatment plants. Municipal waste sludge is a significant threat for the environment due to its amount and chemical composition.

However, dynamic development of individual sewage treatment systems and increase in the number of domestic sewage treatment plants has recently led to significant increase in the amount of sludge generated in those locations. In Poland there were 2,355,000 domestic sewage disposal systems in 2017. Figure 1 presents the share of domestic sewage disposal systems in 2017 (GUS 2018). According to Statistics Poland's data (GUS 2016; GUS 2018), the number of domestic sewage treatment plants grew from 181,000 in 2014 to ca. 203,000 in 2015 and from 217,000 in 2016 to ca. 234,000 in 2017. The majority (nearly 86%) of domestic sewage disposal systems were located in rural areas in 2017. This is where ca. 92% of the overall number of domestic sewage treatment plants were found (GUS 2018).

© Springer Nature Switzerland AG 2020
M. Ochowiak et al. (Eds.): PAIC 2019, *Practical Aspects of Chemical Engineering*, pp. 294–304, 2020.
https://doi.org/10.1007/978-3-030-39867-5_31

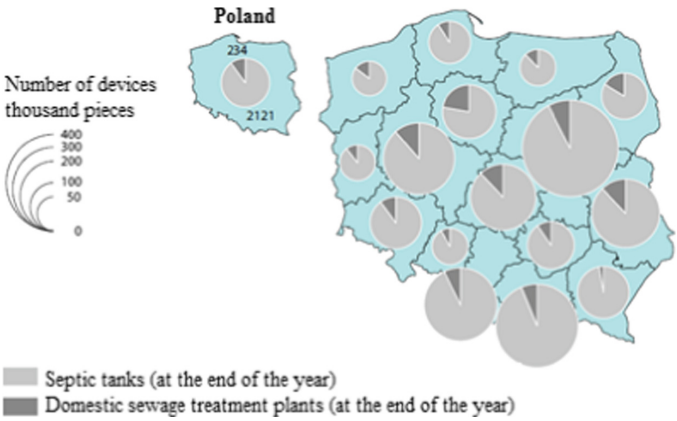

Fig. 1. Domestic sewage disposal systems in 2017 (GUS 2018).

The variability of physicochemical properties of sludge from domestic sewage treatment plants causes that some municipal (mechanical-and-biological) treatment plants, due to the destabilisation of sewage treatment, do not accept them to process in their processing chains. Therefore, other venues to manage the sludge are being sought.

Despite a range of conducted tests on the production of biogas from waste, new substrates are still being sought that could be used in the process of biogas production and to facilitate its effective and that could be used as a cheap and easily accessible substrate or co-substrate in biogas production. The conducted studies (Pawlita-Posmyk et al. 2016; Pawlita-Posmyk et al. 2017; Pawlita-Posmyk et al. 2018) indicate that the use of waste from rural areas for biogas production may lead to limiting the amount of waste nationwide and may have an impact on the general condition of the environment. The said solution could also cause numerous energy-related benefits thanks to biomass and the biogas made out of it as a valuable source of electric and thermal energy.

The determination of rheological parameters, such as viscosity or yield strength, is very important to manage sewage sediments, e.g. to the designing and efficient work of the mixing and pumping process (Tixier et al. 2003). The properties of sludge such as decomposition, particle size, shape and density, particle-particle interaction, capacity of flocculation, superficial physicochemical properties etc. have an impact on their rheology (Sanin 2002). Eshtiaghi et al. (2013) claim that optimal and efficient designing and work of sludge processing require accurate forecasting of the hydrodynamics of the functioning of various devices, such as pumps, heat exchangers and mixing systems. The forecasting of proper flowing behaviour of those engineering hydrodynamic processes requires deep knowledge of the rheology of sludge. Eshtiaghi et al. (2012) claim that the rheology of sludge is complex and always evolves over time due to ageing and microbiological activity.

The literature reports many different results, which indicate that sludge is non-Newtonian (Eshtiaghi et al. 2012; Eshtiaghi et al. 2013; Ségalen et al. 2015). Eshtiaghi et al. (2013) also claim that:

– exhibits yield stress or not,
– is shear-thinning and thixotropic,
– at high shear rate, sludge behaves as thixotropic colloidal suspension, but
– at low shear rate exhibits polymeric behaviour.

Sewage sludge at high solids concentrations (3–10%) behaves as a complex mixture the rheological behaviour of which is highly dependent on the treatment process it is undergoing.

As waste subjected to fermentation may have various forms, they have solids in their composition, the so-called fermentation sludge, which – depositing on the bottom of the chamber – blocks the occurring biochemical processes in the entire volume of the chamber and, in turn, the production of biogas. Therefore, to prevent the stratification of material, it is necessary to agitate substrates (Kowalczyk-Juśko 2013; Matheri et al. 2017; Płaczek et al. 2018). Industrial practice shows that effective mixing of biomass materials enables to: (Kowalczyk-Juśko 2013; Kaparaju et al. 2008; Matheri et al. 2017).

– uniform heat-flux and nutrients distributions in the reactor,
– prevent formation of foam on the surface of the ferment materials,
– facilitate release of the produced biogas.

However, studies (Stroot et al. 2001; Kaparaju et al. 2008) also show that improper mixing intensity may have a negative effect on the structure of microorganisms and so reduce the efficiency of the process.

The aim of this paper is to analyse the rheological properties of the selected sewage sludge of various origin, intended for biogas production. The determination of rheological parameters is important from the point of view transport and sludge processing, including the mixing process in fermentation reactors for biogas production.

2 Materials and Methods

For the testes sewage sludge from the municipal (MWTP) and domestic sewage treatment plant (DSTP) were selected. The characteristic of the analysed sewage sludge is presented in Table 1. Municipal sewage sludge came from a mechanical-and-biological sewage treatment plant with biogenic substance removal. The treatment plant serves 225,000 PEs (Population Equivalent) and the average inflow of sewage to the treatment plant is 45,000 m^3/day.

Table 1. Characteristics of sewage sludge.

Parameter	Unit	Sewage sludge	
		MWTP	DWTP
Color	–	Black	Dark brown-black visible particles of solids
pH	–	5.98	6.45
Water content*	%	97.63	98.95
Density	kg/m^3	994	989

*PN-EN 12880:2004

The annual amount of treated sewage is ca. 11,373,500 m^3/year (including 16.6% of industrial sewage) (WIOŚ 2018). Municipal sewage sludge was collected from the sludge-mixing chamber (sludge from thickening machines, partially dehydrated in the thickening machine and the preliminary sludge trap).

The other type of sludge came from a domestic biological sewage treatment plant serving a single-family house occupied by a 4-member family. The treatment plant has been continuously used for 5 years. The cycle of treatment has 6 phases (Fig. 2).

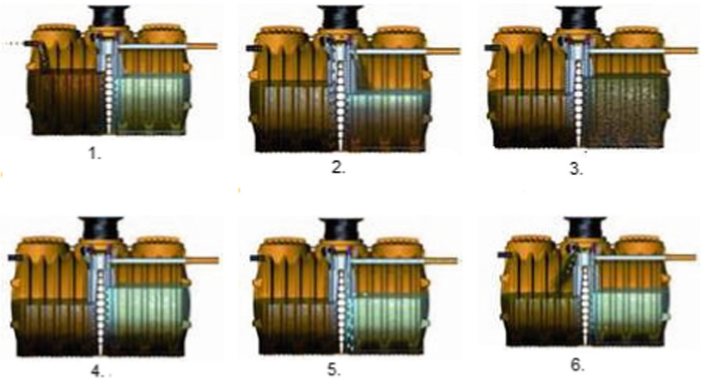

Fig. 2. Principle of treatment plant operation (Kessel Sp. z o.o.). 1. Inlet of "black sewage", 2. Filling in the chamber of active sediment, 3. Treatment/aeration of sewage, 4. Sedimentation phase, 5. Drainage of clean water, 6. Sediment drainage to the setting tank

To measure the viscosity of sewage sludge under various shearing conditions rotary viscometer Rheotest 2 with spinning coaxial cylinders manufactured by Prüfschein were used. All measurements were taken with one set of cylinders. Gap dimension between cylinders was 5 mm.

In the case of that instrument (Fig. 3), the tested sample of sludge (100 mL) was placed between the walls of cylinders. The inner one is the rotating cylinder with variable angular speeds at which the torque of resistance transferred onto the fixed cylinder can be measured. The viscometer was in a bath of constant temperature, which allowed to determine flow curves for various temperatures.

The tests were conducted within the shear rate from 3 s^{-1} to 800 s^{-1}, adequately for the process of mixing, pumping of the fluid. Sludge samples were collected from wastewater treatment plants directly before measurement. The testes were taken at mesophilic temperature in which anaerobic fermentation is planned to be conducted: 33 °C, 35 °C, 38 °C, 40 °C (±0.1 °C).

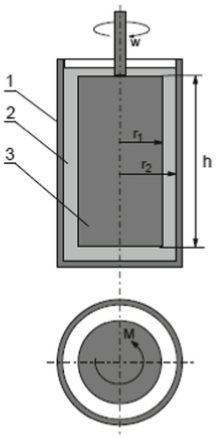

Fig. 3. The operating principle of viscometer with coaxial cylinders. 1 – fixed cylinder, 2 – tested liquid, 3 – rotatable cylinder, r_1, r_2 - the radii of the rotating and stationary cylinder, respectively; h - the height of the liquid layer between the cylinders; ω - angular velocity of the rotating cylinder; M - resisting torque transmitted to the stationary cylinder.

For the sludge from the domestic sewage treatment plant (DSTP), the constant value of the torsion dynamometer was 0.569 N/(m^2•graduation) for the sludge from the municipal sewage treatment plant (MSTP) was 5.55 N/(m^2•graduation). Shear stress was determined from the following equation:

$$\tau = z \cdot \alpha \tag{1}$$

where: z – constant of the dynamometer, α – indication of the analogue gauge of the instrument.

The apparent viscosity of the tested liquid sample was determined on the basis of the following equation:

$$\eta_p = \frac{\tau}{\dot{\gamma}} = \frac{z \cdot \alpha}{\dot{\gamma}} \cdot 10^{-3}\ \text{Pa} \cdot \text{s} \tag{2}$$

where: z, α – as in Eq. (1); $\dot{\gamma}$ – shear rate.

In addition, the selected sewage sludge was observed microscopically. For the observation Inverted Microscope AE2000 manufactured by Motic was used (Fig. 4). Microscopic pictures were done with 40X magnification.

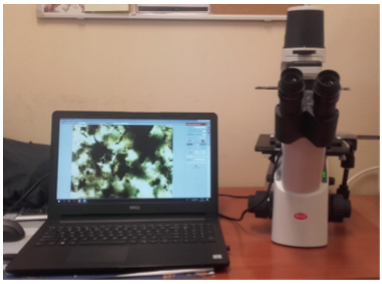

Fig. 4. Test stand for microscopic observations.

3 Result and Discussion

The conducted analysis of physicochemical properties (Table 1) indicate that the tested two type of sewage sludge is characterised by similar density, close to 1000 kg/m^3 and contains a similar amount of dry mass.

Tests of rheological properties of sludge conducted under conditions of mesophilic temperatures for various shear rates (from 3 s^{-1} to 800 s^{-1}) and the determined shear stresses and apparent viscosity of the liquid at various shear rates determined on the basis of Eqs. (1) and (2) are presented in Figs. 5, 6, 7 and 8.

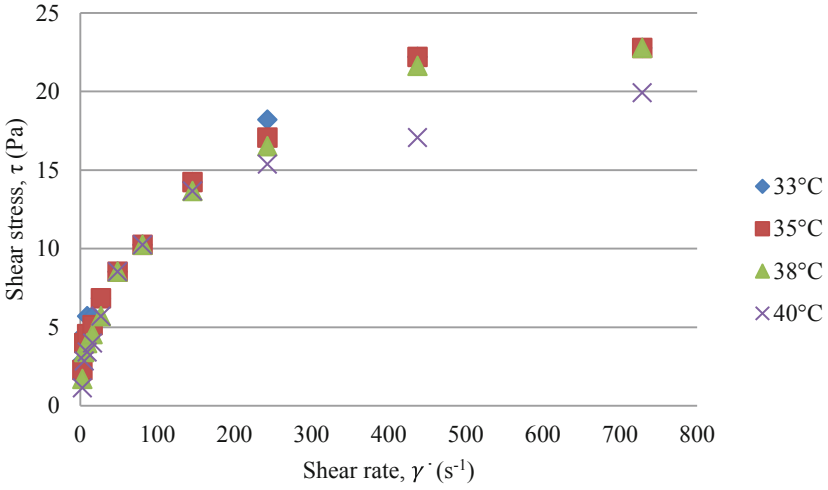

Fig. 5. Impact of shear stresses on the shear rate of sludge from the domestic sewage treatment plant (DSTP).

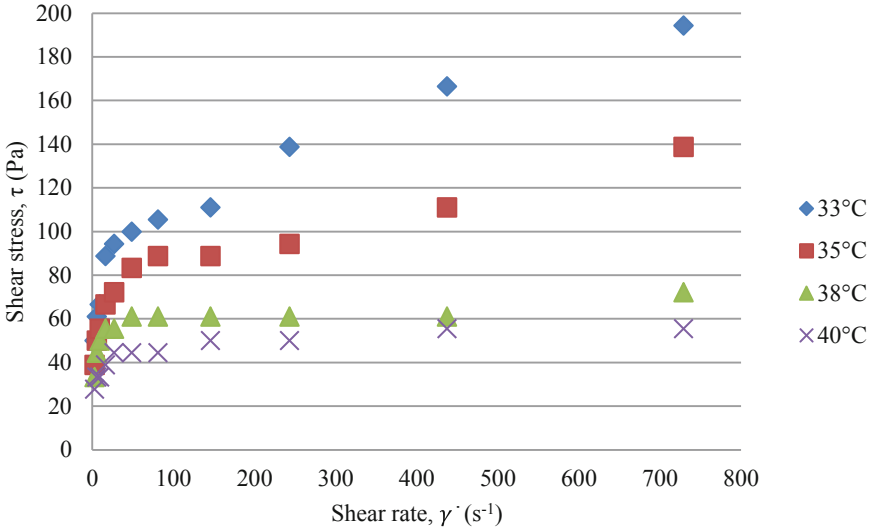

Fig. 6. Impact of shear stresses on the shear rate of sludge from the municipal sewage treatment plant (MSTP).

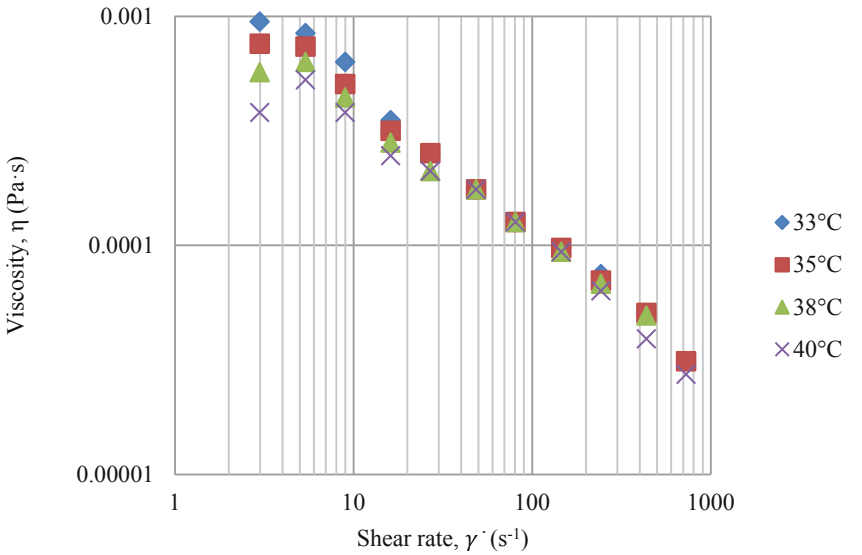

Fig. 7. Impact of shear rate on the apparent viscosity of sludge from the domestic sewage treatment plant (DSTP).

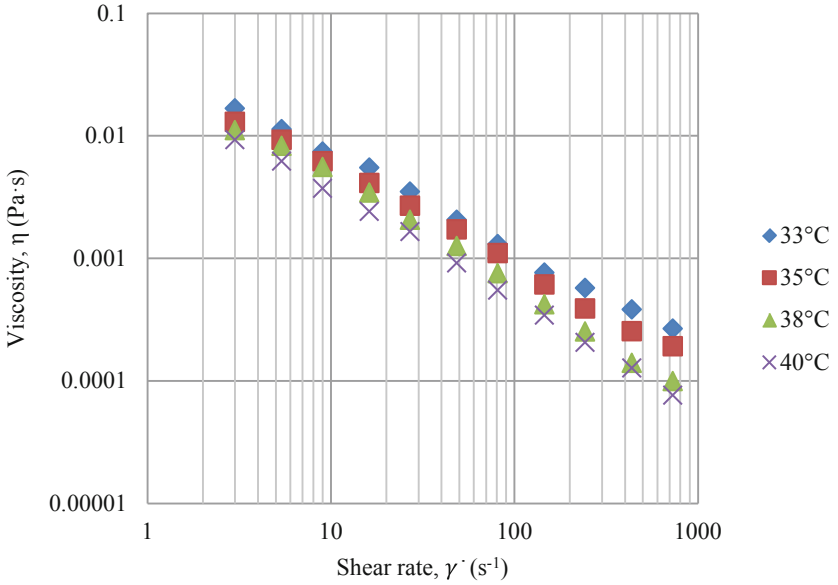

Fig. 8. Impact of shear rate on the apparent viscosity of sludge from the municipal sewage treatment plant (MSTP).

As the shear rate grows, the shear stresses go up both for the domestic and the municipal sewage sludge and it can be characterized as non-linear (non-Binghamian) fluid. As the shear rate grows, the apparent viscosity of the sludge decreases (Figs. 7 and 8). The highest viscosity of 0.00095 Pa·s was obtained (at the shear rate of 3 s^{-1}) at 33 °C for domestic sewage sludge.

For the sludge from the municipal sewage treatment plant, the highest apparent viscosity was 0.01665 Pa·s. The lowest values were obtained at 40 °C: 0.00038 Pa·s for domestic sludge and 0.00925 Pa·s for municipal sludge. The sludge from the municipal sewage treatment plant had the apparent viscosity by 0.016 Pa·s higher than the sludge from the domestic sewage treatment plant (at 33 °C).

Wolski and Zawieja (2013) claim that they obtained the lowest value of 0.002 Pa·s for the sludge conditioned with polyelectrolyte 853 and 610 and the highest – for the sludge conditioned with polyelectrolyte 852 (0.004 Pa·s). Ségalen et al. (2015) state that when the temperature is higher, the rheological parameters are lower.

Mu and Yu (2006) also claim, that temperature is important factor affecting the rheological properties of sludge and the thermal motion of particles is more violent at a higher temperature, and then the network strength between particles is weakened, resulting in a decrease in viscosity. The viscosity of the analysed sludges decreases as the temperature grows (Table 2). The viscosity of the domestic sludge is higher by $2 \cdot 10^{-4}$ Pa·s higher at 33 °C and by $4 \cdot 10^{-5}$ Pa·s at 35 °C, compared to the viscosity of water at 33 °C and 35 °C, respectively. Sanin (2002) states that the concentration of solids has an effect on the rheological properties of sludge.

Table 2. The effect of temperature (33 °C, 35 °C on the apparent viscosity of sludge of various origin at given shear rate (3 s^{-1}).

Parameter	Unit	Apparent viscosity, Pa•s	
		Sewage sludge DSTP	Sewage sludge MWTP
Dry mass	%	1.05	2.37
Temperature at 30	°C	0.00095	0.01665
Temperature at 35	°C	0.00076	0.01295

As the concentration of solids increases, viscosity increases sharply and the flow behaviour index decreases significantly, indicating that the flow tends to be more pronouncedly non-Newtonian at high solid contents. Example microscopic pictures of the sludge are presented in Fig. 9. The sludge has a form of a flaky suspension. The sludge from the municipal sewage treatment plant is black and the sludge from the domestic sewage treatment plant is dark with visible traces of solids.

The flakes in the sludge in both instances are compact (Fig. 9). The sludge from the domestic sewage treatment plant is less dense and condensed than the sludge form the municipal sewage treatment plant, which may result from higher water content in the sample (98.95%).

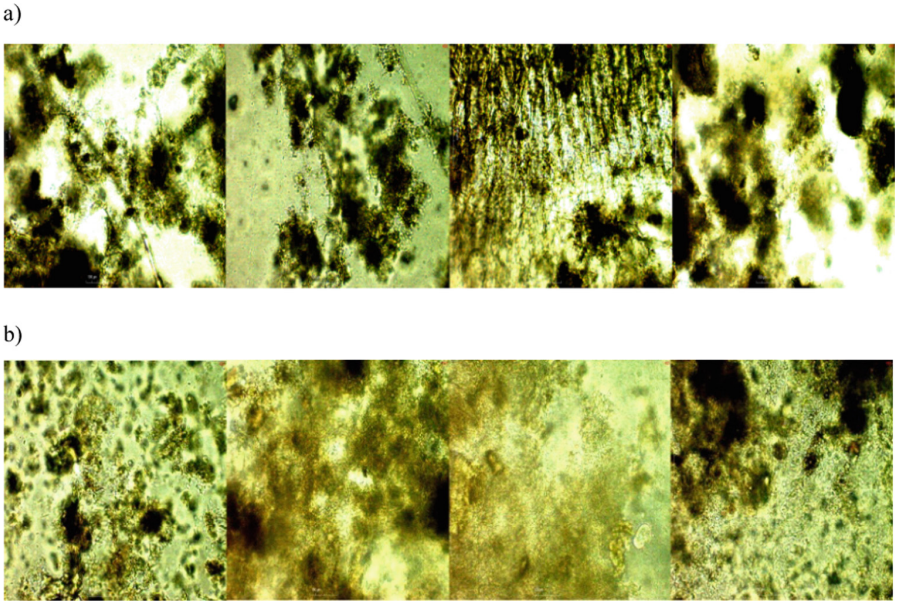

Fig. 9. Example microscopic pictures of sewage sludge: (a) from the municipal sewage treatment plant, (b) domestic biological sewage treatment plant.

4 Summary

The characteristics of sewage sludge depend on a range of factors, e.g. organic substance content, hydration or rheological properties. Pumping and mixing of sewage sludge require the knowledge of such aspects as physical, rheological or hydraulic parameters.

The analysis of all results shows that the shear stresses grew as the shear rate grew but viscosity was decreased. Significant differences were found in sludge viscosity for municipal and domestic sewage sludge. The range of apparent viscosity at various low shear rates was determined for temperatures corresponding to mesophilic fermentation.

The conducted rheological tests may be the basis for optimisation of processes related to sludge processing. The analysis of results of rheological properties of the tested sludge allows to perform preliminary tests e.g. with changing manners of mixing striving to increase the effectiveness of biogas production.

References

Eshtiaghi, N., Markis, F., Yap, S.D., Baudez, J.C., Slatter, P.: Rheological characterisation of municipal sludge: a review. Water Res. **47**, 5493–5510 (2013)

Eshtiaghi, N., Yap, S.D., Markis, F., Baudez, J.C., Slatter, P.: Clear model fluids to emulate the rheological properties of thickened digested sludge. Water Res. **46**, 3014–3022 (2012)

Kaparaju, P., Buendia, I., Ellegaard, L., Angelidakia, I.: Effects of mixing on methane production during thermophilic anaerobic digestion of manure: lab-scale and pilot-scale studies. Bioresour. Technol. **99**(11), 4919–4928 (2008)

Kessel Sp. z o.o. http://www.kessel.pl

Kowalczyk-Juśko, A.: Biogas plants as an opportunity for agriculture and the environment. In: Grzybek, A. (ed.) Foundation for the Development of Polish Agriculture (2013). (in Polish)

Matheri, A.N., Ndiweni, S.N., Belaid, M., Muzenda, E., Hubert, R.: Optimising biogas production from anaerobic co-digestion of chicken manure and organic fraction of minicipal solid waste. Renew. Sustain. Energy Rev. **80**, 756–764 (2017)

Mu, Y., Yu, H.-Q.: Rheological and fractal characteristics of granular sludge in an upflow anaerobic reactor. Water Res. **40**, 3596–3602 (2006)

Pawlita-Posmyk, M., Wzorek, M.: Analysis of domestic sewage treatment system. Chemik **01**(70), 620–625 (2016)

Pawlita-Posmyk, M., Wzorek, M.: Assessment of application of selected wastes for production of biogas. In: E3S Web of Conferences, vol. 19, p. 02017 (2017). https://doi.org/10.1051/e3sconf/20171902017

Płaczek, A., Patyna, A., Witczak, S.: Technical evaluation of photobioreactors for microalgae cultivation. In: E3S Web of Conferences, vol. 19, p. 02032 (2017)

Pawlita-Posmyk, M., Wzorek, M., Płaczek, M.: The influence of temperature on algal biomass growth for biogas production. In: MATEC Web of Conferences, vol. 240, p. 04008 (2018). https://doi.org/10.1051/matecconf/201824004008

Sanin, F.D.: Effect of solution physical chemistry on the rheological properties of activated sludge. Water SA **28**(2), 207–211 (2002)

Ségalen, C., Dieudé-Fauvel, E., Clément, J., Baudez, J.C.: Relationship between electrical and rheological properties of sewage sludge - impact of temperature. Water Res. **73**, 1–8 (2015)

Statistic Poland: Infrastruktura Komunalna w 2017, GUS, Warszawa (2018). www.stat.gov.pl

Statistic Poland: Infrastruktura Komunalna w 2015, Warszawa (2016). www.stat.gov.pl
Stroot, P.G., Mcmahon, K.D., Mackie, R.I., Raskin, L.: Anaerobic codigestion of municipal solid waste and biosolids under various mixing conditions – I. Digester performance. Water Res. **35**(7), 1804–1816 (2001)
Tixier, N., Guibaud, G., Baudu, M.: Determination of some rheological parameters for the characterization of activated sludge. Bioresour. Technol. **90**, 215–220 (2003)
Wolski, P., Zawieja, I.: Analysis of rheological parameters of pre-conditioned sewage sludge subjected to fermentation. Ann. Set Environ. Protect. **15**, 1645–1657 (2013)

The Effect of Airborne Particles on Human Body Fluids

Agata Penconek(✉), Urszula Michalczuk, and Arkadiusz Moskal

Faculty of Chemical and Process Engineering,
Warsaw University of Technology, Warsaw, Poland
agata.penconek@pw.edu.pl

Abstract. The uptake pathways and areas of airborne particles' deposition in human body are known. Also, the first side effects of inhaled particles' omnipresence on various cells have been defined. But there is still a very important question from the chemical engineering perspective. Do particles present in the biological fluids affect their rheological properties, and thus on their functions? Therefore, the aim of this study was to investigate the influences of particles' presence in the human body on various body fluids. Four models of body fluids (saliva, mucus, tears, and cerebrospinal fluid) were used instead of real biological fluids. Two types of airborne particles were selected for the study: natural particles (transported desert dust particles [TDDP]), and toxic air pollution particles (diesel exhaust particles [DEP]). The obtained results show that Non-Newtonian, shear thinning body fluids like mucus or saliva react to the presence of airborne particles, changing their apparent viscosity. The effect caused by the presence of particles depends not only on their origin, but also depends on the interaction of the particle-mucin, and on the concentration of mucins. However Newtonian body fluids do not change their rheological properties under the influence of the presence of exogenous particles.

1 Introduction

Airborne particles, irrespective of origin (natural or anthropogenic) can cause an adverse effect on the human body due to their size, shape and chemical compounds adsorbed on the surface. In addition, due to the increasing use of nanoparticles in various technology including cars' or airplanes' production, chemical, biochemical, environmental engineering, industrial electronic, optical, telecommunications pharmacology and medicine as well as food, cosmetics or nutritional supplements productions the probability of their passage into the human body increases, and thus increases the exposure to unwanted interaction of nanoparticles with the body.

Exponential growth of nanoparticles' number in the environment is natural consequence of their numerous applications. However, many kinds of nanoparticles present in the environment were not created for direct contact with living objects. Furthermore, even if nanoparticles were designed for the medical purposes, for example, for diagnosis, or as drug carriers, the effect of specific nanostructures on the human body must be determined separately, since the physical and biological

© Springer Nature Switzerland AG 2020
M. Ochowiak et al. (Eds.): PAIC 2019, *Practical Aspects of Chemical Engineering*, pp. 305–313, 2020.
https://doi.org/10.1007/978-3-030-39867-5_32

properties of materials are strictly connected to their size, and various effects are observed for micro and nanoparticles formed from the same material.

There are two major routes of entry of the particles into the organisms. Particles of therapeutic and diagnostic applications, for example nanoparticles of gold or carbon (graphene) are administered by injection directly into the bloodstream. While the particles present in the environment deposit in the lungs and then enter the body. In the first case the number of particles is more or less known, and it is directly dependent on the dosage of a pharmaceutics. However, the quantities of environmental particles entering human bodies can only be estimated taking into account that about 15 m^3 of air (containing particles present in the environment) flows through the lungs of healthy, adult man daily. The number of particles in the air depends mainly on the location, weather conditions and the time of year.

Animal studies provide evidence that gold, silver, iridium, titanium dioxide, polystyrene, and carbon nanoparticles ranging from 5 nm to 100 nm translocate across the air-blood barrier. Nanoparticles were found in bones and organs in the amounts corresponding to approx. 5% of the delivered lung dose (Kreyling et al. 2002; Semmler et al. 2004; Geiser et al. 2005; Semmler et al. 2007; Geiser and Kreylingiem 2010).

The effects of nanoparticles on tissue they settle on depend on the material that they are made of and their size, but also of their shape, electric charge, and other compounds adsorbed on their surface.

Nearly 10% of inhaled 20 nm iridium nanoparticles move to organs and tissues such as bones, whereas only 2% in case of 25 nm carbon nanoparticles (except liver) (Kreylingiem and Geiser 2010). The ability to translocate to bones and soft tissues of inhaled 80 nm iridium nanoparticles is about one order of magnitude less than 20 nm ones (Kreylingiem and Geiser 2010). Similarly, significant differences were observed in the translocation of the gold nanoparticles. Nearly 8% of inhaled 1.4 nm gold nanoparticles moved beyond the respiratory system within 24 h of inhalation, whereas nanoparticles of 18 nm counted only 0.2%. The translocated fraction of spherical gold nanoparticles with a smooth surface is smaller in comparison to dendritic agglomerates of similar size formed by iridium or carbon.

Environmental particles were transported to organs where they were found in with the use of various body fluids. Particles had to contact with saliva, nasal mucus, bronchial mucus and blood before reaching, for example liver. In case of therapeutic particles, the contact is usually limited to the blood. Moreover, tear fluid and cerebrospinal fluid (CSF) should also be taken into consideration since environmental particles have contact with tears, just like the therapeutic nanoparticles with modified surface with CSF. Therefor, there is an extremely important question (at least from the chemical and process engineering as well as toxicology and health care perspective). Do particles present in biological fluids affect rheological properties of these fluids? And, hence, do they lead to changes in, for example, liquids' viscosity or whether they can cause the disruption of their original functions?

The main component of all these fluids is water. They also consist of proteins, lipids and minerals, but in various proportions leading to differences in their rheological properties and functions. Most of these fluids are non-Newtonian (shear thinning fluid)

only the cerebrospinal fluid is Newtonian fluid. The viscosity or apparent viscosity (for non-Newtonian fluids) is listed in Table 1.

Table 1. The viscosity/apparent viscosity of selected body fluids

	Saliva	Tear fluid	Nasal mucus	Bronchial mucus	Cerebrospinal fluid
Viscosity/apparent viscosity, m Pa·s	5–25 (1)	1–10 (2)	10^4–10^6 (3)	10^4–10^6 (3)	0,7–1 (5)

The most important functions of these fluids are well known, but the impact of fluids' rheological properties on their functions is not always recognized to an enough extent. Suitable "viscosity" of saliva, tears, nasal and bronchial mucus are necessary to create a film layer on the surface of the mouth, eyes, nose and respiratory tract protecting against ingress of pathogens. The appropriate viscosity of the cerebrospinal fluid provides its free movement in the chambers of the brain covering the central nervous system against mechanical damage and enabling rapid adjustments to intracranial pressure.

Conducting researches on the impact of particles on biological fluid using real biological fluids would be complicated both methodologically and ethically. However, this type of research and its results are extremely needed. They allow, for example, to estimate the risk of exposure to air pollution. The solution to this problem, to some extent, is the use of biological fluid models. Even though they will not give an unequivocal answer, but they may indicate directions for further research.

2 Materials and Methods

2.1 Body Fluids

Four biological fluids were selected for the study: nasal/bronchial mucus, saliva, tears and cerebrospinal fluid. Because there is lack of reproducibility between body fluids obtained from different person the artificial body fluids were used in the study. The biological fluids were prepared considering their natural composition and literatures' data about artificial body fluids.

Nasal/Bronchial Mucus

The two-components model of mucus (McGill and Smith 2010) previously used in our work (Penconek and Moskal 2016; Penconek et al. 2019) was also used in the study.

The mucins type II was obtained form Sigma Aldrich. The NaN_3 was obtained from POCH (Poland). The mucin was used at 200 g/l, the NaN_3 at 0.01 g/l, and dissolved in deionized water. The solution was stirred for 2 h, and the pH was adjusted to level 7.4. The mucus was stored at 4 °C.

Saliva

The saliva model was prepared based on the Christersson et al. (2000). The benzalkonium chlorides, EDTA, xylitol, methylparaben and mucins (type II) was purchased from Sigma-Aldrich. The NaF was obtained from Chempur (Poland). The benzalkonium chlorides was used at 0.02 g/l, EDTA at 0.5 g/l, NaF at 0.0042 g/l, xylitol at 20 g/l, methylparaben at 1 g/l, mucins (type II) at 35 g/l, and dissolved in deionized water. The solution was stirred for 2 h, and the pH was adjusted at 7.00. The sample was stored at 4 °C.

Cerebrospinal Fluid

The cerebrospinal fluid (CF) was prepared based on the procedure of preparation of commercially available CF (ALZET 2017). The $MgCl_3 \cdot 6H_2O$ (Chempur, Poland) (0.163 g/l), KCl (Sigma Aldrich) (0.224 g/l), NaCl (Sigma Aldrich) (8.66 g/l), $CaCl_2 \cdot 2H2O$ (Chempur, Poland) (0.206 g/l) was dissolved in deionized water (solution A). The $Na_2HPO_4 \cdot 2H_2O$ (POCH, Poland) (0.135 g/l) solution in deionized water was prepared separately (solution B). The solution A and B was stirred at 1 h, after this time, they were combined, and the pH was adjusted at 7.0. The obtained solution was kept at 4 °C no longer than 4 weeks.

Tears

The tears model (the water layer) was prepared based on the chemical composition of the water layer of real tears. The NaCl (Sigma Aldrich) (6.98 g/l), KCl (Sigma Aldrich) (2.31 g/l), $NaHCO_3$ (Sigma Aldrich) (1.93 g/l), $C_2H_4OHCOOH$ (Sigma Aldrich) (0.33 ml/l), $CH_3COCOOH$ (Sigma Aldrich) (0.014 ml/l), $CaCl_2$ (Sigma Aldrich) (0.11 g/l), $MgCl_2 \cdot 6H_2O$ (Sigma Aldrich) (0.142 g/l), urea (Sigma Aldrich) (0.27 g/l), glucose (Sigma Aldrich) (0.063 g/l), TRIS (Sigma Aldrich) (6.0 g/l) was dissolved in deionized water in the indicated order. The pH of solution was adjusted at 7.0. The solution was not stored.

2.2 Airborne Particles

Two types of airborne particles were selected for the study: natural particles (transported desert dust particles [TDDP]), and toxic air pollution particles (diesel exhaust particles [DEP]).

The TDDP were purchased from Powder Technology Incorporated (Arizona Dust Nominal 0–3 micron). The DEP was generated by diesel engine without particulate filter (Mercedes Benz 240D, engine power 53 kW at 4200 rpm; torque 137 Nm at 2400 rpm; engine displacement 2399 cm^3) described in detail e.g. in Penconek et al. (2019). The shape of TDDP and DEP was determined based on the SEM photos. The TDDP and DEP form dendritic aggregates with an extensive shape. The TDDP size distribution in the air was determined using a spectrometer (Portable Aerosol Spectrometer, Model 1.109, Grimm, Germany). The DEP size distribution in the air was determined using a spectrometer (FAPES, Grimm, Germany). The average TDDP and DEP size in the air was 1.97 μm and 111 nm, respectively. The TDDP and DEP size distribution in buffer was determined using a Zetasizer (Malvern Instruments, UK).

The TDDP and DEP suspension in buffer was subjected to ultrasound in order to obtain a better degree of deaggregation. The average TDDP and DEP size in the buffer was 513 nm and 250 nm, respectively.

2.3 Methods

The concentration of TDDP and DEP in saliva, mucus and CF fluids was 0.06 mg/ml and in tears was 0.5 μg/ml and 0.0012 μg/ml, respectively.

Basic rheological parameters (flow curve and viscosity dependence as a function of shear stress) were determined for particle suspensions in body fluids models. The tests were performed on an oscillatory rheometer (MCR102, Anton Paar, Austria) equipped with a Peltier system in a plate-plate system for a 1 mm wide gap, at 36.6 °C for saliva, mucus and CF and at 34 °C for tears.

Each measurement was repeated a minimum of three times. The presented results are an average value (the standard deviation was not shown in the graph).

3 Results and Discussion

The apparent viscosity of saliva model has been changed by the presence of exogenous particles (Fig. 1). The TDDP caused the increasing of apparent viscosity of saliva while the presence of DEP lead to the decrease of apparent viscosity. However, the shape of flow curves did not change - regardless of particles' origin (Fig. 2).

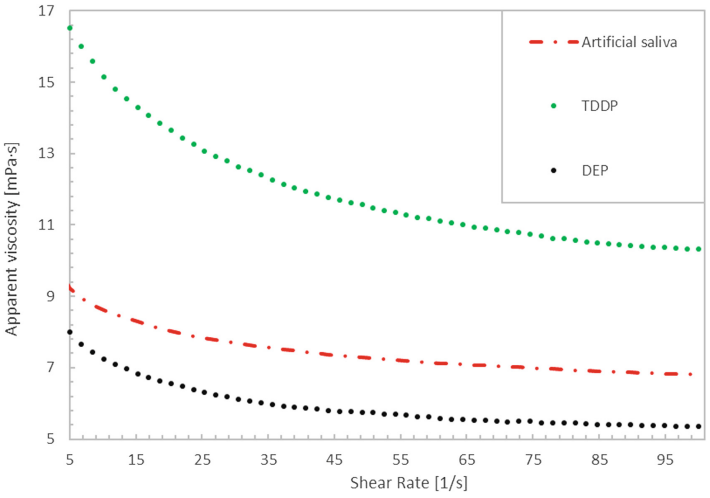

Fig. 1. The influence of exogenous particles on apparent viscosity of saliva model

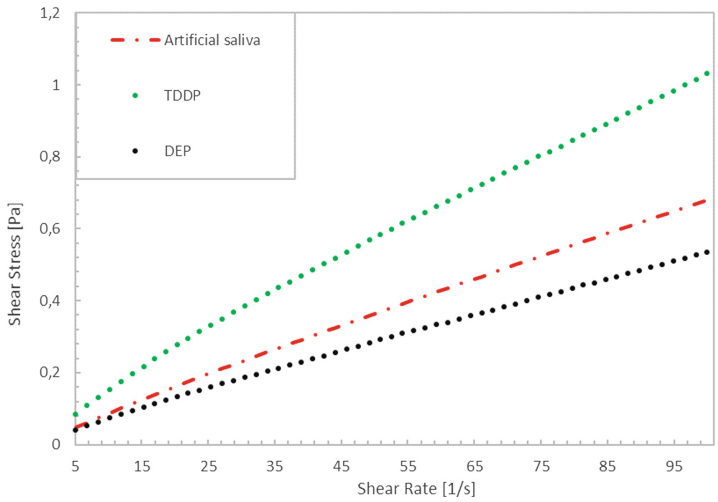

Fig. 2. The influence of exogenous particles on flow curves of saliva model

Both observed effects may affect the function of saliva. When the apparent viscosity increases the removal of bacteria from the mouth is disturbed, the risk of tooth decay also increases. Moreover saliva with higher apparent viscosity is harder to swallow. However, lowering saliva viscosity can lead to faster enamel wear.

The apparent viscosity of mucus model has also been changed by the presence of exogenous particles (Fig. 3). Both, TDDP and DEP caused the increasing of apparent viscosity of mucus. The shape of flow curve did not change - regardless of particles' origin (Fig. 4). Mucus with higher apparent viscosity is more difficult to remove

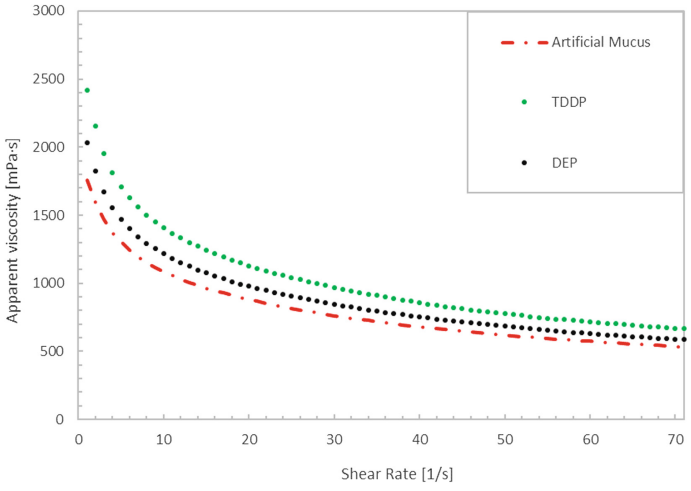

Fig. 3. The influence of exogenous particles on apparent viscosity of mucus model

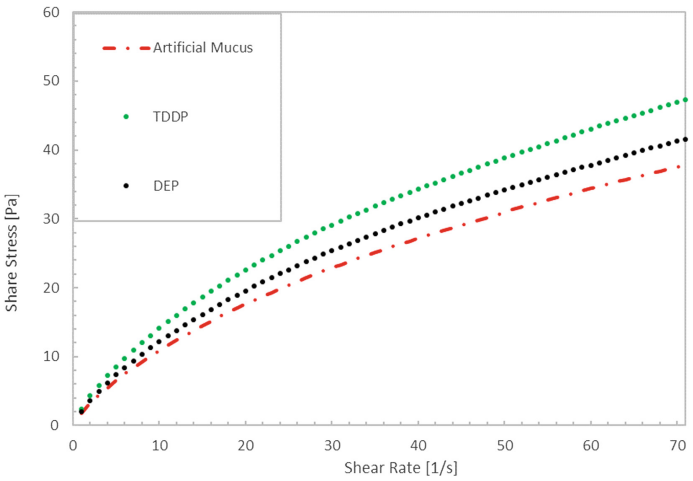

Fig. 4. The influence of exogenous particles on flow curves of mucus model

through ciliary movement, stays longer in the respiratory tract and may contribute to local inflammation. Moreover, the time of drugs diffusion through mucus is higher, therefore the therapeutic effect of aerosol therapy is smaller.

The effect of DEP on mucus apparent viscosity is different than the effect on saliva apparent viscosity. Both saliva and mucus contain mucins, but in different concentration (mucins are large glycoprotein mainly responsible for viscosity). The observed effect may suggest that the influence of exogenous particles on body fluids which contain mucins may be caused not only by the origin of the particle, but also by its interaction with mucins. Moreover, the interaction particle-mucins may also dependents on the concentration of mucins.

The viscosity of tears model (water layer) and CF has not been changed by the presence of exogenous particles (Figs. 5 and 6). Also the shape of flow curves did not change - regardless of particles' origin.

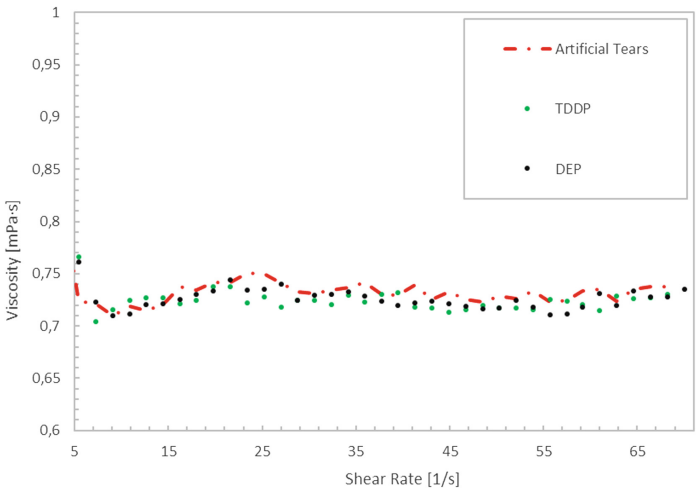

Fig. 5. The influence of exogenous particles on viscosity of tears model (water layer)

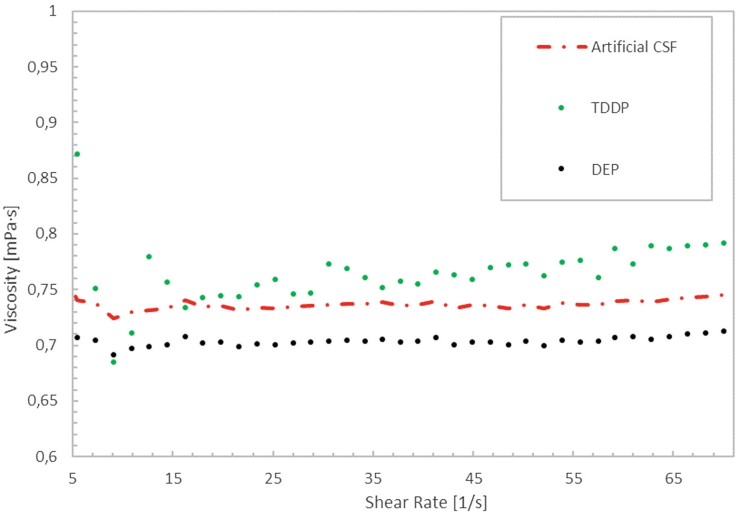

Fig. 6. The influence of exogenous particles on viscosity of CF model

4 Conclusion

The presented models of body fluids are a useful tool for estimating the threat arising from exposure to airborne particles, indicating the direction for further research. Compared to real biological fluids, they have only a few ingredients. But they always have the same composition, which allows to obtain universal results. The obtained results showed that Non-Newtonian, shear thinning body fluids i.e. mucus or saliva react to the presence of airborne particles, changing their apparent viscosity. The effect

caused by the presence of particles depends not only on their origin, but also depends on the interaction of the particle-mucin, and on the concentration of mucins. However Newtonian body fluids do not change their rheological properties under the influence of the presence of exogenous particles.

Acknowledgments. This work was supported by the National Science Centre, Poland [grant number UMO-2015/19/B/ST8/00599].

Authors wish to thank MSc Michał Sirodzki and MSc Ewelina Wojewoda for conducting the part of the experiments.

References

ALZET 2017: ALZET Osmotic Pumps. http://www.alzet.com/products/guide_to_use/cfs_preparation.html. Accessed 13 Oct 2017

Christersson, C.E., Lindh, L., Arnebrant, T.: Film-forming properties and viscosities of saliva substitutes and human whole saliva. Eur. J. Oral Sci. **108**(5), 418–425 (2000)

Kreyling, W.G., Semmler, M., Erde, F., Mayer, P., Takenaka, S., Schulz, H.: Translocation of ultrafine insoluble iridium particles from lung epithelium to extrapulmonary organs is size dependent but very low. J. Toxicol. Environ. Health **65**, 1513–1530 (2002)

Semmler, M., Seitz, J., Erde, F., Mayer, P., Heyder, J., Oderdörster, G., Kreyling, W.G.: Long-term clearance kinetics of inhaled ultrafine insoluble iridium particles from the rat lung, including transient translocation into secondary organs. Inhal. Toxicol. **16**, 453–459 (2004)

Semmler-Dehnke, M., Takenaka, S., Fertsch, S., Wenk, A., Seitz, J., Mayer, P., Oderdörster, G., Kreyling, W.G.: Efficient elimination of inhaled nanoparticles from the alveolar region: evidence for interstitial uptake and subsequent reentrainment onto airways epithelia. Environ. Health Perspect. **115**, 728–733 (2007)

Geiser, M., Rothen-Rutishauser, D., Kapp, N., Schürch, S., Kreyling, W., Schulz, H., Semmler, M., Im Hof, V., Heyder, J., Gehr, P.: Ultrafine particles cross cellular membranes by non-phagocytic mechanisms in lungs and in cultured cells. Environ. Health Perspect. **113**, 1555–1560 (2005)

Geiser, M., Kreyling, W.G.: Deposition and biokinetics of the inhaled nanoparticles. Part. Fiber Toxicol. **7**(1), 2 (2010)

McGill, S.L., Smith, H.D.C.: Disruption of the mucus barrier by topically applied exogenous particles. Mol. Pharm. **7**(6), 2280–2288 (2010)

Penconek, A., Moskal, A.: The influence of pH and concentration of mucins on diesel exhaust particles (DEPs) transport through artificial mucus. J. Aerosol Sci. **102**, 83–95 (2016)

Penconek, A., Michalczuk, U., Sienkiewicz, A., Moskal, A.: The effect of desert dust particles on rheological properties of saliva and mucus. Environ. Sci. Pollut. Res. **26**(12), 12150–12157 (2019)

Analysis of the Steady-State Properties of a Bifunctional Catalyst for the Synthesis of Renewable Fuels

Dominik Pędzich, Natalia Reczek, Krzysztof Skrzypek-Markiewicz, and Katarzyna Bizon(✉)

Faculty of Chemical Engineering and Technology, Cracow University of Technology, Kraków, Poland
kbizon@chemia.pk.edu.pl

Abstract. The chapter reports on the influence of the structure of a bifunctional catalyst pellet on the yield of dimethyl ether (DME) produced directly via methanol from synthesis gas. Theoretical studies were conducted with the aid of a mathematical model of a single isothermal porous bifunctional pellet integrating metallic catalyst for methanol synthesis and acidic catalyst for its dehydration into DME. Evaluation of the pellet performance was done for three arrangement of the catalytic active sites within the pellet, and for various volume fractions of the pellet occupied by each type of active sites. It was shown that, in case of relatively large pellets, a substantial enhancement in the DME yield can be obtained by using the core-shell structure with metallic catalyst located in the pellet core and acidic catalyst located in the pellet shell. Moreover, the proportions between the two catalysts within the pellet showed a marked influence on the DME yield calculated with respect to hydrogen.

1 Introduction

The global energetic crisis and the continuously rising air pollution has led over the last decades to increased interest in alternative, cleaner fuels for internal combustion engines. One of the first solutions that is already commonly applied in the spark ignition (SI) engines is the so-called autogas, i.e. liquified petroleum gas (LPG). However, due to the low cetane number, LPG cannot be utilized in compression ignition (CI) engines (Górski and Jabłońska 2012). An alternative clean diesel fuel for automotive applications is dimethyl ether (DME). Dimethyl ether can be produced from synthesis gas (syngas) obtained both from fossil fuels and renewable sources through a two-step synthesis or, alternatively, through direct synthesis on a bifunctional catalyst.

The two-step synthesis of DME from synthesis gas consists of methanol synthesis on a copper catalyst $CuO/ZnO/Al_2O_3$ (Graaf et al. 1990):

$$CO + 2H_2 \leftrightarrow CH_3OH \tag{1}$$

© Springer Nature Switzerland AG 2020
M. Ochowiak et al. (Eds.): PAIC 2019, *Practical Aspects of Chemical Engineering*, pp. 314–323, 2020.
https://doi.org/10.1007/978-3-030-39867-5_33

$$CO_2 + H_2 \leftrightarrow CO + H_2O \tag{2}$$

$$CO_2 + 3H_2 \leftrightarrow CH_3OH + H_2O \tag{3}$$

and methanol dehydration to DME in the presence of acidic catalyst, for example γ-Al_2-O_3 (Berčič and Levec 1992):

$$2CH_3OH \leftrightarrow CH_3OCH_3 + H_2O \tag{4}$$

More efficient and economic direct synthesis of DME from syngas on bifunctional catalyst combining both methanol formation and dehydration active sites is also already employed on the industrial scale. However, while there are some reports concerning the preparation of bifunctional catalysts and their activity (Ge et al. 1998), only in the recent years more attention has been paid to the additional advantages that can be obtained via catalyst pellet structuring (Sánchez-Contador et al. 2019). In fact, many issues concerning performance, design and feasibility of the technological implementation of multifunctional catalyst pellets are still open, since the enhancement of the product yield through particle microstructuring depends on many factors, including the reaction rate and composition of the gaseous phase (Grünewald and Agar 2004).

For this reason, in this work a theoretical analysis of the influence of the structure of a single bifunctional catalyst on the yield of dimethyl ether produced from synthesis gas was conducted. Three possible arrangements of the catalytic active sites within the pellet were evaluated, i.e. a uniform distribution of both types of active centers and two core-shell structures: the first one with the metallic functionality located in the core and the acidic functionality located in the pellet shell, and the second one with the reverse arrangement of the catalytic active sites (Fig. 1a).

2 Mathematical Model of a Single Bifunctional Pellet

A simplified mathematical model of a spherical catalyst pellet was formulated to evaluate the influence of the catalysts pellet structure on the DME yield. Under the assumption that the process takes place isothermally, the species mass balance (i = 1, 2,…, K – 1) and continuity equations can be written as (Solsvik et al. 2012):

$$\varepsilon_p \frac{\partial}{\partial t}(Cx_i) + \frac{1}{r^2}\frac{\partial}{\partial r}(r^2 u Cx_i) = -\frac{1}{r^2}\frac{\partial}{\partial r}(r^2 J_i) + S_i \tag{5}$$

$$\varepsilon_p \frac{\partial C}{\partial t} + \frac{1}{r^2}\frac{\partial}{\partial r}(r^2 u C) = \sum_{i=1}^{K} S_i \tag{6}$$

where:

$$S_i = f_1(1-\varepsilon_p)\rho_p \sum_{k=1}^{3} v_{k,i} r_i + f_2(1-\varepsilon_p)\rho_p v_{4,i} r_4, \quad i = 1,\ 2, \ldots, K \tag{7}$$

Symbols f_1 and f_2 in Eq. (7) denote, respectively, the pellet volume fraction occupied, respectively, by the metallic and acidic catalyst. They are functions of the pellet radius, r. Kinetic models proposed in (Graaf et al. 1990) and (Berčič and Levec 1992) were employed to describe, respectively, methanol synthesis (Eqs. (8)-(10)) and methanol dehydration (Eq. (11)) step:

$$r_1 = \frac{k_1 K_{CO}\left(p_{CO} p_{H_2}^{3/2} - p_{CH_3OH}\Big/\left(p_{H_2}^{1/2} K_{p1}^{o}\right)\right)}{\left(1 + K_{CO} p_{CO} + K_{CO_2} p_{CO_2}\right)\left(p_{H_2}^{1/2} + \left(K_{H_2O}\Big/K_{H_2}^{1/2}\right) p_{H_2O}\right)} \tag{8}$$

$$r_2 = \frac{k_2 K_{CO_2}\left(p_{CO_2} p_{H_2} - p_{H_2O} p_{CO}\Big/K_{p2}^{o}\right)}{\left(1 + K_{CO} p_{CO} + K_{CO_2} p_{CO_2}\right)\left(p_{H_2}^{1/2} + \left(K_{H_2O}\Big/K_{H_2}^{1/2}\right) p_{H_2O}\right)} \tag{9}$$

$$r_3 = \frac{k_3 K_{CO_2}\left(p_{CO_2} p_{H_2}^{3/2} - p_{CH_3OH} p_{H_2O}\Big/\left(p_{H_2}^{3/2} K_{p3}^{o}\right)\right)}{\left(1 + K_{CO} p_{CO} + K_{CO_2} p_{CO_2}\right)\left(p_{H_2}^{1/2} + \left(K_{H_2O}\Big/K_{H_2}^{1/2}\right) p_{H_2O}\right)} \tag{10}$$

$$r_4 = \frac{k_4 K_{CH_3OH}^2\left(C_{CH_3OH}^2 - C_{H_2O} C_{DME}/K_p\right)}{\left(1 + 2\sqrt{K_{CH_3OH} C_{CH_3OH}} + K'_{H_2O} C_{H_2O}\right)^4} \tag{11}$$

Assuming further steady-state conditions, constant pressure within the pellet and making use of Eq. (6), the species mass balance for components $i = 1, 2, \ldots, K - 1$ can be transformed into the following form:

$$-\frac{1}{r^2}\frac{d}{dr}\left(r^2 J_i\right) + S_i - \sum_{i=1}^{K} S_i = 0 \tag{12}$$

with the molecular fluxes expressed as:

$$J_i = -C D_{i,eff}\frac{dx_i}{dr} \tag{13}$$

The species mass balance and the molecular flux for component $i = K$ are given, respectively, by:

$$\sum_{i=1}^{K} x_i = 1; \qquad \sum_{i=1}^{K} J_i = 0 \tag{14}$$

Effective diffusion coefficients, $D_{i,eff}$, in Eq. (13) were calculated according to the Wilke-Bosanquet model for multicomponent diffusion, combining bulk and Knudsen flux using the Fickian formulation (Solsvik et al. 2012):

$$\frac{1}{D_i} = \frac{1}{D_{i,W}} + \frac{1}{D_{i,K}}; \quad D_{i,W} = \frac{1 - x_i}{\sum_{\substack{j=1 \\ j \neq i}}^{K} x_j / D_{ij}}; \quad D_{i,K} = \frac{97}{2} d_{pore} \sqrt{\frac{T}{M_i}} \tag{15}$$

and accounting for the pore geometry (Solsvik et al. 2012):

$$D_{i,eff} = \frac{\varepsilon}{\tau} D_i \tag{16}$$

Under the assumption that the ideal gas law is obeyed, the binary coefficients required to determine Wilke coefficients were calculated based on the Chapman-Enskog kinetic theory (Pooling et al. 2000).

Following the methodology proposed in (Solsvik et al. 2012) to avoid differentiating the flux expressions, the model equations (Eqs. (12)-(13)) were solved using the method of shooting as a system of first order differential equations with the following boundary conditions:

$$J_i(r = 0) = 0, \quad i = 1, 2, \ldots, K - 1 \tag{17}$$

$$J_i(r = R_p) = -k_{i,m}\left(C_{i,bulk} - C(R_p)x_i(R_p)\right) \tag{18}$$

and with the mass transfer coefficients $k_{i,m}$ calculated using a correlation of the Sherwood number for a fixed bed:

$$\mathrm{Sh} = 2 + 1.8\mathrm{Re}_p^{0.5}\mathrm{Sc}^{0.33} \tag{19}$$

3 Results and Discussion

The main physical parameters used in the numerical simulations are reported in Table 1. In the base case it was assumed that the pellet volume fraction occupied by each type of catalyst is equal to 0.5. Thus, introducing the dimensionless radial coordinate defined as:

$$\zeta = r / R_p \in [0, 1] \tag{20}$$

the 50%/50% proportion corresponds to a dimensionless radius of the pellet core equal to ζ_{core} = 0.7937 (Fig. 1b).

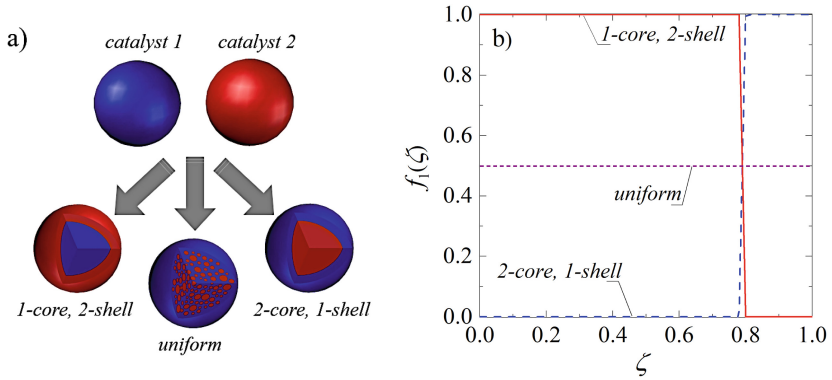

Fig. 1. Schematic of the functionalities structuring at catalyst pellet level (**a**) and radial distribution f_1 of the metallic catalyst for methanol synthesis in the bifunctional pellets for the base case simulations (**b**) (note that $f_2 = 1 - f_1$).

Table 1. Main parameters used in numerical simulations.

Quantity	Value	Quantity	Value
Pore diameter, d_{pore}	10^{-8} m	Pellet density, ρ_p	1775 kg/m^3
Pellet porosity, ε_p	0.5	Temperature, T	503 K
Pressure, P	50–70 bar	Tortuosity, τ	4
Pellet radius, R_p	10^{-4}, 2.5×10^{-3} m	Gas velocity, u_{bulk}	1 m/s

Numerical simulations were made for two different bulk gas compositions, one corresponding to syngas obtained from natural gas, the other to syngas characterized by a high content of nitrogen (Table 2). Since the analysis was limited to a single bifunctional catalyst pellet, setting the bulk gas composition equal to the raw syngas composition can be interpreted in two ways: either the simulated pellet is located near the inlet of a fixed-bed reactor, or it is located in a fluidized-bed reactor during the start-up phase.

Table 2. Syngas composition (Hu et al. 2008).

Source	x_{CO}	x_{CO2}	x_{CH3CO}	x_{H2O}	x_{DME}	x_{CH4}	x_{N2}	x_{H2}
Syngas from natural gas	0.13	0.13	0	0	0	0	0.04	0.7
Syngas with N_2 high content	0.1716	0.0409	0.003	0.0002	0.0018	0.044	0.316	0.4225

Figure 2 shows the profiles of methanol and DME molar fractions obtained using the distributions of the active centers from Fig. 1b and bulk gas conditions corresponding to syngas from natural gas determined for two values of the pellet radius, i.e. $R_p = 10^{-4}$ m (Fig. 2a-b) and $R_p = 2.5 \times 10^{-3}$ m (Fig. 2c-d).

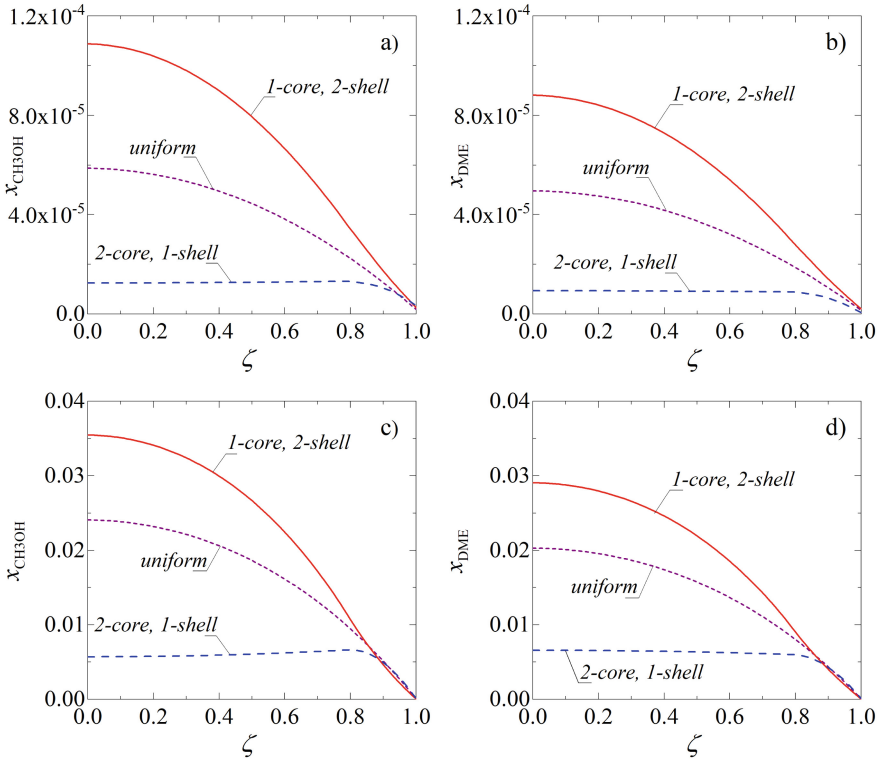

Fig. 2. Distribution of methanol and DME molar fraction within the pellet for $R_p = 10^{-4}$ m (**a**)-(**b**) and $R_p = 2.5 \times 10^{-3}$ m (**c**)-(**d**); $P = 60$ bar, $T = 503$ K, syngas from natural gas.

Both the qualitative and the quantitative difference in the DME concentration within the pellet obtained using a different arrangement of the active sites within the pellet is clearly visible. However, it is practically impossible, basing only on the reactant distribution within the pellet, to assess which structure performs best. Therefore, the yield of DME with respect to hydrogen was used to assess pellet performance.

Following Reference (Morbidelli et al. 2001), the yield of dimethyl ether was defined as the ratio between the actual production rate of DME and the consumption rate of hydrogen in the absence of external and internal mass transport resistances, i.e.:

$$Y_{\mathrm{DME,\,H_2}} = \frac{3\int_0^1 f_2(\zeta) r_4(\mathbf{K}_1, \mathbf{C}(\zeta), \mathbf{x}(\zeta))\zeta^2 d\zeta}{\sum_{k=1}^{3} \left|\nu_{k,\mathrm{H_2}}\right| r_k(\mathbf{K}_2, \mathbf{C}_{bulk}(\zeta))} \tag{21}$$

Table 3 reports the variation of the DME yield for two core-shell structures calculated in relation to the yield obtained for the uniform distribution of metallic and acidic active sites within the pellet. In all simulations, the pellet volume fraction occupied by each type of the two catalytic active sites was set to 0.5 (Fig. 1).

Table 3. Enhancement in the yield of DME with respect to H_2, $Y_{\mathrm{DME,H2}}$, calculated in relation to $Y_{\mathrm{DME,H2}}$ obtained for uniform distribution of catalysts within the pellet.

	R_p	Catalyst arrangement	P = 50 bar	P = 60 bar	P = 70 bar
Syngas from natural gas	10^{-4}	1-core, 2-shell	−39.43%	−36.85%	−34.56%
	10^{-4}	2-core, 1-shell	−40.08%	−36.55%	−33.41%
	2.5×10^{-3}	**1-core, 2-shell**	**44.17%**	**51.22%**	**57.76%**
	2.5×10^{-3}	2-core, 1-shell	−17.13%	−16.72%	−15.38%
Syngas with high N_2 content	**10^{-4}**	**1-core, 2-shell**	**1.70%**	**1.76%**	**1.82%**
	10^{-4}	2-core, 1-shell	−1.43%	−1.39%	−1.34%
	2.5×10^{-3}	**1-core, 2-shell**	**44.33%**	**49.73%**	**55.02%**
	2.5×10^{-3}	2-core, 1-shell	−31.45%	−30.45%	−30.04%

It can be observed (Table 3) that, both for the syngas from natural gas and syngas with high content of nitrogen, a substantial (about 50%) enhancement in the DME yield with respect to hydrogen consumed, $Y_{\mathrm{DME,H2}}$, can be obtained using larger pellets, i.e. $R_p = 2.5 \times 10^{-3}$ m, and 1-core, 2-shell structure, i.e. the bifunctional pellet with the metallic catalyst located in the pellet core and acidic catalyst located in the pellet shell. This is due to the strong influence of internal and external mass transport on the overall process performance. Methanol which is synthesized in the pellet core diffuses towards the surface through the shell, where it makes contact with the acidic catalyst and is dehydrated to DME. In case of uniform distribution of both catalysts, a part of the intermediate product (methanol) may diffuse unconverted into the bulk gas. When the methanol is produced in the pellet shell (2-core, 1-shell arrangement) also only a part of it reaches the pellet core when it undergoes further transformation into DME.

In the case of smaller pellets, i.e. $R_p = 10^{-4}$ m, the process yield is strongly influenced by the bulk gas conditions. While for the syngas characterized by a high content of nitrogen, a slight performance in the DME yield obtained using 1-core, 2-shell arrangement was observed when compared to the uniform distribution of both catalysts, employing as the bulk gas conditions the composition of syngas from natural gas caused a significant decrease of $Y_{DME,H2}$. This means that the optimal structure of the bifunctional pellet depends a lot on the gas composition, and thus – if dealing with a fixed-bed reactor – also on the location of the pellet in the reactor.

As expected, the DME yield is also influenced by the process conditions. Regardless of the pellet structure employed, it gets higher as the total pressure, P, is increased (Table 3).

Another important design parameter in bifunctional pellet structuring are the proportions between the two types of active centers within the pellet. Figure 3 shows the values of $Y_{DME,H2}$ obtained for the same structures of the pellet but with different values of f_1 and f_2 (note that $f_2 = 1 - f_1$). It must be underlined that very low values of $Y_{DME,H2}$ result from bulk gas conditions (Table 2) corresponding, as already mentioned, to the pellet located near the inlet of a fixed-bed reactor or to the pellet located in a fluidized-bed reactor being at the start-up phase.

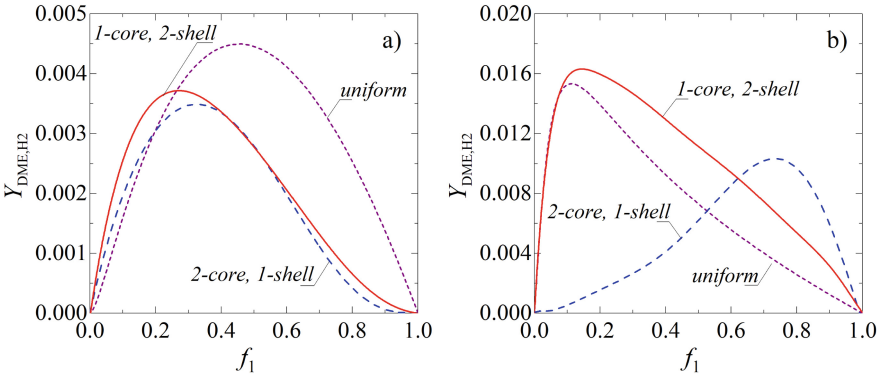

Fig. 3. Comparison of the yield of DME with respect to H_2, $Y_{DME,H2}$, obtained for different catalyst arrangement within the pellet as a function of the pellet volume fraction occupied by the first catalyst, f_1, for $R_p = 10^{-4}$ m (**a**) and $R_p = 2.5 \times 10^{-3}$ m (**b**); $P = 60$ bar, $T = 503$ K, syngas from natural gas.

For smaller pellets ($R_p = 10^{-4}$ m, Fig. 3a) the uniform distribution of the active centers gives the highest $Y_{DME,H2}$ practically in the entire range of f_1. An improvement in the DME yield can be obtained using both 2-core, 1-shell and 1-core, 2-shell catalyst arrangements, however, it is so small that, considering the technological difficulties and the manufacturing cost of structured pellets it may not have economic justification. Moreover, for the assumed bulk gas composition the pellet in which the volume fraction occupied by each type of the catalyst is close to 0.5 results to perform best.

When dealing with relatively large pellets ($R_p = 2.5 \times 10^{-3}$ m, Fig. 3b) both the structure and the fractions (by volume) of active centers play a very important role, and appropriate design of the catalyst pellet may result in a substantial intensification of the process. Both for the uniform and 1-core, 2-shell catalyst arrangement, the maximum of $Y_{DME,H2}$ is obtained with the pellet characterized by a relatively low fraction (by volume) of the metallic active centers ($f_1 \approx 0.1$), and thus a high fraction of the acidic active centers for methanol dehydration ($f_2 \approx 0.9$). In case of 2-core, 1-shell arrangement of the active centers within the catalyst the maximum of $Y_{DME,H2}$ is shifted towards a high fraction of f_1. Interestingly, for larger pellets, 2-core, 1-shell structure may give a higher yield of DME than uniform and 1-core, 2-shell structure; however, this is predicted only for a relatively high fraction of the metallic active centers, f_1. For $f_1 < 0.6$ the optimal pellet structure is the one with 1-core, 2-shell arrangement of the active centers. It ensures the enhancement in the DME yield up to about 50% as compared to the uniform arrangement of the active centers.

4 Conclusions

The analysis of the performance of a bifunctional catalyst pellet for direct synthesis of dimethyl ether (DME) via methanol from synthesis gas, performed with the aid of a mathematical model of a single spherical pellet, confirmed that structuring of bifunctional pellets is a powerful tool for multistep process intensification. Proper arrangement of different types of active centers within a single pellet may be an efficient way to control the intraparticle catalytic process and to increase the desired product yield.

It was demonstrated that particle structure has a great influence, especially when dealing with larger pellets, with radius typical for fixed-bed reactor application. The most advantageous structure of the pellet in this case was the 1-core, 2-shell structure (the metallic catalyst for methanol synthesis step located in the pellet core, and the acidic dehydration catalyst located in the outer shell).

In the case of smaller pellets the best solution appears to be the uniform distribution of the two types of active centers within the pellet. As demonstrated, the yield of the desired product, here DME, may also be substantially increased by a proper selection of the proportions of different active sites within the structured particle.

Acknowledgments. The research was financed by the Polish National Science Centre, project number 2017/26/D/ST8/00509.

References

Berčič, G., Levec, J.: Intrinsic and global reaction rate of methanol dehydration over γ-Al_2O_3 pellets. Ind. Eng. Chem. Res. **31**(4), 1035–1040 (1992)

Ge, Q., Huang, Y., Qiu, F., Li, S.: Bifunctional catalyst for conversion of synthesis gas to dimethyl ether. Appl. Catal. A-Gen. **167**(1), 23–30 (1998)

Górski, W., Jabłońska, M.M.: Etery dimetylowy – uniwersalne, ekologiczne paliwo XXI wieku. Nafta Gaz **68**(9), 631–641 (2012)

Graaf, G.H., Scholtens, H., Stamhuis, E.J., Beenackers, A.A.C.M.: Intraparticle diffusion limitations in low-pressure methanol synthesis. Chem. Eng. Sci. **45**(4), 773–783 (1990)

Grünewald, M., Agar, D.V.: Enhanced catalyst performance using integrated structured functionalites. Chem. Eng. Sci. **59**(22–23), 5519–5526 (2004)

Hu, Y., Nie, Z., Fang, D.: Simulation and model design of pipe-shell reactor for the direct synthesis of dimethyl ether from syngas. J. Nat. Gas Chem. **17**(2), 195–200 (2008)

Morbidelli, M., Gavriilidis, A., Varma, A.: Catalyst Design. Optimal Distribution of Catalyst in Pellets, Reactors, and Membranes. Cambridge University Press, Cambridge (2001)

Poling, B.E., Prausnitz, J.M., O'Connell, J.P.: The Properties of Gases and Liquids. McGraw-Hill, New York (2000)

Sánchez-Contador, M., Ateka, A., Ibánez, M., Bilbao, J., Aguayo, A.T.: Influence of the operating conditions on the behavior and deactivation of a CuO-ZnO-ZrO_2@SAPO-11 core-shell-like catalyst in the direct synthesis of DME. Renew. Energ. **138**, 585–597 (2019)

Solsvik, J., Tangen, S., Jakobsen, H.: On the consistent modeling of porous catalyst pellets: mass and molar formulations. Ind. Eng. Chem. Res. **51**(24), 8222–8236 (2012)

Algae as a Raw Material for Third Generation Biofuels Production

Małgorzata Płaczek(✉)

Department of Process Engineering,
Opole University of Technology, Opole, Poland
m.placzek@po.opole.pl

Abstract. The chapter describes the current state of the art regarding the possibility of production of biofuels from algae, indicates potential benefits arising from their use as well as the methods of acquiring the algae biomass on an industrial scale. The latest technologies employed to process the algae biomass into biofuels, such as biodiesel, biogas or bioethanol is presented. The paper describes also the potential effect of industrial algae production on the environment. It points to specific factors, i.e. water management, supply of carbon dioxide and nutrients as those that may limit the possibilities in terms of design and implementation of the system on a large scale.

1 Introduction

Development of the contemporary societies and global economy requires an increase of energy resources and is inseparably connected with the increase of the environmental and economic pressure of the human activity. Nowadays, energy is an indispensable element of all human activities in which devices, available technical or transport infrastructure are used. The growth pace of the developing countries as well as the expected expansion of the global population to at least 9 billion in 2050 correlates with the global growth in energy consumption from 533 billiard kJ in 2008 to 812 billiard kJ in 2035 (Rogers et al. 2014). Global forecasts show that maintenance of social, political and climatic security for the growing human population to 2050 will require, first and foremost, satisfaction of the growing demand for food (increase by ca. 70%), guaranteed access to water (consumption increase by 50%), with concurrent reduction of carbon dioxide (CO_2) emission to the atmosphere by 50–80% (Yang et al. 2016). The International Energy Agency (IEA) reports that the global demand for energy from 2005 to 2030 will increase by 55%, with the annual increase rate at the level of 1.8% (Lee 2011). Currently, almost 80% of the energy produced around the world originates from non-renewable sources, i.e. from fossil fuels such as coal, oil or natural gas (Zhu et al. 2018). It is estimated that the transport sector accounts for even 28% of total energy consumption in the economy and is responsible for emission of harmful substances - CO_2, NO_X, SO_X and PM2.5 dusts to the atmosphere. Nowadays, when sustainable development and environmental issues are considered one of the most important contemporary problems in the world, the idea of search for alternatives for the shrinking fossil fuel resources, reduction of greenhouse gases to the atmosphere,

© Springer Nature Switzerland AG 2020
M. Ochowiak et al. (Eds.): PAIC 2019, *Practical Aspects of Chemical Engineering*, pp. 324–335, 2020.
https://doi.org/10.1007/978-3-030-39867-5_34

improvement of air quality and limitation of progressing climatic changes is under intensive development (Klein et al. 2018). In order to meet the international legal regulations, intensive research works are conducted on potential obtaining of energy from environmentally friendly sources and aiming at development of new technologies that will allow to process the CO_2 that has already been emitted, e.g. through its mineralisation (Praharyawan et al. 2018). In this context, renewable energy (bioenergy) offers an environmentally friendly solution for the escalating environmental problems and issues connected with energy security. It allows for diversification of energy sources and becoming independent from supplies of resources from politically unstable countries that are the main suppliers of conventional fuels (Ramanna et al. 2017). Bioenergy is obtained from organic matter, i.e. biomass of animal or derived from microorganism biomass. It includes biogas or syngas (biomethane, biohydrogen), liquid fuels (biodiesel, bioethanol), matter from which electricity and heat are obtained (wood chips, pellet). Figure 1 presents sources and types of biomass and methods of its conversion to heat, electricity, useful solid, liquid and gas fuels.

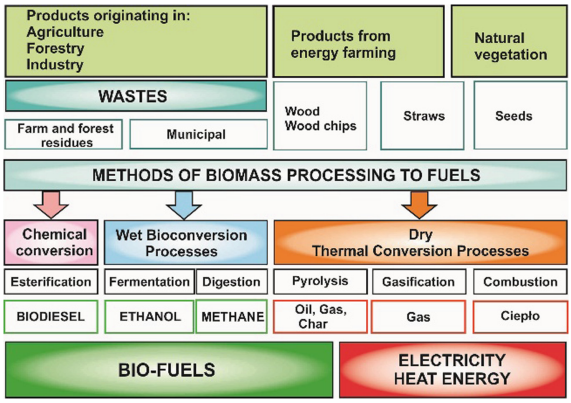

Fig. 1. Methods of biomass conversion into energy and fuels. Worked out based on (Grant 2007)

Liquid biofuels have a specific advantage over other forms of renewable energy such as wind, solar, wave or tidal energy - they can be stored or used directly, e.g. by means of road transport. Selection of the raw material for biofuel production depends on its availability and price. Depending on the type of raw material process in production of biofuels, three generations of biofuels are differentiated. First generation biofuels are produced from alimentary plants, such as sugarcane, corn, oil plants, and animal fats (Slade and Bauen 2013). In Europe, a popular raw material for first generation biofuel (biodiesel) production is rapeseed, in the USA it is soy, while in Malesia, Indonesia or Thailand, biofuels are produced based on palm and coconut oil (Ramanna et al. 2017). Although global production of biofuels based on these raw materials is increasing, controversies connected mostly with food security (food vs. biofuel industry competition) and "land hunger" can become factors limiting broader

use of these energy carriers (Lee 2011). The production of second generation fuels (e.g. cellulosic ethanol) based on inedible parts of plants containing lignocellulose, such as grass, wood chips, is an attractive alternative for the first generation fuels, but it still remains unprofitable due to technological barriers in biomass processing that have not been overcome yet.

The microalgae biomass is free from the above defects and, due to fast growth in comparison to conventional oil plants, ability to accumulate significant amounts of fats, carbohydrates and proteins, is perceived as one of the most promising raw materials for production of third generation biofuels (Scott et al. 2010, Praharyawan et al. 2018). Algae grow 5–20 times faster in comparison to field plants, such as rapeseed or corn, which also demonstrate low amounts of oil, not exceeding 5% of the total mass (Ramanna et al. 2017). In principle, the microalgae cell division takes place once a day, but in the exponential growth phase, its mass may be doubled within 3–4 h (Patel et al. 2017). In comparison to field plants, algae contain higher amounts of fats, from 40 up to 90% of dry mass (Jena and Das 2011). Table 1 presents the comparison of production efficiency of biodiesel obtained from microalgae with respect to the production capacities of typical field plants. According to the presented data, greater amounts of biodiesel can be produced from microalgae with use of significant smaller land areas (Rydzewska-Włodarczyk et al. 2017).

Table 1. Comparison of selected raw materials for biodiesel production (Rydzewska-Włodarczyk et al. 2017).

Raw material	Oil content % w/w	Oil yield L/(ha year)	Land use m^2year/kg biodiesel	Biodiesel productivity kg/(ha year)
Soybean	18	636	18	562
Rape seeds	41	974	12	862
Palm seeds	36	5366	2	4747
Microalgae Low oil cont.	30	58700	0.2	51927
Microalgae High oil cont.	70	136900	0.1	121104

Various studies associated with the productivity of algae cultures as one of the factors conditioning the use of algae in the fuel mass production regard the strategy of their cultivation, determination of the factors directly affecting the biomass growth to obtain a high quantity of algae cells with high fat content. Algae with high lipid accumulation potential - over 20% - include: *Ankistrodesmus falcatus* (59.9%), *Nannochloropsis oceanica* (54.3%), *Schizochytrium sp.* (50–77%), *Chaetoceros calcitrans* (40.9%), *Chlorella vulgaris* (53%), *Pavlova lutheri* (35.5%), *Synechococcus sp.* (29%), *Neochloris oleoabundans* (35–54%) (Razeghifard 2013, Abomohra et al. 2016). One of the methods to improve algae productiveness are immobilisation techniques (Praharyawan et al. 2018). Hameed and Ebrahim (2007) present the example of 19

immobilised microorganisms (*Anabaena azollae*, *Nostoc muscorum*, *Scenedesmus obliquus*) that were used successfully in the production of hydrogen and examples of microorganisms used for ammonia, polysaccharides and glycerol production. The immobilised biomass is used in production of modern energy carriers ("living electrodes") as well as in removal of heavy metals, phosphorus or nitrogen from water and waste.

The potential of macroalgae for biogas production is rather low because of low lipid content that reaches to 0.4–3.5% of dry mass. On the other hand, high content of carbohydrates (3–64%) in the form of starch, cellulose, sugars and other polysaccharides makes macroalgae a desired substrate in anaerobic fermentation. The results of the presented analysis concerning the lipid content in algae cells and the analysis of their chemical suitability, i.e. proportions of triglycerides, level of fatty acid saturation, length of their chains, show clearly the substantial potential of algae with respect to biofuel production and form a direct premise for the search for factors that could significantly improve the profitability of this process.

2 A Favorable Characteristics of Algae as a Raw Material for Biofuel Production

Macro and microalgae are diverse group of prokaryotic and eukaryotic organisms that live in almost any type of the ecosystem in fresh and saltwater, cold and warm waters in all geographic zones (Membere and Sallis 2018). They have found application mainly in the food, cosmetic, pharmaceutical industry as well as a fertilizer in agriculture. Microalgae are miniature biological factories (size of cells between 1 to 30 μm) that convert CO_2 and sunlight into the biomass rich in minerals and produce oxygen in the process of photosynthesis. They are characterised by high photosynthesis efficiency, theoretically 12.6% higher that field plants. For comparison, sugar cane with relatively high photosynthetic effectiveness can convert only 3.5–4% of solar energy into bioenergy (Su et al. 2017). Assimilating CO_2 from the industrial flue gas, algae take part in CO_2 bio-fixation (to produce 1 kg of biomass they use 1.83 kg of CO_2), contributing to reduction of greenhouse gas concentration in the atmosphere (Slade and Bauen 2013). In the process of bioremediation, industrial and municipal waste water becomes the source of nutrients necessary for growth, such as phosphorus or nitrogen (Pawlita-Posmyk and Wzorek 2016, Patel et al. 2017). Many papers point to the possibility of obtaining higher productivity of algae biomass and high fat content in heterotrophic and mixotrophic conditions rather than in the autotrophic culture. Therefore, combination of waste water treatment with algae cultivation seems to be a cost-efficient and environmentally friendly solution in terms of bioenergy production (Slade and Bauen 2013). Depending on the culture species and conditions, the algae biomass can have a diversified chemical composition and efficiency of its growth can diversified over time. The algae productivity may reach 20–30 g/(m^2d) and even 50 g/(m^2d) in its peak. The maximum theoretical productivity of algae for an area demonstrating high insolation can be even 100–120 g/(m^2d). Thus, the biomass productivity and its chemical composition are key parameters taken into consideration when developing profitable and energy-saving methods of biofuel production.

Selection of the highly efficient strain and proper cultivation conditions in relation to the assumed cultivation purpose, for instance liquid or gaseous fuel production and/or obtaining specific bioproducts, gives a change for commercialisation of biofuel production. Among the vast group of algae found on Earth, only 30000 species have been identified so far out of the estimated total number of species ranging from 40000–100000, with only 100 species having a commercial application (Su et al. 2017). Currently, the researchers focus on metabolic engineering and genetic tests aiming at development of a fast growing strain with high lipid content (Patel et al. 2017). In the anaerobic fermentation processes, with participation of specific bacteria, the consecutive reactions may result in generation of 60% of methane and 30% of CO_2. The algae biomass is rich in carbon, nitrogen or phosphorus which are the basic nutrients for anaerobic organisms. The biogas production efficiency is affected by the content of moisture, fats, carbohydrates, ash and lignin (Montingelli et al. 2015, Pawlita-Posmyk and Wzorek 2017).

3 Factors Affecting the Growth of Algae

Algae growth is conditional upon many factors that can be classified as abiotic (temperature, concentration of O_2, CO_2, light with proper intensity, adequate exposure time, pH, salinity, presence of toxic substances), biotic (pathogens, such as viruses, bacteria and presence of other competitive algae strains) and process factors (biomass concentration and frequency of its harvesting, an intensity of mixing (Patel et al. 2017, Płaczek et al. 2017)).

The basic component of the culture medium is water, e.g. cheap seawater rich in natural phosphorus, nitrogen compounds and other microelements. The culture medium is enriched with substances being the source of carbon ($\sim$50% of dry mass), nitrogen, iron, phosphorus, mineral substances and vitamins.

Mixing of the culture can be carried out using multiple methods, i.e. as mechanical mixing, gas mixing (air-lift column, bubble column) or liquid mixing. The mixing method depends on the sensitivity of the given strain to the shear forces that can cause cell destruction. Mixing ensures continuous circulation of the algae suspension in the bioreactor, preventing their separation and, thus, ensuring a uniform cultivation environment. In addition, this has effect on even distribution of nutrients, CO_2 and effective removal of O_2. Cells carried by the liquid have similar access to light, moving cyclically between worse and better lit zones in the bioreactor (Płaczek et al. 2017). Maintenance of the optimum culture temperature (usually 20–30 °C) is decisive in terms of high productivity. Algae are sensitive to temperature changes. They can survive at a temperature 10–15 °C below optimum but die at a temperature 2–3 °C above it (Patel et al. 2017). Therefore, large photobioreactors (PBRs) are placed in greenhouses where temperature control is easy. Pawlita-Posmyk et al. (2018) describe the effect of temperature typical for mesophilic anaerobic fermentation (35–40 °C) on the growth of *Chlorella vulgaris*. The research results showed that excessive temperature first caused inhibition of the algae growth and decline of culture productivity, and finally lead to algae death. In certain algae cultivation systems due to fluctuations in temperature, cooling systems are used, i.e. heat exchangers, internal coils.

Algae, as photosynthetic organisms, absorb and process CO_2 and other substances emitted to the atmosphere as undesirable pollution (Wu et al. 2008). Presence of CO_2 in the culture medium, the basic component of the cellular mass, is indispensable. CO_2 may originate, for instance, from a combined power plant as a component of flue gas from the conventional fuel combustion process. It influences acidity of the culture, i.e. reduced pH - another important parameter determining the algae growth. Most algae species is capable of developing on culture media with pH ranging from 7.0 to 9.0. Control of environmental factors such as change of availability of nutrients, limitation of access to light, application of the proper cultivation method can have a significant effect on the lipid content in the cells. The stress connected with insufficiency of nutrients, especially nitrogen, causes increased lipid production (*C. emersonii* - growth by 63%, *C. minutissima* - 56%, *C. vulgaris* - 40%). This strategy has been applied successfully in commercial installations. Although changes of other cultivation parameters, such as temperature, pH, salinity, can also stimulate lipid accumulation, controlling all listed parameters in large scale production is unfeasible (Patel al. 2017).

4 Microalgae Cultivation Systems and Harvesting Techniques

Increase of the share of algae-based alternative fuels on the global fuel market requires obtaining the adequate quantities of good quality raw materials - biomass, to be converted into valuable biofuels. Industrial cultivation of microalgae can be performed in open systems, i.e. raceway ponds or closed systems referred to as PBRs (Płaczek et al. 2017). Nowadays, the dominant algae culture type are open systems which account for 90% of the global algae production. Raceway pond is shallow concrete or plastic channel in the form of a closed loop equipped with a paddle wheel that forces liquid circulation and prevents algae sedimentation (Patel al. 2017). Low depth (15–40 cm) and large area of the cultivation ponds ensures algae optimal access to the sunlight. The cultivation time is 7–10 days. Open systems have, however, limited production capacities and they are exposed to loss of water and biological contamination (Płaczek et al. 2017, Wądrzyk et al. 2017). In the climatic zones where the nature of daily and annual changes of temperature is not conducive to intensive algae growth and where the insolation is insufficient, PBRs ensuring stabilisation of key culture parameters are used. PBR reduces the possibility of infection with bacteria competing with algae in terms of access to nutrients. Biomass productivity in PBR is at least several times higher than in the open pond. It entails, however, higher capital expenditures resulting mostly from expensive constructive materials of the bioreactor. Photobioreactors such as bubble column, airlift column, flat panel or spiral tube structure are more complex than their open equivalents and they are considered more cost consuming. These costs result from increased energy consumption, sterilisation of culture medium and the use of qualified employees. Many of the PBRs, due to the problem with scale up and operating difficulties, cannot be currently used for production of algae on a global scale. Tubular photobioreactors or a flat panels are usually used for commercial algae cultivation. Mixing the culture liquid is usually carried out using pumps. Aerators are not

very popular as they require periodical cleaning and disinfection. Detailed information regarding the structure and operating parameters of the PBRs is presented in the paper of Płaczek et al. (2017).

Microalgae can be used for production of various types of energy carriers (biomethane produced by anaerobic biomass digestion, biodiesel produced from oil obtained from algae or photobiologically synthesised biohydrogen (Wądrzyk et al. 2017)). The fuel production begins with obtaining the algae biomass which then undergoes multiple stages of processing. The profitability of algae production is affected not only by the production-related costs, i.e. the costs of the nutrients, artificial lighting, CO_2 supply, electric energy, but also by the costs connected with separation of the biomass. The algae biomass is strongly hydrated and contains typically 78–90% of moisture. For the purpose of processing at a later stage, strongly diluted microalgae culture, containing frequently only 0.1 to 2.0 g wt% of dry biomass, must be concentrated to at least 10–30 g wt%, which is an energy-consuming process (Su et al. 2017). Removal of algae from the liquid using convention methods is much more complicated than removal of inorganic particles due to the microscopic size of the cells, their morphology, suspension density similar to water density ($\sim$1.16 kg/m^3) and negative surface charge. It is estimated that the cost of algae dehydration for energy purposes accounts for 20–30% of total biofuel production costs (Rawat et al. 2013, Barros et al. 2015). High costs of dehydration and drying make the fuel obtained from algae less attractive in terms of costs. Taking into account the high costs of microalgae separation which, to a great extent, are decisive in terms of the cost-efficiency of the entire process of biofuel production from algae, methods to improve effectiveness of their separation from culture media are sought for (Sheehan et al. 1998). Separation of the solid-liquid systems can be carried out through centrifugation, flocculation, filtration, sedimentation, floatation or electrophoresis (Uduman et al. 2010). Application of a specific algae biomass dewatering is frequently determined also by the degree of technical proficiency in use of this method on the industrial scale. For instance the dominant technological methods in algae biomass processing are those that proved successful in technology of water treatment for removal of organic contamination. Presence of algae in the drinking water supply sources can cause a number of operating issues i.e. coagulation difficulties, filter clogging or biofilm development (Chen and Yeh 2005). To remove algae from drinking water, pre-oxidants are frequently used, such as ozone as well as a number of chemical substances in the form of coagulants and flocculants. Sedimentation is one of the cheapest algae separation methods, but also the least effective one (Uduman et al. 2010, Patyna et al. 2018). In order to improve effectiveness and reduce time of gravity separation, the preliminary algae flocculation process is carried out, resulting in increased sizes of falling particles. This, however, requires using proper chemical compounds, such as $Al_2(SO_4)_3$, $FeCl_3$, $Fe_2(SO_4)_3$ (Rawat et al. 2013). On the other hand, many algae strains undergo the autoflocculation process the intensity of which depends on the cultivation conditions. This process is most frequently connected with the electrostatic interaction between negatively charged surface of the cells and positively charged ions in the culture liquid, precipitation of salt sediments or generation of extracellular polymer compounds. Many papers indicate that algae produce extracellular polymeric substances in the conditions of change of light intensity, temperature or the concentration of oxygen. In

the batch cultures, this process is a result of cell ageing and the best conditions for sedimentation arise at the end of the exponential and stationary growth phase (Patyna et al. 2018).

5 Production of Biofuel from Microalgae

Liquid algae biofuels are produced subjecting the biomass to thermochemical processes, i.e. pyrolysis, hydrogenation, liquification, gasification, which result in bio-oils as well as biochemical processes, i.e. fermentation, transesterification, the products of which are biodiesel and bioethanol.

Pyrolysis is a reaction of chemical decomposition of biomass under the influence of high temperature (ca. 500 °C) in an environment deprived of oxygen and other oxidising factors. The products are pyrolytic oil (75%), charcoal (12%) and a mixture of flammable gases (13%). The physicochemical properties of bio-oil from microalgae obtained at the temperature of 450° are presented in Table 2 (Su et al. 2017). On the other hand, hydrogenation consists in production of fuel from algae in conditions of high pressure and temperature, in the presence of catalysts and a solvent (Patyna et al. 2018). The developed liquefaction process does not require drying of the biomass which allows to reduce the amount of energy needed to remove water from cells. The process takes place in the aquatic environment at the temperature of ca. 300 °C and pressure of ca. 10 MPa, without reduction of such gases as hydrogen or CO, and consists in recovery of phases: gaseous, oil, water and residues. In the gasification process, biomass is converted in a thermal reaction into a gaseous product which generates energy only after combustion. The first stage of gasification takes place at the temperature of 450–800 °C in the conditions of oxygen deficit which leads to fuel degasification - a flammable gas and the residual minerals are formed. At the second stage, gas is combusted in the temperature of 1000–1200 °C (Amin 2009).

Table 2. Physiochemical properties of microalgae bio-oil (Su et al. 2017).

Parameter	Pyrolysis bio-oil
Density, kg/dm^3	1.01
Kinematic viscosity at 40 °C, mm^2/s	56.8
Flash point, °C	126
Water content, mg/g	598
The calorific value, MJ/kg	27–29
Ash content, wt%	<0.5

Bioethanol is obtained from two-stage process of fermentation of carbohydrates present in the algae. The first stage consists in starch extraction and the second one is the initiation of the proper fermentation process using *Saccharomyces cerevisiae* yeast. The obtained bioethanol undergoes the distillation process. A product of fermentation is also biomethane. This process takes place in fermentation chambers and the generated

gas is stored in tanks. In turn, production of biodiesel involves a different process than biomethane production. The obtained biomass is first dried using electric energy, residual heat or solar energy. In order to release fats from the cells, cellular wall degradation is necessary, for instance by means of ultrasounds. The end stage of biodiesel production is transesterification conducted in high temperature with use of methanol and a catalyst. The fuel obtained in this process undergoes purification. Vegetable oils which, due to high viscosity and composition (they contain free fatty acids, phospholipids, sterols, water), cannot be used directly as engine fuel, undergo transesterification. Transesterification is catalysed by acids, bases or enzymes, and use of an alkaline catalyst guarantees an over 4000 times faster reaction. The most frequently used alkaline catalysts are sodium and potassium hydrocarbons, whereas sulphuric, phosphoric and chloric acids can be acidic catalysts.

6 Environmental Impacts

Industrial production of microalgae can have both a positive and a negative effect on the environment. An example of this can be use of the electric energy originating mostly from fossil fuels and used for the purpose of utilities pumping, gas compression, mixing, photobioreactor lighting, biomass dehydration or drying. Optimisation of energy consumption also through use of waste energy from a combined power plant can effectively improve profitability of fuel production from algae. A reliable cheap water source in the vicinity of the culture is crucial for successful biomass production. Obviously, salty sea water, could be used, but it often requires preliminary processing for the purpose of elimination of components inhibiting the growth of algae and is connected with energy consumption. On the other hand, use of recirculation water in the cultivation processes exposes it to infection and the necessary filtration processes applied to remove contamination from water require significant financial expenditures. In open ponds, to compensate water losses resulting from evaporation, it is necessary to supplement it continuously which also generates costs. An advantage is the fact that the culture can be located on wastelands exposed to very good insolation, but unsuitable for economic use.

Full replacement of fossil fuels with algae based fuels would be connected with increase of demand for fertilisers. Growth in production of fertilisers would contribute to increase of the negative effects of the chemical industry on the environment. Certain conceptual designs of algae production system include circulation of nutrients, especially those obtained from waste water remediation (Slade and Bauen 2013). Algae production systems associated with the power engineering sector may have a positive effect on the air condition, solving the CO_2 sequestration issue. The theoretical effectiveness of CO_2 use can be 20–90% but in practice in open cultivation systems can be lower than 10% while in closed cylindrical photobioreactors (PBRs) it can reach 75%. It arises from the above considerations that a significant part of the gas supplied to the open cultures would be emitted in high amounts at the ground level which may be unacceptable. The demand for CO_2 has effect on the production location and energy balance of the system. If CO_2 from flue gases was used, the production site would have to be located close to the power plant or another big CO_2 source. These sources are

concentrated mostly in the main industrial and urban areas and only a relatively low number of them is located near the oceans from which cheap water could be obtained. Since generation of CO_2 from flue gases is an energy-consuming process, direct use of flue gases would be beneficial in energy terms if algae would tolerate the contamination in the gas.

Improper management of post-culture liquid containing residues of nutrients through its discharge to the environment can result in undesirable changes in the structure and function of water ecosystems (eutrophication). On the other hand, incorporation of eutrophicated ecosystems in the algae production system could solve the issue of excessive supply of nutrients in the waters. Algae placed in a scrubber are capable of capturing 60–80% of nitrogen and from 70% to 100% of phosphorus from the slurry.

Temperature control of the culture must be also included in the energy-consuming processes. It is believed that reducing energy consumption for algae cultivation can be achieved through genetic modification of microalgae. Transgenic algae would be characterised with lower nutritional requirements, would exhibit tolerance to temperature changes, faster growth rates, higher oil yield, translating directly into increased quantities of produced fuel. There is, however, a threat of uncontrolled release of transgenic algae to the environment. Management of waste resulting from the fuel production process can be problematic as many algae species produce toxins at a certain stage of their growth. Prior to sale of these substances or their deposition, the manufacturer will, thus, be obliged to prove that the product is safe (Slade and Bauen 2013).

7 Conclusions

Nowadays, the search for favourable biofuel sources focus on algae which do not compete with food production and, additionally, contribute to reduction of greenhouse gas emission. Financial support for research projects implemented on a global scale, mostly by the US government, EU member states and investment groups, allowed for development of the technology of cultivation and processing of algae into biofuels. Despite significant technological advances, the costs of production of biofuels from the algae are still too high in comparison to price of oil which is a barrier for their commercialisation. Nevertheless, taking into account the growing needs of the transport sector, the demand for cheap raw materials for various branches of the industry as well as the normative requirements connected with the necessity to systematically increase the share of energy from renewable sources in the general supply of energy, new concepts of integrated algae biomass cultivation and processing system have a real change for development. Efficient production and processing will, however, require highly efficient strains of algae and using technologically advanced production systems allowing to reduce the cost and improve its competitiveness to the conventional systems.

References

Abomohra, A.E.-F., Jin, W., Tu, R., Han, S.-F., Eid, M., Eladel, H.: Microalgal biomass production as a sustainable feedstock for biodiesel: current status and perspectives. Renew. Sustain. Energy Rev. **64**, 596–606 (2016)

Amin, S.: Review on biofuel oil and gas production process from microalgae. Energy Convers. Manag. **50**, 1834–1840 (2009)

Barros, A.I., Goncalves, A.L., Simoes, M., Pires, J.C.M.: Harvesting techniques applied to microalgae: a review. Renew. Sustain. Energy Rev. **41**, 1489–1500 (2015)

Chen, J.-J., Yeh, H.-H.: The mechanisms of potassium permanganate on algae removal. Water Res. **39**, 4420–4442 (2005)

Grant, B.-T.: Opportunities for biomass energy programmes. experiences & lessons learned by UNDP in EU & the CIS, Final Report (2007). https://www.uncclearn.org/sites/default/files/inventory/undp42.pdf. Accessed 23 Sept 2019

Hameed, M.S.A., Ebrahim, O.H.: Review biotechnological potential uses of immobilized algae. Int. J. Agric. Biol. **9**(1), 183–192 (2007)

Jena, U., Das, K.C.: Comparative evaluation of thermochemical liquefaction and pyrolysis for bio-oil production from microalgae. Energy Fuels **25**, 5472–5482 (2011)

Klein, B.C., Bonomi, A., Filho, R.M.: Integration of microalgae production with industrial biofuel facilities: a critical review. Renew. Sustain. Energy Rev. **82**(1), 1376–1392 (2018)

Lee, D.H.: Algal biodiesel economy and competition among bio-fuels. Biores. Technol. **102**, 43–49 (2011)

Membere, E., Sallis, P.: Effect of temperature on kinetics od biogas production from macroalgae. Biores. Technol. **263**, 410–417 (2018)

Montingelli, M.E., Tedesco, S., Olabi, A.G.: Biogas production from algal biomass, review. Renew. Sustain. Energy Rev. **43**, 961–972 (2015)

Patel, A., Gami, B., Patel, P., Patel, B.: Microalgae: antiquity to era of integrated technology. Renew. Sustain. Energy Rev. **71**, 535–547 (2017)

Patyna, A., Płaczek, M., Witczak, S.: Study of *Chlorella vulgaris* sedimentation process. In: MATEC Web of Conferences, vol. 240, Article ID 05023, pp. 1–5 (2018)

Pawlita-Posmyk, M., Wzorek, M.: Analysis of domestic sewage treatment system. Chemik **10** (70), 620–625 (2016)

Pawlita-Posmyk, M., Wzorek, M.: Assessment of application of selected wastes for production of biogas. In: E3S Web of Conferences, vol. 19, Article ID 02017, pp. 1–6 (2017)

Pawlita-Posmyk, M., Wzorek, M., Płaczek, M.: The influence of temperature on algal biomass growth for biogas production. In: MATEC Web of Conferences, vol. 240, Article ID 04008, pp. 1–7 (2018)

Płaczek, M., Patyna, A., Witczak, S.: Technical evaluation of photobioreactors for microalgae cultivation. In: E3S Web of Conferences, vol. 19, Article ID 02032, pp. 1–10 (2017)

Praharyawan, S., Rahman, D.Y., Susilaningsih, D.: Influence of light intensity on lipid productivity and fatty acids profile of Choricystis sp. LBB13-AL045 for biodiesel production. Res. J. Life Sci. **5**(2), 128–139 (2018)

Ramanna, L., Rawat, I., Bux, F.: Light enhancement strategies improve microalgal biomass productivity. Renew. Sustain. Energy Rev. **80**, 765–773 (2017)

Rawat, I., Ranjith, K.R., Mutanda, T., Bux, F.: Biodiesel from microalgae: a critical evaluation from laboratory to large scale production. Appl. Energy **103**, 444–467 (2013)

Razeghifard, R.: Algal biofuels. Photosynth. Res. **117**, 207–219 (2013)

Rogers, J.N., Rosenberg, J.N., Guzman, B.J., Oh, V.H., Mimbela, L.E., Ghassemi, A., Betenbaugh, M.J., Oyler, G.A., Donohue, M.D.: The critical analysis of paddlewheel-driven raceway ponds for algal biofuel production at commercial scales. Algal Res. **4**, 76–88 (2014)

Rydzewska-Włodarczyk, M., Drozłowska, E., Sobieraj, M.: Wybrane zagadnienia identyfikacji, wyceny i kalkulacji kosztów produkcji biopaliw trzeciej generacji. Ekonomiczne Problemy Usług **2**, 229–242 (2017)

Scott, S.A., Davey, M.P., Dennis, J.S., Horst, I., Howe, C.J., Lea-Smith, D.J., Smith, A.G.: Biodiesel from algae: challenges and prospects. Curr. Opin. Biotechnol. **21**(3), 277–286 (2010)

Sheehan, J., Dunahay, T., Benemann, J., Roessler, P.: A look back at the U.S. Department of Energy's Aquatic Species Program – Biodiesel from algae. National Renewable Energy Laboratory: Golden, Colorado. NREL/TP-580-24190:1–328 (1998)

Slade, R., Bauen, A.: Micro-algae cultivation for biofuels: cost, energy balance, environmental impacts and future prospects. Biomass Bioenerg. **53**, 29–38 (2013)

Su, Y., Song, K., Zhang, P., Su, Y., Cheng, J., Chen, X.: Progress of microalgae biofuel's commercialization. Renew. Sust. Energy Rev. **74**, 402–411 (2017)

Uduman, N., Qi, Y., Danquah, M.K.: Dewatering of microalgal cultures: a major bottleneck to algae-based fuels. J. Renew. Sustain. Energy **2**, Article ID 012701 (2010)

Wądrzyk, M., Janus, R., Dziok, T.: Produkcja biokomponentów paliwowych drugiej i trzeciej generacji poprzez procesy termochemiczne – bioolej z mikroalg. Nafta-gaz **9**, 641–650 (2017)

Wu, N., Li, Y., Horsman, M., Lan, C.Q., Dubois-Calero, N.: Biofuels from microalgae. Biotechnol. Prog. **24**, 815–820 (2008)

Yang, I.-S., Salama, E.-S., Kim, J.O., Govindwar, S.P., Kurade, M.B., Lee, M., Roh, H.-S., Jeon, B.-H.: Cultivation and harvesting of microalgae in photobioreactor for biodiesel production and simultaneous nutrient removal. Energy Convers. Manag. **117**, 54–62 (2016)

Zhu, L., Li, Z., Hiltunen, E.: Microalgae chlorella vulgaris biomass harvesting by natural flocculant: effects on biomass sedimentation, spent medium recycling and lipid extraction. Biotechnol. Biofuels **11**(183), 1–10 (2018)

The Use of Micro Additives in Building Gypsum Materials

Karol Prałat(✉), Mirosław Grabowski, and Justyna Ciemnicka

Faculty of Civil Engineering, Mechanics and Petrochemistry,
Warsaw University of Technology, ul. Łukasiewicza 17, Płock, Poland
karol.pralat@pw.edu.pl

Abstract. The paper presents the experimental measurement of the thermal conductivity of the modified gypsum and the influence of added micro additives on this thermal parameter. The polymer and the aerogel are used as additives in the weight fractions 0.5%, 1% and 2% of pure gypsum and the microspheres in the weight fractions 5%, 10% and 15% of gypsum. The water-to-gypsum ratio (w/g) for all specimens was 0.75. For the purpose of measuring of the thermal conductivity λ, a novel non-stationary method was used. Based on the experimental measurements found the gypsum with polymer content resulted in more than 44% lower thermal conductivity in comparison to the specimen without hydroxyethylmethylcellulose as a result of the different porosity of the modified specimens. Decrease in thermal properties, were observed as an effect of microstructure modifications of the gypsum product. The gypsum with aerogel and microspheres content resulted in more than 35% and 42% respectively lower values in comparison to the reference sample without micro additives.

1 Introduction

Modern countries and world economies understand that we have to protect environment. They try to lower greenhouse gas emission, protect waters, soils, reduce noise, recycling, look for an alternative sources of energy and energy efficiency (Ciemnicka et al. 2019; Milošević 2012; Węglorz 2014). Modern construction industry, in which we spend up to 80% of our life, is an important element of our environment and landscape. Ensuring an appropriate state of internal environment is very important when we design and build a building, both in health and comfort of use aspects. For many people, taking care about natural environment is also a priority.

Science and industry are used to reduce thermal losses of internal environment. Different methods allow to decrease demand for energy and its consumption. The subject of energy efficiency is the most important in most of the buildings. Energy efficiency is becoming a standard in modern construction industry.

Different methods of reduction of energy consumption are introduced in the ecological buildings in order to reduce consumption of conventional energy and, as a consequence, to protect environment.

© Springer Nature Switzerland AG 2020
M. Ochowiak et al. (Eds.): PAIC 2019, *Practical Aspects of Chemical Engineering*, pp. 336–345, 2020.
https://doi.org/10.1007/978-3-030-39867-5_35

Above goal is achieved mainly through:

- use of energy from alternative sources (renewable),
- use of systems of heat recovery,
- introduction of unconventional methods of obtaining, storing and conversion of energy.

High-tech energy efficient construction industry uses different methods of exchange of solar radiation energy. The basic methods include:

1. Passive solar solutions, which make use of a shape, setting of a building solid to manage available solar energy. It transforms into proper architectural and construction project. Passive systems use and absorb solar radiation from the elements of a building. Proper walls accumulating energy acting as storehouses are used. Heated air (obtained energy) is distributed through channels to the rooms.
2. Active solar solutions, which are usually installation solutions. Photothermal conversion emerges in such systems, that is, conversion of solar radiation energy into thermal energy or photovoltaic conversion, that is, conversion into electric energy.
3. Construction-material-installation solutions aiming at applying other unconventional methods of obtaining energy contained in natural environment, for example, using heat pumps and unconventional methods of its storing in the soil, stone deposits, substances with a low temperature of phase changes. Modern solutions may include: systems of heat recovery, controlling conditions of internal environment microclimate, measurements of energy consumption, non-classic constructions of windows with low values of a coefficient of thermal transmission. Nowadays, very broad field of science within the framework of modern, pro-environmental material solutions is focused on looking for insulations and construction composites with low values of a coefficient of thermal conductivity λ (Ciemnicka et al. 2019, Prałat 2015).

Low values of a coefficient of thermal conductivity λ of insulating and construction materials is obtained with the help of an addition or building phase change materials (PCM) in their structure, which are able to absorb, accumulate and release large amount of energy within the range of a phase change temperature. During absorption of energy, temperature of material does not change. The materials used in the articles are inorganic (hydrated salts) and organic compounds (paraffin, fatty acids, ionic liquids).

A new way to lower value of a coefficient λ is to add micro additives to construction materials. It is assumed that adding a polymer has a considerable impact on crystallization of calcium sulphate (gypsum) and on rate and the way of binding water in it.

It is important to have a basic knowledge aiming at finding material constants of aqueous solutions of polymers, such as: viscosity η, thermal conductivity λ or specific heat C_p. Another important aspect is the impact of micro additives on the value of conductivity of prepared construction materials – mainly gypsums (Prałat 2015).

2 Materials

This paper presents the results of measurement of the thermal conductivity λ of modified gypsum. Specimens were modified with the following micro additives: polymer (hydroxymethyl ethyl cellulose), microspheres and aerogel. Measurements were based on a designed, novel experimental set up using the non-stationary method. The composites were characterized by different concentrations of additives. The gypsum sample was modified by additive of polymer and aerogel in different amounts - 0.5, 1.0 and 2.0% and microspheres - 5, 10 and 15% of gypsum.

The material, mechanical and thermal properties of pure gypsum and its components are very well known and described in the literature (Adrien 2016; Karni and Karni 1995; Yu and Brouwers 2012). As a traditional, unmodified building product, it has the thermal conductivity λ, varying in the range of 0.23 to 1.00 W/(m·K), and density ρ = 1000 kg/m^3 for gypsum boards and blocks. The averaged specific heat is approximately 840 J/(kg·K) (Yu and Brouwers 2012; Heim et al. 2018). The influence of various additives like: aerogels, microspheres and polymers on the thermal conductivity of gypsum is currently not well recognized (Ciemnicka et al. 2019).

Hydroxyethyl methyl cellulose is a nonionic polymer characterized by high viscosity and nontoxic and water-soluble properties. HEMC is one of the cellulose ethers and is widely applied in the building construction sector. It can be used to modify building materials that are made based on any mortars, such as cement or gypsum (Kamsen et al. 2013; Ru et al. 2006, Heim et al. 2018). The particle size of polymer added to gypsum was in the range 150–250 μm.

Nowadays aerogels are one of the best thermal insulation materials. For this work, silica aerogel in the form of particles of fraction 0.7–4.0 mm was used (Garbalińska and Strzałkowski 2016). The granules feature hydrophobic properties and their specific density ranges between 120 and 150 kg/m^3. They are the only fire resistant materials that offer thermal conductivity values as low as 0.012–0.018 W/(m·K) without the need for vacuum or gas sealed systems (Schiovani 2016). This is achieved by forming the structure in a supercritical drying process. Supercritical drying is performed to replace the liquid in a material with a gas to isolate the solid component from the material without destroying the material's nanostructured pore network of diameter of approximately 20 nm.

Microspheres are light, thin-walled hollow spheres which are by-products of the combustion of pulverized coal at thermal power plants. Due to their properties they are a potentially interesting filler and may be used for cement-based composites production (Pichór 2009). The particle size of microspheres from fly ash, added to gypsum was in the range 50–150 μm. The main chemical constituents in used microspheres: Al_2O_3 (34–38%), Fe_2O_3 (1–3%), SiO_2 (50–60%), CaO (1–4%), MgO (0.2–2%) and TiO_2 (0.5–3%) (Ciemnicka et al. 2019).

In order to present the structure of micro additives, images of the substances used were made by laboratory stereoscopic microscope, with the use of 100x magnification and the Moticam camera, allowing observation of details with a size up to 20 μm (Fig. 1). Because of the visible differences in the structure of the micro additives it was assumed that micro additives will reduce the thermal conductivity of gypsum composites to a different extent.

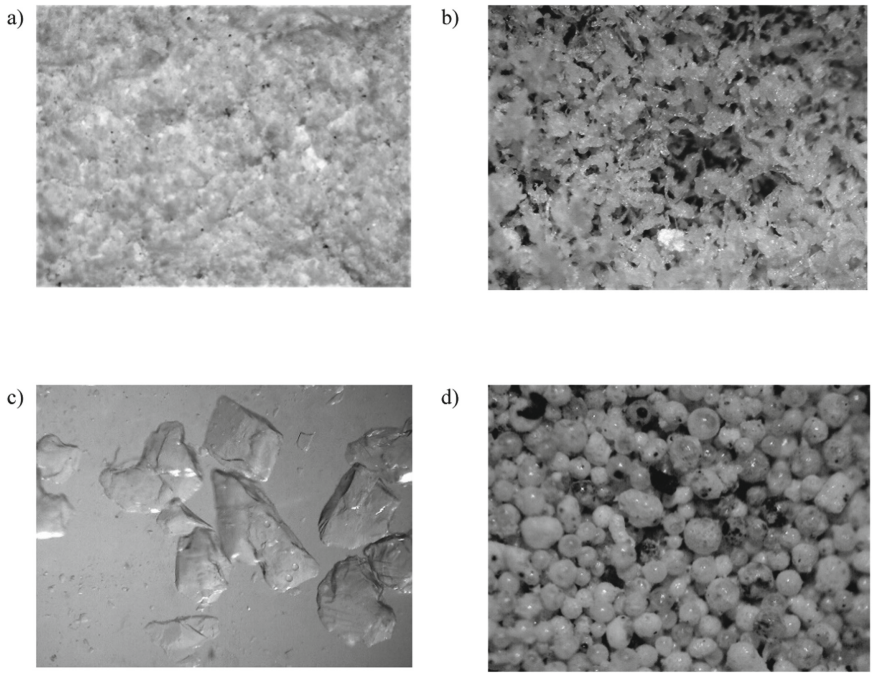

Fig. 1. Microscopic images (magnification x100) of: **a** gypsum, **b** polymer, **c** aerogel, **d** microspheres (Ciemnicka 2019)

3 Experimental Set-Up

Presented solution of a device is an elaboration of so called linear thermal probe with constant disbursement. Idea of device consists in the placement inside material, constant source of heat powered by constant electric current in such a way that giving off stream of heat is constant.

Theoretical bases of "hot wire" method gave Van der Held and Van Drunen (Van der Held and Van Drunen 1949). A field temperature describes Fourier Eq. (1), where ϑ means relative temperature, r radius and t time:

$$c_p \rho \frac{\partial \vartheta}{\partial t} = \lambda \left(\frac{\partial^2 \vartheta}{\partial r^2} + \frac{1}{r} \frac{\partial \vartheta}{\partial r} \right) \tag{1}$$

Pace of heating up the wire depends on properties of the centre in which it can be found. With an assumption of negligible small diameter of heating wire $2r$ in relation to its length L, and with following boundary conditions are obtained general solutions (2):

- initial condition: $t = 0$, r: $\vartheta = \vartheta_o = 0$
- boundary conditions: $t \geq 0$, $r = \infty$: $\vartheta = \vartheta_\infty = 0$

$$r \to 0, q = -2\pi r\lambda(\partial\vartheta/\partial r)_{r\to 0} = const.$$

$$\vartheta = \frac{q}{4\pi\lambda}\int_x^\infty \frac{1}{x} exp(-x)dx = \frac{q}{4\pi\lambda}\left(-C - ln\,x + \frac{x}{1\cdot 1!} - \frac{x^2}{2\cdot 2!} + \ldots\right) \quad (2)$$

where:

$x = r^2/(4at)$,
C = 0,5772 – Euler constant,
$a = \lambda/(c_p\rho)$ – coefficient of thermal diffusion,
$q = Q/L$ – power unit of heating wire.

For very small values x, a value of integral can be written down as $-C - lnx$, and then Eq. (2) takes the form (3):

$$\vartheta = \frac{\mathrm{q}}{4\pi\lambda}\left(ln\frac{4at}{r_0^2} - 0,5772\right) \quad (3)$$

Carrying out two measurements of T in moments t_1 and t_2 value of coefficient of thermal conductivity can be determined from dependencies (4):

$$\lambda = \frac{Q}{4\pi L}\cdot\frac{ln\frac{t_2}{t_1}}{T_2 - T_1} = \frac{q}{4\pi}\cdot\frac{ln\frac{t_2}{t_1}}{T_2 - T_1} \quad (4)$$

where:

Q – quantity of heat emitted by the source of heat, W;
L – length of heating element, m;
t – time, s;
T – temperature of heating element, °C.

Quantity of heat Q emitted by heating element is equal to quantity of heat seized by studied material in a unit of time, with an assumption of lack of losses and omission of heat accumulation in heating element (Heim et al. 2016):

$$Q = U \cdot I \quad (5)$$

where:

U – current voltage, A;
I – current strength, V.

For the purpose of conductivity measurements, an improved "hot wire" method was used. The "hot wire" method, based on transient heat exchange, belongs to one of the most interesting methods because of its simplicity, accuracy and ease of implementation. It involves placing the heating wire inside the tested material and measuring its temperature as a function of time. The idea of the experiment assumes placing in the material a source of heat, supplied with electric current in such a way that the heat flow emitted in time is constant. The measurement takes place under the heating conditions

of the material indirectly by determining the rate of heating. In the *T-ln(t)* coordinates system, after the transitional period, the dependence takes on a linear character (Van der Held and Van Drunen 1949, Heim et al. 2016).

For the purpose of measuring the thermal conductivity λ a computer-controlled experimental stand was used described in detail in (Heim et al. 2016, Prałat et al. 2019). The basic element was a gypsum specimen measuring 50 × 50 × 305 mm, containing an axially placed Kanthal resistance wire heater with a diameter of 0.2 mm. A miniature resistance temperature sensor type Pt100 has been permanently attached to the heater. A characteristic feature of platinum resistance sensors is the increase of their resistance as a function of temperature. In a small temperature range, this increase can be treated as linear (Heim et al. 2016, Prałat et al. 2019).

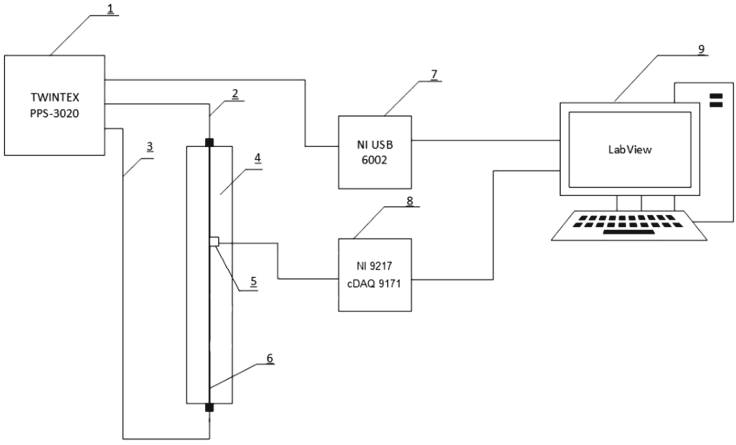

Fig. 2. Experimental set up for measurement of thermal conductivity by "hot wire" method: 1 – adjustable power supply of direct current, 2 and 3 – power cables, 4 – tested specimen, 5 – sensor Pt100, 6 – hot wire, 7 – data recorder, 8 – input module of the resistance temperature sensor, 9 – computer (Prałat et al. 2019)

The temperature sensor was connected with the measuring module NI-9217 produced by National Instruments, which was then connected to the intermediary module cDAQ 9171 transmitting the encoded temperature signal to computer controlling the process. The measuring module NI-9217 can operate in two modes: sampling with high resolution or high frequency sampling (Fig. 2). The dedicated software in the LabView was written for the operation of the measurements procedure. The software made it possible to set the voltage and the current supply limitation, and indirectly heating power, to read the actual parameters, as well as write them to a computer disk. The program also enabled the selection of required power and data logging time sequences (Prałat et al. 2019).

Thermal conductivity measurements are interdependent measurements, also called simultaneous measurements, because the measurement and recording of all measured values were carried out under the same conditions. The estimation of measurement

error of thermal conductivity was calculated for gypsum specimens after 35 days of maturation and drying. The uncertainty assessment is based on a theory that assumes that measurement error is random and therefore subject to relevant statistics. In this case, the final measurement error is determined mainly by "evaluation of measurement uncertainty type B" of the measuring instruments used, methodology or random errors. It can be assumed that random and methodical errors are very small and can be neglected. Therefore, the uncertainty of the final measurement will be affected by measurement errors of the instruments. The uncertainty assessment is the ratio of the error margin of the instrument to the measured value and decreases with the increase of this value. The relative uncertainty of the complex, independent, random measurement of the thermal conductivity of gypsum was calculated from Eq. (6) (Heim 2016):

$$\frac{u(\lambda)}{\lambda} = \sqrt{\delta(U)^2 + \delta(I)^2 + \delta(l)^2 + \left[\frac{\delta(t_1)}{\ln t_1}\right]^2 + \left[\frac{\delta(t_2)}{\ln t_2}\right]^2 + \delta(T_1)^2 + \delta(T_2)^2} = 0.861\% \quad (6)$$

where: δU - uncertainty of voltage measurement on the heating wire, δI - uncertainty in measuring the intensity of the current flowing through the heating wire, δl - uncertainty in measuring the length of the heating wire, δt_1 - uncertainty of time measurement t_1, δt_2 - uncertainty of time measurement t_2, δT_1 - uncertainty of temperature measurement T_1, δT_2 - uncertainty of temperature measurement T_2.

4 Results

Specimens were conditioned in temperatures of 20 ÷ 22 °C and RH = 40 ± 1% for 28 days. After this time they were dried at a temperature of 65 °C for 7 days. During the experiment, thermal conductivity values on the specimens were determined successively at 1, 3, 7, 21, 28 and 35 days after they were made. At the same time, the values of density of gypsum blocks were determined.

Bulk density was determined as a ratio of mass and volume of the gypsum specimens. Total porosity p was calculated based on bulk density with reference to the density of the structure (7).

$$p = \left(1 - \frac{\rho}{\rho_g}\right) \cdot 100\% \quad (7)$$

The obtained values of bulk density and total porosity are presented in Table 1. The specific density of tested specimens was assumed ρ_g = 2,350 kg/m^3.

When measuring the thermal conductivity based on "hot wire" method, a low heating power of 0.2 W was used. For all gypsum specimens tested, graphs of the dependencies $T - T_0 = f(ln(t))$ were made and the slope S for the latter was determined. Figure 3 shows the graphs for the gypsum without micro additives.

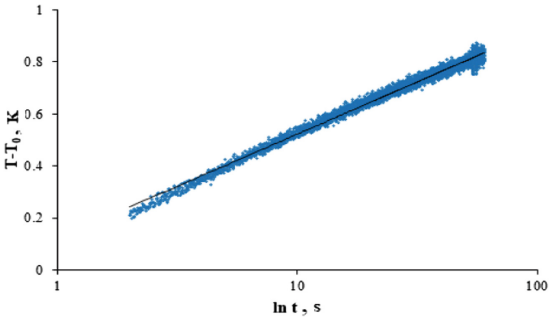

Fig. 3. Sample graph of the temperature change of the heating wire of the gypsum specimen as a function of the natural logarithm of time

Table 1. Bulk density ρ, porosity p and thermal conductivity λ of gypsum specimens after 35 days of maturing.

Gypsum specimens	λ, W/(m·K)	ρ, kg/m^3	p, %
Gypsum + 0.5% polymer	0.2685	1011	57
Gypsum + 1% polymer	0.2664	1233	48
Gypsum + 2% polymer	0.1948	947	60
Gypsum + 5% microspheres	0.2083	1011	57
Gypsum + 10% microspheres	0.2797	1208	49
Gypsum + 15% microspheres	0.2027	999	57
Gypsum + 0.5% aerogel	0.2481	1026	56
Gypsum + 1% aerogel	0.3261	1206	49
Gypsum + 2% aerogel	0.2266	908	61
Gypsum	0.3465	1309	44

The thermal conductivity of the specimens was calculated using Eq. (8). The density and porosity of all the tested gypsum specimens were determined. The values obtained experimentally are shown in Table 1. In addition, the thermal conductivity of gypsum was compared with the literature data.

$$\lambda = \frac{Q}{4\pi L} \cdot \frac{1}{S} = \frac{q}{4\pi} \cdot \frac{1}{S} \tag{8}$$

Experimental values of thermal conductivity of gypsum specimens with the addition of polymer, aerogel and microspheres were respectively over 44% (with 2% polymer addition), 35% (with 2% aerogel addition) and 42% (with 15% microspheres addition) lower than the reference specimen, made of gypsum without additives.

On this basis, the thermal conductivity change in time diagrams were made (Fig. 4) and in the function of varying density (Fig. 5). It was observed that since the 14th day of the specimens maturation, the thermal conductivity has stabilized.

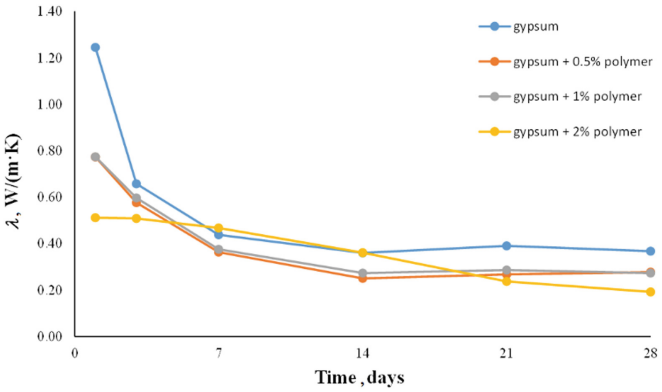

Fig. 4. Changes in thermal conductivity of gypsum specimens during the aging process of pure gypsum and gypsum with micro additives

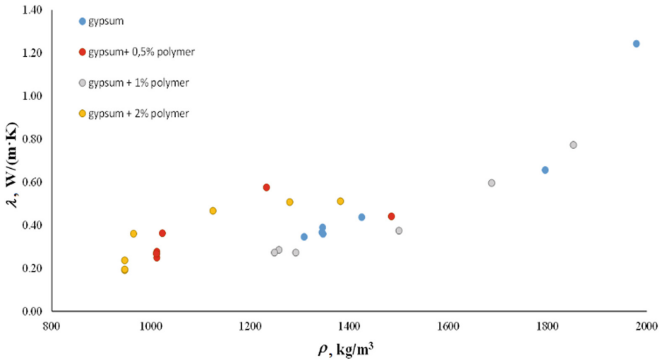

Fig. 5. Graph of the dependence of $\lambda = f(\rho)$ of gypsum specimens with different moisture content

5 Conclusions

The gypsum with polymer content results in more than 44% lower thermal conductivity in comparison to the specimen made of pure gypsum as a result of the different density and total porosity of the material. Experimental values of thermal conductivity of modified gypsum specimens with the addition of aerogel were 35% and microspheres 42% lower than that made of pure gypsum. The analysed gypsum composites with micro additives are thus environmentally friendly materials with improved insulating performance.

The relative uncertainty of the complex, independent, random measurement of the thermal conductivity of gypsum after 35 days aging process was lower than 0.9%. The experimental value of λ = 0.3465 W/(m·K) of the specimen with the content of pure

gypsum differed from the literature value $\lambda = 0.3537$ W/(m·K) by 1.0% (PN-EN 12524:2003). It has been confirmed that the novel experimental set up based on "hot wire" method was designed and made properly.

References

Adrien, J., Meille, S., Tadier, S., Maire, E., Sasaki, L.: In-situ X-ray tomographic monitoring of gypsum plaster setting. Cem. Concr. Res. **82**, 107–116 (2016)

Ciemnicka, J., Jaskulski, R., Kubissa, W., Prałat, K.: Influence of selected micro additives content on thermal properties of gypsum. Archit. Civ. Eng. Environ. **3**, 69–79 (2019)

Ciemnicka, J.: Analysis of thermal parameters of gypsum modified with micro additives. Ph.D. thesis. Warsaw University of Technology (2019)

Garbalińska, H., Strzałkowski, J.: Thermal and strength properties of lightweight concretes with the addition of aerogel particles. Adv. Cem. Res. **28**(9), 567–575 (2016)

Heim, D., Mrowiec, A., Prałat, K.: Analysis and interpretation of results of thermal conductivity obtained by the hot wire method. Exp. Tech. **40**(2), 513–519 (2016)

Heim, D., Mrowiec, A., Prałat, K., Mucha, M.: Influence of tylose MH1000 content on gypsum thermal conductivity. J. Mater. Civ. Eng. **30**(3), 04018002 (2018)

Kamseu, E., Bignozzi, M.C., Melo, U.C., Leonelli, C., Sglavo, V.M.: Design of inorganic polymer cements: Effects of matrix strengthening on microstructure. Constr. Build. Mater. **38**, 1135–1145 (2013)

Karni, J., Karni, E.: Gypsum in construction: origin and properties. Mater. Struct. **28**(2), 92–100 (1995)

Milošević, P.: Sustainable eco planning strategies in East Europe (case study of Belgrade). Archit. Civ. Eng. Environ. **5**(4), 29–42 (2012)

Pichór, W.: Properties of fiber reinforced cement composites with cenospheres from coal ash. In: Brandt, A.M., Olek, J., Marshall, I.H. (eds.) Proceedings of International Symposium on Brittle Matrix Composites, vol. 9, pp. 245–254 (2009)

Prałat, K.: Habilitation dissertation (Summary of professional accomplishments). Properties of selected heat-insulating polymers significant in reduction of thermal losses of internal environment (2015)

Prałat, K., Grabowski, M., Kubissa, W., Jaskulski, R., Ciemnicka, J.: Application of experimental setup for the thermal conductivity measurement of building materials using the "hot wire" method. Sci. Rev. Eng. Environ. Sci. **28**(1), 153–160 (2019)

Ru, W., Xin-Gui, L., Pei-Ming, W.: Influence of polymer on cement hydration in SBR-modified cement pastes. Cem. Concr. Res. **36**(9), 1744–1751 (2006)

Schiavoni, S., D'Alessandro, F., Bianchi, F., Astrubali, F.: Insulation materials for the building sector: a review and comparative analysis. Renew. Sustain. Energy Rev. **62**, 988–1011 (2016)

Węglorz, M.: Selected aspects of sustainable civil engineering in research works of professor Andrzej Ajdukiewicz. Archit. Civ. Eng. Environ. **7**(1), 41–47 (2014)

Van der Held, E., Van Drunen, F.: A method of measuring the thermal conductivity of liquids. Physica XV **10**, 865–881 (1949)

Yu, Q.L., Brouwers, H.J.H.: Thermal properties and microstructure of gypsum board and its dehydration products: a theoretical and experimental investigation. Fire Mater. **36**(7), 575–589 (2012)

European Standard: PN-EN 12524:2003: Building materials and products. Thermal and moisture properties

The Influence of External Recirculation Loop Design on the Hydrodynamic Properties of a Hybrid Fluidized Bed Apparatus

Mateusz Prończuk(✉) and Katarzyna Bizon

Faculty of Chemical Engineering and Technology,
Cracow University of Technology, Kraków, Poland
mpronczuk@chemia.pk.edu.pl

Abstract. The chapter presents the results of experimental and numerical studies of the impact of the design of selected zones of a hybrid fluidized-bed apparatus on its hydrodynamic properties. In particular experimental tests were carried out to characterize the hydrodynamics of the bottom zone and of the degassing zone. The analysis of liquid flow through these zones was performed using tracer experiments done with the stimulus-response method to determine the presence of local liquid circulation that could lead to local oxygen deficiency in the apparatus (dead zones) or privileged flow channels. In addition, CFD simulations of the liquid flow through the bottom zone of the apparatus were carried out assuming different design solutions for this zone.

1 Introduction

Three-phase airlift apparatuses are used more and more frequently to run microbiological processes (Merchuk 2003). They have a number of advantages that have contributed to the growing popularity of this type of construction. The presence of a solid phase on the surface of which a layer of microorganisms is deposited results in the increase in the overall biomass concentration in the apparatus, and thus increase in the bioprocess rate. The introduction of a gas phase, usually air, into the apparatus has two functions: beyond introducing oxygen into the system, the presence of gas bubbles in the airlift apparatus induces flow of the liquid phase, so such apparatuses do not need additional devices to force the liquid phase circulation. Circulation of the liquid also helps distribute reagents throughout the entire apparatus (Merchuk 2003). However, rising gas bubbles create additional shear stress that may damage the delicate biofilm layer and detach it off the surface of the solid support, which is a serious problem when growing delicate cells (Guo et al. 1997; Olivieri et al. 2010).

Hybrid airlift fluidized-bed apparatus is a modification of a classical three-phase airlift apparatus. The main modification consists in the lack of direct contact between solid and gas phase. This is achieved by separating fluidization and bubbling zones by placing them one above the other (Fig. 1) (Guo et al. 1997). Thanks to this, the advantages of the three-phase airlift apparatus are preserved and one of the major disadvantages of a classical design is eliminated.

© Springer Nature Switzerland AG 2020
M. Ochowiak et al. (Eds.): PAIC 2019, *Practical Aspects of Chemical Engineering*, pp. 346–354, 2020.
https://doi.org/10.1007/978-3-030-39867-5_36

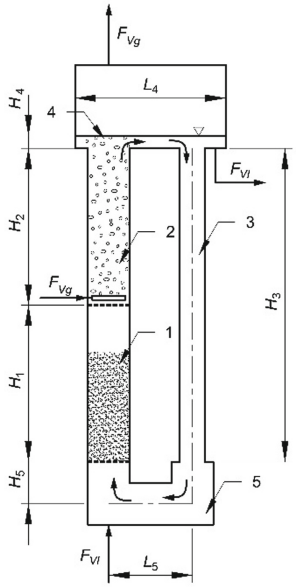

Fig. 1. Hybrid fluidized-bed apparatus with external liquid circulation: 1 – fluidization zone, 2 – bubbling zone, 3 – downcomer zone, 4 – degassing zone, 5 – bottom zone

The hybrid apparatus is a relatively new design, therefore there are few reports in the scientific literature concerning such apparatuses (Guo et al. 1997; Olivieri et al. 2010; Prończuk et al. 2016, 2017, 2018, 2019), and their properties have not yet been completely understood. In the hybrid apparatus, liquid circulation is caused by the introduction of a gas phase. The flow velocity of the circulating liquid, however, depends not only on the flow rate of the gas phase but also on the design of the apparatus itself. There are many possible design variants of two- and three-phase airlift apparatuses (Rujiruttanakul and Pavasant 2011). Each of the construction solutions has a number of advantages and disadvantages. In some cases, even a slight change in the design may cause a significant change in the apparatus operating conditions.

The aim of this work was to analyze the construction of an external recirculation loop and its effect on hydrodynamics of the apparatus. Particular attention was paid to the zones connecting the recirculation loop "3" with fluidization "1" and bubbling "2" zones, i.e. the degassing "4" and the bottom "5" zones. An analysis of the liquid flow through these zones (i.e. "4" and "5") was performed to identify areas of local liquid circulation and to identify local privileged flow channels. Tracer experiments were carried out to visualize the liquid flow and to determine the residence time distribution in the selected zones. Moreover, CFD simulations of liquid flow through the bottom zone characterized by various construction were carried out to determine the influence of the bottom zone design on liquid mixing.

2 Experimental Set-up

The test stand is schematically shown in Fig. 1. The fluidization zone "1" is located at the bottom of the riser. Above it, the bubbling zone "2" is located. The downcomer zone "3" is situated in parallel to the riser (zones "1" and "2") and is connected at the top with the bubbling zone by means of the degassing zone "4" and at its outlet with the bottom zone "5". The fluidization zone was restricted by two meshes: at the bottom to provide a base on which the bed of solid particles rests, and at the top to prevent the bed from entering into the bubbling zone. To ensure rigidity, the meshes consisted of two layers. The first layer of mesh with openings of 1 mm served as a support and the second mesh with openings of 0.315 mm rested on it. The apparatus was built using pipes and sheets made of PMMA (Plexiglas), so it was possible to observe the flow of process media during the apparatus operation. Its design allowed also the use of circulation pipes of various diameters. Table 1 reports the main dimensions of the apparatus.

Table 1. Main dimensions of the external-loop hybrid fluidized-bed apparatus, d – diameter, H – height, L – length, W – width

Dimension	Value	Dimension	Value
d_1	0.08 m	H_3	1 m
d_2	0.08 m	H_4	1 m
d_3	0.03 m, 0.08 m	H_5	0.12 m
d_5	0.08 m	L_4	0.34 m
H_1	1 m	L_5	0.17 m
H_2	1 m	W_5	0.12 m

Tap water and atmospheric air were used as process media to evaluate the hydrodynamics of the apparatus, whereas polyoxymethylene (POM) granulate was used as the fluidized-bed material. The physical properties of media at 18 °C were employed in the calculations. Tracer experiments were carried out in two different manners. The first consisted in the introduction of a colored tracer into the flowing liquid, thanks to which it was possible to visualize the flow. An aqueous solution of blue ink was used as a tracer. The tracer flow was recorded using a high speed video camera. The second technique was the classic stimulus-response method (Levenspiel 2011) with an aqueous KCl solution used as a tracer. The concentration of the tracer was determined by measurement of the conductance. It was measured at the inlet and outlet of each zone to determine the response to the stimulus introduced and, based on the response, to determine the value of the Peclet number for the analyzed zones of the apparatus (Levenspiel 2011). In both cases, the tracer was introduced into the apparatus in the form approaching the Dirac distribution.

3 Results

The first zone to be analyzed was the degassing zone ("4" in Fig. 1). This zone has the shape of a rectangular tank that connects the bubble zone "2" and the downcomer zone "3" at the top of the apparatus. As the name implies, the gas phase was separated from the liquid phase in this zone. Experimental studies have shown that the liquid in the upper tank was completely degassed in zone "4" in all experiments conducted.

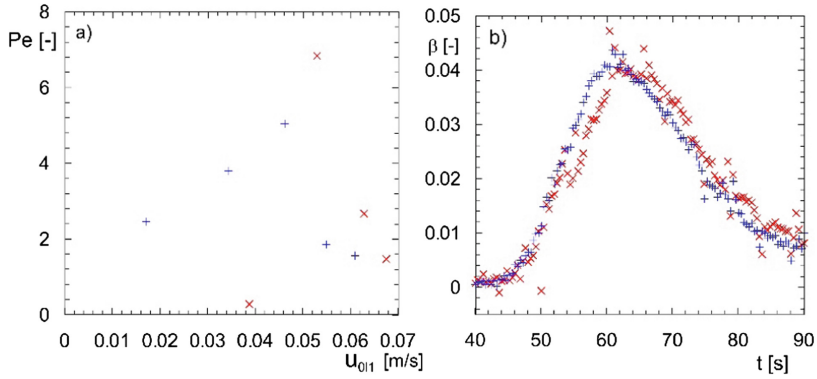

Fig. 2. Results of the tracer experiments with KCl for the degassing zone "4": (a) calculated Peclet number value versus superficial liquid velocity, u_{0l1}, for d_3 = 0.03 m (blue "+") and d_3 = 0.08 m (red "x"); (b) representative inlet (blue "+") and outlet (red "x") dimensionless tracer concentration, β, versus time

The stimulus-response tracer experiments permitted to determine the values of axial Peclet number defined as:

$$\mathrm{Pe} = \frac{uL}{D} \tag{1}$$

for zone "4" (Fig. 2a), where u is the mean flow velocity, L is the zone length and D is the axial mass dispersion coefficient.

Depending on the superficial liquid velocity, u_{0l1}, the Pe value fluctuated between 0–8, suggesting that the type of flow in this zone is close to ideal mixing. However, when analyzing the response to a given stimulus at the outlet of the degassing zone (Fig. 2b, red "x"), some discontinuities were found in the tracer concentration distribution. It can be observed in Fig. 2b that initially the concentration of the tracer in the stream leaving zone "4" was approximately equal to the concentration of the tracer in the stream entering this zone. However, after some time, one can observe a sudden decrease in the concentration of the tracer, despite a continuous increase in its concentration in the inflow stream. This suggests that the flow in this zone was transient and the type of flow changed over time.

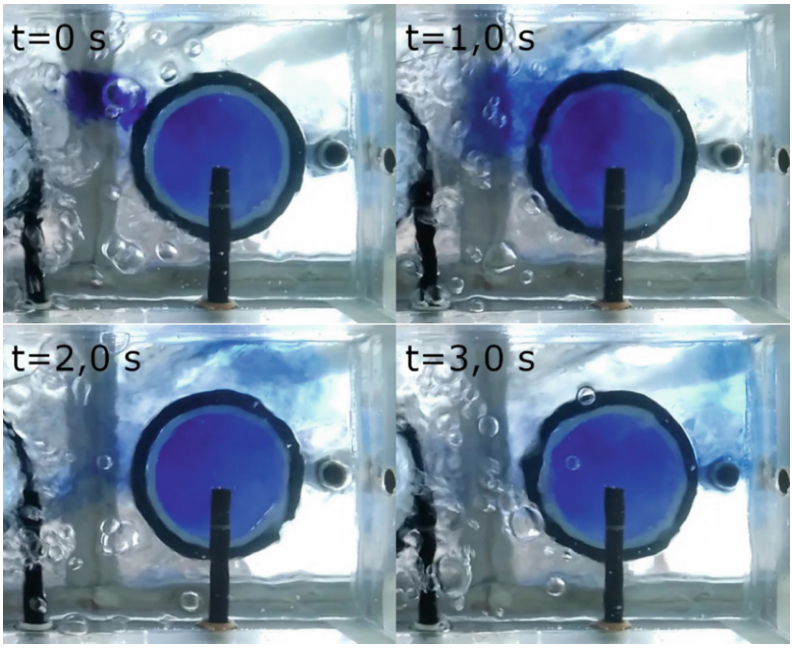

Fig. 3. Colored tracer experiments for degassing zone "4" (top view)

In order to visualize the flow through the degassing zone, experiments with a colored tracer were performed. The tracer was injected in the upper tank, near the liquid outflow from the bubbling zone "2". The results obtained (Fig. 3) confirm the complex nature of the flow in this zone. It can be seen that the tracer, initially introduced in the form of a compact cloud (Fig. 3a, $t = 0$ s), was quickly dispersed in the liquid (Fig. 3b, $t = 1$ s). The tracer cloud increased its volume considerably and it partially moved above the outflow from zone "4". However, only a certain portion of the tracer entered the downcomer and the remainded portion moved clockwise around the inlet to the downcomer zone ($t = 2$ s and $t = 3$ s in Fig. 3c and 3d). When the part of tracer flowed from the degassing zone to the downcomer zone, the tracer concentration near the conductivity probe mounted on the discharge from this zone dropped momentarily. When the tracer circulating around the inlet to the downcomer zone was directed towards it, its concentration near the conductivity probe increased again. The visual observations made are therefore consistent with the results of the tracer experiments conducted with KCl as a tracer. They also confirm the hypothesis that the flow character changes as the liquid flows through the degassing zone.

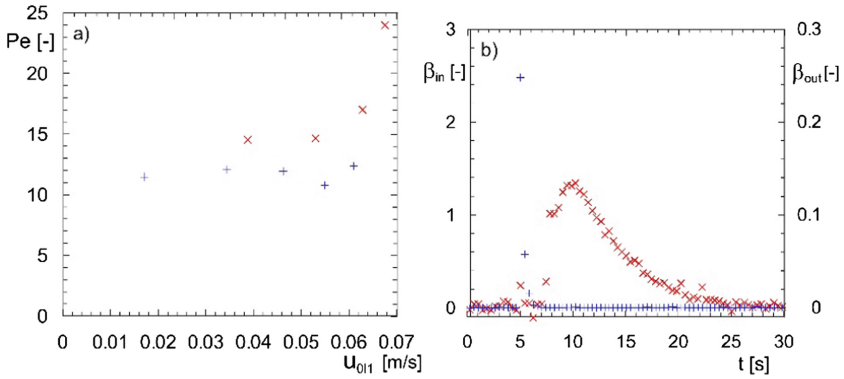

Fig. 4. Results of the tracer experiments with KCl for the bottom zone "5": (a) calculated Peclet number value versus superficial liquid velocity, u_{0l1}, for d_3 = 0.03 m (blue "+") and d_3 = 0.08 m (red "x"); (b) representative inlet (blue "+") and outlet (red "x") dimensionless tracer concentration, β, versus time

The second zone analyzed in this work was the bottom zone "5". It consisted of a U-shaped pipeline with a diameter of d_5 = 0.08 m. It was made of three straight parts connected together at an angle of 90°. Depending on the diameter of the downcomer zone (when it was different from the bottom zone diameter), a sudden extension of the flow cross-section at the bottom zone inlet occurred (see Fig. 1).

The tracer experiments performed using KCl permitted to determine the value of the Pe number for this zone (Fig. 4a). It can be seen that the values of the Pe number for this zone depend not only on the liquid flow velocity, but also on the downcomer diameter. The flow through the bottom zone for the apparatus with the downcomer zone of the same diameter as the bottom zone (i.e. 0.08 m) is characterized by Pe values between 15 and 25. For the apparatus with a smaller downcomer diameter, the Pe values are in the range of 10–13, which means that the flow was approaching the ideal mixing. This suggests that the presence of a sudden extension of the flow cross-section creates an area where additional mixing occurs. To identify this area, additional tracer experiments using a KCl solution (Fig. 4b) and a colored marker (Fig. 5) were performed.

In the experiments done using KCl solution, the tracer was introduced into the downcomer zone, in a short distance before entering the bottom zone. The inlet tracer concentration was measured directly below its injection point. Representative results of the experiments are shown in Fig. 4b. It can be observed that, despite a short mean residence time in this zone (for the case shown in Fig. 4b it was τ = 7.3 s), the time span of the response signal is several times greater than the stimulus RTD time span. However, the maximum tracer concentration is much higher in the case of the stimulus signal. This type of RTD is characteristic for dispersed flows characterized by low values of the Pe (close to ideal mixing).

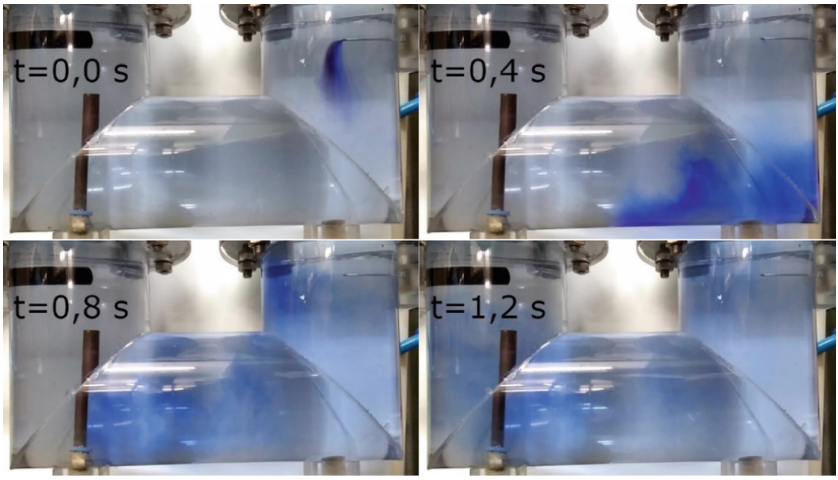

Fig. 5. Colored tracer experiments for bottom zone "5" (front view), d_3 = 0.03 m

In the experiments performed using the colored tracer the injection point was located in the bottom zone, directly below the outflow from the downcomer zone (see Fig. 5, t = 0.0 s). It can be seen that the liquid flowing out of the downcomer zone "3" has a much higher average velocity than the liquid in the bottom zone (d_3 = 0.03 m). The tracer quickly moved away from the injection point and flowed towards the bottom wall of the apparatus (Fig. 5b, t = 0.4 s). As a result of the collision with the wall, the tracer smudge was significantly dispersed in the entire volume of the liquid. Then the tracer cloud was split into two parts, one of which flowing towards the outlet from zone "5" and the other returning towards the entrance of zone "5" directly below the downcomer (Fig. 5c, t = 0.8 s). Eventually, near the outlet from zone "3", the tracer cloud intensively mixed with the flowing liquid and flowed towards the outlet from the bottom zone (Fig. 5d, t = 1.2 s). Thus, near the outlet from the downcomer zone, a volume characterized by a local liquid circulation was identified.

In order to analyze the impact of the zone "5" construction on the liquid flow, CFD simulations were conducted. Figure 6 shows streamlines of the liquid flow through the bottom zone. Figure 6a shows the results obtained for the same geometry as in case of the experimental device, whereas Fig. 6b presents the case in which the outlet from the downcomer zone enters the bottom zone not on in its middle but at its wall. The last two figures show the results of CFD simulations obtained for the downcomer zone with changed shape. In Fig. 6c the downcomer zone of rounded shape (half of the torus with straight fragments attached at both ends) was analyzed. Figure 6d shows the streamlines in the bottom zone that consists of more straight elements (5 instead of 3). In all cases the bottom zone dimensions were selected in such a way that the external dimensions (width and height in Table 1) correspond to those of the tested apparatus (Fig. 6a).

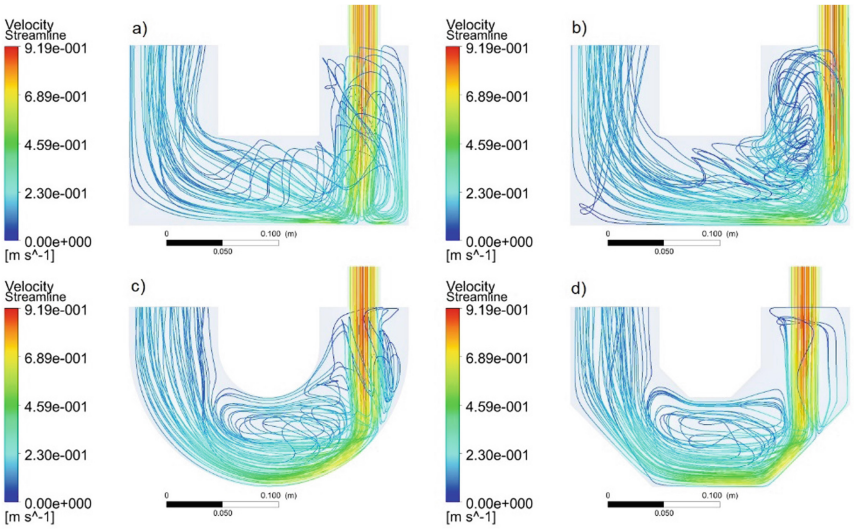

Fig. 6. Results of CFD simulations obtained for different shapes and configurations of the bottom zone: (a) 3-part, (b) 3-part with inlet on the right side, (c) rounded and (d) 5-part

It can be observed in Fig. 6a that, for the geometry corresponding to the experimental setup the results of numerical simulations are very similar to those obtained during the tracer experiments with a colored tracer (Fig. 5). The obtained streamlines indicate that the liquid stream flowing from the downcomer zone "3" to the bottom zone "5" collides with the opposite wall and splits into two parts. One of them flows towards the outlet from the zone and the other circulates below the outflow from the downcomer before heading towards the outlet from the bottom zone. Changing the inlet position (Fig. 6b) results in more intense mixing near the inlet to zone "5". The effects of local circulation are much more visible than in the previous case. The structure with the rounded shape of zone "5" (Fig. 6c) has a slightly lower mixing intensity near the inlet than in case of the geometry shown in Fig. 6a. However, it can be observed that near the bottom wall of the analyzed zone the liquid stream has a much higher velocity than the average velocity in this zone. In addition, in the central part of the bottom zone, near the upper wall, there is an additional region of local liquid circulation. Similar results were obtained in the last simulation (Fig. 6d), however, in this case the liquid circulation near the outlet from the downcomer zone was less intensive.

4 Conclusions

The experimental and numerical studies performed on the hybrid fluidized-bed apparatus allowed to analyze the hydrodynamics of the selected zones of the apparatus. The performed analysis of tracer (KCl) RTD demonstrated some discontinuities in the tracer concentration at the outlet of zone "4". The experiments conducted using colored tracer confirmed that this is due to the presence of vortices near the outlet from the degassing

zone to the downcomer zone. It was observed that in the bottom zone, near the outlet from the downcomer zone, there is a region responsible for intensive mixing. Moreover, CFD simulations confirmed that change in the bottom zone design could contribute to the reduction of turbulence near the inlet of zone "5", which could lead to reduction of hydraulic resistance. However, the design change may also lead to the formation of dead zones in the apparatus. The analysis performed showed, that identification of hydrodynamic phenomena is an important issue when designing the hybrid apparatus. The experiments conducted permitted to explain and to understand the hydrodynamics of a hybrid fluidized-bed apparatus.

References

Guo, Y.X., et al.: Hydrodynamic and mass transfer studies in a novel external-loop airlift reactor. Chem. Eng. J. **67**, 205–214 (1997)

Levenspiel, O.: Tracer Technology: Modeling the Flow of Fluids, vol. 96. Springer, Heidelberg (2011)

Merchuk, J.C.: Airlift bioreactors: review of recent advances. Can. J. Chem. Eng. **81**(3–4), 324–337 (2003)

Olivieri, G., et al.: A novel three-phase airlift reactor without circulation of solids. Can. J. Chem. Eng. **88**, 574–578 (2010)

Prończuk, M., Bizon, K.: Investigation of the liquid mixing characteristic of an external-loop hybrid fluidized-bed airlift reactor. Chem. Eng. Sci. **210**, 115231 (2019)

Prończuk, M., Grzywacz, R.: Wpływ geometrii hybrydowego reaktora airlift na wybrane parametry przepływu płynów. Przem. Chem. **95**, 2003–2007 (2016)

Prończuk, M., et al.: Experimental investigations of hydrodynamic characteristics of a hybrid fluidized bed airlift reactor with external liquid circulation. Chem. Eng. Res. Design. **126**, 188–198 (2017)

Prończuk, M., et al.: Doświadczalne wyznaczanie współczynników dyspersji wzdłużnej w hybrydowym aparacie fluidyzacyjnym airlift. Prace Naukowe IICh PAN 22 (2018)

Rujiruttanakul, Y., Pavasant, P.: Influence of configuration on the performance of external loop airlift contactors. Chem. Eng. Res. Design. **89**, 2254–2261 (2011)

Impact of Electrodes Design on Their Activity in the Oxidation of Organic Pollutants

Tomasz Rozmanowski(✉), Piotr Krawczyk, and Jakub Wolańczyk

Institute of Chemistry and Technical Electrochemistry,
Poznan University of Technology, Poznań, Poland
tomasz.rozmanowski@put.poznan.pl

Abstract. In the present work the influence of the design of exfoliated graphite based electrodes on their catalytic activity towards phenol and methanol electro-oxidation was examined. Exfoliated graphite (EG) and EG/Pd composite were used as electrodes for phenol and methanol oxidation. EG was obtained by thermal exfoliation of graphite intercalation compound with sulfuric acid and the EG/Pd composite was prepared by electrochemical deposition of palladium onto exfoliated graphite. Morphology of the obtained materials was characterized by scanning electron microscopy (SEM). Three types of electrode design, in the form of a tablet, with polyvinylidene fluoride binder (PVDF) and a powder type electrode placed in a polymeric pocket were examined. The processes of phenol and methanol oxidation were examined in alkaline electrolyte using cyclic voltammetry and potentiostatic methods. Electrochemical results revealed that electrode design has a crucial influence on its catalytic activity towards process of phenol and methanol electro-oxidation. According to results of cyclic voltammetry measurements, the highest activity exhibit powder type electrodes. Furthermore it is proved that electrode construction is strongly related with the chemical composition of material used for its preparation.

1 Introduction

The continuous development of industry leads to a dramatic increase of the generated wastes and pollutions becoming serious threat for natural environment. In literature one can find many works devoted to utilization of substances considered as dangerous and toxic. For this purpose chemical (Cordova Villegas 2016; Meunier 1997), photochemical (Cordova Villegas 2016; Ahmed 2010), electrochemical (Cordova Villegas 2016; Smychkova 2015) and biological (Cordova Villegas 2016) methods are used. Among them, electrochemical processes are especially interesting due to their many advantages such as high selectivity, better energetic efficiency (a higher ratio of mass product to the energy used), usually ambient temperature and pressure, environmentally friendly character and easy control of whole process by exact set up of current-voltage parameters (Ciszewski 2004). Additionally, electrochemical reactions are recognized mostly as heterogeneous processes which allows to separate the products of the reaction from the employed electrocatalyst (electrode material). Efficiency of the electrochemical processes depends on many factors such as type of electrode material (chemical composition), electrode design, cell construction and the conditions of the

© Springer Nature Switzerland AG 2020
M. Ochowiak et al. (Eds.): PAIC 2019, *Practical Aspects of Chemical Engineering*, pp. 355–364, 2020.
https://doi.org/10.1007/978-3-030-39867-5_37

process (current-voltage parameters), temperature and pressure. The design of electrode should be considered as one of the most important. Taking into account the shape and structure, electrodes might be classified as solid, porous, powder, fluid and gas-diffusion (Ciszewski 2004). High catalytic activity is usually displayed by the electrode materials consisting of metal catalyst deposited onto porous matrix providing high specific surface area. The latter role can be served by carbon cloth (Ciszewski 2004), fibers and nanofibers (Zaragoza-Martin 2007; Guo 2016), nanotubes (Jha 2008), exfoliated graphite (Krawczyk et al. 2016a), graphene (Xu 2008) and some polymer materials (Mayer 1997; Athawale 2006). Most of these materials exist in powder form which makes the formation of the electrodes more complicated compared to solid-bulk materials.

The purpose of this work was to study the influence of the electrodes design on their electrochemical activity towards phenol and methanol oxidation. Exfoliated graphite and EG/Pd based electrodes in form of a tablet, with PVDF as a binder and a powder type electrode placed in a polymeric pocket were investigated.

2 Experimental

Exfoliated graphite was prepared in two-step method. Within the first one graphite intercalation compound with sulfuric acid (H_2SO_4–GIC) was obtained using chemical method. Purified flaky graphite (99.98 wt% C, flakes 100 μm in diameter) was immersed in the solution mixture of sulfuric and nitric acids with molar ratio 3:1. As prepared H_2SO_4–GIC was rinsed with water and dried in air at ambient temperature. Afterwards its thermal exfoliation at the temperature of 800 °C for 4 min in air atmosphere was carried out.

In order to obtain EG/Pd composite the process of electrochemical deposition of palladium onto exfoliated graphite was performed. For this purpose acidic bath composed of 0.11 M $PdCl_2$ in 1 M HCl was used. Pd electrodeposition was realized for 4 h at current density of 0.1 mA g^{-1}. The obtained composite was rinsed with water and dried in air at ambient temperature.

Morphology of the exfoliated graphite and EG/Pd composite was observed by scanning electron microscopy (SEM) (Hitachi S-3400 N).

Both obtained materials, exfoliated graphite and EG/Pd composite were subsequently used to prepare three types of electrodes; in the form of a tablet, with PVDF binder and a powder type electrode placed in a polymeric pocket. Tablet electrode with 10 mm in diameter was prepared by compressing 90 mg of selected material for 2 min at pressure force of 8 tons. The second type of electrode was formed using 90 mg of chosen material mixed with 20 mg of PVDF and 2 ml of acetone. Such a mixture was placed around the graphite rod playing a role of current collector and dried at 50 °C to form solid electrode. The powder-type electrode composed of exfoliated graphite or EG/Pd composite loosely placed in a pocket made of porous polymer material, in which graphite rod playing a role of current collector was beforehand inserted. All types of designed electrodes are shown in Fig. 1.

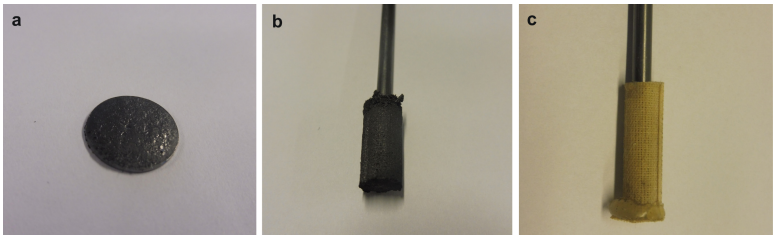

Fig. 1. Electrodes design: (a) tablet form, (b) with PVDF binder, (c) powder type in polymeric pocket

Cyclic voltammetry (CV) and potentiostatic method were used to study the electrochemical activity of all designed electrodes. Electrochemical measurements were performed at ambient temperature with potentiostat-galvanostat PGSTAT30 AutoLab (EcoChemie B.V.). All electrochemical measurements were carried out in a three-electrode cell in 6 M KOH solution with addition of 0.1 M phenol or 1 M methanol. Hg/HgO/6 M KOH (0.098 V vs. NHE) electrode and graphite rod served as reference and counter electrode, respectively.

CV measurements of phenol and methanol oxidation were performed with scan rate 0.1 and 10 mV s^{-1}, respectively. All measurements were started from the rest potential of the examined electrode (E_R) towards the most positive potentials. To verify the electrocatalytic activity of examined electrodes the potentiostatic measurements were conducted under chosen potential.

3 Results and Discussion

Information on morphology of the exfoliated graphite (EG) and EG/Pd composite are provided in Fig. 2. As one can see in Fig. 2 aexfoliated graphite has a accordion-like structure composed of splitted and wrinkled graphene layers thus exhibiting desirable properties such as developed surface area, high adsorption capability and low density (Chung 2002). The morphology of the EG/Pd composite is characterized by homogeneous distribution of palladium particles (bright spots) onto exfoliated graphite

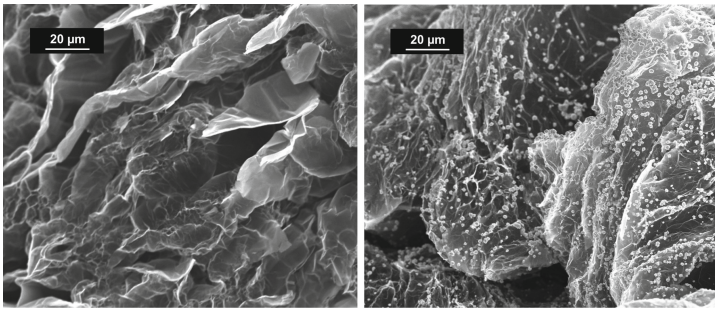

Fig. 2. SEM images of exfoliated graphite (a), EG/Pd composite (b).

matrix (Fig. 2b). The amount of the deposited palladium, calculated from the mass change of the EG electrode before and after the process of Pd electrodeposition was equal to 22 mg per 40 g of EG.

Cyclic voltammograms depicting the process of phenol oxidation at electrodes composed of exfoliated graphite with different design are shown in Figs. 3, 4 and 5. After starting the measurement in the anodic direction, at the potential of 0.35 V an increase in anodic currents lasting up to 0.6 V is observed. This effect illustrates the reaction of phenol electro-oxidation (Skowroński 2004). On continuing the anodic potential sweep further increase in current density related with the process of anodic evolution of oxygen take place (Krawczyk 2010). After the reversal of polarization any cathodic peaks have been recorded which suggests irreversible character of the conducted process. From the literature data, it is well known that electro-oxidation of phenol leads to the formation of insoluble oligomer films being an intermediate products of incomplete oxidation of phenol (Tahar 2009). The deposited film blocks the active surface area of the electrode material leading to the significant decrease in its activity. In contrast, on the presented voltammograms a slight increase in activity of all electrodes upon cycling is noted. The reason for a such behavior seems to be process of oxygen evolution occurring carried out after the reaction of phenol oxidation. Active oxygen reacts with the deposited oligomer increasing its porosity and, in consequence active surface area of the examined material. Additionally, surface of the electrodes undergoes modification of its chemical composition by building up the functionalities groups, mainly composed of C = O. This phenomena is especially pronounced in strong alkali media in which the process of oxygen evolution occurs immediately after the reaction of phenol electro-oxidation (Krawczyk 2012; Krawczyk et al. 2016a). From the comparison of voltammograms it can be noted that the highest activity in the reaction of phenol oxidation exhibits powder type electrode. The current density of phenol oxidation equals to 0.6 A g^{-1} and it is about ten times higher than the values recorded for other two types of electrodes (tablet and with PVDF binder). Such a difference in catalytic activity of the examined electrodes is likely related with the development of active surface area which is significantly higher in case of powder type electrode due to its composition of loosely packed exfoliated graphite flakes.

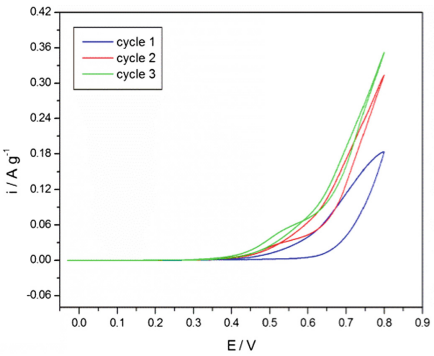

Fig. 3. Cyclic voltammograms recorded in 0.1 M phenol/6 M KOH solution for tablet electrode composed of exfoliated graphite. Scan rate of 0.1 mV s^{-1}, scan range: $E_R \leftrightarrow 0.8$ V.

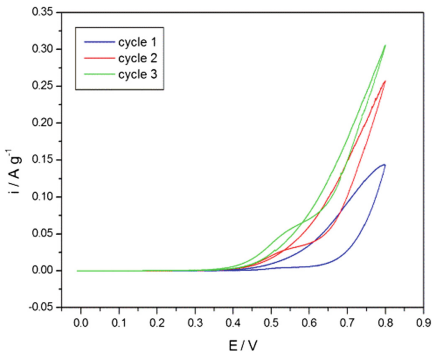

Fig. 4. Cyclic voltammograms recorded in 0.1 M phenol/6 M KOH solution for electrode composed of exfoliated graphite with PVDF binder. Scan rate of 0.1 mV s^{-1}, scan range: $E_R \leftrightarrow 0.8$ V.

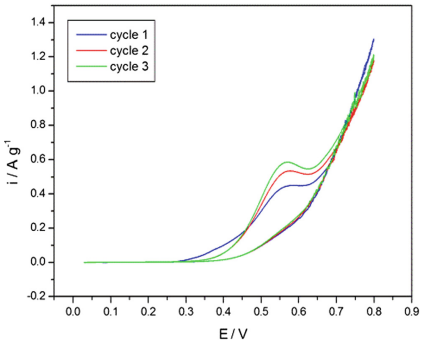

Fig. 5. Cyclic voltammograms recorded in 0.1 M phenol/6 M KOH solution for powder type electrode composed of exfoliated graphite. Scan rate of 0.1 mV s^{-1}, scan range: $E_R \leftrightarrow 0.8$ V.

Figure 6 presents potentiostatic curves of phenol oxidation recorded under constant potential of 0.53 V for all types of electrode designs. As can be seen, current density of phenol oxidation is much higher for powder type electrode than appropriate values noted for tablet electrode and electrode with PVDF binder. Anodic density charge generated through the 2 h reaction of phenol oxidation at powder type electrode reaches 1450.66 C g^{-1}. This value is significantly higher than those calculated for other investigated electrodes (4.14 C g^{-1} and 19.61 C g^{-1}). The most pronounced difference in recorded current densities is noted during the first half an hour of the examined process. After that the activity of powder type electrode stabilizes due to its partial deactivation by the formed oligomer film. The highest development of surface area of EG powder contributes to its highest susceptibility for deactivation.

Summarizing, potentiostatic experiments revealed that the powder type electrode displays significantly higher activity towards reaction of phenol electro-oxidation compared to the other types of electrodes.

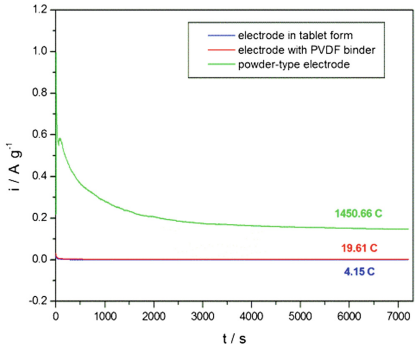

Fig. 6. Potentiostatic curves of phenol oxidation recorded under constant potential of 0.53 V.

Cyclic voltammograms depicting process of methanol oxidation at different electrode designs based on EG/Pd composite are shown in Figs. 7, 8 and 9. As can be seen during anodic polarization a sharp anodic peak is recorded for all examined electrodes. This effect is associated with the reaction of methanol electro-oxidation occurring onto palladium catalyst (Rozmanowski 2018; Chowdhury 2016). For all designed electrodes, the regarded peak gradually increase upon cycling thus allowing the conclusion that some kind of their activation takes place. One of the possible explanation of a such behavior is gradual improvement in wettability of EG/Pd composite. The highest activity towards the reaction of methanol oxidation exhibits a powder type electrode. High current density noted for this electrode is related with the easier access of methanol molecules to Pd catalyst caused by loosely packed EG/Pd deposit. The differences in the activity between the examined electrode designs are adequate to the values noted in the process of phenol oxidation. Additionally, after the reversal of polarization from anodic to cathodic, an anodic peak corresponding to the reactivation of electrode surface has been recorded (Rozmanowski 2018). Taking into account the mutual ratio of both anodic peaks recorded during positive and negative polarization, the best efficiency of the regeneration process is noted for electrode prepared with PVDF addition.

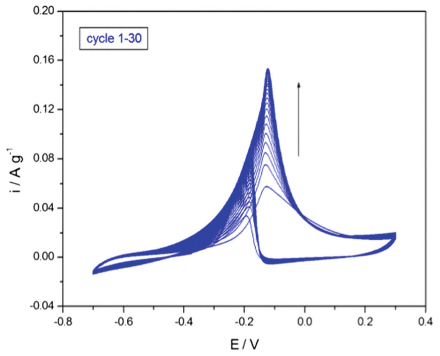

Fig. 7. Cyclic voltammograms recorded in 1 M methanol/6 M KOH solution for tablet electrode composed of EG/Pd composite. Scan rate of 10 mV s^{-1}, scan range: −0.7↔0.3 V.

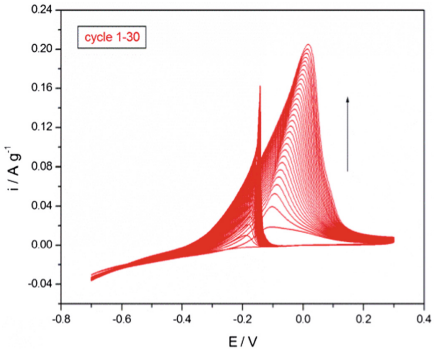

Fig. 8. Cyclic voltammograms recorded in 1 M methanol/6 M KOH solution for electrode composed of exfoliated graphite with PVDF binder. Scan rate of 10 mV s^{-1}, scan range: −0.7↔0.3 V.

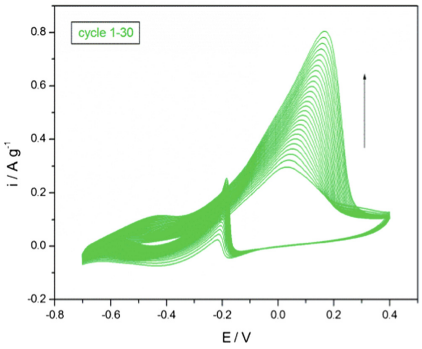

Fig. 9. Cyclic voltammograms recorded in 1 M methanol/6 M KOH solution for powder type electrode composed of exfoliated graphite. Scan rate of 10 mV s^{-1}, scan range: −0.7↔0.3 V.

In order to determine the durability and stability of the prepared EG/Pd electrodes a long-lasting CV measurements were performed in 1 M CH_3OH/6 M KOH. The dependence of current density of methanol oxidation peak on number of cycles performed is depicted in Fig. 10. Three different types of behavior can be distinguished. In case of tablet electrode, after initial increase (first 15 cycles) a steady state values of methanol oxidation current density is achieved. Significant increase in current density, especially between tenth and twentieth cycle has been noted for powder type electrode. Current density of methanol oxidation reaches maximum value in 80^{th} cycle, after that its lightly decreases. Completely different behavior is noted for electrode prepared with PVDF binder. Continuous increase of methanol oxidation current density can be observed throughout all 100 cycles. This effect can be related with the gradual increase in penetration ability of methanol molecules into inner regions of electrode material.

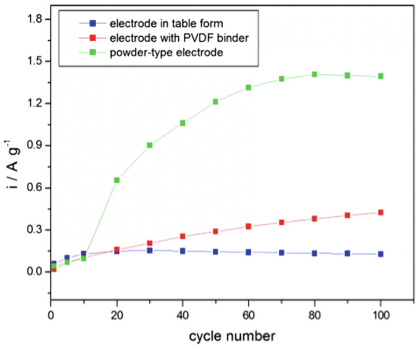

Fig. 10. Cyclic stability of electrodes composed of EG/Pd composite in 1 M methanol/6 M KOH solution.

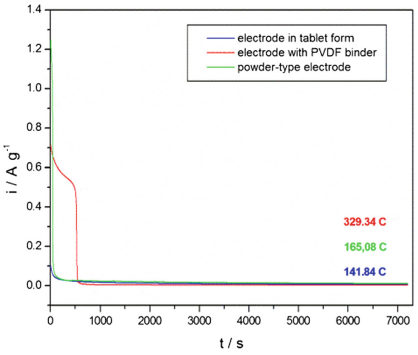

Fig. 11. Potentiostatic curves of methanol oxidation at electrodes composed of EG/Pd composite.

The course of two-hour potentiostatic oxidation of methanol onto all examined electrode designs are given in Fig. 11. The highest anodic density charge of methanol oxidation has been noted for electrode prepared with addition of PVDF binder (329.34 C g^{-1}). This value is about 2 times higher compared to those obtained for tablet and powder type electrodes (141.84 C g^{-1} and 16.08 C g^{-1}, respectively). The differences in the potentiostatic results can be assigned to the poisoning effect of palladium catalyst by adsorbed intermediate products of methanol oxidation, especially CO. A careful observation of potentiostatic curves allows to one can notice that during first dozens of seconds the methanol oxidation current density is significantly higher for powder type electrode (green curve in Fig. 11). Unfortunately, high activity of this electrode contributes to the faster poisoning of the contained Pd catalyst displayed by dramatic decrease in current density. On the other hand, the activity of electrode with PVDF addition (red curve), is about 2 times lower meaning that the deactivation of the palladium catalyst by generated CO species is much slower (drop of current density

occurs after 600 s). Therefore, electrode prepared with addition of PVDF exhibits higher total anodic charge density of methanol oxidation than powder type electrode.

4 Conclusions

Electrochemical measurements showed that the effectiveness of the mineralization/oxidation process of selected alcohols depends on the electrodes design. According to cyclic voltammetry results, the highest catalytic activity was recorded for powder type electrodes prepared in the form of a loose bed of graphite material placed in a polyamide pocket. Such a result can be explain in term of the easiest access of phenol and methanol molecules to the active sites of employed electrode material. The acquired results also proved that the impact of electrode design on demonstrated electrochemical activity is closely related to their chemical composition. Potentiostatic studies indicated that the greatest differences in electrochemical activity of the studied electrodes appear within the initial stages of the conducted processes. This fact is closely related with the gradual deactivation of electrode material by generated products of the reaction of alcohols oxidation.

Acknowledgments. This work was supported by National Science Centre of Poland research grant no. 2015/17/B/ST8/00371.

References

Ahmed, S., Rasul, M.G., Martens, W.N., Brown, R., Hashib, M.A.: Heterogeneous photocatalytic degradation of phenols in wastewater: a review on current status and developments. Desalination **26**, 3–18 (2010)

Athawale, A.A., Bhagwat, S.V., Katre, P.P.: Nanocomposite of Pd–polyaniline as a selective methanol sensor. Sen. Actuat B **114**, 263–267 (2006)

Chowdhury, S.R., Mukherjee, P., Bhattachrya, S.K.: Palladium and palladium-copper alloy nanoparticles as superior catalyst for electrochemical oxidation of methanol for fuel cell applications. Int. J. Hydrogen Energy **41**, 17072–17083 (2016)

Chung, D.D.L.: Review Graphite. J. Mater. Sci. **37**, 1475–1489 (2002)

Ciszewski, A.: Podstawy inżynierii elektrochemicznej. Wydawnictwo Politechniki Poznańskiej, Poznań (2004)

Cordova Villegas, L.G., Mashhadi, N., Chen, M., Mukherjee, D., Taylor, K.E., Biswas, N.: A short review of techniques for phenol removal from wastewater. Curr. Pollut. Rep. **2**, 157–167 (2016)

Guo, J., Sun, G., Wang, Q., Wang, G., Zhou, Z., Tang, S., Jiang, L., Zhou, B., Xin, Q.: Carbon nanofibers supported Pt–Ru electrocatalysts for direct methanol fuel cells. Carbon **44**, 152–157 (2016)

Jha, N., Reddy, A.L.M., Shaijumon, M.M., Rajalakshmi, N., Ramaprabhu, S.: Pt–Ru/multiwalled carbon nanotubes as electrocatalysts for direct methanol fuel cell. Int. J. Hydrogen Energy **33**, 427–433 (2008)

Krawczyk, P., Rozmanowski, T., Gurzęda, B., Osińska, M.: Process of phenol electrooxidation on the expanded graphite electrode accompanied by the in-situ anodic regeneration. J. Appl. Electrochem. **775**, 228–234 (2016a)

Krawczyk, P., Rozmanowski, T., Osińska, M.: Electrochemical sorption of hydrogen in exfoliated graphite/nickel/palladium composite. Int. J. Hydrogen Energy **41**, 20433–20438 (2016b)

Krawczyk, P., Skowroński, J.M.: Modification of expanded graphite resulting in enhancement of electrochemical activity in the process of phenol oxidation. J. Appl. Electrochem. **40**, 91–98 (2010)

Krawczyk, P., Skowroński, J.M.: Electrochemical reactivation of expanded graphite electrodes covered by oligomeric products of phenol electrooxidation. Electrochim. Acta **79**, 202–209 (2012)

Mayer, A.B.R., Mark, J.E.: Platinum nanocatalysts immobilized on latex supports. J. Polym Sci Pol Phys **35**, 1207–1216 (1997)

Meunier, B., Sorokin, A.: Oxidation of pollutants catalyzed by metallophthalocyanines. Acc. Chem. Res. **30**, 470–476 (1997)

Rozmanowski, T., Krawczyk, P.: Influence of chemical exfoliation process on the activity of $NiCl_2$-$FeCl_3$-$PdCl_2$-graphite intercalation compound towards methanol electrooxidation. Appl. Catal. B-Environ. **224**, 53–59 (2018)

Shmychkova, O., Luk'yanenko, T., Yakubenko, A., Amadelli, R., Velichenko, A.: Electrooxidation of some phenolic compounds at Bi-doped PbO_2. Appl. Catal. B: Environ. **162**, 346–351 (2015)

Skowroński, J.M., Krawczyk, P.: Electrooxidation of phenol at exfoliated graphite electrode in alkaline solution. J. Solid State Eletrochem. **8**, 442–447 (2004)

Skowroński, J.M., Rozmanowski, T., Osińska, M.: Reuse of nickel recovered from spent Ni–Cd batteries for the preparation of C/Ni and C/Ni/Pd layered electrodes for energy sources. Process. Saf. Environ. **93**, 139–146 (2014)

Tahar, N.B., Savall, A.: Electropolymerization of phenol on a vitreous carbon electrode In alkaline aqueous solution at different temperatures. Electrochim. Acta **55**, 465–469 (2009)

Xu, Ch., Wang, X., Zhu, J.: Graphene − metal particle nanocomposites. J. Phys. Chem. C **112** (50), 19841–19845 (2008)

Zaragoza-Martín, F., Sopeña-Escario, D., Morallón, E., Salinas-Martínez de Lecea, C.: Pt/carbon nanofibers electrocatalysts for fuel cells: effect of the support oxidizing treatment. J. Power Sourc. **171**, 302–309 (2007)

Extensional Flow of Wormlike Micellar Solutions

Sylwia Różańska(✉), Jacek Różański, and Patrycja Wagner

Institute of Chemical Technology and Engineering,
Poznań University of Technology, Poznań, Poland
sylwia.rozanska@put.poznan.pl

Abstract. This chapter presents typical measurement results obtained for semidilute wormlike micellar solutions (WLM) using capillary breakup extensional rheometry. Experimental studies were carried out for aqueous solutions of a mixture of cocamidopropyl betaine and sodium dodecylbenzenesulfonate. Just like in shear flow, there is a high degree of qualitative similarity between extensional viscosity curves generated for semidilute solutions of polymers and WLM. The differences resulting from the different structure of polymer chains and WLM can be observed primarily at late times of thinning. The results presented in the literature also suggest that extensional rheology can be used to identify branching in wormlike micelle solutions.

1 Introduction

A distinct property of surfactants, inseparably connected with their rheological characteristics, is their ability to form micelles in solutions. Depending on the structure of the surfactant molecule and surfactant concentration, as well as the presence of substances enhancing the process of micelle formation in the solution (inorganic and organic salts), the type of solvent, and pH and temperature of the solution, a range of micelle types may be formed including spherical, cylindrical, vesicle, lamellar and reverse. From the viewpoint of the ability of surfactants to modify the rheological properties of products, the most interesting solutions are those in which very long cylindrical associates called wormlike micelles (WLM) are formed. WLM have been used in the formation of the rheology home and personal care products (e.g., cosmetics and detergents) (Zięba et al. 2019) and are becoming increasingly important in, e.g., enhanced oil recovery (Ezrahi et al. 2006), agrochemical spraying (Xue et al. 2008), and drag reduction agents in district heating and cooling systems (Różański 2011). In all cases mentioned above, both rheological properties in extensional and shear flow are important.

As with polymer solutions, WLM solutions can be divided into dilute, semidilute and concentrated. In dilute solutions, there are no interactions between wormlike micelles. In contrast, in semidilute and concentrated solutions micelles become entangled and form a spatial micellar network. Another possibility is the formation of branched wormlike micelles (Lerouge and Berret 2010).

© Springer Nature Switzerland AG 2020
M. Ochowiak et al. (Eds.): PAIC 2019, *Practical Aspects of Chemical Engineering*, pp. 365–373, 2020.
https://doi.org/10.1007/978-3-030-39867-5_38

There are many similarities between the properties of entangled wormlike micellar solutions and entangled polymer solutions. Between polymer mers covalent bonds are present, while between surfactant molecules occur physical interactions. For these reasons, micelles can undergo break and reform under shear.

According to the model proposed by Cates (1987), the total relaxation time of WLM solutions will depend on reptation time τ_r and breaking time τ_b. Breaking time is the average time for such a warm to break into two pieces (Cates 1987).

Extensional flow is much less known than the shear flow of WLM solutions. The measurement results published in the literature were obtained by various techniques: opposed jet experiments, four-roll mill experiments, entrance flow, two-dimensional squeeze flow, flow through porous media, filament stretching and capillary breakup extensional rheometry. Among the enumerated techniques, only the application of filament stretching extensional rheometer (FiSER) and capillary breakup extensional rheometer (CaBER) has the capacity to produce a purely extensional flow field. What is more, measurement results obtained using different techniques vary significantly both in terms of quantity and quality. The aim of this paper is to present the typical results of measurements performed for semidilute wormlike micellar solutions using capillary breakup extensional rheometry.

2 Extensional Flow of Low Viscosity Liquids

Ensuring equilibrium conditions during extensional flows presents a number of difficulties, and in practice it can be achieved only approximately for high viscosity liquids (above 1,000 Pa·s) (Ferguson et al. 1997). High viscosity fluids are primarily molten polymers, whereas most polymer and surfactant solutions are low viscosity liquids (below 100 Pa·s). With respect to low viscosity liquids, it is only possible to determine instantaneous values of tensile stresses and calculate so-called transient extensional viscosity on their basis.

However, the most challenging task is to determine the rheological properties of fluids in extensional flow with a viscosity value less than 1 Pa·s. In this case, mainly two experiments are used: stagnation flow between opposed nozzles and capillary breakup extensional experiments. The conducted by Dontula et al. (1997) analysis of the advantages and disadvantages opposed nozzle devices results, that this devices should be considered as useful rather than indexers rheometers. A purely extensional flow of a low viscosity liquid can be achieved with the capillary thinning of a liquid filament (within a so-called capillary break-up extensional rheometer (CaBER)). This solution was proposed by Bazilevsky et al. (1997). The CaBER technique can be applied to liquids covering a wide range of viscosities, from about 0,05 Pa·s up to 10 Pa·s (McKinley 2005; Sachsenheimer et al. 2014). The principle of measurement using a CaBER rheometer is shown in Fig. 1. A sample is placed between two plates of the same diameter. At time $t = 0$, one or both plates are put into rapid motion with an exponential profile, at a constant extension rate $\dot{\epsilon}_0$ from the initial length of L_0 to the final length of L_f.

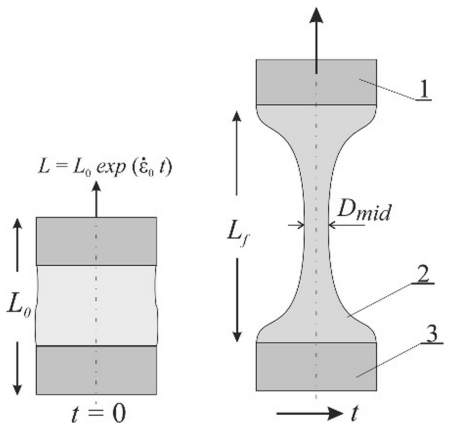

Fig. 1. Schematic of the Capillary Breakup Extensional: 1 – movable plate, 2 – stretching sample, 3 – stationary plate

Next, the motion of the plates is halted, sample extension is stopped, and the measured parameter is the change in the diameter of the formed liquid bridge (filament) D_{mid} at half of the distance between the plates as a function of time. The measurement ends following the breakup of the liquid filament.

Measurement results obtained with the method of capillary filament breakup are usually presented as a relationship between the midpoint diameter of the filament D_{mid} and the initial diameter of the filament D_0 as a function of its thinning time (D_{mid} – the midpoint diameter of the fiber, D_0 – the initial diameter of the fiber). Figure 2 shows the relationship $D_{mid}/D_0 = f(t)$ for Newtonian fluids, power-law fluids and elastic fluids. Transient extensional viscosity can be calculated from the equation proposed by Anna and McKinley (2001).

$$\eta_E^+(\dot{\varepsilon}, t) = \frac{\sigma_E(t)}{\dot{\varepsilon}(t)} = \frac{2 \cdot \Gamma}{D_{mid}(t) \cdot \dot{\varepsilon}(t)} = -\frac{\Gamma}{dD_{mid}/dt} \tag{1}$$

where Γ – surface tension.

The determination of apparent extensional viscosity is possible if the effect of inertia and gravity on the filament thinning process is negligible. The effect of inertia on capillary thinning can be determined based on values of the Ohnesorge number and the Deborah number.

$$Oh = \frac{\eta}{\sqrt{\rho \cdot \Gamma \cdot (D_{mid}/2)}} \tag{2}$$

$$De = \frac{\lambda}{\sqrt{\frac{\rho \cdot (D_{mid}/2)^3}{\Gamma}}} \tag{3}$$

where ρ is the density of fluids. Fluid inertia does not affect filament thinning when values of the Ohnesorge number and the Deborah number are greater than 1 (Clasen et al. 2012; Vadillo et al. 2012).

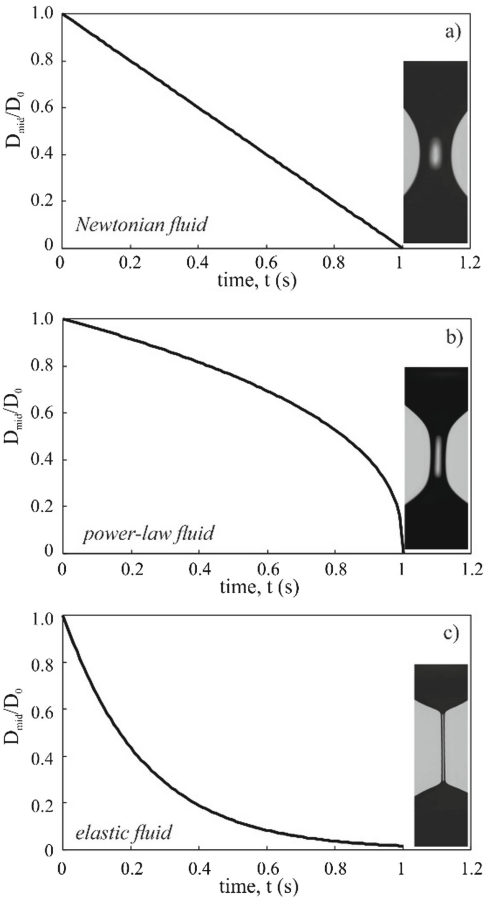

Fig. 2. Examples of the relationship between dimensionless fiber diameter and thinning time

Gravity has a significant impact on fluid deformation, especially when thinning affects a sample of considerable diameter. If a measurement is carried out correctly, there should be symmetry of the sample around its axis and the plane passing through the central part of the filament. Gravitational forces cause an additional axial flow along the fluid filament from a quasi-tank found at the top plate, which leads to delayed filament thinning. The values of extensional viscosity calculated on the basis of such measurement results will rise apparently along with increasing thinning time (Anna and McKinley 2001).

The impact of gravitational forces on filament thinning can be determined based on the Bond number:

$$Bo = \frac{g \cdot \rho \cdot D_{mid}^2}{4 \cdot \Gamma} \tag{4}$$

where g is the gravitational constant. The strong effect of gravity is manifested in the initial period of capillary thinning, when the diameter of the filament is large, and it is negligibly small when the values of the number Bo < 0.2.

3 Materials and Methods

Zwitterionic cocamidopropyl betaine (CAPB) was purchased from PCC Exol (Poland), commercial name is Rokamina K30, and contained 29,8% of active matter and 3,9% of NaCl. Anionic surfactant sodium dodecylbenzenesulfonate (SDBS) was purchased from Aldrich. Its average molecular weight was 348.48 g/mol.

Rheological measurements in the extensional flow were carried out using a CaBER 1 rheometer (Thermo Fisher Scientific, Germany) while in shear flow using a Physica MCR501 rheometer (Anton Paar). The capillary thinning fluid was generated by sudden shifts of two cylindrical plates with diameters of 4 mm to a distance of h = 5.08 mm (initial gap 2 mm). A high-speed camera was used to record the course of capillary thinning bridge, with a temporal resolution down to 0.33 ms and a spatial resolution of 1.9 μm/pixel.

Frequency sweep measurements were performed in the linear viscoelastic regime of the samples, as determined previously by the dynamic strain sweep measurements. All rheological tests were performed at a stabilized temperature of 20 ± 0.1 °C.

4 Capillary Breakup Extensional Rheometry of WLM Solutions

Figure 3 shows the results of CaBER measurements performed for CAPB/SDBS solutions in the form of the relationships $\eta_E = f(\varepsilon)$ and $D_{mid}/D_0 = f(t)$. Four distinct filament thinning regimes can be distinguished. Regimes I and II of filament thinning are controlled by a viscocapillary balance.

If the values of the extension rate $\dot{\varepsilon}$ are sufficiently small, the Newtonian thinning regime (regime I) occurs, in which mid-filament diameter decreases linearly in time according to the equation (Papageorgiou 1995; Haward and McKinley 2012).

$$D_{mid}(t) = 0.1418 \frac{\Gamma}{\eta_0}(t_c - t) \tag{5}$$

where η_0 is the zero shear viscosity, t_c is the critical time to breakup. At higher values of the extension rate $\dot{\varepsilon}$, disentanglement and orientation of the WLM occur (regime II). In this regime, filament thinning is still controlled by a viscocapillary balance (Doshi et al. 2003).

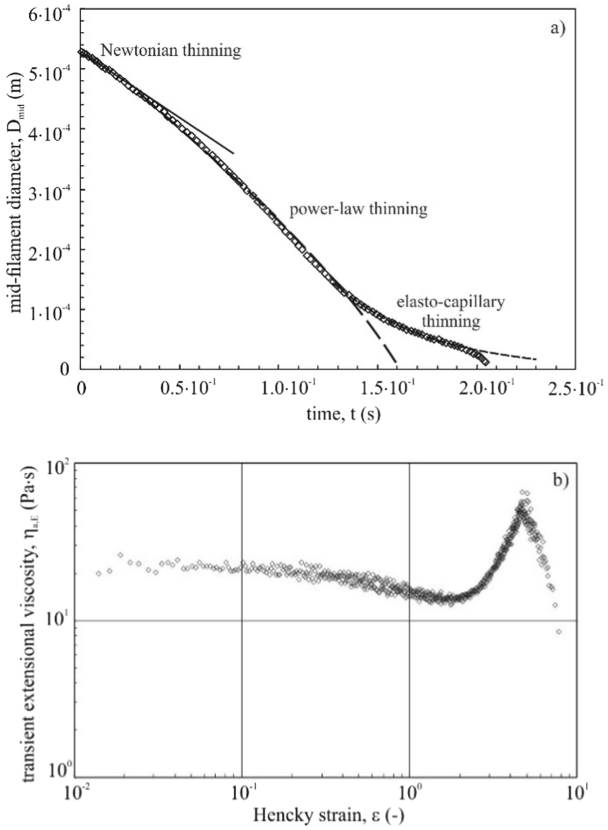

Fig. 3. Results of CaBER measurements performed for CAPB/SDBS solutions in the form of the relationships $D_{mid} = f(t)$ (a) and $\eta_{a,E} = f(\varepsilon)$ (b)

At high extension rate viscous stresses are assumed to be negligible, and elastic and capillary contributions to the total force balance each other (regime IV). Regarding the elastocapillary regime, Entov and Hinch (1997) showed that for an Oldroyd-B fluid the diameter decreased exponentially with time according to the equation:

$$D_{mid}(t) = D_0 \left(\frac{GD_0}{4\Gamma} \right)^{1/3} e^{-\frac{t}{3\lambda_E}} \tag{6}$$

where G is the elastic modulus of the material, D_0 is the initial diameter and λ_E is the extensional relaxation time. From the equation in (6) it follows that elastocapillary thinning occurs at a constant value of the strain rate:

$$\dot{\varepsilon} = \frac{2}{3 \cdot \lambda_E} \tag{7}$$

or at the value of the Weissenberg number equal to 2/3:

$$Wi = \lambda_E \dot{\varepsilon} \tag{8}$$

The data presented in Fig. 4 show that elastocapillary thinning of WLM solutions is consistent with the Oldroyd-B fluid model.

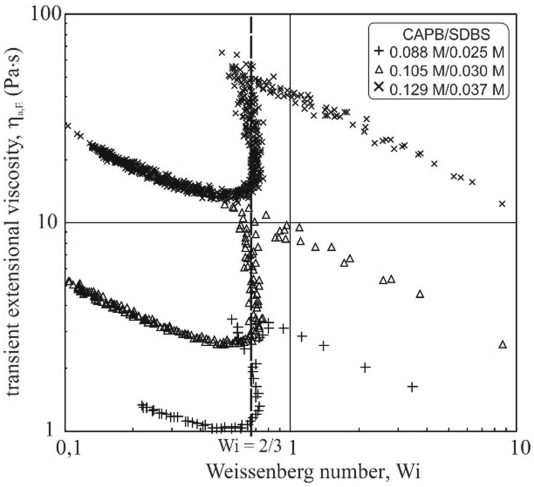

Fig. 4. Dependence of apparent extensional viscosity on the Weissenberg number for aqueous solutions of the CAPB/SDBS mixtures

At late times, regime IV also occurs, with a notable rapid decrease in extensional viscosity. In regimes I to III, the shape of apparent extensional viscosity curve generated for semidilute WLM solutions is similar to the curves reported in the literature for semidilute polymer solutions. However, differences are noted in regime IV. As demonstrated by Entov and Hinch (1997) and Anna and McKinley (2001), in polymer solutions the diameter approaches linear behaviour at late times, which means that apparent extensional viscosity has a constant value ($\eta_{E,\infty}$). This is due to the fully stretched polymer chain – the elastic stresses can no longer grow to resist the increasing capillary pressure.

The causes of the rapid decrease in extensional viscosity in regime IV have not yet been fully explained (Rothstein 2003). Covalent bonds are known to exist between polymer mers, while the formation of wormlike micelles is a result of relatively weak physical interactions between surfactant molecules. Thus, at high strain rates $\dot{\varepsilon}$ tensile stresses may lead to the breakup of micellar associates, which may result in the observed decrease in apparent extensional viscosity. Another important point to

consider is that wormlike micelles constantly disintegrate and reassemble in the solution. This phenomenon may also contribute to a rapid decrease in extensional viscosity and filament breakup.

Based on measurement results obtained in elastocapillary regime and the equation given in (6), it is possible to determine extensional relaxation time λ_E. Both in polymer solutions and WLM solutions, extensional relaxation time is comparable to terminal relaxation time:

$$\lambda_s = \lim_{\omega \to 0} \frac{G'}{G'' \omega} \tag{9}$$

Studies by Sachsenheimer et al. (2012) show that in the case of wormlike cationic surfactant solutions the value of the ratio λ_E/λ_s also depends on the relationship between breaking time τ_b and reptation time τ_r, with three distinguishable cases:

1. $\lambda_E/\lambda_s \approx 1$ if $\tau_b << \tau_r$
2. $\lambda_E/\lambda_s << 1$ if $\tau_b >> \tau_r$ (as in the case of entangled polymer solutions)
3. $\lambda_E/\lambda_s >> 1$ if flow induced structure buildup

For CAPB/SDBS solutions $\lambda_E/\lambda_s << 1$ (for example $\lambda_E/\lambda_s = 0.0157$ for CAPB/SDBS = 0.129/0.037), which shows that the relaxation of stresses in shear flow is dominated by reptation.

There are also literature reports suggesting that extensional rheology can be used for differentiating between entangled linear and branched wormlike micellar solutions. Chellamuthu and Rothstein (2008) showed that an increase in micelle branching induced a rapid decrease of the maximum values of the Trouton ratio and the ratio of extensional relaxation time to the Maxwell relaxation time measured in shear. These changes are probably due to new stress relief mechanisms available to branched micelles, which appear to be extremely efficient in extensional flows.

5 Conclusions

The paper discusses typical measurement results obtained for semidilute wormlike micellar solutions using capillary breakup rheometry. Just like in shear flow, there is a high degree of qualitative similarity between extensional viscosity curves generated for semidilute solutions of polymers and WLM. However, there are also differences, including a rapid drop in extensional viscosity in regime IV, and $\lambda_E/\lambda_s \approx 1$ if breaking time is considerable shorter than reptation time ($\tau_b << \tau_r$). These discrepancies stem from different structures of the polymer chains and WLM (presence of covalent bonds between polymer mers and weak physical interactions between surfactant molecules). The results presented in the literature also suggest that extensional rheology can be used to identify branching in wormlike micelle solutions.

Acknowledgments. This work was supported by PUT research grant no. 0912/SBAD/2002.

References

Anna, S.L., McKinley, G.H.: Elasto-capillary thinning and breakup of model elastic liquids. J. Rheol. **45**, 115–138 (2001)

Bazilevskii, A.V., Entov, V.M., Lernee, M.M., Rozhkov, A.N.: Failure of polymer solution filaments. Polym. Sci. A **39**, 316–324 (1997)

Cates, M.E.: Reptation of living polymers: dynamics of entangled polymers in the presence of reversible chain-scission reactions. Macromolecules **20**, 2289–2296 (1987)

Chellamuthu, M., Rothstein, J.P.: Distinguishing between linear and branched wormlike micelle solutions using extensional rheology measurements. J. Rheol. **52**(3), 865–884 (2008)

Clasen, C., Phillips, P.M., Palangetic, L., Vermant, J.: Dispensing of rheologically complex fluids: the map of misery. AIChE J. **58**, 3242–3255 (2012)

Dontula, P., Pasquali, M., Scriven, L.E., et al.: Can extensional viscosity be measured with opposed-nozzle devices? Rheol. Acta **36**, 429–448 (1997)

Doshi, P., Suryo, R., Yildirim, O.E., et al.: Scaling in pinch-off of generalized Newtonian fluids. J. Non-Newton. Fluid **113**(1), 1–27 (2003)

Entov, V.M., Hinch, E.J.: Effect of a spectrum of relaxation times on the capillary thinning of a filament of elastic liquid. J Non-Newton Fluid **72**, 31–53 (1997)

Ezrahi, S., Tuval, E., Aserin, A.: Properties, Main Applications and Perspectives of Worm Micelles. Adv. Colloid Interface Sci. **128–130**, 77–102 (2006)

Ferguson, J., Hudson, N.E., Odriozola, M.A.: The interpretation of transient extensional viscosity data. J Non-Newton. Fluid **68**, 241–257 (1997)

Haward, S.J., McKinley, G.H.: Stagnation point flow of wormlike micellar solutions in a microfluidic cross-slot device: effects of surfactant concentration and ionic environment. Phys. Rev. E **85**, 031502–031514 (2012)

Lerouge, S., Berret, J.F.: Shear-induced transitions and instabilities in surfactant wormlike micelles. Adv. Polym. Sci. **230**, 1–71 (2010)

McKinley, G.H.: Visco-Elasto-Capillary Thinning and Break-Up of Complex Fluids, British Soc. Rheol. HML Report Number 05-P-04, pp. 1–49 (2005)

Papageorgiou, D.T.: On the breakup of viscous liquids threads. Phys. Fluids **7**, 1529–1544 (1995)

Rothstein, J.P.: Transient extensional rheology of wormlike micelle solutions. J. Rheol. **47**, 1227–1247 (2003)

Rozanski, J.: Flow of drag-reducing surfactant solutions in rough pipes. J. Non-Newton. Fluid **1**, 279–288 (2011)

Sachsenheimer, D., Hochstein, B., Buggisch, H., Willenbacher, N.: Determination of axial forces during the capillary breakup of liquid filaments - the tilted CaBER method. Rheol. Acta **51**, 909–923 (2012)

Sachsenheimer, D., Oelschlaeger, C., Müller, S., et al.: Elongational deformation of wormlike micellar solutions. J. Rheol. **58**, 2017–2042 (2014)

Xue, Z., Corvalan, C.M., Dravid, V., et al.: Breakup of shear-thinning liquid jets with surfactants. Chem. Eng. Sci. **63**, 1842–1849 (2008)

Vadillo, D.C., Mathues, W., Clasen, Ch.: Microsecond relaxation processes in shear and extensional flows of weakly elastic polymer solutions. Rheol. Acta **51**, 755–769 (2012)

Zieba, M., Wieczorek, D., Klimaszewska, E., et al.: Application of new synthesized zwitterionic surfactants as hair shampoo components. J. Dispersion Sci. Technol. **40**, 1189–1196 (2019)

Heat Transfer Enhancement During the Flow of Drag-Reducing Surfactant Solutions

Jacek Różański(✉) and Sylwia Różańska

Institute of Chemical Technology and Engineering,
Poznan University of Technology, Poznań, Poland
jacek.rozanski@put.poznan.pl

Abstract. This chapter presents a review of methods for enhancing the heat transfer during flow of the drag reducing surfactant solutions proposed in the literature. For that type of fluids, the main goal is to increase the heat transfer coefficient to the level obtained during the flow of pure water. Based on the performed analysis of different methods for enhancing the heat transfer, it is clear that none of them can be treated as the universal one. The values of the heat transfer coefficient depend not only on the temperature and concentration of the solution but also on the type of surfactant used. In addition, the experimental results on heat transfer enhancement are presented only in graphical form. This means that the results published in the literature may be applied in practice only in the case when a flow system used is the same as a solution of surfactant in modelling studies and temperature conditions are similar.

1 Introduction

The flow of some surfactant solutions is accompanied by a marked decrease in turbulent pressure losses. The phenomenon of drag reduction occurs only when long micelles (referred to as wormlike micelles) are formed in the solution. An addition of surfactants of this type to water flowing in central heating and cooling systems may significantly reduce the consumption of electricity supplied to pumps (Broniarz-Press et al. 2007). Unfortunately, a decrease in pressure losses is associated with a significant decline of the heat transfer coefficient. For these reasons, it became necessary to develop methods for intensifying heat transfer during the flow of surfactant solutions (Matthys 1991; Gasljevic and Matthys 1997; Aguilar et al. 1999; Gasljevic et al. 2000; Aguilar et al. 2001; Aly et al. 2006; Sears and Yang 2006; Hadri et al. 2011; Wang et al. 2011; Różański 2012). The primary goal in fluids of this type is to increase the heat transfer coefficient to the level characterising the flow of pure water. The extent of

© Springer Nature Switzerland AG 2020
M. Ochowiak et al. (Eds.): PAIC 2019, *Practical Aspects of Chemical Engineering*, pp. 374–382, 2020.
https://doi.org/10.1007/978-3-030-39867-5_39

drag reduction and heat transfer reduction are determined by means of suitably defined quantitative parameters (Gasljevic and Matthys 1999):

$$DR = \frac{\lambda_n - \lambda_s}{\lambda_n} \cdot 100 \tag{1}$$

$$HTR = \frac{Nu_n - Nu_s}{Nu_n} \cdot 100 \tag{2}$$

In the relations above the λ_n and Nu_n describe the values of the friction factor and the Nusselt number for the turbulent flow of Newtonian fluids, and the λ_s and Nu_s are the values characteristic for the flow of surfactant solution, at the same flow rate.

Methods for improving heat transfer during the flow of drag-reducing surfactant solutions can be divided into two main groups (Fig. 1). One group consists of methods in which the micellar microstructure is destroyed upstream of the heat exchanger (Li et al. 2001; Qi et al. 2003, b; Wei et al. 2009; Shi et al. 2011b; Wang et al. 2012; Shi et al. 2013). If the recovery of the micellar microstructure takes a sufficiently long time, during the flow of a surfactant solution through the heat exchanger the values of the heat transfer coefficient are comparable to the values recorded during the flow of pure water. The other group includes methods based on modifications of the heat exchanger design (Qi et al. 2001; Sato et al. 2003; Inaba et al. 2005; Shi et al. 2011; Zhou et al. 2006).

Improvements in heat transfer can be achieved either by destroying the micellar microstructure or changing flow patterns associated with heat transportation from the heat transfer surface. In recent years, attempts have also been made to use nanoparticles to increase the heat transfer coefficient during the flow of surfactant solutions (Liu and Liao 2010; Yang et al. 2012; Yang et al. 2013). This paper provides an overview of heat transfer enhancement methods which can be employed during the flow of drag-reducing fluids.

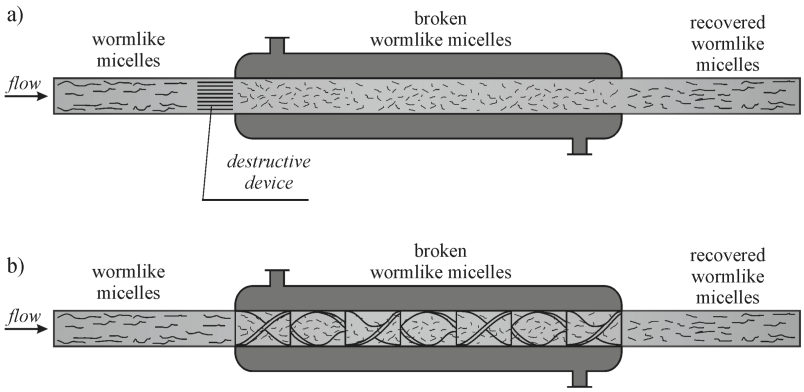

Fig. 1. Idea of improving heat transfer during the flow of drag-reducing fluids through the application of destructive devices (a), and modification of heat exchanger design (b)

2 Destructive Devices

Several methods have been proposed in the literature for destroying the micellar microstructure through the placement of:

- a centrifugal pump,
- small-diameter tubes or orifice,
- static mixers,
- ultrasonic generator,
- UV lamp.
- upstream of the heat exchanger.

The first two methods listed above have no practical relevance. It is unlikely that a pump can be positioned upstream of the heat exchanger, while placing a small-diameter tube is associated with a great increase in drag.

Another method employed for the destruction of the micellar microstructure involves placing plugs made of small-opening wire mesh upstream of the heat exchanger (Fig. 2c). Such plugs, made of wire mesh with the side lengths of mesh openings equal to 0.125 mm and 0.1 mm, were used by Gasljevic and Matthys (1997) to enhance heat transfer during the flow of Ethoquad T13/NaSal solution. Relatively satisfactory results were obtained for the heat transfer coefficient at the solution flow rates of 5 m/s to 9 m/s, but the pressure losses were very high, reaching several bars.

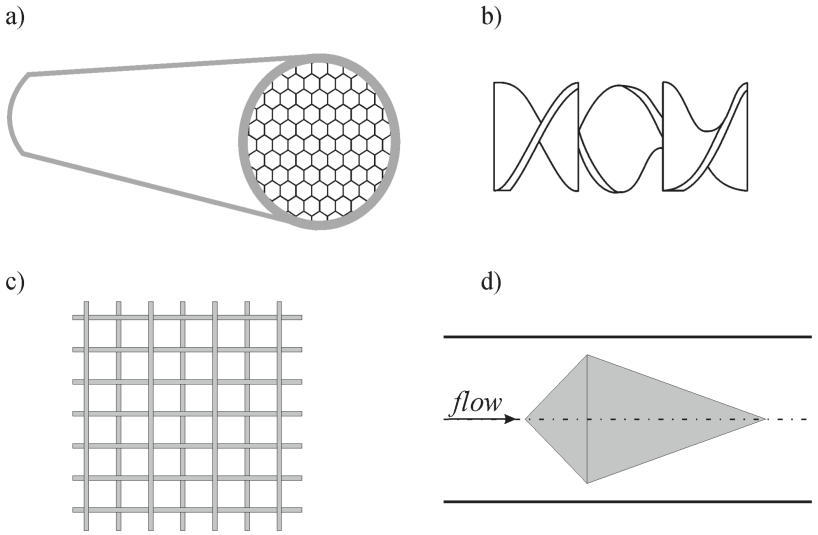

Fig. 2. Destructive devices: honeycombs (a) static mixers (b) wire meshes (c) and special construction of block (d)

Studies on the application of wire mesh with openings of different diameters during the flow of CTAC/NaSal solutions in a flat channel were carried out by Li et al. (2001).

The values of the heat transfer coefficients reported by the authors were comparable to those obtained during the flow of pure water for the CTAC concentration of 30 ppm at Reynolds numbers similar to the critical Reynolds number Re_c (where Re_c is the first critical Reynolds number; above it there is a rapid decline of the drag reduction phenomenon). At higher CTAC concentrations, the use of mesh failed to produce an increase in heat transfer coefficient.

Qi et al. (2003) analysed the possibility of using helical static mixers and honeycombs as destructive devices for the micellar microstructure (Fig. 2a, b). The authors conducted their studies with solutions of two different surfactants marketed under the trade names Ethoquad T13-50/NaSal and SPE98330. Honeycombs did not increase the value of the heat transfer coefficient in the solutions of both surfactants. Helical static mixers were shown to be far more effective in this application. Depending on the length and the number of segments used, and the temperature of the solution, the value of the HTR parameter for Ethoquad T13-50/NaSal was 20% to 40% (for comparison, during the flow of the solution with an intact microstructure the parameter reached 70%). Better results were obtained during the flow of SPE98330 solution, where the value of HTR ranged between 0% and 20%. The results discussed above were achieved at pressure drops induced by static mixers, ranging from $0.18 \cdot 10^5$ Pa to approximately $0.35 \cdot 10^5$ Pa.

Wei et al. (2009) proposed using a specially designed insert, which the authors named a "block", for the destruction of the micellar microstructure (Fig. 2d). Experimental studies were conducted for the amphoteric surfactant oleyl trimethylaminimide dissolved in an aqueous solution of ethylene glycol (20%) in the concentration range from 0.005% to 0.1%. The block device caused a significant increase in the value of the heat transfer coefficient only in the immediate downstream area ($x/H = 1.9$). Further downstream of the location of the device, the recorded values of the heat transfer coefficient were the same as during surfactant flow through an empty channel.

Another interesting method proposed by Qi et al. (2003b) for the destruction of the micellar microstructure was based on the application of ultrasounds. In their experiments, the authors used three different surfactant solutions: Ethoquad T13-50/NaSal, SPE98330/HCHO/Trilon A and Arquad S-50/NaSal. The first two of the systems used were characterised by viscoelastic properties, while the third did not exhibit such characteristics. Measurements of the heat transfer coefficient performed on the laboratory scale showed that the use of ultrasounds caused an increase in the heat transfer coefficient only in viscoelastic surfactant solutions.

If photorheological fluids (PR) are used as additives inducing the phenomenon of drag reduction, the destruction of the micellar microstructure can be achieved by exposing the solution to radiation at an appropriate wavelength (Ketner et al. 2007; Kumar and Raghavan 2009; Lee et al. 2011; Shi et al. 2011; Wang et al. 2012). An example of such a system is cetyltrimethylammonium bromide (CTAB) with an addition of sodium salt of trans-O-methyl-o-coumaric acid (trans-OMCA). Electron microscope images demonstrate the formation of long wormlike micelles in solutions of the CTAB/trans-OMCA mixture. Under the influence of UV radiation, the trans-OMCA form is gradually converted to the cis-OMCA form. In the CTAB/cis-OMCA mixture, short cylindrical micelles are formed, which is manifested by the disappearance of viscoelastic properties of the solution, and a decline in its viscosity.

The phenomenon was used by Shi et al. (2011b) to improve heat transfer during the flow of Ethoquad O/12PG/trans-OMCA solution. During the turbulent flow of this solution, a significant decrease was observed both in pressure losses and the heat transfer coefficient. Under the influence of UV radiation, trans-OMCA is converted to cis-OMCA, which leads to the breakdown of the micellar microstructure, thus triggering an increase in drag and the heat transfer coefficient (DR ≈ 70%, HTR ≈ 80%). However, this method has one essential disadvantage. The authors of the paper (Shi et al. 2011b) failed to propose a method leading to the conversion of the cis-OMCA form into trans-OMCA, and the recovery of the micellar microstructure.

Shi et al. (2013) in their study replaced OMCA with sodium salt of 4-phenylazo benzoic acid (ACA). Trans-ACA is a form which has the ability to form mixed wormlike micelles with cationic surfactants, while the cis form produces relatively short micelles. Azobenzene derivatives easily undergo reversible photoisomerisation under the influence of UV and VIS radiation. Consequently, in the case of Ethoquad O/12PG/ACA, it was possible to partially destroy the micellar microstructure by irradiation with UV light upstream of the heat exchanger, and then restore it through exposure to VIS light downstream of the heat exchanger (Shi et al. 2013).

3 Modification of Heat Exchanger Design

A number of methods have been proposed in the literature for modifying heat exchangers to adapt them to the flow of surfactants exhibiting the phenomenon of drag reduction. Heat transfer can be enhanced through the application of a fluted tube (Qi et al. 2001), triangle ribs (Sato et al. 2003), low-profile vortex generators, HEV and helical static mixers and dynamic mixers (single rectangular bar, two parallel rods and pin rods) (Shi et al. 2011).

Data reported by Qi et al. (2001) show that the pressure losses Δp_s and the heat transfer coefficient observed during the flow of a cationic surfactant (Ethoquad T13-50/NaSal) through the heat exchanger with a fluted tube (Fig. 3a) depend on the temperature of the solution. For $T = 50$ °C, the ratio $\Delta p_s/\Delta p_n$ was in the range of 15 to 9, and the ratio Nu_s/Nu_n ranged between 2.4 and 2.6 (Δp_n is the pressure loss occurring in the flow of distilled water through a straight tube). A rise in the temperature of Ethoquad T13-50 solution to 60 °C caused a decrease in the ratio $\Delta p_s/\Delta p_n$ to approximately 3, and the ratio $\mathrm{Nu}_s/\mathrm{Nu}_n$ to approximately 1.2. Also, a fluted tube was found to be a more effective method for enhancing the process of heat transfer in the flow of a solution of the amphoteric surfactant SPE98330 ($\mathrm{Nu}_s/\mathrm{Nu}_n \approx 1.4$ and $\Delta p_s/\Delta p_n = 2.5$).

Zhou et al. (2006) used low-profile vortex generators (LPV) to improve heat transfer during the flow of CTAC/NaSal solutions (concentrations 90 ppm, molar ratio 1:2) (Fig. 3b). LPV increased the values of the heat transfer coefficient in CTAC/NaSal solution at a concentration of 0.009% by approximately 25% relative to the values recorded during the flow of pure water through an empty channel. At the same time, pressure losses increased only by approximately 10%. According to Zhou et al. (2006) an increase in the value of the heat transfer coefficient in this case is not due to the destruction of the micellar microstructure but rather the formation of longitudinal vortices downstream of LPV generators.

Sato et al. (2003) placed triangle ribs inside the tube in order to improve heat transport during the flow of surfactant solutions. The authors conducted their experiments on aqueous CTAC/NaSal solutions in the SPC concentration range of 50 ppm to 500 ppm. Three ribs of different height (from 7.3 mm to 13.6 mm) and opening angle θ(30° and 60°) were placed in the cross-section plane of the tube every 120° (Fig. 3c). The most effective ribs were 12.1 mm in height, and had the opening angle θ = 30°, leading to the ratio Nu_s/Nu_n values of approximately 1.25 for solutions at concentrations ranging from 50 ppm to 100 ppm, with an approximately threefold increase in drag. At higher surfactant concentrations the effectiveness of triangle ribs was shown to decline.

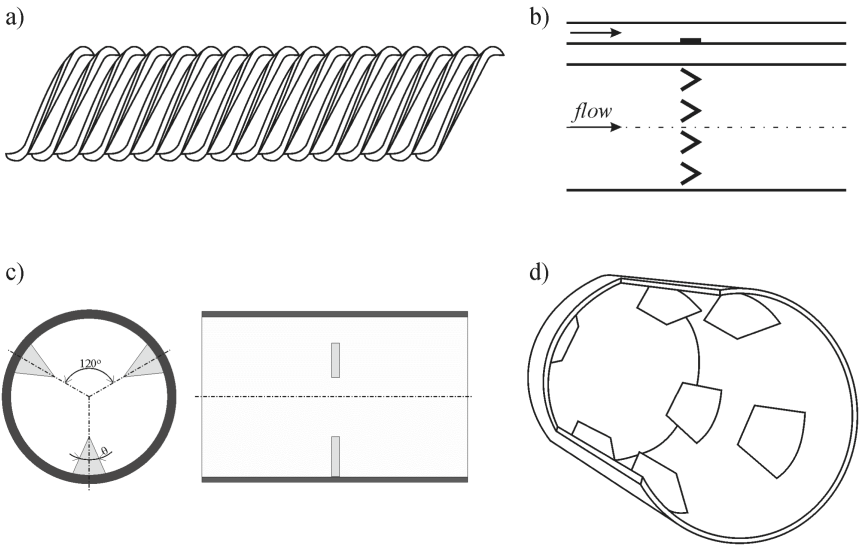

Fig. 3. Surface heat exchanger modification through application flute tube (a) low-profile vortex generator (b), triangle ribs (c) and HEV static mixers (d)

Shi et al. (2011) used helical and HEV static mixers to intensify heat transfer during the flow of an aqueous solution of Ethoquad O/12 PG/NaSal (Fig. 3d). For HEV mixers in the Reynolds number range from approximately 10,000 to 18,800, the ratio $\Delta p_s/\Delta p_n$ reached a value of approximately 5, while the value of the ratio Nu_s/Nu_n was approximately 0.76. Research results reported in the literature for helical static mixers are ambiguous. Measurements performed by Shi et al. (2011) showed the use of helical static mixers to be a completely ineffective method. The measured values of the heat transfer coefficient were comparable during the flow of Ethoquad O/12 PG/NaSal solution through an empty tube and a tube fitted with helical static mixers. In contrast, Maxson et al. (2017) recorded a significant improvement in heat transfer for solutions of the same surfactant.

Studies exploring the possibility of using dynamic mixers to enhance heat transfer were conducted by Maxson et al. (2017). The authors determined the heat transfer

coefficients during the flow of Ethoquad O/12/NaSal solutions through a tube fitted with three types of mixers: single rectangular bar, two parallel rods and pin rods. The application of two parallel rods was shown to be the most effective method. This is most likely due to the "open" axis of the agitator which allows warm fluid displaced from the wall by the agitator to flow radially into the centre of the tube. Hence, Maxson et al. (2017) recommend designing dynamic agitators in such a manner as to maximise radial fluid displacement. The effectiveness of two parallel rods was strongly correlated with the surfactant concentration, which means that their effective performance is also affected by the mechanical degradation of the micellar microstructure.

4 Nanofluids

Also, attempts have been made to enhance heat transfer through the addition of nanoparticles to drag-reducing surfactant solutions (Liu and Liao 2010; Yang et al. 2012; Yang et al. 2013). Liu and Liao (2010) conducted experimental studies on drag and heat transfer during the flow of CTAC/NaSal solutions with added carbon nanotubes (CNT). An addition of CNT increased the value of the thermal conductivity coefficient from 7% to 40% depending on the concentration of nanoparticles and the temperature of the solution. The results of studies on convective heat transfer during the flow of CTAC/NaSal/CNT solutions conducted by Liu and Liao (2010) are inconclusive. An addition of nanotubes to CTAC/NaSal solutions triggered a relatively slight increase in the coefficient of friction (from 5% to 10%), while the values of the heat transfer coefficient were strongly correlated with the temperature of the solution.

Yang et al. (2012, 2013) analysed the effect of spherical copper nanoparticles with a diameter of about 50 nm on the heat transport rate in aqueous CTAC/NaSal solutions. The addition of copper nanoparticles was found to increase the value of the thermal conductivity coefficient. In a CTAC solution at a concentration of 0.1%, an addition of Cu (0.25% by volume) induced an increase in the thermal conductivity coefficient by 25.43%. The results of measurements of pressure losses and the heat transfer coefficient showed that an addition of Cu nanoparticles to CTAC/NaSal solutions primarily reduced the value of the critical Reynolds number Re_c (in the original paper the authors use the Péclet number). Above the critical value of Re_c, both the heat transfer coefficient and pressure losses were shown to rise.

5 Conclusions

The above description of different methods for enhancing heat transfer during the flow of drag-reducing surfactant solutions indicates that none of them can be regarded as universal. Their effectiveness depends to a large extent on the type of surfactant used, and the temperature and concentration of the solution. Destructive devices can be used in short heat exchangers. Also, a relatively good method for intensifying heat transfer during the flow of cationic surfactant solutions is based on fluted tubes, however tubes of this type can only be used for building new heat exchangers. In contrast, HEV static mixers, which were also shown to produce satisfactory results, can be employed to

enhance heat transfer in existing systems. Even though their practical application still requires more in-depth research, photosensitive surfactant solutions and nanofluids may in the future provide an interesting alternative to traditional drag-reducing surfactant solutions.

Acknowledgments. This work was supported by PUT research grant no. 03/32/SBAD/0902.

References

Aguilar, G., Gasljevic, K., Matthys, E.F.: Asymptotes of maximum friction and heat transfer reductions for drag-reducing surfactant solutions. Int. J. Heat Mass Transf. **44**, 2835–2843 (2001)

Aguilar, G., Gasljevic, K., Matthys, E.F.: Coupling between heat and momentum transfer mechanisms for drag reducing polymer and surfactant solutions. J. Heat Transf. **121**, 796–802 (1999)

Aly, W.I.A., Inaba, H., Haruki, N., et al.: Drag and heat transfer reduction phenomena of drag-reducing surfactant solutions in straight and helical pipes. J. Heat Transf. **128**, 800–810 (2006)

Broniarz-Press, L., Różański, J., Różańska, S.: Drag reduction effect in pipe systems and liquid falling film flow. Rev. Chem. Eng. **23**, 149–245 (2007)

Gasljevic, K., Aguilar, G., Matthys, E.F.: Buoyancy effects on heat transfer and temperature profiles in horizontal pipe flow of drag-reducing fluids. Int. J. Heat Mass Transf. **43**, 4267–4274 (2000)

Gasljevic, K., Matthys, E.F.: Experimental investigation of thermal and hydrodynamic development region for drag-reducing surfactant solutions. J. Heat Transf. **119**, 80–119 (1997)

Gasljevic, K., Matthys, E.F.: Improved quantification of the drag reduction phenomenon through turbulence reduction parameters. J. Non-Newtonian Fluid Mech. **84**, 123–130 (1999)

Hadri, F., Besq, A., Guillou, S., et al.: Temperature and concentration influence on drag reduction of very low concentrated CTAC/NaSal aqueous solution in turbulent pipe flow. J. Non-Newtonian Fluid Mech. **166**, 326–331 (2011)

Inaba, H., Aly, W.I.A., Haruki, N., et al.: Flow and heat transfer characteristic of drag reducing surfactant solution in helically coiled pipe. Heat Mass Transf. **41**, 940–952 (2005)

Ketner, A.M., Kumar, R., Davies, T.S., et al.: A simple class of photorheological fluids: surfactant solutions with viscosity tunable by ligot. J. Am. Chem. Soc. **129**, 1553–1559 (2007)

Kumar, R., Raghavan, S.R.: Photogelling fluids based on light-activated growth of zwitterionic wormlike micelles. Soft Matter **5**, 797–803 (2009)

Lee, H.Y., Diehn, K.K., Sun, K., et al.: Reversible photorheological fluids based on spiropyran-doped reverse micelles. J. Am. Chem. Soc. **133**, 8461–8463 (2011)

Li, P., Kawaguchi, Y., Daisaka, H., Yabe, A., et al.: Heat transfer to the drag-reducing flow of surfactant solution in two-dimensional channel with mesh-screen inserts at the inlet. J. Heat Transf. **123**, 779–789 (2001)

Liu, Z.H., Liao, L.: Forced convective flow and heat transfer characteristics of aqueous drag-reducing fluid with carbon nanotubes added. Int. J. Therm. Sci. **49**, 2331–2338 (2010)

Matthys, E.F.: Heat transfer, drag reduction, and fluid characterization for turbulent flow of polymer solutions: recent results and research needs. J. Non-Newtonian Fluid Mech. **38**, 313–342 (1991)

Maxson, A., Watson, L., Karandikar, P., et al.: Heat transfer enhancement in turbulent drag reducing surfactant solutions by agitated heat exchangers. Int. J. Heat Mass Transf. **109**, 1044–1051 (2017)

Qi, Y., Kawaguchi, Y., Christensen, R.N., et al.: Enhancing heat-transfer ability of drag reducing surfactant solutions with static mixer and honeycombs. Int. J. Heat Mass Transf. **46**, 5161–5173 (2003a)

Qi, Y., Kawaguchi, Y., Lin, Z., et al.: Enhanced heat transfer of drag reducing surfactant solutions with fluted tube-in-tube heat exchanger. Int. J. Heat Mass Transf. **44**, 1495–1505 (2001)

Qi, Y., Weavers, L.K., Zakin, J.L.: Enhancing heat-transfer ability of drag reducing surfactant solutions with ultrasonic energy. J. Non-Newtonian Fluid Mech. **116**, 71–93 (2003b)

Różański, J.: Heat transfer in the thermal entrance region for drag reduction surfactant solutions in pipe flow. Int. J. HeaMass Transf. **55**(4), 1113–1125 (2012)

Sears, P.L., Yang, L.: Heat transfer in a surfactant drag-reducing solution a comparison with predictions for laminar flow. J. Heat Transf. **128**, 557–563 (2006)

Sato, K., Chu, R., Kumada, M.: Heat transfer enhancement using turbulent promoters for drag-reducing surfactant aqueous solution flow. J. Enhanc. Heat Transf. **10**(3), 301–310 (2003)

Shi, H., Ge, W., Fang, B.: Enhancing heat transfer of drag-reducing surfactant solution by an HEV static mixer with low pressure drop. Adv. Mech. Eng. **2011**, 1–10 (2011a)

Shi, H., Wang, Y., Fang, B., et al.: Light-responsive threadlike micelles as drag reducing fluids with enhanced heat-transfer capabilities. Langmuir **27**, 5806–5813 (2011b)

Shi, H., Ge, W., Oh, H., et al.: Photoreversible micellar solution as a smart drag-reducing fluid for use in district heating/cooling systems. Langmuir **27**, 102–109 (2013)

Wang, Y., Shi, H., Fang, B., et al.: Heat transfer enhancement for drag-reducing surfactant fluid using photo-rheological counterion. Exp. Heat Transf. **25**(3), 139–150 (2012)

Wang, Y., Yu, B., Zakin, J.L., et al.: Review on drag reduction and its heat transfer by additives. Adv. Mech. Eng. **2011**, 1–17 (2011)

Wei, J.J., Kawaguchi, Y., Li, F.C., et al.: Drag-reducing and heat transfer characteristics of a novel zwitterionic surfactant solution. Int. J. Heat Mass Transf. **52**, 3547–3554 (2009)

Yang, J.Ch., Li, F.Ch., He, Y.R., et al.: Experimental study on the characteristics of heat transfer and flow resistance in turbulent pipe flows of viscoelastic-fluid-based Cu nanofluid. Int. J. Heat Mass Transf. **62**, 303–313 (2013)

Yang, J.Ch., Li, F.Ch., Zhou, W.W., et al.: Experimental investigation on the thermal conductivity and shear viscosity of viscoelastic-fluid-based nanofluids. Int. J. Heat Mass Transf. **55**, 3160–3166 (2012)

Zhou, T., Leong, K.C., Leo, K.H.: Experimental study of heat transfer enhancement in a drag-reducing two-dimensional channel flow. Int. J. Heat Mass Transf. **49**, 1462–1471 (2006)

Separation of Erythritol from Fermentation Broth Using Preparative Chromatography

Beata Rukowicz(✉), Kinga Polaszek, and Krzysztof Alejski

Institute of Chemical Technology and Engineering,
Poznan University of Technology, Poznań, Poland
beata.rukowicz@put.poznan.pl

Abstract. Biologically obtained erythritol is produced by microorganisms during the fermentation of the carbon source. In this paper a process of erythritol desalination based on ion exchange chromatography is proposed. A strongly acidic cation exchanger in sodium form was used as the stationary phase. Experimental overload profiles were determined for the chromatographic separation of erythritol and sodium chloride (assuming a constant desalting of 96%). As a result, it was determined that the separation efficiency decreases with volume overload, and the process carried out for a 30–40% column load allows to obtain the highest separation efficiency.

1 Introduction

The low-caloric sweetener erythritol is a sugar alcohol which can be obtained by biotechnological synthesis (Park et al. 2016). This polyol has no effect on blood sugar or blood insulin level. Erythritol is a natural sweetener with applications in food and pharmaceutical industries and it is commonly used in low-sugar and sugar-free products (Moon et al. 2010; Saran et al. 2015). The biologically-derived erythritol is produced by microorganisms during the fermentation of a carbon source as a glycerol or glucose. Biotechnological production of erythritol use yeasts that can tolerate high osmotic pressures like Trichosporonoides sp., Torula sp,. Monilella sp. or Candida magnoliae (Jovanovic et al. 2014; Lin et al. 2010). A high-yield production of erythritol can be achieved by osmophilic mutant of Yarrowia lipolytica Wratislavia K1 (Mirończuk et al. 2015). Studies have shown that the high osmotic pressure (including high substrate concentration and high salinity) strongly enhanced erythritol yield and productivity (Tomaszewska et al. 2014a, b; Yang et al. 2015). NaCl addition to the medium improves erythritol biosynthesis and consequently it is present in the fermentation broth after the fermentation process.

The fermentation broth in erythritol producing bioreactor contains the main product within a complex mixture of many components, including biomass, inorganic salts as well as organic acid by-products Therefore, economical and efficient downstream processing of erythritol is essential. Several separation methods have been reported to purify erythritol, including ion exchange (Chida and Ochiai 2000; Lin et al. 2005),

© Springer Nature Switzerland AG 2020
M. Ochowiak et al. (Eds.): PAIC 2019, *Practical Aspects of Chemical Engineering*, pp. 383–391, 2020.
https://doi.org/10.1007/978-3-030-39867-5_40

chromatographic methods (Marioka et al. 2000; Maeda et al. 1993; Paananen et al. 2006), membrane methods (Staszak et al. 2013) and crystallization (de Troostembergh et al. 2002).

Ion-exclusion chromatography is useful method for the separation of ionic and nonionic substances and can be applied to desalination of the fermentation broth. This separation technique is used both at analytical scale and at preparative scale for the separation of strong electrolytes from weak electrolytes and nonelectrolytes (Lodi et al. 2017). Ion exclusion can be performed on the anion or cation-exchange resins – the resin has the same charge as ionic substances. As a result ionized samples are excluded from the pores of the support and elute first, while the nonionic compounds elute later.

The main purpose of preparative chromatography is to purify and to isolate compounds at a high yield, high purity or high productivity. Productivity, defined as an amount of isolate target compound per unit mass of feed and per unit time is the most important factor. To increase productivity samples are applied on the column with much higher concentrations or volumes than in analytical chromatographic process. A differently shaped profile is obtained for mass overload (or otherwise called as concentration overload) and volume overload as shown in Fig. 1 (Poole 2003; Schmidt-Traub 2005; Vajda et al. 2014). Overloading of the chromatographic column and the required purity of the product affect the efficiency of the process. As column overload increases, higher productivity can be achieved with lower product purity.

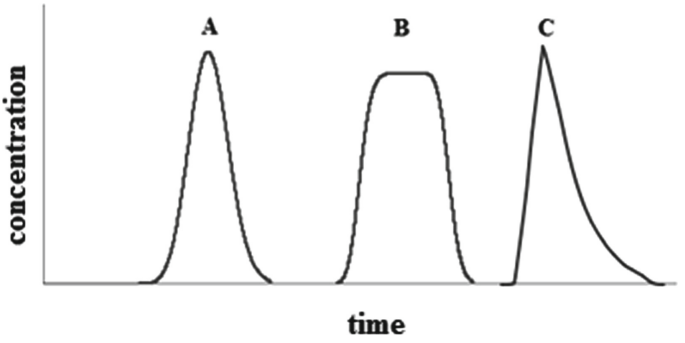

Fig. 1. Different types of elution profiles for analytical separation (A), volume overload (B), mass overload (C)

Mass overload can be applied for concentrated solutions while the process for fermentation broth is carried out with volume overload. Separation with a small feed volume causes a large dilution of the product while an increase of the volume of the feed affects the extension of profiles and causes peak broadening. Theoretical profiles are shown in Fig. 2. The paper presents research on the experimental determination of the level of chromatographic column overload. The experimental volume overloaded profiles were determined for the chromatographic separation of erythritol and sodium chloride.

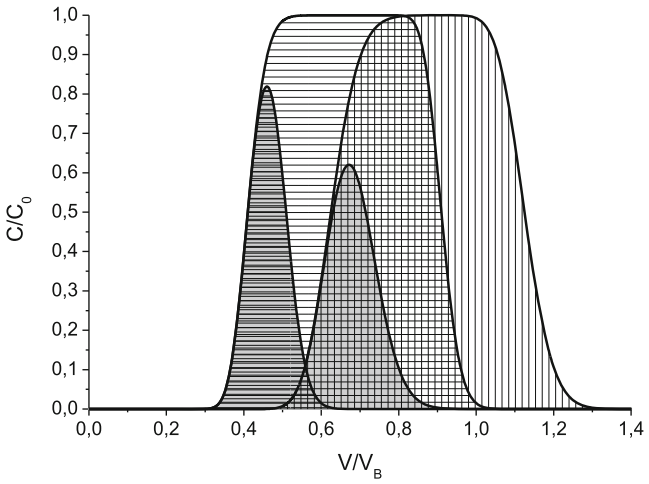

Fig. 2. Comparison of theoretical two-component separation profiles for different column load: 10% volume loading (gray fill color of chromatograms of compounds A and B) and 50% volume loading (hatched fill of chromatograms of compounds A and B)

2 Materials and Methods

2.1 Materials

Experiments were conducted for model aqueous solution composed of 150 g/L erythritol and 30 g/L sodium chloride. The model test solution was selected based on the composition of erythritol fermentation broth. Sodium chloride (99.8%, salt) was purchased from Avantor Corporation. Erythritol (food product) was purchased from Biofan Corporation. Chromatographic separation experiments were carried out using monospheric strongly acidic cation exchange resin in sodium form (based on a styrene-divinylbenzene copolymer, Lewatit S1567, 0.6 mm).

2.2 Analytical Method

An HPLC system with RI detector was used to measure the concentration of erythritol and inorganic salt in collected product fractions. Rezex-ROA Organic Acid column (4.6 mm × 250 mm, Phenomenex) was used as a HPLC analytic column and 5 mM H_2SO_4 as a mobile phase. The flow rate of the mobile phase was maintained at 0.4 mL/min with a column temperature of 50 °C. In addition, the process was monitored by continuous direct measurement of conductivity. On-line measurements were performed using a multifunction meter (Elmetron) measuring the pH, temperature and conductivity of working solutions.

2.3 Chromatographic Separation Step

Studies on the effect of volume overload on process efficiency have been carried out at room temperature (20 °C). Ion exchange resin in sodium form was used for batch ion exclusion chromatography. The model feed solution was composed of 150 g/L erythritol and 30 g/L sodium chloride. The preparative chromatography system was composed of a pump, a chromatographic column (26 mm i.d. × 100 cm length), a multifunction meter and fraction collector. The feed solution was loaded into the packed column with the amount converted into the column capacity in the range of 10–60% of the total bed volume. Distilled water was used as a mobile phase with flow rate 10.5 mL/min and space velocity 1.2 h^{-1} (ratio of flow rate of the mobile phase to the total bed volume). Fractions from the column were collected and analyzed using the HPLC system. Chromatograms of erythritol and salt were determined based on quantitative analysis. The results are presented in charts on a dimensionless scale to compare the tests carried out for different separation conditions. The dimensionless form of the total volume of the mobile phase dosed per column (V) related to the bed volume in the column (V_B) was defined as the ratio of the eluate volume and the bed volume (V/V_B, where V_B = 530 mL). Graphs in non-dimensional form were also made for the concentration of components determined by HPLC. The ratio of the concentration in the test sample to the initial concentration of erythritol (C = 150 g/L) or sodium chloride (C = 30 g/L) in the feed was determined (C/C_0, where C_0 is the initial concentration of the component in the feed solution).

Erythritol and sodium chloride curves and conductivity profiles are set on a common graph and the eluate two fractions were isolated: saline waste and a product solution with 96% desalination degree (Fig. 3).

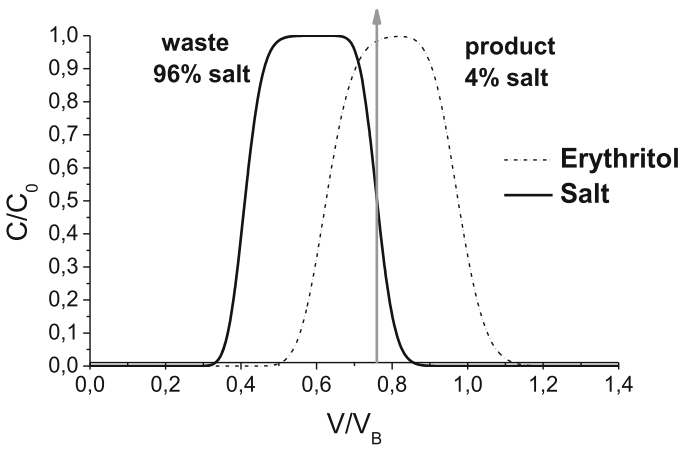

Fig. 3. Exemplary concentration profiles separated into waste fraction and product fraction with 96% desalination degree (part of the waste fraction can be separated as recycle which is subject to retreatment)

3 Results and Discussion

In the research, 4% of the salt content in the product (96% purity after the desalination of the aqueous solution) was assumed. Tests were conducted for various column loads with a constant 96% degree of desalination and constant 1.2 h^{-1} space velocity of mobile phase.

Figure 4 shows the result for a 10% column load system (10% bed volume, 10% V_B). The model solution (53 mL) was dosed onto the column. As a result a very high degree of separation erythritol from salt was obtained. Degree of desalting of product fraction above 96% was obtained with a yield approx. 72% (calculated as the ratio of erythritol in the product to the amount in feed solution). As a result of low column load the sample elution time was the shortest and the concentration profile surfaces are the smallest for this system. Elution profiles have shape symmetrical peaks resemble the analytical profiles. This is an example where the best separation efficiency was obtained but at high product dilution. As a result of desalting a 29 g/L erythritol solution was obtained.

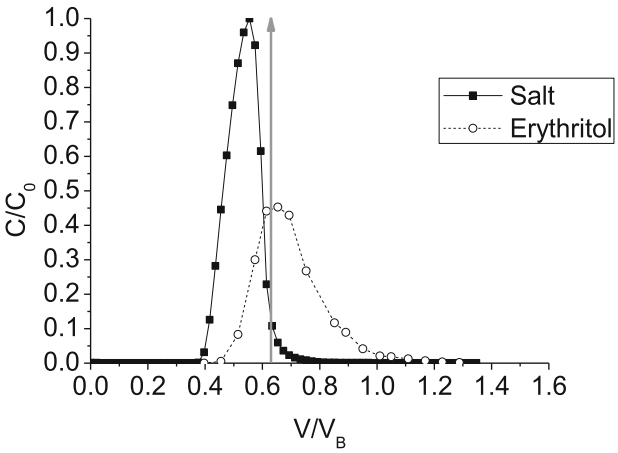

Fig. 4. Elution profiles of erythritol and salt for 10% V_B (V_B = 530 mL)

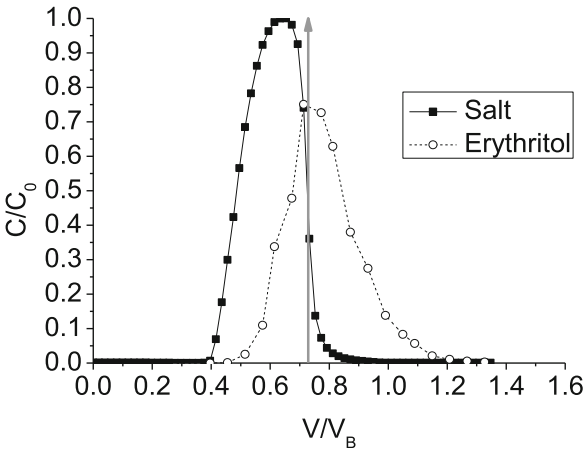

Fig. 5. Elution profiles of erythritol and salt for 20% V_B (V_B = 530 mL)

Figure 5, 6, 7, 8 and 9 show the effect of column loading (20–60% of the total bed volume) on the erythritol separation yield. The amount of solution loaded has a significant impact on the efficiency of the process. Figure 9 shows the results for 60% column loading. 318 ml of model solution was introduced into the column, which significantly reduced the degree of separation. The erythritol and salt profiles (conductivity) overlap. The conductivity profile is trapezoidal and significantly lengthened. The amount of erythritol in the final product was 32% (for 96% degree of desalination). On the basis of elution profiles the efficiency of the desalting process was calculated for the tested column loads (results are presented in Table 1).

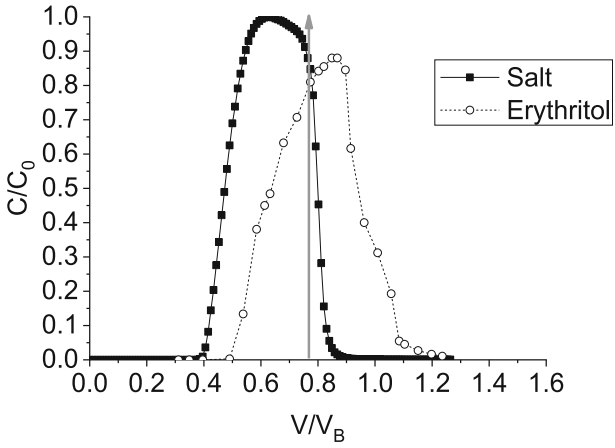

Fig. 6. Elution profiles of erythritol and salt for 30% V_B (V_B = 530 mL)

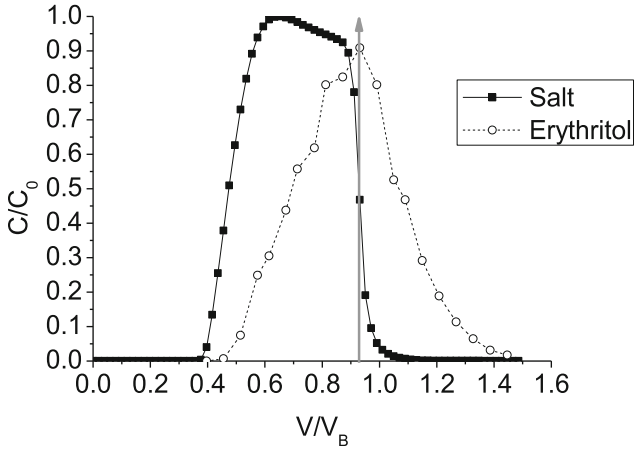

Fig. 7. Elution profiles of erythritol and salt for 40% V_B (V_B = 530 mL)

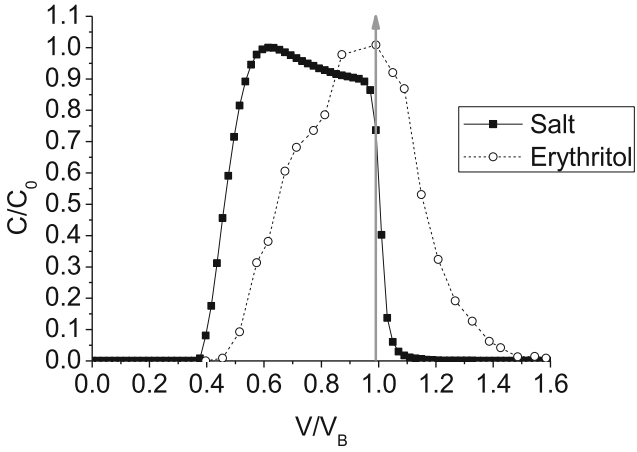

Fig. 8. Elution profiles of erythritol and salt for 50% V_B (V_B = 530 mL)

Based on the research (assuming a constant separation degree of 96%), it was found that the separation efficiency decreases with volume overloading. For low overload (10–20%) very high dilution of the erythritol solution was obtained. At 50–60% column loading, the smallest degree of product dilution (approx. 2 times relative to the feed) as well as the lowest separation efficiency (32–38%) was obtained. As a result, it was determined that the process carried out for a 30–40% column load allows obtain the highest possible separation efficiency (in the range of 42–58%).

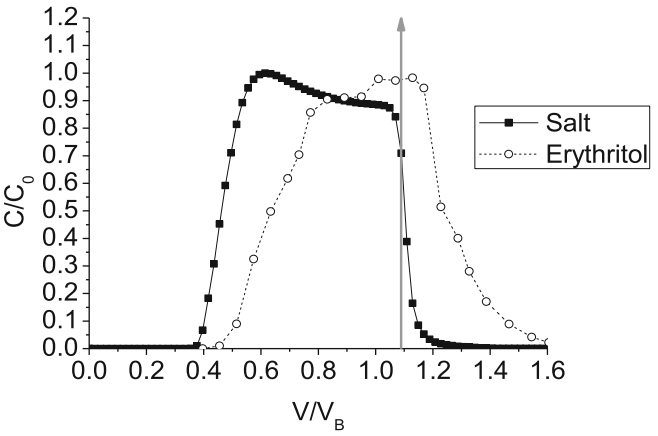

Fig. 9. Elution profiles of erythritol and salt for 60% V_B (V_B = 530 mL)

Table 1. Process efficiency for tested column loads (96% degree of desalination).

Volume overload	Separation yield
10%	72%
20%	69%
30%	58%
40%	42%
50%	38%
60%	32%

4 Conclusions

The separation of erythritol and sodium chloride can be obtained using ion exchange chromatography and this method can be applied to desalination of the fermentation broth. The efficiency of the separation process depends, among others from the column overload and the required product purity. Volume overload increases the efficiency of the process, however, decreases the separation of impurities. Ion exclusion chromatography carried out for 30–40% column overload allows obtain the highest possible separation efficiency. The main disadvantage of the process is obtaining a diluted product, which requires concentration.

Acknowledgments. This work was supported by the Ministry of Science and HigherEducation 2020. The study is a continuation of the project "Biotechnological conversion of glycerol to polyols and dicarboxylic acids," realized within the Operational Programme – Innovative Economy, 2007–2013, co-financed by the European Union PO IG 01.01.02.074/09.

References

Chida, S., Ochiai, T.: Method for producing erythritol using a microorganism. Patent US 6110715 (2000)

de Troostembergh, J.C.M.P., Debonne, I.A., Obyn, W.R.: Process for producing and recovering erythritol from culture medium containing the same. Patent US 6440712 B2 (2002)

Jovanovic, B., Mach, R.L., Mach-Aigner, A.R.: Erythritol production on wheat straw using Trichoderma reesei. AMB Express **4**(1), 34 (2014)

Lin, S.J., Wen, C.Y., Huang, C.C., Chu, W.S.: Erythritol-producing Moniliella strains. Patent US 6916639 B2 (2005)

Lin, S.J., Wen, C.Y., Wang, P.M., Huang, J.C.: High-level production of erythritol by mutants of osmophilic Moniliella sp. Process Biochem. **45**, 973–979 (2010)

Lodi, G., Storti, G., Pellegrini, L.A., Morbidelli, M.: Ion exclusion chromatography: model development and experimental evaluation. Ind. Eng. Chem. Res. **56**, 1621–1632 (2017)

Marioka, S., Abe, T., Maeda, T., Taki, A., Sawada, K., Ishitsuka, H.: Process for producing high-purity erythritol crystal. Patent US 6030820 (2000)

Maeda, T., Kombu, T., Nakazawa, I.: Process for isolating and recovering erythritol from culture medium containing the same. Patent EP 0327016 B1 (1993)

Mirończuk, A.M., Dobrowolski, A., Rakicka, M., Rywińska, A., Rymowicz, W.: Newly isolated mutant of Yarrowia lipolytica MK1 as a proper host for efficient erythritol biosynthesis from glycerol. Process Biochem. **50**, 61–68 (2015)

Moon, H.J., Jeya, M., Kim, I.W., Lee, J.K.: Biotechnological production of erythritol and its applications. Appl. Microbiol. Biotechnol. **86**, 1017–1025 (2010)

Paananen, H., Kuisma, J., Heikkila, H., Ravanko, V., Lewandowski, J., Karki, A.: Separation system and process. Patent US 7060188 B2 (2006)

Park, Y.C., Oh, E.J., Jo, J.H., Jin, Y.S., Seo, J.H.: Recent advances in biological production of sugar alcohols. Curr. Opin. Biotech. **37**, 105–113 (2016)

Poole, C.F.: The Essence of Chromatography. Elsevier, Amsterdam (2003)

Saran, S., Mukherjee, S., Dalas, J., Saxena, R.K.: High production of erythritol from Candida sorbosivorans SSE-24 and its inhibitory effect on biofilm formation of Streptococcus mutans. Bioresour. Technol. **198**, 31–38 (2015)

Schmidt-Traub H.: Preparative chromatography. Wiley-VCH, Weinheim (2005)

Staszak, K., Woźniak, M.J., Karaś, Z., Staniewski, J., Prochaska, K.: Application of nanofiltration in the process of the separation of model fermentation broths components. Pol. J. Chem. Tech. **15**(4), 1–4 (2013)

Tomaszewska, L., Rymowicz, W., Rywińska, A.: Mineral supplementation increases erythrose reductase activity in erythritol biosynthesis. Appl. Biochem. Biotechnol. **172**(6), 3069–3078 (2014a)

Tomaszewska, L., Rywińska, A., Rymowicz, W.: High selectivity of erythritol production from glycerol by Yarrowia lipolytica. Biomass Bioenergy **6**(4), 309–320 (2014b)

Vajda, P., Kamarei, F., Felinger, A., Guiochon, G.: Comparison of volume and concentration overloadings in preparative enantio-separations by supercritical fluid chromatography. J. Chromatogr. A **1341**, 57–64 (2014)

Yang, L.B., Dai, X.M., Zheng, Z.Y., Zhu, L., Zhan, X.B., Lin, C.C.: Proteomic analysis of erythritol-producing Yarrowia lipolytica from glycerol in response to osmotic pressure. J. Microbiol. Biotechnol. **25**(7), 1056–1069 (2015)

Spent Automotive Converters as a Secondary Resource of Metals

Martyna Rzelewska-Piekut[1(✉)], Mariola Saternus[2], Agnieszka Fornalczyk[2], and Magdalena Regel-Rosocka[1]

[1] Institute of Chemical Technology and Engineering, Poznan University of Technology, Poznań, Poland
martyna.rzelewska-piekut@put.poznan.pl
[2] Faculty of Materials Engineering, Silesian University of Technology, Katowice, Poland

Abstract. Chapter describes a possibility of recovery of metal ions (especially platinum group metals) from spent automobile converters by hydrometallurgical method. Also, the composition of the automobile catalyst is reported. Moreover, the results of leaching of metal ions from spent catalysts with organic and inorganic acids were presented. Carboxylic acids were considered as potential leaching agents for treatment of spent automotive converters. These acids show leaching potential towards base metals, and could be used in the first step of leaching prior to platinum group metals leaching in more stringent conditions.

1 Introduction

Rapid depletion of natural metal sources and the increasing environmental requirements encourage scientists to look for efficient and selective techniques for recovery of metals from secondary raw materials. Due to technological progress the demand for metals, especially platinum group metals (PGM) or rare earth metals is still growing (Benson et al. 2000; Kucharski 2010). An important source of PGM are spent automobile converters which are made of a ceramic or metal support, on which an intermediate layer (aluminum oxide) and an active substance (specific catalyst) are applied, i.e. noble metals, mainly Pt, Pd and Rh (Saternus and Fornalczyk 2009; Wołowicz 2013).

In recent years, the popularity of hydrometallurgical methods (extraction, leaching) for the recovery of metal ions from solid waste increased, mainly due to the significantly lower operating temperatures than in pyrometallurgical processes and complete use of raw material (Rzelewska and Regel-Rosocka 2018).

The aim of this work is to present efficiency of hydrometallurgical methods for recovery of valuable metals from spent automobile catalysts.

© Springer Nature Switzerland AG 2020
M. Ochowiak et al. (Eds.): PAIC 2019, *Practical Aspects of Chemical Engineering*, pp. 392–400, 2020.
https://doi.org/10.1007/978-3-030-39867-5_41

2 Spent Automotive Catalysts - Characteristics

Catalytic reactors are devices that significantly reduce the amount of hazardous chemicals emitted into the air. Currently, virtually all cars on the road should have installed catalytic converters. There are different types of engines, and therefore there are various types of automotive catalytic converters. Spark ignition engines most often use TWC reactors (Three Way Catalyst), which reduce nitrogen oxides (NO_x) and at the same time oxidize hydrocarbons (HC) and carbon monoxide (CO). In contrast, oxidative reactors are used in compression-ignition engines that oxidize HC and CO. A brief description of the catalytic converters currently used in various types of cars is presented in Table 1.

Table 1. Characteristics of basic types of automotive catalytic converters (Bailey 1997; Hagelüken 2006; Wolak 2008; DCL 2017)

Type	Characteristics
TWC Three Way Catalyst	Allows reduction of NO_x and oxidation of CO and HC with precise control of the air/fuel ratio; consists of a of ceramic or metallic carrier, an intermediate layer and an active or catalytic layer, depending on the operating conditions of the engine and the exhaust gas composition, conversion rates of close to 100% can be achieved at close to stoichiometric (lambda one) conditions
DOC Diesel Oxidation Catalyst	Oxidation catalytic reactor, very effective in controlling the level of carbon monoxide (II), hydrocarbons, compounds responsible for smell and volatile organic fractions, the disadvantage of this type of reactors is a small reduction of nitrogen oxides
DPF Diesel Particulate Filter	Filters used to remove solid particles, are made of a ceramic element placed in a metal casing, similar to a traditional catalytic converter, with the difference that one of the two channels is blind - the walls of both channels are made of SiC coated with Al_2O_3 and CeO_2, platinum particles are deposited on these oxides; exhaust gases can penetrate between the channels due to the porous structure of the filter, thanks to which solid particles are retained in the walls and at the bottom of the clogged channels
NAC NO_X Adsorbers Catalyst	Store nitrogen oxides in excess oxygen in the air/fuel ratio and then release and catalytically reduce stored NO_x in excess oxygen in the air/fuel ratio; most of the NO_x emitted by the car is NO, this oxide is oxidized to NO_2 and then adsorbed on another metal oxide, e.g. barium, and stored as barium nitrate

Generally, catalytic converters are built from stainless steel shell, non-woven fabric preventing the carrier from moving and the carrier itself. Ceramic or metallic materials are most often used as carriers in automotive catalytic converters (Umicore Precious Metals Refining 2009). Currently, the majority of car catalytic converters are produced on ceramic carriers (approximately 96%), however, the percentage share in the market

of new generation metal catalytic converters (Metal Substrate Converters), initially used in sports and racing cars, is still growing (Kucharski 2010).

The basic material of the ceramic carrier is a crystalline mass consisting of Al_2O_3 with the addition of other oxides, e.g. CeO_2 (15–30 wt%). Precious metals, usually platinum, palladium or rhodium, are applied to a properly prepared carrier surface. Such design allows the active surface to be increased, and consequently the contact zone of the catalytic substances (Pt, Pd, Rd) with the exhaust gas that flows through the carrier channels (see Fig. 1). The combustion process is inseparably accompanied by the formation of the following toxic compounds: carbon oxides (CO), unburned hydrocarbons (HC) and nitrogen oxides (NO_x). In order for these compounds to be harmless to the environment, they must undergo certain transformations, and as a result neutral compounds for the environment, such as carbon dioxide, water or nitrogen are obtained.

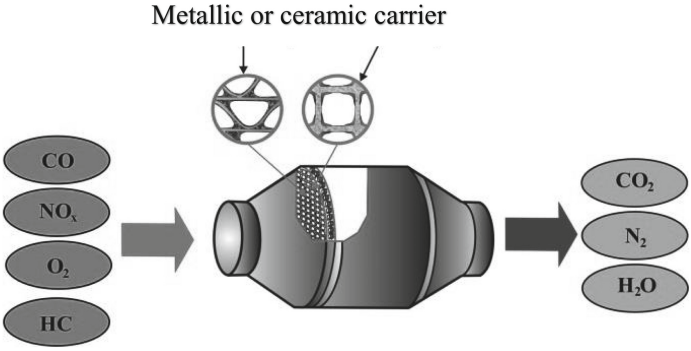

Fig. 1. Scheme of automotive catalytic converter (Fornalczyk 2016)

An advantage of ceramic carriers (see Fig. 2a) is low thermal expansion and good surface development, which enables good distribution of the catalytically active phase. At the same time, the basic disadvantages include lower thermal and mechanical strength of the carriers and the need to use mats made of ceramic fibers, protecting against cracking during shocks and reducing differences in thermal expansion in relation to the metal shell. The structure of honeycomb is the best geometrical form of the ceramic carriers due to large contact area of the exhaust gases with the catalyst (Kucharski 2010).

Automotive catalytic converters with metallic carriers (see Fig. 2b) are made of heat-resistant Fe-Cr-Al foil with platinum coatings. This foil is rolled up in a way that maximally increases the contact area with catalytic substances. Metallic carriers have – in relation to ceramic carriers – a number of advantages; are more resistant to thermal shocks and mechanical damage. These monoliths quickly reach operating temperature and, above all, are characterized by low exhaust gas flow resistance. Another advantage of this type of catalytic converters is the fact that metallic carriers are not as brittle as ceramic ones and their walls can be much thinner. Thus, metallic carriers enable to

obtain a larger contact surface of exhaust gases with catalytic substances using the same volume of carrier. Metallic carriers heat up much faster and more evenly because they have a lower specific heat capacity and the heat transfer coefficient has a higher value (Kucharski 2010). Another advantage of metallic carriers is the ability to more easily manufacture channels in various shapes to increase exhaust gas flow (Suiter 2012). The disadvantage of these carriers is the complicated process of obtaining catalytically active coating (Umicore Precious Metals Refining 2009).

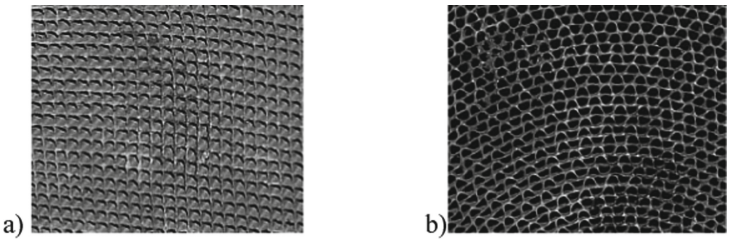

Fig. 2. Catalytic carrier structure: (a) ceramic, (b) metallic

The content of platinum metals in automotive catalytic converters varies widely from 1.42 to 1.76 g/dm^3 of carrier capacity, depending on the vehicle manufacturer, model, engine capacity and even the serial number of the catalytic converter. Some cars use catalytic converters in which the catalytic layer is made only of palladium or only platinum, or platinum-palladium layer and those in which platinum, palladium and rhodium together are used. As was mentioned before, gasoline and diesel engines use completely different catalytic converter systems. Thus, spent or scrapped catalytic converters are a valuable source of platinum, despite the fact that they are composed of more than 99% ceramic material or Fe-Cr-Al steel as well as combustion products and organic substances. Both types of catalysts available on the automotive market, i.e. with metallic and ceramic carriers, contain similar amounts of PGM (Kucharski 2010).

The recycling of spent automotive catalytic converters is currently very cost-effective and even necessary due to the fact that platinum group metals, especially platinum, palladium and rhodium, are considered critical metals, i.e. those whose natural sources are limited and shrinking. The use of PGM is constantly growing due to their catalytic properties (Johnson Matthey 2019). The availability of PGM in the future is questionable considering their high demand in recent years (see Table 2), social, economic, environmental as well as political aspects connected with their production.

To almost exclusive producers of primary platinum belong South Africa – nearly 70%, while the largest share of the recovered platinum group comes from the USA and Canada, this is mainly due to the fact that regulations on exhaust emissions were introduced very early in the US. The very restrictive legal regulations currently in force regarding the obligation to obtain specific recovery rates for end-of-life vehicles and the mandatory removal of catalytic converters (they are waste intended for further segregation and processing) have improved the situation of the European Union in the area of platinum recovery.

Table 2. Supply, demand and recycling of platinum, palladium and rhodium in 2018 (Johnson Matthey 2019)

Metal	Supply (kg)	Demand (kg)	Recycling (kg)
Pt	169400	222400	56000
Pd	187020	287800	82950
Rh	21260	29710	9180

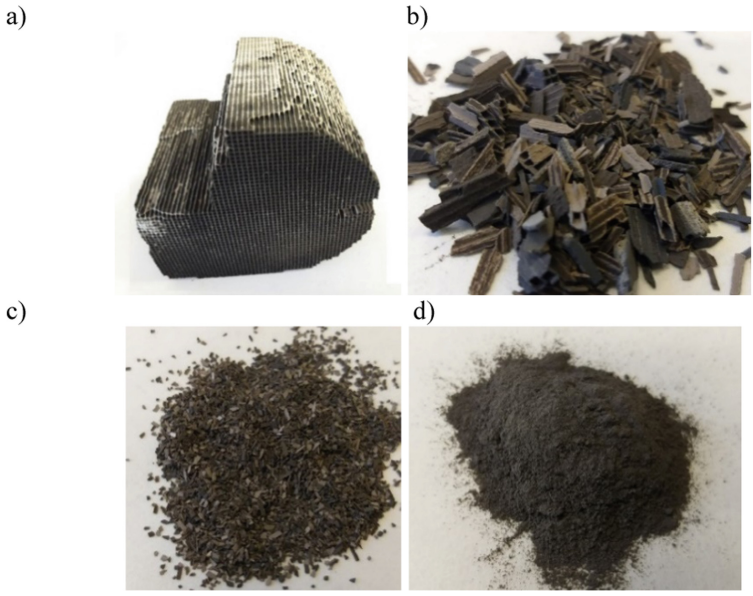

Fig. 3. Spent automotive converter: (a) before grinding and various mixed converters after grinding: (b) >1 mm, (c) > 0.5 mm, (d) <0.063 mm

However, the process of catalytic converters treatment is difficult and complicated due to fact that the level of platinum and other precious metals in carriers is rather small. Therefore, the catalytic converter carriers (see Fig. 3a) should be appropriately prepared, mainly ground (see Fig. 3b–d). After this operation pyrometallurgical or hydrometallurgical treatment is applied. In the pyrometallurgical treatment, catalytic converter carriers are smelted with various metals such as copper, iron or lead, in which, as a result, the alloy of metal collector with platinum is obtained, while the alumina carrier forms a slag. In industry pyrometallurgy is often used because it is effective but, on the other hand, it is slow and energy-consuming. The other treatment method is based on hydrometallurgical processes such as leaching in various media, such as chlorine, chlorides, aqua regia, with addition of H_2O_2, sulfuric acid with H_2O_2 or cupric ions. Hydrometallurgical methods in comparison with the pyrometallurgical ones consume less energy but the recycling efficiency is not so high and, additionally, large amount of waste solutions is generated.

3 Leaching of Metals from Spent Automotive Catalysts

Principals on leaching process and kinetics of leaching reactions are given in the chapter ***Metal leaching from e-waste with ionic liquids*** of this book. Generally, as leaching agents of metals from spent automotive catalysts are applied strong solutions of mineral acids that have oxidative properties, e.g. nitric acid, aqua regia (1:3 mixture of nitric and hydrochloric acids). As Pt, Pd and Rh, which are of the main interest of spent automotive catalyst treatment, are noble metals, the minimum oxidizing potential to overcome during leaching is high, e.g. for Pt with and without the Cl^- complexing ions is +0.77 V and +1.18 V (Saguaru et al. 2018). To increase leaching efficiency additional chlorination (Mišić et al. 2013, Sinisalo and Lundström 2018), oxidative agents, such as $AlCl_3$/NaOCl solution (Angelidis 2001), H_2O_2 (Sarioğlan 2013) or $FeCl_3$ (Ding et al. 2019), or microwave energy (Suoranta et al. 2015) are used.

4 Carboxylic Acids as Metal Leaching Agents from Spent Catalysts

Carboxylic acids, such as formic acid, can be used for catalyst pretreatment by reducing the PGMs to their metallic form to improve subsequent leaching. Formic acid reduces Pt and Rh according to the following reactions (Upadhyay et al. 2013; Trinh et al. 2017):

$$PtO_{2(s)} + 2HCOOH \rightarrow Pt + 2H_2O + 2CO_2 \quad (1)$$

$$PdO_{(s)} + HCOOH \rightarrow Pd + H_2O + CO_2 \quad (2)$$

$$Rh_2O_{3(s)} + 3HCOOH \rightarrow 2Rh + 3H_2O + 3CO_2 \quad (3)$$

Owing to the reductive pretreatment, PGM recoveries increased from 71 to 97%, 60 to 94% and 58 to 90% for Pt, Pd and Rh, respectively. Moreover, the pre-reduction step provides minimized environmental impact of PGM recovery and reduction in cost of reagents, while keeping the maximum yield of PGMs in a less acidic solution.

To the best of our knowledge no information on use of carboxylic acids as leaching agents for spent automotive converters has been reported. Carboxylic acids are not strong enough to react directly with noble PGMs, therefore it seems that their role in the treatment of spent automotive catalysts can be assigned to auxiliary operations. For example, acetic acid was proposed for Pb dissolution from Pb-Pt-Rh precipitation in the final step of a hydrometallurgical procedure of a pure PGM powder recovery from spent automotive catalysts (Angelidis 2001).

Some organic acids (e.g. oxalic, citric) were used in treatment of other catalysts, for example spent hydrodesulfurisation Mo-V. Oxalic acid, particularly buffered oxalic acid, was proposed for iron removal from hydroprocessing catalysts containing Co, Mo, Re and the Pt group metals on alumina, silica-alumina or a zeolite support (McVicker et al. 1985). It was also used as a complexing agent for selective vanadium recovery from the spent catalyst, while citric acid leached not only vanadium but also

molybdenum, nickel and aluminium affecting negatively the selectivity of V recovery (Zeng and Cheng 2009). Effectiveness (Mo and V extraction) of five acids (organic and inorganic) used in spent hydroprocessing catalyst leaching was ranked in the following order (Al-Sheeha et al. 2013): oxalic acid = EDTA > citric acid > H_2SO_4 > HNO_3 >> acetic acid.

It was concluded that the role of organic acids for metal leaching was more significant than that of the inorganic acids. It was clearly indicated that the acids with more than one carboxylic group (lower K_a value) had greater strength of the acid, and, thus, leached metals more effectively than monocarboxylic acid (acetic).

The carboxylic acid based processes could be more effective, recoverable, and reusable providing high efficiency of metal extraction, ease of stripping, and low corrosive environment (Al-Sheeha et al. 2013). Citric acid was shown to be more active leaching agent than H_2SO_4 for Mo, V, and Ni ultrasonic-assisted digestion from spent hydroprocessing catalysts (Marafi and Stanislaus 2011). 10% citric acid was reported to be effective leaching agent for V, K and Fe from spent vanadium catalyst at atmospheric pressure, 50 °C for 4 h, at S/L ratio below 0.1 (Mazurek 2014). Under these conditions about 90% of vanadium and potassium compounds and more than 60% of iron contained in the catalyst were dissolved. Hydrothermal treatment at 80 °C, S/L = 1/8 for 10 h with 0.1 M citric acid provided more than 70% dissolution of Al, Ni and Mo from spent hydro-processing catalysts (Shen et al. 2012).

These observations for petrochemical catalysts were not confirmed by the authors of this chapter for leaching of metal ions from spent automobile converters. Results (obtained by the authors) of metal leaching with two carboxylic (citric and oxalic) and inorganic acids are shown in Table 3. The following leaching mixtures were used:

- **solution 1** - aqua regia (3:1 mixture of 36% HCl and 65% HNO_3),
- **solution 2** - mixture of 36% HCl and 95% H_2SO_4 acids and 30 wt% H_2O_2,
- **solution 3** - 1 M citric acid,
- **solution 4** - 1 M oxalic acid.

It has been proved that Pt(IV) and Rh(III) can be leached from spent automobile converters only with inorganic acid mixtures, which is not possible with citric or oxalic acids (Table 3). The solutions after leaching are multicomponent mixtures and contain not only noble metal ions (Pt(IV), Rh(III)) but also base metal ions (Fe(III), Mg(II), Zn (II), Cu(II), Pb(II), Al(III)). The results for leaching of non-noble metals show leaching potential of oxalic acid to dissolve base metals (e.g. Fe(III), Al(III)) prior to further PGM leaching in more stringent conditions. Further separation of precious metals from non-precious needs another step, e.g. liquid-liquid extraction.

Table 3. Mass of metal ions in leaching solutions 1–4 after leaching at 70 ± 3 °C for 3 h, S/L = 1 g/45 cm^3 (own research)

Leaching solution	Mass of metal ions, mg							
	Pt(IV)	Rh(III)	Fe(III)	Mg(II)	Zn(II)	Cu(II)	Pb(II)	Al(III)
1	1.8	0.6	2.4	2.8	3.8	0.1	3.5	15.8
2	1.6	0.5	0.4	2.5	3.0	0.1	1.2	54.0
3	0.0	0.0	0.4	1.0	1.6	0.4	<0.1	22.6
4	0.0	0.0	4.2	0.9	1.7	0.6	<0.1	63.0

Not only synthetic organic acids are used as leaching agents. Carboxylic acids may be produced directly in the place of treatment by microorganisms. For example, Pt was leached from refinery reforming catalyst with oxalic acid produced by *Aspergillus niger*. At the optimum conditions, i.e. 1% for the pulp density, pH 0.5, 70 °C almost 40% of Pt was recovered (Malekian et al. 2019). Thus, it puts a new perspective on oxalic acid use as the leaching agent for PGMs from automotive catalysts.

5 Summary

Currently, production and sale of cars is still increasing, therefore the demand for platinum group metals also grows. As the natural resources (with their intensive exploitation) are limited and can quickly exhaust, there is a strong need to find alternative sources of this critical element. Spent PGM-containing materials are considered a valuable and metal-rich resources that could be recycled. It is not only economically viable, but also environmentally friendly. In the chapter, carboxylic acids were considered as potential leaching agents for treatment of spent automotive converters. However, it can be concluded that they show leaching potential towards base metals, and could be used in the first step of leaching prior to PGM leaching in more stringent conditions.

Acknowledgements. The work was supported by the Polish Ministry of Science and Higher Education (Grant No. 0912/SBAD/2010) and co-financed by National Agency of Academic Exchange NAWA (Grant No. PPN/BIL/2018/1/00200).

References

Al-Sheeha, H., Marafi, M., Raghavan, V., Rana, M.S.: Recycling and recovery routes for spent hydroprocessing catalyst waste. Ind. Eng. Chem. Res. **52**, 12794–12801 (2013)

Angelidis, T.N.: Development of a laboratory scale hydrometallurgical procedure for the recovery of Pt and Rh from spent automotive catalysts. Top. Catal. **16**, 419–423 (2001)

Bailey, O.H.: NO_x Adsorbers for diesel applications: general considerations and operational issues. Diesel Net Technical report, ASEC Manufacturing (1997)

Benson, M., Bennett, C.R., Harry, J.E., Patel, M.K., Cross, M.: The recovery mechanism of platinum group metals from catalytic converters in spent automotive exhaust systems. Resour. Conserv. Recycl. **31**, 1–7 (2000)

Ding, Y., Zheng, H., Li, J., Zhang, S., Liu, B., Ekberg, C.: An efficient leaching of palladium from spent catalysts through oxidation with Fe(III). Materials **12**, 1205 (2019)

DCL (2017). http://www.dcl-inc.com. Accessed 1 Oct 2017)

Fornalczyk, A: Analiza możliwości wykorzystania magnetohydrodynamiki do intensyfikacji odzysku platyny ze zużytych katalizatorów samochodowych. Wydawnictwo Politechniki Śląskiej, Gliwice (2016). (in Polish)

Hagelüken, C.: Markets for the catalyst metals platinum, palladium and rhodium. Metall **1–2**, 31–42 (2006)

Johnson Matthey (2019).http://www.platinum.matthey.com/. Accessed 21 Sept 2019
Kucharski, M.: Recykling metali nieżelaznych. Wydawnictwa AGH, Kraków (2010). (in Polish)
Malekian, H., Salehi, M., Biria, D.: Investigation of platinum recovery from a spent refinery catalyst with a hybrid of oxalic acid produced by *Aspergillus niger* and mineral acids. Waste Manage. **85**, 264–271 (2019)
Marafi, M., Stanislaus, A.: Waste catalyst utilization: extraction of valuable metals from spent hydroprocessing catalysts by ultrasonic-assisted leaching with acids. Ind. Eng. Chem. Res. **50**, 9495–9501 (2011)
Mazurek, K.: Removal of vanadium, potassium and iron from spent vanadium catalyst by leaching with citric acid at atmospheric pressure. Pol. J. Chem. Technol. **16**, 59–62 (2014)
McVicker, G.B., Carter, J.L., Murrell, L.L., Ziemiak, J.J.: Removal of metal contaminants from catalysts using buffered oxalic acid. US patent: 4522928 (1985)
Mišić, L., Kovačević, R., Gardić, V., Marković, R., Petrović, J.: Leaching process of platinum metals from spent autocatalysts. In: 17th International Research/Expert Conference on Trends in the Development of Machinery and Associated Technology, Istanbul, Turkey, pp. 169–172 (2013)
Rzelewska, M., Regel-Rosocka, M.: Wastes generated by automotive industry–spent automotive catalysts. Phys. Sci. Rev. **3**(8), 20180021 (2018)
Saguaru, C., Ndlovu, S., Moropeng, D.: A review of recent studies into hydrometallurgical methods for recovering PGMs from used catalytic converters. Hydrometallurgy **182**, 44–56 (2018)
Sarioğlan, Ş.: Recovery of palladium from spent activated carbon-supported palladium catalysts. Platin. Met. Rev. **57**, 289–296 (2013)
Saternus, M., Fornalczyk, A.: Zużyte katalizatory samochodowe jako źródło platynowców. Rudy Metale **54**(2), 59–67 (2009). (in Polish)
Shen, W., Li, T., Chen, J.: Recovery of hazardous metals from spent refinery processing solid catalyst. Procedia Environ. Sci. **16**, 253–256 (2012)
Sinisalo, P., Lundström, M.: Refining approaches in the platinum group metal processing value chain—a review. Metals **8**, 203 (2018)
Suiter, J.: Al_2O_3 Oxide Morphology for Two Fe-Cr-Al Stainless Steel Foils Used in Gasoline Engine Catalytic Converters (2012). http://digitalcommons.calpoly.edu/cgi/viewcontent.cgi?article=1068&context=matesp
Suoranta, T., Zugazua, O., Niemelä, M., Perämäki, P.: Recovery of palladium, platinum, rhodium and ruthenium from catalyst materials using microwave-assisted leaching and cloud point extraction. Hydrometallurgy **156**, 56–62 (2015)
Trinh, H.B., Lee, J.C., Srivastava, R.R., Kim, S., Ilyas, S.: Eco-threat minimization in HCl leaching of PGMs from spent automobile catalysts by formic acid prereduction. ACS Sustain. Chem. Eng. **58**, 7302–7309 (2017)
Umicore Precious Metals Refining (2009). http://www.umicore.com/storage/migrate/2009sept_PMR.pdf
Upadhyay, A.K., Lee, J., Kim, E., Kim, M., Kim, B.S., Kumar, V.: Leaching of platinum group metals (PGMs) from spent automotive catalyst using electro-generated chlorine in HCl solution: Leaching of platinum group metals from spent automotive catalyst. J. Chem. Technol. Biotechnol. **88**, 1991–1999 (2013)
Wolak, P.: Motoryzacja a środowisko. Otwarty Uniwersytet Ekonomiczny (2008). (in Polish)
Wołowicz, A.: Zastosowanie palladu i jego związków ze szczególnym uwzględnieniem katalizy. Przem. Chem. **92**(7), 1237–1245 (2013). (in Polish)
Zeng, L., Cheng, C.Y.: A literature review of the recovery of molybdenum and vanadium from spent hydrodesulphurisation catalysts: part I: metallurgical processes. Hydrometallurgy **98**, 1–9 (2009)

Risk Assessment in Process Industries Using Fuzzy Logic Approach

Dorota Siuta[1(✉)], Agata Kotynia[2], Bożena Kukfisz[3], and Waldemar Szaferski[4]

[1] Safety Engineering Department, Faculty of Process and Environmental Engineering, Lodz University of Technology, Lodz, Poland
dorota.siuta@p.lodz.pl
[2] BHP Consulting, Warsaw, Poland
[3] Faculty of Security Engineering and Civil Protection, The Main School of Fire Service, Warsaw, Poland
[4] Institute of Chemical Technology and Engineering, Faculty of Chemical Technology, Poznan University of Technology, Poznan, Poland

Abstract. Process risk assessment is the most effective way to design safety and security safeguards in order to ensure the safety of people and the environment. The key issue is to estimate the frequency of occurrence and consequences as well as the risk of major accident scenarios with the lowest level of uncertainty. In order to deal with all knowledge-based uncertainties a new process risk assessment methodology based on fuzzy logic was proposed. The methodology utilized the fuzzy representative loss events selection model, the fuzzy bow-tie model and the fuzzy risk matrix. The case study for isobutane storage tank was used to illustrate the proposed methodology. Preliminary tests confirmed that final results of the risk index of accident scenarios were determined in a more precise and realistic manner and more appropriate selection of safety systems can be achieved.

1 Introduction

Intensive development of new manufacturing technologies, the use of hazardous materials, more complicated installations and extreme process conditions have resulted in a series of major incidents and accidents in recent years. These events have led to massive loss of human life, environmental damage and economic loss. At present, the total elimination of potential hazards and their consequences is not possible in chemical industries (Markowski and Siuta 2013). Therefore, it is vital to carry out risk assessment in process plants, especially that nowadays such assessment is legally required in different countries as a way to quantify risk as a probability distribution function of the occurrence and consequences of major accident scenarios. Risk assessment provides a basis for identifying, evaluating, defining and justifying the selection or rejection of risk reduction measures. Numerous risk assessment techniques, including qualitative, quantitative, and semiqualitative approaches, have been developed. The hazard and operability study (HAZOP), fault tree analysis (FTA), event tree analysis (ETA), bow-tie (BTA), layer of protection analysis (LOPA), and failure model effect criticality

© Springer Nature Switzerland AG 2020
M. Ochowiak et al. (Eds.): PAIC 2019, *Practical Aspects of Chemical Engineering*, pp. 401–411, 2020.
https://doi.org/10.1007/978-3-030-39867-5_42

analysis (FMECA), fire and explosion index (F&EI) (Mitkowski and Bal 2015) are the most popular risk assessment methods used in the chemical process industry. However, these techniques are static by nature and ineffective in handling uncertainties (Zarei, Khakzad, Cozzani, and Reniers 2019; Khan, Rathnayaka, and Ahmed 2015). Uncertainties in the process of risk analysis are associated with incomplete and ambiguous knowledge concerning mainly data and reliability models necessary to determine the frequency of the accident scenario and associated with the assumptions and parameters used to assess their consequences. To help in risk assessment conventional techniques account for uncertainties in a more efficient way, some authors have combined conventional techniques with Bayesian network (Pasman and Rogers 2012), Petri nets (Nivolianitou et al. 2004), Monte Carlo approach (Siuta et al. 2013), evidence theory (Dutta 2015), and rough sets. One promising method for dealing with uncertainties concerning the lack of knowledge in process safety assessment is fuzzy logic. Fuzzy logic is a form of multi-valued logic derived from the fuzzy set theory. This method provides a natural way of dealing with problems in which the source of imprecision is the absence of sharply defined criteria of class membership rather than the presence of random variables. The main advantage of such a method is the use of qualitative human knowledge and mapping it into quantitative and much more precise values. Fuzzy logic has found a number of applications in different stages of reliability and risk assessment (Mangeli, Shahraki, and Saljooghi 2019; Renjith et al. 2018; Hong et al. 2016; Wu et al. 2013). However, these studies did not involve process risk assessment methodology based on the fuzzy representative loss events selection model, fuzzy bow-tie model and fuzzy risk matrix for proper calculation of the risk index, and more appropriate selection of safety systems.

2 Proposed Risk Assessment Methodology Based on Fuzzy Logic Approach

The process risk assessment methodology based on fuzzy sets approach is divided into five parts: systems and hazards identification i.e. identifying the events that may have adverse effects on systems; representative accidental events selection using the fuzzy risk ranking model described in (Markowski and Siuta 2017); likelihood estimation of accident scenarios using the fuzzy "bow—tie" model shown in (Markowski and Kotynia 2011); consequence estimation of accident scenarios based on fuzzy consequence model presented in (Siuta et al. 2013); and risk characterization based on the fuzzy risk matrix shown in (Markowski et al. 2010).

Calculations using proposed methodology were carried out on the basis of principles and stages of the fuzzy logic system such as fuzzification, fuzzy inference process and defuzzification. For the proposed methodology a Mamdani fuzzy inference algorithm was applied along with a Max method for the aggregation step and a centroid method for the defuzzification. In case of frequency calculations using the fuzzy bow-tie model, the inference process was implemented on the basis of expert knowledge and mathematical calculation. The case study for isobutane storage tank was used to illustrate the methodology. Results obtained using fuzzy logic approach were compared to traditional risk assessment methodology.

3 Case Study

Storage installation for isobutane (Fig. 1) was used as a case study to demonstrate the application of the proposed methodology. Installation includes three spherics pressure isobutane vessels the capacity of 300 m^3 each, pumps system, heaters and appropriate connecting pipelines. Safety and protection systems of the installation divided into three layers: prevention, protection and mitigation are shown in Table 1.

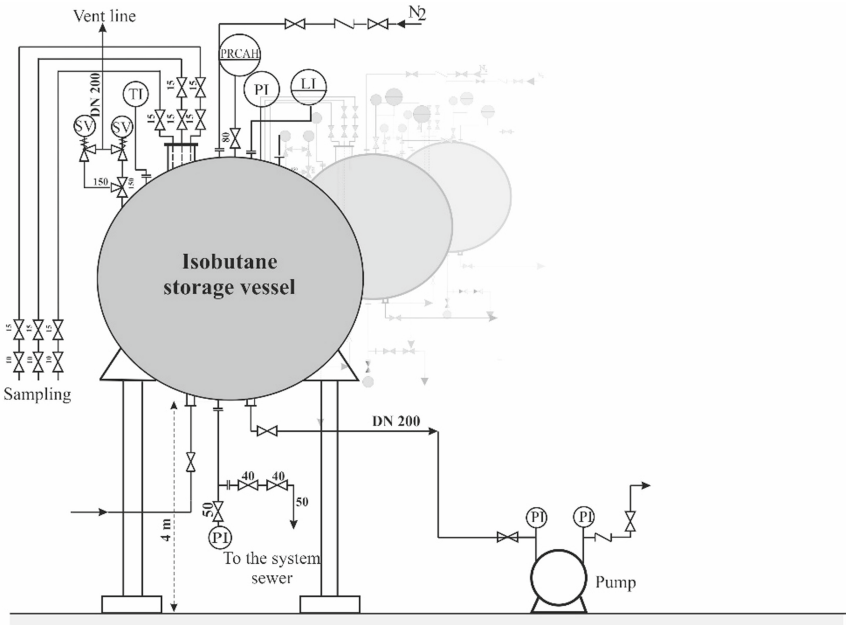

Fig. 1. Isobutane storage installation

Table 1. Safety and protection systems for isobutane storage installation

Safety layer	Measure
Layer I – prevention systems	Good engineering practice (GEP) Maintenance and inspections Basic Process Control Systems (BPCS) in central room: LI, TI, PI & PRCAH
Layer II – protection systems	Pressure safety valves with vent line Dike
Layer III – mitigation systems	Deluge system Fire brigade (FB)

The method presented in publication (Markowski and Siuta 2017) was used to select representative accidental events (RAE). Hazard and operability analysis revealed six accidental events (AE). The fuzzy and classical initial risk indicators of AEs were calculated and are presented in Table 2.

Table 2. List of accidental events for isobutane storage vessel

Accidental events	Traditional risk ranking index (R)	Fuzzy risk ranking index (R_f)
1. Catastrophic rupture of the isobutane tank	4 (NA)	3.87 (13% TNA, 87% NA)
2. Tank over-pressurization and release from the pressure relieve valve	4 (NA)	3.76 (24% TNA, 76% NA)
3. Rupture of the inlet line	2 (TA)	2.41 (59% TA, 41% TNA)
4. Release of isobutane from the inlet line (failure of valve, flange packing, seal leakage in pumps)	2 (TA)	2.67 (33% TA, 67% TNA)
5. Release of isobutane from the outlet line (failure of valve, flange packing)	2 (TA)	2.67 (33% TA, 67% TNA)
6. Thermal expansion	1 (A)	1.38 (62% A, 38% TA)

It was assumed that all accidental events for which the fuzzy risk ranking index is higher than "R, $R_f > 2$" were classified as a representative accidental event. Two representative accident scenarios (1, 2) were identified using the traditional risk ranking index. In case of fuzzy approach the five representative accident scenarios (1, 2, 3, 4, 5) should be selected. For simplification one accidental event named the catastrophic release from storage tank of isobutane was selected as a representative loss event. As can been seen in Table 2, the advantage of the fuzzy model consists in a more precise selection of the RAEs from the list of accidental events compared to the traditional approach. The contribution of each initial risk index represented by fuzzy sets (A - acceptable, TA - tolerable-acceptable, TNA - tolerable-unacceptable and NA - unacceptable) to the total value of initial risk ranking index is also evident. Bow-tie (BT) model used for the representative loss event scenario (LES) is shown in Fig. 2.

The minimal cut sets equations of the top event (TE) and two outcome events (OEs) in which fatalities can occur obtained from the bow-tie model are as follows (Eq. 1–3)

$$\sum MCS_{TE} = AD + BD + CD + AE + BE + CE \tag{1}$$

$$\sum MCS_{OE1} = TE \cdot II \cdot CE \tag{2}$$

$$\Sigma\ MCS_{OE2} = TE \cdot \overline{II} \cdot LI \cdot CE \tag{3}$$

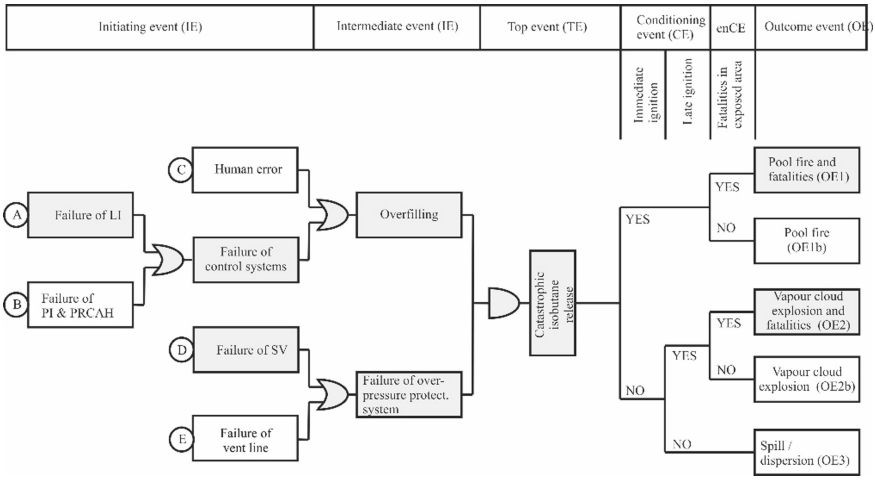

Fig. 2. Bow- tie model for a representative loss event scenario

Frequency calculation with the use of fuzzy logic is performed based on the fuzzy frequency sets scale (Fig. 3) for initiating events (IEs), safety functions (SF) and in a form of traditional variables for conditioning events (CEs) which are given in Table 3.

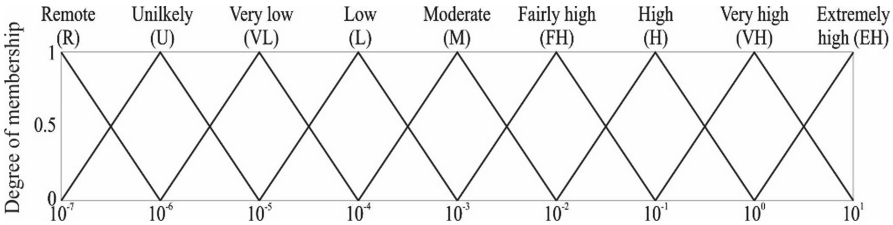

Fig. 3. Fuzzy numbers frequency scale established for a bow-tie model

Table 3. Traditional probability values for conditioning events

Symbol	Conditioning event (CE)	Probability value
II	Immediate ignition	0.1
LI	Late ignition	0.5
Enabling CE	Staff in affected area	0.1
	Fatalities	0.5

Fuzzy numbers for the representative loss event scenario concerning the catastrophic release from storage tank of isobutane are chosen by experts from the fuzzy numbers scale and are shown in Table 4. Traditional frequency/probability values of

initiating events and failure of safeguards were proposed by LOPA authors (CCPS 2014, 2015).

Table 4. Fuzzy numbers and traditional values for IE frequency (F)/probability (P) used in this study

Symbol	A	B	C	D	E
IE	LI failure	PI failure	Human error	PSV failure	Vent line failure
F [1/yr]/P	F	F	F	P	P
Fuzzy number	H	H	FH	FH	FH
Traditional value	10^{-1}	10^{-1}	10^{-2}	10^{-2}	10^{-2}

Calculations of fuzzy sets according to the minimal cut sets Eqs. (1–3) follow the fuzzy algebra principles. The cases in which there are no losses are not taken into consideration. The combined frequency is calculated for the paths where fatalities occur. Table 5 presents results of fuzzy frequency calculations of top event and outcome events. Table 6 shows results of traditional frequency calculations.

Table 5. Results of fuzzy frequency calculations for accident scenario

Symbol	Event		Fuzzy set		Crisp value
		Left boundary value	Mean value	Right boundary value	
TE	Isobutane storage tank rupture	4.20E-05	4.20E-03	4.20E-01	7.85E-03
OE1	Pool fire and fatalities	2.10E-07	2.10E-05	2.10E-03	3.92E-05
OE2	Vapour cloud explosion and fatalities	9.45E-07	9.45E-05	9.50E-03	1.80E-04
OE	Combined consequences (OE1 + OE2)	1.16E-06	1.16E-04	1.16E-02	2.19E-04

Table 6. Results of traditional frequency calculations for accident scenario

Symbol	Event	Traditional value
TE	Isobutane storage tank rupture	4.20E-03
OE1	Pool fire and fatalities	2.10E-05
OE2	Vapour cloud explosion and fatalities	9.45E-05
OE	Combined consequences (OE1 + OE2)	1.16E-04

Calculations of the severity of consequences of an accident scenario are made in accordance with the methodology proposed by Markowski et al. 2010 based on the flash point of the substance and its released amount. For the LES the quantity of isobutane released during tank rupture is the whole tank capacity (178000 kg). To assess the severity of the consequences of LES fuzzy logic system was applied. Surfaces for the severity of the consequences are illustrated in Fig. 4. Table 7 presents results of fuzzy and traditional severity of the calculation of consequences.

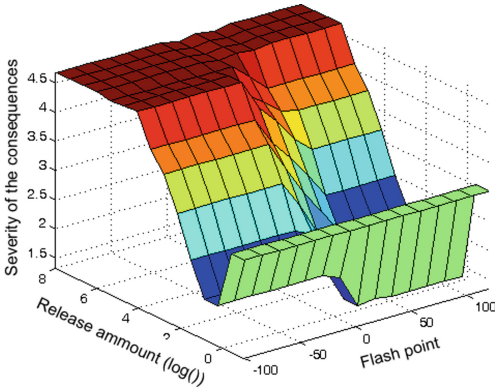

Fig. 4. Fuzzy surface for the calculation of the severity of consequences

Table 7. Results of the calculations of the severity of consequences

Isobutane			Severity of the consequences	
Symbol	Flash Point [^{0}C]	Released quantity [kg]	Fuzzy logic calculations	Traditional calculations
LES	−60	178 000	4.66	5

To determine the risk of representative accident scenarios, the frequency with safeguards and the severity of the consequences were taken into account. These crisp values of frequency and the severity of consequences were introduced into the fuzzy risk matrix. Figure 5 presents a three-dimensional plot which shows the relationship between frequency, severity of consequences and risk obtained by the mapping from two inputs (fuzzy frequency and severity) to one output (fuzzy risk).

Results of the final risk calculations are shown in Table 8. A defuzzified crisp value (3.37) belongs to two risk sets – TNA (tolerable not acceptable) and NA (not acceptable) as shown in Fig. 6. It informs that additional safety measures are required to make the analysed installation safe. The safety goal requires at least 75% of TA (tolerable acceptable) fuzzy set and no more than 25% of TNA fuzzy set.

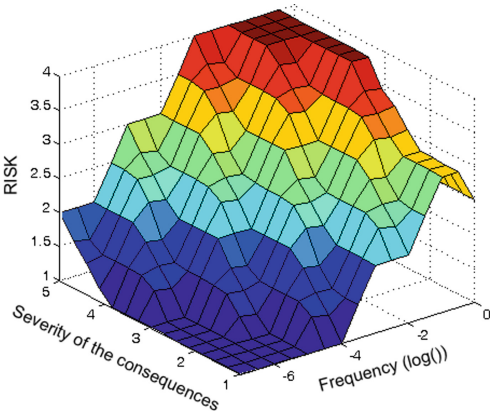

Fig. 5. Fuzzy risk surface used for risk assessment of accident scenario

Table 8. Risk index calculation results

Frequency calculation method	Outcome event	Crisp value/traditional value			Membership of risk set
		Frequency	Consequences	Risk	
Fuzzy logic	Combined consequences (OE1 + OE2)	2.19E-04	4.66	3.37	TNA – 63%, NA – 37%
Traditional calculations		1.16E-04	5	NA	–

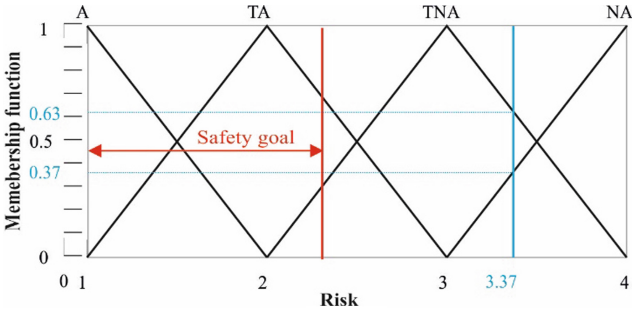

Fig. 6. Crisp risk value membership to fuzzy risk sets

One of the ways to increase the safety of installations is to reduce the frequency of the occurrence of an accident scenario through the use of effective safeguard systems operating at independent safeguard levels. These additional safeguards may consist in introducing other technical or organizational solutions or increasing the reliability of existing systems by adding additional devices or replacing the existing ones. In this case in order to reach the safety goal additional safety measures need to be applied. One

way to minimalize the risk level an additional level control system with high level alarm (I layer of protection), LAH, can be proposed. Another way to reduce the risk level is to increase the reliability of applied PI & PRCAH system from about 10^{-1}/yr to about 10^{-2}/yr. The third option to improve safety can be vocation of an internal fire brigade. The effectiveness and the promptness of firefighting and rescue operations can reduce severity of the consequences (III layer of protection). Table 9 presents results of fuzzy frequency, severity of the consequences (C) and risk of the loss event scenario calculations. Case I is an option with additional LAH having an impact on frequency. Case II is an option with more reliable PI & PRCAH system. Case III is an option with vocation of FB having an impact on severity of the consequences. Case IV is an option with all of above mentioned additional safety measures.

Table 9. Results after implementation of additional safety measures

Case no.	Additional safety measure	Frequency [1/yr]				C	Risk	Degree of membership to risk level
		Left boundary value	Mean value	Right boundary value	Crisp value			
I	LAH	6.11E-08	6.60E-06	1.16E-03	1.72E-05	4.66	2.63	TA-37% TNA-63%
II	PI & PRCAH	6.60E-07	6.60E-05	6.60E-02	1.22E-04	4.66	3.13	TNA-87% NA-13%
III	FB	1.16E-06	1.16E-04	1.16E-02	2.19E-04	4.18	3.24	TNA-76% NA-24%
IV	All the above	1.16E-08	1.65E-06	6.60E-04	8.23E-06	4.18	2.22	TA-78% TNA-22%

Indeed, the application of all additional safety measures (case IV) enabled a significant reduction of the risk level. An acceptable level of risk is obtained. Attention should be paid to the first case (No. I), in which the proposed LAH system reduced the risk level by almost one level. However, the acceptable risk level is still exceeded (by 38%). Since the determination of the risk acceptance criteria is subjective, this solution can be considered during making decisions regarding the risk reduction. A cost-benefit analysis is suggested. In the second (No. II) and third (No. III) cases, the application of the proposed safety measures reduced the risk level only to a small extent - by less than one level. These propositions are not sufficient to ensure the safety of installations.

4 Conclusions

A new process risk assessment methodology based on fuzzy logic was proposed in this study. The advantage of the proposed methodology lies in a more precise selection of representative events from the list of accidental events with available data and expert judgments compared to what would have been possible using the traditional approach.

In addition, it provides a better assessment of the accident scenario, proper calculation of the risk index and a more optimal selection of safety systems. A case study of the isobutane tank confirmed that the contribution of each fuzzy set into the final result of risk level is clear, that it may help in understanding the uncertainties and provide a better insight into the selection of preventive and mitigating safety strategies in process plants.

References

Center for Chemical Process Safety, CCPS: Guidelines for Enabling Conditions and Conditional Modifiers in Layers of Protection Analysis. American Institute of Chemical Engineers, New York (2014)

Center for Chemical Process, CCPS: Guidelines for Initiating Events and Independent Protection Layers in Layer of Protection Analysis. American Institute of Chemical Engineers, New York (2015)

Dutta, P.: Uncertainty modeling in risk assessment based on dempster-shafer theory of evidence with generalized fuzzy focal elements. Fuzzy Inf. Eng. **7**, 15–30 (2015). https://doi.org/10.1016/j.fiae.2015.03.002

Hong, Y., Pasman, H.J., Sachdeva, S., Markowski, A.S., Mannan, M.S.: A fuzzy logic and probabilistic hybrid approach to quantify the uncertainty in layer of protection analysis. J. Loss Prev. Process Ind. **43**, 10–17 (2016). https://doi.org/10.1016/j.jlp.2016.04.006

Khan, F., Rathnayaka, S., Ahmed, S.: Methods and models in process safety and risk management: Past, present and future. Environ. Prot. Trans. Inst. Chem. Eng. Part B, Process Saf. (2015). https://doi.org/10.1016/j.psep.2015.07.005

Mangeli, M., Shahraki, A., Saljooghi, F.H.: Improvement of risk assessment in the FMEA using nonlinear model, revised fuzzy TOPSIS, and support vector machine. Int. J. Ind. Ergon. **69**, 209–216 (2019). https://doi.org/10.1016/j.ergon.2018.11.004

Markowski, A.S., Kotynia, A.: Bow-tie model in layer of protection analysis. Process Saf. Environ. Prot. **89**(4), 205–213 (2011). https://doi.org/10.1016/j.psep.2011.04.005

Markowski, A.S., Mannan, M.S., Kotynia (Bigoszewska), A., Siuta, D.: Uncertainty aspects in process safety analysis. J. Loss Prev. Process Ind. **23** (2010). https://doi.org/10.1016/j.jlp.2010.02.005

Markowski, A.S., Siuta, D.: Selection of representative accident scenarios for major industrial accidents. Process Saf. Environ. Prot. **111** (2017) https://doi.org/10.1016/j.psep.2017.08.026

Markowski, A.S., Siuta, D.: Application of fuzzy logic approach to consequence modeling in process industries. Chem. Eng. Trans. (2013). https://doi.org/10.3303/CET1331027

Mitkowski, P.T., Bal, S.K.: Integration of fire and explosion index in 3D process plant design software. Chem. Eng. Technol. **38**, 1212–1222 (2015). https://doi.org/10.1002/ceat.201400644

Nivolianitou, Z.S., Leopoulos, V.N., Konstantinidou, M.: Comparison of techniques for accident scenario analysis in hazardous systems. J. Loss Prev. Process Ind. **17**, 467–475 (2004). https://doi.org/10.1016/j.jlp.2004.08.001

Pasman, H.J., Rogers, W.J.: Risk assessment by means of Bayesian networks: a comparative study of compressed and liquefied H2transportation and tank station risks. Int. J. Hydrogen Energy **37**, 17415–17425 (2012). https://doi.org/10.1016/j.ijhydene.2012.04.051

Renjith, V.R., Jose kalathil, M., Kumar, P.H., Madhavan, D.: Fuzzy FMECA (failure mode effect and criticality analysis) of LNG storage facility. J. Loss Prev. Process Ind. (2018). https://doi.org/10.1016/j.jlp.2018.01.002

Siuta, D., Markowski, A.S., Mannan, M.S.: Uncertainty techniques in liquefied natural gas (LNG) dispersion calculations. J. Loss Prev. Process Ind. **26** (2013). https://doi.org/10.1016/j.jlp.2012.07.020

Wu, W., Cheng, G., Hu, H., Zhou, Q.: Risk analysis of corrosion failures of equipment in refining and petrochemical plants based on fuzzy set theory. Eng. Fail. Anal. **32**, 23–34 (2013). https://doi.org/10.1016/j.engfailanal.2013.03.003

Zarei, E., Khakzad, N., Cozzani, V., Reniers, G.: Safety analysis of process systems using Fuzzy Bayesian Network (FBN). J. Loss Prev. Process Ind. **57**, 7–16 (2019). https://doi.org/10.1016/j.jlp.2018.10.011

Adsorption of Phosphates on Modified Eggshells - Batch and Fixed-Bed Column Process

Dawid Skrzypczak[1(✉)], Katarzyna Mikula[1], Daria Kocek[2], Grzegorz Izydorczyk[2], Rafał Taf[2], and Anna Witek-Krowiak[1]

[1] Department of Chemical Engineering, Faculty of Chemistry, Wroclaw University of Science and Technology, Wrocław, Poland
dawid.skrzypczak@pwr.edu.pl
[2] Department of Advanced Material Technologies, Faculty of Chemistry, Wrocław University of Science and Technology, Wrocław, Poland

Abstract. The aim of this study was to develop a method for removing phosphate from an aqueous solution using iron (III) chloride-modified eggshells. The physicochemical properties of the modified biomass (FTIR, pH_{PZC}) were examined. The sorption capacity of the modified sorbents was tested. The kinetic rate constant was determined using the general model and equals 1.82 10^{-10} min^{-1}. The maximum sorption capacity of modified eggshells was determined using the Langmuir model (Q_{max} = 42.3 mg g^{-1}). Kinetic experiments were also carried out in a fixed-bed column. To establish the adsorption parameters in the bed column, the Thomas, Yoon-Nelson, and MDR models were used to describe the experimental data. The maximum sorption capacity in the column was 58.4 mg g^{-1}. Based on the result, modified eggshells could be used in the future as an effective sorbent for removing phosphate ions from aqueous solutions.

1 Introduction

Phosphorus is essential for the biological growth of plants and animals. It is not a building block of proteins, but none of these structures could be produced without its participation. Due to high-energy, reversible phosphorus binding, the process of transition from adenosine diphosphate (ADP) to adenosine triphosphate (ATP) is a "fuel" for reactions occurring inside cells. Phosphorus is also used in the production of fertilizers and various types of detergents, which is the reason for the growing share of this biogenic element in wastewater.

The largest part of total phosphorus in raw wastewater is orthophosphates, with as much as 20 to 50%. They most often occur in the form H_2PO_4- and H_2PO4^2. Polyphosphates, as well as organic phosphorus, are another significant part (Przywara 2014). Too high phosphate levels in the aquatic environment may lead to excessive proliferation of blue-green algae, which have a high oxygen demand. The uncontrolled multiplication of anaerobic organisms causes the formation of lake silt, which results in a slow shallowing the water reservoir and its transformation into a swamp or bog.

© Springer Nature Switzerland AG 2020
M. Ochowiak et al. (Eds.): PAIC 2019, *Practical Aspects of Chemical Engineering*, pp. 412–422, 2020.
https://doi.org/10.1007/978-3-030-39867-5_43

This can create a huge threat to fish, algae and other aquatic organisms, as well as infect water with various parasites. (Nguyen et al. 2014). This phenomenon is called eutrophication and promotes the growth of cyanobacteria, which produce a dangerous toxin - microcystin. After entering the human body, this substance can cause extremely dangerous hepatocellular carcinoma (Ye et al. 2017).

There are many methods of phosphate removal from wastewater like electrocoagulation, chemical precipitation, biological methods of removal, but they are uneconomical or require continuous process control (Hoon 2012). An alternative method to remove phosphate from aqueous solutions is adsorption. The process of adsorption occurs mainly on the surface of biomass, which means that its modification can significantly increase sorption possibilities. Before making any modifications, one should be extremely careful with the selection of substances, because some can cause serious losses of adsorbent mass, as well as damage to its structure, or a decrease in adsorbent capacity. Better adsorbents can be obtained by strengthening or modifying functional groups present on the surface. Biomass may also have adsorption inhibiting groups on the surface, which, in this case, would have to be removed, which would facilitate the process (Park et al. 2010).

This paper presents the possibility of removing phosphates from an aqueous solution with eggshells modified with iron(III) chloride using adsorption processes. Studies on the physicochemical properties of the adsorbent (FTIR) were carried out. Sorption properties of materials (equilibrium, process kinetics) were tested. A fixed-bed column process was also carried out.

2 Materials and Methods

2.1 Materials

Eggshells (EG) were obtained from a local producer. The adsorbent was washed several times with distilled water to remove various impurities and then dried in an oven at 40 °C for 24 h. EG were crushed and sieved into various fractions. Iron (III) chloride CHEMPUR ($FeCl_3 \cdot 6\ H_2O$- 270.3 g/mol) was used for eggshells modification. Potassium dihydrogen phosphate POCH (KH_2PO_4 - 136.09 g/mol) was used to prepare solutions containing appropriate concentrations of phosphate ions by dissolving it in distilled water. Phosphate Test SPECTROQUANT HC554346 (o - phosphate) was used to determine the phosphate content. Phosphate concentration measurements were performed on a THERMO SCIENTIFIC - EVOLUTION 201 spectrophotometer (UV - Visible Spectrophotometer).

2.2 Modification of Adsorbents

0.2 dm^3 of the solution thus prepared was taken into the cylinder, and 20 g of iron(III) chloride was added. 10 g of EG was added to the mixture, which had been previously cleaned and comminuted. The flask was placed on a magnetic stirrer and stirred

for 1.5 h. After this time, the NaOH solution (2 M) was added dropwise to adjust pH 5. After this operation, the solution was filtered, and the obtained adsorbent was dried in an oven for 24 h.

2.3 Characteristics of Biomass

Functional group analysis (Fourier infrared transformation) was performed using the PERKIN-ELMER SYSTEM 2000 FT-IR apparatus. The spectrum was recorded in infrared in the range 3500-500 cm^{-1}.

2.4 Kinetics and Equilibrium Studies

2.4.1 Kinetics

A solution containing 90 mg dm^{-3} of PO_4^{3-} ions (2 dm^3) was prepared. Then 0.15 g of EG modified with hydrated iron(III) chloride was weighed and poured into the previously prepared solution. The vessel was placed on a magnetic stirrer, and samples were taken at 24-hour intervals.

2.4.2 Equilibrium

A solutions containing 5, 10, 20, 50, 75 and 90 mg dm^{-3} PO_4^{3-} ions with pH 5 were prepared. Next, 0.1 g of EG modified with hydrated iron(III) chloride was weighed into six flasks, and then 0.1 dm^3 of previously prepared solutions were measured and poured into flasks. The prepared mixtures were placed on a shaker and left for 24 h. After this time, it was filtered, and samples were taken.

2.5 Adsorption on a Fixed-Bed Column

A mesh was inserted at the bottom of the column to prevent packing from falling out, then 1 cm glass balls (2 mm) were placed, onto which a 2 cm bed composed of iron(III) chloride shells were placed. It was covered with an insulating mesh and another 1 cm glass balls. The solution containing PO_4^{3-} ions was fed to the column using a peristaltic pump at a rate of 3.75 ml min^{-1}. Samples were taken during the process for 24 h.

3 Results and Discussion

3.1 Characteristics of the Biomass

The adsorbent surface before and after modification is shown in Fig. 1 a, b. It can be seen that hydrated iron(III) oxides precipitated on the surface of the adsorbents during the modification.

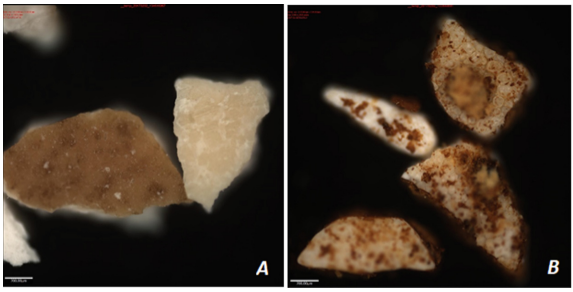

Fig. 1. Eggshells before (A) and after (B) modification with iron(III) chloride

3.1.1 Fourier Infrared Transformation (FTIR)

To examine the surface characteristics of adsorbents, FT-IR analysis was performed for modified EG before and after phosphate ion adsorption. Figure 2 presents the spectra of adsorbents before and after the process. The presence of given functional groups on the surface is closely related to the respective wavelengths in the spectrum.

The presented spectra show that for wavelengths above 3000 [1 cm^{-1}] a significantly larger peak is shown by modified EG with bound PO_4^{3-} ions, which indicates a much higher occurrence of - H stretching groups on the surface than in the case of modified EG before adsorption. Analogous observations can be made up to the wavelength range 3000–1200, where on the adsorbent surface after the process there is a much larger number of C - H stretching groups, C = H stretching and C - O stretching groups. This indicates that the carboxyl groups present on the adsorbent surface have a very important role in binding phosphate ions. At lower wavelengths, a larger peak exhibits the adsorbent before carrying out the process. Namely, within the waves of 400–1200 [1 cm^{-1}], where these waves are responsible for the occurrence of stretching groups C - O, - OH and C - C, as well as for bending groups O - C - O.

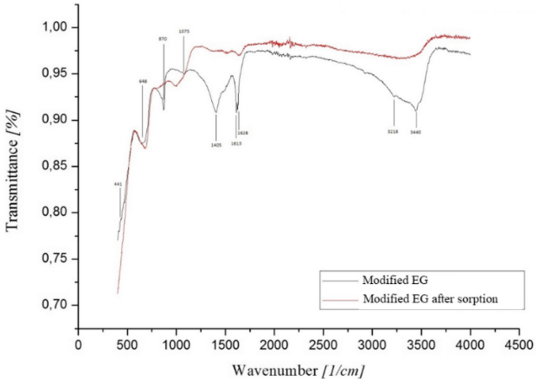

Fig. 2. FTIR spectrum for modified EG before and after phosphate ions adsorption

3.2 Kinetics and Equilibrium

3.2.1 Equilibrium

To optimize the phosphate removal process from aqueous solutions, it is extremely important to determine the balance of adsorption. Therefore, it was decided to base on two main mathematical models, namely the Langmuir isotherm Eq. (1) (Pastoriza-Santos and Liz-Marzán 1999) and the Freundlich isotherm Eq. (2) (Freundlich 1907):

$$Q_e = \frac{Q_{max}^t \cdot K_L \cdot C_e}{1 + K_L \cdot C_e} \tag{1}$$

$$Q_e = K_F \cdot C_e^{1/n_F} \tag{2}$$

where: Q_e - equilibrium adsorbents capacity [mg g^{-1}], Q_{max} - maximum sorption capacity of the sorbent [mg g^{-1}], K_L - constant in Langmuir's equation [dm^3 mg^{-1}], C_e - equilibrium phosphate concentration in solution [mg dm^{-3}], K_F - constant in Freundlich's equation [(mg g^{-1})·(dm^3 mg^{-1})1 n^{-1}], n_F - constant in Freundlich's equation.

To determine the equilibrium parameters of the process, diagrams of the adsorbent sorption capacity dependence on the phosphate concentration in the aqueous solution at equilibrium were drawn (Fig. 3). The equilibrium process parameters obtained from non-linear regression are shown in Table 1.

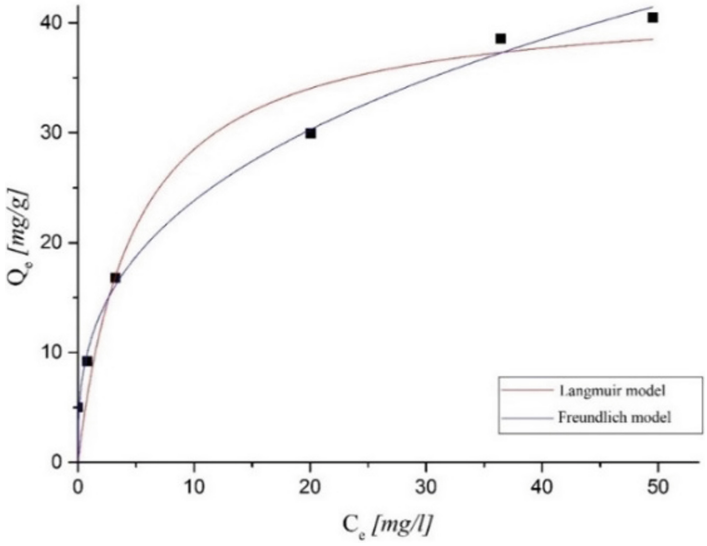

Fig. 3. Equilibrium of removal PO_4^{3-} ions (dashed line: Langmuir and Freundlich models; T:20 °C; sorbent dosage: 100 mg dm^{-3}; contact time: 48 h; pH:5; C0: 5–90 mg dm^{-3})

Table 1. Parameters obtained by non-linear regression – isotherm

Langmuir's model		Freundlich's model	
Q_{max} [mg·g^{-1}]	42.3	K_F [dm^3·mg^{-1}]	10.7
K_L [dm^3·mg^{-1}]	0.207	n_F	2.89
R^2	0.989	R^2	0.968

The adsorption isotherm expresses the specific relationship between the adsorbate concentration and its accumulation on the adsorbent surface at a constant temperature. As mentioned before, two models were used to describe the obtained experimental data - Langmuir and Freundlich models. The correlation coefficient R^2 was used to assess the fit of the respective model. For the process carried out using EG modified with hydrated iron(III) chloride, it was shown that the experimental data is best described by the Freundlich equation. Thus, in this case, most likely, it is a heterogeneous surface, and the adsorption process itself is multilayered. A slightly smaller R^2 coefficient, in this case, was obtained by fitting the Langmuir isotherm model, but the value of the maximum adsorption capacity (42.3 mg g^{-1}) is very close to the set value (40.47 mg g^{-1}). For comparison, Table 2 shows the maximum adsorption capacity of phosphate ions of selected adsorbents.

Table 2. The maximum adsorption capacity of phosphate ions on selected adsorbents

Lp.	Adsorbent	Q_{max} [mg g^{-1}]	Reference
	Zirconium-loaded reduced graphene oxide	27.7	(Luo et al. 2016)
	Zirconium/aluminum-pillared montmorillonite (Zr/Al-Mt)	17.2	(Huang et al. 2015)
	La-doped vesuvianite	6.7	(Li et al. 2016)
	Al-pillared bentonite	12.7	(Yan et al. 2010)
	Fe-pillared bentonite	11.2	(Dai et al. 2011)
	Aluminum pillared clays (Al-PILC)	10.3	(Tian et al. 2009)
	Lanthanum/aluminum pillared clays (LaAl-PILC)	13.0	(Wang et al. 2016)
	Montmorillonite	20.5	(Kasama et al. 2004)
	Beidellite	24.5	(Kasama et al. 2004)
	Saponite	25.1	(Kasama et al. 2004)
	Fluor-tetrasilicic expandable mica pillared with Keggin ion-like Al clusters	27.0	(Kasama et al. 2004)
	Dolomite	4.76	(Yuan et al. 2015)
	Magnetic diatomite clay (MDC)	11.9	(Chen et al. 2016)
	Magnetic illite clay (MIC)	5.48	(Chen et al. 2016)
	Eggshells (without modification)	13.1	(Guo et al. 2017)
	Eggshells modified $FeCl_3$	**42.4**	**This research**

3.2.2 Kinetics

Two equations are used to describe the rate of adsorption reaction, which take into account the order of the reaction, namely pseudo-first and pseudo-second-order, and the kinetic equation for the generalized model. The pseudo-first kinetic model is the Lagergren Eq. (3) (Lagergren 1898). It assumes that adsorption is preceded by diffusion through the boundary layer (Wänke et al. 2001):

$$\frac{dQ_t}{dt} = k_1^{'} \cdot (Q_e - Q_t) \tag{3}$$

where: Q_t - sorption capacity that changes over time [mg g^{-1}], t – time [min], k_1'- reaction rate constant [1 s^{-1}].

The pseudo-second kinetic model, which assumes that the process takes over the mechanism of chemisorption is the Blanchard model (4) (Dubey and Mishra 2016):

$$\frac{dQ_t}{dt} = k_2^{'} \cdot (Q_e - Q_t)^2 \tag{4}$$

where: k_2' - reaction rate constant [dm^3 mol min^{-1}].

Because the adsorption process very rarely occurs according to the chemisorption or physical adsorption itself, a general rate raw kinetic model (5) (Park et al. 2010) is very often used, which assumes a mixed process mechanism:

$$\frac{dQ_t}{dt} = k_n \cdot (Q_e - Q_t)^n \tag{5}$$

where: k_n – n-th order reaction rate constant, n - reaction order.

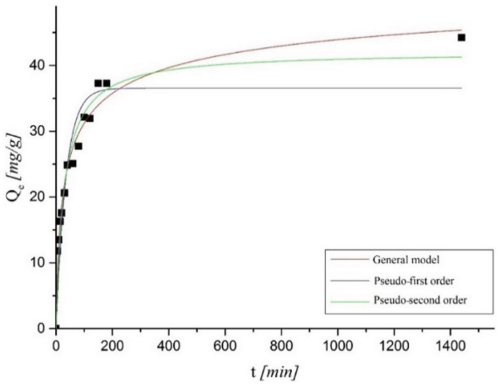

Fig. 4. Kinetics of removal of PO_4^{3-} ions by modified EG (dashed line: pseudo-first-order equation, pseudo-second-order equation, and general rate law equation model) (T:20 °C; sorbent dosage 75 mg dm^{-3}; contact time: 24 h; pH:5; C0: 90 mg dm^{-3})

The kinetics of the sorption process is shown in Fig. 4. The kinetic process parameters obtained from non-linear regression are shown in Table 3.

Table 3. Kinetic process parameters obtained from non-linear regression

Pseudo- first order		Pseudo- second order		General model	
Q_e [mg·g^{-1}]	36.2	Q_e [mg·g^{-1}]	41.7	Q_e [mg·g^{-1}]	63.8
k'_1 [min^{-1}]	0.029	k'_2 [min^{-1}]	8.590E-04	k′ [min^{-1}]	1.820E-10
				n	5.64
R^2	0.863	R^2	0.947	R^2	0.974

The graph shows that the adsorption rate is the highest in the first 120 min of contact with the adsorbent with phosphate ions. This is probably due to the large concentration difference, which is also the driving force of the process. The process stabilizes after about 200 min but does not yet reach equilibrium. Pseudo-first and pseudo-second kinetics models did not satisfactorily match the experimental data, so it can be concluded that the process does not occur only through the mechanism of chemisorption or physical adsorption. The R^2 correlation shows that the best fit was obtained using a general rate model that assumes that adsorption occurs according to complex mechanisms.

3.3 Fixed Bed Column

Experimental determination of the adsorption efficiency in a fixed-bed column, under various conditions, is extremely expensive; however, mathematical models have been developed that allow predicting the effectiveness of this process. Three mathematical models were used to determine process parameters: the Thomas model (6) (Riazi et al. 2016), the Yoon-Nelson model (7) (Martín-Lara et al. 2013) and the MDR model (8) (D. Rocha et al. 2015).

Thomas' model is one of the most general and widely used to assess column performance. The assumption of this theory is the lack of external and internal diffusion resistance. Thomas's model assumes no axial dispersion, as well as a constant flow rate of the solution in the bed column. Also, it fixed-bed that the description of equilibrium settling follows the Langmuir isotherm, and the reaction rate describes the equation of the secondary, reversible reaction kinetics.

$$\ln\left(\frac{C_0}{C} - 1\right) = k'' \cdot (t - t_1) \tag{6}$$

where: $k'' = k_T \cdot C_0$ oraz $t_1 = \frac{q_0 \cdot M}{Q \cdot C_0}$, C_0 – input concentration of phosphate to column [mg dm^{-3}], C - output concentration of phosphate from column [mg dm^{-3}], k_{Th} - Kinetic coefficients of the Thomas model, q_o - expected adsorbent capacity in the fixed-bed column [mg g^{-1}], M - total mass of adsorbent in column [g].

The Yoon - Nelson model is based on the assumption that the rate of decrease in adsorption on each molecule of adsorbate is proportional to the adsorption on the adsorbent. The model is not only less complicated but requires less detailed data on adsorbate properties or physical properties of the bed.

$$\ln \frac{C}{C_0 - C} = K_{YN} \cdot t - \tau \cdot K_{YN} \tag{7}$$

where: K_{YN} - Yoon-Nelson constant, τ - time required to adsorb 50% of the adsorbate [min].

The modified dose-response (MDR) model was originally developed in pharmacological studies. The use of this model to develop experimental results minimizes the error that results from the use of the Thomas model, especially in the short and long time of the curve breakthrough. This model presents the following equation:

$$\frac{C}{C_0} = 1 - \frac{1}{1 + \left(\frac{C_0 \cdot V_e}{1000 \cdot q_0 \cdot M}\right)^{a_{mdr}}} \tag{8}$$

where: V_e – volume of phosphate solution [dm^3] a_{MDR} - MDR model constant, the total volume of purified solution [dm^3].

The results obtained from fitting the curve to the experimental data are shown in Table 4.

Table 4. Summary of parameters obtained from non-linear regression for a column with a bed using modified EG

Thomas model		MDR model		Yoon – Nelson model	
k_{Th}	3.485e-06	a_{mdr}	1.055	K_{YN}	0.108
q_0 [mg g^{-1}]	42.8	q_0 [mg g^{-1}]	58.4	τ [min]	19.6
R^2	0.905	R^2	0.991	R^2	0.905

Experimental data was best described by the MDR model, which eliminates errors resulting from the use of Thomas's model. The predicted adsorption capacity in the column for modified EG was determined to be 58.4 mg g^{-1}. Nguyen et al. (Nguyen et al. 2014) in their work presented the possibility of phosphate removal using modified ocara Zr (IV). The process was carried out in a fixed-bed column. The maximum sorption capacity, determined by the Thomas model, was 16.4 mg g^{-1}. Woumfo et al. (Woumfo et al. 2015) in their work presented phosphate removal using volcanic soil as a sorbent. The use of sorbent alone did not bring the expected results due to the very low permeability. To increase permeability, sugar cane process residues were used in a 50/50 ratio. The maximum sorption capacity was 4.18 mg g^{-1}.

4 Conclusion

Eggshells modified with iron(III) chloride are a very good adsorbent for PO_4^{3-} ions. The sorption equilibrium was best described by the Langmuir model. The maximum sorption capacity was 42.4 mg g^{-1}. The modification resulted in the expected effect of increasing the sorption capacity of the adsorbent, three times compared to eggshells without modification (literature data). The kinetics data of the process in the fixed-bed column was best described by the MDR model. The maximum sorption capacity was 58.4 mg g^{-1}. The results showed that eggshells modified with iron (III) chloride are very good materials for potential use as sorbents for removing phosphate ions from wastewater.

Acknowledgments. The work was financed by a statutory activity subsidy from the Polish Ministry of Science and Higher Education for the Faculty of Chemistry of Wroclaw University of Science and Technology Number 049U/0063/19.

References

Chen, J., Yan, L.G., Yu, H.Q., Li, S., Qin, L.L., Liu, G.Q., Li, Y.F., Du, B.: Efficient removal of phosphate by facile prepared magnetic diatomite and illite clay from aqueous solution. Chem. Eng. J. **287**, 162–172 (2016). https://doi.org/10.1016/j.cej.2015.11.028

Rocha, P.D., Franca, A.S., Oliveira, L.S.: Batch and column studies of phenol adsorption by an activated carbon based on acid treatment of corn cobs. Int. J. Eng. Technol. **7**, 459–464 (2015). https://doi.org/10.7763/ijet.2015.v7.837

Dai, J., Yang, H., Yan, H., Shangguan, Y., Zheng, Q., Cheng, R.: Phosphate adsorption from aqueous solutions by disused adsorbents: Chitosan hydrogel beads after the removal of copper (II). Chem. Eng. J. **166**, 970–977 (2011). https://doi.org/10.1016/j.cej.2010.11.085

Dubey, A., Mishra, A.: A novel plant-based biosorbent for removal of copper (II) from aqueous solutions: biosorption of copper (II) by dried plant biomass. J. Renew. Mater. **5**, 54–61 (2016). https://doi.org/10.7569/jrm.2016.634127

Freundlich, H.: Über die Adsorption in Lösungen. Zeitschrift für Phys Chemie **57**(1), 385–480 (1907). https://doi.org/10.1515/zpch-1907-5723

Guo, Z., Li, J., Guo, Z., Guo, Q., Zhu, B.: Phosphorus removal from aqueous solution in parent and aluminum-modified eggshells: thermodynamics and kinetics, adsorption mechanism, and diffusion process. Environ. Sci. Pollut. Res. **24**, 14525–14536 (2017). https://doi.org/10.1007/s11356-017-9072-8

Hoon, C.H.: The Removal Methods of Phosphorus/Phosphate and Nitrogen/Nitrate from Water and Wastewater. 83 (2012)

Huang, W., Chen, J., He, F., Tang, J., Li, D., Zhu, Y., Zhang, Y.: Effective phosphate adsorption by Zr/Al-pillared montmorillonite: Insight into equilibrium, kinetics and thermodynamics. Appl. Clay Sci. **104**, 252–260 (2015). https://doi.org/10.1016/j.clay.2014.12.002

Kasama, T., Watanabe, Y., Yamada, H., Murakami, T.: Sorption of phosphates on Al-pillared smectites and mica at acidic to neutral pH. Appl. Clay Sci. **25**, 167–177 (2004). https://doi.org/10.1016/j.clay.2003.09.005

Lagergren, S.: Zur theorie der sogenannten adsorption gelöster stoffe. K. Sv. Vet. Akad. Handl. **24**, 1–39 (1898)

Li, R., Wang, J.J., Zhou, B., Awasthi, M.K., Ali, A., Zhang, Z., Gaston, L.A., Lahori, A.H., Mahar, A.: Enhancing phosphate adsorption by Mg/Al layered double hydroxide functionalized biochar with different Mg/Al ratios. Sci. Total Environ. **559**, 121–129 (2016). https://doi.org/10.1016/j.scitotenv.2016.03.151

Luo, X., Wang, X., Bao, S., Liu, X., Zhang, W., Fang, T.: Adsorption of phosphate in water using one-step synthesized zirconium-loaded reduced graphene oxide. Sci. Rep. **6**, 1–13 (2016). https://doi.org/10.1038/srep39108

Martín-Lara, M.A., Blázquez, G., Ronda, A., Pérez, A., Calero, M.: Development and characterization of biosorbents to remove heavy metals from aqueous solutions by chemical treatment of olive stone. Ind. Eng. Chem. Res. **52**, 10809–10819 (2013). https://doi.org/10.1021/ie401246c

Nguyen, T.A.H., Ngo, H.H., Guo, W.S., Zhou, J.L., Wang, J., Liang, H., Li, G.: Phosphorus elimination from aqueous solution using "zirconium loaded okara" as a biosorbent. Bioresour. Technol. **170**, 30–37 (2014). https://doi.org/10.1016/j.biortech.2014.07.069

Park, D., Yun, Y.S., Park, J.M.: The past, present, and future trends of biosorption. Biotechnol. Bioprocess Eng. **15**, 86–102 (2010). https://doi.org/10.1007/s12257-009-0199-4

Pastoriza-Santos, I., Liz-Marzán, L.M.: Formation and stabilization of silver nanoparticles through reduction by *N*, *N* -Dimethylformamide. Langmuir **15**, 948–951 (1999). https://doi.org/10.1021/la980984u

Przywara, L.: Warunki i możliwości usuwania fosforanów i fosforu ogólnego ze ścieków przemysłowych (2014)

Riazi, M., Keshtkar, A.R., Moosavian, M.A.: Biosorption of Th (IV) in a fixed-bed column by Ca-pretreated Cystoseira indica. J. Environ. Chem. Eng. **4**, 1890–1898 (2016). https://doi.org/10.1016/j.jece.2016.03.017

Tian, S., Jiang, P., Ning, P., Su, Y.: Enhanced adsorption removal of phosphate from water by mixed lanthanum/aluminum pillared montmorillonite. Chem. Eng. J. **151**, 141–148 (2009). https://doi.org/10.1016/j.cej.2009.02.006

Wang, Z., Shen, D., Shen, F., Li, T.: Phosphate adsorption on lanthanum loaded biochar. Chemosphere **150**, 1–7 (2016). https://doi.org/10.1016/j.chemosphere.2016.02.004

Wänke, H., Brückner, J., Dreibus, G., Rieder, R., Ryabchikov, I.: Chemical composition of rocks and soils at the pathfinder site. Space Sci. Rev. **96**, 317–330 (2001). https://doi.org/10.1023/A:1011961725645

Woumfo, E.D., Siéwé, J.M., Njopwouo, D.: A fixed-bed column for phosphate removal from aqueous solutions using an andosol-bagasse mixture. J. Environ. Manage. **151**, 450–460 (2015). https://doi.org/10.1016/j.jenvman.2014.11.029

Yan, L.G., Xu, Y.Y., Yu, H.Q., Xin, X.D., Wei, Q., Du, B.: Adsorption of phosphate from aqueous solution by hydroxy-aluminum, hydroxy-iron and hydroxy-iron-aluminum pillared bentonites. J. Hazard. Mater. **179**, 244–250 (2010). https://doi.org/10.1016/j.jhazmat.2010.02.086

Ye, Y., Ngo, H.H., Guo, W., Liu, Y., Li, J., Liu, Y., Zhang, X., Jia, H.: Insight into chemical phosphate recovery from municipal wastewater. Sci. Total Environ. **576**, 159–171 (2017). https://doi.org/10.1016/j.scitotenv.2016.10.078

Yuan, X., Xia, W., An, J., Yin, J., Zhou, X., Yang, W.: Kinetic and thermodynamic studies on the phosphate adsorption removal by dol mineral. J. Chem. **2015**, 8 (2015). https://doi.org/10.1155/2015/853105

Experimental Analysis of the Deposition of Aerosol Droplets in the Upper Airways of Human

Tomasz Robert Sosnowski(✉)

Faculty of Chemical and Process Engineering,
Warsaw University of Technology, Warsaw, Poland
tomasz.sosnowski@pw.edu.pl

Abstract. This chapter presents some examples of the application of chemical engineering approach in solving problems of drug delivery using aerosolized liquids. Both aerosol formation and the subsequent transport of micrometer-sized droplets through the upper airways of human: nose, mouth and throat, have been investigated by experiments "in vitro" on anatomical models of these parts of the respiratory system. The results allowed to identify the basic physicochemical and aerodynamic/mass transfer phenomena which are responsible for the local separation of aerosol droplets from the air stream and their deposition and displacement in the studied regions of the human body. The influence of liquid properties (e.g., the surface tension, rheological characteristics) and inhalation dynamics have been shown to be essential factors for predicting the efficiency of drug delivery using aerosols.

1 Introduction

Inhalation of aerosolized medicines is a convenient and effective way of treatment of lung diseases (e.g. asthma, COPD, bronchitis, pneumonia, etc.), (Pirożyński and Sosnowski 2016). Drugs which are expected to deposit in the bronchial tree, obviously must penetrate beyond the upper airways, UA, i.e. the mouth and throat region (the oropharynx). This is challenging because many inhalers do not generate sufficiently small particles or droplets, and a high fraction of released aerosol is captured in the UA. In addition, the actual breathing pattern, which may be different in individual patients, strongly influences the way in which aerosol particles/droplets are carried along the successive parts of the respiratory system. As a consequence, usually only 40–60% of the prescribed drug dose reaches the target area in the lungs.

Nasal sprays form another group of aerosolized medicines and they are used to treat local diseases of the nose (e.g., allergic rhinitis). In this case, the application of sprayed drugs is expected to result in the homogenous deposition inside the nasal cavity without drug penetration beyond this region. Obviously, such aerosols must have a different characteristics that those targeted to the lungs.

The knowledge on the process of aerosol transport in the human airways is still unsatisfactory, although the chemical engineering approach, such as CFD or other

© Springer Nature Switzerland AG 2020
M. Ochowiak et al. (Eds.): PAIC 2019, *Practical Aspects of Chemical Engineering*, pp. 423–429, 2020.
https://doi.org/10.1007/978-3-030-39867-5_44

computational studies ("*in silico*" analysis) shed more light on this problem (e.g., Moskal and Gradon 2002; Sosnowski et al. 2007; Sosnowski and Kramek-Romanowska 2016; Moskal and Sosnowski 2018; Asgari et al. 2019). However, the fundamental research in this field can be enhanced by *"in vitro"* experiments, i.e. physical measurements with anatomical models of human airways, which are conducted under controlled and reproducible conditions (e.g., Sosnowski et al. 2006).

This chapter reports recent results of the studies related to generation of liquid aerosols (mists) in selected medical atomizing devices, and deposition of emitted droplets in anatomically-based models of the oro-pharynx and the nasal cavity.

2 Methods

All experiments were done at room temperature. Different types of aerosol dosing devices and anatomically-based models (ABMs) of the upper airways of human were used:

- nasal atomizers - studied with two anatomical models (adult and child) of nasal cavity;
- jet nebulizers - studied with the model of oro-pharynx (adult).

In the first case, the study was focused on identification of factors facilitating the homogeneous distribution in the nasal cavity of aerosol released from the dedicated atomizers (nasal pumps). In the second case, the main aim of the research was to evaluate the role of size and velocity of droplets released from the nebulizer on their local deposition in the mouth and throat. All liquids used in spraying processes were characterized regarding the surface tension and rheological properties, since it has been recognized that these factors may influence the size distribution of droplets and other properties of the aerosol cloud (e.g., Ochowiak et al. 2017, 2019). Size distributions of droplets produced by all tested atomizing devices were evaluated by laser diffraction (Spraytec – Malvern, UK). ABMs used in the studies were derived from CT and MRI scans and prepared by rapid prototyping technique in a way which allowed to assemble them from two parts: left-side and right-side (Rapiejko et al. 2015; Copley Scientific 2019). This was necessary because of the applied method of visualization of drug deposition in both types of ABMs. Deposition of droplets was studied using two experimental systems:

- in case of nasal deposition, the colorimetric method adapted after Kundoor and Dalby (2011) was used. In brief, the inner surface of the ABMs was covered with a thin layer of water-sensitive paste. All studied drugs were water-based, so after deposition of aerosols sprayed with nasal pumps, the clear change in color at the deposition areas could be observed. This allowed to identify the deposition regions, and - after image capturing (EX-F1 Exilim, Casio) and digital processing – to evaluate the differences in the deposition pattern caused by droplet size, cloud characteristics and the airflow rate through the system.

- in case of deposition of nebulized aerosols in the model of the mouth-throat region, the fluorescein doped liquid was used. The deposition of droplets in the ABM could be clearly detected under UV light. The high sensitivity of this method is important since the mass of deposited liquid was much lower than in the case of nasal drugs studies. Image acquisition and processing was done in the similar way as in the studies with the nose models. The relationships between aerosol droplet size and airflow rate were evaluated.

3 Results

Figure 1 shows the examples of local deposition of aerosol drugs delivered from two different atomizers (i.e. nasal pumps) to the nasal cavity of an adult. Since the measured average size of sprayed droplets (Dv50) is in the range of 60–70 μm and the jet has high kinetic energy, the homogenous distribution of sprayed drugs in the nasal interior is impossible. The droplets are deposited mainly at the entrance to the nasal cavity (in the vicinity of the nasal valve) and they do not reach deeper regions. This effect can be easily explained by a simple experiment where the nasal spray is pushed through the converging tube used as a model of the nostril. It is seen that in spite of good aerosolization of the drug during spraying to the open space (Fig. 2a), the aerosol cloud cannot develop to this from when it is released inside the channel, so the drug is administered as a narrow jet of large droplets (Fig. 2b and 2c). Similar situation is expected during drug spraying in the nostril.

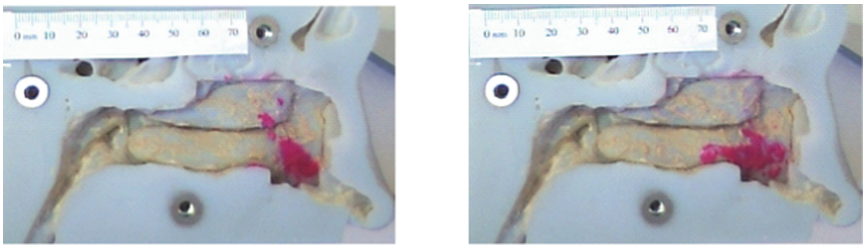

Fig. 1. Deposition of aerosol sprayed to the nasal cavity of an adult (two different drugs).

Based on the data presented it can be argued to what extent sprayed droplets can be efficient as a drug carriers to the nasal mucosa? The response was partially found during the studies continued on the pediatric nose model. The results of this research showed that airflow applied during drug administration or shortly after spraying of the drug to the nose, was capable of displacing the layer of deposited liquid (i.e. drug) along the nasal surface, Fig. 3. Such transport should allow the drug to induce a quick therapeutic effect also in a deeper parts of the nasal cavity.

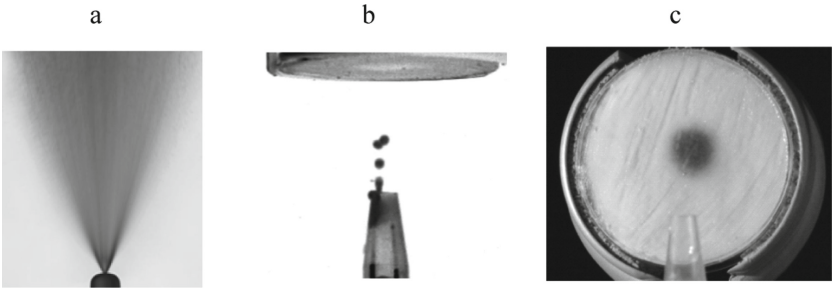

Fig. 2. Cloud of the nasal aerosol in the open space (a) and inside the constricted tube as a model of the nostril (b). Picture (c) shows the deposition spot of the liquid jet emerging from the constricted tube.

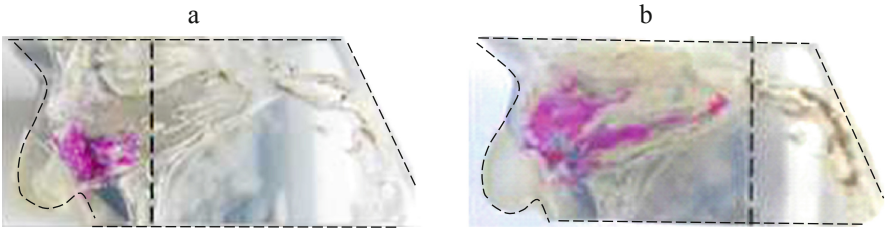

Fig. 3. Deposition of spray in the pediatric nose model: without airflow (a), with additional airflow (b).

The observed displacement of liquid layer along the solid surface due to aerodynamic shear induced by flowing gas is a recognized phenomenon and it has been discussed by several authors in the relation to other applications (e.g., Roisman et al. 2015; Fan et al. 2011). It should be stressed that in case of intranasal drug delivery, physicochemical properties of sprayed liquids influence not only the cloud geometry/velocity and droplet size distribution (Sosnowski et al. 2020), but also the possibility of the lateral displacement of deposited layer along the nasal interior. More viscous drugs will drain more slowly, so probably they can be more easily spread along the surface in horizontal direction. Therefore, the use of viscosity modifiers in such drugs may have additional beneficial effect.

In the initial studies of deposition of nebulized mists in the model oro-pharynx it was found that aerosols composed of droplets with the average size below 5 μm penetrated almost completely through the tested geometry when aerosol flow rate corresponded to the tidal breathing (15 dm^3/min), i.e. the typical breathing pattern of inhalation done with nebulizers. However, the enhanced deposition in the mouth-throat region was observed at higher flow rates (30 dm^3/min), in particular for aerosols composed of droplets with the average size larger than 5 μm. It can be easily explained by inertial effects expressed by the Stokes number:

$$\mathrm{Stk} = \frac{\rho d^2 U}{18 \mu R} \tag{1}$$

where d stands for aerodynamic diameter of a droplet, ρ – liquid density, U – droplet (aerosol) velocity, μ – air viscosity and R – the characteristic length in the system (e.g., the distance to the wall). The "hot-spots" of aerosol deposition were found on the hard palate area and inside the pharynx, i.e. in the regions which are characterized the airway bend or narrowing (decrease of R in Eq. 1). Examples are shown in Fig. 4.

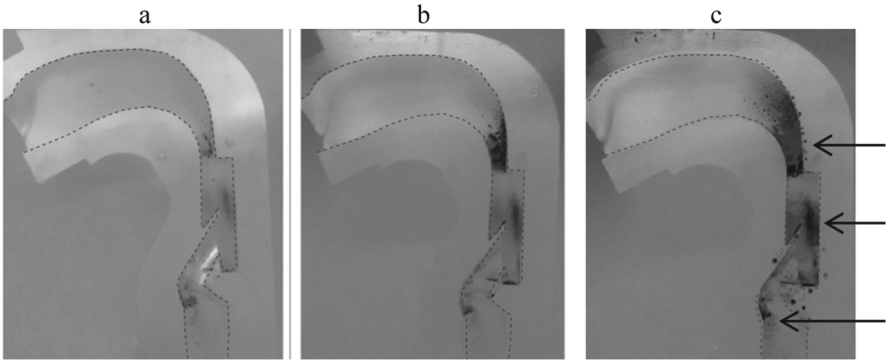

Fig. 4. Deposition of nebulized drugs in the model of the oro-pharynx. Aerosol flow rate: 30 dm^3/min, the average droplet size: 3 μm (a), 5 μm (b), 8 μm (c). Arrows show the "hot-spots" of deposition.

4 Discussion

Results of *"in vitro"* physical experiments show that deposition of aerosol sprays in the models of nasal cavity takes place mainly in the anterior regions, i.e. in the vestibule and the areas adjacent to the nasal valve. In spite of the fact that the drug is converted into relatively fine droplets ($\sim$60 μm) which might be expected to penetrate the nasal cavity, the initial velocity of the aerosol jet results in the intense impaction of the droplets in the narrow air passages close to the nose inlet. It has been demonstrated, however, that nasal drugs can be displaced towards deeper regions of the nose interior due to the dynamic interactions of flowing air with the deposited layer of the liquid. These aerodynamic forces can be responsible for the efficient drug delivery to the nasal mucosa and the induction of beneficial therapeutic effects. Rheological properties of a given drug, but also the volume of applied dose, should influence the efficiency of the spreading process. Liquids with high viscosity do not drain quickly, so they can be pushed more horizontally. If the volume of the applied/deposited drug is large, then the layer of liquid on the nasal surface is thicker and can be more easily displaced by inspired air due to a larger area of the aerodynamic interactions (Fig. 5a and 5b). Probably, in some cases the air passage in the nose can be completely plugged by the deposited drug (Fig. 5c) which may lead to the re-opening of this passage by the

airflow, and transporting of the drug to deeper nose regions. The flow of air in the nose after drug application is usually intensified by sniffing being the typical behavioral response to the feeling of drug dripping from the nose.

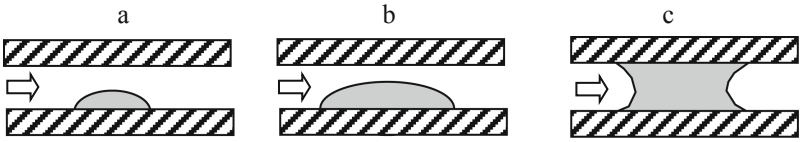

Fig. 5. Schematic illustration of the role of liquid volume (i.e. thickness of liquid layer in relation to the dimensions of air passage) on the shearing action of the flowing air: a – small volume of deposited drug, b – larger volume of drug, c – very large volume of drug and the resultant liquid bridge formed inside the narrow channel. The arrow shows direction of the interacting airflow.

In case of aerosol deposition in the oro-pharynx, the process is evidently governed by droplets momentum. The classical description of this effect analyzes the corresponding values of either Stk or the *IP* (inertial parameter), where factors d^2U or d^2Q (where Q – the aerosol flow rate) play the crucial role. It may be noted, however, that the increase of deposition with Stk or *IP* is always observed for steady flows but may not hold for oscillatory flows, which are typical for breathing (rather than Q = const). As shown by Sosnowski et al. (2006, 2007), the time-dependent aerodynamic effects in this region may increase the deposition of ultrafine particles, even if Stk or *IP* values are low. In the current studies we used only the constant flows of 15 and 30 dm^3/min, and visually confirmed that – according to Eq. 1 – the increase in d has stronger influence on local deposition in the oro-pharynx than the increase in Q. Such effect was also confirmed in the heated system (i.e. at physiological temperature 37 °C - data not shown) where the deposition was notably decreased as a result of partial evaporation of droplets, i.e. due to a reduction of their diameter, d.

5 Conclusions

The reported research demonstrated that experimental approach and data analysis which are commonly used in many problems of chemical engineering can be also efficiently applied in the analysis of problems related to drug delivery by aerosol inhalation. Direct visualization experiments helped to identify the dependence of aerosol deposition pattern in selected parts of human breathing system on the operation parameters of drug atomization and inhalation processes, including:

- the physicochemical properties of drugs (surface tension, rheological characteristics),
- type and working regime of the atomization device, and
- the inhalation flow rate.

The results of such studies are useful in explaining the mechanisms of aerosol deposition in the upper airways, and they may also help to verify the findings of computational analysis which are being developed for such systems. Finally, this should take effect in better designs of the devices used for generation of therapeutic aerosols (atomizers and inhalers) and increased effectiveness of inhalation therapy.

Acknowledgments. Work done under the support of NCN, project No. 2018/29/B/ST8/00273. The author expresses his gratitude to Arkadiusz Kuczaj PhD (PMI, Neuchatel, Switzerland) for his help in the arrangement of selected experiments and fruitful discussion.

References

Asgari, M., Luccia, F., Kuczaj, A.K.: Multispecies aerosol evolution and deposition in a bent pipe. J. Aerosol Sci. **129**, 53–70 (2019)

Copley Scientific (2019). www.copleyscientific.com/home/inhaler-testing/aerodynamic-particle-size/improved-in-vitro-in-vivo-correlation-ivivc/alberta-idealised-throat-ait. Accessed 22 May 2019

Fan, J., Wilson, M.C.T., Kapur, N.: Displacement of liquid droplets on a surface by a shearing air flow. J. Coll. Interface Sci. **356**, 286–292 (2011)

Kundoor, V., Dalby, R.N.: Effect of formulation- and administration-related variables on deposition pattern of nasal spray pumps evaluated using a nasal cast. Pharm. Res. **28**, 1895–1904 (2011)

Moskal, A., Sosnowski, T.R.: Chemical engineering in biomedical problems – selected applications. In: Ochowiak, M., et al. (eds.) Practical Aspects of Chemical Engineering, pp. 307–318. Springer, Cham (2018)

Moskal, A., Gradoń, L.: Temporary and spatial deposition of aerosol particles in the upper human airways during breathing cycle. J. Aerosol Sci. **33**, 1525–1539 (2002)

Ochowiak, M., Kasperkowiak, A., Doligalski, M., Sosnowski, T.R., Matuszak, M., Włodarczak, S., Markowska, M., Krupińska, K., Jabłczyńska, K.: The thermostated medical jet nebulizer: aerosol characteristics. Int. J. Pharmaceutics **567**, 118475 (2019)

Ochowiak, M., Matuszak, M., Włodarczak, S.: The analysis of pneumatic atomization of Newtonian and non-Newtonian fluids for different medical nebulizers. Drug Dev. Ind. Pharm. **43**, 1999–2010 (2017)

Pirożyński, M., Sosnowski, T.R.: Inhalation devices: from basic science to practical use, innovative vs generic products. Expert Opin. Drug Del. **13**, 1559–1571 (2016)

Rapiejko, P., Sosnowski, T.R., Sova, J., Jurkiewicz, D.: Deposition of intranasal glucocorticoids – preliminary study. Otolaryngol. Pol. **69**(6), 30–38 (2015)

Roisman, I.V., Criscione, A., Tropea, C.: Dislodging a sessile drop by a high-Reynolds-number shear flow at subfreezing temperatures. Phys. Rev. E **92**, 023007 (2015)

Sosnowski, T.R., Kramek-Romanowska, K.: Predicted deposition of e-cigarette aerosol in the human lungs. J. Aerosol Med. Pulm. Drug Del. **29**, 299–309 (2016)

Sosnowski, T.R., Moskal, A., Gradoń, L.: Mechanims of aerosol particle deposition in the oro-pharynx under non-steady airflow. Ann. Occup. Hyg. **51**, 19–25 (2007)

Sosnowski, T.R., Rapiejko, P., Sova, J., Dobrowolska, K.: Impact of physicochemical properties of nasal sprays products on drug deposition and transport in a pediatric model of the nasal cavity. Int. J. Pharmaceutics **574**, 118911 (2020)

Sosnowski, T.R., Moskal, A., Gradoń, L.: Dynamics of oro-pharyngeal aerosol transport and deposition with the realistic flow pattern. Inhal. Toxicol. **18**, 773–780 (2006)

Spherical Particle Technology and Engineering: Fabrication and Practical Utility

Małgorzata Stanisz, Łukasz Klapiszewski(✉), and Teofil Jesionowski(✉)

Institute of Chemical Technology and Engineering, Poznan University of Technology, Poznań, Poland
{lukasz.klapiszewski,teofil.jesionowski}@put.poznan.pl

Abstract. Recent development of industry has resulted in an increased interest in the preparation of various structures of micro- and nanometric sizes. Intensified experimental research in the field of micro- and nanotechnology has facilitated the explanation of many scientific phenomena and enabled the production of micro- and nanodevices. Spherical structures can be designed to obtain unique properties and find applications in science and industry. In addition, they can be prepared using biodegradable and by-products materials. Micro- and nanomaterials can be used as novel drug delivery systems, adsorbents, supports, catalysts and many other. In this chapter general description of technology of spherical particles is presented.

1 Spherical Particles - Introduction

The increasing interest in nanotechnology enabled the development of micro- and nanosized particles formation. First particles were observed in nature and then researchers tried to recreate them under laboratory conditions. Moreover, their synthesis could be designed to ensure their specified features and characteristic. The surface of the particles can be modified and combined with a variety of compounds in order to change and improve their properties. Spherical particles may be obtained in many forms such as solids, core-shells and hollow spheres. Each group is characterized by various structure or morphology and can be used in different sectors of science and industry.

Solid particles (SP) with different morphologies were observed for the first time in a nature. They were commonly found in a dispersed form such as interstellar dust, mud, clay and volcanic ashes. Interestingly, amorphous silica spheres form colloids, known as opals, which are very popular and desired by collectors. It was shown that particles can present a variety of different forms such as rods, boxes and tubes, but the most interest was aroused by particles with a spherical shape, which rarely occur in nature. Preparation of spherical particles might be challenging for scientists and because of that several complex methods have to be used (Matijević 1993).

Core-shell particles (CS) consists of a solid core and at least a single layer of another substance, different from the core. There are several types of core-shell

© Springer Nature Switzerland AG 2020
M. Ochowiak et al. (Eds.): PAIC 2019, *Practical Aspects of Chemical Engineering*, pp. 430–440, 2020.
https://doi.org/10.1007/978-3-030-39867-5_45

particles depending on the used material, for example particles in which core and shell are both organic or inorganic, but there are also hybrid CS particles in which core and shell are belong to different classes of materials. To enhance the characteristic of solid particles and create novel functional applications, SP can be coated with layers of another compound and establish CS particles. Core-shell particles are very unique because mostly core possesses different characteristic than its shell and together, they exhibit special properties. Several researches indicate that, core-shell particles possess improved magnetic and optical properties, enhanced thermal and chemical stability and high surface area that their solid precursor (Sadjadi et al. 2017).

The term hollow spheres (HS) was first used in philosophy, geography, astronomy and mathematics by thinkers in ancient Greece (Augustin and Hungerbach 2009). HS have a void inside, which provides new properties and application paths. Perfect hollow particles possess great mechanical and chemical stability, their shell is resistant to any substance leakage and exhibits fantastic loading and releasing capacities (Wei et al 2015). The morphology of a shell which builds the sphere is very important. Shells protect loaded substances from a harsh reaction environment and control the pace and time of compounds diffusion. Moreover, the thickness of a shell has a significant influence on its future applications (Mirzaei et al. 2018).

2 Morphology of Spherical Particles

The morphology of particles is strictly related to the material, from which they were prepared. They could be prepared of compounds such as silica, several metal oxides, gold, silver and copper nanoparticles as well as polymers e.g. polyaniline and polystyrene (Wang et al. 2016). A new group of spherical particles consists of biopolymers, especially chitin, arginine and lignin.

Depending on the used substance, spherical particles may exhibit different properties such as high surface area, low density and good loading capacity (Yu et al. 2018).

2.1 Metallic Particles

Metallic nanoparticles are widely used for the synthesis of hollow spheres and core-shell particles. Moreover, they can also be used as solid particles and added for enrichment of material properties. Gold, silver and copper nanoparticles are the most well-known and commonly used metallic nanoparticles (Klapiszewski et al. 2015; Modrzejewska-Sikorska et al. 2017).

Gold nanoparticles (AuNPs) are added to other materials to enhance or change their properties. Silica decorated with gold nanoparticles is used in phototherapy and targeted medicine for cancer treatment. Some drugs absorb photon energy and scatter it partially as heat. If nanoparticles are located near cancer tissues, the increased temperatures may damage the cancer cells. Moreover, silica and gold particles are resistant at a wide range of pH values. The obtained particles also enhanced Raman scattering signal for inorganic and biological samples (Janetanakit et al. 2017).

Li and co-workers (2018) presented titanium dioxide and zinc oxide double-shelled hollow spheres. TiO_2 was deposited on the functionalized surface layer of polystyrene,

then silver, gold, platinum or palladium particles were adsorbed and the particle was coated with a zinc oxide shell. TiO_2@ZnO spheres with metallic nanoparticles were tested as benzyl alcohol photo-oxidants. The highest photooxidation rates were observed in case of particles with silver and the lowest in case of spheres without metallic nanoparticles. The unique structure of double-shelled hollow spheres with metallic particles as co-catalysts may be used in future as an efficient photocatalyst in heterogenous catalysis (Li et al. 2018).

Silver nanoparticles (AgNPs) exhibit significant antibacterial properties against many microorganisms, including *E. coli*. Silver ions from silver nanoparticles mostly influence the enzymatic and structural proteins. It should also be taken into consideration, that silver particles might be transferred and accumulated in humans and other living organisms. Moreover, the possible after effects are strictly related to their properties, applications and concentration. For further uses all risks should be evaluated and, if possible, minimized (Sondi and Salopek-Sondi 2004).

AgNPs are often combined with other spherical particles, such as silica, to improve their properties. Kerdlap and co-workers (2019) showed that silver nanoparticles attached to silica spheres release antibacterial Ag^+ ions more efficiently and for a longer time compared to larger AgNPs (Kerdlap et al. 2019). Another functional and biocompatible material prepared with a use of silver nanoparticles was presented by Klapiszewski et al. (2015). Kraft lignin and silica hybrid material were combined with AgNPs and their antibacterial activity was tested against a variety of Gram-positive and Gram-negative bacteria. It was reported that the addition of silver nanoparticles to lignin/silica hybrid material resulted in an increased inhibition of microbial growth, while both precursors and hybrid material itself did not exhibit any antibacterial activity (Klapiszewski et al. 2015).

Copper hollow spheres are sensitive to catalysed oxidation process of glucose, therefore they can be used as biosensors. Different amounts of electron flows are detected and registered as a power, the volume of which depends on glucose concentration (Kong et al. 2014).

Moreover, not only copper element but also its oxides can be used for preparation of spheres. Xu and Wang (2007) prepared copper(I) oxide multi-shelled hollow spheres using CTAB as a micellar template. The particles exhibited different morphologies, depending on the amount of added surfactant. The number of shells increased with higher concentration of CTAB. In the future, multi-shelled Cu_2O hollow particles may be used as advanced carriers, in which every void may be loaded with different compounds (Xu and Wang 2007).

2.2 Polymer Particles

Polymer particles are one of the most popular products due to their low density, good chemical stability, relatively high surface area and the fact that they can also possess numerous nanometer holes in their surface. Polymer spheres can also be modified by organic or inorganic compounds to sanitize them for environmental signals. Polymer spheres sensitive to pH, temperature and magnetic field were obtained during several studies (Wang et al. 2015).

A novel group of polymeric particles includes particles which consist of biopolymers, such as lignin. This biopolymer is nontoxic, renewable and is obtained as a by-product in paper industry. One of the first reports was published by Yiamsawas with co-workers (2014), who prepared capsules with a liquid core. During the preparation of spheres, polyaddition of lignin occurred on water droplet surface with the use of reverse microemulsion. The presented lignin spherical particles were stable in organic and aqueous conditions for several weeks (Yiamsawas et al. 2014).

Natural rubbers are great for preparation of hollow spheres because such materials are cheap, are a by-product in concentrated natural rubber production and can be easily removed by calcination at 550 °C using air conditions. Kerdlap et al. (2019) reported the preparation of silica hollow spheres using natural rubber spherical particles as a template. Tetraethyl orthosilicate (TEOS) was used as a silica precursor and silica shell was formed on a hard rubber template (Kerdlap et al. 2019).

2.3 Hybrid and Composite Particles

Hybrid and composite spherical particles are characterized by specific and unique properties, because they were prepared with more than one compound, mostly from inorganic and organic precursors. Hybrid and composite materials combined with silica exhibit great characteristic and novel applications possibilities. Mesoporous silica possesses an ability to encapsulate several metallic nanoparticles and oxides to perform as a nanoreactor during a catalysis reaction. Silica shell also protects the encapsulated particles from harsh reaction conditions. Moreover, the porous structure enables the permeation and sorption of organic compounds (Kumar et al. 2016). Gao et al. presented silica particles decorated with $MnSiO_3$. The particles were characterized by a spherical shape, with a mesoporous core and high surface area and pore volume. Deposition of $MnSiO_3$ had no significant influence on the silica structure. Results showed that higher amount of silica in comparison to $MnSiO_3$ reduces the coupling ability of pyroxymangite, which lowers its application possibilities. Particles exhibited great adsorption capacities and were used for the removal of Pb^{2+} ions (Gao et al. 2017). Wang and co-workers (2018) prepared organically modified silica and titanium carbide shells *via* pickering emulsion polymerization, in which phase changing material was encapsulated. Spherical particles possessed good thermal stability and exhibited great ability to store and release thermal energy. Organic-inorganic hybrid shells might be used in future as energy storage systems (Wang et al. 2018).

Silica and iron oxide spheres may be used as catalysts for several synthesis and heterogenous synthesis reactions. Such material can also be decorated with metallic nanoparticles, such as silver, to enhance their properties. As catalysts, the spherical particles can be easily separated from the reaction environment and reused up to seven times. Moreover, they exhibit high efficiency and reaction rate (Sadjadi et al. 2017; Snoussi et al. 2018).

3 Preparation Methods

Specific synthesis conditions have a high impact on the properties of future particles such as miscibility, phase stability and magnetic appearance. Moreover, there is a possibility to design the shape, size and unique properties such as multi-shells, additional pores and channels in the structure of particles. Chemical and mechanical methods can be used during the preparation of spherical particle (Fig. 1). Moreover, there are methods suitable only for hollow spheres and core-shells, respectively (Wang et al. 2015).

3.1 Sol-Gel Method

The sol-gel method is a well-known procedure used to prepare not only solid nanomaterials silica, titanic, zirconia or zinc oxide particles from organic precursors, but also to deposit one or several layers on a solid matrix to prepare core-shell or hollow spheres. This method occurs in aqueous and non-aqueous media, when water or organic solvent e.g. ethanol is used, respectively. Oxygen is mostly provided from the solvent in which hydrolysis and condensation reactions take place. In comparison to the aqueous solvent, the particle size, shape, morphology and reproducibility can be easily controlled in non-aqueous media (Rao et al. 2017; Muresan 2015; Mitra and De 2016). Stöber method enables the preparation of silica particles (Stöber et al. 1968). The method consists of two steps: first hydrolysis and then condensation of silane compounds. Type of catalysts influences the morphology of product. Using a basic catalyst enables the synthesis of spherical particles and using an acidic catalyst results in more linear products (Esquena and Solans 2001). Klapiszewski et al. (2014) modified Stöber method and obtained silica nanospheres. In their research, TEOS was used as a silica precursor and 25% ammonia was used as a catalyst. The synthesis process occurred in ethyl alcohol as the reaction medium. Researchers tested whether various different factors, such as TEOS and ammonia quantity or temperature and time of the process, influence the properties of the particles. The particles (478–875 nm) were synthetized when excess ammonia solution over TEOS was used and, on the other hand smaller, particles (below 300 nm) were prepared with a use of excess TEOS (Klapiszewski et al. 2014).

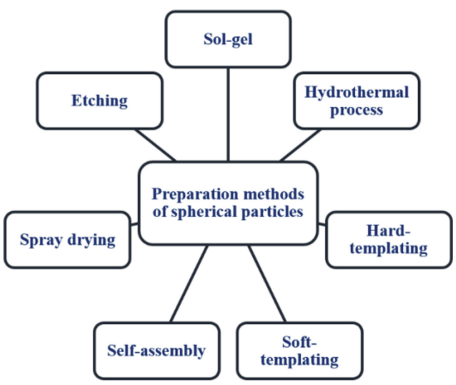

Fig. 1. The most important methods for fabrication of spherical particles

3.2 Hard-Templating Method

Hard-templating is a very efficient and widely used method of core-shell and hollow spheres preparation (Fig. 2).

First, solid particles including spheres are designed and then used as a template and mostly modified before the deposition of the first compound layer. There are several compounds which are efficiently used as templates e.g. silica, polystyrene, carbon or calcium carbonate. Modification is mostly necessary in order to ensure higher efficiency of the process. Matrix surface can be improved to obtain polar or ion-exchange properties. The spherical matrix has an influence on the shape of the core-shell particle or its void in hollow spheres, whereas the thickness of the particle is determined by type of method used for particle preparation. Mostly the sol-gel and hydrothermal processes are used for layer deposition on a hard matrix. Ultimately, the hard template has to be removed during the preparation of hollow spheres. There are various methods for removal of the matrix, including chemical etching, calcination and dissolution. Hard template and its removal method have to be selected very precisely in order to not destroy the obtained hollow sphere. Unfortunately, spherical particles prepared by hard-templating method exhibit low resistance to high temperatures and poor quality (Hu et al. 2011).

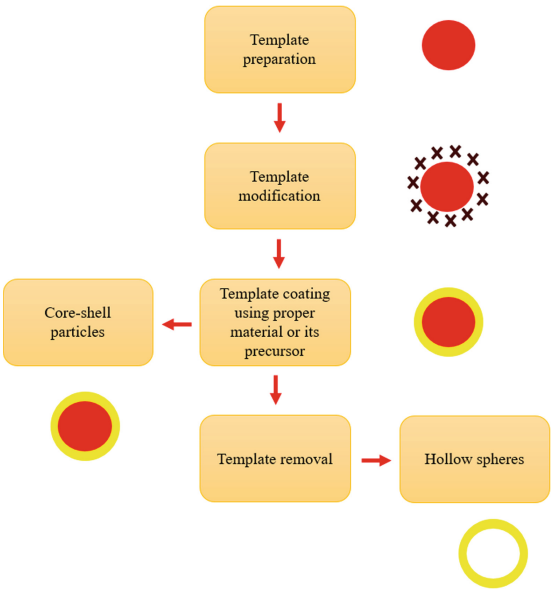

Fig. 2. Hard-templating method preparation diagram

3.3 Self-assembly Method

Self-assembly method is mostly used to prepare hollow spheres. The process includes two steps: (i) first, the material for template is selected very carefully and (ii) then it is

modified to obtain the hollow sphere from a simple matrix. The type of compounds which are used to build the matrix have to be selectively reactive and preferably cheap. The self-assembly method has recently become one of the most frequently used procedures for preparation of hollow spheres. It is a relatively cheap and easy procedure and, more importantly, the morphology of product can be controlled. Three main methods can be used for preparation of hollow spheres without template: (i) controlled etching, (ii) outward diffusion and (iii) heterogenous contraction (Yu et al. 2017).

3.4 Spray Drying

Spray drying is a method widely used for the production of particles with different morphologies. Using spray drying has many advantages such as low costs, product stability, simple procedure and continuous synthesis. It could be used for encapsulation of specific compounds and to prepare solid particles with novel properties and application possibilities. During the synthesis of particles, their shape and size can be easily controlled to produce spheres which are suitable for inhalation to lungs for targeted drug delivery. This method consists of the basic steps which include the preparation of a dispersion, homogenization and spraying in a drying chamber. First, the liquid phase is atomized into droplets and then they are quickly dried in a hot stream of gas. Using spray drying enables better physicochemical properties of final product than simple stationary dryer. Moreover, particles show lower ability to form aggregates and higher surface area (Jesionowski and Krysztafkiewicz 1996).

The aerosol flow reactor method is a great technique for production of lignin spheres in the size range of 330 nm and 1050 nm. First, aqueous and non-aqueous alkali and kraft lignin solution are prepared, the of which concentration varied from 1 to 3%. For preparation of solid lignin spheres, the following laboratory equipment was used: an atomizer, heating tube and particle collector. Droplets were suspended in nitrogen gas, dried and cooled before collection. Further obtained lignin particles were used as a core for preparation of hollow spheres (Tardy et al. 2018).

4 Practical Application of Spheres

4.1 Environmental Utilities

Spherical particles can be effectively used in environment protection. Most of the spheres adsorb organic and reactive dyes, chlorophenols and toxic water pollutants. Moreover, the use of hollow spheres accelerates water purification, removes pollutions from soil and underground water, and adsorbs hazardous metal ions. Photodegradation is a very efficient method for removal of harmful compounds from wastewater. During this procedure, hazardous metal ions are transformed into different forms which are environmentally safe. One of the greatest advantages of this method is that the whole procedure can be performed in the polluted location without additional transport and removal of contaminations (Ghasemzadeh et al. 2014).

Spherical particles, especially hollow ones, are great for immobilization of enzymes. Immobilized proteins inside of the sphere exhibit good thermal stability and can be easily reused (Wang et al. 2015).

Hollow particles can be applied as novel sensors of gasses (CO, H_2, H_2O and CH_2O) as well as metal ions (Hg^{2+} and Cu^{2+}), biosensors and pressure sensors. HS are characterized by short response time and good reproducibility. Depending on their function and application, HS should exhibit specific active sites, size and shape (Wang et al. 2016). Hollow spheres are more often used as sensors than solid particles because of their better in terms performance in terms of gas diffusion and mass transfer, hence they could be successfully used as carbon monoxide detectors (Prockop and Chichkova 2007). Biosensors are widely used to indicate chemical compounds which occur during several physicochemical reactions (Kong et al. 2014; Jędrzak et al. 2018; Jędrzak et al. 2019).

4.2 Engineering Applications

Spherical particles, depending on their morphology and synthesis method, possess many potential applications. Hollow spheres (HS) are mostly used as a packaging for drugs and biological material. Moreover, they could be used as micro- and nanoreactors for expensive and sensitive compounds. They also exhibit good release rates, which prevent premature reactions and leaking. Use of HS as drug delivery systems has to be safe and controlled on every process step. An accurate encapsulation method and surface modification is very important for targeted drug delivery. Mostly, hollow particles are located in a harsh environment and have to be resistant to high temperatures and strong acidic conditions. Some of them cooperate well with mucus in the human intestine which enables prolonged substance sorption. There are several reports which indicate that HS can be used during cancer therapy. Cancer cells are characterized by lower pH and higher temperature than tissues around them. It was shown, that drug from the anthracycline group placed inside a hollow sphere exhibits higher anti-cancer activity compared to the pure substance. Such an approach to anti-cancer therapy possesses less side effect and is more comfortable for the patient (Kolesnikova et al. 2010; Wei et al. 2015). Rafi and co-workers (2016) presented mesoporous silica nanoparticles coated with a pH-sensitive polymer. The materials were tested as drug delivery systems for cancer therapies. It was shown that drug release depends on the pH value. The carrier is closed at higher pH values and it opens with repulsive forces between positively charged polymer chains and acidic environment. The drug may be released near cancer cells because they exhibit lower pH values compared to healthy tissues (Rafi et al. 2016). Moreover, hollow spheres could be used in bioimaging and position emission tomography (PET). They are potentially good disease diagnostic materials due to their low toxicity toward healthy tissues.

Spherical particles are widely used in electrochemistry. Hollow particles store energy and are used as lithium-ion and lithium-sulfur batteries or supercapacitors. They not only form great novel electrodes, which could be used as fuel cells and chemically charged batteries, but also as anti-corrosion functional films. Addition of the spheres into a polymeric matrix inhibits the corrosion process and allows for the repair of small cracks on material surface (Shchukin et al. 2006; Wei et al. 2015).

Spheres play also a significant role in catalysis. Conducting a catalytic reaction with the use of hollow particles prevents catalyst migration and improves its efficiency. It should be noted that the shell of a hollow particle can also be used as a catalyst, therefore additional filling is not necessary. Hollow particles are used during oxidation and reduction reactions, photodegradation of methyl orange and Suzuki reaction. They are also employed as selective photocatalysts, which easily separate charges and reduce the time of electron-void pair formation (Liu et al. 2012; Nguyen et al 2015). Kumar et al. (2016) prepared silica and palladium nanoparticles which were used as homogeneous catalysts during alkene and alkyne hydrogenation reactions. Silica was modified with several saccharides, but the best results were obtained with a use of D-glucose. Pallidum can be incorporated inside of the SiO_2 particle but also on its surface. Silica-palladium nanoparticles are mild catalysts and could be used up to 5 times in organic synthesis without the loss of efficiency (Kumar et al. 2016).

5 Conclusions

Spherical particles are novel materials with unique properties. Spheres with different morphologies such as solid, core-shell and hollow, can be designed for specific parameters including high surface area, pore volume, chemical and thermal stability in order to find applications in scientific and industrial fields. Their micro- and nanometric sizes enable easier transport to targeted location. The increased interest in the use of microcontainers in medicine has contributed to the search for capsules which will consist of non-toxic and friendly materials for living organisms. During several tests, it was found that silica is an excellent material for the production of microcontrollers. It is chemically stable and possesses numerous hydroxyl functional groups. Moreover, biopolymers such as lignin or chitin can also be effectively used for preparation of microspheres due to their eco-friendly properties. Spheres may be used as targeted delivery systems, advanced, eco-friendly adsorbents or catalysts in heterogeneous catalysis.

Acknowledgments. This work was supported by Ministry of Science and Higher Education Poland as PUT research project no. 03/32/SBAD/0906.

References

Augustin, C., Hungerbach, W.: History and Production of Hollow Spheres, pp. 5–30. Springer, Heidelberg (2009)

Esquena, J., Solans, J.: Phase changes during silica particle formation in water-in-oil emulsions. Colloid Surf. A **183**, 533–540 (2001)

Gao, Q., Li, H.T., Ling, Y., et al.: Synthesis of $MnSiO_3$ decorated hollow mesoporous silica spheres and its promising application in environmental remediation. Microporous Mesoporous Mater. **241**, 409–417 (2017)

Ghasemzadeh, G., Momenpour, M., Omidi, F., et al.: Applications of nanomaterials in water treatment and environmental remediation. Front. Environ. Sci. Eng. **8**, 1–12 (2014)

Hu, J., Chen, M., Fang, X., et al.: Fabrication and application of inorganic hollow spheres. Chem. Soc. Rev. **40**, 5472–5491 (2011)

Janetanakit, W., Wang, L., Santacruz-Gomez, K., et al.: Gold–embedded hollow silica nanogolf balls for imaging and photothermal therapy. ACS Appl. Mater. Interface **9**, 27533–27543 (2017)

Jesionowski, T., Krysztafkiewicz, A.: Production of a highly dispersed sodium-aluminium silicate to be used as a whitepigment or as a polymer filler. Pigm. Resin Technol. **25**, 4–14 (1996)

Jędrzak, A., Rębiś, T., Nowicki, M., et al.: Polydopamine grafted on an advanced Fe_3O_4/lignin hybrid material and its evaluation in biosensing. Appl. Surf. Sci. **455**, 455–464 (2018)

Jędrzak, A., Rębiś, T., Kuznowicz, M., et al.: Bio-inspired magnetite/lignin/polydopamine-glucose oxidase biosensing nanoplatform. From synthesis, *via* sensing assays to comparison with others glucose testing techniques. Int. J. Biol. Macromol. **127**, 677–682 (2019)

Kerdlap, W., Thongpitaka, C., Keawmaungkom, S., et al.: Natural rubber as a template for making hollow silica spheres and their use as antibacterial agents. Microporous Mesoporous Mater. **273**, 10–18 (2019)

Klapiszewski, Ł., Królak, M., Jesionowski, J.: Silica synthesis by the sol–gel method and its use in the preparation of multifunctional biocomposites. Cent. Eur. J. Chem. **12**, 173–184 (2014)

Klapiszewski, Ł., Rzemieniecki, T., Krawczyk, M., et al.: Kraft lignin/silica–AgNPs as a functional material with antibacterial activity. Colloids Surf. B **134**, 220–228 (2015)

Kolesnikova, T.A., Gorin, D.A., Fernandes, P., et al.: Nanocomposite microcontainers with high ultrasound sensitivity. Adv. Funct. Mater. **20**, 1189–1195 (2010)

Kong, C.C., Tang, L.L., Zhang, X.Z., et al.: Templating synthesis of hollow CuO polyhedron and its application for nonenzymatic glucose detection. J. Mater. Chem. A **2**, 7306–7312 (2014)

Kumar, B.S., Amali, A.J., Pitchumani, K.: Mesoporous microcapsules through D-glucose promoted hydrothermal self–assembly of colloidal silica: Reusable catalytic containers for palladium catalyzed hydrogenation reactions. ACS Sustain. Chem. Eng. **5**, 667–674 (2016)

Li, S., Cai, J., Wua, X., et al.: Sandwich–like TiO_2@ZnO–based noble metal (Ag, Au, Pt, or Pd) for better photo–oxidation performance: synergistic effect between noble metal and metal oxide phases. Appl. Surf. Sci. **443**, 603–612 (2018)

Liu, J., Yang, H.Q., Kleitz, F., et al.: Yolk–shell hybrid materials with a periodic mesoporous organosilica shell: ideal nanoreactors for selective alcohol oxidation. Adv. Funct. Mater. **22**, 591–599 (2012)

Matijević, E.: Preparation and properties of uniform size colloids. Chem. Mater. **5**, 412–426 (1993)

Mirzaei, A., Kim, J.H., Kim, H.W., et al.: How shell thickness can affect the gas sensing properties of nanostructured materials: survey of literature. Sens. Actuator B Chem. **258**, 270–294 (2018)

Mitra, A., De, G.: Sol–gel synthesis of metal nanoparticle incorporated oxide films on glass in Glass Nanocomposites. In: Karmakar, B., Rademann, K., Stepanov, A.L. (eds.) Glass Nanocomposites: Synthesis, Properties and Applications, pp. 145–163. Elsevier Inc., Amsterdam (2016)

Modrzejewska-Sikorska, A., Konował, E., Cichy, A., et al.: The effect of silver salts and lignosulfonates in the synthesis of lignosulfonate-stabilized silver nanoparticles. J. Mol. Liq. **240**, 80–86 (2017)

Muresan, L.M.: Corrosion protective coatings for Ti and Ti alloys used for biomedical implants. In: Tiwari, A., Rawlins, J., Hihara, L.H. (eds.) Intelligent Coatings for Corrosion Control, pp. 585–602. Elsevier Inc., Amsterdam (2015)

Nguyen, C.C., Vu, N.N., Do, T.-O.: Recent advances in the development of sunlight–driven hollow structure photocatalysts and their applications. J. Mater. Chem. A **3**, 18345–18359 (2015)

Prockop, L.D., Chichkova, R.I.J.: Carbon monoxide intoxication: an updated review. Neurol Sci **262**, 122–130 (2007)

Rafi, A.A., Mahkam, M., Davaran, S., et al.: A smart pH–responsive nano–carrier as a drug delivery system: a hybrid system comprised of mesoporous nanosilica MCM–41 (as a nano–container) & a pH–sensitive polymer (as smart reversible gatekeepers): preparation, characterization and in vitro release studies of an anti–cancer drug. Eur. J. Pharm. Biopharm. **93**, 64–73 (2016)

Rao, B.G., Mukherjee, D., Reddy, B.M.: Novel approaches for preparation of nanoparticles. In: Ficai, D., Grumezescu, A. (eds.) Nanostructures for Novel Therapy, pp. 1–36. Elsevier Inc., Amsterdam (2017)

Sadjadi, S., Malmir, M., Heravi, M.M.: A green approach to the synthesis of Ag doped nano magnetic g–Fe_2O_3@SiO_2–CD core–shell hollow spheres as an efficient and heterogeneous catalyst for ultrasonic–assisted A3 and KA2 coupling reactions. RSC Adv. **7**, 36807–36818 (2017)

Shchukin, D.G., Köhler, K., Möhwald, H.: Microcontainers with electrochemically reversible permeability. J. Am. Chem. Soc. **128**, 4560–4561 (2006)

Snoussi, Y., Bastide, S., Manef, A., et al.: Sonochemical synthesis of Fe_3O_4@NH_2–mesoporous silica@Polypyrrole/Pd: a core/double shell nanocomposite for catalytic applications. Ultrason-Sonochem **41**, 551–561 (2018)

Sondi, I., Salopek-Sondi, B.: Silver nanoparticles as antimicrobial agent: a case study on *E. coli* as a model for Gram–negative bacteria. J. Colloid Interface Sci. **275**, 177–182 (2004)

Stöber, W., Fink, A., Bohn, E.: Controlled growth of monodisperse silica spheres in the micron size range. J. Colloid Interface Sci. **26**, 62–69 (1968)

Tardy, B.L., Richardson, J.J., Guo, J., et al.: Lignin nano– and microparticles as template for nanostructured materials: formation of hollow metal–phenolic capsules. Green Chem. **20**, 1335–1344 (2018)

Wang, H., Zhao, L., Song, G., et al.: Organic–inorganic hybrid shell microencapsulated phase change materials prepared from SiO_2/TiC–stabilized pickering emulsion polymerization. Sol. Energy Mater. Sol. Cells **175**, 102–110 (2018)

Wang, J., Zhao, G., Wang, X., et al.: Synthesis of magnetic thermosensitive microcontainers for enzyme immobilization. J. Nanopart. Res. **17**, 1–11 (2015)

Wang, X., Feng, J., Bai, Y., et al.: Synthesis, properties, and applications of hollow micro–/nanostructures. Chem. Rev. **16**, 10983–11060 (2016)

Wei, H., Wang, Y., Guo, J., et al.: Advanced micro/nanocapsules for self–healing smart anticorrosion coatings. J. Mater. Chem. A **3**, 469–480 (2015)

Wu, H., Wang, Y., Zheng, C., et al.: Multi–shelled NiO hollow spheres: easy hydrothermal synthesis and lithium storage performances. J. Alloys Compd. **685**, 8–14 (2016)

Xu, H., Wang, W.: Template synthesis of multishelled Cu2O hollow spheres with a single–crystalline shell wall. Angew. Chem. **119**, 1511–1514 (2007)

Yiamsawas, D., Baier, G., Thines, E., et al.: Biodegradable lignin nanocontainers. RSC Adv. **4**, 11661–11663 (2014)

Yu, L., Wu, H.B., Lou, X.W.D.: Self–templated formation of hollow structures for electrochemical energy. Acc. Chem. Res. **50**, 293–301 (2017)

Yu, L., Yu, X.Y., Lou, X.W.: The design and synthesis of hollow micro–/nanostructures: present and future trends. Adv. Mater. **30**, 1–27 (2018)

Analysis and Modeling of the Process of Metal Separation from the Aqueous Phase in a Pseudo-emulsion Based Hollow Fiber Strip Dispersion

Katarzyna Staszak[1(✉)], Karolina Wieszczycka[1], Maciej Staszak[1], M. Teresa A. Reis[2], and M. Rosinda C. Ismael[2]

[1] Institute of Chemical Technology and Engineering, Poznan University of Technology, Poznan, Poland
Katarzyna.Staszak@put.poznan.pl
[2] CERENA – Centre for Natural Resources and the Environment, Department of Chemical Engineering, Instituto Superior Técnico, Universidade de Lisboa, Lisbon, Portugal

Abstract. Novelty extractants from the group of pyridine derivatives: N-(2-ethylhexyloxy)pyridine-3-cabroxyimidoamide and N-decyloxy-1-pyridin-3-yl) ethaneimine as the carriers in the palladium(II) ions extraction from chloride media through pseudo-emulsion based Hollow Fiber membrane strip dispersion (PEHFSD) were presented. The recovery of Pd(II) was around 99% for conditions tested. Moreover usefulness of quantum molecular modeling and engineering calculations in description palladium(II) ions separation process was showed. Quantum molecular modeling results indicated that there is no intermolecular bond between molecules of extractant, thus extractant association do not occur in this system. It is very important because the association phenomena change the optimum strength of the extractant needed to obtain a maximal metal transfer. The application of mass balance equations allow to estimate overall mass transfer coefficient and in consequence describe the kinetics of metal permeation in PEHFSD system. The transport of palladium(II) was investigated as a function of extractant concentrations. The overall mass transfer coefficient of permeation was calculated from the experimental data, the values being found in the range of $5.0 \cdot 10^{-6}$ to $0.14 \cdot 10^{-6}$ m/s.

1 Introduction

The current situation on the global metal market, associated with the rapid depletion of natural sources and the growing requirements in the field of environmental protection, makes it necessary to look for cheap, efficient and selective methods of recovery of metal ions from wastewater. This problem is very important especially in the case of platinum group metals (PGMs), because the recovery from secondary sources is more profitable than their mining from increasingly poorer ores (Wieszczycka et al. 2018).

© Springer Nature Switzerland AG 2020
M. Ochowiak et al. (Eds.): PAIC 2019, *Practical Aspects of Chemical Engineering*, pp. 441–451, 2020.
https://doi.org/10.1007/978-3-030-39867-5_46

Commonly used methods for concentrating and separating of metals from aqueous solutions are mainly precipitation methods (Raju et al. 2012), ion exchange (Wołowicz et al. 2019), electrolysis (Rögener et al. 2012) or liquid-liquid extraction (Rzelewska-Piekut et al. 2018). Unfortunately, in the case of precipitation and ion exchange methods, the purity of the separated metal is often insufficient and requires additional purification methods, while in the case of liquid-liquid extraction it is recommended to use rather high concentration of metal. Therefore the novel methods are still being searched. One of the proposition are membrane methods, such as nanofiltration (Al-Rashdi et al. 2013), ultrafiltration (Staszak et al. 2012), diffusion or Donnan dialysis (Çengeloğlu et al. 2001), and electrodialysis (Mohammadi et al. 2005). Moreover more specific solutions by enhanced membrane technique with extractant are also proposed. In this case, there is possibility to prepare novel liquid membranes such as polymer inclusion membranes (Baczyńska et al. 2018) or emulsion liquid membranes (Dong et al. 2018). However, the development of such methods is mainly associated with the possibility of using Hollow Fiber membrane modules (HF) for the selective separation of metals from multi-component solutions. Such modules carry out both single extraction or re-extraction (stripping) processes (Chaudhury et al. 2019) as well as simultaneous extraction and re-extraction in pseudo-emulsion systems (Pseudo-Emulsion based Hollow Fiber Strip Dispersion - PEHFSD) (Sonawane et al. 2010; Roy et al. 2008; Wieszczycka et al. 2015; Staszak et al. 2017; Wojciechowska et al. 2018). The use of the HF module in a pseudo-emulsion system, where the process is additionally supported by a selective and efficient extractant, promotes the selective separation of metal ions, which allows them to be obtained from waste solutions.

The separation and purification in PEHFSD processes strongly depend on the properties of extractants applied. Therefore the novel metal carriers based on synthesized compounds containing both the N-alkoxyimine (CH_3(H)-C=N-OR) or N-alkoxyimidamide (NH_2-C=N-OR) and pyridine ring were proposed here. Previous investigations showed that these extractants, as well as metal complexes, were characterized by high stability in contact with strong inorganic acids. Moreover, the classical extraction with such compounds showed high efficiency for metal ions recovery (Wojciechowska et al. 2017; 2019).

The aim of this study was to investigate the possibility of using quantum molecular modeling and engineering calculations in the process of palladium(II) ions separation from aqueous solutions using pseudo-emulsion based Hollow Fiber strip dispersion technique with employing new extractants from the group of pyridine derivatives: *N*-(2-ethylhexyloxy)pyridine-3-cabroxyimidoamide (Eh-3-IA) and *N*-decyloxy-1-pyridin-3-yl)ethaneimine (D-3-EI).

2 Experimental

The PEHFSD experiments were carried out using Liqui-Cel® Extra-Flow 2.5 in. ×8 in. membrane contactor from Celgard (USA). Two tanks, each with 800 mL volume: one with feed solutions containing aqueous solutions of 100 ppm Pd(II) and 1.5 M HCl, and second one with mixture of organic phase (0.08–0.83% of selected extractants

in toluene) and stripping solutions (aqueous solutions of 0.01 M thiourea and 0.1 M HCl). The aqueous feed solution flowed through the lumen (tube side) of the fibers, while pseudo-emulsion flowed through the shell side of the fibers. Before each experiment, pores of the membrane were wetted by the organic phase and stable liquid membrane supported was formed. To avoid the leakage of the organic solution (strip dispersion) to the aqueous side through the pores a low pressure differential (about 30 kPa) between the aqueous feed solution side and the strip dispersion side was used. Both phases were circulated in a closed circuit to a constant value of the palladium(II) concentration in the aqueous phase (30 min–3 h, depending on the experimental conditions). The schema of the experimental is shown in Fig. 1.

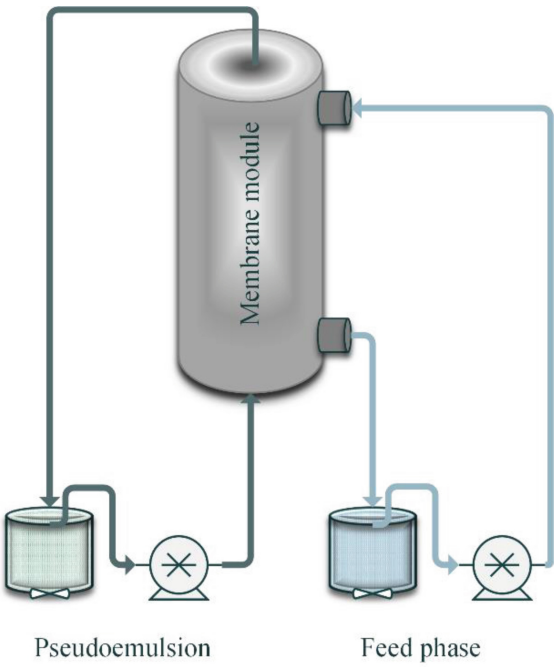

Fig. 1. PEHFSD experimental setup

At various time intervals, samples of the aqueous phase were taken to determine the content of Pd(II) ions using AAS Perkin Elmer-AAnalyst 200 in the air-acetylene flame.

From the practical point of view, it was important to keep the stable pseudoemulsion during the process and to separate the stripping and organic phases as soon as the process stopped, to avoid further transport. Because of the formation and separation of emulsions depends on interfacial phenomena and the presence of surface-active compounds, interfacial tension of extractants was also measured using the Du Noüy ring method with K12 tensiometer from Krűss (Germany).

3 Results and Discussions

3.1 Topology of the Electron Density

Quantum molecular modeling was applied to obtain information about the behavior of extractants molecules in the system. The geometric properties of atoms and molecules are determined by the distribution of electron density. According to VSEPR theory (Sidgwick and Powell 1940; Petrucci et al. 2002) (Valence Shell Electron Pair Repulsion) the molecular geometry results from the valence electrons which may constitute bonds or exist as lone pairs. The repulsion forces between electrons are the key element, which shapes the molecule. The implementation of the VSEPR theory can be done by calculating the molecule electron density spatial distribution and applying Laplacian functional on it. The electron density field for a molecule can be obtained by means of Schrödinger equation solving for quantum many-body problem, namely system of many interacting particles.

There exist several general techniques to solve this equation, for example Density Functional Theory (DFT), Quantum Monte Carlo family of methods, approximation algorithms of Perturbation Theory, Hartree-Fock and post-Hartree-Fock methods, to name a few. This work contains the results obtained by the latter, Hartree-Fock, due to its robustness. Main concept of this well-known method is to describe the quantum multibody system by Slater determinant, a formulation which defines the wave function of a multi-electron or in general multi-fermionic systems. The assumption which is often held in the Hartree–Fock method is that the N-body wave function can be described by a single Slater determinant as an approximation to the solution of the Schrödinger equation. Accurate representation of molecular structure was considered by selecting specific basis function. To account for asymmetry of molecular orbitals, the chosen basis set is 6-311G++(d, p). The d-type functions with valence p orbitals were added to a basis set together with the diffuse functions indicated by + sign, which more precisely characterize the distant parts of the atomic orbitals, which are remotely located from the atomic nuclei.

Estimated electron density field (expressed in atomic units e/a_0^3) by Hartree-Fock method is then used for Laplacian calculation, defined as the divergence of the gradient, according to the following formula (1):

$$\Delta\rho = \nabla^2\rho = \nabla \cdot \nabla\rho \tag{1}$$

The Laplacian density field obtained is then used to construct the relief map of selected molecule. The electron density Laplacian renders the shell character of a molecule by presenting equivalent number of interchanging shells of high charge and low charge concentrations. For a free atom the uniform sphere of charge concentration is expected in the valence electron orbit, on the other side in the molecule structure of atoms it is distorted by chemical rearrangement to create local maxima and minima.

The high values of Laplacian refer to the electron shells of nucleophilic character while the minimum values correspond to electrophilic character. The zero value iso-surface is defined as reactive surface, which envelops the space of highest electronic charge.

The Fig. 2 clearly presents that no electron pair between ring nitrogen atom of one molecule and oxygen of other molecule forms any type of bond. The distance between both atoms is 8.18764 Å, which is indicated by the arrowline on the graphical presentation of both molecules. The calculations performed do not confirm existence of intermolecular bond between both atoms. Moreover, the confirmation of the lack of interaction between two molecules of Eh-3-IA are presented in Fig. 3. Observes maximums of Laplacian of electron density correspond to the presence of electronic shells in molecules.

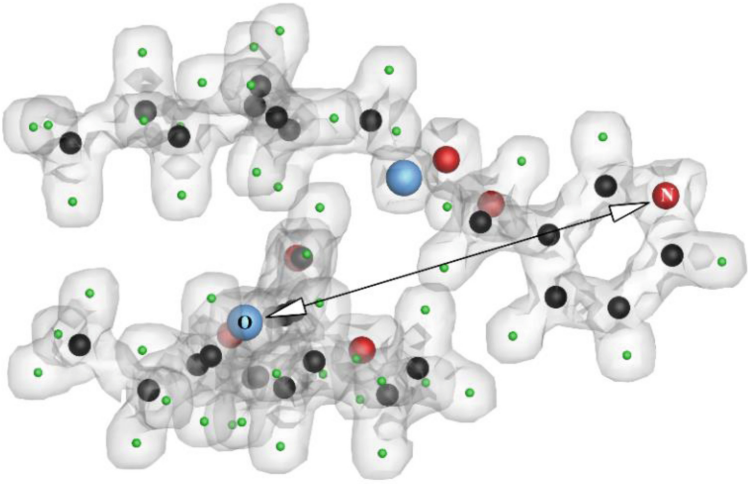

Fig. 2. Bonding regions indicted by Laplacian of isovalue -0.0001 for two Eh-3-IA molecules (indicated distance is 8.18764 Å).

Thus, according to the quantum molecular modeling results it could be concluded that extractant association do not occur in this system. It is very important because the association phenomena (extractant association, modifier association and extractant-modifier co-association) change the optimum strength of the extractant needed to obtain a maximal metal transfer. The change of extraction properties may be due to the change of the mobility of self-associates. On the other hand the surface concentration of the extractant molecules, which are able to complex metal ions, can be reduced by formation of extractant-extractant associates at the hydrocarbon/water interface. Moreover, there is no competition in access to the active complex-forming extractant group for metal ions.

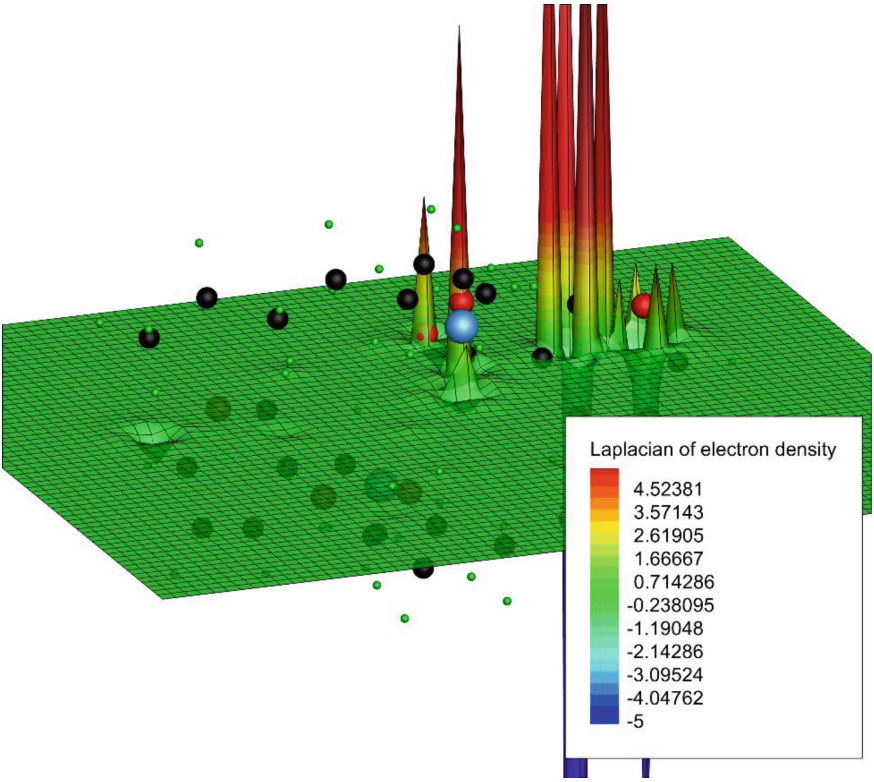

Fig. 3. Relief map of Laplacian of electron density for two Eh-3-IA molecules, in $[e/a_0^5]$.

3.2 PEHFSD

Preliminary study showed that extractants studied adsorb at the liquid-liquid interface and reduce the interfacial tension (see Fig. 4). These studies confirmed possibility to apply these carriers in PEHFSD investigations. The pseudo-emulsions formed in the system were stable during whole processes and did not show any adverse coalescence phenomenon. Moreover, after the end of the processes, its rapid separation occurred.

The exemplary results of transport Pd(II) ions in PEHFSD system are presented in Fig. 5. Almost complete extractions of palladium ions were obtained irrespective of extractant's concentration – 98.6, 98.6 and 99.1%, for c = 0.08, 0.28 and 0.83%, respectively. Nevertheless, the time needed to reach equilibrium strongly depends on the amount of extractant in the system – from 15 min for the highest concentration of D-3-EI (0.83%) to 2.5 h for the lowest concentration of D-3-EI (0.08%). Thus, it could be concluded that kinetics of Pd(II) extraction strongly depend on pyridine oxime-ether carrier. Similar relationship was observed by Reis et al. (2019) for zinc(II) ions.

The model for the transport of palladium(II) ions in PEHFSD is based on several mass balance equations (Agarwal et al. 2014).

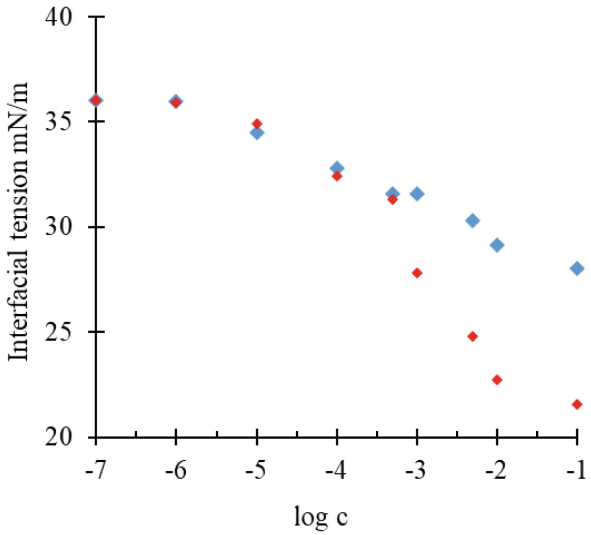

Fig. 4. Equilibrium interfacial tensions isotherms for Eh-3-IA (red) and D-3-EI (blue) in water/toluene systems, c in mol/dm^3.

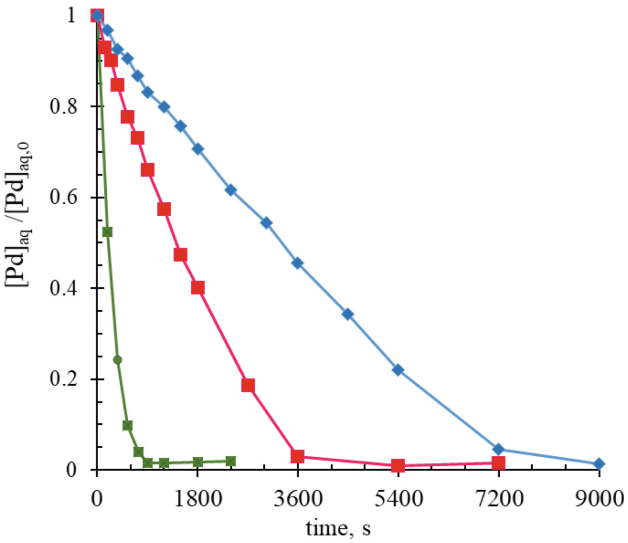

Fig. 5. Effect of the extractant concentration (D-3-EI) on Pd(II) ions extraction in PEHFSD, c = 0.83% (green), 0.28% (red) and 0.08% (blue).

Module mass balance for the feed solution:

$$\frac{d[Pd]_{aq}^{M}}{dt} = -u_{aq}\frac{d[Pd]_{aq}^{M}}{dz} - \left(\frac{A}{V_M}\right)_{in} \cdot K_p([Pd]_{aq}^{M} - [Pd]_{str}^{M}) \tag{2}$$

Tank mass balance for the feed solution:

$$\frac{d[Pd]_{aq}^{T}}{dt} = \frac{Q_{aq}}{V_{aq}}([Pd]_{aq,z=L}^{M} - [Pd]_{aq,z=0}^{M}) \tag{3}$$

Module mass balance for the stripping solution:

$$\frac{d[Pd]_{str}^{M}}{dt} = -u_{str}\frac{d[Pd]_{str}^{M}}{dz} - \left(\frac{A}{V_M}\right)_{out} \cdot K_p([Pd]_{aq}^{M} - [Pd]_{str}^{M}) \tag{4}$$

Tank mass balance for the stripping solution:

$$\frac{d[Pd]_{str}^{T}}{dt} = \frac{Q_{str}}{V_{str}}([Pd]_{str,z=0}^{M} - [Pd]_{str,z=L}^{M}) \tag{5}$$

With the assumption that the stripping reaction is instantaneous, thus $[Pd]_{str}^{M} = 0$ and $[Pd]_{str}^{T} = 0$, the solution of Eqs. (2)–(5) is as follows:

$$V_{aq}\ln\frac{[Pd]_{aq,t=0}^{T}}{[Pd]_{aq}} = Q_{aq}\left[1 - \exp\left(\frac{2K_pL}{u_{aq}r_i}\right)\right]t = S \cdot t \tag{6}$$

In these equations L is the fiber length, Q is the flow rate of the phases, u is the linear velocity, V is the volume of each phase, K_P is the overall mass transfer coefficient, r_i is inner radii of the hollow fiber, S is the slope of this linear relationship which is illustrated in Fig. 6. The superscripts M and T refer to the membrane module and tank, respectively. The subscripts *aq* and *str* refer to the aqueous feed and stripping phase, respectively.

Based on the experimental results values of the overall mass transfer coefficient for all experiments are presented in Fig. 6.

The influence of the concentration of D-3EI on the kinetics of Pd(II) extraction was confirmed also by the value of overall mass transfer coefficient. The decrease in the concentration of extractant reduced the K_P coefficient from $5.0 \cdot 10^{-6}$ to $0.14 \cdot 10^{-6}$ m/s. However, it should be noted that this change is not proportional - reducing the concentration ten times resulted in a reduction in the value of overall mass transfer coefficient up to 30 times. In fact, the decrease in K_P coefficient might be due to the significant increase in the contribution of the reaction resistance with the reduction of the extractant concentration.

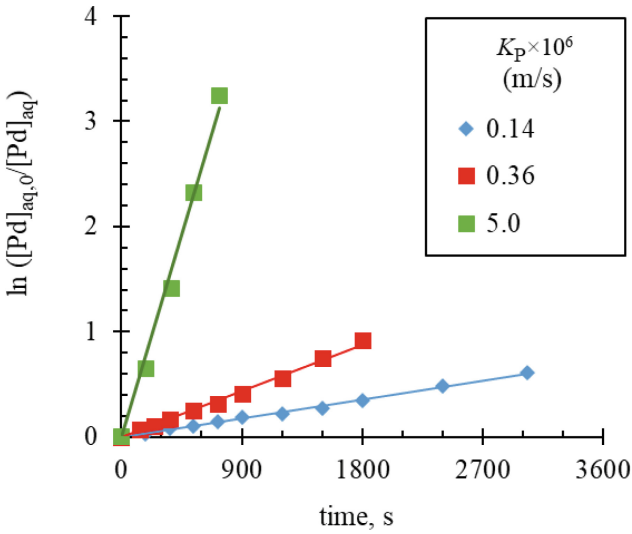

Fig. 6. Determination of the overall mass transfer coefficient K_P of Pd(II) with the effect of extraction concentration: c = 0.83% (green), 0.28% (red) and 0.08% (blue).

4 Conclusions

The investigations showed that the proposed novel extractants can be used to separate metals from the aqueous phase in a pseudo-emulsion system using Hollow Fiber type membrane modules.

The usefulness of quantum molecular modeling in the assessment of interactions between extractant molecules has been demonstrated. Obtained results suggested that there is no intermolecular bond between molecules of extractant.

The application of mass balance equations allow to estimate overall mass transfer coefficient and in consequence describe the kinetics of metal permeation in PEHFSD system.

Acknowledgements. This work is co-financed by the Polish National Agency for Academic Exchange (Grant No PPN/BIL/2018/1/00200) "Novel carriers at HF system for selective recovery of precious metal ions from waste sources" and by the Polish Ministry of Science and Higher Education (Grants No. 03/32/SBAD/0910).

PEHFSD studies were realized in the frame of Polish-Portuguese scientific and technological cooperation for the years 2019–2020. "Novel carriers at HF system for selective recovery of precious metal ions from waste sources". Financial support through the project UID/ECI/04028/2019 from the "Fundação para a Ciência e a Tecnologia" (FCT, Portugal) is also acknowledged.

References

Agarwal, S., Reis, M.T.A., Ismael, M.R.C., Carvahlo, J.M.R.: Zinc extraction with Ionquest 801 using pseudo-emulsion based hollow fibre strip dispersion technique. Sep. Purif. Technol. **127**, 149–156 (2014)

Al-Rashdi, B.A.M., Johnson, D.J., Hilal, N.: Removal of heavy metal ions by nanofiltration. Desalination **315**, 2–17 (2013)

Baczyńska, M., Słomka, Ż., Rzelewska, M., Waszak, M., Nowicki, M., Regel-Rosocka, M.: Characterization of polymer inclusion membranes (PIM) containing phosphonium ionic liquids and their application for separation of Zn(II) from Fe(III). Chem. Technol. Biotechnol. **93**(6), 1767–1777 (2018)

Çengeloğlu, Y., Kir, E., Ersöz, M.: Recovery and concentration of Al(III), Fe(III), Ti(IV), and Na(I) from red mud. J. Colloid Interf. Sci. **244**(2), 342–346 (2001)

Chaudhury, S., Ansari, S.A., Mohapatra, P.K., Noronha, D.M., Pillai, J.S., Srivastave, A., Pius, I. C.: Demonstration of Hollow Fiber membrane technique for the recovery of plutonium from analytical laboratory waste. Nuclear Technol. **205**(5), 727–735 (2019)

Dong, K., Xie, F., Kuang, K., Wang, W.: Recovery of copper and cyanide through emulsion liquid membrane with quaternary amine salt as the mobile carrier. Min. Proc. Ext. Met. Rev. (2018). https://doi.org/10.1080/08827508.2018.1538984

Mohammadi, T., Moheb, A., Sadrzadeh, M., Razmi, A.: Modeling of metal ion removal from wastewater by electrodialysis. Sep. Purif. Technol. **41**(1), 73–82 (2005)

Petrucci, R.H., Harwood, W.S., Herring, F.G.: General Chemistry: Principles and Modern Applications, 8th edn. Prentice-Hall, Upper Saddle River (2002)

Raju, B., Kumar, J.R., Lee, J.-Y., Kwonc, H.-S., Kantam, M.L., Reddy, B.R.: Separation of platinum and rhodium from chloride solutions containing aluminum, magnesium and iron using solvent extraction and precipitation methods. J. Hazard. Mater. **227–228**, 142–147 (2012)

Reis, M.T.A., Ismael, M.R.C., Wojciechowska, A., Wojciechowska, I., Aksamitowski, P., Wieszczycka, K., Carvalho, J.M.R.: Zinc(II) recovery using pyridine oxime-ether – novel carrier in pseudo-emulsion hollow fiber strip dispersion system. Sep. Purif. Technol. **223**, 168–177 (2019)

Rögener, F., Sartor, M., Bán, A., Buchloh, D., Reichardt, T.: Metal recovery from spent stainless steel pickling solutions. Resour. Conserv. Recy. **60**, 72–77 (2012)

Roy, S.C., Sonawane, J.V., Rathore, N.S., Janarda, P., Changrani, R.D., Dey, P.K., Bharadwaj, S.R.: Pseudo-emulsion based hollow fiber strip dispersion technique (PEHFSD): optimization, modelling and application of PEHFSD for recovery of U(VI) from process effluent. Sep. Sci. Technol. **43**(11–12), 3305–3332 (2008)

Rzelewska-Piekut, M., Janiszewska, M., Staszak, K., Regel-Rosocka, M.: Study on transport of metal ions in selected separation systems. Przem. Chem. **97**(12), 2045–2049 (2018)

Sidgwick, N.V., Powell, H.M.: Bakerian Lecture. stereochemical types and valency groups. Proc. Roy. Soc. Lond. Ser. A, Math. Phys. Sci. **176**(965), 153–180 (1940)

Sonawane, J.V., Pabby, A.K., Sastre, A.M.: Pseudo-emulsion based hollow fibre strip dispersion (PEHFSD) technique for permeation of Cr(VI) using Cyanex-923 as carrier. J. Hazard. Mater. **174**(1–3), 541–547 (2010)

Staszak, K., Konopczyńska, B., Prochaska, K.: Micellar enhanced ultrafiltration as a method of removal of chromium(III) ions from aqueous solutions. Sep. Sci. Technol. **47**(6), 802–810 (2012)

Staszak, K., Wojciechowska, A., Reis, M.T.A., Wojciechowska, I., Wieszczycka, K., Ismael, M. R.C., Carvalho, J.M.R.: Recovery of zinc(II) from chloride solutions using pseudo-emulsion based hollow fiber strip dispersion with pyridineketoxime extractants. Sep. Purif. Technol. **177**, 152–160 (2017)

Wieszczycka, K., Regel-Rosocka, M., Staszak, K., Wojciechowska, A., Reis, M.T.A., Ismael, M. R.C., Gameiro, M.L.F., Carvalho, J.M.R.: Recovery of zinc(II) from chloride solutions using pseudo-emulsion based hollow fiber strip dispersion (PEHFSD) with 1-(3-pyridyl) undecan-1-one oxime or tributylphosphate. Sep. Purif. Technol. **154**, 204–210 (2015)

Wieszczycka, K., Tylkowski, B., Staszak, K.: Metals in Wastes. De Gruyter (2018)

Wojciechowska, A., Reis, M.T.A., Wojciechowska, I., Ismael, M.R.C., Gameiro, M.L.F., Wieszczycka, K., Carvalho, J.M.R.: Application of pseudo-emulsion based hollow fiber strip dispersion with task-specific ionic liquids for recovery of zinc(II) from chloride solutions. J. Mol. Liq. **254**, 369–376 (2018)

Wojciechowska, I., Wieszczycka, K., Aksamitowski, P., Wojciechowska, A.: Copper recovery from chloride solutions using liquid extraction with pyridinecarboximidamides as extractants. Sep. Purif. Technol. **187**, 319–326 (2017)

Wojciechowska, I., Wieszczycka, K., Wojciechowska, A., Aksamitowski, P.: Ether derivatives – efficient Fe(III) extractants from HCl solution. Sep. Purif. Technol. **209**, 756–763 (2019)

Wołowicz, A., Staszak, K., Hubicki, Z.: Static sorption of heavy metal ions on ion exchanger in the presence of sodium dodecylbenzenesulfonate. Adsorption **25**, 393–404 (2019)

Comparison of Emulsification in a Sieve Emulsification Mixer, Homogenizer and Mechanical Mixer

Waldemar Szaferski[1(✉)], Dorota Siuta[2], Bożena Kukfisz[3], and Krystian Czernek[4]

[1] Institute of Chemical Technology and Engineering, Faculty of Chemical Technology, Poznan University of Technology, Poznań, Poland
waldemar.szaferski@put.poznan.pl
[2] Faculty of Process and Environmental Engineering, Lodz University of Technology, Lodz, Poland
[3] Faculty of Security Engineering and Civil Protection, The Main School of Fire Service, Warsaw, Poland
[4] Department of Process Engineering, Opole University of Technology, Opole, Poland

Abstract. The formation of liquid-liquid mixtures is frequently required in the chemical industry and related sectors. Improvement or introduction of new methods and constructions which reduce the energy consumption, without compromises in terms of final product quality, is important. This study discusses three types of emulsion preparation methods, among which mechanical mixing and homogenization are well known, while the sieve emulsification mixing (SEM) is less known. The application of the last method is foreseen in the preparation of cosmetic emulsions and in the metallurgical industry during mechanical levelling of metal alloy objects. The tested apparatus is designed to produce a highly dispersed oil-water mixture, with the smallest possible size of the droplets created. Droplets were analysed on the basis of the average diameters d_{32} and d_{43}. The used SEM configuration allowed to achieve smaller droplet diameters than the standard mechanical mixer, although they were not as small as in the case of the homogenizer.

1 Introduction

Emulsions are systems which possess a wide range of applications. They are used in the paint industry to produce emulsion paints and in pharmaceuticals to manufacture medicines for both external and internal use. They are also employed in the bitumen industry as materials for the construction of road surfaces. The possibility of obtaining a high degree of dispersion of the particles and the phenomenon of coalescence which occurs in emulsions determine the special value of emulsions in the food industry as edibles. On other hand, dairy products can be emulsions of natural origin, such as milk and cream, or artificially made sauces and mayonnaises. With respect to the cosmetics

© Springer Nature Switzerland AG 2020
M. Ochowiak et al. (Eds.): PAIC 2019, *Practical Aspects of Chemical Engineering*, pp. 452–460, 2020.
https://doi.org/10.1007/978-3-030-39867-5_47

industry, emulsions can be used in liquid form, as cosmetic lotions, and in the semi-solid form, as creams. During the preparation of cosmetic emulsions, it is crucial to ensure that they do not cause skin irritation, as the skin easily absorbs components of O/W (Oil-in-Water) emulsions, despite its low affinity for hydrophobic substances. Artificial emulsions are prepared in a process called emulsification, which can be carried out using mechanical mixing, a static mixer, homogenizer, vortex atomizer, with the use of ultrasound, membranes or in flow through porous media.

Mechanical mixing is one of the most popular techniques, which utilizes an agitator. As a result of rotation of the agitator, the mechanical power is used to disperse phases by delivering turbulences into the system, which cause the movement of fluids elements, break the phases and distort large droplets, breaking and mixing them. Consequently, the emulsion is formed. In general, emulsification consists of two stages. The first is focused on the preparation of a pre-emulsion in which the two phases and the emulsifier are mixed to form a primary emulsion. Structural elements, geometry of the mixer and the type of material influence the size of internal droplets. Physico-chemical properties and volume fraction of emulsion phases are extremely important. Intensity of mixing, amount of delivered power and the frequency of rotations are also very important, because smaller size of droplets are usually formed when the frequency of rotations increases.

High-speed mixers, turbine and propeller mixers in particular, are the most popular among mechanical mixers. The selection of the agitator is one of the most important parameters which influences the properties of the emulsion. The diameters of droplets produced during mechanical mixing are a result of the dynamic equilibrium between the scattering and the coalescence forces (Koch 1992). The effectiveness and wide use of mechanical mixers are confirmed by numerous publications. Broniarz-Press and Tarnicka (2013) showed that the droplet diameters of the internal phase decreases with the increase of mixing time using a mechanical agitator and then become fixed at a constant level. The particle size obtained by this technique also depends on the used stabilizer.

Another method of emulsification utilizes homogenizers, which can be equipped with various types of endings, mostly with the rotor-stator type. Usually, that method consists of three stages. The first is the initial emulsification, namely the mixing of the emulsifier with the emulsion phases. Then the second part occurs, during which the droplets are deformed and disintegrated. The last step is stabilization, which involves the formation of a stabilizing film around the droplets constituting the inner phase. If rapid adsorption occurs, the droplets are not formed. In order to obtain the largest possible disintegration of the dispersed phase, the process of emulsion production should be carried out at high frequency of rotation of the homogenizer rotor (Bąk and Podgórksa 2015).

In order to optimize the process of producing emulsions used in the cosmetic, industrial machine tools and the automotive industry, an attempt was made to develop a novel method of producing emulsions using the sieve emulsification mixer (SEM). This apparatus, in addition to mechanical mixing, uses a sieve bottom and pump configuration to create droplets during the introduction of dispersed phase and to homogenize

the whole mixing volume during circulation mode. The first tests for such construction were carried out using a 20 μm sieve and a tank with an internal diameter of 210 mm (Mitkowski and Szaferski 2016). The researchers used vegetable oil and a 2% aqueous solution of polyoxyethylenesorbitan monopalmitate Tween 40 to demonstrate the potential possibilities of that apparatus and, at the same time, direct future work to find relationships between different mesh sizes, distances between adjacent meshes and process parameters (liquid flow rate, agitator rotational frequency) (Mitkowski and Szaferski 2016; Różanski et al. 2018).

2 Experimental Set-Up and Analysis

The experiments were performed with use of three experimental configurations: sieve emulsification mixer (Fig. 1a), mechanical mixer (Fig. 1b) and homogenizer (Fig. 1c). A tank with an internal diameter of 110 mm was the common element for all configurations. Regardless of which configuration was used, the elevation height was equal to 30 mm. In case of the mechanical mixer and the SEM, the dispersion element was a standard disk agitator with six blades (i.e. Rushton turbine). In case of SEM, constant rotational frequency of 5 s^{-1} was applied. The stirrer's rotation was selected to ensure that the stirrer's movement spreads the mixture in the apparatus, but at the same time it does not directly influence the emulsion production. Similarly, the lack of baffles was employed to avoid the influence of these elements on the process and to ease the cleaning process.

In the SEM configuration, the oil phase was introduced through the sieve bottom with 200 μm or 400 μm mesh delivered by Metalex (Gliwice, Poland). All substrates were introduced into the mixer using the TH-15 peristaltic pump from Aqua-Trend (Łódź, Poland). In case of the homogenizer, the Ultra Turrax T-50 digital homogenizer with dispersing tip G45F was used, which was also used in (Rózańska et al. 2013, 2014).

Rheological measurements were carried out using the Anton Paar Physica MCR 501 rheometer. The selection of oils was based on the possibility of comparing the impact of the oil phase on the work of individual apparatus and in order to checking the possibility of using the SEM mixer in various sectors of the industry.

In case of mechanical mixing and homogenizer, the analysis of emulsion samples consisted of taking microscopic images using the MultiScaneBase program and a Nikon Eclipse 50i microscope equipped with an Opta-Tech camera with a tenfold zoom. Measurements were conducted 5 min after delivering all components, and subsequent samples were taken every 15 min for a period of 75 min.

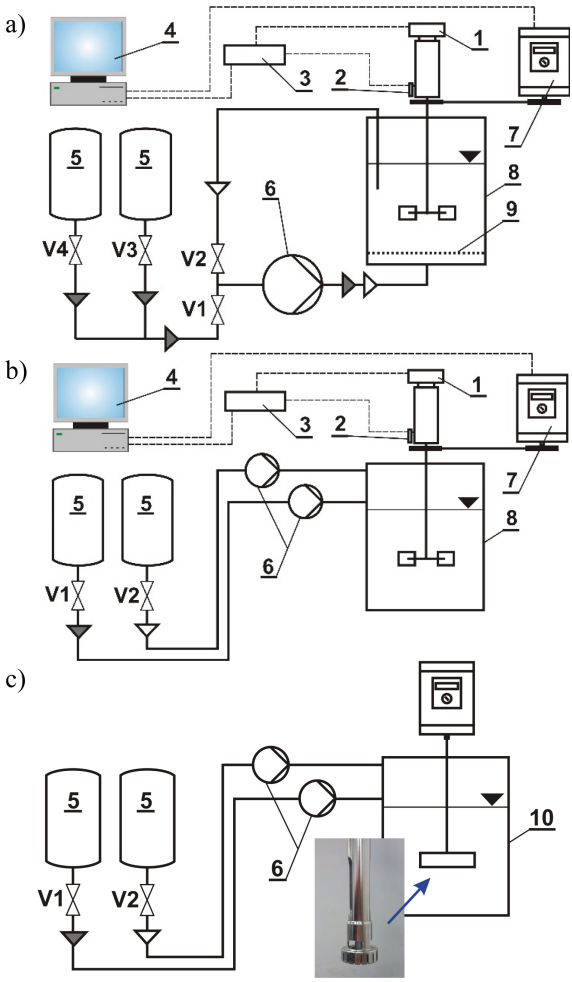

Fig. 1. Diagram which presents the experimental set-up used in experimental tests: (a) sieve emulsification mixer, (b) mechanical mixer, (c) homogenizer 1 - system of clamping and bearing of the stirrer shaft, 2 - turning sensor, 3 - torque meter, 4 - computer, 5 - substrate tank, 6 - pump, 7 - motor and inverter, 8 - tank, 9 - sieve bottom, V1, V2, V3, V4 - valves

In case of the SEM mixer, the measurements were carried out during several stages. The first stage ended when all the components of the emulsion were delivered to the apparatus, and the measurement was carried out after 5 min. At this point, the second stage followed, during which closed circulation was activated, which allowed the resulting emulsion to continuously pass through the sieve bottom. Measurements were also carried out every 15 min for a period of 75 min. Closed loop was carried out for mass flow rate of 326.4 g/min.

After taking microscopic images using the MultiScaneBase program, each image was analysed using the MatLab 2017 program with the imfindcircles function, which is

based on the Hough transformation. Hough's method is based on the detection of regular shapes in computer vision. The first stage of analysis in that program was to write a formula according to which the program will run and to use functions which improve its quality. Before starting the process, an analysis of a single photo from a series of tests was performed for all photos in order to select appropriate parameters such as diameter range, sensitivity and edge gradient threshold.

3 Materials

Oil-in-water emulsions consisted of commercial almond or mineral oils, and aqueous solution containing 5% of Tween 80 as emulsifier. Almond oil is characterized by density of 915 g/cm^3 and viscosity of 0.0747 Pa•s and mineral oil Lotos 15 W/40 by density of 860 g/cm^3 and viscosity of 0.168 Pa•s.

4 Analysis of Experimental Researches

Based on the analysis of the microscopic images taken during the experiments, histograms were plotted for each sample which show the breakdown of droplets in given size ranges. All histograms were prepared based on 3500 up to approx. 5000 droplets. Figure 2 represents a histogram for an O/W emulsion of almond oil in SEM (Fig. 1a). Each column represents the specific range of droplets which is explicitly defined under the figure. It is noticeable that none of the droplet ranges reached 40%. In case of droplets with the smallest diameters range (6.24–30 μm) an increasing trend with emulsification time can be observed while in the range of 60–120 μm a decreasing trend occurred. Based on the obtained results, it can be assumed that prolonged mixing will increase the number of smallest droplets, however, noticeable stability of the number of droplets in the range of 30–60 μm may suggest that their content remains approximately constant over time in range of 33–38%. On the other hand, fractions containing bigger droplets did not change significantly over the processing time. Improvement of emulsion, understood as the increase of the fraction of smallest droplets, can be achieved by increasing the processing time.

When the process was carried out in a mechanical mixer (Fig. 1b), droplets in the range of 150–300 μm initially prevailed but their quantity decreased with the increase of the processing time. In turn, the number of droplets with diameters from slightly lower ranges (30–90 μm) began to increase with the processing time. Initially, the lowest range (6.24–30 μm) accounted for only 30% of all droplets, but with the next measurement their number increased by more than two times, followed by a further decrease of their content to 20% after 60 min. Failure to initiate a downward trend for this droplet size from the very beginning of sampling (10 min) may be caused by inaccurate breakage of the droplets by the mechanical mixer. The best result i.e. the

maximum number of droplets in the smallest range, was obtained after 20 min of mixing while after 60 min the number of very large droplets was still significant (more than 10%).

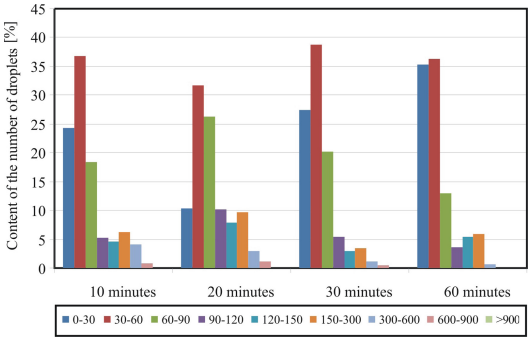

Fig. 2. Histogram obtained in SEM (see Fig. 1a) with mass flow rate of 326.4 g/min

All experiments were also analysed on the basis of differences in the values of mean equivalent diameters d_{32} and d_{43} over time defined according to Eqs. 1 and 2.

$$d_{32} = \frac{\sum_{i=1}^{N} n_i \cdot d_i^3}{\sum_{i=1}^{N} n_i \cdot d_i^2} \tag{1}$$

$$d_{43} = \frac{\sum_{i=1}^{N} n_i \cdot d_i^4}{\sum_{i=1}^{N} n_i \cdot d_i^3} \tag{2}$$

where: n – number of droplets in a given range, d – difference between the upper and lower range value.

Figures 3 and 4 present the dependence between d_{43} and time for emulsion of almond oil in water and mineral oil in water, respectively, for all three experimental set-ups. The data are qualitatively similar to the dependence of the d_{32} presented in Figs. 5 and 6. Both types of emulsions obtained the smallest equivalent diameters in the homogenizer configuration, regardless of the considered time. It can be seen that in comparison to the measurements carried out for the SEM configuration after 10 min, the SEM with 200 sieve gives better results for the system with mineral oil, while the SEM with 400 sieve is inferior. For both types of oils, the largest equivalent droplet diameters were obtained during experiments performed with use of a mechanical mixer (Fig. 1b).

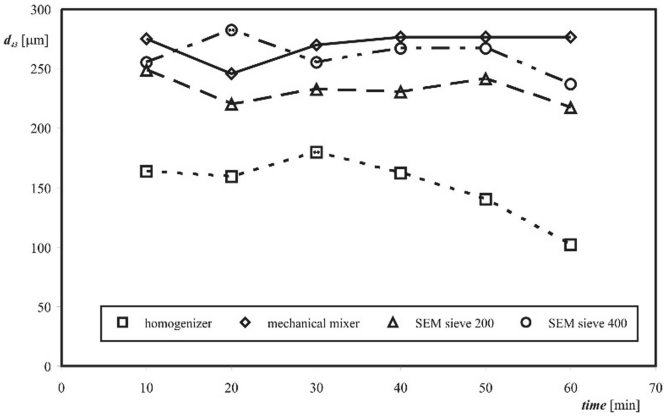

Fig. 3. Mean equivalent diameter d_{43} versus mixing time for almond oil

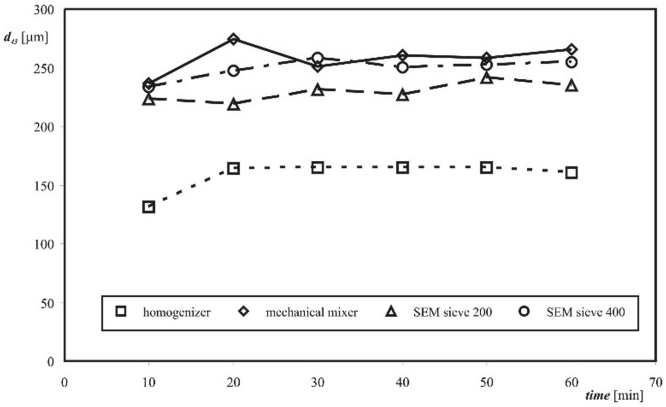

Fig. 4. Mean equivalent diameter d_{43} versus mixing time for miner oil

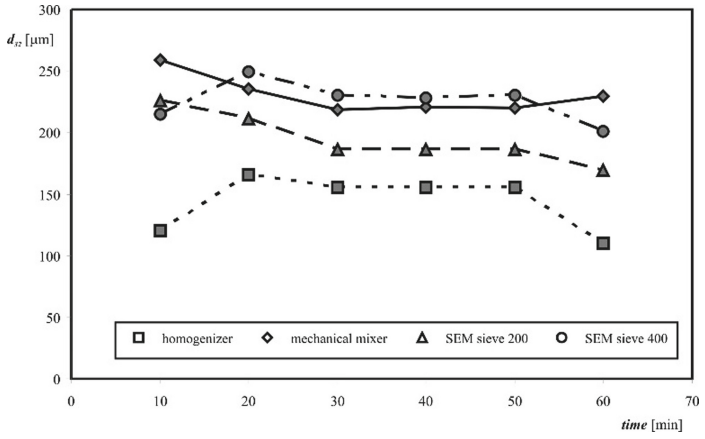

Fig. 5. Mean equivalent diameter d_{32} versus mixing time for almond oil

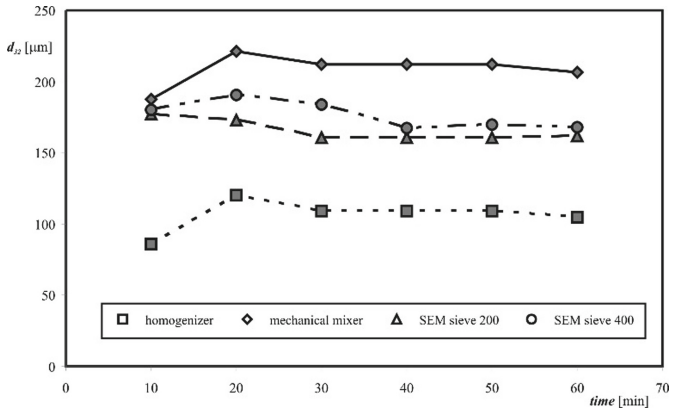

Fig. 6. Mean equivalent diameter d_{32} versus mixing time for miner oil

5 Conclusions

The determination of the emulsion production efficiency was based on the quality of the dispersed phase, namely the droplet size obtained in three different mixer configurations, which were compared in terms of the equivalent droplet diameters (d_{32} and d_{43}). The best emulsion was unequivocally obtained using the homogenizer, because the obtained values of equivalent diameters were the lowest. The least favourable results, which correspond to droplets with the largest diameters, were obtained using a mechanical mixer. The results obtained for SEM sieve 200 and SEM sieve 400 were similar.

Acknowledgements. This research was supported by the Ministry of Science and Higher Education in Poland subsidy for Poznan University of Technology, Faculty of Chemical Technology (Grand No.: 03/32/SBAD/0902). Authors would like to express many thanks for assistance in experimental work to Patrycja Jarmicka and Wiktoria Głowicka.

References

Bąk, A., Podgórksa, W.: Rozpad i koalescencja kropel w obecności aktywnego powierzchniowo polimeru PVA 88% (85000–124000). Inżynieria i Apar. Chem. **54**, 304–305 (2015)

Broniarz-Press, L., Tarnicka, Z.: Wpływ czasu mieszania na wielkośc kropli w emulsjach na bazie oleju rzepakowego. Inżynieria i Apar. Chem. **52**, 293–295 (2013)

Koch, R.: Procesy mechaniczne w inżynierii chemicznej. WNT, Warszawa (1992)

Mitkowski, P.T., Szaferski, W.: Production of emulsion in tank mixer with sieve bottom. Chem. Eng. Res. Des. **109**, 618–627 (2016). https://doi.org/10.1016/j.cherd.2016.03.014

Rózańska, S., Broniarz-Press, L., Rózański, J., et al.: Extensional viscosity of o/w emulsion stabilized by polysaccharides measured on the opposed-nozzle device. Food Hydrocolloids **32**, 130–142 (2013)

Różańska, S., Różański, J., Ochowiak, M., Mitkowski, P.T.: Extensional viscosity measurements of concentrated emulsions with the use of the opposed nozzles device. Brazilian J. Chem. Eng. **31**, 47–55 (2014). https://doi.org/10.1590/S0104-66322014000100006

Różanski, J., Różanska, S., Mitkowski, P.T., et al.: The flow of single- and multiphase fluids through nets and beds of spherical particles. Przem. Chem. **97**, 2040–2044 (2018)

Application of Flow Simulation Results in the Calculation of Gas Networks

Jolanta Szoplik(✉)

Faculty of Chemical Technology and Engineering,
West Pomeranian University of Technology, Szczecin, Poland
jolanta.szoplik@zut.edu.pl

Abstract. The paper presents examples of the possibility of an application of gas flow simulation results in the pipeline network to transport natural gas under low pressure. The study was carried out for a selected existing low-pressure network and real data, taking into account the variability of network load depending on the ambient temperature. The methodology of network characteristics preparation based on the results of gas flow simulation in the network and development of equations for estimating gas demand depending on the heating degree days index is presented. Next, two examples of practical application of flow simulation results in gas network calculations are presented. The first example presents the development of relationships between the minimum overpressure of the supply stream and the size of that stream, which makes it possible to maintain a lower overpressure in the whole network. The second example concerns the analysis of the storage capacity of the gas pipeline network for alternative gaseous fuels produced from surplus energy from renewable sources.

1 Introduction

Pipeline networks, commonly used to transport gaseous fuels over long distances, have a very complex structure and fluid dynamics that are difficult to describe. An additional difficulty in flow analysis is variability of the transported stream over time, depending on weather (temperature), calendar (day of the week, hour of the day) and economic (national income) factors. On the other hand, literature reports show that well-designed and optimally utilized network capacity may contribute to the reduction of gas transport costs, reduce gas losses resulting from network leakage or pipeline failure and have a positive impact on the environment.

One of the ways to obtain information about the dynamics of complex network systems operating in different conditions is to simulate the flow of gas in the network pipelines and to verify the results obtained with the actual data collected during system operation in given conditions. To describe changes occurring in network pipelines, depending on the level of gas overpressure in the network, classical equations of numerical fluid dynamics in differential form are used. The use of transient models is necessary for analyzing gas flow in the high-pressure network, while simpler steady state models can be used to describe changes in the low-pressure pipeline flow (Osiadacz 1987). However, regardless of the form of the equations adopted, the network

© Springer Nature Switzerland AG 2020
M. Ochowiak et al. (Eds.): PAIC 2019, *Practical Aspects of Chemical Engineering*, pp. 461–472, 2020.
https://doi.org/10.1007/978-3-030-39867-5_48

model consists of more or less detailed forms of the mass, momentum and heat balance equations and the flow equations. Osiadacz and Chaczykowski (2001), Chaczykowski (2010) analyzed the influence of thermal model type or state equation on the basic parameters characterizing the flow (pressure drop and gas temperature) and the accuracy of the numerical solution in a high-pressure gas pipeline. On the other hand, Matko et al. (2000) analyzed the influence of the model type (linear or nonlinear distributed parameter or linear lumped parameter) on the differences between the values of gas streams and pressures at the end of a high-pressure pipeline, obtained during simulation and using actual data.

The results of gas flow simulation in a gas pipeline or pipeline network provide a lot of information about changes in the flow and distribution of basic parameters characterizing the stream. Askari et al. (2015), Szoplik (2015) demonstrated that the results of gas flow simulation in the network can be used, for example, for fuel demand forecasting and pipeline capacity planning, while Monforti and Szikszai (2010), Lochner (2011), Voropai et al. (2012), Szoplik (2016; 2019) show that the results of the simulation can be used to increase network capacity and improve transportation. In turn, Reddy et al. (2006), Sun (2012) and Damavandi et al. (2011) indicate the possibility of using the results of the simulation to detect pipeline damages and localize gas leakages from the network. The vast majority of examples analyzed in the literature of numerical methods application in the calculation of gas networks are aimed at reducing the costs of gas transport to the consumers. Optimization of the gas network structure is based on minimizing the costs of gas transport and at the same time maximizing the efficiency of the network (2000), therefore, it is advisable to conduct research on lowering the costs of maintenance of the most energy-consuming elements of the network equipment. Depending on the structure and complexity of the network, the authors used various additional detailed models, which, in their opinion, have a significant impact on the modeling results obtained. Gato and Henriques (2005) stated that atypical changes in the gas flow may depend on the type of characteristics of the regulator or valve used in the calculations. Fasihizadeh et al. (2014) proposed a change in the network structure and basic input parameters, which was reflected in a reduction in the costs of gas transport. Nguyen and Chan (2006) used artificial intelligence methods to optimize the operation of compressors in high-pressure gas compressor stations. In turn, Staibach (2007) studied the effect of compressor switching on and off and valve opening and closing on the cost of fuel consumption in a gas compression plant. Simulation methods can also be used to increase the capacity of long-distance pipelines (Voropai et al. 2012) or to identify bottlenecks (Lochner 2011) that may arise in the future due to the growing demand for gas in Europe, while Lise and Hobbs (2008) analyzed the impact of changes in gas sales on the price and security of gas supply to Europe.

A brief description of the low-pressure pipeline network used to transport fuels, a methodology for preparing input data to simulate gas flow and two examples of practical use of the results of flow modeling in the network to control the gas flow in the network in order to minimize gas losses in case of pipeline failure and to estimate the storage capacity of the network for other gaseous fuels obtained from alternative energy sources will be presented. The analysis was prepared on the basis of actual gas pipeline network and data on network load.

2 Methods of Natural Gas Transport

Depending on the distance between the place of natural gas production and consumption and its composition, gaseous fuel may be transported in liquefied form by sea by methane carriers or in gaseous form by pipelines located below the surface of the earth (Thomas and Dawe 2003). However, regardless of the method of gas transporting to the country, gas is transported to final consumers via a three-stage pipeline network. The main streams of gas supplied to Poland are distributed throughout the country by means of a network of high-pressure pipelines (Szoplik 2012). Then, at the gas reduction station, the overpressure of the gas stream is reduced to the average value and the transport of gas through the medium-pressure network begins. Another reduction of the overpressure of the gas stream from medium to low value takes place in the second stage gas station, which is the beginning of the low-pressure gas network. The limitation for each network is the overpressure of the gas stream and the velocity of the stream in the pipeline. In the case of low-pressure network, the maximum gas velocity is 5 m/s and the gas overpressure can vary from 1700 Pa to 2500 Pa.

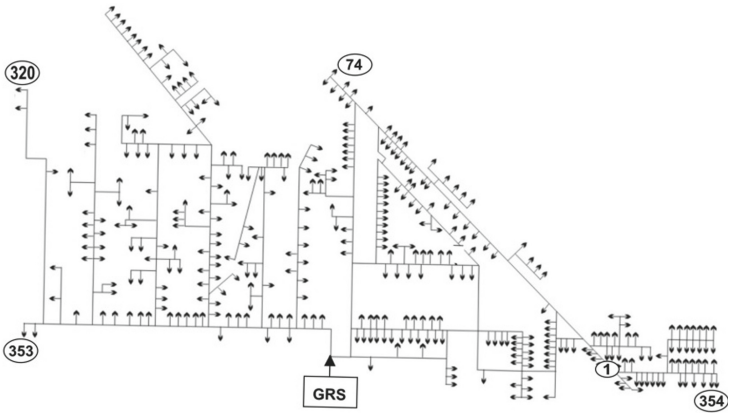

Fig. 1. Scheme of real low-pressure gas pipeline network; GRS – gas reduction station, 1 ÷ 354 – connections in which consumers receive gas (Szoplik 2016; 2019)

Failure to meet the condition of gas overpressure in the low-pressure network results in malfunctioning of the gas appliances installed in the customers, while the amount of gas overpressure in the network pipelines depends directly on the network load.

The diagram of the existing low-pressure gas network with one supply point (reduction and measurement station of the second stage GRS) and 354 exit points (end users) is shown in Fig. 1. The network is mostly made of steel gas pipelines (about 70% of the total length of the network) and polyethylene gas pipelines. The total length of all gas pipelines in the network is approximately 14.5 km of pipelines with nominal diameters ranging from 45 mm to 250 mm.

3 Preparation of Network Characteristics

The characteristics of the gas network are prepared on the basis of the results of gas flow simulation and are a map of the gas dynamics in the network pipelines, on the basis of which it is possible to analyze the operation of the network in different conditions. On the basis of data collected during many years of research and published in works (Szoplik 2012; 2015; 2016; 2019), it can be concluded that the network load is strongly dependent on the air temperature and time of day. Significantly higher network load is characteristic for days with lower temperature and in the morning hours compared to the network load at night on the days of the summer season. Example results of annual and daily variability of network load in one of the small towns are shown in Fig. 2.

Simulation of gas flow in the gas network (Fig. 1) requires the preparation of input data in the form of hourly gas streams drawn from the network at 354 exit points for different ambient temperatures. The daily demand for natural gas by the customer ($Q_{(NG)}$ [m^3/day]), depending on the air temperature T, can be presented by means of Eq. (1), which should be determined individually for each exit point from the network, because each customer has a different gas consumption characteristic.

$$Q_{(NG)} = a \cdot Sd + b = a \cdot (18 - T) + b \tag{1}$$

Air temperature T in Eq. (1) is presented as an indicator of heating degree days (Sd = 18 − T), which presents the demand for energy necessary to heat a room from temperature T to temperature 18 °C. The Sd value is greater than zero when T < 18 °C or Sd = 0 when T ≥ 18 °C. It was assumed in the calculations that the demand for gas in the connection depends on the air temperature (Eq. 1) only in case of recipients heating apartments, whereas for recipients who use gas only for the preparation of meals, the Eq. (1) is simplified to $Q_{(NG)} = b$. Parameters a and b of Eq. (1) are determined on the basis of the actual demand for natural gas in the connection registered in different periods of the year and for the actual air temperatures. The methodology of determining the parameters of the model (1) is presented on the example of data characterizing the gas consumption by the customer, which is settled on the basis of only three bills issued by the seller in a given calendar year. Table 1 summarizes the data necessary to determine the parameters of the model. The absolute term b represents gas consumption independent of the ambient temperature, so it is calculated as the quotient of gas consumption in the summer period (Sd = 0) and the number of days in that period (b = 88/61 = 1.44). The directional coefficient of the model (1) represents the gas consumption depending on the ambient temperature and, based on the data from Table 1 is calculated as follows:

$$a = \frac{\sum Q_{(NG)} - (\sum n \cdot b)}{\sum Sd} = \frac{1654 - (344 \cdot 1.44)}{2179} = 0.53$$

Based on Eq. (1), it is possible to estimate the daily gas demand in the network connection for any ambient temperature T (Sd = 18 − T).

Table 1. Data to determine the parameters a and b of the model (1)

Period	n number of days in period	Sd in period	$Q_{(NG)}$ [m^3/period]	$Q_{(NG)calc(1)}$ = 0.53Sd + 1.44n [m^3/period]	$\Delta Q_{(NG)}$ [%]
23.01 ÷ 12.06	141	1444	962	968	0,6
13.06 ÷ 12.08	61	0	88	88	0
13.08 ÷ 31.12	142	735	604	592	1,7
	Σn = 344	ΣSd = 2179	$\Sigma Q_{(NG)}$ = 1654		

Equation (1) enables to estimate the demand for natural gas (NG) by a customer or a group of customers depending on the temperature T of air (Sd = 18 − T) during a 24-h period, whereas hourly streams of gas taken in individual network connections from Fig. 1 are determined on the basis of hourly flow characteristics of gas through a reduction and measurement station supplying a given network. The methodology of determining hourly demand for gas in any network connection is described in detail in the following work (Szoplik 2016).

An example of the annual variation in gas demand by all consumers taking gas from the network as shown in Fig. 1 and the variation in ambient temperature (Sd index) on subsequent days of the year is shown in Fig. 2a. Higher gas demand is observed on days with lower air temperatures, which correspond to higher Sd values. On the other hand, the variability of gas demand by the customer in the connection (determined on the basis of relationship 1 and the characteristics of the flow through the station) in the following hours of the day for three selected days with different air temperature is shown in Fig. 2b. Lower demand for gas is characteristic for night hours (between 11 p.m. and 5 a.m.).

On the basis of data on network load depending on ambient temperature, simulations of natural gas flow in the network were carried out and the characteristics of the network operating in various conditions were developed. Modeling of gas flow in the network was performed in GasNet program, in which the calculation of gas streams and overpressure in the network pipelines was carried out using the mesh method based on the analogy to the current flow in electrical circuits. The result of flow simulation is the distribution of streams, velocities and overpressure of gas in all gas pipelines of the network. Simulations carried out for different input data sets made it possible to determine the minimum overpressure of the gas stream feeding the network, at which the gas of specified quality parameters can be transported to all customers under overpressure greater than the minimum of 1700 Pa. In this way, the minimum gas overpressure at the entry to the network was determined for various gas streams collected at 354 exit points from the network (depending on the ambient temperature and time of day) and for various gas quality parameters (heat of gas combustion of H_s).

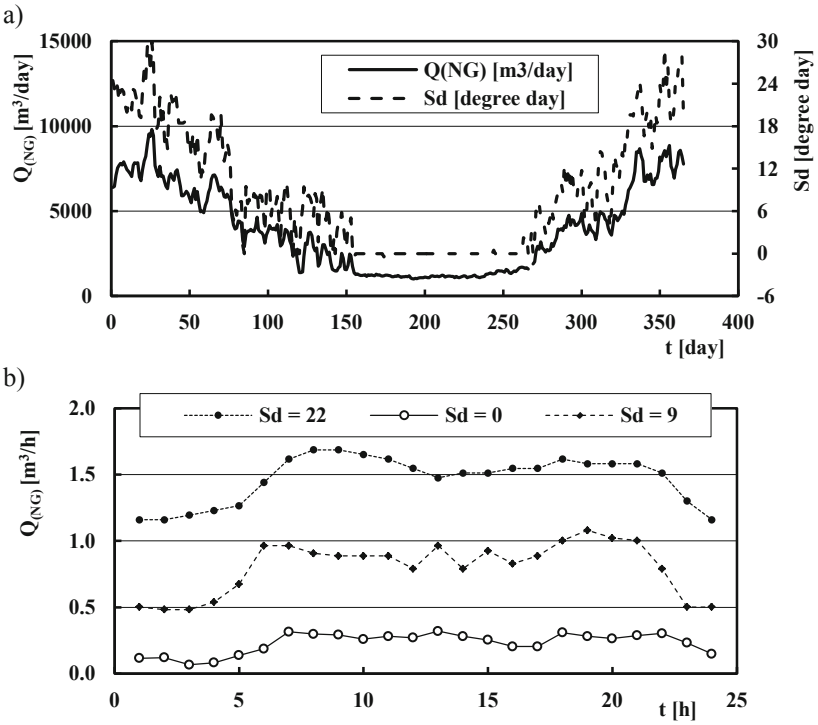

Fig. 2. Variability of gas demand $Q_{(NG)}$; (a) daily in pipeline network, (b) hourly in connection; Sd = 0 when T $\geq$ 18 °C; Sd = 9 when T = 9 °C; Sd = 22 when T = −4 °C

4 Steering of Gas Flow in the Network

One of the parameters determining the proper operation of the network and safe transport of gas to consumers is the overpressure of gas in the network. The amount of overpressure of gas stream in low-pressure network pipelines should be in the range from 1700 to 2500 Pa. From a practical point of view, it is beneficial to maintain the lowest possible overpressure in the network, as the potential gas losses caused by pipeline failure, leakage of the network or methane penetration through the pipeline walls will be the lowest. The value of overpressure of the gas stream feeding the network depends on the network load, i.e., gas consumption by consumers, and is higher the higher the gas consumption from the network, i.e., in the winter season and in the morning hours. The paper (Szoplik 2016) describes examples of methods of adjusting the overpressure of the supply stream depending on the size of this stream. Figure 3 shows a schematic representation of the methodology of gas overpressure control in the network in order to reduce it to the minimum level under given conditions of network operation. The GRS gas reduction station supplying the sample

network is supplied with a flow of gas with a constant overpressure (e.g. P_{in} = 2.5 bar) and a time-varying flow ($Q_{in} \neq$ const). At the GRS station, the overpressure of the stream P_{in} is reduced to values in the range (1700 ÷ 2500 Pa) depending on the size of the stream Q_{in} according to an experimentally determined control algorithm (Szoplik 2016):

$$P_{out} = aQ_{in}^2 + bQ_{in} + c \tag{2}$$

As a result, the gas stream Q_{out} leaving the GRS reduction station is not only characterised by a lower overpressure (in relation to P_{in}), but above all by the fact that it is dependent on the size of the gas stream Q_{in}.

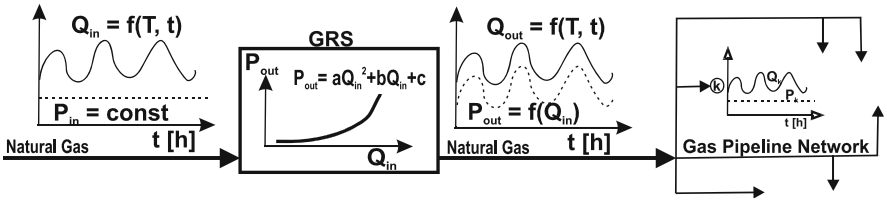

Fig. 3. Scheme of gas system pressure steering in the network

Parameters a, b and c of the control algorithm (2) can be determined only on the basis of the results of simulation of gas flow in the network, performed for various ambient temperatures, during which the minimum overpressure of the gas supplying the network is selected, depending on the size of gas streams collected from the network. The control algorithm shall be developed individually for each gas network on the basis of the actual network load data. Figure 4 shows a fragment of the overpressure and gas flow change record directly before and after the introduction of the developed algorithm for controlling the overpressure in the network. Analyzing the data from Fig. 4 one can notice a dynamic change of the stream overpressure (red line) leaving the GRS station depending on the stream size (pink line). Thanks to this, the overpressure of the supply stream will be maintained at a minimum level, depending on the size of the supply stream, i.e., the total volume of gas streams received at 354 points of exit from the network. In the paper (Szoplik 2016) it was shown that the application of such a pressure control method allows to reduce the annual gas stream entering the network by about 0.4%. It can be assumed that the savings resulting from the use of such a control system will be greater the larger the network and the higher the permissible overpressure of gas in the network (medium or high pressure network).

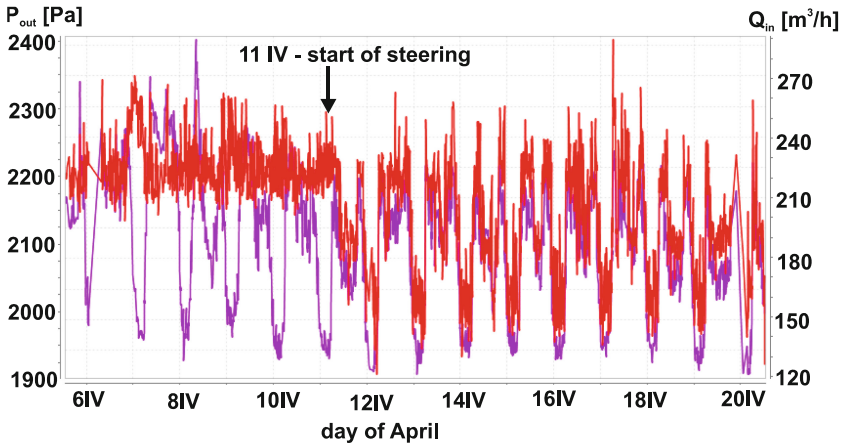

Fig. 4. The relationship between the overpressure and gas stream before and after steering system run (red line – gas overpressure, pink line – gas stream)

5 Storage Capacity of Alternative Gaseous Fuels in the Gas Pipeline Network

Storage of alternative gaseous fuels (af) in the gas network consists in the continuous or periodic addition of gaseous fuels from surplus energy generated from renewable sources (sun, wind, biomass) to the natural gas transported through the pipeline network. Examples of alternative gaseous fuels that can be fed into the natural gas network are, for example, biomethane from biomass gasification or hydrogen from water hydrolysis using surplus electricity from renewable sources.

The paper (Szoplik and Stelmasińska 2019) analyzed two possible ways of biomethane introducing to the low pressure gas network as shown in Fig. 1 and showed that regardless of the network load, biomethane can constitute approximately 39% of the regasified LNG and biomethane mixture stream and approximately 29% in the case of the natural gas and biomethane mixture stream. In this case, the size of the biomethane stream entering the network depended on the size of the natural gas stream supplied to consumers (i.e., the ambient temperature). On days with a lower ambient temperature, significantly more biomethane can be introduced into the network, as the network load is higher on these days.

The size of a mixture of natural gas and any alternative gaseous fuel $Q_{(NG\text{-}af)}$ entering the network depends on the heat combustion value of the gas biofuel ($H_{s(af)}$) and the natural gas ($H_{s(NG)}$). Assuming that gas network in Poland can transmit gas fuels with a minimum value of combustion heat $H_{s(NG\text{-}af)} = 34$ [MJ/m^3], it is possible to estimate the stream of the mixture of natural gas (or regasified natural gas) and alternative gaseous fuel with a value of combustion heat known from the following relationship:

$$Q_{(NG-af)} = \frac{H_{s(NG)} \cdot Q_{(NG)}}{H_{s(NG-af)}} \tag{3}$$

Assuming that the daily demand for natural gas $Q_{(NG)}$ for any ambient temperature can be determined from the model (1), the maximum share of y_{af} gaseous alternative fuel (biomethane or hydrogen) in the mixture of natural gas and biofuels can be estimated from the heat combustion values of natural gas ($H_{s(NG)}$), biofuels ($H_{s(af)}$) and mixtures ($H_{s(NG\text{-}af)}$) based the following relationship:

$$y_{af} = \frac{H_{s(NG)} - H_{s(NG-af)}}{H_{s(NG)} - H_{s(af)}} \tag{4}$$

Figure 5 shows the results of calculations in the form of the size of the mixture of natural gas and hydrogen $Q_{(NG\text{-}H2)}$ and hydrogen $Q_{(H2)}$ stream, which can be fed into the network (from Fig. 1) on the following days of the year (assuming $H_{s(NG\text{-}H2)}$ = 34 [MJ/m^3], $H_{s(NG)}$ = 41.306 [MJ/m^3], $H_{s(H2)}$ = 12 [MJ/m^3]). The percentage share of hydrogen in the mixture of natural gas and hydrogen estimated from the relationship (4) is 25%, whereas in the mixture of regasified liquid natural gas and hydrogen the share of hydrogen is greater and amounts to 34%. Based on the data presented in Fig. 5, it was found that in the low pressure network from Fig. 1, the maximum storage capacity is about 427459 m^3 of hydrogen in natural gas and 439455 m^3 of hydrogen in regasified LNG. The advantage of alternative fuels storage in low-pressure networks is that alternative fuels do not need to be compressed to high pressures (which is the case with high-pressure networks) and that alternative fuels can be produced in close proximity to low-pressure networks. Such a way of hydrogen introducing into the network is beneficial for the network operator because it allows to generate a mixture of gases with a constant value of combustion heat over time, which makes it much easier to account for the consumed energy. However, from the point of view of the alternative fuel manufacturer, such a way of fuel supplying may be burdensome because the production of alternative fuel is not constant over time.

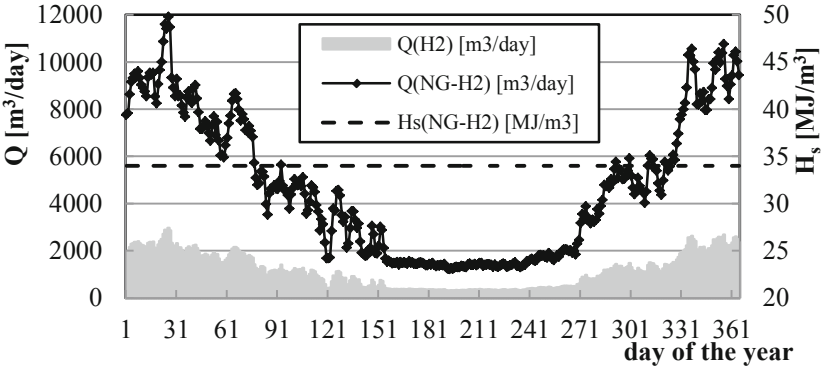

Fig. 5. Variability of mixture $Q_{(NG\text{-}H2)}$ network load and $Q_{(H2)}$ hydrogen stream on subsequent days of the calendar year; $H_{s(NG\text{-}H2)}$ = 34 [MJ/m^3]

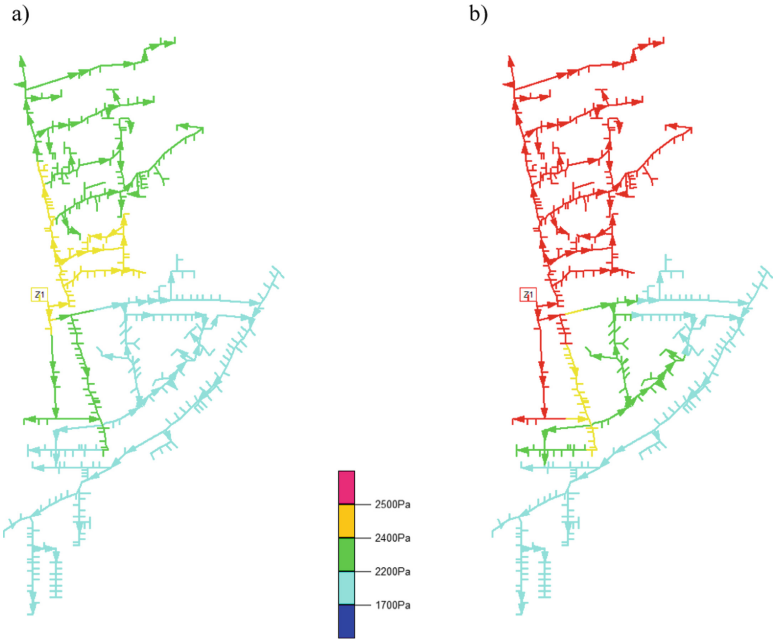

Fig. 6. Distribution of gas overpressure in pipelines, T = −17 °C; (a) natural gas $Q_{in(NG)}$ = 332 [m^3/h], $P_{z1,min}$ = 2475 Pa; (b) mixture natural gas and hydrogen $Q_{in(NG-H2)}$ = 403 [m^3/h], $P_{z1,min}$ = 2799 Pa

Alternative gaseous fuels (hydrogen, biomethane) have a much lower heat combustion value than natural gas (natural gas or regasified liquid natural gas) transmitted through the network, which always results in a reduction in the quality of the mixture produced and the transport of larger streams of the mixture of fuels and an increase in the pressure drop in the network. The results of the simulation in the form of overpressure distribution (Fig. 6a and b) of natural gas $Q_{(NG)}$ and mixture of natural gas and hydrogen $Q_{(NG-H2)}$ in the network pipelines on a day of temperature T = −17 °C clearly show the increase of network load and decrease of overpressure in the network in case of alternative fuel introducing into the network. In this case, the use of flow simulation is necessary to analyze the storage capacity of the network for alternative fuels, as it may be that an increase in the gas mixture streams collected from the network may require the use of too much overpressure in the low-pressure network supply stream. This must result in the alternative fuel stream being reduced to a value that allows the mixture to be transported under appropriate overpressure.

6 Summary

Simulations of gas flow in network pipelines provide data on the most important flow characteristics (flow, velocity and overpressure distribution) from which it is possible to map the network and estimate the maximum capacity of the network to store

alternative gaseous fuels produced indirectly from renewable energy sources. In turn, the results of simulating the flow of gas or gas/alternative fuel mixtures in the form of a minimum overpressure of the supply stream can be used to develop the relationship between overpressure and supply stream, so that the lowest possible overpressure can be maintained in the network. In addition, flow simulations may be a good method for testing the behavior of the network under different operating conditions of the system and for planning the possible expansion or modernization of the network.

Acknowledgements. The calculations presented in the paper were made on the basis of the results provided by the Gas Plant in Szczecin, during my internship stay carried out in the framework of the project "Time for an internship. Science and Business Cooperation".

References

Askari, S., Montazerin, N., Fazel Zarandi, M.H.: Forecasting semi-dynamic response of natural gas networks to nodal gas consumptions using genetic fuzzy systems. Energy **83**, 252–266 (2015)

Chaczykowski, M.: Transient flow in natural gas pipeline–the effect of pipeline thermal model. Appl. Math. Model. **34**(4), 1051–1067 (2010)

Damavandi, M.Y., Kiaei, I., Sheikh-El-Eslami, M.K., Seifi, H.: New approach to gas network modeling in unit commitment. Energy **36**, 6243–6250 (2011)

Fasihizadeh, M., Sefti, M.V., Torbati, H.M.: Improving gas transmission networks operation using simulation algorithms: case study of the National Iranian Gas Network. J. Nat. Gas Sci. Eng. **20**, 319–327 (2014)

Gato, L.M.C., Henriques, J.C.C.: Dynamic behaviour of high-pressure natural-gas flow in pipelines. Int. J. Heat Fluid Flow **26**, 817–825 (2005)

Lise, W., Hobbs, B.F.: Future evolution of the liberalised European gas market: simulation results with a dynamic model. Energy **33**, 989–1004 (2008)

Lochner, S.: Identification of congestion and valuation of transport infrastructures in the European natural gas market. Energy **36**(5), 2483–2492 (2011)

Matko, D., Geiger, G., Gregoritza, W.: Pipeline simulation techniques. Math. Comput. Simul. **52**, 211–230 (2000)

Monforti, F., Szikszai, A.: A Monte Carlo approach for assessing the adequacy of the European gas transmission system under supply crisis conditions. Energy Policy **38**, 2486–2498 (2010)

Nguyen, H.H., Chan, Ch.W.: Application of artificial intelligence for optimization of compressor scheduling. Eng. Appl. Artif. Intell. **19**, 113–126 (2006)

Osiadacz, A.J.: Simulation and Analysis of Gas Networks. Gulf Publishing Company, Houston (1987). ISBN 9780872018440

Osiadacz, A.J., Chaczykowski, M.: Comparison of isothermal and non-isothermal pipeline gas flow models. Chem. Eng. J. **81**(1), 41–51 (2001)

Reddy, H.P., Narasimhan, S., Bhallamudi, S.M.: Simulation and state estimation of transient flow in gas pipeline networks using a transfer function model. Ind. Eng. Chem. Res. **45**, 3853–3863 (2006)

Steinbach, M.C.: On PDE solution in transient optimization of gas networks. J. Comput. Appl. Math. **203**, 345–361 (2007)

Sun, L.: Mathematical modeling of flow in a pipeline with a leak. Math. Comput. Simul. **82**, 2253–2267 (2012)

Szoplik, J.: The gas transportation in a pipeline network. In: Al-Megren, H. (ed.) Advances in Natural Gas Technology. InTech (2012). ISBN 978-953-51-0507-7. https://doi.org/10.5772/36902. http://www.intechopen.com/books/advances-in-natural-gas-technology/the-gas-transportation-in-a-pipeline-network

Szoplik, J.: Forecasting of natural gas consumption with artificial neural networks. Energy **85**, 208–220 (2015)

Szoplik, J., Stelmasińska, P.: Analysis of gas network storage capacity for alternative fuels in Poland. Energy **172**, 343–353 (2019)

Szoplik, J.: Improving the natural gas transporting based on the steady state simulation results. Energy **109**, 105–116 (2016)

Thomas, S., Dawe, R.A.: Review of ways to transport natural gas energy from countries which do not need the gas for domestic use. Energy **28**, 1461–1477 (2003)

Voropai, N.I., Senderov, S.M., Edelev, A.V.: Detection of "bottlenecks" and ways to overcome emergency situations in gas transportation networks on the example of the European gas pipeline network. Energy **42**, 3–9 (2012)

Metal Leaching from E-Waste with Ionic Liquids

Stefaan Verwimp[1,2], Magdalena Emmons-Burzyńska[1], Abhishek Dutta[2], and Magdalena Regel-Rosocka[1(✉)]

[1] Institute of Chemical Technology and Engineering, Poznan University of Technology, Poznań, Poland
magdalena.regel-rosocka@put.poznan.pl
[2] Faculteit Industriële Ingenieurswetenschappen, Campus Groep T, KU Leuven, Leuven, Belgium

Abstract. The chapter presents some aspects of metal leaching from e-waste. It focuses on new leaching systems containing ionic liquids (ILs) for recovery of copper (mainly) from waste printed circuit boards (PCBs). It is reported that the most efficient are acidic ILs with bisulfate anion, and they perform even better than sulfuric acid. However, the results of the leaching show that IL agent should be supported by the presence of some oxidants (e.g. H_2O_2) to increase the process efficiency. Nonetheless, the use of ILs seems to be a perspective option to make the leaching more intensive and effective, a lot of basic research is necessary to investigate the mechanism of the Cu leaching, and to find optimum process conditions.

1 Introduction

Recovery of metal ions from secondary sources, such as waste electric and electronic equipment (WEEE), called also e-waste, has become an important issue to be solved. On the one hand, e-waste is the fastest growing waste stream which is increasing at an alarming rate. WEEE fraction in all the municipal waste amounts to 3–5% annually (in developing countries even 8%) and is still not recycled enough (Widmer et al. 2005). Approximately 45 million tons of e-waste (6.1 kg per inhabitant) was generated globally in 2016 and is expected to grow to 52 million tons (6.8 kg/inh) by 2021. Only 20% of the e-waste is recycled appropriately. The total worth of e-waste today exceeds 55 billion euros. In 2016, Europe alone produced 12.3 mln tons of e-waste, including 0.45 million tons in Poland (Baldé et al. 2017) and 0.24 mln tons in Belgium. The leaders in e-waste production are China and the USA with 7.2 mln and 6.3 mln tons in 2016 (Baldé et al. 2017). On the other hand, printed circuit boards (PCB) from WEEE contain valuable metals (depending on a device: Cu, Au, Ag, Pd) that could be recovered and recycled becoming a crucial chain link in European circular economy focused on a sustainability (Regel-Rosocka 2018).

© Springer Nature Switzerland AG 2020
M. Ochowiak et al. (Eds.): PAIC 2019, *Practical Aspects of Chemical Engineering*, pp. 473–482, 2020.
https://doi.org/10.1007/978-3-030-39867-5_49

2 Waste Electric and Electronic Equipment

WEEE, e-waste or e-scrap, is waste including all consumables, components, and sub-assemblies which are part of the electronic product at time of discarding. The waste stream of end-of-life electronic devices must normally be processed according to the WEEE management regulations of the country where it was discarded. However, large amounts of e-waste remain poorly managed as is evidenced by the low global rates of recycled WEEE. Most e-waste (70–85%) is illegally shipped to developing countries in Asia and Africa under the disguise of a donation or recycling purposes through gaps in current e-waste regulations (Wang et al. 2013; Awasthi and Li 2017). In these developing countries, incineration, landfilling and coarse recycling methods such as crushing and acid leaching are widely practiced (Perkins et al. 2014; Bakhiyi et al. 2018). It leads to the release of harmful gases into the atmosphere and the contamination of soil and groundwater with heavy metals and non-metallic compounds (polychlorinated biphenyls, dioxins, furans) (Fu et al. 2011; Birloaga et al. 2013) resulting in accumulation of contaminants in plants, which can lead to their introduction into the food chain (Quan et al. 2014).

The printed circuit board (PCB) is a component that mechanically supports and electrically connects all the components in almost all electronical devices. The basic structure consists of a non-conducting substrate or laminate with thin copper sheet that is deposited on one or either side. The most used substrate for making PCBs are glass-fiber reinforced epoxy resins that contain bromine which act as a fire retardant. Depending on the construction of the PCBs they can be classified as single-sided, double-sided or multi-layered. Single-sided and double-sided PCBs have a copper sheet on one or both sides of the substrate. Multi-layered boards are made up of multiple layers of copper sheets separated by layers of insulation material. After mounting the components to the outer layer of the PCB, a solder mask and silk screen are added, completing the PCB (Verwimp 2019).

Waste PCBs represent only 3 wt% of the total e-waste produced globally but they are the most valuable part of the e-waste accounting for about 40% of metal recovery value (Dalrymple et al. 2007; Zhou and Qiu 2010). The most common metal on a PCB is copper, there are also large amounts of solder, nickel, iron and precious metals (Golev et al. 2016). Valuable metals such as Au, Ag and Pd are used as contact materials between the connection of components due to their high chemical stability and good conductivity. Also other metals such as Ga, In, Ti, Si, Gi, As, Sb, Se, Te, Ta are usually derived from the components mounted on the PCBs (Ghosh et al. 2015). From an economic point of view, Au is the most interesting component of a PCB since it alone covers 59% of the estimated value of major metals that are contained in waste PCBs (Dalrymple et al. 2007).

The PCB composition differs greatly depending on the device it comes from, the manufacturer and the age. Various estimates indicate that a typical PCB consists of about 30% organic, 30% ceramics and 40% metals (Duan et al. 2011), while other claim that in general, PCBs contain about 28% metals, 23% plastics and the remaining are ceramics and glass material (Zhou and Qiu 2010) and yet another study (Chen et al. 2015a, b) reports it to consist of 50% polymers, 20% glass fibers and 30% metals.

3 Metal Leaching from E-Waste with Ionic Liquids

3.1 Recycling of E-Waste

Recycling starts with the collection of WEEE from consumers, followed by a series of mechanical operations for dismantling, often together with magnetic separation, to classify different materials followed by a crushing operation to reduce the size of the particles. After separation and reduction of size, further treatment for the recovery of valuable metals happens in the form of metallurgy. Three different metallurgical treatment options are pyro-, hydro- and/or biometallurgy (Verwimp 2019).

This chapter focuses on hydrometallurgical treatment of PCBs with addition of ILs to recover valuable metals. Currently, hydrometallurgical processes on an industrial scale are mostly used as an additional step in pyrometallurgy to further purify molten metals. However, hydrometallurgy have advantages over pyro-processes as they are easier to control, are more predictable, require simpler and less costly equipment, there are no emissions of toxic gases and operate at lower temperatures. However, large quantities of solutions are used which can be corrosive or toxic. These harmful solutions or sludge need to be managed or recycled (Ghosh et al. 2015; Golev et al. 2016).

3.2 General Information on Leaching

Leaching is a heterogeneous operation, used in hydrometallurgy, where soluble or suspended reactants (B, Eq. 1) are extracted by a liquid (A, Eq. 1), called leaching agent. The fluid which contains the extracted solid (C, Eq. 1) is called a leachate:

$$aA_{(fluid)} + bB_{(solid)} \rightarrow cC_{(fluid)} + dD_{(solid)} \quad (1)$$

Leaching has been intensively investigated as a method for metal recovery from e-waste recently. As a result of leaching two fractions are distinguished: a material that is free from valuable components and is dumped (D, Eq. 1), and the other – the metal pregnant leach solution (PLS) (rich in separated component, C, Eq. 1) that is advanced for further processing by adsorption, cementation, ion-exchange or liquid-liquid extraction, etc. (Rzelewska and Regel-Rosocka 2018).

Selection of a leaching agent depends on the composition of a material and properties of the separated metals. The most frequently applied leaching agents are mineral acids (H_2SO_4, HCl, HNO_3, aqua regia), hydroxides (NaOH, NH_4OH) and chlorides (NH_4Cl, $CuCl_2$, $FeCl_3$) (Gupta 2003). Recently, some water-soluble ionic liquids (IL) were reported as leaching agents for copper from primary and secondary resources (Chauhan et al. 2018).

3.3 Ionic Liquids (ILs) for Treatment of PCBs

ILs are a group of liquid salts that generally consist of an organic cation and organic or inorganic anion and have a melting point that is lower or equal to 100 °C (Wasserscheid and Keim 2000). The wide range of possible cation and anion combinations (10^{18} possibilities) makes it so that ILs can be developed to fit a particular application

which is why they are often called designer solvents. ILs have properties that make them more appealing than many solvents used today. These useful properties include high thermal stability, very low flammability, high ionic conductivity, tuneable solubility and miscibility, wide range of viscosities, a large electrochemical window and a very low to negligible vapour pressure (Welton 1999; Wasserscheid and Keim 2000).

Recently ILs (particularly water soluble) have been proposed for metal leaching from e-waste. Reports on IL use for recovery of metals from PCBs indicate, mainly, a Brønsted acidic ionic liquid, i.e. 1-butyl-3-methylimidazolium bisulfate [BMIM][HSO_4] as a leaching agent (Table 1). This IL provides a robust anion that, in the contrary to such anions as [BF_4] and [PF_6], is resistant to hydrolysis to strong acids (e.g. HF for fluorinated anions) and can be recycled without decomposition or transfer losses (Whitehead et al. 2004).

Table 1. Ionic liquids applied for metal leaching from e-waste.

IL name	Remarks	Efficiency	Ref.
[EMIM][BF_4] 1-ethyl-3-methylimizadolium tetrafluoroborate	Dissolution of bromine epoxy resins of PCBs at 260 °C, 10 min or solders at 240 °C, 10 min	no data	Zhu et al. (2012a, b)
[BMIM][HSO_4] 1-butyl-3-methylimidazolium bisulfate	With H_2O_2 addition	L_{Cu} = 99.17% from particles of 0.1–0.25 mm size	Huang et al. (2014)
	Without H_2O_2 addition	L_{Cu} and L_{Au} details in Table 2	Verwimp (2019)
[CM-MIM][HSO_4] 1-carboxymethyl-3-methylimidazolium bisulfate	With H_2O_2 addition,	L_{Cu} = 89.19%	Zhang et al. 2018b
[BSO_4HPy][HSO_4] N-sulfobutylpyridinium bisulfate, **[BSO_3HMIm][HSO_4]** 1-sulfobuty-3-methylimidazolium bisulfate, **[BSO3HMIm][OTf]** N-sulfobutylpyridinium trifluoromethanesulfonate, **[MIm][HSO_4]** methylimidazolium bisulfate, **[BSO_3HPy][OTf]** 1-sulfobutyl-3-methylimidazolium trifluoromethanesulfate	With H_2O_2 addition, Zn leaching from PCBs	L_{Zn} > 60% with **[BSO_4HPy][HSO_4]** and **[MIm][HSO_4]** L_{Zn} ~ 20% with **[OTf] ILs** L_{Cu} = 99.77% with **[BSO_3HPy][OTf]**	Chen et al. (2015), Li and Chen (2017)
[BSO_4HPy][HSO_4] N-sulfobutylpyridinium bisulfate	Slurry electrolytic system from electrolyte: 30 g/dm^3 $CuSO_4 \cdot 5H_2O$, 60 g/dm^3 NaCl,170 g/dm^3 H_2SO_4 partly replaced by IL	L_{Cu} = 90.94%	Zhang et al. (2018a)

[BMIM][HSO_4] has been found to behave like an acid when it is present in an aqueous solution (Whitehead et al. 2004). The acidity of the aqueous [BMIM][HSO_4] solution is reported to be much higher than that of aqueous $KHSO_4$ solution and, as a consequence, activity of the hydrogen ions released from this IL is higher than that from inorganic salt aqueous solution. From this behavior it can be assumed that the

leaching reaction occurs as seen in eq. 2 (Dong et al. 2009; Huang et al. 2014; Zhang et al. 2018b). Thus, hydrogen sulfate ILs are expected to be efficient leaching agents.

$$4Cu + 4H_2SO_4^- + O_2 \rightarrow 4CuSO_4^- + 2H_2O \quad (2)$$

Zhang et al. (2018b) has observed that volume of the imidazole cation greatly enhances the affinity of an anion towards it. As a consequence, the hydrogen ions in the solution are concentrated on the surface of the imidazole cation affecting positively Cu leaching with bisulfate ILs relative to the conventional H_2SO_4 use.

$[BSO_3HPy][HSO_4]$ was used not only as a leaching agent but also to replace H_2SO_4 in a slurry electrolytic system (in a cylindrical electrolyzer at room temperature with a graphite rod anode and a titanium net cathode, at 0.5 A current, for 3 h) to recover metallic copper from waste PCBs in one-step (Zhang et al. 2018a). This substitution of H_2SO_4 by the bisulfate IL reduces effectively the particle size of the obtained Cu powders, and increases current efficiency and Cu recovery rate from e-waste without pretreatment.

Table 2. Effect of IL presence on leaching efficiency (L) of metals from waste PCBs at 75 °C, S/L = 1/20 (based on experiments of the authors of the chapter).

		Without IL	With 0.5 M IL	With H_2SO_4 + IL
After burning in furnace at 1200°C for 2 h		0.5 M H_2SO_4 L_{Cu} = 7.2% L_{Au} = 23% 5 M H_2SO_4 L_{Cu} = 7.2% L_{Au} = 22%	L_{Cu} = 8.4% L_{Au} = 23%	0.5 M + 0.5 M L_{Cu} = 10% L_{Au} = 4.0% 5 M + 0.5 M L_{Cu} = 18% L_{Au} = 3.4%
After cutting to pieces of av. size: 32.0 mm²		0.5 M H_2SO_4 L_{Cu} = 0.06% L_{Au} =19% 5 M H_2SO_4 L_{Cu} = 0.16% L_{Au} = 24%	L_{Cu} = 0.03% L_{Au} = 4.7%	0.5 M + 0.5 M L_{Cu} = 0.06% L_{Au} = 7.1% 5 M + 0.5 M L_{Cu} = 0.06% L_{Au} = 4.8%

The leaching efficiency was calculated according to the following equation:

$$L = \frac{\text{amount of metal extracted}}{\text{total amount of metal content in sample}} \cdot 100\% \quad (3)$$

The leaching efficiency of Cu with sulfuric acid and its mixtures with [BMIM][HSO_4] obtained by the authors of the chapter is shown in Table 2. A synergy in leaching with mixture of H_2SO_4 and IL is visible for Cu leaching from powder, while antagonistic effect is noted for Au. In case of PCB pieces opposite results are reported: Cu is almost not dissolved, while Au leaching efficiency amounts to 20%. Much higher

Cu leaching yield (almost 100%) was reported by Huang et al. (2014) when an oxidant (H_2O_2) was added to waste PCBs powder at solid/liquid ratio (S/L) of 1/25, at 70 °C, leaching solution composition 25 cm^3 80% (v/v) [BMIM][HSO_4], 10 cm^3 30% H_2O_2.

Apart from use of ILs as metal leaching agents, non-aqueous ILs can play also an important role in the pretreatment of PCBs. For example, [EMIM][BF_4] has been proposed to dissolve (at 260 °C for 10 min) bromine epoxy resins of waste PCBs (Zhu et al. 2012a) or solder – at 240 °C for 10 min – (Zhu et al. 2012b) to ease recovery of copper foils and glass fibers. As a result, a new, clean and non-polluting method to recycle valuable materials from PCBs was elaborated.

3.4 Leaching Kinetics

The overall leaching reaction involves the following steps (Levenspiel 1999) (Fig. 1):

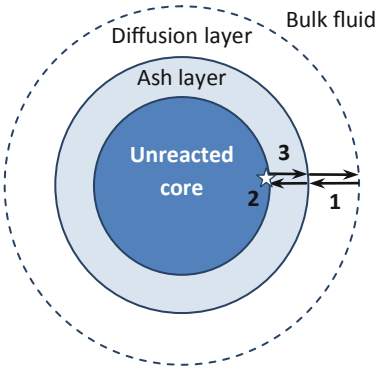

Fig. 1. Overall leaching reaction process: **1** external mass transfer, **2** chemical reaction, **3** internal mass transfer

1 external mass transfer: diffusion of reactant or product through diffusion layer
2 chemical reaction: reaction between reactant in fluid and solid
3 internal mass transfer: diffusion of reactants or products through the ash layer to the unreacted core.

At the boundary between the solid and liquid phase, there is a stationary aqueous diffusion layer where the concentration differs from that of the rest of the bulk liquid. The slowest of the leaching steps is called the rate controlling step and will determine the overall rate of the reaction. However, this rate controlling step can change according to the reaction conditions (Chauhan et al. 2018).

Kinetic Models for Leaching with ILs. The major models developed for an idealized non-catalytic liquid-solid reaction are the shrinking core, shrinking particle, homogeneous and grain models (Table 3). Of these models, the shrinking core has been widely used to model leaching kinetics of PCBs (Levenspiel 1999, Chen et al. 2015a, b). If a

model fits well to the experimental data, then the rate equation will accurately predict and describe the reaction kinetics (Huang et al. 2014).

The shrinking core model (SCM) assumes a non-porous particle where reaction only occurs at the surface of an unreacted core inside the particle while the total particle size remains unchanged. The reaction at the surface is faster than at the interior of the particle which causes the reactant in the outer layer of the solid to be leached out, leaving behind an inert, reacted layer (also called the ash layer). It means that the SCM takes into account all three leaching steps shown in Fig. 1. The shrinking core model has models for spherical particles and also for flat plate particles (shown in Table 3).

The reaction controlled model for flat plate particles and film diffusion models for spherical and flat plate particles are the same and therefore give the same result. The value for the apparent rate constants will be identical, however, the constants are not identical, they differ from each other since they are function of different variables. This all means that when one of these models fits the experimental data the best, it will be impossible to determine which of these are the correct model for the reaction based on the experimental data for the fraction reacted alone.

Table 3. Kinetic models for leaching (Levenspiel 1999; Georgiou and Papangelakis 1998).

Model	Particle	Film layer diffusion controlled	Ash layer diffusion controlled	Chemical control
Shrinking core model (SCM)	Sphere	$kt = x$ with $k = \frac{3bC_b k_l}{\rho_B R}$	$kt = 1 - \frac{2}{3}x - (1-x)^{\frac{2}{3}}$ with $k = \frac{6bC_b D_e}{\rho_B R^2}$	$kt = 1 - (1-x)^{\frac{1}{3}}$ with $k = \frac{bC_b k'}{\rho_B R}$
	Flat plate	$kt = x$ with $k = \frac{bC_b k_l}{\rho_B L}$	$kt = x^2$ with $k = \frac{2bC_b D_e}{\rho_B L^2}$	$kt = x$ with $k = \frac{bC_b k'}{\rho_B L}$
Shrinking particle model (SPM)	Always assumed to be a spherical particle	$kt = 1 - (1 - X_B)^{\frac{2}{3}}$ with $k = \frac{2bC_b D_e}{\rho_B R_0^2}$	Not applicable	$kt = 1 - (1-x)^{\frac{1}{3}}$ with $k = \frac{bC_b k'}{\rho_B R_0}$
Homogeneous model	Small lumps uniformly distributed	Not applicable	$\theta_v \theta_v^* = 1 - \frac{2}{3}x - (1-x)^{\frac{2}{3}}$ with $\theta_v = k_v C_b t$	$\theta_v \theta_v^* = x$
Grain model	Pellets made up of individual grains	Not applicable	$\theta^* \hat{\sigma}^2 = 1 - \frac{2}{3}x - (1-x)^{\frac{2}{3}}$	$\theta^* \hat{\sigma}^2 = x$

x - fraction reacted or leaching rate, k - apparent rate constant, k' - reaction rate constant, k_l - mass transfer coefficient of the liquid film layer, k_v - reaction rate constant based on volume, t - time, b - stoichiometric coefficient for reacting substance B (Eq. 1), C_b - bulk concentration, D_e - effective diffusivity, ρ_B - molar density, R - radius of the spherical particles, R_0 - original radius of the particle, L - half thickness of a flat plate particle, θ_v - dimensionless time, θ_v^* - dimensionless time for the complete reaction, $\hat{\sigma}$ - grain model parameter (a function of the reaction rate constant, external surface area and volume, the radius, the porosity of the pellet)

The shrinking particle model (SPM) assumes a non-porous particle, where no ash layer is formed. Instead, the particle behaves like an unreacted core in the SCM which shrinks during the course of the reaction but without any ash layer around it (Fig. 1). Since the ash layer is absent, only film diffusion (1) and reaction controlled rate (2) can be the limiting steps. The SPM contains no model equations to fit flat plate particles, only spherical ones (Huang et al. 2014; Verwimp 2019). The chemical reaction rate controlled step in the SPM is identical to that of the SCM where the particles have a constant size throughout the reaction, meaning that the equation for both models is exactly the same. However, since the particle shrinks, the R is replaced by R_0 (Huang et al. 2014).

The homogeneous model considers the solid phase to be made out of small lumps that are uniformly distributed. Similar to the SCM, an ash layer is formed during the reaction. Also similar to the SCM are the equations for ash diffused controlled reaction and chemical controlled reaction.

The grain model assumes the solid particles to be pellets made up of individual grains that are densely packed together (Georgiou and Papangelakis 1998). The liquid reagent diffuses through the gaps of the grains while every grain reacts individually according to the SCM. The equation that the grain model gives is the same as that of the SCM and homogeneous model, meaning that it is impossible to determine which model is the correct model for the reaction based on the experimental data of the fraction reacted alone.

In practice, kinetics of Pb leaching with various ILs, i.e. $[BSO_4HPy][HSO_4]$, $[BSO_3HMIm][HSO_4]$, $[MIm][HSO_4]$, $[BSO_3HMIm]OTf$, $[BSO_3HPy]OTf$, (Chen et al. 2015c) from waste PCBs did not show unambiguous process limiting step, either surface chemical reaction or mass transfer. Neither of the two models showed an acceptable correlation for Pb, while Cu leaching was limited by diffusion. It was indicated by various authors that result of kinetics modelling was influenced by content of the leached metals, form of the leached material, and, thus, by accessibility of the metals to the leaching agents. For Zn leaching it was indicated that diffusion plays more important role than the surface reaction (Chen et al. 2015a, b).

The authors of the chapter also observed that non-homogenity and large size of PCB pieces negatively affected the results of kinetic model fitting, whereas leaching from homogeneous powder of burned PCBs was reported to be controlled by ash diffusion (Verwimp 2019).

4 Summary

Up to now, some ILs have been proposed for leaching of copper (mainly) and zinc from waste PCBs. The most efficient are acidic ILs with bisulfate anion, and they perform even better than sulfuric acid. However, the results of the leaching show that IL agent should be supported by the presence of oxidants (e.g. H_2O_2) to increase the process efficiency. Nonetheless, the use of ILs seems to be a perspective option to make the leaching more intensive and effective, a lot of basic research is necessary to investigate the mechanism of the Cu leaching, and to find optimum process conditions.

Acknowledgements. The work was supported by the Polish Ministry of Science and Higher Education (Grant No. 0912/SBAD/2010).

References

Awasthi, A.K., Li, J.: An overview of the potential of eco-friendly hybrid strategy for metal recycling from WEEE. Resour. Conserv. Recycl. **126**, 228–239 (2017)

Bakhiyi, B., Gravel, S., Ceballos, D., Flynn, M.A., Zayed, J.: Has the question of e-waste opened a Pandora's box? An overview of unpredictable issues and challenges. Environ. Int. **110**, 173–192 (2018)

Baldé, C.P., Forti, V., Gray, V., Kuehr, R., Stegmann, P.: The Global E-waste Monitor – 2017. United Nations University (UNU), International Telecommunication Union (ITU) & International Solid Waste Association (ISWA), Bonn/Geneva/Vienna (2017)

Birloaga, I., De Michelis, I., Ferella, F., Buzatu, M., Vegliò, F.: Study on the influence of various factors in the hydrometallurgical processing of waste printed circuit boards for copper and gold recovery. Waste Manage. **33**, 935–941 (2013)

Chauhan, G., Ram Jadhao, P., Pant, K.K., Nigam, K.D.P.: Novel technologies and conventional processes for recovery of metals from waste electrical and electronic equipment: challenges & opportunities – A review. J. Environ. Chem. Eng. **6**, 1288–1304 (2018)

Chen, M., Huang, J., Ogunseitan, O.A., Zhu, N., Wang, Y.M.: Comparative study on copper leaching from waste printed circuit boards by typical ionic liquid acids. Waste Manage. **41**, 142–147 (2015a)

Chen, M., Wang, J., Huang, J., Chen, H.: Behaviour of zinc during the process of leaching copper from WPCBs by typical acidic ionic liquids. RSC Adv. **5**, 34921–34926 (2015b)

Chen, M., Zhang, S., Huang, J., Chen, H.: Lead during the leaching process of copper from waste printed circuit boards by five typical ionic liquid acids. J. Clean. Prod. **95**,142–147 (2015c)

Dalrymple, I., Wright, N., Kellner, R., Bains, N., Geraghty, K., Goosey, M., Lightfoot, L.: An integrated approach to electronic waste (WEEE) recycling. Circuit World **33**, 52–58 (2007)

Dong, T., Hua, Y., Zhang, Q., Zhou, D.: Leaching of chalcopyrite with Brønsted acidic ionic liquid. Hydrometallurgy **99**, 33–38 (2009)

Duan, H., Hou, K., Li, J., Zhu, X.: Examining the technology acceptance for dismantling of waste printed circuit boards in light of recycling and environmental concerns. J. Environ. Manage. **92**, 392–399 (2011)

Fu, J., Wang, Y., Zhang, A., Zhang, Q., Zhao, Z., Wang, T., Jiang, G.: Spatial distribution of polychlorinated biphenyls (PCBs) and polybrominated biphenyl ethers (PBDEs) in an e-waste dismantling region in Southeast China: use of apple snail (Ampullariidae) as a bioindicator. Chemosphere **82**, 648–655 (2011)

Ghosh, B., Ghosh, M.K., Parhi, P., Mukherjee, P.S., Mishra, B.K.: Waste printed circuit boards recycling: an extensive assessment of current status. J. Clean. Prod. **94**, 5–19 (2015)

Golev, A., Schmeda-Lopez, D.R., Smart, S.K., Corder, G.D., McFarland, E.W.: Where next on e-waste in Australia? Waste Manage. **58**, 348–358 (2016)

Georgiou, D., Papangelakis, V.G.: Sulphuric acid pressure leaching of a limonitic laterite: chemistry and kinetics. Hydrometallurgy **49**, 23–46 (1998)

Gupta, C.K.: Chemical metallurgy: principles and practice. Wiley-Vch Verlag GmbH & Co KGaA, Weinheim (2003)

Huang, J., Chen, M., Chen, H., Chen, S., Sun, Q.: Leaching behavior of copper from waste printed circuit boards with brønsted acidic ionic liquid. Waste Manage. **34**, 483–488 (2014)

Levenspiel, O.: Chemical Reaction Engineering. Wiley, New York (1999)

Li, F., Chen, M.: Copper recovery from waste printed circuit boards and the correlation of Cu, Pb, Zn by ionic liquid. Environ. Protect. Eng. **43**, 55–66 (2017)

Perkins, D.N., Brune Drisse, M.N., Nxele, T., Sly, P.D.: E-waste: a global hazard. Ann. Global Health **80**, 286–295 (2014)

Quan, S.X., Yan, B., Lei, C., Yang, F., Li, N., Xiao, X.M., Fu, J.M.: Distribution of heavy metal pollution in sediments from an acid leaching site of e-waste. Sci. Total Environ. **499**, 349–355 (2014)

Regel-Rosocka, M.: Electronic wastes. Phys. Sci. Rev. **3**, 20180020 (2018)

Rzelewska, M., Regel-Rosocka, M.: Wastes generated by automotive industry – spent automotive catalysts. Phys. Sci. Rev. **3**, 20180021 (2018)

Verwimp, S.: Recycling of metals from waste printed circuit boards. Master thesis, KU Leuven, Belgium (2019)

Wang, D.G., Alaee, M., Byer, J.D., Brimble, S., Pacepavicius, G.: Human health risk assessment of occupational and residential exposures to dechlorane plus in the manufacturing facility area in China and comparison with e-waste recycling site. Sci. Total Environ. **445–446**, 329–336 (2013)

Wasserscheid, P., Keim, W.: Ionic liquids—new 'solutions' for transition metal catalysis. Angew. Chem. **39**, 3772–3789 (2000)

Welton, T.: Room-temperature ionic liquids. solvents for synthesis and catalysis. Chem. Rev. **99**, 2071–2084 (1999)

Whitehead, J.A., Lawrance, G.A., McCluskey, A.: 'Green' leaching: recyclable and selective leaching of gold-bearing ore in an ionic liquid. Green Chem. **6**, 313–315 (2004)

Widmer, R., Oswald-Krapf, H., Sinha-Khetriwal, D., Schnellmann, M., Böni, H.: Global perspectives on e-waste. Environ. Impact Assess. Rev. **25**, 436–458 (2005)

Zhang, D.J., Chen, M., Tan, Q., Wang, B., Chen, S.: Recovery of copper from WPCBs using slurry electrolysis with ionic liquid $[BSO_3HPy]{\cdot}HSO_4$. Hydrometallurgy **175**, 150–154 (2018a)

Zhang, D.J., Dong, L., Li, Y.T., Wu, Y., Ma, Y.X., Yang, B.: Copper leaching from waste printed circuit boards using typical acidic ionic liquids recovery of e-wastes' surplus value. Waste Manage. **78**, 191–197 (2018b)

Zhou, Y., Qiu, K.: A new technology for recycling materials from waste printed circuit boards. J. Hazard. Mater. **175**, 823–828 (2010)

Zhu, P., Chen, Y., Wang, L.Y., Zhou, M.: Treatment of waste printed circuit board by green solvent using ionic liquid. Waste Manage. **32**, 1914–1918 (2012a)

Zhu, P., Chen, Y., Wang, L.Y., Zhou, M.: A new technology for recycling solder from waste printed circuit boards using ionic liquid. Waste Manage. Res. **30**, 1222–1226 (2012b)

Influence of Annealing on Structure and Corrosion Resistance of Duplex and Super Duplex Stainless Steel

Sylwia Włodarczak[1(✉)], Andżelika Krupińska[1], Tomasz Kachlicki[2], Magdalena Matuszak[1], Małgorzata Markowska[1], Piotr Krawczyk[3], Tomasz Rozmanowski[3], Marcin Janczarek[1], and Marek Ochowiak[1]

[1] Institute of Chemical Technology and Engineering, Poznan University of Technology, Poznan, Poland
sylwia.wlodarczak@put.poznan.pl
[2] Institute of Materials Engineering, Poznan University of Technology, Poznan, Poland
[3] Institute of Materials Engineering, Institute of Chemistry and Technical Electrochemistry, Poznan University of Technology, Poznan, Poland

Abstract. One of the basic criteria determining the suitability as a structural material is its corrosion resistance. In addition, abrasion resistance, heat resistance, mechanical strength are also important. The properties of austenitic-ferritic two-phase Duplex steels resulted in its various applications, among others, in radiators, dryers, structures working in aggressive environments. In this paper the changes in the structure of Duplex steel and Super Duplex steel subjected to long-lasting annealing processes at two different temperatures were investigated. The aim of these studies was demonstrating changes in properties resulting from the effects of elevated temperature and assessing whether such steels can work in a given temperature range.

1 Introduction

Production of corrosion resistant steels is still developing (Alshemary et al. 2018). Undoubtedly among the most popular steels are austenitic ferritic steels (García-Junceda et al. 2019; Varbai et al. 2019). Duplex steels have been known for about 80 years, but their new features, new application possibilities are still being explored. They are characterized by increased chromium content, with a reduced nickel content, resulting in a biphasic structure. In the annealed state these steels usually have up to 40–50% of austenite in the ferritic matrix. In addition to Cr and Ni, other alloying elements can also include N, Mo, Cu, Si and W. These are added to stabilize the structure and improve corrosion resistance (Haghdadi et al. 2019a). It is believed that nitrogen is necessary because it delays the formation of unfavorable intermetallic phases (which cause the properties to deteriorate). One of the aforementioned phases can be the σ phase which causes the brittleness of steel.

© Springer Nature Switzerland AG 2020
M. Ochowiak et al. (Eds.): PAIC 2019, *Practical Aspects of Chemical Engineering*, pp. 483–490, 2020.
https://doi.org/10.1007/978-3-030-39867-5_50

1.1 Duplex Steels

The special characteristics of Duplex steel include: high yield strength, good fatigue resistance, intergranular and pitting corrosion, weldability, good thermal conductivity (Chen and Yang 2001; Yaoa et al. 2012; Haghdadi et al. 2019a; de Lima et al. 2019). Satisfactory mechanical properties are the result of the presence of ferrite, which is characterized by high strength and fine-grained microstructure (Linton et al. 2004; Olsson and Snis 2007; Wei et al. 2008; Lasebikan and Akisanya 2014; Salvador and Antunes 2016). These steels easily become fragile at low temperatures and are therefore not suitable for low temperature applications (Azevedo et al. 2019; Pereira and Azevedo 2019).

Duplex steels exhibit high corrosion resistance in most environments where austenitic steels are normally used (Potgieter et al. 2008). However, they have several features that definitely promote them to specific applications (Ravindranath and Malhotra 1995; Ahn and Kang 2000; Dillea et al. 2017). This results directly from their chemical composition, specifically the increased amount of chromium, the content of molybdenum and nickel. These alloying elements generate the resistance of biphasic steels to the aerobic environment. In addition, chromium, molybdenum and nitrogen are responsible for good resistance to stress and pitting corrosion (Lothongkum et al. 2006; Luchtenberg et al. 2019). Duplex steel structure is a special advantage in the chloride environment (Perren et al. 2001; Böhni et al. 2002). It has been proven that if there is at least 30% ferrite in such a structure, Duplex steels are much more resistant to stress corrosion than austenitic steels (Chen and Yang 2001; Sieurin and Sandstrom 2007; Haghdadi 2019b; Gerald et al. 2020). However, it should be borne in mind that ferrite is sensitive to hydrogen embrittlement, so Duplex steel cannot be used in environments where this hydrogen could penetrate deep into steel and cause this effect. Also given their Cr content and presence of ferrite, Duplex steels exhibit good corrosion resistance in alkaline environment.

With their satisfactory properties and affordability, Duplex steels are used in many places, for example in devices such as coolants, heaters, condensers, desalination, desulphurisation and purification equipment, heat exchangers, dynamically loaded units - centrifuges, dryers (Knyazeva and Pohl 2013; Naeem et al. 2019). The clean and smooth surface under normal weather conditions is used in contact with food and pharmaceuticals. Chemical neutrality and non-toxicity in contact with many types of food and drug ingredients, as well as in contact with various detergents used in the purification of plant and equipment are also important. Duplex steels can also be used in very aggressive corrosive environments (such as in the manufacture of mustard, vinegar, cheese fermentation, fish processing), where other types of stainless steel fail to meet the requirements. These steels can also be used in the pharmaceutical industry, in environments with chlorides above 500 mg/l.

2 Experimental Section

The use of Duplex steel, as a construction material for chemical and industrial equipment, is often related to the work at elevated temperatures. The purpose of this paper was to investigate the effect of elevated temperature on properties and

microstructure changes and to assess whether the steel still exhibits adequate corrosion resistance under specified conditions.

The samples were made of Duplex 2205 and Super Duplex 2507 steel. The 2205 steel sample was in the form of a profile, while the 2507 steel was a flat sheet. The chemical composition of the samples was examined using the EDS method as shown in Table 1.

Table 1. Chemical composition of the test samples obtained during EDS microanalysis [% by weight].

Steel	Si	Cr	Mn	Ni	Mo
2205	0.36	21.53	0.79	4.94	4.15
2507	0.43	26.06	0.78	5.57	5.18

The samples were annealed in the following way:

- 2 samples were annealed for 250 h at 600 °C,
- 2 samples were annealed for 500 h at 600 °C,
- 2 samples were annealed for 250 h at 800 °C,
- 2 samples were annealed for 500 h at 800 °C.

During the annealing the samples were placed in a hermetically sealed steel tube with charcoal pieces to protect them against oxidation.

After the heat treatment, metallographic specimens were made to examine the microstructure (quantitatively and qualitatively) and compare it with the microstructure that the sample had before annealing - in the initial state. Microhardness measurements were made for samples subjected to annealing under all mentioned conditions and in the initial state. In addition, EDS microanalysis and potentiostatic tests were performed after heat treatment.

Figure 1 shows the microstructures of Duplex 2205 observed with optical microscope in the initial state and after the most restrictive annealing (500 h, 800 °C).

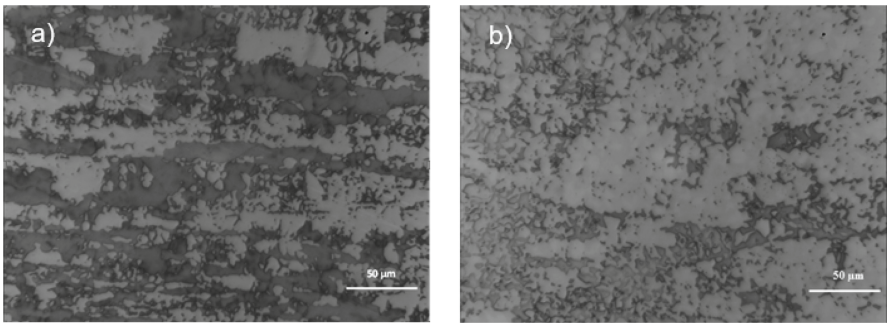

Fig. 1. Microstructure of Duplex 2205 steel (500x magnification): **a** before annealing, **b** after annealing.

Samples of Duplex and Super Duplex steel characterized by a typical two-phase, austenitic-ferritic structure. Bright areas of the figure are austenite, whereas dark - ferrite. As a result of the heat treatment, the ferrite zone and the austenite expansion are noticeable (secondary austenite is formed). In addition, point separations are visible, which is most likely to be σ phase. Table 2 shows quantitative microstructure analysis for selected measurement points.

Table 2. Quantity analysis of microstructures.

Sample	Mean share [%] ferrite + phase σ	Mean share [%] austenite
2205 - initial state	52.4	47.6
2205 - 250 h, 600 °C	44.6	55.4
2205 - 500 h, 600 °C	43.4	56.6
2205 - 250 h, 800 °C	12.6	87.4
2205 - 500 h, 800 °C	17.0	83.0
2507 - initial state	47.8	52.2
2507 - 250 h, 600 °C	40.2	59.8
2507 - 500 h, 600 °C	40.8	59.2
2507 - 250 h, 800 °C	32.8	67.2
2507 - 500 h, 800 °C	39.6	60.4

The secant method was used to estimate the percentages of the individual phases in the analyzed samples, as shown in Fig. 2.

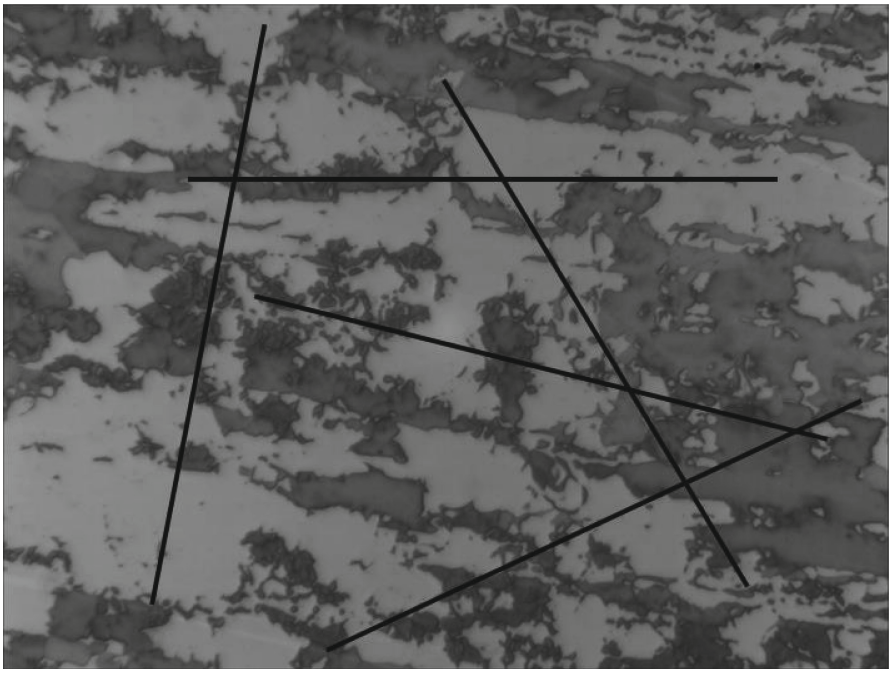

Fig. 2. Quantity analysis (secant method).

In both steels the ferrite content decreases as the annealing temperature rises. During annealing at 800 °C the content of ferrite slightly increases with the passage of heat treatment time. Probably the reason for this is the formation of δ ferrite.

A further study showing the effect of the annealing process on the structure and properties of the analyzed steel was Vickers' microhardness measurement. The test was performed at a 50 g load. for each of the samples tested, 3 microhardness measurements per phase were carried out. Example average results are summarized in Table 3.

Table 3. Micro-hardness test results (HV0,05).

Sample	2507		2205	
Phase	Ferrite	Austenite	Ferrite	Austenite
Initial state	307.9	330.6	264.2	231.5
600 °C/500 h	440.3	339.6	348.7	311.6
800 °C/250 h	500.8	432.7	449.0	416.3

By analyzing the obtained data, it can be seen that as the annealing time and temperature increase, the hardness increases as well. After heat treatment, another chemical composition was measured using the EDS microanalysis, as shown in Table 4.

Table 4. EDS microanalysis after annealing.

Steel	Si	Cr	Mn	Ni	Mo
2205 - 800 °C/250 h	0.83	23.88	64.19	4.51	6.6
2507 - 800 °C/250 h	0.91	23.30	60.89	6.02	8.88

As can be seen, the chemical composition of samples after annealing slightly deviates from the composition before treatment as shown in Table 1. The magnetic properties of the samples were tested by applying a magnet to each of them. It was observed that only samples annealed at 800 °C showed no magnetic properties.

In order to assess of the effect of thermal process parameters on the electrochemical properties of the passive layer, potentiostatic tests of samples were carried out. Before the test, the surface of the samples was appropriately prepared by polishing with abrasive paper. Samples were immersed in a 3M NaCl aqueous solution and potentiostatically polarized at +700 mV SCE for 120 s at 25 °C. The reference electrode was a calomel electrode. The result of the study is shown in Fig. 3.

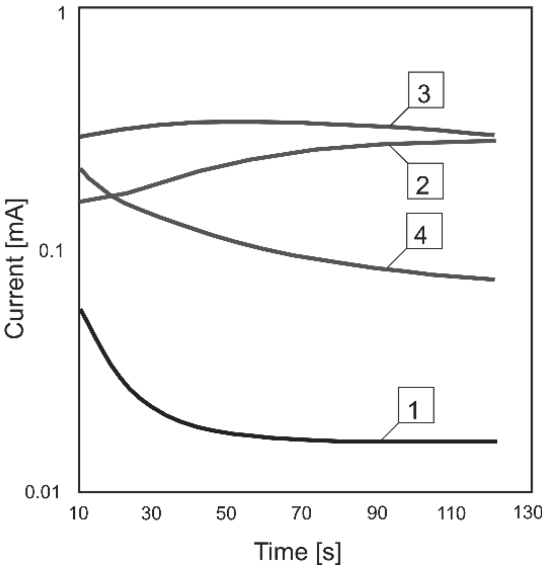

Fig. 3. Development in corrosion current at 700 mV SCE and 25 °C when testing Duplex 2205 stainless steel heat-treated: 1 - at 600 °C for 250 h, 2 - at 800 °C for 250 h, 3 - at 800 °C for 500 h, 4 - at 600 °C for 500 h.

The untreated sample showed excellent corrosion resistance - no current flow was recorded. As a result of annealing the resistance decreased. The more restrictive annealing conditions were applied, the lower the corrosion resistance was characterized by the sample - the higher current value was obtained. In the case of samples at 600 °C, a decreasing trend is noticeable. This indicates passive behaviour resulting from a much smaller amount of σ phase than in the case of higher temperature treatment. Samples annealed at 800 °C tend to increase and high end current, which indicates weak corrosion resistance.

3 Summary

Samples in the initial state showed a typical two-phase structure composed of austenite grains and ferrite. The heat treatment carried out even under the least restrictive conditions (600 °C, 250 h) caused the intermetallic phase (σ phase) precipitation and the expansion of the austenite areas - secondary austenite. The reaction of ferrite breakdown into σ phase and secondary austenite is an eutectoid reaction. Phase σ is formed inside ferrite, which is due to the fact that it is thermodynamically more stable than austenite and the chromium solubility in ferrite is higher than in austenite. During σ phase formation, the system achieves a thermodynamic balance (El Koussy et al. 2004).

The increase in hardness of samples is due to the formation of a hard and brittle σ phase and occurs along with the increase in temperature and time of annealing.

The loss of magnetic properties of both samples after annealing at 800 °C may be due to the formation of a large number of secondary paramagnetic austenite and δ ferrite possibly devoid of the magnetic properties.

The decrease in corrosion resistance in relation to the initial state was apparent for all samples, with the annealed material at 600 °C subjected to passivation. Annealed samples at higher temperatures (800 °C) showed worse corrosion resistance than annealed samples at 600 °C. This is due to the conversion of ferrite to secondary austenite and the release of excess chromium in the form of σ phase.

The study has clearly shown that the working temperature of Duplex and Super Duplex must be clearly lower than 600 °C. Literature specifies the working temperature range for these steels from −50 °C to +300 °C.

Acknowledgments. This research was supported by Ministry of Science and Higher Education through grant PUT 03/32/SBAD/0902.

References

Ahn, Y.S., Kang, J.P.: Effect of annealing temperature on the corrosion behavior of duplex stainless steel studied by in situ techniques. Mater. Sci. Technol. **16**, 382–388 (2000)

Alshemary, A., et al.: Accuracy of duplex stainless steel feature generated by electrical discharge machining (EDM). Measurement **130**, 137–144 (2018)

Azevedo, C.R.F., et al.: An overview of the recurrent failures of duplex stainless steels. Eng. Fail. Anal. **97**, 161–188 (2019)

Böhni, H., et al.: Corrosion resistance of super duplex stainless steels in chloride ion containing environments: investigations by means of a new microelectrochemical method. Corros. Sci. **43**(4), 727–745 (2002)

Chen, T.H., Yang, J.R.: Effects of solution treatment and continuous cooling on σ-phase precipitation in a 2205 duplex stainless steel. Mat. Sci. Eng. **A311**, 28–41 (2001)

Dillea, J., et al.: Microstructural evolution during aging at 800 °C and its effect on the magnetic behavior of UNS S32304 lean duplex stainless steel. J. Magn. Magn. Mater. **426**, 102–107 (2017)

El Koussy, M.R., et al.: Effects of thermal aging on microstructure and mechanical properties of duplex stainless steel weldments. Mater. Sci. Technol. **20**, 375–381 (2004)

García-Junceda, A., et al.: Analysis of the interface and mechanical properties of field-assisted sintered duplex stainless steels. Mat. Sci. Eng. **740–741**, 410–419 (2019)

Gerald, O.J., et al.: Corrosion behaviour of 2205 duplex stainless steel in marine conditions containing Erythrobacter pelagi bacteria. Mater. Chem. Phys. **239** (2020, in press)

Haghdadi, N., et al.: Microstructure dependence of impact toughness in duplex stainless steels. Mater. Sci. Eng., A **745**, 369–378 (2019a)

Haghdadi, N., et al.: The effect of phase transformation route on the intergranular corrosion susceptibility of 2205 duplex stainless steel. Mater. Lett. **238**, 26–30 (2019b)

Knyazeva, M., Pohl, M.: Duplex Steels: Part I: genesis, formation, structure. Metallogr. Microstruct. Anal. **2**, 113–121 (2013)

Lasebikan, B.A., Akisanya, A.R.: Burst pressure of super duplex stainless steel pipes subject to combined axial tension, internal pressure and elevated temperature. Int. J. Press. Vessels Pip. **119**, 62–68 (2014)

Linton, V., et al.: Failure of a super duplex stainless steel reaction vessel. Eng. Fail. Anal. **11**, 243–256 (2004)

de Lima, H.M.L.F., et al.: The effect of copper addition on the corrosion resistance of cast duplex stainless steel. J. Mater. Res. Technol. **8**(2), 2107–2119 (2019)

Lothongkum, G., et al.: Effect of nitrogen on corrosion behavior of 28Cr – 7Ni duplex and microduplex stainless steels in air-saturated 3.5 wt% NaCl solution. Corros. Sci. **48**, 137–153 (2006)

Luchtenberg, et al.: Effect of welding energy on the corrosion and tribological properties of duplex stainless steel weld overlay deposited by GMAW/CMT process. Surf. Coat. Tech. **375**, 688–693 (2019)

Naeem, M., et al.: Enhanced wear and corrosion resistance of AISI-304 steel by duplex cathodic cage plasma treatment. Surf. Coat. Tech. **375**, 34–45 (2019)

Olsson, J., Snis, M.: Duplex - a new generation of stainless steels for desalination plants. Desalination **205**, 104–113 (2007)

Perren, R.A., et al.: Corrosion resistance of super duplex stainless steels in chloride ion containing environments: investigations by means of a new microelectrochemical method, II. Influence of precipitates. Corros. Sci. **43**(4), 727–745 (2001)

Pereira, H.B., Azevedo, C.R.F.: Can the drop evaporation test evaluate the stress corrosion cracking susceptibility of the welded joints of duplex and super duplex stainless steels? Eng. Fail. Anal. **99**, 235–247 (2019)

Potgieter, J.H., et al.: Influence of nickel additions on the corrosion behaviour of low nitrogen 22% Cr series duplex stainless steels. Corros. Sci. **50**, 2572–2579 (2008)

Ravindranath, K., Malhotra, S.N.: The influence of aging on the intergranular corrosion of 22 chromium-5 nickel duplex stainless steel. Corros. Sci. **37**, 121–132 (1995)

Salvador, C.F., Antunes, R.A.: FCAW repair welding cycles, HAZ microstructure and corrosion resistance of 2304 duplex stainless steel. Corros. Eng., Sci. Technol. **51**, 573–580 (2016)

Sieurin, H., Sandstrom, R.: Sigma phase precipitation in duplex stainless steel 2205. Mat. Sci. Eng. **A444**, 271–276 (2007)

Varbai, B., et al.: Effect of heat input and role of nitrogen on the phase evolution of 2205 duplex stainless steel weldment. Int. J. Press. Vessels Pip. 176 (2019, in press)

Wei, Z., et al.: Study of mechanical and corrosion properties of a Fe-21.4Cr-6Mn-1.5Ni-0.24 N-0.6Mo duplex stainless steel. Mater. Sci. Eng., A **497**((1–2)), 501–504 (2008)

Yaoa, Y.H., et al.: Effect of long-term thermal aging on the mechanical properties of casting duplex stainless steels. Mater. Sci. Eng., A **551**, 116–121 (2012)

Application of Morison Equation in Unsteady Mixing Characteristics

Szymon Woziwodzki(✉)

Institute of Chemical Technology and Engineering,
Poznan University of Technology, Poznań, Poland
szymon.woziwodzki@put.poznan.pl

Abstract. Unsteady mixing is one of the methods increasing mixing intensity, especially in an unbaffled stirred vessel. However, because of the unsteady motion of the impeller, it is difficult to describe it. One of the most important mixing parameters is mixing power. It is not constant and depends on the Reynolds number than well as the oscillation frequency. Therefore, knowledge about forces acting on an impeller is essential. In marine engineering and fluid dynamics, the Morison equation is commonly used to describe wave forces acting on offshore structures. In this way, the motion of waves is considered as sinusoidal unsteady flow. Therefore, the Morison equation could describe forces acting on a rotating impeller, however, it requires consideration of all forces, beside drag and inertia force, acting in a stirred vessel.

1 Introduction

Mechanical mixing is commonly used in many industries. Usually is used to achieve mixing degree, homogeneity ratio or to increase heat or mass exchange. However, mixing in such a way faces limitations mainly because of baffles in the vessel. Baffle presence is not welcome in case of i.e. crystallization or pharmaceutical purposes (imitations because of the cleaning of equipment).

Unsteady mixing is when its properties depend on time, i.e. mixing power. Unsteady conditions can be realized in various ways, unsteady rotation of an impeller (Yoshida et al. 2011, 2012; Woziwodzki 2017; Frankiewicz and Woziwodzki 2018), reciprocating movement of the impeller (Komoda et al. 2000, 2012; Kamieński and Wójtowicz 2001).

The main problem to describe unsteady mixing is that mixing power depends on time. I turbulent flow regime and steady mixing according to the Newton law mixing power number is a constant, independent of Reynolds number. In unsteady flow, the Reynolds number also depends on the flow and the flow range is changing from laminar to turbulent. In addition, the forces which in the steady mixing are omitted i.e. the inertia force, are important in the unsteady mixing. Influence of inertia force, and a drag force, usually depends on the oscillation frequency. Therefore, knowledge about them is very important i.e. to describe unsteady mixing power demand.

© Springer Nature Switzerland AG 2020
M. Ochowiak et al. (Eds.): PAIC 2019, *Practical Aspects of Chemical Engineering*, pp. 491–499, 2020.
https://doi.org/10.1007/978-3-030-39867-5_51

2 Morison Equation

The Morison equation was first introduced in 1950 by Morison, O'Brien, Johnson and Schaaf (because of this, it is sometimes called the MOJS equation in honour of all four authors). This equation describes the surface forces exerted on piles (Morison et al. 1950). According to Morison, O'Brien, Johnson and Schaff, the total force F exerted on a fixed body comprises two main forces (1): drag force F_D and inertia force F_I

$$F = F_D + F_I \tag{1}$$

According to this the force in the x-direction is

$$\frac{F}{L_c} = \frac{1}{2}\rho D_c C_D |U|U + \frac{\pi D^2 \rho}{4} C_I \frac{dU}{dt} \tag{2}$$

The left side of the above equations is equal to force per length of cylinder L_c then on the right side of Eq. (2) U and dU/dt is, respectively, flow velocity and acceleration of the fluid. The concept of Morison et al. (1950) necessitates the introduction of drag C_D and inertia C_I coefficients.

In sinusoidally oscillating flow, where velocity U depends on the time

$$U = U_m sin(\omega t) \tag{3}$$

and velocity amplitude U_m and angular velocity ω. Hence for sinusoidally oscillating flow, the Morison Eq. (2) takes the following form (Sarpkaya 2010)

$$\frac{F}{L_c} = \frac{1}{2}\rho D_c C_D U_m^2 |sin(\omega t)|sin(\omega t) + \frac{\pi D^2 \rho}{4} C_I U_m \frac{d(U_m sin(\omega t))}{dt} \tag{4}$$

or

$$\frac{F}{L_c} = \frac{1}{2}\rho D_c C_D U_m^2 |sin(\omega t)|sin(\omega t) + \frac{\pi D^2 \rho}{4} C_I U_m \omega cos(\omega t) \tag{5}$$

Morison et al. (1950) used only two-component force but there could be more. The total force F can be divided into three or even four components, which may take into account, for example, the inertia of the liquid displaced by the rotating cylinder or the so-called memory effect of resistance force and inertia (Sarpkaya 2010).

3 Morison Equation for Unsteady Mixing

Morison equation uses geometrical parameters of a cylinder. Let's assume that cylinder is an impeller with diameter D (or radius r) and height H_{im} and Eq. (2) takes the form

$$\frac{F}{H_{im}} = \frac{1}{2}\rho D C_D |U| U + \frac{\pi D^2 \rho}{4} C_I \frac{dU}{dt} \tag{6}$$

The impeller rotates with velocity U which is the velocity at the impeller blade tip.

$$U = \omega r \tag{7}$$

Angular velocity ω for the impeller blade is constant at each r (Yoshida et al. 1999). The Eq. (6) may write as

$$\frac{F}{H_{im}} = \frac{1}{2}\rho D C_D r^2 |\omega| \omega + \frac{\pi D^2 \rho}{4} C_I r \frac{d\omega}{dt} \tag{8}$$

The total force on the left side above equation in mixing is related to a torque T. The torque T on the mixer shaft is the product of the force F and the impeller radius r, which can be written as

$$T = Fr \tag{9}$$

The Eq. (8) may be rewritten as

$$\frac{T}{H_{im}} = \frac{1}{2}\rho D C_D r^3 |\omega| \omega + \frac{\pi D^2 \rho}{4} C_I r^2 \frac{d\omega}{dt} \tag{10}$$

For the impeller, the length L_c is its height. Introducing in the Eq. (10) the diameter of the impeller ($r = D/2$) we get

$$\frac{T}{H_{im}} = \frac{1}{16}\rho D^4 C_D |\omega| \omega + \frac{\pi D^4 \rho}{16} C_I \frac{d\omega}{dt} \tag{11}$$

Impeller height H_{imp} is usually shown as projection height (Fig. 1) and commonly is presented as a function of impeller diameter and constant C_1: $H_{imp} = C_1 D$. Using this relationship in Eq. (11) gives

$$T = \frac{1}{16}\rho C_1 D^5 C_D |\omega| \omega + C_1 \frac{\pi D^5 \rho}{16} C_I \frac{d\omega}{dt} \tag{12}$$

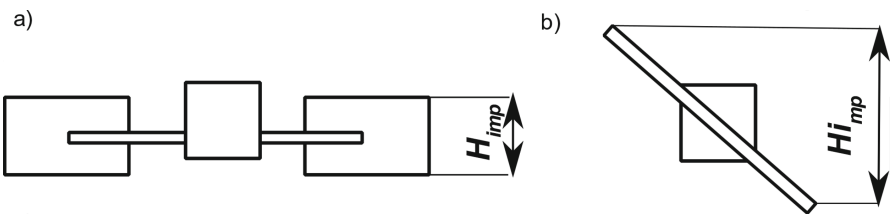

Fig. 1. Impeller projection height a) flat blade impeller, b) pitched blade impeller

Angular velocity of unsteady rotating impeller depends on time-course of impeller speed

$$\omega = 2\pi N(t) \tag{13}$$

Table 1 presents various variation in impeller speed.

Table 1. Exemplary time-courses of impeller speed (Yoshida et al. 2001; Woziwodzki 2017)

Type of impeller time course	Equation	
Sinusoidal	$N = N_{max}\sin(2\pi ft)$	(14)
Triangular	$N = \frac{8}{\pi^2} N_{max}\left(sin(2\pi ft) - \frac{1}{9}sin(6\pi ft) + \frac{1}{25}sin(10\pi ft)\right)$	(15)
Triangular (without change of rotation direction)	$N = \frac{8}{\pi^2} n_{max}\left\lvert\left(sin(2\pi ft) - \frac{1}{9}sin(6\pi ft) + \frac{1}{25}sin(10\pi ft)\right)\right\rvert$	(16)
Asymmetrical triangular	$N = N_{max}\left(\frac{a_0}{2} + \sum_{n=1}^{H}(a_n cos(n\omega t) + b_n sin(n\omega t))\right)$	(17)
Triangular with brake	$N = N_{max}\left(\sum_{n=1}^{H}(a_n cos(n\omega t) + b_N sin(n\omega t))\right)$	(18)

a_N, b_N, a_0 – Fourier series constants
N_{max} – maximal impeller speed
f – oscillation frequency
n – integer

Introducing Eq. (15) to (13) gives an angular velocity for triangular time-course of angular velocity.

$$\omega = \frac{16}{\pi} N_{max}\left(sin(2\pi ft) - \frac{1}{9}sin(6\pi ft) + \frac{1}{25}sin(10\pi ft)\right) \tag{19}$$

Combination of Eqs. (19) and (12) gives triangular time-course of torque T.

$$\begin{aligned} T = {} & \tfrac{16}{\pi^2} C_1 C_D N_{\max}^2 D^5 \rho \left\lvert sin(2\pi ft) - \tfrac{1}{9}sin(6\pi ft) + \tfrac{1}{25}sin(10\pi ft)\right\rvert \times \\ & \left(sin(2\pi ft) - \tfrac{1}{9}sin(6\pi ft) + \tfrac{1}{25}sin(10\pi ft)\right) + \\ & D^5 \rho C_1 C_I N_{\max} \tfrac{d\left(sin(2\pi ft) - \frac{1}{9}sin(6\pi ft) + \frac{1}{25}sin(10\pi ft)\right)}{dt} \end{aligned} \tag{20}$$

To determine torque time-course knowledge about C_D and C_I coefficients is required. There are few methods of determination of drag and inertia coefficients (Jurnee and Massie 2001; Sarpkaya 2010; Woziwodzki 2017). The most useful method is the application of the Fourier transform. In this method, the left side of the Eq. (20) is expansion into Fourier series.

$$\frac{T3\pi^3}{128C_1N_{\max}^2D^5\rho} = C_D\left(sin(2\pi ft) - \frac{1}{9}sin(6\pi ft) + \frac{1}{25}sin(10\pi ft)\right) + \frac{3\pi^3C_I}{128N_{max}}\frac{d\left(sin(2\pi ft) - \frac{1}{9}sin(6\pi ft) + \frac{1}{25}sin(10\pi ft)\right)}{dt} \tag{21}$$

Here, it relates the characteristic Fourier series constants to the drag coefficient and inertia coefficient:

$$C_D = a_1 \tag{22}$$

$$C_I = \frac{128N_{max}b_1}{3\pi^3} \tag{23}$$

The Keulegan-Carpenter (Keulegan and Carpenter 1958) solution (25) was used in Eq. (21) to solve the expression

$$T \propto \left|sin(2\pi ft) - \frac{1}{9}sin(6\pi ft) + \frac{1}{25}sin(10\pi ft)\right| \times \left(sin(2\pi ft) - \frac{1}{9}sin(6\pi ft) + \frac{1}{25}sin(10\pi ft)\right) \tag{24}$$

$$T \propto \frac{8}{3\pi}\left(sin(2\pi ft) - \frac{1}{9}sin(6\pi ft) + \frac{1}{25}sin(10\pi ft)\right) \tag{25}$$

Another method to calculate C_D and C_I coefficients is the use of the least square method.

Equation (20) can be easily used to determine mixing power P ($P = 2\pi NT$)

$$P = \frac{32}{\pi}C_1C_DN_{\max}^3D^5\rho\left|sin(2\pi ft) - \frac{1}{9}sin(6\pi ft) + \frac{1}{25}sin(10\pi ft)\right| \times \left(sin(2\pi ft) - \frac{1}{9}sin(6\pi ft) + \frac{1}{25}sin(10\pi ft)\right) + 2\pi D^5\rho C_1C_IN_{\max}^2\frac{d\left(sin(2\pi ft) - \frac{1}{9}sin(6\pi ft) + \frac{1}{25}sin(10\pi ft)\right)}{dt} \tag{26}$$

or power number Ne

$$Ne = \frac{P}{N_{\max}^3D^5\rho} = \frac{32}{\pi}C_1C_D\left|sin(2\pi ft) - \frac{1}{9}sin(6\pi ft) + \frac{1}{25}sin(10\pi ft)\right| \times \left(sin(2\pi ft) - \frac{1}{9}sin(6\pi ft) + \frac{1}{25}sin(10\pi ft)\right) + \frac{2\pi}{N_{\max}}C_1C_I\frac{d\left(sin(2\pi ft) - \frac{1}{9}sin(6\pi ft) + \frac{1}{25}sin(10\pi ft)\right)}{dt} \tag{27}$$

4 Experimental Verification

Experimental verification of modified Morison Eq. (20) for unsteady mixing was performed in an experimental set-up presented in Fig. 2.

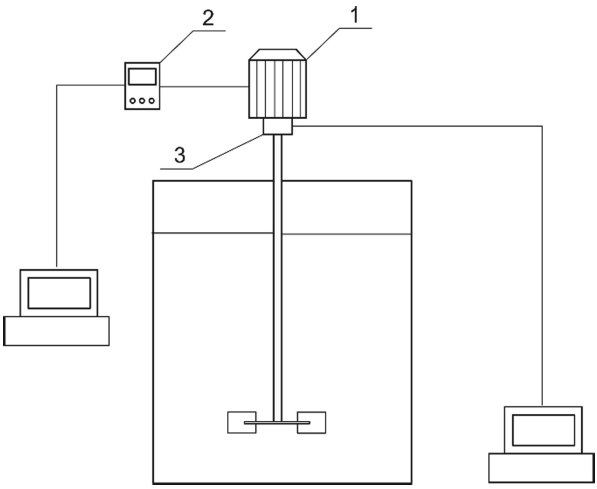

Fig. 2. Experimental set-up 1 – electric motor, 2 – inverter, 3 – torque meter

The experimental set-up consisted of an electric motor delivered by EMA Indukta (2.2 kW), an inverter (Schneider Electric MX Eco) and torque meter Sensor-AT MT2. Unbaffled stirred vessel with diameter D_V = 0.29 m was used and liquid height H_L = 0.29 m. In experimental verification, various impellers were tested (radial and axial impellers) (Fig. 3): Rushton turbine, PBT, A315, SC-3, HE-3 W. The diameter of impellers was D = 0.1 m and impeller bottom height C = 0.1 m.

Verification of modified Morison Eq. (20) was performed for various time-courses of impeller speed: triangular (symmetrical, with the change in direction of impeller rotation) FR1, FR3 (symmetrical, with a change in direction of impeller rotation and brake) and F1 (without a change in direction of rotation).

The experiment was conducted in a turbulent flow regime and in the range of drag force domination, $KC > 15$ (Woziwodzki 2017) where KC is Keulegan-Carpenter number

$$KC = \frac{N_{max}}{f} \tag{28}$$

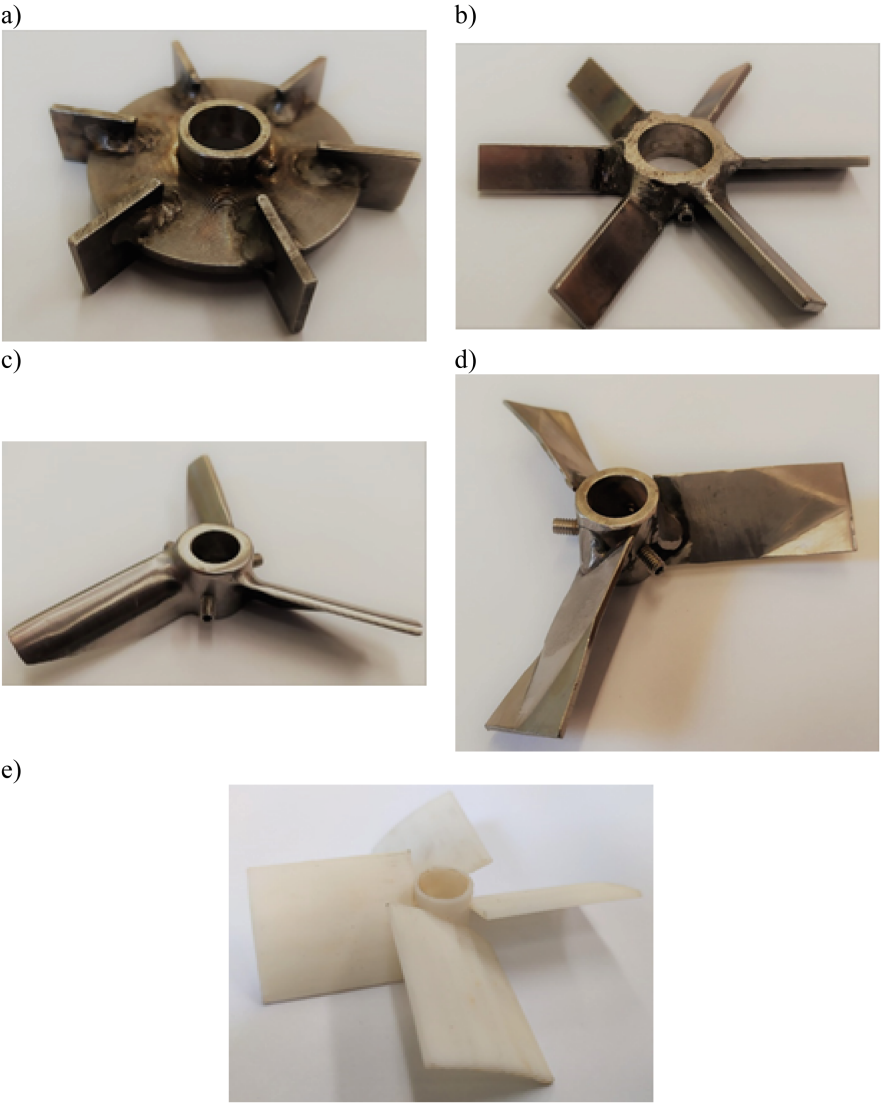

Fig. 3. Impellers: a) Rushton turbine, b) PBT, c) SC-3, d) HE-3 W, e) A315

Comparison of modified Morison equation and experimental data was performed for radial and for axial impellers.

Figure 4a–d presents torque-course for radial impeller RT (Fig. 4a), and axial impellers (Figs. 4b–d).

The obtained data show that for radial impellers (Fig. 4a) there is good compliance between the modified Morison equation for unsteady mixing and experimental data. For radial impeller coefficient of determination is in range R^2 = 0.97–0.99 for all tested time-courses of impeller speed.

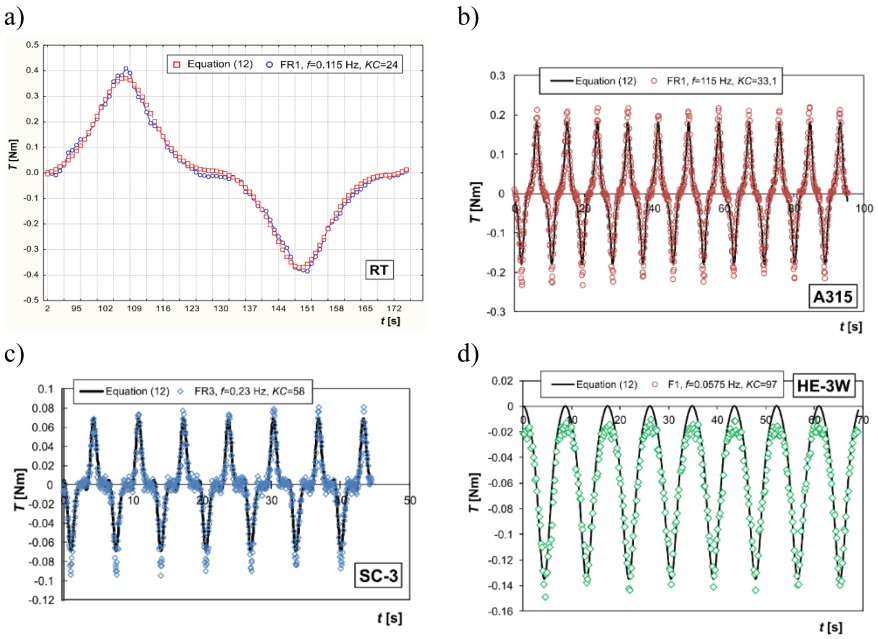

Fig. 4. Comparison of torque time-course of experimental data and obtained from Eq. (12) a) Rushton turbine, b) A315, c) SC-3, d) HE-3 W

For axial impellers (A315, SC-3, PBT and HE-3 W) and all time-courses of impeller speed, the compliance between experimental data and Eq. (12) was no so good as for radial impeller. The differences were observed especially for maximal impeller speed N_{max}. For FR1 time-course (Fig. 4b) experimental maximal torque T_{max} is independent of the direction of impeller rotation, while for FR3 time-course maximal torque depends on the rotation direction. Higher T_{max} was observed for the clockwise direction of rotation. A similar relation was observed for F1. In addition, the difference between T_{min} was observed. It suggests a need to change Eq. (12) and include an additional force than drag and inertia force.

5 Conclusions

The obtained results show that the modified Morison equation for unsteady mixing well describes the changes in torque as a function of time for radial mixers with flat blades and for pitched blade impellers. In the latter's case, deviations in torque time-course are related to the change of the drag coefficient C_D depending on the direction of rotation and the change toward axial circulation. It suggests that the proposed equation should be modified and it should include an additional force i.e. axial forces or lift force. The observations are in good agreement with Sarpkaya (1998) suggested modification of Morison equations using higher harmonic frequencies.

Acknowledgments. This work was supported by the Polish Ministry of Science and Higher Education (Grant no. 03/32/SBAD/0902).

References

Frankiewicz, S., Woziwodzki, S.: Effect of blade shape on unsteady mixing of gas-liquid systems. In: Practical Aspects of Chemical Engineering, pp 127–136. Springer, Cham (2018)

Jurnee, J.M.J., Massie, W.W.: Offshore Hydromechanics. Delft University of Technology, Delft (2001)

Kamieński, J., Wójtowicz, R.: Power input for a vibromixer. Inżynieria Chemiczna i Procesowa **22**, 603–608 (2001)

Keulegan, G.H., Carpenter, L.H.: Forces on cylinders and plates in an oscillating fluid. J. Res. Nat. Bur. Stan. **60**, 423–440 (1958)

Komoda, Y., Inoue, Y., Hirata, Y.: Mixing performance by reciprocating disk in cylindrical vessel. J. Chem. Eng. Jpn **33**, 879–885 (2000). https://doi.org/10.1252/jcej.33.879

Komoda, Y., Senda, S., Takeda, H., et al.: 2D fluid deformation induced by a rotational reciprocating plate impeller in a cylindrical vessel. In: Proceedings of 14th European Conference on Mixing, Warsaw, pp. 211–216 (2012)

Morison, J.R., O'Brein, M.P., Johnson, J.P., Schaaf, S.C.: The force exerted by surface waves on piles. Pet. Trans. AIME **189**, 149–157 (1950)

Sarpkaya, T.: Wave Forces on Offshore Structures. Cambridge University Press, Cambridge (2010)

Sarpkaya, T.: Resistance in Unsteady Flow: Search for a Model. Naval Postgraduate School, Department of Mechanical Engineering, Monterey (1998)

Woziwodzki, S.: Mieszanie nieustalone - analiza i wybrane zastosowania. Wydawnictwo Politechniki Poznańskiej, Poznań (2017)

Yoshida, M., Ito, A., Yamagiwa, K., et al.: Power characteristics of unsteadily forward-reverse rotating impellers in an unbaffled aerated agitated vessel. J. Chem. Technol. Biotechnol. **76**, 383–392 (2001)

Yoshida, M., Kimura, A., Yoneyama, A., Tezura, S.: Design and operation of unbaffled vessels agitated with an unsteadily forward–reverse rotating impeller handling solid–liquid dispersions. Asia-Pac. J. Chem. Eng. **7**, 572–580 (2012). https://doi.org/10.1002/apj.609

Yoshida, M., Mikazuki, K., Yamagiwa, K., Tezura, S.: Liquid flow characteristics inside impeller rotational region of an unbaffled vessel agitated with an unsteadily angularly oscillating impeller. J. Chem. Chem. Eng. **5**(4), 348–354 (2011)

Yoshida, M., Yamagiwa, K., Ohkawa, A., et al.: Torque of drive shaft with unsteadily rotating impellers in an unbaffled aerated agitation vessel. Mater. Technol. **17**, 19–31 (1999)

Author Index

A
Adamski, Mariusz, 1, 241, 252
Adamski, Robert, 10, 252
Aksamitowski, Przemysław, 17
Alejski, Krzysztof, 69, 383

B
Bachosz, Karolina, 110
Bizon, Katarzyna, 314, 346
Burda, Tomasz, 153

C
Ciemnicka, Justyna, 336
Czernek, Krystian, 27, 452

D
Dobrołowicz, Paweł, 37
Dołęgowska, Barbara, 171
Dorosz, Agata, 47
Dutta, Abhishek, 473
Dyga, Roman, 58

E
Emmons-Burzyńska, Magdalena, 69, 473

F
Fathordoobady, Farahnaz, 122
Fornalczyk, Agnieszka, 392
Frankiewicz, Sebastian Szymon, 79

G
Ginter-Kramarczyk, Dobrochna, 144, 191
Golczak, Aleksandra, 89
Grabowski, Mirosław, 336
Grygorcewicz, Bartłomiej, 171
Guo, Yigong, 122

I
Ismael, M. Rosinda C., 441
Izydorczyk, Grzegorz, 412

J
Janczarek, Marcin, 99, 483
Jankowska, Katarzyna, 110
Jarzębski, Maciej, 122
Jędrzejczak-Silicka, Magdalena, 132
Jesionowski, Teofil, 110, 161, 430

K
Kachlicki, Tomasz, 483
Kiersnowska, Zofia, 144
Klapiszewski, Łukasz, 430
Klimczak, Franciszek, 153
Kocek, Daria, 412
Kołodziejczak-Radzimska, Agnieszka, 161
Konopacki, Maciej, 171, 282
Kordas, Marian, 171, 282
Kotynia, Agata, 401
Kowalska, Ewa, 99

© Springer Nature Switzerland AG 2020
M. Ochowiak et al. (Eds.): PAIC 2019, *Practical Aspects of Chemical Engineering*, pp. 501–502, 2020.
https://doi.org/10.1007/978-3-030-39867-5

Krawczyk, Piotr, 355, 483
Krupińska, Andżelika, 153, 183, 261, 483
Kruszelnicka, Izabela, 144, 191
Kuczora, Adrianna, 199
Kukfisz, Bożena, 209, 401, 452

L
Legawiec, Krzysztof Jan, 216
Lukosek, Marek, 69

M
Macioszek, Łukasz, 223
Markowska, Małgorzata, 183, 231, 261, 483
Martínez Cánovas, Paula, 47
Masewicz, Łukasz, 122
Matuszak, Magdalena, 183, 231, 261, 483
Michalczuk, Urszula, 305
Michalkiewicz, Michał, 144, 191
Mijowska, Ewa, 132
Mikula, Katarzyna, 412
Mioduszewska, Natalia, 241
Mitkowski, Piotr Tomasz, 1, 89, 252
Moskal, Arkadiusz, 47, 305
Muszyński, Przemysław, 191

O
Ochowiak, Marek, 153, 183, 231, 261, 483
Odziomek, Marcin, 271
Okoń, Patryk, 27
Ośkiewicz, Igor, 37

P
Padiasek, Joanna, 282
Pakowski, Zdzisław, 10
Pawlita-Posmyk, Monika, 294
Pędzich, Dominik, 314
Penconek, Agata, 305
Płaczek, Małgorzata, 324
Polaszek, Kinga, 383
Polewski, Krzysztof, 122
Polowczyk, Izabela, 216
Prałat, Karol, 336
Prończuk, Mateusz, 346

R
Rakoczy, Rafał, 132, 171, 282
Ratajczak, Kamil, 122
Reczek, Natalia, 314
Regel-Rosocka, Magdalena, 392, 473
Reis, M. Teresa A., 441
Różańska, Sylwia, 365, 374
Różański, Jacek, 199, 365, 374
Rozmanowski, Tomasz, 355, 483
Rukowicz, Beata, 383
Rybski, Ryszard, 223
Rzelewska-Piekut, Martyna, 392

S
Saternus, Mariola, 392
Sawerski, Arkadiusz, 122
Siejak, Przemysław, 122
Singh, Anubhav Pratap, 122
Siuta, Dorota, 209, 401, 452
Skrzypczak, Dawid, 412
Skrzypek-Markiewicz, Krzysztof, 314
Sosnowski, Tomasz Robert, 423
Stanisz, Małgorzata, 430
Stasiak, Maksymilian, 122
Staszak, Katarzyna, 441
Staszak, Maciej, 441
Szaferski, Waldemar, 10, 27, 89, 209, 241, 252, 401, 452
Szoplik, Jolanta, 461
Szulc, Tomasz, 183
Szymańska, Karolina, 132

T
Taf, Rafał, 412
Tomaszewska, Jolanta, 191

V
Verwimp, Stefaan, 473

W
Wagner, Patrycja, 365
Wieszczycka, Karolina, 17, 441
Witczak, Stanisław, 27
Witek-Krowiak, Anna, 412
Włodarczak, Sylwia, 153, 183, 223, 231, 261, 483
Wolańczyk, Jakub, 355
Woziwodzki, Szymon, 37, 79, 491
Wróbel, Kamil, 10
Wzorek, Małgorzata, 294

Z
Zając-Woźnialis, Anna, 144
Zajchowski, Stanisław, 191
Zdarta, Jakub, 110
Zembrzuska, Joanna, 144